OCS Study
MMS 89-0068

Gulf of Mexico Physical Oceanography Program Final Report: Year 5

Volume II: Technical Report

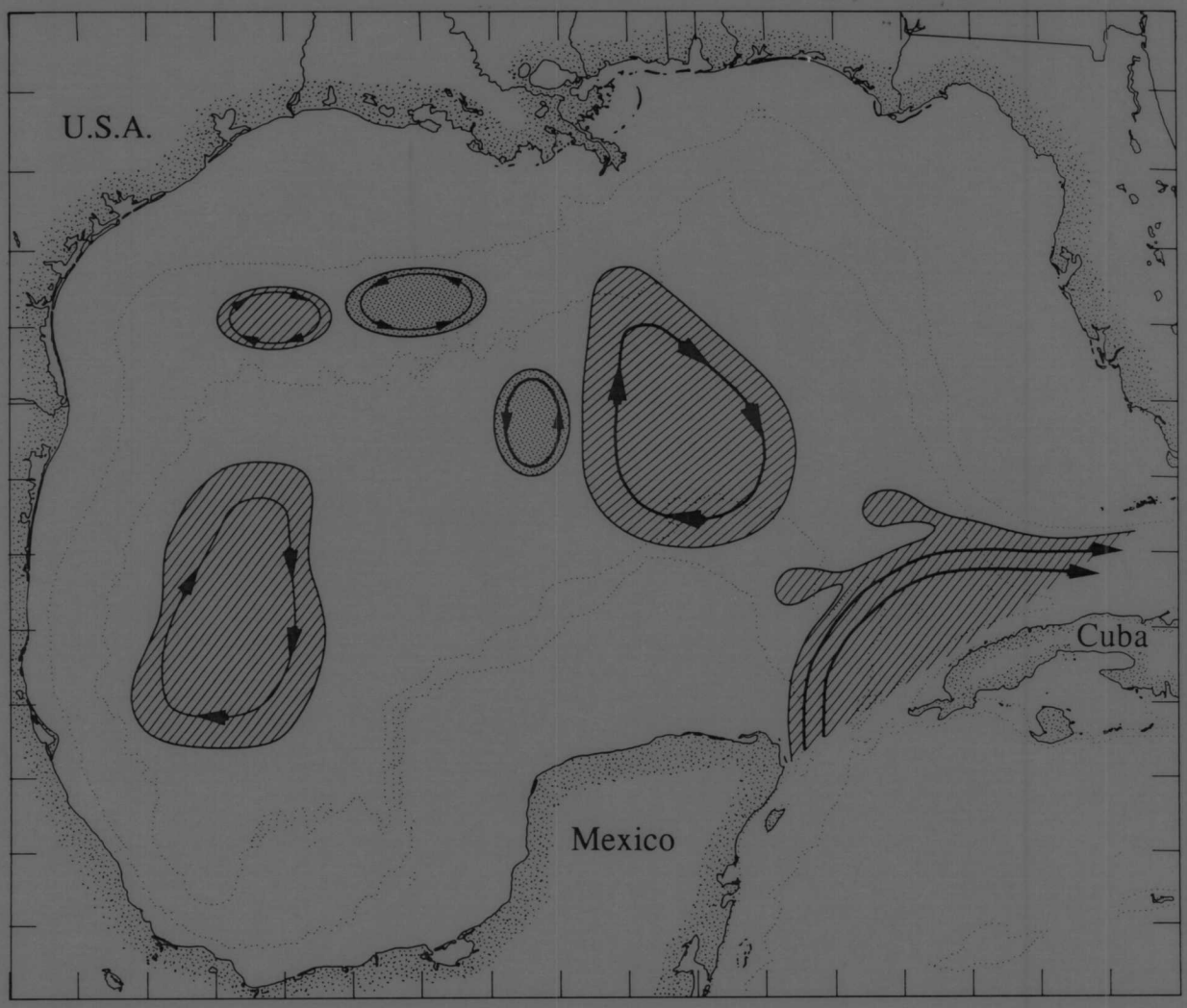

U.S. Department of the Interior
Minerals Management Service
Gulf of Mexico OCS Region

OCS Study
MMS 89-0068

Gulf of Mexico Physical Oceanography Program Final Report: Year 5

Volume II: Technical Report

Author

Science Applications International Corporation

Prepared under MMS Contract
14-12-0001-30289
by
Science Applications International Corporation
Raleigh, North Carolina 27606

Program Manager:
Evans Waddell, Ph.D.
Science Applications International Corporation
Raleigh, North Carolina 27606

Project Officer:
Murray L. Brown, Ph.D.
Minerals Management Service,
Gulf of Mexico OCS Regional Office

Published by

U.S. Department of the Interior
Minerals Management Service
Gulf of Mexico OCS Regional Office

New Orleans
October 1989

DISCLAIMER

This report was prepared under contract between the Minerals Management Service (MMS) and Science Applications International Corporation (SAIC). This report has been technically reviewed by the MMS and approved for publication. Approval does not signify that the contents necessarily reflect the views and policies of the Service, nor does mention of trade names or commercial products constitute endorsement or recommendation for use. It is, however, exempt from review and compliance with MMS editorial standards.

REPORT AVAILABILITY

Extra copies of the report may be obtained from the Public Information Unit (Mail Stop OPS-3-4) at the following address:

U.S. Department of the Interior
Minerals Management Service
Gulf of Mexico OCS Regional Office
1201 Elmwood Park Boulevard
New Orleans, Louisiana 70123-2394

Attention: Public Information Unit (OPS-3-4)

Telephone Number: (504) 736-2519

CITATION

Science Applications International Corporation, 1989, Gulf of Mexico Physical Oceanography Program, Final Report: Year 5. Volume II: Technical Report. OCS Report/MMS - 89-0068, U.S. Dept. of the Interior, Minerals Management Service, Gulf of Mexico OCS Regional Office, New Orleans, La. 333 pp.

ABOUT THE COVER

The cover illustration suggests the richness of the mesoscale eddy field in the Gulf of Mexico. Clockwise and counterclockwise rotating features have a wide range of sizes, are seen in most areas of the Gulf and are a major influence on circulation patterns.

TABLE OF CONTENTS

Section	Page
List of Figures	ix
List of Tables	xxxi
Acknowledgements	xxxv
I. INTRODUCTION	1
1.1 Program Overview	1
1.2 Program Observations	3
1.3 Program Principal Investigators and Primary Support Personnel	3
1.4 Report Organization	4
II. DATA ACQUISITION	5
2.1 Introduction	5
2.2 Lagrangian Drifters	5
2.3 Hydrography	5
2.3.1 Introduction	5
2.3.2 Mooring Servicing Cruises	7
2.3.2.1 Introduction	7
2.3.2.2 Hydrographic Equipment and Sampling Procedures	7
2.3.3 ARGOS Drifter Deployment Surveys	17
2.3.4 Aerial XBT (AXBT) Surveys	21
2.3.5 Ship-of-Opportunity (SOOP) Cruises	21
2.3.6 Horizontal Temperature Composites	30
2.4 Marine Optics	30
2.4.1 Introduction	30
2.4.2 Instrumentation	36
2.4.2.1 Introduction	36
2.4.2.2 F-Meter	36
2.4.2.3 Q-Meter	37
2.4.2.4 B-Meter	37
2.4.2.5 C-Meter	38
2.4.2.6 Chlorophyll A-Meter	38
2.4.2.7 UV-B Meter	39
2.4.2.8 Secchi Disc	40
2.5 Remote Sensing	40

TABLE OF CONTENTS

Section		Page
2.5.1	Introduction	40
2.5.2	Thermal Imagery	40
2.5.3	GEOSAT Altimetry	41
2.6	Subsurface Moorings	42
2.6.1	Introduction	42
2.6.2	Currents and Temperature	42
2.6.3	Transmissometry	45
2.6.4	Inverted Echo Sounders (IES's)	48
III.	DATA ANALYSIS	51
3.1	Introduction	51
3.2	Lagrangian Drifters	51
3.3	Hydrography	51
3.4	Marine Optics	53
3.4.1	Introduction	53
3.4.2	Nomenclature and Definitions	53
3.5	Remote Sensing	59
3.5.1	AVHRR Data	59
3.5.2	Satellite Altimetry	60
3.6	Subsurface Observations	63
3.6.1	Inverted Echo Sounder Data	63
3.7	Oceanic Frontal Analyses	64
3.7.1	SOOP Data	64
3.7.2	Thermal AVHRR and Coastal Zone Color Scanner (CZCS) Imagery	71
IV.	TECHNICAL DISCUSSION	75
4.1	Introduction	75
4.2	Long-term Variability	76
4.2.1	Loop Current Variability	76
4.2.1.1	Introduction	76
4.2.1.2	Frontal Variability	77
4.2.1.3	Loop Current Variability and Currents	82
4.2.2	Frontal Analysis Statistics	85

TABLE OF CONTENTS

Section	Page
4.2.2.1 Loop Current	85
4.2.2.2 Warm Eddies	89
4.2.2.3 Shelf-Slope Fronts	89
4.3 Eddy Movement and Dynamics	95
4.3.1 Gulf Eddies, August 1986-December 1988	95
4.3.2 Kinematics of Eddies E and F	119
4.3.3 Physical Processes of Interest	129
4.3.3.1 Dynamics Related to the Stalling of Eddy E	132
4.3.3.2 Ejection of Mass from Eddy F	132
4.3.3.3 Dynamics of Cyclones on the Northern Slope	141
4.3.3.4 A Possible Scenario	142
4.4 Slope Circulation	143
4.4.1 Current Meter Statistics	143
4.4.2 Warm Eddies and Cold Cyclones Over the Lower Slope	149
4.4.2.1 General Overview	149
4.4.2.2 Summer 1987	152
4.4.2.3 Summer 1988	158
4.4.2.4 Discussion of Cyclones on the Slope	163
4.4.2.5 Warm Eddies	168
4.4.2.6 A Note on Tides	172
4.4.3 Eddy Current Structure	173
4.4.3.1 Introduction	173
4.4.3.2 Subsurface Circulation from Current Meter Records	173
4.4.3.3 Dynamic Normal Mode Decomposition of Currents	192
4.4.3.4 Frequency Domain Description	207
4.4.3.4.1 Introduction	207
4.4.3.4.2 Autospectra	207
4.4.3.4.3 Vertical Coherence of U and V	215
4.4.3.4.4 Discussion	215
4.5 Deep Currents	221
4.5.1 Introduction	221
4.5.2 Water Column Analysis	221

TABLE OF CONTENTS

Section		Page
4.5.3	Horizontal Energy Distribution	227
4.5.4	Local Phase Propagation and Wave Numbers	232
4.5.5	Energy Propagation	237
4.5.6	Deep Currents and Warm Eddies	241
4.5.7	Mean Currents	242
4.5.8	Summary	246
4.6	Shelf Circulation and Hydrography	247
4.6.1	Introduction	247
4.6.2	General Current Meter Statistics	248
4.6.3	Spectrum Analysis Results	256
4.6.4	Empirical Orthogonal Function Results	270
4.6.5	Discussion and Interpretation	276
4.6.6	Shelf Hydrography	278
4.6.6.1	Introduction	278
4.6.6.2	Seasonal Thermal Structure	278
4.6.6.3	Temperature, Salinity and Density	281
4.6.6.4	Dissolved Oxygen	286
4.6.6.5	Suspended Solids	290
4.7	Shelf Optics	290
4.7.1	Introduction	290
4.7.2	Inter-Station Comparison	290
4.7.3	Optical Water Mass Classification	312
4.7.4	Conclusions	323
REFERENCES		327

LIST OF FIGURES

Figure No.	Caption	Page
1.1-1.	General Map of the Gulf of Mexico	2
2.3-1a,b.	Cruise track and station locations for R/V PELICAN Cruise PN8713 for (a) Section A-B and (b) Section C-D	9
2.3-1c,d.	Cruise track and station locations for R/V PELICAN Cruise (c) PN8715 (Section E-F) and (d) PN8803 (Section G-H). Boxes are CTD casts and X's are XBT drops	10
2.3-1e,f.	Cruise track and station locations for R/V PELICAN Cruise PN8814 for (e) Section I-J and (f) Section K-L	11
2.3-1g.	Cruise track and station locations for R/V PELICAN Cruise PN8820 (Section M-N). Boxes are CTD casts	12
2.3-1h,i.	Cruise track and station locations for R/V PELICAN Cruise PN8823 for (h) Sections O-P, P-Q and Q-R; and (i) Section S-T. X's are XBT drops	13
2.3-1j,k.	Cruise track and station location for R/V PELICAN Cruise (j) PN8903 (Section U-V) and (k) PN8913 (Section W-X). Boxes are CTD casts and X's are XBT drops	14
2.3-2a.	Cruise track for dedicated ARGOS drifter deployment cruise for the R/V PELICAN on January 13-14, 1987	18
2.3-2b.	Cruise track for dedicated ARGOS drifter deployment cruise for the R/V SEAWARD EXPLORER on November 3-10, 1987	19
2.3-2c.	Cruise track for dedicated ARGOS drifter deployment cruise for the R/V PELICAN on October 18-22, 1988	20
2.3-3a.	Flight track for aerial XBT survey during the Year 5 program for the period of July 31 to August 3, 1988	22
2.3-3b.	Flight track for aerial XBT survey during the Year 5 program for the period of October 19-22, 1988	23
2.3-4.	Examples of cruise tracks for the two primary Ship-of-Opportunity sections during the Year 5 program	25

LIST OF FIGURES

Figure No.	Caption	Page
2.3-5.	Examples of standard data products produced for the NMFS E.M. QUEENY Ship-of-Opportunity section (Note the Loop Current at Stations 4 to 16)	26
2.3-6.	Examples of standard data products produced for the M/V SENATOR MMS Ship-of-Opportunity section (Note the cold eddy at Station 10)	27
2.3-7.	Example of a GYRE Ship-of-Opportunity cruise track	28
2.3-8.	Example of a JUSTO SIERRA Ship-of-Opportunity cruise track	29
2.3-9.	Sample composite plot of the 15°C temperature surface (mooring locations are indicated by black dots)	32
2.4-1.	Station locations for the April 1987 study of the optical properties of the Louisiana shelf	33
2.4-2.	Station locations for the February 1988 study of the optical properties of the Louisiana shelf	34
2.4-3.	Station locations for the July 1988 study of the optical properties of the Louisiana shelf	35
2.6-1.	Mooring locations during Year 5 of the MMS-sponsored Gulf of Mexico Physical Oceanography Program	43
2.6-2.	Time line of deployment periods and data return for each current meter level during Year 5 of the Gulf of Mexico Physical Oceanography Program. The solid lines are for currents and the dashed lines are for temperature	47
2.6-3.	Examples of the transmissometry data obtained during the Year 5 program	49
3.5-1.	Raw and detrended GEOSAT height data from an October 8, 1988 descending pass in the central Gulf of Mexico. Subtraction of the linear regression line from the "raw" data gives detrended data	61

LIST OF FIGURES

Figure No.	Caption	Page
3.5-2.	Sea surface height and isotherm depth for (a) concurrent sea surface height from an ascending pass and the 14°C isotherm depth from AXBT Stations 1 through 22 (Figure 2.3-3b) and (b) sea surface height data from a descending pass and 14°C isotherm depth from AXBT Stations 1 through 22	62
3.6-1a,b.	Correlations from raw and 3-HLP median travel times from IES #1 record MGG6 and (a) synthetic dynamic heights and (b) the depth of the 20°C isotherm	65
3.6-1c,d.	Correlations from raw and 3-HLP median travel times from IES #1 record MGG6 and (c) the depth of the 14°C isotherm and (d) the depth of the 8°C isotherm	66
3.6-2.	Forty-HLP IES #1 median and mode travel times for record MGG6. The eddies moving through the site are identified along with the approximate dates of hydrographic cruises and the occurrence of ARGOS drifters	67
3.7-1.	Available QUEENY east-west Ship-of-Opportunity transects between 1980 and 1987. The positions of Moorings C and E on the west Florida shelf are marked. The mean transect with the position of the origin used in the analysis is marked on the map	68
3.7-2.	A typical QUEENY section through the Loop Current and the eastern side of a detached warm eddy showing the (a) zero to 500 m isotherm structure and (b) zero to 200 m isotherm structure	69
3.7-3.	Available New Orleans to Yucatan Straits Ship-of-Opportunity transects from 1983 to 1986. The mean transect with the position of the origin used in the analysis is marked on the map	70
3.7-4.	The analysis of the critical depth of the 20°C isotherm (125 m) from a representative QUEENY section. The designations: EE, LW, LC and LE are front positions; AW and AE are cross-sectional areas and DC is the maximum depth of the isotherm in the Loop Current	72

LIST OF FIGURES

Figure No.	Caption	Page
3.7-5.	Example of the digitization, using a 1/2° x 1/2° grid, of the Loop Current and warm eddy fronts (•) and the areas contained by these fronts (*). The fronts are from monthly composites of thermal satellite imagery	74
4.2-1.	The variability of the positions of the frontal parameters derived from the QUEENY transects	78
4.2-2a.	The variability of the position of the frontal parameters (LW, LC and LE) derived from the QUEENY transects for 1983 through 1986	79
4.2-2b.	The variability of the position of the frontal parameter (LN) derived from the NESTOR transects for 1983 through 1986	80
4.2-3.	The variance preserving spectra of LW (solid) and LE (dashed) from the QUEENY analysis	83
4.2-4.	The 40-HLP along-shelf current velocity and temperature at the 50-m level for Moorings C and E for the years 1983 to 1985. The positions of the eastern Loop Current front (LE) and the north boundary (LN), from the QUEENY and NESTOR transects, are also plotted as time series	84
4.2-5.	The percent occurrence of the Loop Current front from the 10 years of monthly frontal analyses Superimposed are the mean and standard deviation of the frontal positions derived from the QUEENY and NESTOR transects	86
4.2-6.	The percent occurrence of Loop Current water from the monthly frontal analyses	87
4.2-7.	A comparison of the positions of the fronts (LN, LE and LW) derived from the QUEENY and NESTOR transects (solid) and from the monthly frontal analyses (dashed)	88
4.2-8.	Scatter plot of the northward extent versus the computed area of the Loop Current from the frontal analyses	90
4.2-9.	The percent occurrence of warm eddy fronts from monthly frontal analyses	92

LIST OF FIGURES

Figure No.	Caption	Page
4.2-10	The percent occurrence of warm eddy water from monthly frontal analyses	93
4.2-11.	The percent occurrence of shelf-slope fronts from monthly frontal analyses	94
4.3-1.	Drifter trajectory for July 27 to September 16, 1986. The asterisk represents the initial position of the drifter. Depth contours are in meters	96
4.3-2.	XBT transect through the Loop Current region for September 1 to 2, 1986	97
4.3-3.	Drifter trajectory for September 16 to November 29, 1986. The asterisk represents the initial position of the drifter. Depth contours are in meters	98
4.3-4.	Conditions for October 18 to 25, 1986. SST's are in °C and the asterisk represents the initial position of the drifter. Arrows denote flow at the edges of Eddy D. Dotted lines indicate the location of eddy water	99
4.3-5.	Drifter trajectories for November 29, 1986 to January 20, 1987. The asterisks represent the initial positions of the drifters. Depth contours are in meters	100
4.3-6.	Conditions for the week of January 20 to 27, 1987. SST's are in °C and the asterisks represent the initial positions of the drifters. Arrows denote flow at the edges of Eddy D. Dotted lines indicate the location of eddy water	101
4.3-7.	Drifter trajectories for January 27 to March 17, 1987. The asterisks represent the initial positions of the drifters. Depth contours are in meters	102

LIST OF FIGURES

Figure No.	Caption	Page
4.3-8.	Conditions for the week of March 31 to April 7, 1987. SST's are in °C. Arrows denote the flow at the edges of Eddy D (western Gulf) and the flow of the Loop Current (eastern Gulf) while dotted lines indicate the location of eddy water or Loop Current water (based on XBT data)	103
4.3-9.	Drifter trajectories for April 14 to June 9, 1987. The asterisks represent the initial positions of the drifters. Depth contours are in meters	105
4.3-10.	The depth of the 15°C isothermal surface as constructed from XBT data collected during the period of April 5 to May 30, 1987	106
4.3-11.	Drifter trajectories for June 9 to August 15, 1987. The asterisks represent the initial positions of the drifters. Depth contours are in meters.....	107
4.3-12.	Drifter trajectories for August 15 to October 27, 1987. The asterisks represent the initial positions of the drifters. Depth contours are in meters	108
4.3-13.	The depth of the 8°C isothermal surface as constructed from XBT data collected during the period of October 14 to November 24, 1987	109
4.3-14.	Drifter trajectories for November 7, 1987 to March 22, 1988. The asterisks represent the initial positions of the drifters. Depth contours are in meters	111
4.3-15.	Conditions for the week of March 22 to 29, 1988. SST's are in °C. Arrows denote the flow at the edges of Eddy E while dotted lines indicate the location of eddy water (based on XBT data)	112
4.3-16.	Drifter trajectories for April 12 to May 17, 1988. The asterisks represent the initial positions of the drifters. Depth contours are in meters	113
4.3-17.	Drifter trajectories for May 17 to September 6, 1988. The asterisks represent the initial positions of the drifters. Depth contours are in meters	114

LIST OF FIGURES

Figure No.	Caption	Page
4.3-18.	The depth of the 8°C isothermal surface as constructed from XBT data collected during the period of July 5 to August 3, 1988	115
4.3-19.	Vertical plot of temperature for Stations 1 to 17 for July 31, 1988 AXBT section in Eddy F	116
4.3-20.	Drifter trajectories for September 6 to October 18, 1988. The asterisks represent the initial positions of the drifters. Depth contours are in meters.....	117
4.3-21.	Drifter trajectories for October 18, 1988 to January 1, 1989. The asterisks represent the initial positions of the drifters. Depth contours are in meters	118
4.3-22.	The depth of the 8°C isothermal surface as constructed from XBT data collected during the period of October 17 to 31, 1988	120
4.3-23a,b.	Sea surface height vs isotherm depth for (a) concurrent sea surface height from an ascending pass and the 14°C isotherm depth from AXBT Stations 1 through 22 (2.3-3b) and (b) sea surface height data from a descending pass and 14°C isotherm depth from AXBT Stations 1 through 22	121
4.3-24.	Drifter trajectories for December 13, 1988 to January 1, 1989. The asterisks represent the initial positions of the drifters. Depth contours are in meters	122
4.3-25.	For Drifter 3344, the (a) vorticity, normal deformation rate and shear deformation rate for Eddy E, and (b) divergence for Eddy E	124
4.3-26.	For Drifter 3344, the (a) east-west and north-south translation velocities and swirl magnitudes for Eddy E, and (b) variations in the lengths of the major and minor axes for Eddy E	125
4.3-27.	East-west and north-south speed components of Drifter 3353	126
4.3-28.	For Drifter 3353, the (a) vorticity, normal deformation rate and shear deformation rate for Eddy E, and (b) divergence for Eddy E	127

LIST OF FIGURES

Figure No.	Caption	Page
4.3-29.	For Drifter 3345, the (a) vorticity, normal deformation rate and shear deformation rate for Eddy F, and (b) divergence for Eddy F	128
4.3-30.	For Drifter 3347, the (a) vorticity, normal deformation rate and shear deformation rate for Eddy F, and (b) divergence for Eddy F	130
4.3-31.	Period of rotation, distance to the center, and eccentricity for Eddy E as determined from the trajectory of Drifter 3344	133
4.3-32.	Potential vorticity for Eddy E as determined from the trajectory of Drifter 3344	134
4.3-33a.	Period of rotation, distance to the center and eccentricity for Eddy F as determined from the trajectory of Drifter 3345	136
4.3-33b.	Period of rotation, distance to the center and eccentricity for Eddy F as determined from the trajectory of Drifter 3347	137
4.3-34a.	Potential vorticity for Eddy F determined from Drifter 3345	138
4.3-34b.	Potential vorticity for Eddy F determined from Drifter 3347	139
4.3-35.	A schematic indicating the initial conditions of the coalescing of two anticyclones. Shown are tentacles of water from the exteriors of each eddy which flow outward to wrap around the other eddy	140
4.4-1.	Current rose and table of joint frequency distribution of speed and direction for the period from November 11, 1987 through September 5, 1988 (Period I) at Mooring EE at depths of (a) 100 m and (b) 725 m (based on hourly 3-HLP currents)	144
4.4-2.	Current rose and table of joint frequency distribution of speed and direction for the period from November 11, 1987 through September 5, 1988 (Period I) at Mooring FF at depths of (a) 100 m and (b) 725 m (based on hourly 3-HLP currents)	145

LIST OF FIGURES

Figure No.	Caption	Page
4.4-3a,b.	Current rose and table of joint frequency distribution of speed and direction for the period from November 11, 1987 through September 5, 1988 (Period I) at Mooring GG at depths of (a) 100 m and (b) 725 m (based on hourly 3-HLP currents)	146
4.4-3c.	Current rose and table of joint frequency distribution of speed and direction for the period from November 11, 1987 through September 5, 1988 (Period I) at Mooring GG at a depth of 2500 m (based on hourly 3-HLP currents)	147
4.4-4.	Forty-HLP IES #1 median and mode travel times for record MGG6. The eddies moving through the site are identified along with the approximate dates of hydrographic cruises and the occurrence of ARGOS drifters	150
4.4-5.	Depth of the 15°C isotherm from Composite Two	151
4.4-6a.	Depth of the 15°C isotherm from Composite One	153
4.4-6b.	Depth of the 8°C isotherm from Composite One	154
4.4-7.	Available SENATOR Ship-of-Opportunity transects with the mean transect and origin marked. The position of Mooring GG is noted	155
4.4-8a.	Contours of the depth of the 8°C isotherm as a function of distance along the transect, and time for the SENATOR sections	156
4.4-8b.	Contours of the depth of the 20°C isotherm as a function of distance along the transect, and time for the SENATOR sections	157
4.4-9.	A plot of 40-HLP isotherm depths from the upper three current meters at Mooring GG and the IES #1 travel time record	159
4.4-10.	A sketch of the eddy features observed in a NOAA 9 image for May 7, 1988 (JD 128). The smoothed trajectory for ARGOS Drifter 3353, in Eddy E, is shown for the period May 2 to 12, 1988 with crosses marking the beginning of each day	160

LIST OF FIGURES

Figure No.	Caption	Page
4.4-11a.	Forty-HLP stick and temperature data from the indicated slope instruments for April to October 1988	161
4.4-11b.	Forty-HLP U (solid), V (dashed) and temperature data for the indicated slope instruments for April to October 1988	162
4.4-12.	Depth of the 8°C isotherm from Composite Three	164
4.4-13a.	Depth of the 8°C isotherm from Composite Four	165
4.4-13b.	Depth of the 15°C isotherm from Composite Four	166
4.4-14.	The track of ARGOS Drifter 3353 for October to December 1988. The ticks are at daily intervals	167
4.4-15a.	Forty-HLP stick and temperature data from the indicated slope instruments for October 1987 to May 1988	169
4.4-15b.	Forty-HLP U (solid), V (dashed) and temperature data from the indicated slope instruments for October 1987 to May 1988	170
4.4-16a.	Stick vector plots of 40-HLP currents at Mooring EE for the period from October 27, 1987 through March 11, 1988. Vertically up (+V) is east	175
4.4-16b.	Stick vector plots of 40-HLP currents at Mooring EE for the period from February 9, 1988 through June 24, 1988. Vertically up (+V) is east	176
4.4-16c.	Stick vector plots of 40-HLP currents at Mooring EE for the period from June 8, 1988 through October 22, 1988. Vertically up (+V) is east	177
4.4-17a.	Stick vector plots of 40-HLP currents at Mooring FF for the period from October 27, 1987 through March 11, 1988. Vertically up (+V) is east	178
4.4-17b.	Stick vector plots of 40-HLP currents at Mooring FF for the period from February 9, 1988 through June 24, 1988. Vertically up (+V) is east	179
4.4-17c.	Stick vector plots of 40-HLP currents at Mooring FF for the period from June 8, 1988 through October 22, 1988. Vertically up (+V) is east	180

LIST OF FIGURES

Figure No.	Caption	Page
4.4-18a.	Stick vector plots of 40-HLP currents at Mooring GG for the period from October 27, 1987 through March 11, 1988. Vertically up (+V) is east	181
4.4-18b.	Stick vector plots of 40-HLP currents at Mooring GG for the period from February 9, 1988 through June 24, 1988. Vertically up (+V) is east	182
4.4-18c.	Stick vector plots of 40-HLP currents at Mooring GG for the period from June 8, 1988 through October 22, 1988. Vertically up (+V) is east	183
4.4-18d.	Stick vector plots of 40-HLP currents at Mooring GG for the period from October 6, 1988 through October 26, 1988. Vertically up (+V) is east	184
4.4-19.	Topography of the 8°C temperature surface based on a composite of XBT data sets collected during the period from October 17 to 31, 1988	185
4.4-20a,b.	Forty-HLP temperature series at 305 m at Mooring GG for the period from (a) October 27, 1988 through March 11, 1988 and (b) February 9, 1988 through June 24, 1988	186
4.4-20c,d.	Forty-HLP temperature series at 305 m at Mooring GG for the period from (c) June 8, 1988 through October 22, 1988 and (d) October 6, 1988 through October 26, 1988	187
4.4-21.	Trajectory of Drifter 3344 during the month of March 1988. Each X indicates a one-day interval	189
4.4-22.	Topography of the 15°C temperature surface based on a composite of XBT data sets collected during the period from July 5 to August 3, 1988	190
4.4-23a.	Gulf of Mexico mean vertical stability profile	195
4.4-23b.	Gulf of Mexico modal structure functions for the barotropic (F_0) and first three baroclinic modes (F_1, F_2 and F_3) for Mooring GG. The solid dots on the vertical axis indicate the depths at which current meters were located	196

LIST OF FIGURES

Figure No.	Caption	Page
4.4-23c.	Gulf of Mexico modal structure functions for the barotropic (F_0) and first three baroclinic modes (F_1, F_2 and F_3) for Mooring FF. The solid dots on the vertical axis indicate the depths at which current meters were located	197
4.4-23d.	Gulf of Mexico modal structure functions for the barotropic (F_0) and first three baroclinic modes (F_1, F_2 and F_3) for Mooring EE. The solid dots on the vertical axis indicate the depths at which current meters were located	198
4.4-24.	Amplitudes of the barotropic (D_0) and first three baroclinic modes (D_1, D_2 and D_3) at Mooring GG for the period from April 14, 1988 through October 26, 1988 (Period IV) for the (a) U component (cross isobath component) of current velocity and (b) V component (along isobath component) of current velocity	201
4.4-25.	Cartoon showing (a) stick vectors for the barotropic mode of current at Mooring GG for the period from July 20, 1988 through October 26, 1988 and (b) a hypothetical vortex pair that would produce a time series of current velocity similar to that shown above, if it moved across a fixed mooring in the direction shown by the heavy line	203
4.4-26.	Amplitudes of the barotropic (D_0) and first two baroclinic modes (D_1 and D_2) at Mooring GG during the period from November 15, 1987 through September 1, 1988 (Period III) for (a) the U component (cross isobath component) of current velocity and (b) the V component (along isobath component) of current velocity	205
4.4-27.	Amplitudes of the barotropic (D_0) and first two baroclinic modes (D_1 and D_2) at Mooring FF during the period from November 15, 1987 through September 1, 1988 (Period III) for (a) the U component (cross isobath component) of current velocity and (b) the V component (along isobath component) of current velocity	206

LIST OF FIGURES

Figure No.	Caption	Page
4.4-28.	Amplitudes of the barotropic (D_0) and first baroclinic mode (D_1) at Mooring EE during the period from November 15, 1987 through September 1, 1988 (Period III) for (a) the U component (cross isobath component) of current velocity and (b) the V component (along isobath component) of current velocity	208
4.4-29.	Spectral coherence between the barotropic and first baroclinic modes at Mooring EE for 292 days beginning on November 15, 1987 for the (a) U component of current velocity and (b) V component of current velocity	209
4.4-30a,b.	Autospectra of the U component of current velocity at 300 m for 292 days beginning November 15, 1987 for (a) Mooring EE and (b) Mooring FF	210
4.4-30c.	Autospectrum of the U component of current velocity at 305 m for 292 days beginning November 15, 1987 for Mooring GG	211
4.4-31a,b.	Autospectra of the V component of current velocity at 300 m for 292 days beginning November 15, 1987 for (a) Mooring EE and (b) Mooring FF	212
4.4-31c.	Autospectrum of the V component of current velocity at 305 m for 292 days beginning November 15, 1987 for Mooring GG	213
4.4-32.	Autospectra of current velocity at 2500 m for Mooring GG for 292 days beginning November 15, 1987 for (a) the U component of current velocity and (b) the V component of current velocity	214
4.4-33.	Phase and coherence squared at Mooring EE for 292 days beginning November 15, 1987 between (a) the U components of current velocity at 100 m and 300 m and (b) the V components of current velocity at 100 m and 300 m	216
4.4-34.	Phase and coherence squared at Mooring FF for 292 days beginning November 15, 1987 between (a) the U components of current velocity at 100 m and 305 m and (b) the V components of current velocity at 100 m and 305 m	217

LIST OF FIGURES

Figure No.	Caption	Page
4.4-35.	Phase and coherence squared at Mooring GG for 292 days beginning November 15, 1987 between (a) the U components of current velocity at 100 m and 305 m and (b) the V components of current velocity at 100 m and 305 m	218
4.4-36.	Phase and coherence squared at Mooring GG for 292 days beginning November 15, 1987 between (a) the U components of current velocity at 305 m and 2500 m and (b) the V components of current velocity at 305 m and 2500 m	219
4.5-1.	Seven-DLP stick plots from eastern Gulf Moorings A and G	222
4.5-2.	Kinetic energy spectra in variance preserving form for deep current records at Mooring G	224
4.5-3.	Seven-DLP stick plots from western Gulf Moorings P, Q, R, S and T	225
4.5-4.	Kinetic energy spectra in variance preserving form for deep current records at (a) Mooring R, and (b) Mooring P	226
4.5-5.	Seven-DLP deep currents from central Gulf Moorings GG and FF. The travel time record from IES #1 (MGG6) at Mooring GG is also shown	228
4.5-6.	Forty-HLP variance ellipses for the indicated records where the half axis lengths are equal to the standard deviation of the velocity fluctuations along the principal axes	229
4.5-7a,b.	Kinetic energy spectra in variance preserving form for records (a) MOG4 and MGG4; and (b) MOG4, MGG4/5 and MOQ4	230
4.5-7c.	Kinetic energy spectra in variance preserving form for records MOA4, MFF4 and MOP4	231
4.5-8a.	The velocity hodographs from the EOF analysis of the deep current records for 18 to 37 day period motions	235
4.5-8b.	The velocity hodographs from the EOF analysis of the deep current records for 38 to 300 day period motions	236

LIST OF FIGURES

Figure No.	Caption	Page
4.5-9.	Time lines of deep current records with selected upper layer records from 1986 to 1988 for the MMS Gulf of Mexico Physical Oceanography Program. Solid lines are velocity and dashed lines are temperature ..	238
4.5-10.	Seven-DLP stick plots of records M0Q4, and M0G4 lagged by 106 days. The lower panel shows the along isobath (V) components. The lagged M0G4 is solid and M0Q4 is dashed	239
4.5-11.	Coherence squared and phase differences for the indicated eastern and western Gulf records. Eastern Gulf records have been lagged by 106 days	240
4.5-12a,b.	Coherence squared and phase differences between upper and lower layer currents in the (a) eastern Gulf of Mexico and (b) central Gulf of Mexico	243
4.5-12c.	Coherence squared and phase differences between upper and lower layer currents in the western Gulf of Mexico	244
4.5-13.	Mean velocity vectors for the indicated records (all available data)	245
4.6-1.	Mean current vectors from all available data for the shelf and upper slope moorings. Current vectors originate at the mooring site and flow toward the letters denoting the individual meters	249
4.6-2.	Variance distribution for current meter records by band and by component	255
4.6-3.	Principal axes of the low-passed current variance ellipses from all available data for the shelf and upper slope moorings	257
4.6-4.	Variance preserving spectra for 274 days, beginning March 29, 1988, at Sabine Pass (SRST2) and Southwest Pass (BURL1) for (a) the U component of wind stress and (b) the V component of wind stress	258
4.6-5.	Variance preserving spectra for 341 days, beginning in April 1987, from the current meter records at (a) Mooring CC at 20 m depth (record MCC3) and (b) Mooring DD at 150 m depth (record MDD4). Spectra are estimated using 20 degrees of freedom ...	259

LIST OF FIGURES

Figure No.	Caption	Page
4.6-6a,b.	Vertical coherence and phase, estimated using 20 degrees of freedom, for the concurrent portions of current records at Mooring CC at 11 and 54 meters depth for (a) the southward component of current velocity and (b) the eastward component of current velocity	261
4.6-6c,d.	Vertical coherence and phase, estimated using 20 degrees of freedom, for the concurrent portions of current records at Mooring DD at 150 and 174 meters depth for (a) the southward component of current velocity and (b) the eastward component of current velocity	262
4.6-7.	Horizontal coherence and phase, estimated using 20 degrees of freedom, for the concurrent portions of the current records at Mooring CC at 28 m and Mooring DD at 150 m for (a) the southward component of current velocity and (b) the eastward component of current velocity	263
4.6-8.	Winds for Southwest Pass and the last 100 days of currents at Meters MAA1 (7 m), MBB3 (18 m), MDD1 (10 m) and MDD4 (150 m)	264
4.6-9.	Vertical coherence and phase between (a) cross isobath and (b) along isobath Mooring BB current meter records MBB1 (12 m) and MBB3 (18 m) for Period VI, estimated using 20 degrees of freedom	266
4.6-10a,b.	Coherence and phase between (a) cross isobath and (b) along isobath current meter records from Mooring BB Meter MBB3 (18 m) and Southwest Pass (BURL1) wind stress during Period VII, estimated using 20 degrees of freedom	267
4.6-10c,d.	Coherence and phase between (c) cross isobath and (d) along isobath current meter records from Mooring DD Meter MCC3 (28 m) and Southwest Pass (BURL1) wind stress during Period VII, estimated using 20 degrees of freedom	268
4.6-11.	Coherence and phase between (a) cross isobath and (b) along isobath current meter records from Mooring AA Meter MAA1 (7 m) and Southwest Pass (BURL1) wind stress during Period VIII, estimated using 20 degrees of freedom	271

LIST OF FIGURES

Figure No.	Caption	Page
4.6-12.	Coherence and phase between (a) cross isobath and (b) along isobath current meter records from Mooring BB Meter MBB3 (18 m) and Southwest Pass (BURL1) wind stress during Period VIII, estimated using 20 degrees of freedom	272
4.6-13.	Forty-HLP time series plots at indicated depths for (a) Mooring BB, (b) Mooring CC and (c) Mooring DD. Note the temperatures are vertically uniform during cooling and vertically stratified during warming	279
4.6-14.	Forty-HLP time series plots of temperatures at a nominal depth of 10 m for the indicated moorings. Note that during shelf cooling a horizontal gradient develops while during warming the near surface layer is approximately isothermal	280
4.6-15.	Cross-shelf sections of (a) temperature, (b) salinity and (c) sigma-t (density) taken during cruise PN8713 on April 9 to 10, 1987. Current meter locations are indicated and labelled	282
4.6-16.	Cross-shelf sections of (a) temperature, (b) salinity and (c) sigma-t (density) taken during cruise PN8715 on April 25 to 26, 1987. Current meter locations are indicated and labelled	283
4.6-17.	Cross-shelf sections of (a) temperature, (b) salinity and (c) sigma-t (density) taken during cruise PN8803 on July 17, 1987. Current meter locations are indicated and labelled	284
4.6-18.	Cross-shelf sections of (a) temperature, (b) salinity and (c) sigma-t (density) taken during cruise PN8814 on November 15 to 16, 1987. Current meter locations are indicated and labelled	285
4.6-19.	Cross-shelf sections of (a) temperature, (b) salinity and (c) sigma-t (density) taken during cruise PN8820 on February 9 to 10, 1988. Current meter locations are indicated and labelled	287
4.6-20.	Cross-shelf sections of dissolved oxygen (DO) for cruises: (a) PN8713 (April 9 to 10, 1987), (b) PN8715 (April 25 to 26, 1987) and (c) PN8803 (July 17, 1987)	288

LIST OF FIGURES

Figure No.	Caption	Page
4.6-21.	Cross-shelf sections of dissolved oxygen (DO) for cruises: (a) PN8814 (November 15 to 16, 1987), (b) PN8820 (February 9 to 10, 1988), and (c) PN8903 (July 21, 1988)	289
4.7-1.	Station locations for the February 1988 study of the optical properties of the Louisiana shelf	295
4.7-2.	The vertical distribution of light fluorescence at Stations AA, BB, CC and DD in February 1988. A signal output of one Volt corresponds approximately to 10 mg m^{-3} of chlorophyll-like pigments depending on the pigment composition	296
4.7-3.	The vertical distribution of total light scattering at Stations AA, BB, CC and DD in February 1988. A signal output of one Volt f. corresponds approximately to b = 0.140 m^{-1} depending on the particle composition and distribution. The wavelength centers around 655 nm	298
4.7-4.	The vertical distribution of the light transmission at Stations AA, BB, CC and DD in February 1988. When the signal output from the transmissometer having a total path length of 0.5 m amounts to one relative unit, the light transmission T(0.5 m) = 0.242. The following relations are valid: $T(1.0\ m) = e^{-c.1} = (T(0.5\ m))^2$ in which c is the beam light attenuation coefficient (m^{-1}). The wavelength applied centers around 631 nm	299
4.7-5.	Relative downward quanta irradiance (350 to 700 nm) versus depth at Stations AA, BB, CC and DD in February 1988. The 100% value is taken to be Q (350 to 700 nm) just below the water surface. The quanta irradiance is a measure for the amount of photons available for photosynthesis (= Photosynthetically Active Radiation, or PAR)	300
4.7-6.	Relative downward UV-B irradiance versus depth at Stations AA, BB, CC and DD in February 1988. The 100% value is taken to be E_d (310 nm) just below the water surface. In the upper meters an averaging procedure is required at stations where the light absorption is high i.e., always at Station AA, sometimes at Station BB depending on the season, but never at Stations CC and DD	302

Figure No.	Caption	Page
4.7-7.	Station locations for the April 1987 study of the optical properties of the Louisiana shelf	303
4.7-8.	The vertical distribution of light fluorescence at Stations AA, BB, CC and DD in April 1987. A signal output of one Volt corresponds approximately to 10 mg m^{-3} of chlorophyll-like pigments depending on the pigment composition	304
4.7-9.	The vertical distribution of total light scattering at Stations AA, BB, CC and DD in April 1987. A signal output of one Volt corresponds approximately to b = 0.140 m^{-1} depending on the particle composition and distribution. The wavelength applied centers around 655 nm	305
4.7-10.	The vertical distribution of the light transmission at Stations AA, BB, CC and DD in April 1987. (See caption to Figure 4.7-4 for further discussion.)	306
4.7-11.	Relative downward quanta irradiance (350 to 700 nm) versus depth at Stations AA, BB, CC and DD in April 1987. The 100% value is taken to be Q (350 to 700 nm)just below the water surface. (See caption to Figure 4.7-5 for further discussion.)	307
4.7-12.	Relative downward UV-B irradiance versus depth at Stations AA, BB, CC and DD in April 1987. The 100% value is taken to be E_d (310 nm) just below the water surface. (See caption to Figure 4.7-6 for further discussion.)	309
4.7-13.	Station locations for the July 1988 study of the optical properties of the Louisiana shelf	310
4.7-14.	The vertical distribution of light fluorescence at Stations AA, BB, CC and DD in July 1988. A signal output of one Volt corresponds approximately to 10 mg m^{-3} of chlorophyll-like pigments depending on the pigment composition	311

LIST OF FIGURES

Figure No.	Caption	Page
4.7-15.	The vertical distribution of total light scattering at Stations AA, BB, CC and DD in July 1988. A signal output of one Volt corresponds approximately to b = 0.140 m^{-1} depending on the particle composition and distribution. The wavelength applied centers around 655 nm	313
4.7-16.	The vertical distribution of the light transmission at Stations AA, BB, CC and DD in July 1988. (See caption to Figure 4.7-4 for further discussion.)	314
4.7-17.	Relative downward quanta irradiance (350 to 700 nm) versus depth at Stations AA, BB, CC and DD in July 1988. The 100% value is taken to be Q (350 to 700 nm) just below the water surface. (See caption to Figure 4.7-5.)	316
4.7-18.	Relative downward UV-B irradiance versus depth at Stations AA, BB, CC and DD in July 1988. The 100% value is taken to be the E_d (310 nm) just below the water surface. (See caption to Figure 4.7-6.)	317
4.7-19.	Profiles of downward quanta irradiance Q as percent of surface value for different optical water types (Jerlov, 1976) together with Q as measured at Stations AA, BB, CC and DD in February 1988. Dashed curves taken from above and downwards represent quanta irradiance profiles from Stations AA, BB, CC and DD (reading down)	319
4.7-20.	Profiles of downward quanta irradiance Q as percent of surface value for different optical water types (Jerlov, 1976) together with Q as measured at Stations AA, BB, CC and DD in April 1987. Dashed curves represent quanta irradiance profiles from Stations AA, BB, CC and DD (reading down)	320
4.7-21.	Profiles of downward quanta irradiance Q as percent of surface value for different optical water types (Jerlov, 1976) together with Q as measured at Stations AA, BB, CC and DD in July 1988. Dashed curves represent quanta irradiance profiles from Stations AA, BB, CC and DD (reading down)	321

Figure No.	Caption	Page
4.7-22.	Empirical relations between the color index F, obtained at zero m depth and selected levels for the downward quanta irradiance Q. Included are the optical water classes I, IA, IB, II, III Oceanic and 1 Coastal (Hojerslev, 1980). x–F^1 versus Z_q (1%) in February 1988. •–F^1 versus Z_q (1%) in April 1987. o–F^1 versus Z_q (1%) in July 1988	322
4.7-23.	Total suspended solids (TSS) (note that the unit is 10 mg l^{-1}) and c(631) (m^{-1}) versus the total light scattering coefficient at 655 nm [b(655) (m^{-1})], respectively	324

LIST OF TABLES

Table No.	Caption	Page
2.2-1.	MMS ARGOS buoys tracked during Year 5	6
2.2-2.	Drifters and their associated oceanographic features	7
2.3-1.	Cruise listing and sampling totals for mooring servicing cruises along 92°W longitude	8
2.3-2.	Station sequences for individual hydrographic cruise sections	15
2.3-3.	Specifications of the Neil Brown Mark IIIB and Sea-Bird SBE-9 CTD Systems	16
2.3-4.	Dedicated MMS-sponsored ARGOS drifter deployment cruises supported with T-7 (760 m) XBT drops	17
2.3-5.	Regular MMS-supported T-7 Ship-of-Opportunity XBT sections from October 1, 1986 to the end of data on March 26, 1988	24
2.3-6.	Nonregular MMS-supported Ship-of-Opportunity T-7 XBT data sets in the Gulf of Mexico from October 1, 1986 through October 30, 1988	24
2.3-7	Component listing of four wide-area horizontal temperature composite plots assembled primarily from available 760 m XBT and AXBT data	31
2.6-1.	Mooring locations and corresponding depths for Year 5 of the MMS-sponsored Gulf of Mexico Physical Oceanography Program	44
2.6-2.	Planned mooring instrumentation levels for Year 5 of the MMS-sponsored Gulf of Mexico Physical Oceanography Program	46
3.3-1.	CTD salinity calibration data for the Gulf of Mexico Year 5 Program	52
3.3-2.	Northwest Regional Calibration Center calibration coefficients for Neil Brown Mark IIIB CTD (April 10, 1986)	52

LIST OF TABLES

Table No.	Caption	Page
3.4-1.	Fundamental quantities, units, and symbols in optical physical oceanography. In this section the IAPSO recommended nomenclature is used. For comparison the nomenclature recommended by IAMAP and the classical American nomenclature are represented as well	54
3.4-2.	Spectral values of vertical attenuation coefficient for the downward irradiance k_w, light absorption coefficient, a_w, for the clearest natural ocean waters, and light scattering coefficient, b_w, for pure artificial sea water. After Morel (1974), Smith and Baker (1981)	58
4.2-1.	Loop current statistics from 98 QUEENY transects (1/80-6/87) and 73 NESTOR transects (5/83-9/86)	81
4.2-2.	Loop Current summary statistics from frontal analysis	91
4.2-3.	Warm eddy summary statistics from frontal analysis	91
4.4-1.	Comparative time periods discussed for Moorings EE, FF and GG	143
4.4-2.	Tidal Analysis of MHH1 (IES #2) pressure record	172
4.4-3	Statistics for deployments three and four (common data period: November 11, 1987 through September 5, 1988 (Period I); 7200 observations)	191
4.4-4.	Rossby radii for the first three baroclinic modes	199
4.4-5.	Relative mean square residuals after fitting the given number of modes	202
4.5-1.	Topographic Rossby wave number estimates	233
4.6-1	Comparative time periods discussed for the shelf Moorings (AA, BB, CC and DD) along with Mooring EE.	248

LIST OF TABLES

Table No.	Caption	Page
4.6-2a.	Low frequency statistics, all available data	250
4.6-2b.	Low frequency statistics, time Period VI	251
4.6-2c.	Low frequency statistics, time Period VII	252
4.6-2d.	Low frequency statistics, time Period VIII	253
4.6-3a.	Empirical orthogonal functions, time Period VI	273
4.6-3b.	Empirical orthogonal functions, time Period VII ...	274
4.6-3c.	Empirical orthogonal functions, time Period VIII ..	275
4.6-4.	Summary of suspended solids data for Mooring AA site	291
4.6-5.	Summary of suspended solids data near Mooring BB site	292
4.6-6.	Summary of suspended solids data near Mooring CC site	293
4.6-7.	Summary of suspended solids dtaa near Mooring DD site	294
4.6-8.	Summary of observed maximums, minimums and averages of total and volatile suspended solids data near the Mooring AA, BB, CC and DD sites	294
4.7-1.	Gulf of Mexico optical observations for February 1988	301
4.7-2.	Gulf of Mexico optical observations for April 1987	308
4.7-3.	Gulf of Mexico optical observations for July 1988	315
4.7-4.	Spectral values of vertical attenuation coefficient for the downward irradiance k_w, light absorption coefficient a_w, for the clearest natural ocean waters, and light scattering coefficient, b_w, for pure artifical sea water. After Morel (1974), Smith and Baker (1981)	318

ACKNOWLEDGEMENTS

To be successful, the MMS Physical Oceanography Program required the work and support of a variety of people. This is not only in the obvious scientific efforts, but also in the administrative, program, and technical support areas. Gail McGee has ably "administered" to this program so that subcontracts and payments happened and on time. Elaine Wiley has typed program material patiently and accurately as I and others rewrote and changed our individual and collective minds. She was the one called on to make it happen "before the overnight delivery man picks up".

Rebecca Weber has patiently and accurately stepped through the essential sequences associated with data QA and analysis utilized by the various scientists involved in this program. Paul deKernion has, with calm, regularity, and dependability, provided the logistic support that is essential to the success of a Ship-of-Opportunity program.

Jim Singer has planned and conducted virtually all the cruise activities associated with the Year 5 program. Those who know him appreciate his conscientious attendance to planning and detail, which are essential for regular and continued success in the field. Bob Wayland has been Data Manager for this program and a valuable contributor to much of the scientific work and discussions.

Thanks are extended to Steve Rabalais (LUMCON) and Captain Bob Cutting and the crew of the R/V PELICAN from which all the surface cruise work was undertaken. They provided the professionalism and flexibility needed to be responsive to this measurement program. Tim Flynn (AMS) and his wife Barbara did their usual excellent job in helping to plan and conduct the AXBT surveys. They were always "on course and on station".

Several other scientists assisted this program in obtaining XBT data, which helped provide a clearer picture of the "setting" of the processes being measured. Dr. Victor Vidal of the Electrical Power Institute of Mexico cooperated by dropping XBT's during his several cruises covering much of the southern and western Gulf. Dr. Doug Biggs, TAMU, also dropped XBT's over "his corner of the ocean" in the northwest Gulf. Dr. George Forristall (Shell Oil) was cooperative with regards to eddy tracking and documentation. Finally, Dr. Jack Kalman of the Applied Physics Laboratory is thanked for supplying altimeter data. When these auxiliary data sets were grouped with other survey data taken during the study, the existence, location, and size of key features became apparent. Without this cooperative effort and the resulting composite surveys, our understanding of deep Gulf conditions would have been diminished.

Dr. Murray Brown, COTR for the Physical Oceanography Study, has provided continuing enthusiasm and energy. His support at MMS and his continuing efforts within the scientific community were fundamental to the success of these programs, and hence to the expanded knowledge base available to scientists and managers who are called upon to make important environmental decisions.

I. INTRODUCTION

1.1 Program Overview

In 1982, the Minerals Management Service (MMS) initiated a series of regional physical oceanographic field measurement programs in the Gulf of Mexico (GOM) (Figure 1.1-1) which have had as an objective the development of an improved documentation and understanding of important current patterns and processes. These insights are to be used to make informed management and operational decisions relating to offshore oil and gas activities.

Since its beginning, the overall program has emphasized three regions:

- west Florida shelf and slope as well as the adjacent Loop Current (LC) during Years 1, 2 and 4
- western Gulf with particular emphasis on the mid- to lower slope during Year 3, and
- north central Gulf from the inner shelf to the deep Gulf during Year 5.

The various data collected were used by program Principal Investigators to develop the desired oceanographic description and process characterization.

In recent years and in part as a direct result of these MMS-funded studies, circulation in the Gulf of Mexico has become increasingly well resolved. On the slope and in the deep Gulf, the first-order elements of circulation include the Loop Current which enters through the Yucatan Straits and exits via the Florida Straits (Figure 1.1-1). At intervals, which may range from four to 17 months, the top part of the Loop Current separates becoming a closed anticyclonic (clockwise circulating) eddy which drifts to the west, transporting considerable heat, salt and momentum.

Circulation over the continental slope and in the deeper Gulf is strongly influenced by the presence and location of LC eddies. Thus, a major component of the regional studies was to examine the local circulation and processes resulting from both the presence and absence of LC eddies and related features. It is apparent that documenting these large evolving features could not be accomplished with strictly a regional focus. As a consequence, each of the regional phases has had a basin-scale component which was to document and better understand LC-eddies as they changed during westward migration. Considering the eddy-shedding interval, this component also required a longer-term commitment.

Shelf circulation on the west Florida shelf and the west Louisiana/east Texas shelf was examined during two of the regional programs. These have produced substantial subsurface current data sets which are combined with concurrent ancillary data (wind velocity and water level) to describe primary circulation patterns on these shelves. The present report

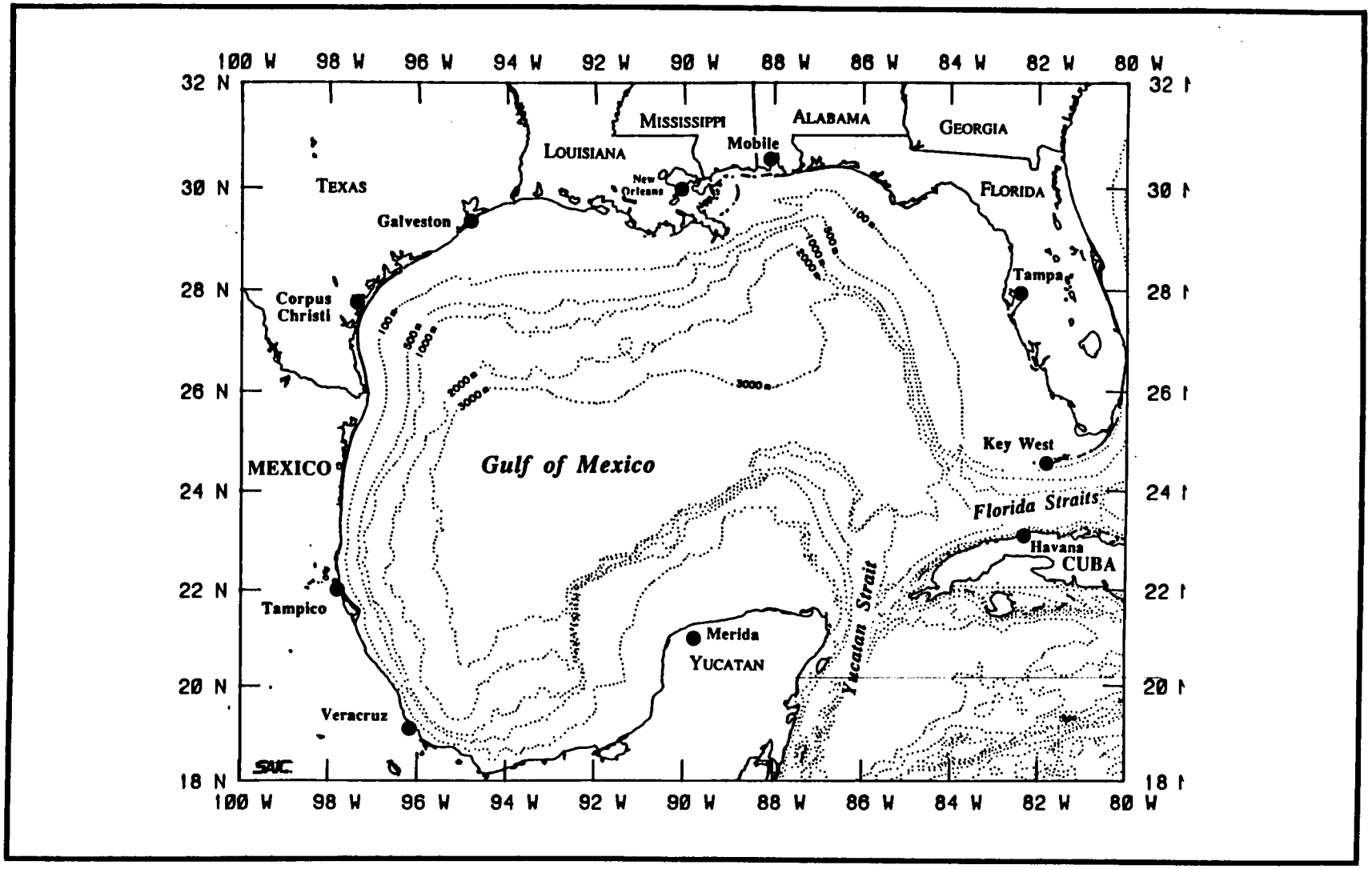

Figure 1.1-1. General Map of the Gulf of Mexico.

describes the activities, measurements and insights developed during Year 5 of the Gulf regional physical oceanographic studies.

1.2 Program Observations

Characterization of the regional conditions and circulation required access to an integrated and coordinated multivariate data set. During Year 5 this included

- Subsurface current velocity and temperature
- Regional and site-specific hydrographic, XBT and AXBT surveys
- Satellite thermal imagery
- GEOSAT altimetry
- Satellite-tracked Lagrangian drifters
- A suite of marine optical measurements

These data were supplemented with data obtained from the National Oceanic and Atmospheric Administration (NOAA), National Climatic Center (coastal wind data) and NOAA/National Ocean Data Center (NODC) [National Data Buoy Center (NDBC) buoy winds, Coastal Marine (C-MAN) winds and coastal water levels].

The survey data available to this program have been substantially enhanced by cooperative cruises conducted as part of the MMS Ship-of-Opportunity Program (SOOP). The SOOP effort had several components which included regular expendable bathythermograph (XBT) transects taken along standard lines from commercial vessels and "opportunistic" cooperative surveys with the Electrical Power Institute of Mexico (Dr. Victor Vidal) and Texas A & M University (TAMU) (Dr. Doug Biggs). In addition, several offshore oil and gas companies provided information regarding their observations and activities.

1.3 Program Principal Investigators and Primary Support Personnel

The various observations cited above have been used by the program's scientific principals:

Dr. T. Berger (SAIC)
Dr. D. Brooks (Texas A&M University)
Dr. P. Hamilton (SAIC)
Dr. N. Højerslev (University of Copenhagen)
Mr. F. Kelly (Texas A&M University)
Dr. W. Wiseman (Louisiana State University)

Primary technical and support personnel were provided by SAIC. Mr. R. Wayland worked with meteorological data and was program data manager. Mr. J. Singer was responsible for field activities and logistics. Dr. E. Waddell (SAIC) was Program Manager.

1.4 Report Organization

This report is structured to allow the reader ready access to specific information and levels of detail. In a separate volume, the Executive Summary provides a descriptive overview of the program content and key insights developed. Within this volume (Technical Volume) the content of the various chapters is structured to make available the level of detail which each reader may require.

- Chapter 1 provides an overview of this program and its relation to overall program objectives.

- Chapter 2 describes topics relating to data acquisition such as where, when, how, and how good.

- Chapter 3 describes important analyses which were applied to the observations. Because some of these techniques have been described in detail in prior reports, those will not be repeated but will be identified and the appropriate reference given.

- Chapter 4 provides a discussion of the data interpretation and synthesis. By separating this chapter from the previous sections, the reader can focus on insights without being diverted by other information.

II. DATA ACQUISITION

2.1 Introduction

Chapter II presents an overview of the extensive multivariate data set collected during the Gulf Year 5 program. The chapter objective is to provide a foundation by which the reader can understand technical details of measurements made during the program. Pre-analysis corrections or adjustments are identified and discussed. When such adjustments are similar or the same as undertaken during previous program years, the reader will be referred to detailed discussions in these earlier reports. The discussion will not be reproduced here. Reading this chapter will provide the reader with a good understanding of the data base available to the program principals. The chapter is also organized so that each of the primary data or measurement types is discussed separately. Data taken during the program will be submitted to the (NODC) and will be available from that source.

2.2 Lagrangian Drifters

The ARGOS drifter tracks available to the Year 5 program are summarized in Table 2.2-1. Eight of these drifters were provided through this MMS program while four data sets (Buoys 1392, 1396, 5837 and 5839) were from other sources. These latter drifter trajectories were provided by the Naval Oceanographic Research and Development Activity (NORDA) as part of an experimental drifter design program, and Continental Shelf Associates as part of an Environmental Protection Agency (EPA) contract.

The drifters were in a number of Gulf of Mexico (GOM) features including cyclonic as well as anticyclonic eddies. Drifter 3379 was originally in an anticyclonic eddy called Eddy C (Lewis et al., 1989). However, it also became entrained in a cyclonic flow field in the Bay of Campeche. Drifter 3352 was placed in a subsequent anticyclonic ring, Eddy D, which was also tracked by Drifter 7234. Drifters 5837 and 5839 were caught in the peripheral flow field of Eddy D. Eddy E, was tracked by Drifters 3348, 3344 and 3353, and Eddy F was tracked by Drifters 3345 and 3347. Table 2.2-2 summarizes the features seen by each drifter.

2.3 Hydrography

2.3.1 Introduction

Vertical temperature data were collected during eight mooring servicing cruises, three ARGOS drifter deployment surveys, two AXBT surveys, and sixty-one Ship-of-Opportunity cruises as part of the Year 5 effort. These data, combined with other types of data (i.e., thermal imagery, GEOSAT altimetry, currents and inverted echo sounder (IES) data, etc.) are considered vital to developing a better understanding of the processes and dynamics of the circulation of the region. Additional information collected during some, but not all, of the mooring servicing cruises included conductivity temperature depth (CTD) salinity, oxygen, optics and suspended solids data. A more detailed discussion of the different data sets follows.

Table 2.2-1. ARGOS buoys tracked during Year 5.

SN	Date Deployed (GMT)	Deployment Location		Description	Deployment Vessel(Vessel Funding)	Date Left Eddy (GMT)	End of Drifting Data (GMT)	Comments
3379	03/07/86	25°11.9'N	90°00.8'W	FRL-TOD with 200m weighted thermistor string.	M/V ERICA (MMS) Cruise ER8601	~09/16/86	01/22/87	1
3352	01/14/87	25°28.9'N	91°25.8'W	FRL Mini-TOD with 100m tether and mini window shade drogue.	R/V PELICAN (MMS) Cruise PN8711	04/01/87	06/11/87	2
7234	04/14/87	26°09.3'N	93°29.6'W	Horizon FHD-B with 50m tether and holey sock drogue.	R/V GYRE (TAMU - Biggs) Cruise 87G04	06/05/87	11/27/87	3
5837	05/12/87	26°38.8'N	93°38.6'W	Draper LCD with 1m tether and 2km holey sock drogue.	OSV PETER W. ANDERSON (EPA)	NA	09/09/87	4
5839	05/12/87	26°39.0'N	93°38.5'W	Draper LCD with 60m tether and 36m holey sock drogue.	OSV PETER W. ANDERSON (EPA)	NA	09/25/87	5
3348	09/10/87	25°46.0'N	87°01.0'W	Triton Mini-D with 50m line drogue.	M/V THUNDER UNIVERSE (Shell Development Corp.)	10/13/87	10/13/87	6
3344	11/08/87	25°20.0'N	88°28.1'W	FRL Mini-TOD with 100m tether and mini window shade drogue.	R/V SEAWARD EXPLORER (MMS) Cruise SE8729	03/20/88	~05/20/88	7
1392	02/09/88	29°36.0'N	87°18.0'W	NORDA experimental buoy with 100m tether & cylinder drogue.	Air deployed (NORDA)	NA	03/18/88	8
1396	02/10/88	29°36.0'N	87°24.0'W	NORDA experimental buoy with 100m tether & cylinder drogue.	Air Deployed (NORDA)	NA	03/12/88	9
3353	04/10/88	24°30.1'N	92°11.8'W	FRL Mini-TOD with 100m tether and mini window shade drogue.	R/V PELICAN (MMS) Cruise PN8823	09/16/88	12/31/88*	10
3345	05/16/88	26°30.1'N	86°29.8'W	FRL Mini-TOD with 100m tether and mini window shade drogue.	M/V LORETTA J (Marathon Oil Company)	NA	12/31/88*	11
3347	10/20/88	24°39.8'N	92°27.5'W	ORE Torpedo with 100m tether and window shade drogue.	R/V PELICAN (MMS) Cruise PN8911	NA	12/31/88*	12

* Continued to transmit useful data beyond this date.

1 Buoy 3379 was deployed in an anticyclonic eddy (Eddy C) studied during the Year 3 program. It left the eddy around 09/16/86, made a cyclonic loop through the Bay of Campeche, returning to Eddy C in early December 1986 and left again in late January 1987. The buoy was apparently recovered by a ship around 03/30/87 near 92°30'W in the Bay of Campeche and transported south into a Mexican port.

2 Buoy 3352 was deployed in an old anticyclonic eddy. It left the eddy around 04/01/87 and later ran aground near 20°30'N in the western Gulf of Mexico.

3 Buoy 7234 was deployed in the same old anticyclonic eddy as Buoy 3352. It left the eddy around 06/05/87 and later gave its last data while drifting in the western Gulf of Mexico. The data from this buoy were erratic, possibly due to a defective transmitter.

4 Buoy 5837 available data begin 06/11/87 when it was northeast of the anticyclonic ring in which MMS Buoy 7234 had been deployed. It remained nearly stationary for eight to 10 days before drifting to the northwest and then to the south. Data became 'noisy' after July 8 as the buoy was programmed to transmit only once per day after this date. Buoy ran aground near 25°36.6'N, 97°13.2'W around 09/09/87.

5 Buoy 5839 available data begin 06/10/87 when it was northeast of the anticyclonic ring in which MMS Buoy 7234 had been deployed. It immediately began a series of cyclonic loops while drifting to the south. Data became 'noisy' after July 8 as the buoy was programmed to transmit only once per day after this date. Buoy was picked up by a fishing vessel on 09/25/87.

6 Buoy 3348 was deployed in a new anticyclonic eddy. It ceased transmitting on 10/13/87 as a minor hurricane passed nearby.

7 Buoy 3344 was deployed in the same anticyclonic eddy as Buoy 3348 had been. It left the ring around 03/20/88 and later ran aground near 24°30'N in the western Gulf of Mexico.

8 Buoy 1392 was deployed in the northeastern Gulf of Mexico as an experimental test of its operation and performance. No specific oceanic feature was targeted. It was recovered after three weeks.

9 Buoy 1396 was deployed in the northeastern Gulf of Mexico as an experimental test of its operation and performance. No specific oceanic feature was targeted. It was recovered after three weeks.

10 Buoy 3353 was to be deployed in the same anticyclonic eddy as Buoys 3348 and 3344 had been. It is not clear that this was achieved. It left its eddy on 09/16/88 and drifted northward following the passage of Hurricane Gilbert to its south.

11 Buoy 3345 was deployed in a new anticyclonic eddy.

12 Buoy 3347 was deployed in the same anticyclonic eddy as Buoy 3345.

Table 2.2-2. Drifters and their associated oceanographic features.

Argos Drifter ID	Feature(s)
3379	Eddy C, Bay of Campeche cyclone
3352	Eddy D
7234	Eddy D, mid-Gulf cyclone
5837	Cyclones associated with Eddy D
5839	Cyclones associated with Eddy D
3348	Eddy E
3344	Eddy E
3353	Eddy E, shelf break cyclones and anticylones
3345	Eddy F
3347	Eddy F

2.3.2 Mooring Servicing Cruises

2.3.2.1 Introduction

Between April 2, 1987 and November 2, 1988, nine mooring related cruises along 92°W longitude were completed aboard the R/V PELICAN. Of these, eight included collection of CTD and/or XBT data and seven included suspended sediment samples at the shelf mooring sites opposite the in-situ transmissometer levels. On three of the cruises, an extensive suite of optical measurements was made, details of which are discussed in Section 2.4. Table 2.3-1 summarizes the cruises and the data obtained. Figure 2.3-1(a-k) shows the station locations and Table 2.3-2 gives a station summary for each of the eight hydrographic cruises conducted during the program. Station spacing was generally on the order of five nautical miles (NM) on the shelf out to the 200 m isobath and then widened to 10 NM offshore.

2.3.2.2 Hydrographic Equipment and Sampling Procedures

During each of the CTD supported cruises a CTD sensor package and a General Oceanics, Inc. Model 1015 Mark V Rosette Multi-Bottle Sampler were used. The Sampler was equipped with 12 ten-liter Niskin bottles, two of which were outfitted with reversing thermometer racks. Each rack contained two protected and one unprotected reversing thermometer.

The data acquisition equipment consisted of a Neil Brown Mark IIIB CTD system and two different SeaBird Model SBE-9 CTD systems, one belonging to Louisiana Universities Marine Consortium (LUMCON) and a second belonging to Texas A&M University (TAMU). The LUMCON CTD fish was employed only for shelf cruises, and the TAMU fish for deep (3000 m +) profiles at the two IES sites. The Neil Brown system was used for two cruises extending into the offshelf area. Specifications for both the Neil Brown and SeaBird systems are presented in Table 2.3-3.

Table 2.3-1. Cruise listing and sampling totals for mooring servicing cruises along 92° W longitude.

Cruise ID	Dates	CTD Casts	XBT Casts	Salinity Samples	Dissolved Oxygen Samples	Suspended Solids Samples	Optics**
PN8713	April 2 - 10, 1987	24	41	38	186	0	0
PN8715	April 24 - 27, 1987	16	2	15	75	9	5
PN8803	July 14 - 18, 1987	11	4	11	53	7	0
PN8814	Nov. 4 - 17, 1987	12	45	15	27	15	0
PN8820	Feb. 6 - 11, 1988	17	0	16	58	14	5
PN8823*	April 7 - 15, 1988	0	57	0	0	4	0
PN8826	May 3 - 5, 1988	0	0	0	0	4	0
PN8903	July 18 - 22, 1988	17	0	17	76	11	11
PN8913	Oct. 28 - Nov. 2, 1988	0	32	0	0	0	0

* Cruise also included ARGOS drifter deployment for Buoy 3353.
** Optical measurements included all or some of the following:

- color index
- downward irradiance
- quanta irradiance
- light scattering
- light transmission
- fluorescence
- Secchi disk

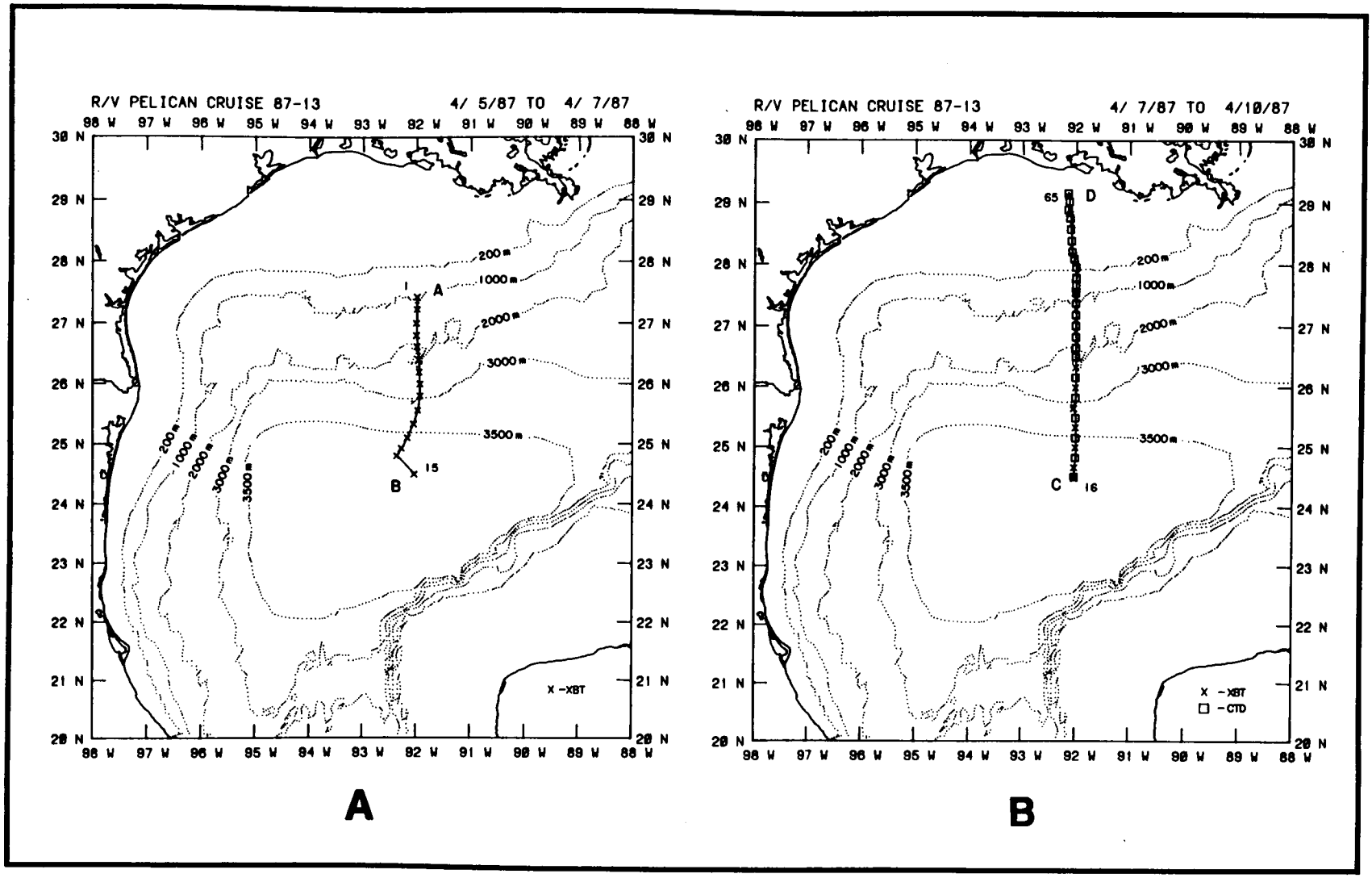

Figure 2.3-1a,b. Cruise track and station locations for R/V PELICAN Cruise PN8713 for (a) Section A-B and (b) Section C-D.

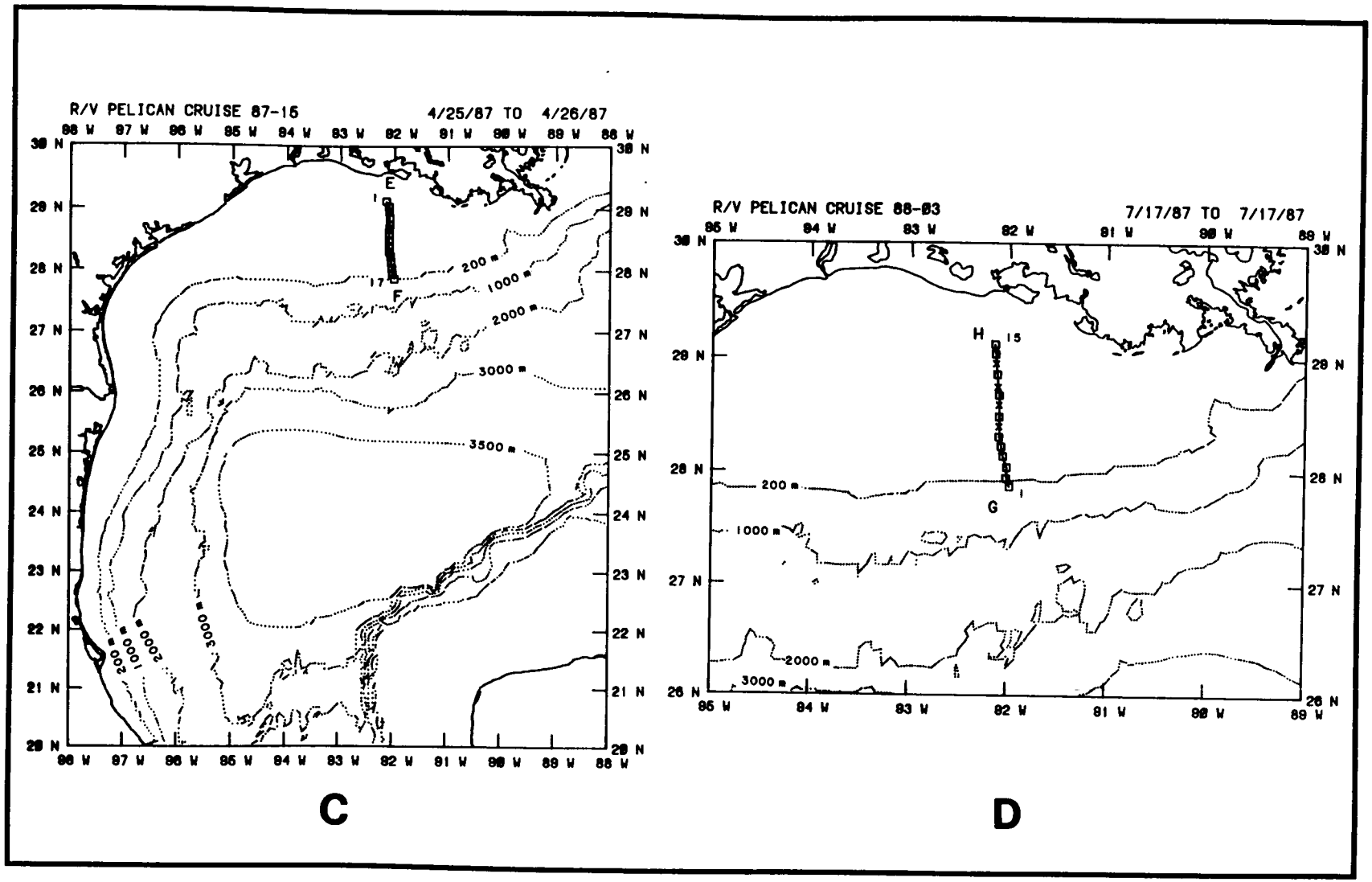

Figure 2.3-1c,d. Cruise track and station locations for R/V PELICAN Cruise (c) PN8715 (Section E-F) and (d) PN8803 (Section G-H). Boxes are CTD casts and X's are XBT drops.

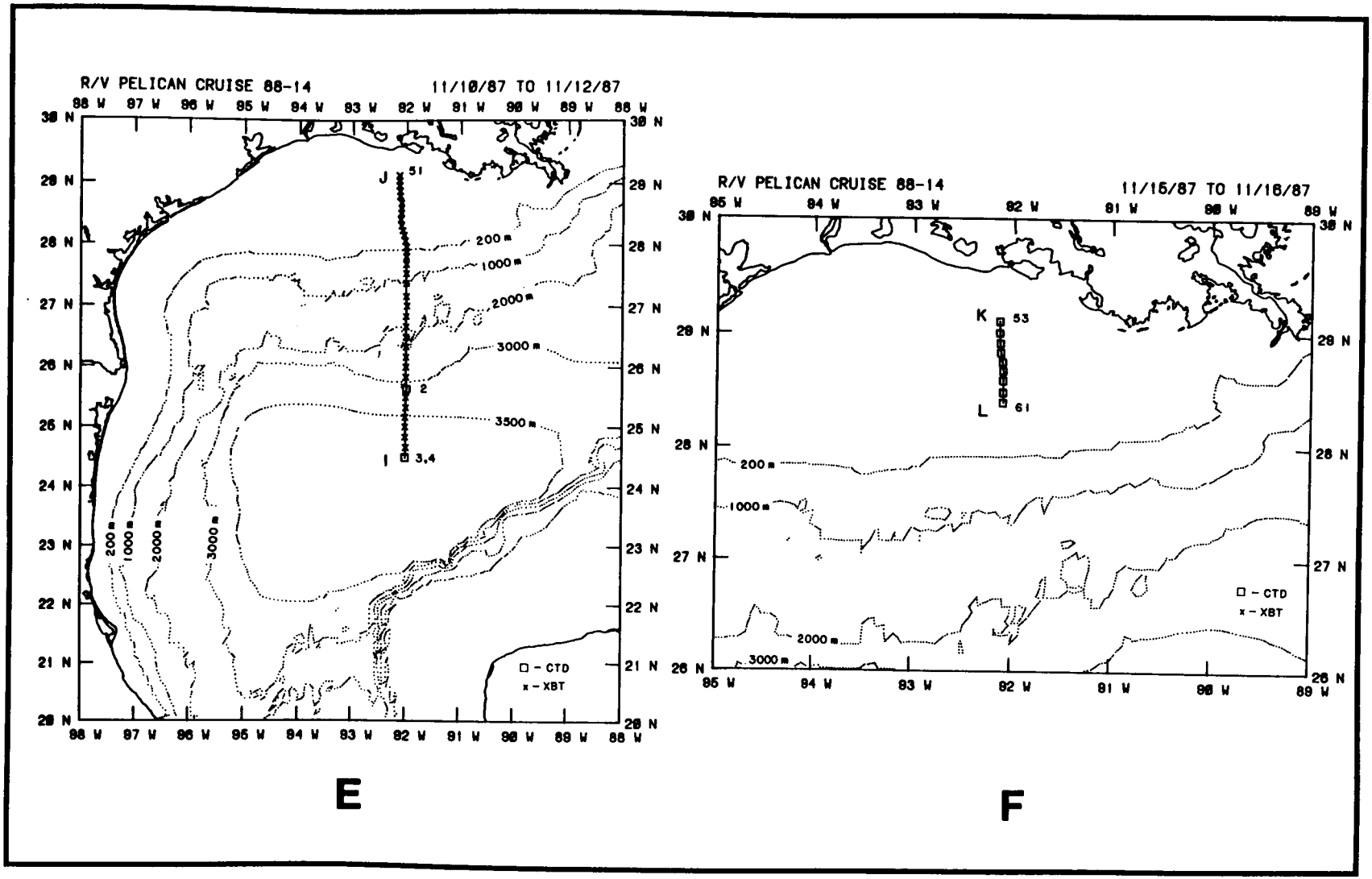

Figure 2.3-1e,f. Cruise track and station locations for R/V PELICAN Cruise PN8814 for (e) Section I-J and (f) Section K-L.

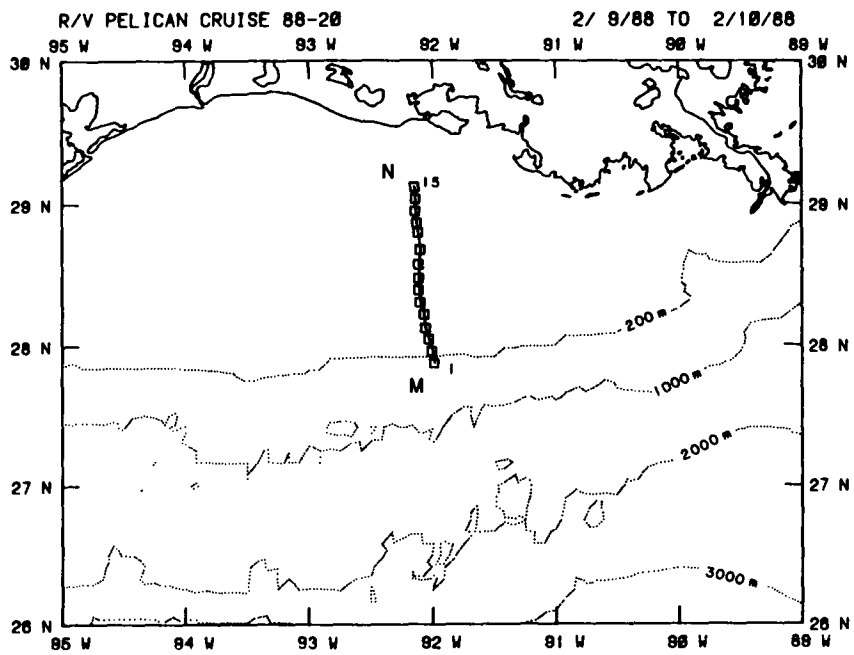

G

Figure 2.3-1g. Cruise track and station locations for R/V PELICAN Cruise PN8820 (Section M-N). Boxes are CTD casts.

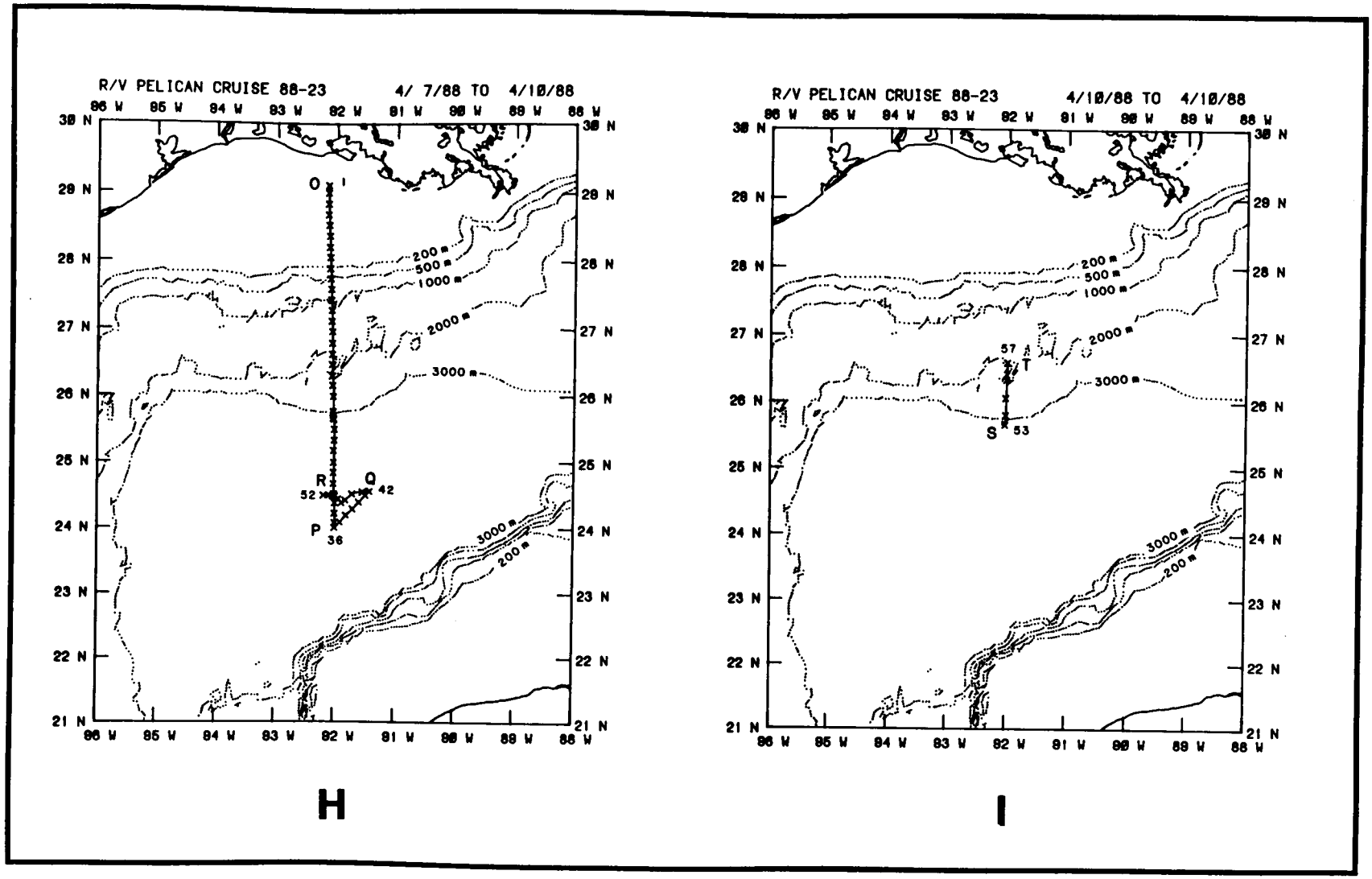

Figure 2.3-1h,i. Cruise track and station locations for R/V PELICAN Cruise PN8823 for (h) Sections O-P, P-Q and Q-R; and (i) Section S-T. X's are XBT drops.

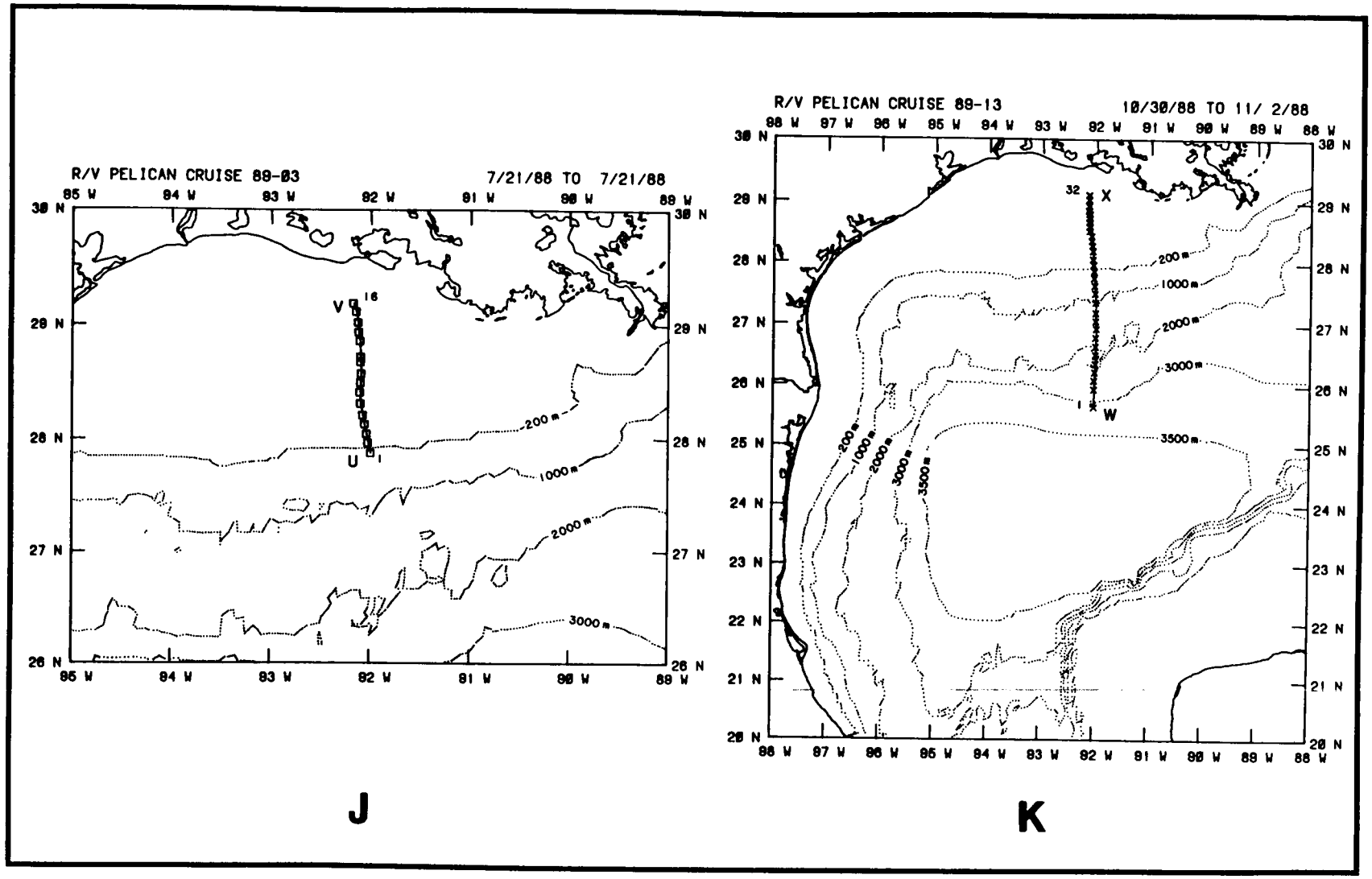

Figure 2.3-1j,k. Cruise track and station location for R/V PELICAN Cruise (j) PN8903 (Section U-V) and (k) PN8913 (Section W-X). Boxes are CTD casts and X's are XBT drops.

Table 2.3-2. Station sequences for individual hydrographic cruise sections.

Cruise ID	Section Name	Station Sequence
PN8713	A-B	1X,2X,3X,4X,5X,6X,7X,8X,9X,10X,11X,12X,13X, 14X,15X
PN8713	C-D	16C(17X),18X,19C,20X,21C,22X,23C,24X(25X), 26C,27X,28C,29X,30C,31C,32X,33C,34X,35C,36X, 37C,38X,39C,40X,41C(42X,43X,44X,45X),46C, 47X,48X,49C,50X,51C,52X,53C,54X,55C,56X,57C, 58X,59C,60X,61C,62X,63C,64X,65C
PN8715	E-F	1C,2C,3C(4X,5X),6C,7C,8C,9C,10C,11C,12C,13C, 14C,15C,16C,17C,18C
PN8803	G-H	1C,2C,3C,4C,5C,6C,7X,8C,9X,10C,11X,12C,13X, 14C,15C
PN8814	I-J	3C(4C),5X,6X,7X(8X),9X,10X(11X),12X,2C(13X, 14X),15X,16X(17X),18X,19X(20X),21X,22X(23X), 25X,26X(27X),28X(29X),30X(31X),32X,33X(34X), 35X,36X,37X,38X,40X,41X,42X,43X,44X,45X,46X, 47X,48X,49X,50X,51X
PN8814	K-L	53C,54C,55C,56C,57C,58C,59C,60C,61C
PN8820	M-N	1C,2C,3C,4C,5C,6C,7C,8C,9C,10C,11C,12C,13C, 14C,15C
PN8823	O-P	1X,2X,3X,4X,5X,6X,7X,8X,9X,10X,11X,12X,13X, 14X,15X,16X,17X,18X,19X,20X,21X,22X,23X,24X, 25X,26X,27X,28X,29X,30X,31X,32X,33X,34X,35X, 336X
PN8823	P-Q	36X,37X,38X,39X,40X,41X,42X
PN8823	Q-R	42X,43X,44X,49X,50X,51X,52X
PN8823	S-T	53X,54X,55X,56X,57X
PN8903	U-V	1C,2C,3C,4C,5C,6C,7C,8C,9C,10C,11C,12C,13C, 14C,15C,16C
PN8913	W-X	1X,2X,3X,4X,5X,6X,7X,8X,9X,10X,11X,12X,13X, 14X,15X,16X,17X,18X,19X,20X,21X,22X,23X,32X, 31X,30X,29X,28X,27X,26X,25X,24X

Table 2.3-3. Specifications of the Neil Brown Mark IIIB and Sea-Bird SBE-9 CTD Systems.

	Conductivity		*Temperature*		*Pressure*	
	Mark IIIB	SBE-9	Mark IIIB	SBE-9	Mark IIIB	SBE-9
Accuracy: (mmho/cm, °C, %FS)	±0.005	±0.01	±0.005	±0.01	±0.1	±0.1
Resolution: (mmho/cm, °C, %FS)	0.001	0.0004	0.0005	0.0003	0.0015	0.0004
Response Time: (msec at 1m/sec drop rate)	40	70	30	70	1	1
Range; (mmho/cm, °C, db)	1-65	0-70	-3 to +32	-5 to +35	0-1600	0-600*

* A second 0-6000 db instrument was also used during this program.
%FS = Percent of Full Scale.

The operation and makeup of the Neil Brown system has been previously described in SAIC (1988) and is not repeated here. A description of the SeaBird system follows: This system digitized CTD data in its underwater unit and transmitted it to an SBE-11 Deck Unit. The deck unit then decoded the data and passed it to a COMPAQ portable computer with 256k memory, a double-sided, double-density disk drive and a 10 megabyte Bernoulli cartridge. Software converted the data to engineering units for display on a video monitor and for output to an EPSON Dot Matrix Printer. As a backup, a SONY audio cassette recorder stored all raw data.

During XBT data acquisition, a Sippican Mk-9 digital XBT system was used. It was controlled by an HP-85B computer and was equipped with an LM-3A hand-held launcher and 100 feet of cable. Data were stored on SCOTCH data cartridges.

Sampling procedures for CTD and XBT data acquisition, bottle salinity and dissolved oxygen sampling were as described in SAIC (1988). For suspended solids analysis large volumes (2 to 10 liters) of water were drawn from Niskin bottles into polyethylene jugs from which known volumes were taken and filtered through pre-weighed 0.3 um glass microfiber filters. The filters were then stored for drying and analysis on shore. Optical measurements were made as described in Section 2.4

2.3.3 ARGOS Drifter Deployment Surveys

Three MMS-funded XBT surveys dedicated solely to ARGOS drifter deployments in eddys are listed in Table 2.3-4. On each occasion, T-7 (760 m) XBT's were dropped at approximately 10 NM intervals using the XBT system described above in Section 2.3.2.2. Figure 2.3-2(a-c) shows the cruise tracks for these cruises.

Table 2.3-4. Dedicated MMS-sponsored ARGOS drifter deployment cruises supported with T-7 (760 m) XBT drops.

Ship	Dates	Cruise ID	No. XBT's	Drifter SN
PELICAN	01/13/87 - 01/14/87	PN8711	27	3352
SEAWARD EXPLORER	11/03/87 - 11/10/87	SE8729	53	3344
PELICAN	10/18/88 - 10/22/88	PN8911	44	3347

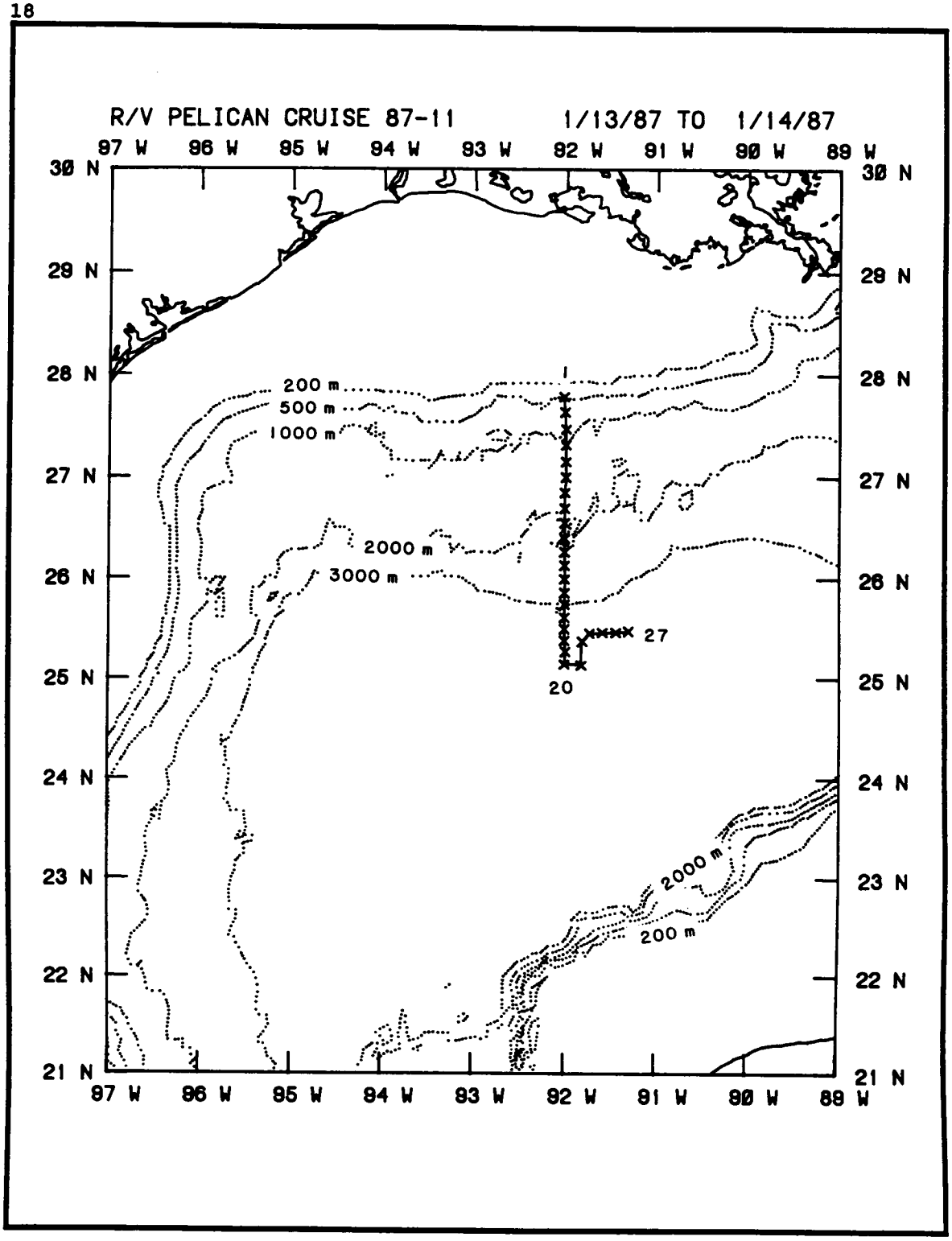

Figure 2.3-2a. Cruise track for dedicated ARGOS drifter deployment cruise for the R/V PELICAN on January 13-14, 1987.

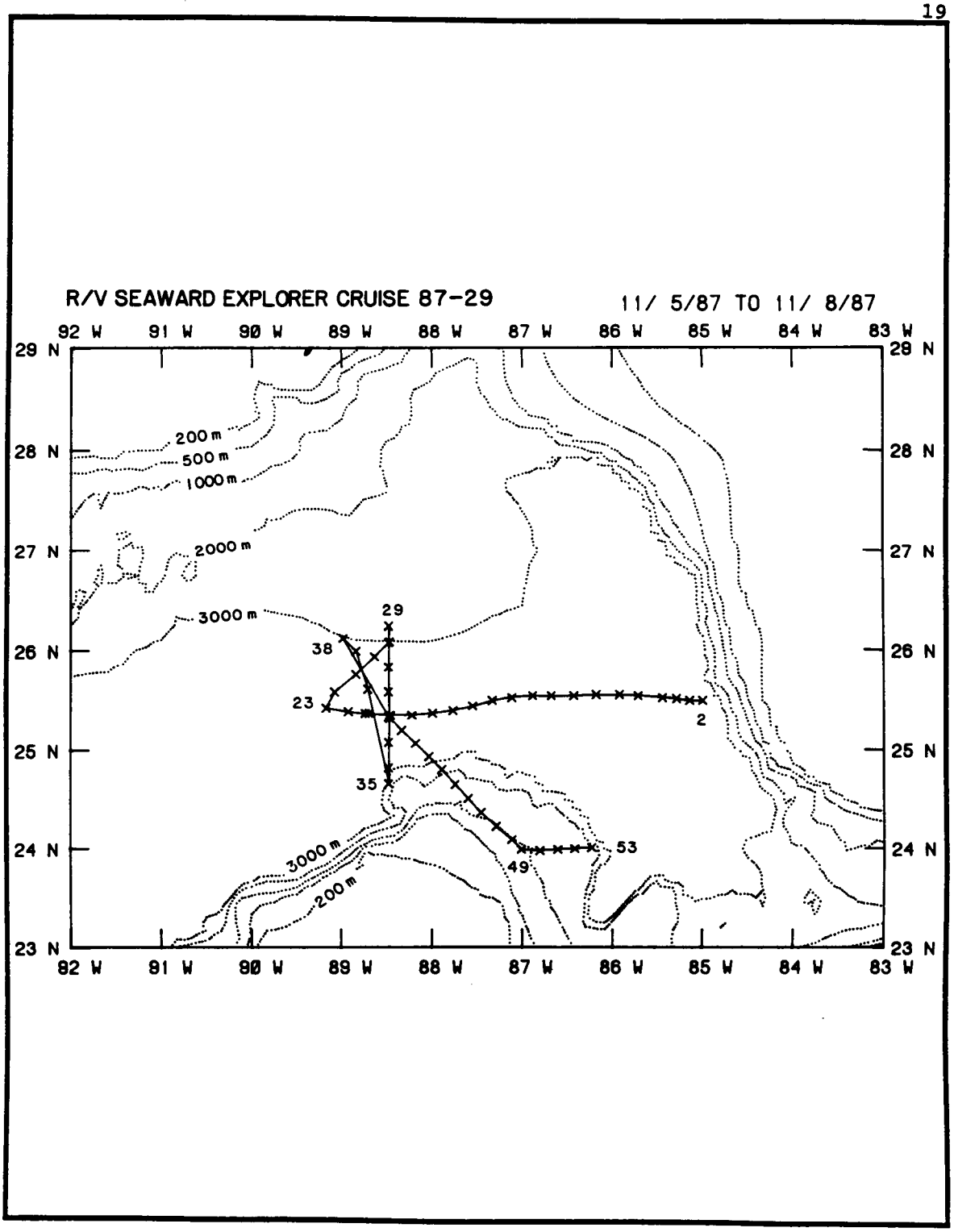

Figure 2.3-2b. Cruise track for dedicated ARGOS drifter deployment cruise for the R/V SEAWARD EXPLORER on November 3-10, 1987.

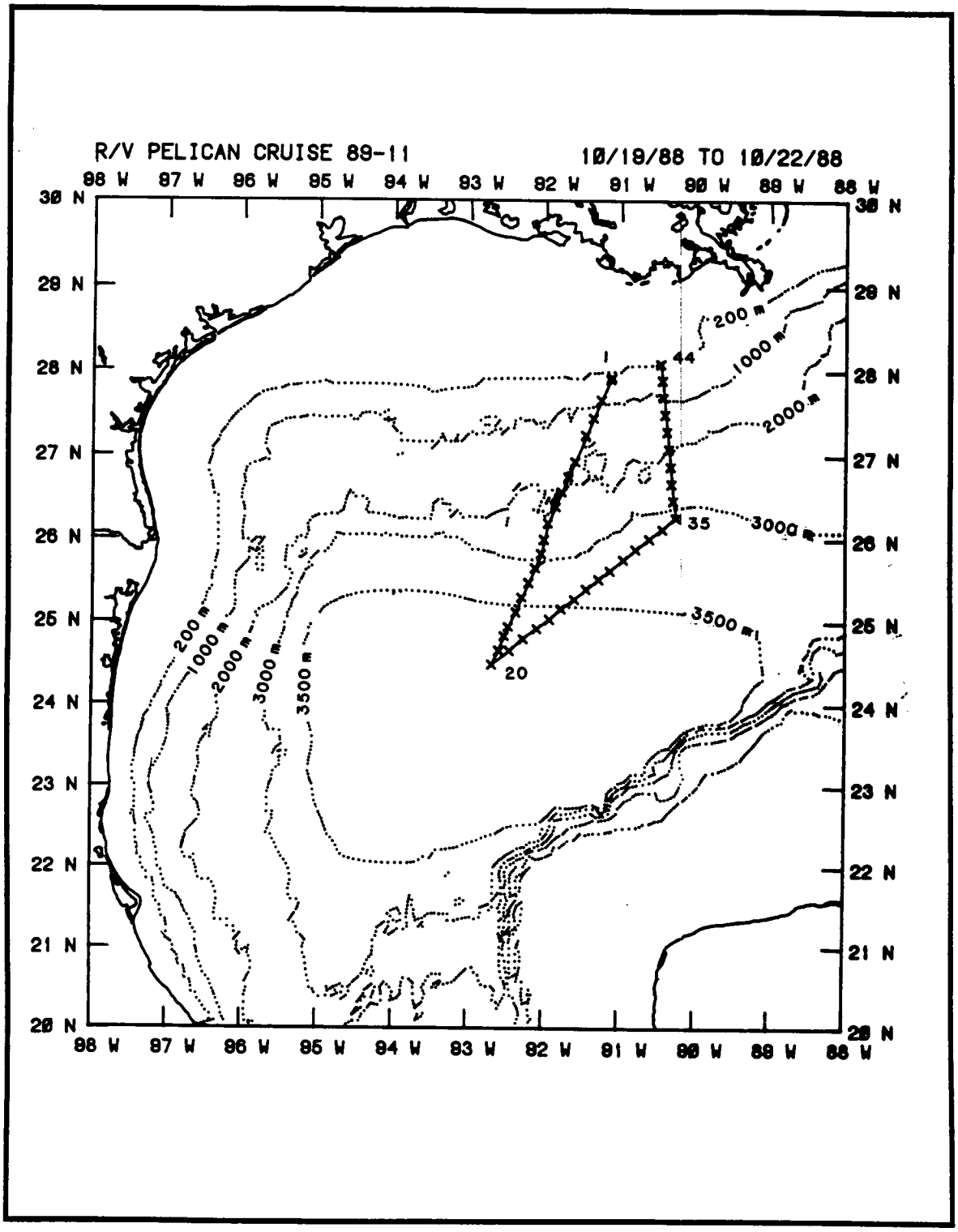

Figure 2.3-2c. Cruise track for dedicated ARGOS drifter deployment cruise for the R/V PELICAN on October 18-22, 1988.

2.3.4 Aerial XBT (AXBT) Surveys

Two AXBT surveys were made, one between July 31 and August 3, 1988, and a second between October 19 and 22, 1988. Both surveys were of the same eddy feature containing ARGOS Drifter 3345 as it migrated towards the western Gulf of Mexico. All of the AXBT's were 760 meter probes, and each survey consisted of 100 probes. However, due to probe failures (11 on the initial survey and 14 on the latter survey) during launch or in the water, the overall data return for both aerial XBT surveys was 87.5%.

The sampling plan was different from that utilized earlier in the Year 3 program (SAIC, 1988). This time, instead of a star pattern about the center of the eddy, the AXBT's were deployed along north northwest to south southeast running GEOSAT lines (see Figure 2.3-3a,b). In addition, the surveys were timed to coincide along one or two of these lines with the passage of a GEOSAT satellite overhead. In particular, lines passing through the eddy centers satisfied these criteria. Along line station spacing was on the order of 10 to 20 NM during the initial survey and 15 NM during the second.

The plane, on-board equipment and personnel were provided by Aero Marine Surveys (AMS). The data aquisition equipment were redundant in positioning, receiving and recording capability and were specifically configured for AXBT data collection. Field procedures were similar to those reported in SAIC (1988) except that the first flight originated from New Orleans, La., and the second from Galveston, Texas.

2.3.5 Ship-of-Opportunity (SOOP) Cruises

As part of the Year 5 effort, the SOOP XBT program continued much as it had during Years 1 through 4 [see SAIC (1986, 1987 and 1988)]. This included continuation of the NMFS/MMS funded E.M. QUEENY cruises from approximately 27.0°N, 90.0°W to 24.5°N, 83.5°W; the MMS Crowley Caribbean Transport (formerly Coordinated Caribbean Transport) cruises running from Lake Charles, La. to the Yucatan Straits; and other irregularly timed opportunistic cruises passing through the Gulf of Mexico. In particular, on three occasions during this period extensive surveys of the western and central Gulf of Mexico were obtained through coordination with a Mexican research vessel, the JUSTO SIERRA. Sampling distances varied significantly from these sources, though during the QUEENY and CCT cruises probes were deployed hourly while the vessels steamed through the area. Almost all of the data were collected using T-7 (760 m) XBT probes and either a Sippican Mk9 or BathySystems SA810 digitizer and an LM-3A handheld launcher. Tables 2.3-5 and 2.3-6 summarize these data and begin October 1, 1986 where earlier reports [SAIC (1987 and 1988)] left off. Vertical section plots of almost all of the data identified in these tables are presented in Brown et al., (1989). Examples of the tracks for the two main SOOP sections and the standard data products produced are presented in Figures 2.3-4, and 2.3-5 and 2.3-6, respectively. Examples of the GYRE and JUSTO SIERRA cruise tracks are presented in Figures 2.3-7 and 2.3-8.

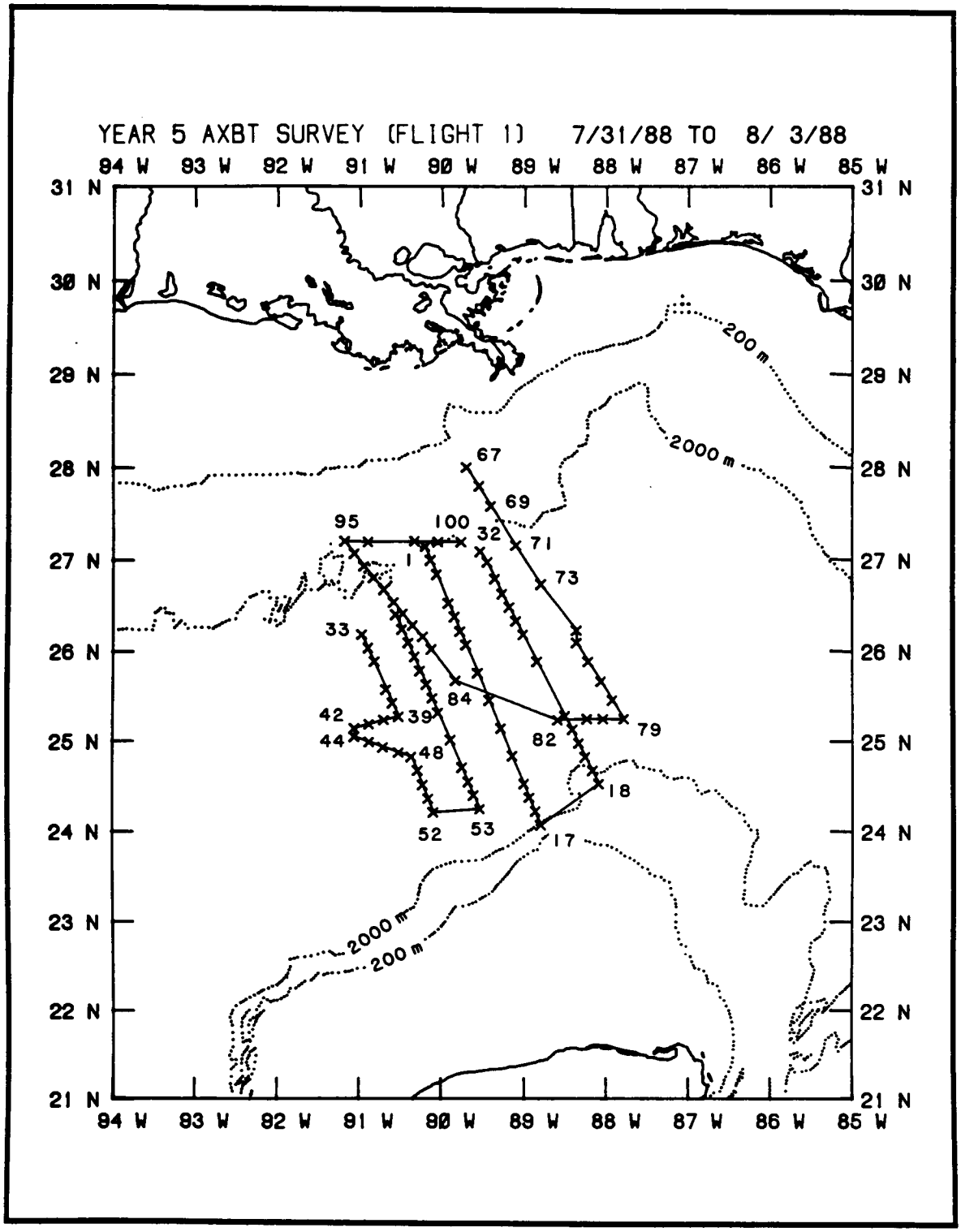

Figure 2.3-3a. Flight track for aerial XBT survey during the Year 5 program for the period of July 31 to August 3, 1988.

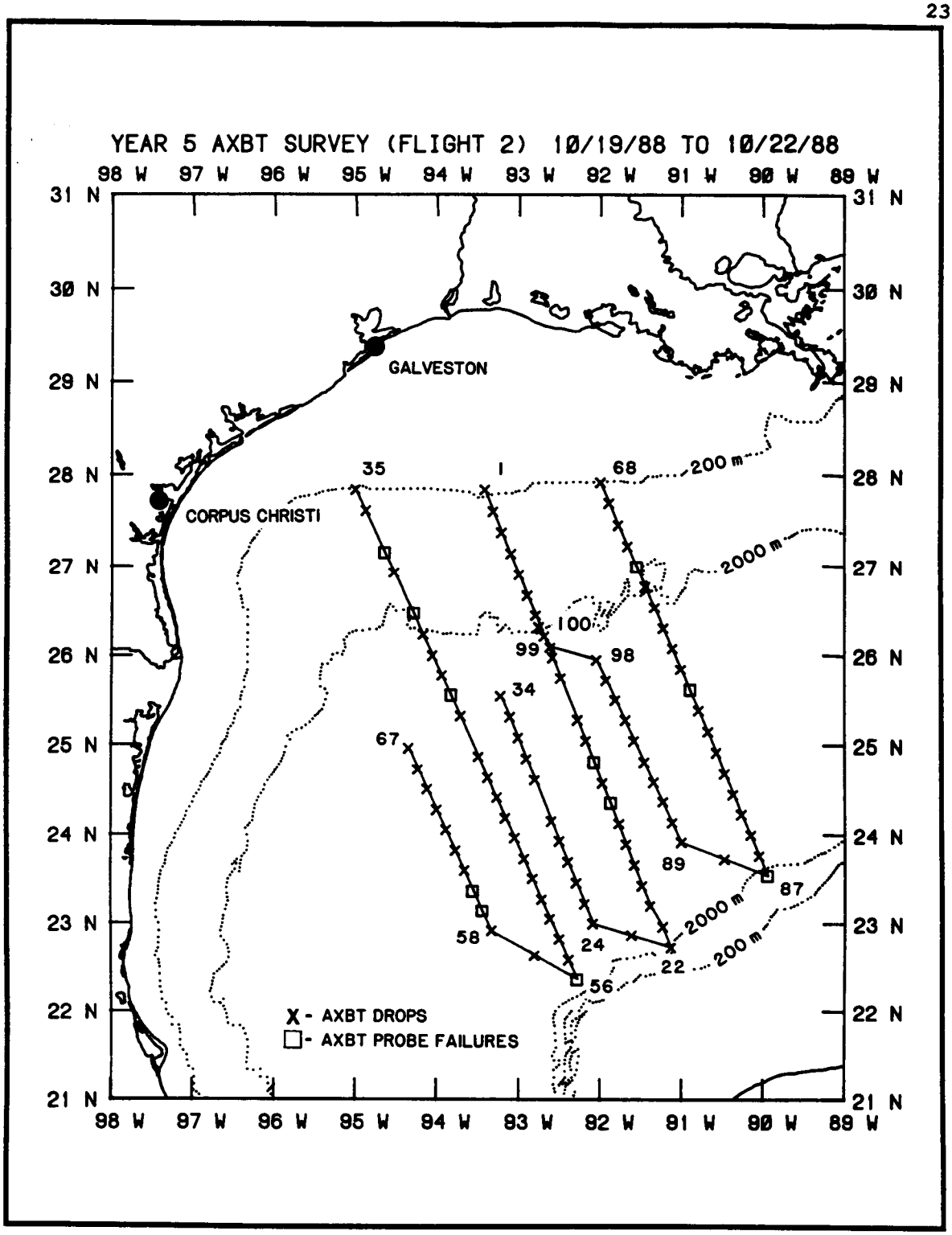

Figure 2.3-3b. Flight track for aerial XBT survey during the Year 5 program for the period of October 19-22, 1988.

Table 2.3-5. Regular MMS-supported T-7 Ship-of-Opportunity XBT sections from October 1, 1986 to the end of data on March 26, 1988.

Section	Ship	Date	No. Trips
I*	SENATOR	10/13/86 - 11/11/87	34
I	AMBASSADOR	01/12/88 - 03/26/88	5
II**	E. M. QUEENY	10/26/86 - 06/13/87	12

* MMS section from Lake Charles, La. to the Yucatan Straits.
** NMFS section from 27.0°N 90.0°W to 24.5°N 83.5°W.

Table 2.3-6. Non regular MMS-supported Ship-of-Opportunity T-7 XBT data sets in the Gulf of Mexico from October 1, 1986 through October 30, 1988.

Ship	Dates	Cruise ID	No. XBT's
SUNCOASTER	03/13/87 - 03/17/87	SC8705	24
GYRE	04/02/87 - 04/02/87	87G03	11
GYRE*	04/12/87 - 04/17/87	87G04	23
JUSTO SIERRA**	05/03/87 - 06/11/87	JS8701	117
SUNCOASTER	09/24/87 - 09/29/87	SC8720	21
JUSTO SIERRA	10/14/87 - 11/16/87	JS8702	139
GYRE	10/27/87 - 10/28/87	87G10	6
GYRE	11/17/87 - 11/24/87	87G11	16
JUSTO SIERRA	07/05/88 - 07/26/88	JS8801	140
GYRE	10/15/88 - 10/23/88	88G05	15

* Cruise also included ARGOS drifter deployment for Buoy 7234.
** Data from T-6 (460 m) probes.

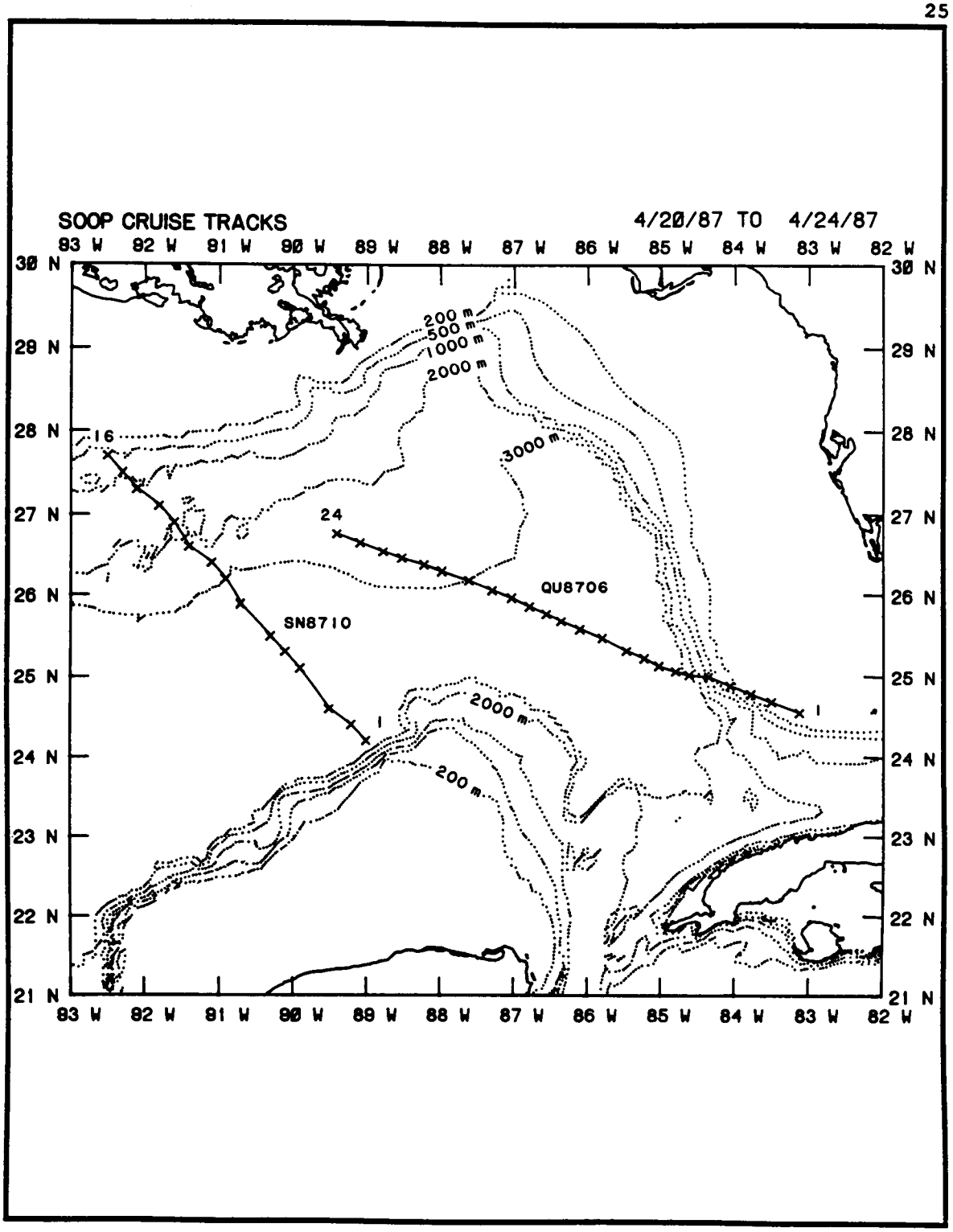

Figure 2.3-4. Examples of cruise tracks for the two primary Ship-of-Opportunity sections during the Year 5 program.

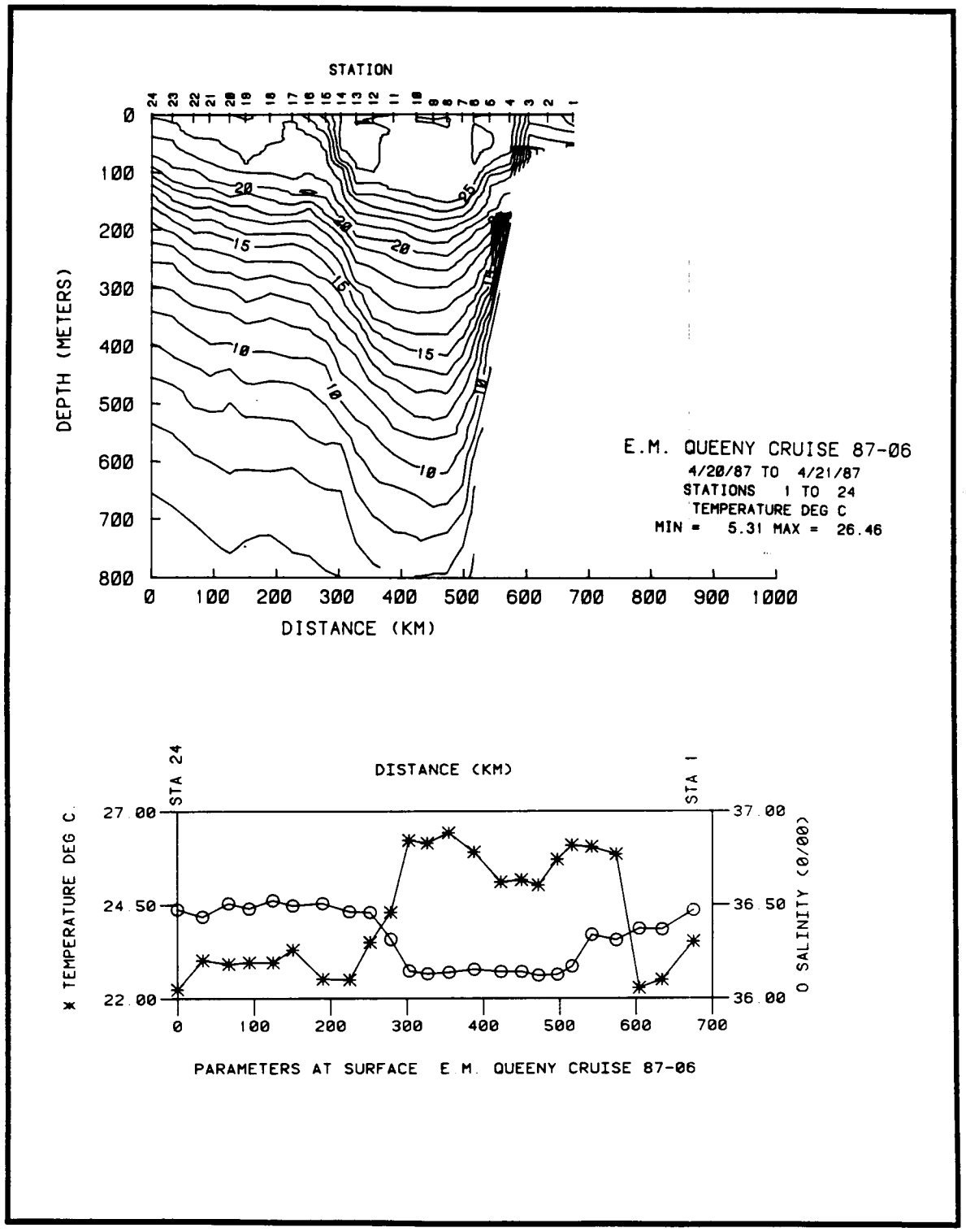

Figure 2.3-5. Examples of standard data products produced for the NMFS E.M. QUEENY Ship-of-Opportunity section (Note the Loop Current at Stations 4 to 16).

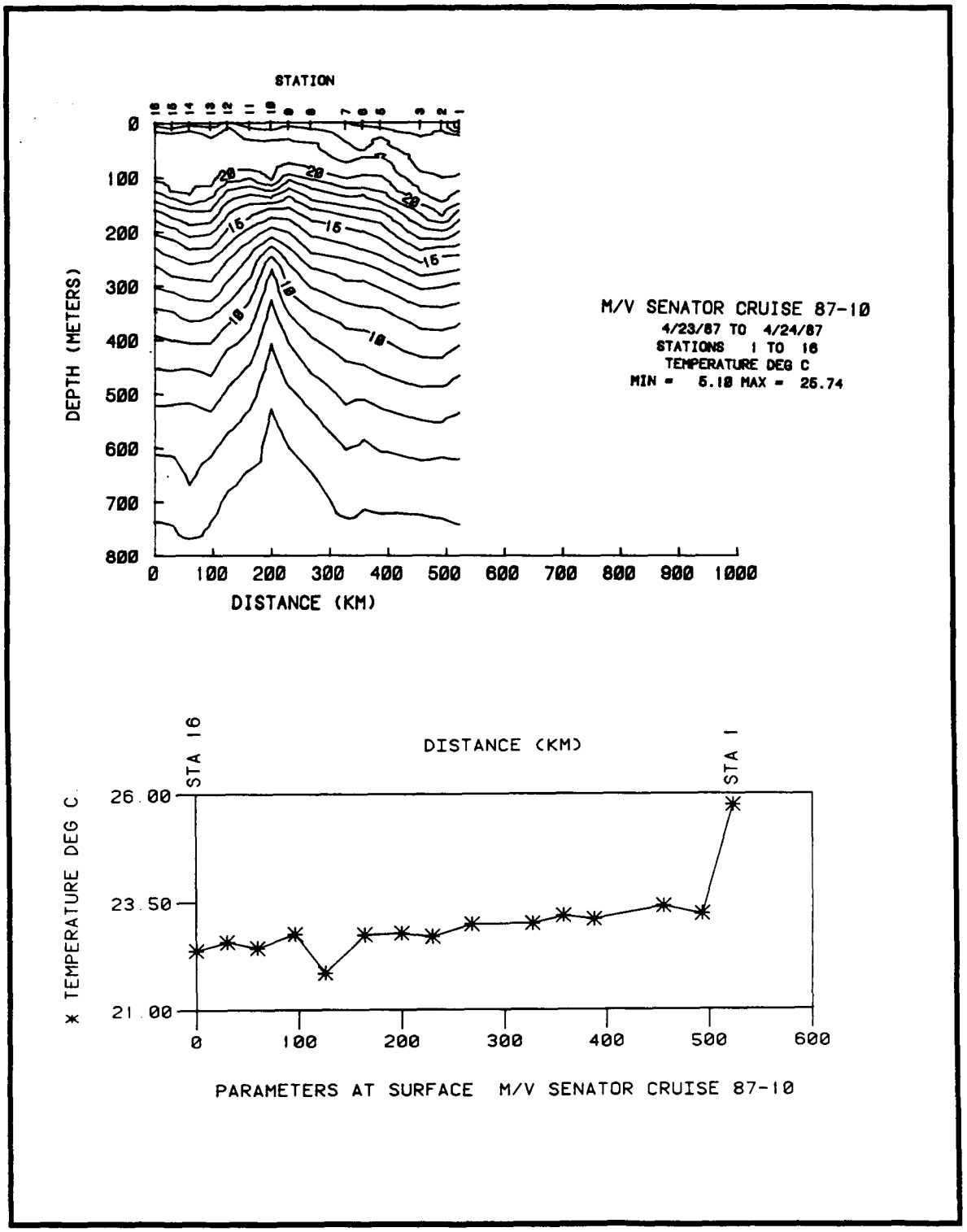

Figure 2.3-6. Examples of standard data products produced for the M/V SENATOR MMS Ship-of-Opportunity section (Note the cold eddy at Station 10).

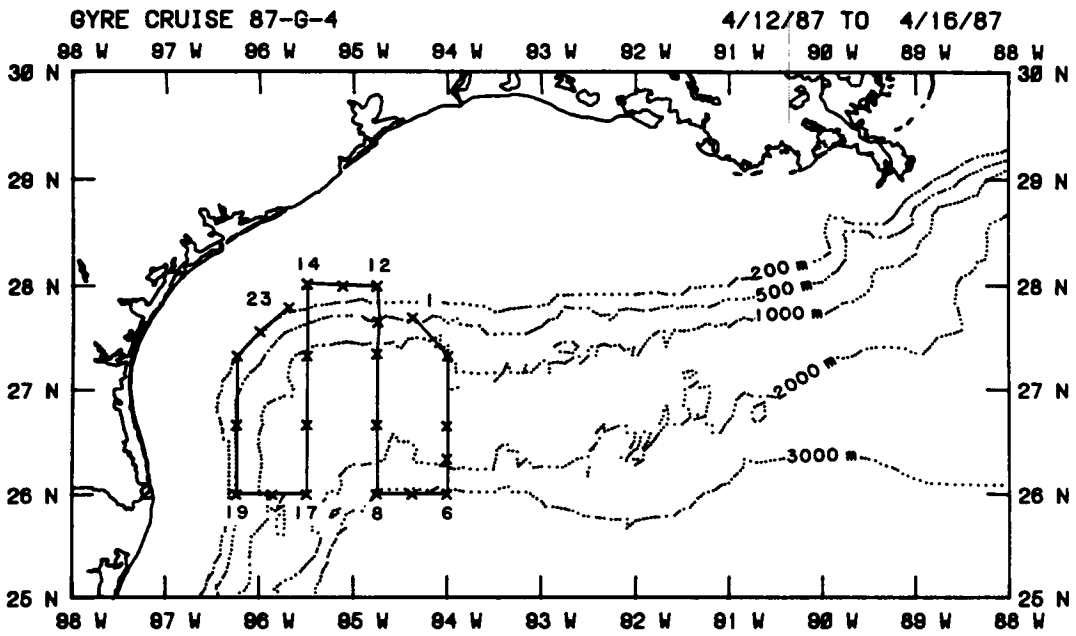

Figure 2.3-7. Example of a GYRE Ship-of-Opportunity cruise track.

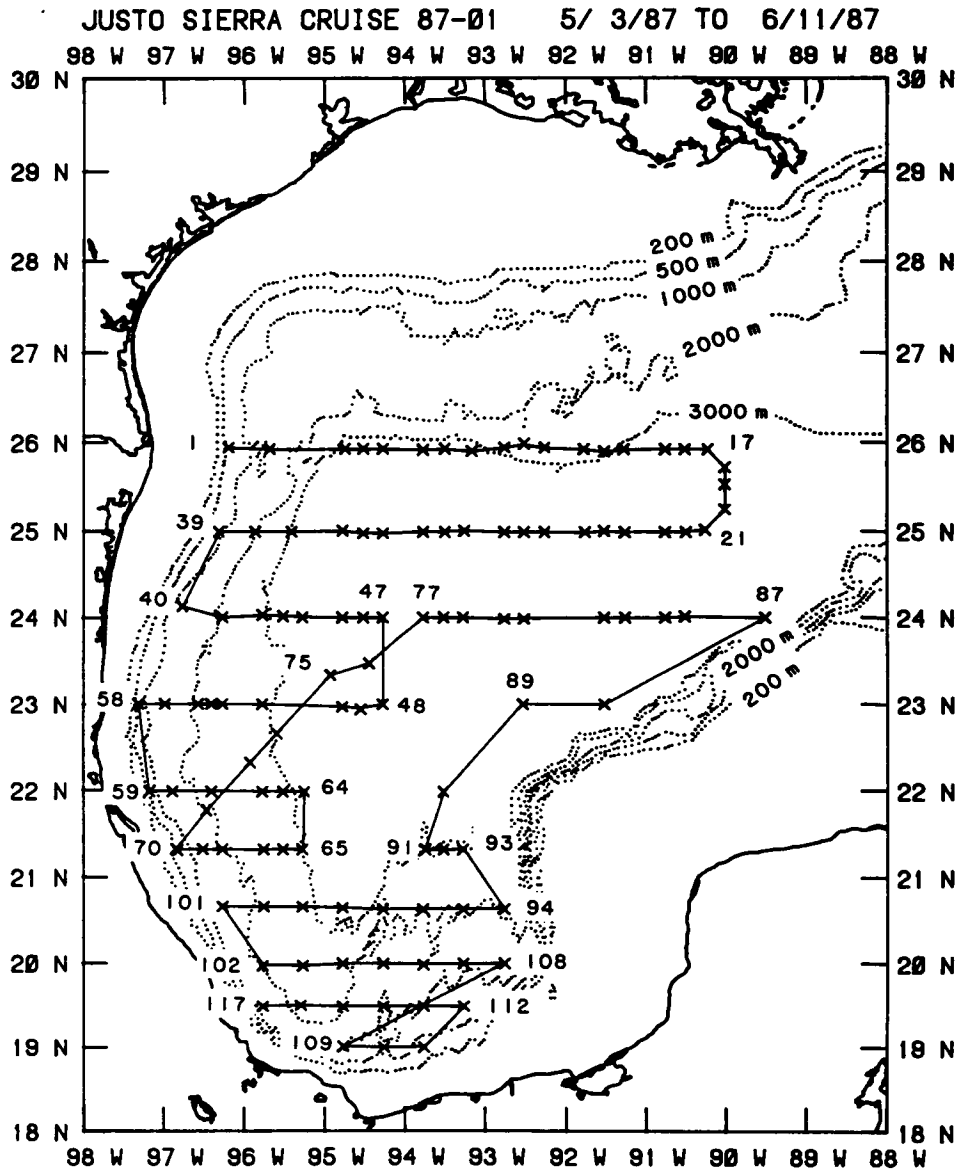

Figure 2.3-8. Example of a JUSTO SIERRA Ship-of-Opportunity cruise track.

2.3.6 Horizontal Temperature Composites

Wide area horizontal composites of the 8, 15 and 21°C temperature surfaces were plotted by combining the various data sources identified above for four different periods of time. These periods and component cruises or flights are identified in Table 2.3-7, and a sample plot is presented in Figure 2.3-9. The plots are derived primarily from unadjusted raw AXBT and XBT data with the exception of GYRE cruise 88G05 for which 0.49°C was subtracted to bring the XBT data in agreement with coincidental CTD temperature data in the surface mixed layer. All of the XBT and AXBT data used are from 760 meter probes with the exception of JUSTO SIERRA Cruise JS8701 which deployed 460 meter probes. Only Composite Three contains any CTD data and that is from the outermost station of PELICAN Cruise PN8903 near the 200 meter isobath and contributes only to the plot of the 21°C temperature surface.

2.4 Marine Optics

2.4.1 Introduction

The Gulf of Mexico has not been subjected to intensive optical studies, although results from some major optical studies have been reported (e.g., Austin, 1980 and Højerslev, 1985). The present investigation can possibly be regarded as a first attempt towards a more complete optical measuring program on the Louisiana shelf.

MMS has focused on the processes taking place on the Louisiana shelf over appreciable time scales. Drifting buoys and current meter moorings have been deployed in order to describe both the long term as well as the short term oceanographic events in the area. Combined with these measurements, an optical program was set up with the aim of describing sediment transport on the shelf over extended periods. In the long term optical program, transmissometers were deployed at four locations selected to cover essentially the shelf along a section being almost perpendicular to the coast line as shown in Figures 2.4-1, 2.4-2 and 2.4-3. In order to calibrate the transmissometer data in terms of the amount of suspended matter, three optical cruises by the University of Copenhagen, Institute of Physical Oceanography were planned to take place when the fresh water discharge essentially from the Mississippi River, could be expected to reach its highest and lowest levels. The three cruises took place in April, 1987 and in February and July, 1988. The optical cruise program involved six different in-situ instruments for making the calibration of the deployed transmissometers as accurate and reliable as possible. At the same time, this permitted a cross checking of the various optical cruise results against one another.

The results from the deployed transmissometers were severely affected (within weeks) by fouling on the lenses. Moreover, their calibration (or at least some calibrations) seemingly suffered from instrumental deficiencies which could not be discovered beforehand. This requires that the planned intercalibration is put aside at present. However, it is felt that the time series from the deployed transmissometers depict the time variation of the light transmission correctly until the onset

Table 2.3-7. Component listing of four wide-area horizontal temperature composite plots assembled primarily from available 760 m XBT and AXBT data.

Composite No.	Cruises/Flights	Data Period (GMT)
1	PELICAN Cruise PN8713	04/05/87 - 04/07/87
	QUEENY Cruise QU8705	04/06/87 - 04/07/87
	SENATOR Cruise SN8709	04/12/87 - 04/13/87
	GYRE Cruise 87G04	04/12/87 - 04/16/87
	JUSTO SIERRA Cruise JS8701*	05/03/87 - 05/30/87
2	JUSTO SIERRA Cruise JS8702	10/14/87 - 11/16/87
	GYRE Cruise 87G10	10/27/87 - 10/28/87
	SENATOR Cruise SN8726	10/28/87 - 10/29/87
	SEAWARD EXPLORER Cruise SE8729	11/05/87 - 11/08/87
	PELICAN Cruise PN8814	11/10/87 - 11/12/87
	GYRE Cruise 87G11	11/18/87 - 11/24/87
3	JUSTO SIERRA Cruise JS8801	07/05/88 - 07/26/88
	PELICAN Cruise PN8903**	07/21/88 - 07/21/88
	AXBT Flight GOMYR5AXBT1	07/31/88 - 08/03/88
4	GYRE Cruise 88G05	10/15/88 - 10/23/88
	PELICAN Cruise PN8911	10/19/88 - 10/22/88
	AXBT Flight GOMYR5AXBT2	10/19/88 - 10/22/88
	PELICAN Cruise PN8913	10/30/88 - 11/02/88

* Data from T-6 (460 m) probes.
** Data from 1 CTD station only.

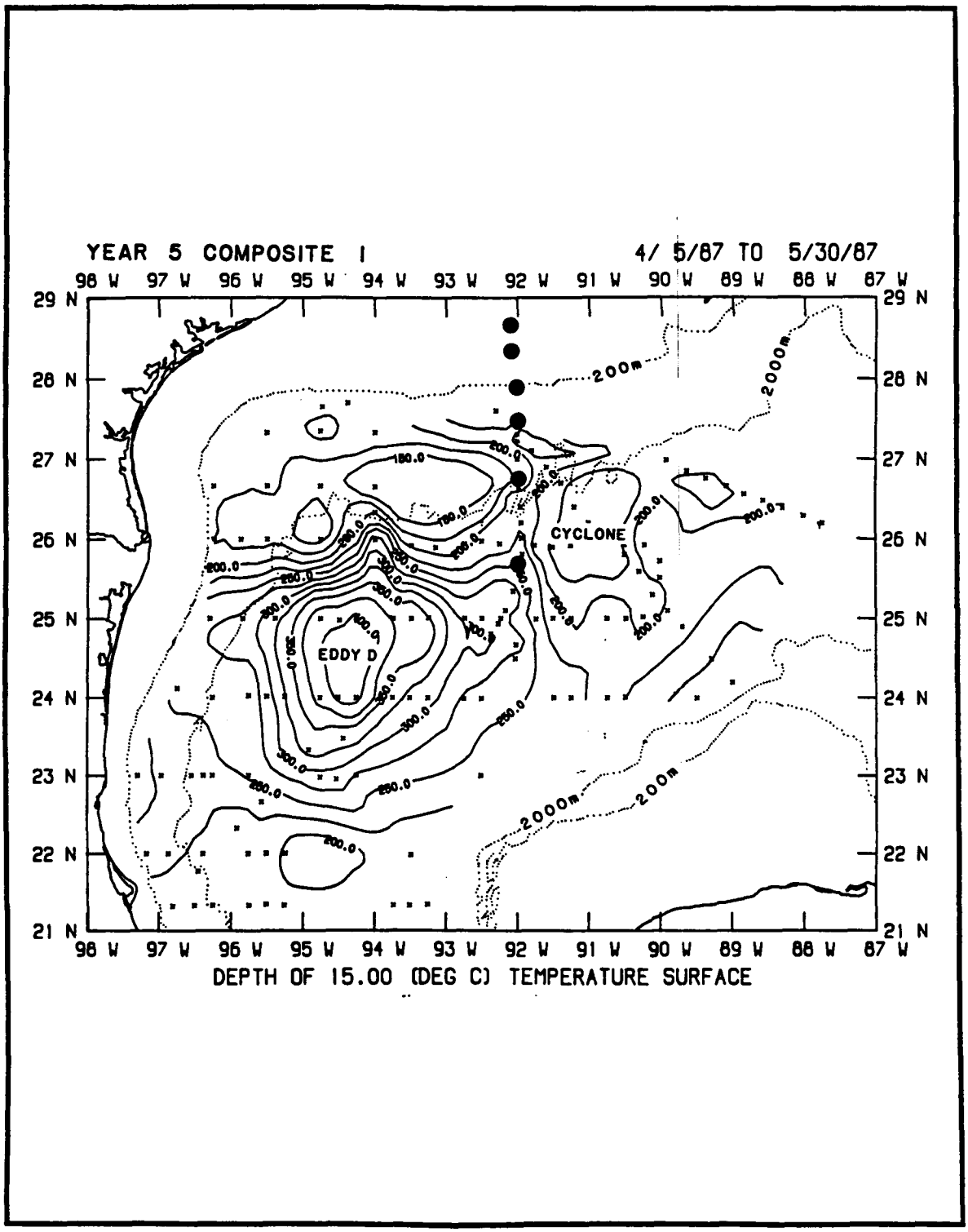

Figure 2.3-9. Sample composite plot of the 15°C temperature surface (mooring locations are indicated by black dots).

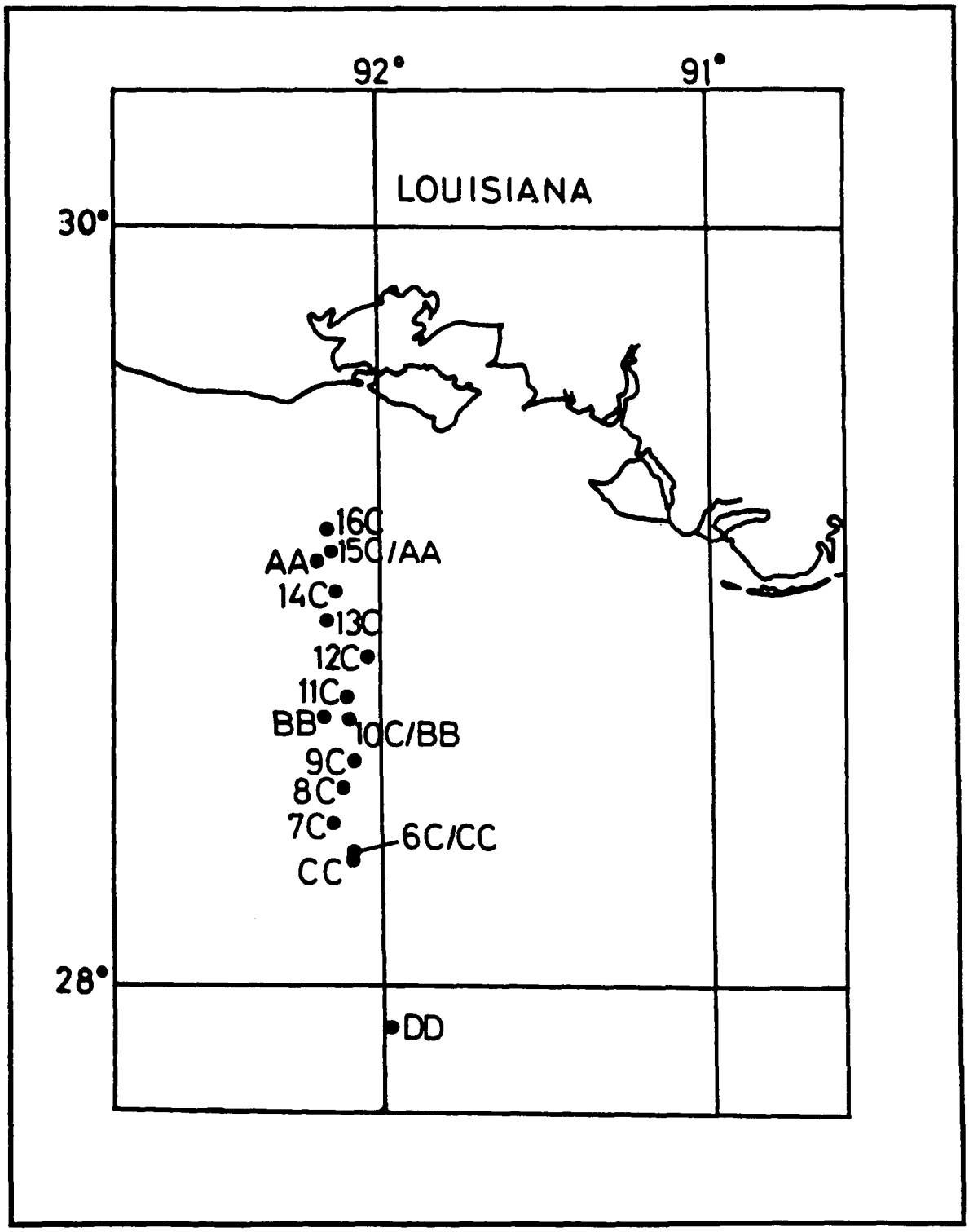

Figure 2.4-1. Station locations for the April 1987 study of the optical properties of the Louisiana shelf.

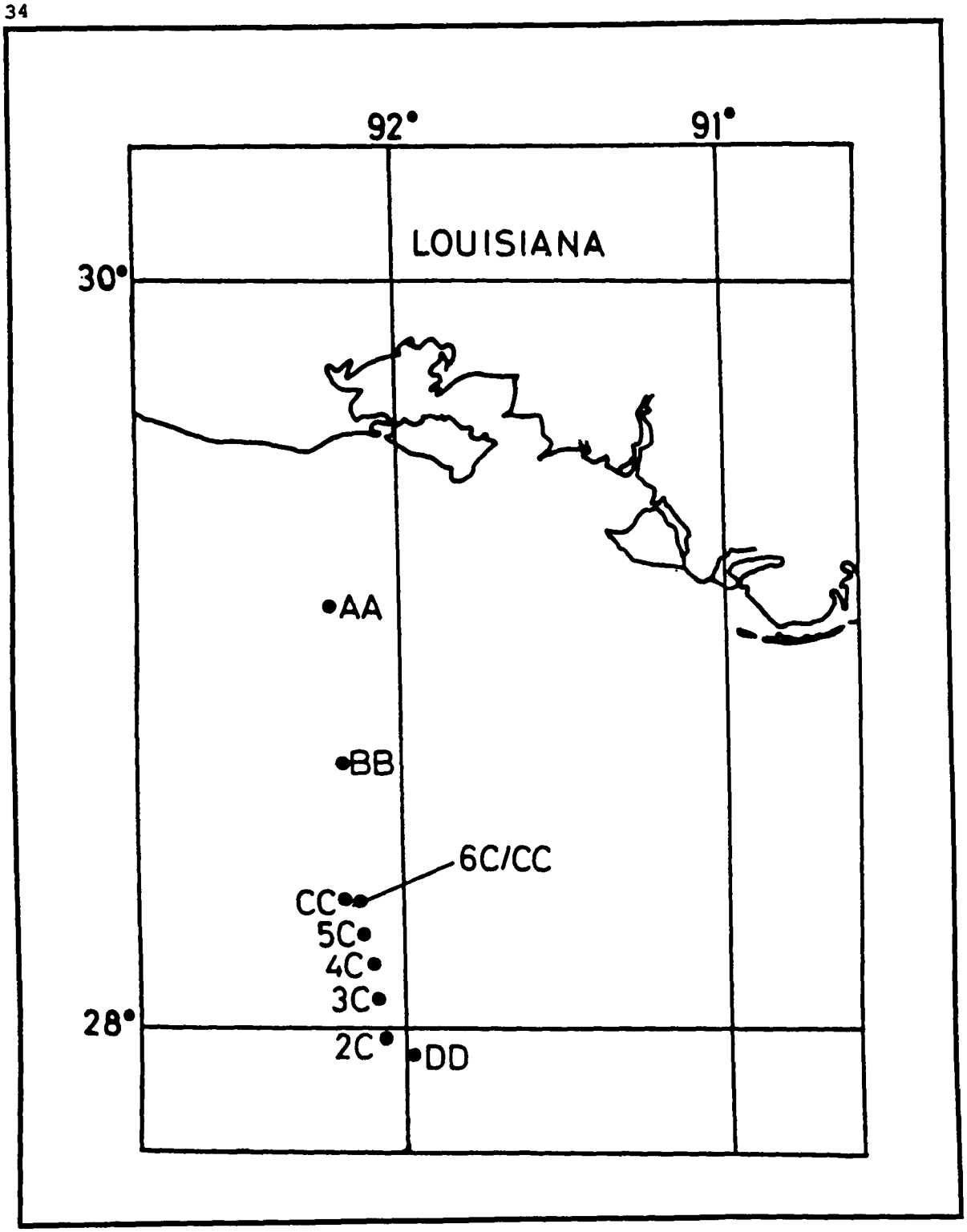

Figure 2.4-2. Station locations for the February 1988 study of the optical properties of the Louisiana shelf.

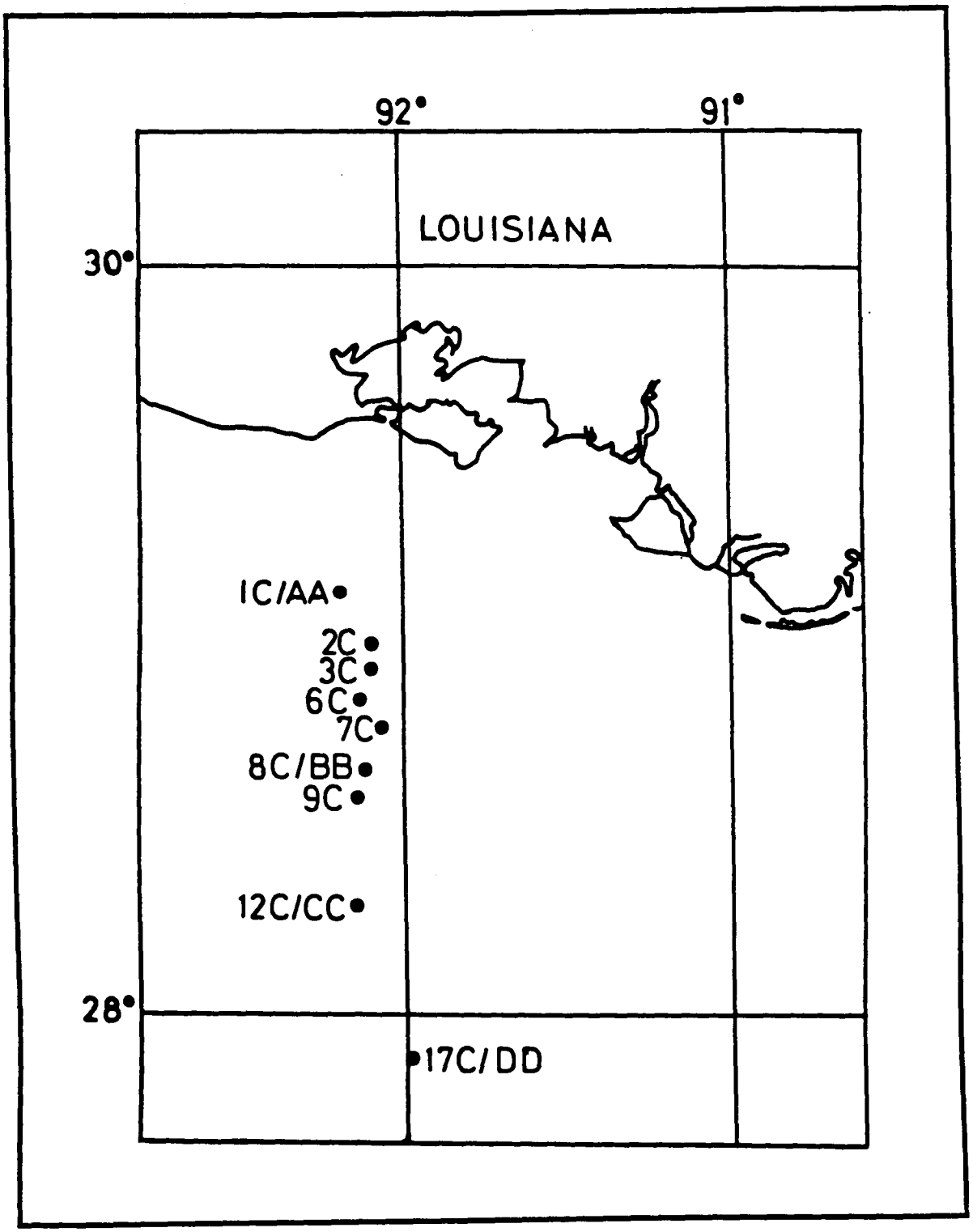

Figure 2.4-3. Station locations for the July 1988 study of the optical properties of the Louisiana shelf.

of fouling substantially attenuated the received signal. Only the absolute values must be regarded as undetermined.

The optical cruise data seem to be of good quality and are consistent. In general, there is a good agreement between the various parameters measured except for a few cases where either pronounced vertical gradients in suspended matter or appreciable time delays between measurements caused disagreements in the results. It has to be emphasized that for measurements of the concentration of suspended matter, this involves a 5-liter Niskin bottle occupying a depth interval of 0.5 m. Moreover, when such a water sampler moves up and down in the sea, the sampling of vertical gradients may lead to appreciable errors. Such variability was observed in some of the data on occasion.

2.4.2 Instrumentation

2.4.2.1 Introduction

Six optical oceanographic sensors and a Secchi disc were used for the Gulf Year 5 Study. These specialized sensors were developed at the University of Copenhagen, Institute of Physical Oceanography for measurement of optical oceanographic parameters in different parts of the world. A review of these sensors has been completed by Højerslev and Larsen (1980) and Hundahl and Holck (1980). In terms of their functions and precision, the sensors are discussed below.

2.4.2.2 F-Meter

The color index meter measures nadir radiances, L (180°) at 447, 521 and 550 nm just below the sea surface. The band half widths in all channels are approximately 15 nm. The ratio between the blue (447 nm) and green (521 nm) signals produces a quantity (defined by Højerslev and Jerlov, 1977) called the color index, F_1. As discussed by Højerslev (1980), the color index is a very convenient quantity for optical oceanic blue and green water studies because a large variety of sea colors can be described by a combination of only two colors. Actually, any color can be described by three primary colors. However, it can be noted that shelf waters in the Gulf of Mexico are generally blue or turquoise ranging to green to yellow. In a few cases, reddish to brownish colors were seen close to the coast. Thus most natural colors encountered in the region can be described by essentially two primary colors rather than three, specifically blue and green.

Further, the color meter wavelengths are quite close to Channels one (443 nm) and two (520 nm) and three (550 nm) of the NIMBUS-7, CZCS which permits an almost direct comparison between measurements taken by both systems. The color meter is calibrated against an Epply standard of spectral irradiance No. EPI-1486. Repeated calibrations of this sensor over a period of two decades have shown overall variations of less than two percent. In terms of field usage, color index measurements are collected as close to the water surface as possible to define the ratio at zero depth (just below the surface). If an estimate for the maximum relative error is sought, then

$$\frac{\Delta F}{F} = \frac{L(180°,\ 447\ \text{nm},\ Z=0)}{L(180°,\ 521\ \text{nm},\ Z=0)} \cdot \frac{1}{2} \cdot \frac{e^{-K_L(447)\,\Delta Z}}{e^{-K_L(521)\,\Delta Z}}$$

where $K_L(447)$ and $K_L(521)$ are the vertical attenuation coefficients for the nadir radiances at 447 and 521 nm, respectively. The uncertainty in depth, ΔZ, is the total vertical displacement of the color index meter from the actual sea surface. In this particular investigation

$$K_L(447) \simeq 0.7\ m^{-1},\ K_L(521) \simeq 0.5\ m^{-1},\ \text{and}\ \Delta Z \leq 0.5\ m.$$

Thus,

$$\frac{\Delta F}{F} \cdot 100 \leq 5.5\%$$

and the overall color index accuracy is within the $\pm$ 7.5% for the worst case (Station AA) but within $\pm$ 2.5% for Station DD. Further details pertaining to this instrument have been presented by Jerlov (1974).

2.4.2.3 <u>Q-Meter</u>

The quanta irradiance meter measures the number of photons incident on a horizontal unit area in a unit time in the 350 to 700 nm spectral range. The q-meter is calibrated to yield a reading that is proportional to the radiant input energy at a given wavelength and the wavelength itself is in the 350 to 700 nm range. Detailed discussions of this sensor have been presented by Jerlov and Nygård (1969) and Højerslev (1978).

In practice, the relative errors in the vertical attenuation coefficient for downward quanta irradiance, K_q, must be examined carefully because of the irradiance variability in the euphotic zone, the significant light fluctuations in shallow depths, the allowance for integration effects in the visible range, and the wavelength dependence of the cosine collector. As such, the maximum relative error may exceed $\pm$ 25% close to the water surface where K_q is high and disturbances due to waves are sometimes appreciable.

2.4.2.4 <u>B-Meter</u>

The light scattering meter integrates the light scattering function, $\beta(\theta)$, from three to 150 degrees at 655 nm. Since $b = \int_{4\pi}\beta(\theta)d\omega$, the sensor provides a measure of the scattering coefficient.

A Lambert emitter mounted in front of a lamp housing is configured to produce a cosine emission at grazing angles; this emission minimizes integration errors caused by the dominant forward scattering. Integration of the light scattering function is performed in the interval

$3° \leq \theta \leq 150°$. An error analysis for this sensor (Højerslev, 1985) utilizing 36 combinations of Junge distribution particles showed that the total light scattering coefficient can be profiled to an accuracy on the order of 5%. Details pertaining to b-meter calibration procedures have been discussed earlier by Jerlov (1961, 1976).

2.4.2.5 C-Meter

This particular light transmission sensor provides a measure of the (beam) light attenuation coefficient, c, at 631 nm over a fixed path length of 0.5 m. Readings in the water column are checked against readings in the air. Absolute c-values can only be obtained if the sensor is calibrated in a tank (Højerslev and Larsen, 1980).

Photodiode output at 631 nm is collimated by a double lens system. In air the collimated beam has a solid angle of acceptance of 10^{-4} steradians; in sea water, the solid angle of acceptance is 0.56×10^{-4} steradians. The beam cross section at the light sensor is around one mm^2.

Transmission is defined as the ratio of the signal reading in water to air over half a meter path length. Its relations to c is given by

$$\text{Transmission} = T = k \cdot e^{-cr}$$

where k is a calibration constant dependent on geometry, wavelength, acceptance angles, and changes in window reflections in air and water, respectively.

An error analysis by Højerslev (1985) for this sensor based on Mie scattering theory shows the error in c to be of the maximum order of $\pm$ 10%.

2.4.2.6 Chlorophyll A-Meter

Chlorophyll distribution in the water column was profiled with a one-channel fluorescence meter. Excitation wavelengths are located in the blue-green part of the spectrum; emission wavelengths are in the red part. The fluorescence technique is approximate, but yields a convenient relative profile for chlorophyll a (Chl a) and to a not negligible degree from phaeophytin a. During earlier experiments, this sensor was calibrated against various plankton monocultures at different Chl a levels (Hundahl and Holck, 1980). Experience has shown that fluorescence yields from monocultures having the same Chl a concentration may differ by a factor of two. For the spring cruise in April 1987, therefore, the fluorescence meter was "field calibrated" so that 100 mV output corresponded to one mg m^{-3} Chl a. This calibration value is chosen to be "average" for the marine plankton populations in the area during the winter, spring and summer. The maximum absolute error introduced by this assumption is of the order of $\pm$ 30% (Højerslev, 1985).

2.4.2.7 <u>UV-B Meter</u>

The UV-B meter measures the downward irradiance around 310 nm, $E_d(310)$. The half width is approximately three nm. The UV-B meter serves as a speedy and practical means for measuring dissolved organic matter in the sea, termed as yellow substance, gelbstoff or gilvin being a complex mixture of fulvic and humic acids (for details see Højerslev, 1982a, 1988 and Harvey et al., 1983). The UV-B meter records the UV-B daylight continuously down through the water column so the vertical attenuation coefficient K(310) can be calculated. K(310) serves together with the light scattering and the light attenuation coefficient, b and c, respectively, as a means to map and quantify the concentration of yellow substance (and suspended matter) in a feasible manner. The overall uncertainty in K(310) increases with increasing concentration of yellow substance, in particular, although high concentrations of suspended matter also influence the accuracy. In general, the overall uncertainty can be expressed as

$$\frac{\Delta K(310)}{K(310)} = 4\,\frac{e^{2K(310)(Z_2 - Z_1)}}{2K(310)(Z_2 - Z_1)} \cdot \frac{\Delta E(310,\ Z_1)}{E(310,\ Z_1)} + \frac{\Delta Z}{Z_2 - Z_1}$$

where $\Delta E(310,\ Z_1)$ represents the maximum daylight fluctuation at depth Z_1 caused by clouds, waves, etc. and $E(310,\ Z_1)$ is the UV-B irradiance at depth Z_1, around which the fluctuations occur. The last term can normally be ignored. $\Delta E(310,\ Z_1)$ decreases with depth but so does $E(310,\ Z_1)$. The term

$$\frac{\Delta E(310)}{E(310)}$$

is typically of the order of 0.02 for all depths as well as for steady surface light conditions and a fairly calm sea which was the case during all three cruises. Accordingly,

$$\frac{\Delta K(310)}{K(310)} = 0.08\,\frac{e^{2K(310)(Z_2 - Z_1)}}{2K(310)(Z_2 - Z_1)}$$

(See Højerslev, 1985 for more details).

The right side has its minimum value for the case where

$$2K(310)(Z_2 - Z_1) = 1$$

This implies that in order to calculate K(310) most accurately the calculation has to be performed between those depths, Z_2 and Z_1, where the

above condition is fulfilled. At Station AA, K(310) ≈ 1.5 m^{-1}, so for this case the calculation of K(310) should be made over depth intervals ≈ 0.33 m. Opposite at Station DD, where K(310) for the extreme case ≈ 0.07 m^{-1} the depth intervals $Z_2 - Z_1 \approx 7$ m. So for the cases described above, the overall lowest possible uncertainty of K(310) amounts to:

$$\frac{\Delta K(310)}{K(310)} = \pm 22\%$$

2.4.2.8 Secchi Disc

A standard Secchi disc was used to estimate the light attenuation coefficient in the green part of the spectrum and the depth of the euphotic zone. A white disc (albedo ≈ 0.80, diameter = 0.3 m) was lowered to its depth of visual disappearance.

A critical correction for these measurements is the accounting for surface wave height along the suspension wire. Højerslev (1982b) has shown that a one-meter wave height causes a 40% decrease in Secchi disc depth when referenced to a calm sea. The correction is applied as

$$D_0 = D_H(1+0.4H)$$

where D_0 is the Secchi disc depth for a completely calm sea, and D_H is the Secchi disc depth measured in the presence of a wave height H(m). For more details the reader is referred to Højerslev (1986a, b).

2.5 Remote Sensing

2.5.1 Introduction

Remotely sensed data have been used extensively in Year 5 for advance planning of hydrographic cruises, identification of mesoscale features, and interpretation of event details seen in both hydrographic and current meter records. Remotely sensed data used in the Year 5 program include sea surface temperatures detected by the NOAA Polar Orbiting satellites and sea surface heights measured by the Navy GEOSAT (Geodetic Satellite).

2.5.2 Thermal Imagery

The NOAA Polar Orbiters carry a variety of sensors including the Advanced Very High Resolution Radiometer (AVHRR), which measures visible and infrared radiation in four or five bandwidths. Each satellite has a slightly different suite of instruments. In general, the even numbered satellites (NOAA-10 during this program) have a four-channel radiometer, and the odd numbered satellites (NOAA-9) have a five-channel radiometer. For the four-channel instrument, the fifth data channel repeats the channel-four radiometer data. Generally, two km resolution imagery was used for full basin AVHRR maps, while one km resolution imagery was obtained for special local study area maps.

Two channels (four and five) of the five-channel radiometer data are useful in determining sea surface temperature. These two-channel data are converted from radiance to temperature and corrected for water vapor in the atmosphere (but not for clouds), remapped to a user selected projection and displayed as color enhanced images. Spatial resolution of the AVHRR is nominally one km, and temperature resolution is 1/8 degree Kelvin (10 bit scale). High resolution data are downlinked essentially in real time if the satellite is in view of a ground station in the High Resolution Picture Transmission (HRPT) mode, or limited time periods are stored for later transmission as Local Area Coverage (LAC) data. Data are also averaged and stored in the satellite in a lower resolution Global Area Coverage (GAC) mode. The GAC data provide global coverage at a maximum resolution of four kilometers.

The satellite ground track and infrared band field-of-view are such that the entire Gulf of Mexico can be seen in one view by a satellite passing over the central part of the Gulf. A polar orbiting satellite passes over a portion of the Gulf of Mexico twice daily. Since two polar orbiters are normally operational, two nighttime and two daytime views of some portion of the Gulf of Mexico are available daily. The infrared sensors also detect clouds so that clear sky images of the entire Gulf of Mexico are relatively rare. Successive views can be composited to alleviate the effects of cloud cover in some cases.

The infrared data provide useful images of the Gulf of Mexico only from mid-October to mid- to late May (late fall to late spring) since the sea surface temperatures tend to be highly uniform during the rest of the year. Over 200 HRPT (one km resolution) images of the Gulf of Mexico have been acquired and processed. These images cover the period from October 15, 1987 to May 31, 1988 with relatively clear images available for 120 days (52 percent) of the period.

2.5.3 GEOSAT Altimetry

The Navy GEOSAT has been in an orbit which exactly repeats its ground track within one km every 17.05 days since November 1986. The Exact Repeat Mission (ERM) orbit is identical to that of the SEASAT which was operational for three months in 1978. GEOSAT uses a 13.5 gigaHertz radar altimeter to measure its altitude above the earth's surface 10 times per second. Ground processing of the raw altimeter data provides a once per second average height of the sea surface above a reference ellipsoid. Data are flagged which do not meet certain validity criteria or which are values over land. The valid sea surface height data include the earth's geoid, the dynamic ocean surface, orbit errors, earth and ocean tides, path length errors due to atmospheric water vapor and among other sources free electrons in the ionosphere. Additional processing of the altimeter data can yield estimates of dynamic topography accurate to about 10 cm. The GEOSTAT altimeter data used for this study were provided by the Applied Physics Laboratory of Johns Hopkins University.

The satellite covers latitudes between 72°N and 72°S along tracks which are spaced approximately 150 km apart at the equator and 145 km apart in the Gulf of Mexico. Thirty ascending and descending tracks provide

coverage of the Gulf of Mexico where alongtrack spacing of the one second data is about 6.7 km. The altimeter footprint is two to 10 kilometers depending on sea state.

The altimeter is not affected by cloud cover as the AVHRR is; however, the altimeter can lose track in heavy rain cells and in crossing coastal areas from land to sea; it also suffers adverse affects of increased solar activity. Data losses were minimal early in the program but increased during 1988. These data losses worldwide appear to coincide with a period of high solar activity.

2.6 Subsurface Moorings

2.6.1 Introduction

Measurements of current and temperature combined with transmissometry and hydrographic measurements on the shelf and with IES and hydrographic data in offshelf waters are valuable in interpreting and understanding oceanic processes. In this study seven taut line current meter moorings and two IES's were deployed along an onshore-offshore section approximately along 92°W longitude off the Louisiana coast (see Figure 2.6-1 and Table 2.6-1). The shelf moorings were equipped with transmissometers in addition to current meters in an effort to estimate the flux of various volatile and non-volatile suspended materials. Offshelf, the IES's were expected to contribute to the detection and documentation of Loop Current eddies crossing 92°W longitude. It was also anticipated that some passing eddies would, in part, influence shelf circulation in the shelf-slope region.

2.6.2 Currents and Temperature

Current and temperature measurements were made from moorings designed according to the methods described in SAIC (1988). During the initial deployment in April 1987, twelve General Oceanics, Inc. Mark II Niskin winged current meters and eight Mark I Niskin winged current meters were deployed. Three months later, during the initial rotation of the shelf moorings, it was discovered that the Mark II instruments were not operating properly in the vector averaging mode. This was later found to be a manufacturing error in the EPROM programming which caused the instrument to advance the tape cassette to end-of-tape (EOT) at unpredictable times, but generally fairly early in the deployment. What data were collected were good but short in duration. As a result and because of the anticipated impact on offshelf current records, plans were made to replace all Mark II instruments with Aanderaa RCM4s and RCM5s or General Oceanics Mark Is in November 1987 during the scheduled six-month rotation. This was accomplished resulting in a mix of Aanderaa instruments with General Oceanics Mark I instruments which do not have a vector averaging mode. As opportunities permitted, prior to and after the Mark II problem had been corrected, a number of additional 'test' and 'comparative' deployments of these instruments in the burst and vector averaging modes were made on the same moorings. These resulted in additional measurements to the program and in a few cases served as timely backups. For the purposes of this report, the repaired Mark II

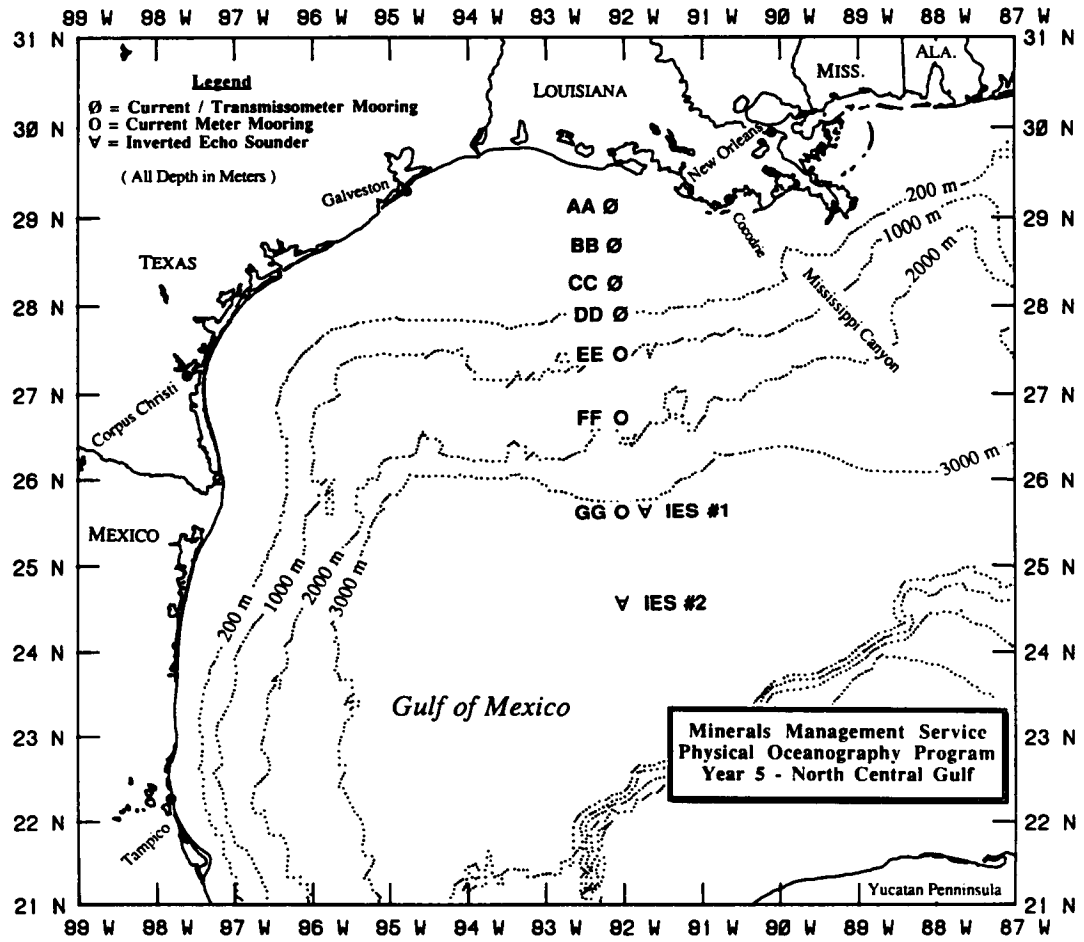

Figure 2.6-1. Mooring locations during Year 5 of the MMS-sponsored Gulf of Mexico Physical Oceanography Program.

Table 2.6-1. Mooring locations and corresponding depths for Year 5 of the MMS-sponsored Gulf of Mexico Physical Oceanography Program.

Moorings	Loran C Time Delays (TDs)	Location Latitude	Longitude	Water Depth (m)
AA	11189.4 27194.6 46870.9 64046.3	29°07.031'N	92°08.658'W	14
BB	11277.2 27099.1 46792.2 64071.6	28°40.52'N	92°05.87'W	40
CC	11343.9 26999.2 46725.5 64080.6	28°18.57'N	92°05.76'W	64
DD	11434.7 26945.7 46641.6	27°53.0'N	91°59.7'W	181
EE	11501.7 26835.2 46561.4	27°28.1'N	92°00.0'W	825
FF	11609.1 26662.4 46419.5 64081.9	26°44.4'N	91°59.7'W	1750
GG	11736.0 26417.2 46213.6 64061.1	25°39.2'N	92°01.9'W	3000
IES1	11734.1 26412.7 46215.1 64061.1	25°39.4'N	92°02.4'W	3000
IES2	11853.6 26241.0 46000.7 64024.9	24°29.57'N	92°00.95'W	3743

instruments when used in the vector averaging mode are referred to as Mark III's though the manufacturer does not make this distinction.

Two other significant problems were encountered during the current measurement program. On September 10, 1988, a Kevlar segment at approximately 600 meters depth at Mooring FF failed causing the 100 m and 300 m instruments to rise to the surface and begin drifting. These were recovered by a tuna fisherman on September 22, 1988. No other mooring failures occurred over the 19-month field effort. A more repetitive problem was fouling observed on shelf instruments at Moorings AA (14 m depth) and BB (40 m depth) where layers (up to an inch or more) of small barnacles were found to have encrusted the instruments after three months. At Mooring CC (64 m depth) barnacle fouling was significantly less intense and of a different, larger type, not covering the entire exposed surface area of the instruments. At Mooring DD (180 m depth) and further offshore no significant fouling besides a thin film layer was ever observed.

The heavy fouling at Moorings AA and BB did not interrupt the time series of current speed and direction because of an instrument design with no moving parts. However, an over-the-side shipborn tow test of a recovered Mooring AA instrument in November 1988 revealed that the current magnitudes were lower for the heavily fouled instrument by as much as 15 to 30 cm s^{-1} from those of an unfouled instrument that had measured towed speeds of up to 110 cm s^{-1}. There was, however, no significant difference in the directional data. This suggests that the current records at sites AA and BB are probably directionally accurate but may have exhibited lower speeds and less energy than actually occurred towards the latter parts of each deployment period. Interestingly, this trend is not visually obvious in examining the current records.

Clearly, more frequent rotations of the instruments would have reduced or eliminated this problem. In addition, the use of an environmentally acceptable antifouling compound may have delayed the onset of fouling. Earlier experience, however, has shown that in this region even the most potent antifouling paints would have failed during the three-month deployments.

Descriptions of the General Oceanics and Aanderaa instruments are provided in SAIC (1986 and 1988), respectively. Table 2.6-2 provides a summary of the planned instrumented depths on each mooring and Figure 2.6-2 provides a time line for the actual recovered data. Data return for the 12 months following correction of the Mark II problem was 92 percent.

2.6.3 Transmissometry

Six Sea Tech Model ST025-A 25 cm transmissometers were deployed at the four shelf mooring sites (Moorings AA, BB, CC and DD) at the depths indicated earlier in Table 2.6-2. These were configured to store data on Aanderaa TR-1 and TR-2 data loggers and were mounted on Aanderaa gimble vane assemblies. They were deployed and rotated at three-month intervals as part of the same moorings which measured current.

Table 2.6-2. Planned mooring instrumentation levels for Year 5 of the MMS-sponsored Gulf of Mexico Physical Oceanography Program.

Mooring	Water Depth (m)	Instrument	Instrument Level (m)
AA	14	Current Meter	7
		Transmissometer	9
BB	40	Current Meter	12
		Transmissometer	14
		Current Meter	18
		Transmissometer	20
CC	64	Current Meter	11
		Transmissometer	14
		Current Meter	28
		Transmissometer	32
DD	181	Current Meter	10
		Transmissometer	11
		Current Meter	100
		Current Meter	150
EE	825	Current Meter	100
		Current Meter	300
		Current Meter	725
FF	1750	Current Meter	100
		Current Meter	300
		Current Meter	725
		Current Meter	1650
GG	3000	Current Meter	100
		Current Meter	300
		Current Meter	725
		Current Meter	1650
		Current Meter	2500

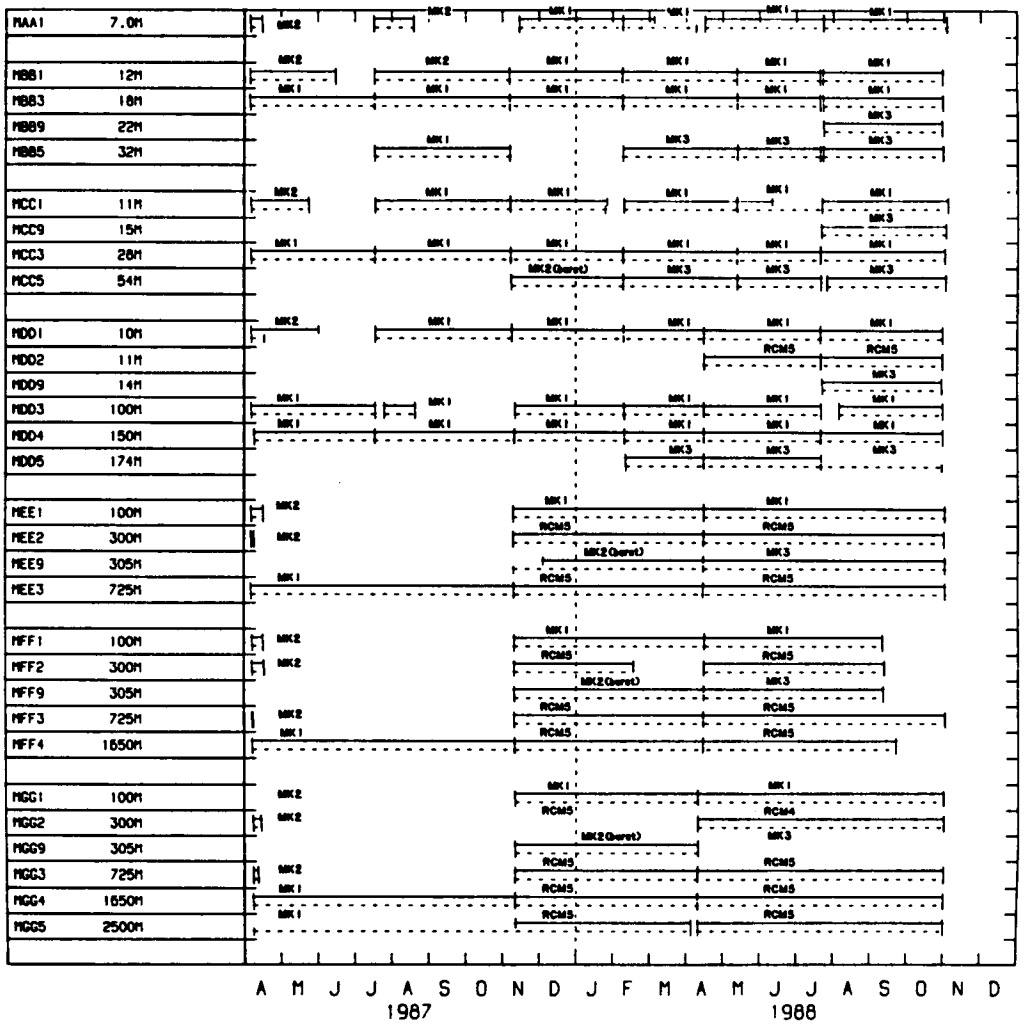

Figure 2.6-2. Time line of deployment periods and data return for each current meter level during Year 5 of the Gulf of Mexico Physical Oceanography Program. The solid lines are for currents and the dashed lines are for temperature.

Immediately following each deployment, suspended solids samples were taken from Niskin bottles tripped at the transmissometer levels as close as possible to the transmissometer sites.

The usefulness of most of the data from these instruments was in part degraded by the high productivity on the shelf. This tended to block completely or degrade significantly the optical paths within two to three weeks, particularly at the near shore stations (Moorings AA and BB) where massive deposits (an inch or more thick) of barnacles were repeatedly found completely encrusting the instrument each time it was rotated. Clearly, more frequent rotations and a means of protecting the optical elements from fouling would have improved the quality of the data. An example of transmissometry time series records for the first deployment are presented in Figure 2.6-3.

2.6.4 Inverted Echo Sounders (IES's)

Two Sea Data Model 1665 IES's were deployed at the locations identified earlier in Figure and Table 2.6-1. These were deployed on April 6 and 7, 1987 and recovered a year later. At the time of the April 1988 recovery it was discovered that IES #2 had malfunctioned. Subsequently only IES #1 was redeployed. It was later recovered on October 30, 1988. Actually, both instruments experienced some problems with IES #2 returning a good temperature and pressure record for the initial 12-month deployment, but no travel time data, and IES #1 returning good travel times for both deployments, but only a partial temperature and pressure record for the initial deployment.

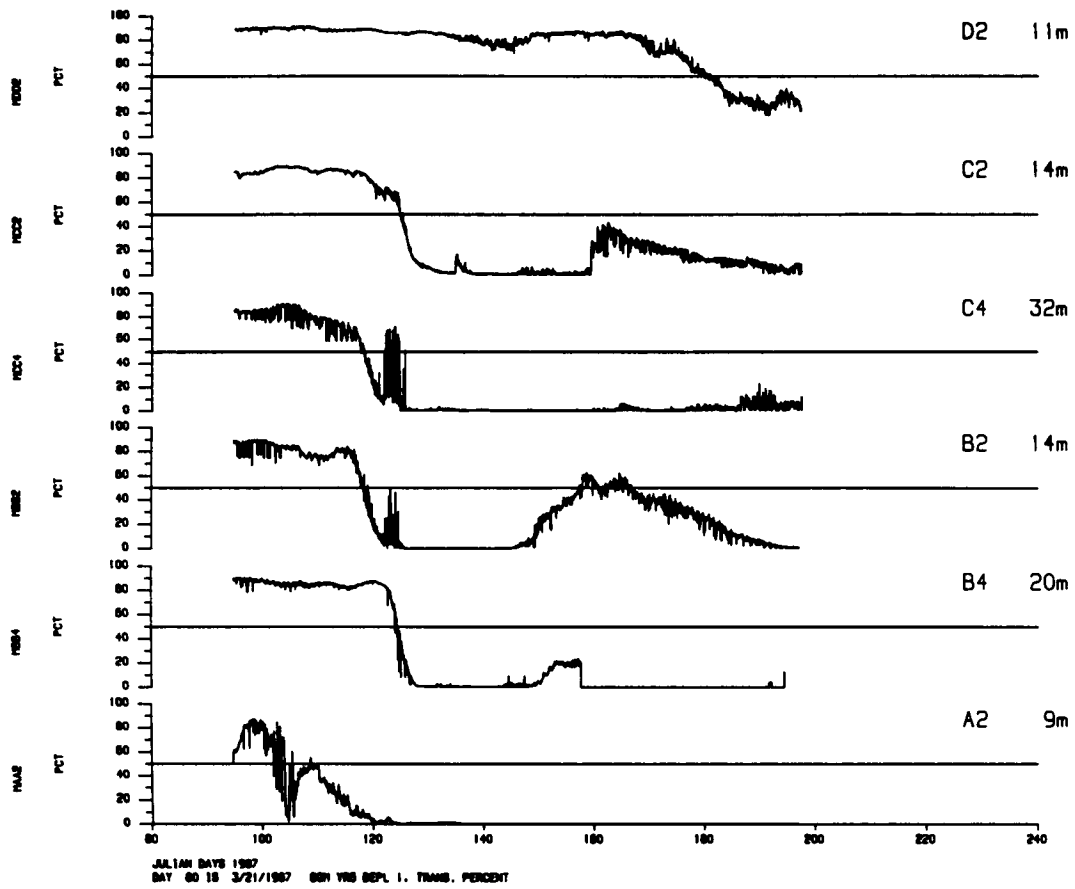

Figure 2.6-3. Examples of the transmissometry data obtained during the Year 5 program.

III. DATA ANALYSIS

3.1 Introduction

Presented in Chapter III are the analyses techniques used on the data described in Chapter II. Results of these analyses provide the basic information used for the technical discussion in this report. Because this program report is part of a series, materials presented in previous reports are not duplicated here. The reader is referred to the prior reports, in particular, Years 1 and 2 (SAIC, 1986). Procedures which are accepted as routine or standard within the oceanographic community have generally not been described. Separating this material from the technical discussion of patterns and physical processes helps maintain the focus and provides a readily identifiable location for analysis procedures.

3.2 Lagrangian Drifters

The analyses of the drifter data follow the work previously performed for MMS in the Gulf of Mexico (SAIC, 1986; 1987; 1988). These include the production of SST maps with drifter tracks, a study of the hydrography of the water column as determined by XBT data, a kinematic analysis of the drifter tracks, and a dynamic analysis based on the conservation of angular momentum. The kinematic analysis provides the time histories of translation velocity U, swirl velocity u (tangential speed about the center of motion), divergence D, vorticity z, normal deformation rate N, and shear deformation rate S (see SAIC, 1986, Section 3.2.1.2). The dynamic analysis uses the vorticity of the water column, the rotation of the earth (a function of latitude), and the divergence of the water column in determining a balance between changes in the total rate of spin and the stretching of the water column (SAIC, 1986, Section 3.2.1.3).

The results of all these analyses are used to produce an understanding of the physical processes in the Gulf of Mexico, especially those related to Loop Current eddys. A synopsis of these results to date can be found in Lewis and Kirwan (1985, 1987) and Lewis et al., (1989).

3.3 Hydrography

CTD salinity, temperature and depth calibration methods were as described earlier in SAIC (1988). Based on these methods, the corrections identified in Table 3.3-1 and Table 3.3-2 were applied. The resulting adjusted mixed layer CTD salinities are characterized by standard deviations of ± 0.001 to ± 0.009 ppt. However, vertical salinity records for cruise PN8903 are suspect due to a degraded CTD thermistor response causing salinity spiking in the thermocline. Temperature and pressure corrections were applied only to data for cruises PN8713 and PN8814 per Table 3.3-2. All other CTD temperatures and pressures were within the range of accuracy of the reversing thermometers and/or the amount of wire used to lower the CTD (wire out). With the exception of GYRE Cruise 88G05 where 0.49°C was subtracted to bring XBT data into agreement with coincidental CTD temperature data in the surface mixed layer, no

Table 3.3-1. CTD salinity calibration data for the Gulf of Mexico Year 5 Program.

Cruise ID	Instrument	Calibration Offset Applied
PN8713	Neil Brown Mark IIIB	(See Table 3.3-2)
PN8715	SeaBird SBE-9 (LUMCON)	+0.015 ppt
PN8803	SeaBird SBE-9 (LUMCON)	+0.011 ppt
PN8814	Neil Brown Mark IIIB SeaBird SBE-9 (TAMU)	(See Table 3.3-2) +0.024 ppt
PN8820	SeaBird SBE-9 (LUMCON)	+0.026 ppt
PN8903	SeaBird SBE-9 (LUMCON)	+0.024 ppt*

* This offset adjusted the mixed layer CTD salinities to agree with bottle salinities. However, it was observed that a degraded thermistor response caused substantial salinity spiking in the thermocline.

Table 3.3-2. Northwest Regional Calibration Center calibration coefficients for Neil Brown Mark IIIB CTD (April 10, 1986).

Parameter*	A(0)	A(1)
Conductivity (mmho/cm)	+0.008	.999597
Temperature (°C)	+0.049	.999749
Pressure (dbar)	+0.1	.999752

* Parameter = A(0) + A(1) x N, where N = Instrument output.

temperature offset corrections were applied to either the XBT or AXBT data. In addition, no drop-rate adjustments were made, though obviously bad drops were discarded.

Dissolved oxygen analysis procedures were according to the modified Winkler method described by Strickland and Parsons (1972). Total suspended and volatile solids were determined by the methods described in American Public Health Association, et al., (1985).

3.4 Marine Optics

3.4.1 Introduction

Presented in this section is a general discussion of the analytical and physical relationships used in evaluating the optical observations made. Because optical properties are not generally encountered by many readers, a representation of nonmenclature and associated engineering units is also provided.

3.4.2 Nomenclature and Definitions

The nomenclature and units follow the recommendations by the International Association of the Physical Sciences of the Ocean (IAPSO) Working Group on Symbols, Units and Nomenclature in Physical Oceanography. In addition, the classical American nomenclature and the nomenclature recommended by the International Association of Meteorology and Atmospheric Physics (IAMAP) Radiation Commission in Atmospheric Physics are presented for reasons of comparison in Table 3.4-1. In this section, spectral densities of radiation quantities (or more simply spectral radiation quantities) are designated by the IAPSO recommended symbol for the respective quantities supplemented by the subscript λ, e.g., L_λ for the spectral density of radiance, i.e., the radiance $L = \int L_\lambda d\lambda$.

Consider the differential amount of radiant energy $dQ(\lambda)d\lambda$ in a specified wavelength interval $(\lambda, \lambda + \Delta\lambda)$ which is transported across a small element of area dA in directions confined to an element of solid angle $d\omega$ during a time interval dt. This energy can be expressed in terms of radiance, $L(\lambda)$, as

$$dQ(\lambda)d\lambda = L(\lambda) \cos \theta \, d\lambda \, dA \, d\omega \, dt$$

where θ is the angle between the direction under consideration and the outward directed normal to dA. Radiance, L, is actually a function of horizontal position, depth, orientation, and time as well as wavelength but normally varies so slowly that it is often assumed to be independent of horizontal position (i.e., x and y).

Radiant flux, Φ, is the time rate of flow of Q and can be expressed simply as

$$d\Phi = \frac{dQ}{dt} = L \cos \theta \, dA \, d\omega$$

Table 3.4-1. Fundamental quantities, units, and symbols in optical physical oceanography. In this section the IAPSO recommended nomenclature is used. For comparison the nomenclature recommended by IAMAP and the classicial American nomenclature are represented as well.

Quantity [1]	Units	Symbols		
		IAPSO	IAMAP	Classical America
Radiant energy	J	Q	Q	U
Radiant flux	W	Φ	Φ	P
Radiant Intensity	Wsr^{-1}	I	I	J
Radiance	$Wm^{-2}sr^{-1}$	L	L	N
Irradiance	Wm^{-2}	E	E	H
Downward irradiance	Wm^{-2}	E_d	E(-),E↓	H(-)
Upward irradiance	Wm^{-2}	E_u	E(+),E↑	H(+)
Wavelength	nm	λ	λ	λ
Light absorption coefficient	m^{-1}	a	σ_a	a
Volume light scattering function	$m^{-1}sr^{-1}$	β	γ_s	σ
(Total) light scattering coefficient	m^{-1}	b	σ_s	s
(Beam) light attenuation coefficient	m^{-1}	c	σ_e	α
Vertical light attenuation coefficient	m^{-1}	K		K

[1] The spectral densities of the radiation quantitites Q, Φ, ...E_u are designated by subscript λ. The corresponding units are those of the radiation quantities per unit wavelength.

Intensity, I, is defined as

$$dI = \frac{d\Phi}{d\omega} = L \cos \theta \, dA$$

Irradiance is the radiant flux per area, or

$$\frac{d\Phi}{dA} = L \cos \theta \, d\omega$$

and is usually considered in five quantities. The two most common are the upward irradiance, E_u,

$$E_u = \int_{-2\pi} L|\cos\theta| d\omega$$

in which the integration is completed over all solid angles in the lower hemisphere, and the downward irradiance, E_d,

$$E_d = \int_{+2\pi} L|\cos\theta| d\omega$$

in which the integration is completed over all solid angles in the upper hemisphere.

Downward quanta irradiance, q, in the visible part of the spectrum (350 to 700 nanometers (nm)) can be related to the downward irradiance as

$$q(350 \text{ to } 700 \text{ nm}) = \int_{300}^{700} Ed(\lambda) \cdot \lambda \cdot h^{-1} \cdot s^{-1} \cdot d\lambda$$

where $h = 6.626 \times 10^{-34}$ joule sec is Planck's constant and $s = 3 \times 10^{8}$ m s^{-1} is the speed of light <u>in vacuo</u>. This is a measure of available light energy for photosynthesis (PAR).

Optical properties can be divided into two classes: the inherent and apparent properties. An inherent property is independent of changes in the radiance distribution; an apparent property is dependent. Inherent properties of interest in this context are the light absorption coefficient a(x,y,z,t), the light scattering coefficient b(x,y,z,t), and the light attenuation coefficient c(x,y,z,t) = a + b. All have units of reciprocal length m^{-1}. The light scattering function $\beta(\theta)$ is defined through the equation

$$dI = \beta(\theta) \cdot E \cdot dV$$

where E is the irradiance in the scattering volume. The term $dV \cdot \beta(\theta)$ is related to the scattering coefficient since

$$b = \int_{4\pi} \beta(\theta) d_{\omega}$$

Apparent properties include the vertical attenuation coefficients for irradiances, such as

$$K_d = -\frac{1}{E_d}\frac{\partial E_d}{\partial Z} \qquad \text{for the downward irradiance}$$

$$K_L = -\frac{1}{L}\frac{\partial L}{\partial Z} \qquad \text{for the radiance}$$

$$K_q = -\frac{1}{q}\frac{\partial q}{\partial Z} \qquad \text{for the quanta irradiance}$$

In practice, the K-functions are calculated as

$$K = \frac{1}{Z_2 - Z_1} \ln\left(\frac{E(Z_1)}{E(Z_2)}\right)$$

Again, all the attenuation coefficients have units of reciprocal length m^{-1}.

It might be noted, however, that since all the K-functions are apparent properties, they are subject to variability with solar elevation, cloud cover, and state of the sea (e.g., Højerslev, 1986b for more details).

Beam transmittance can now be defined in a straight forward manner by considering the ratio of an initial flux $\Phi(o)$ traveling in a narrow near-parallel beam over a distance r to a position where it is measured as $\Phi(r)$. Thus

$$\ln(\Phi(r)/\Phi(o)) = -c\ r \qquad (1)$$

defines the light attenuation coefficient, c. The distance r for the transmissinity measurements in this study was 0.5 m for the Danish transmissometer and 0.25 m for the Sea Tech transmissometer.

The calibration of a transmissometer calls for special attention since it can be done in two fundamentally different ways.

The light transmission T_1 over the pathlength r in a water mass having a light attenuation coefficient equal to c_1 can be written as

$$T_1 = \frac{\Phi_1}{\Phi_a} = k\ e^{-c_1 r} \qquad (2)$$

where Φ_a and Φ_1 are the fluxes recorded by the transmissometer when measuring in air and in water, respectively. k is a calibration constant

depending on: (i) the geometry and optics of the transmissometer, the latter being dependent on wavelength, (ii) the changes in the beam divergence when measuring in air and water, respectively, and (iii) the changes in light reflections at the two windows when facing air and sea water, respectively. For a high quality transmissometer k lies around 0.94. The factor k can be determined by measuring c_1 by means of an independent optical calibration device which often consists of a lamp house, an optical bench and a light sensor where the latter can be set at different distances from the lamp house underwater. Sometimes the calculation of k is done by assuming that the calibration tank contains pure (uncontaminated) water. This means that $c_1 = c_w$ where c_w is the light attenuation coefficient for pure water. Table 3.4-2 gives tabulated values for a_w and b_w which allow calculation of c_w. Consequently, by knowing the wavelength at which the c-meter operates, $c_1 = c_w$ is known more or less accurately and k can be calculated. It shall, however, be emphasized that the test water in the calibration has to be absolute pure. Moreover, the validity of the values given in Table 3.4-2 is still a matter of dispute.

It is possible to go one step further in the calibration scheme. Like before the following relation is valid

$$T_2 = \frac{\Phi_2}{\Phi_a} = k\ e^{-c_2 r} \qquad (3)$$

where the water for this case has a light attenuation coefficient equal to c_2.

Division of Equations (2) and (3) leads to:

$$\frac{T_1}{T_2} = \frac{\Phi_1}{\Phi_2} = e^{-(c_1 - c_2) r} \qquad (4)$$

and

$$c_1 - c_2 = 1/r \ln \frac{\Phi_2}{\Phi_1} \ (m^{-1}) \qquad (5)$$

The Danish transmissometer calibration is performed by taking a batch of fairly pure water and measuring its light attenuation coefficient c_1 by using a calibration bench described earlier. The transmissometer is then dropped into the tank and Φ_1 is measured. According to Equation (5) the only unknowns left are c_2 and Φ_2 since r = 0.5 m. When the transmissometer is applied at sea, Φ_2 is measured versus depth allowing c_2 to be calculated, so that the light attenuation coefficient versus depth is completely determined. The Sea Tech transmissometer calibration formula is given as:

$$c_2 - c_w = 1/r \ln \frac{\Phi_w}{\Phi_2} \ (m^{-1}) \qquad (6)$$

Table 3.4-2. Spectral values of vertical attenuation coefficient for the downward irradiance k_w, light absorption coefficient, a_w, for the clearest natural ocean waters, and light scattering coefficient, b_w, for pure artificial sea water. After Morel (1974), Smith and Baker (1981).

λ nm	K_w m^{-1}	a_w	b_w m^{-1}	λ nm	K_w m^{-1}	a_w	b_w m^{-1}
300	0.154	0.141	0.0262	650	0.350	0.349	0.0010
310	0.116*	0.105	0.0229	660	0.400	0.400	0.0008
320	0.0944	0.0844	0.0200	670	0.430	0.430	0.0008
330	0.0765	0.0678	0.0175	680	0.450	0.450	0.0007
340	0.0637	0.0561	0.0153	690	0.500	0.500	0.0007
350	0.0530	0.0463	0.0134				
360	0.0439	0.0379	0.0120	700	0.650	0.650	0.0007
370	0.0353	0.0300	0.0106	710	0.834	0.839	0.0007
380	0.0267	0.0220	0.0094	720	1.170	1.169	0.0006
390	0.0233	0.0191	0.0084	730	1.800	1.799	0.0006
				740	2.380	2.38	0.0006
400	0.0209	0.0171	0.0076	750	2.47	2.47	0.0005
410	0.0196	0.0162	0.0068	760	2.55	2.55	0.0005
420	0.0184	0.0153	0.0061	770	2.51	2.51	0.0005
430	0.0172	0.0144	0.0055	780	2.36	2.36	0.0004
440	0.0170	0.0145	0.0049	790	2.16	2.16	0.0004
450	0.0168	0.0145	0.0045				
460	0.0176	0.0156	0.0041				
470	0.0175	0.0156	0.0037				
480	0.0194	0.0176	0.0034				
490	0.0212	0.0196	0.0031				
500	0.0271	0.0257	0.0029				
510	0.0370	0.0357	0.0026				
520	0.0489	0.0477	0.0024				
530	0.0519	0.0507	0.0022				
540	0.0568	0.0558	0.0021				
550	0.0648	0.0638	0.0019				
560	0.0717	0.0708	0.0018				
570	0.0807	0.0799	0.0017				
580	0.109	0.108	0.0016				
590	0.158	0.157	0.0015				
600	0.245	0.244	0.0014				
610	0.290	0.289	0.0013				
620	0.310	0.309	0.0012				
630	0.320	0.319	0.0011				
640	0.330	0.329	0.0010				

* Compared with the measured value of 0.069 found in the present data (See Section 4.7.2).

where Φ_w is the received flux when the transmissometer is submerged into the purest water obtainable for which $c_w = 0.364\ m^{-1}$ at 660 nm as claimed by the Sea Tech transmissometer manufacturer B. Bartz (pers. comm. - compare with Table 3.4-2). Since the fluxes Φ_w and Φ_2 are converted into Volts, Equation (6) becomes:

$$c_2 - 0.364 = 4 \ln \frac{V_m}{V_2} \ (m^{-1}) \qquad (7)$$

The Sea Tech transmissometer is constructed electronically to give a voltage output equal to 5V when measuring in a hypothetical water mass, being without light scattering and light absorbing properties. This means, in turn, that the maximum signal V_2 becomes $= V_w = 4.56$ V for which case $c_2 = 0.364 = c_w\ (m^{-1})$. In this study V_2 surpassed 4.56 V in several cases at the blue clear water station DD. This means that the <u>absolute</u> calibration is unreliable. On the other hand the <u>variation</u> of c with depth and time is most likely unaffected by the above mentioned instrumental failure.

Equation (7) can be rewritten as:

$$c_2 = 4 \ln \frac{\Phi_w}{\Phi_2} + 0.364 = 4 \ln \frac{V_w}{V_2} + 4 \ln \frac{5}{V_w} \ (m^{-1}) \qquad (8)$$

in which $V_w = 4.56V$ makes the last term equal to the above $0.364\ m^{-1}$. Rearrangements of Equation (8) results in:

$$c_2 = 4 \ln \frac{5}{V_2} \ (m^{-1}) \qquad (9)$$

from which it is directly seen that V_2 always has to stay below 4.56 V since natural occurring sea waters have a positive light attenuation due to the presence of suspended matter and dissolved organic substances.

3.5 <u>Remote Sensing</u>

3.5.1 <u>AVHRR Data</u>

Infrared images of the Gulf of Mexico were acquired from NESDIS and NORDA on 9-track digital tape in NESDIS 1B format and processed using the University of Miami image processing algorithms. The data were first sectorized to extract the desired geographic area, atmospherically corrected, and remapped to an equirectangular grid. Two versions of the resultant image were saved: one retaining the full one km resolution, the other subsampling every second pixel in a form which reduced memory requirements.

Using the second image allowed addition of overlays such as land masks, bathymetry, and station markers to the image. Once processed in this way, the images were color enhanced to show boundaries between cooler and warmer water. Initially, the palette was chosen to differentiate temperature in one degree increments with cooler water depicted as shades of blue and warmer water in shades of red. The palette can be modified to provide different color schemes or to show finer gradations of temperature.

During fall through late spring, sea surface temperatures can range from 15°C on the west Florida shelf to 26°C in the Loop Current and in warm eddies. During summer and early fall, temperatures are uniform throughout the Gulf of Mexico and generally warmer than 26°C.

3.5.2 Satellite Altimetry

Satellite altimetry data were used on a limited basis during Year 5 to evaluate eddy detection in the western Gulf of Mexico. Two general methods are available for evaluating altimeter data: one uses data from the crossover points of a number of tracks to determine the shape of the ocean surface; the second or collinear track method, the one used here, involves computation of a mean sea surface along a given track from a large number of successive passes.

Collinear track data from segments over deep water are first edited to remove spikes, linearly interpolated to fill short gaps, and resampled at fixed points. Data at the fixed points are averaged to produce a mean surface along the specified track. The mean surface used in this study was computed from the first 14 Exact Repeat Missions (ERM's). The mean surface is the sum of the earth's geoid and the mean ocean dynamic topography over the averaging period. In the Gulf of Mexico the mean surface includes the effects of the Loop Current and persistent warm eddies.

The mean surface is next subtracted from the instantaneous altimeter values along each pass over the track. The difference data include satellite orbit errors, earth and ocean tides, and free path (altimeter range) errors caused by moisture and free electrons in the atmosphere. Free path errors have not been corrected in this data set. Earth and ocean tides can be removed using model data supplied by NOAA or by modelling local tides. Satellite errors can be removed most simply by performing a linear regression of the difference data and then subtracting the regression line from the difference data as shown in Figure 3.5-1.

Corrected difference data along three tracks, two parallel ascending tracks and one descending track crossing the first two, were compared with AXBT data collected in mid October 1988 including one AXBT track (see Figure 2.3-3, track segment indicated by Stations 1 through 22) made at the same time as a GEOSAT overflight. Altimeter data were compared qualitatively with temperature at 250, 300 and 400 m and with the depth of the 14°C isotherm. The 'best' fit of altimetry is with the depth of the 14°C isotherm as shown in Figure 3.5-2. Here data from an ascending

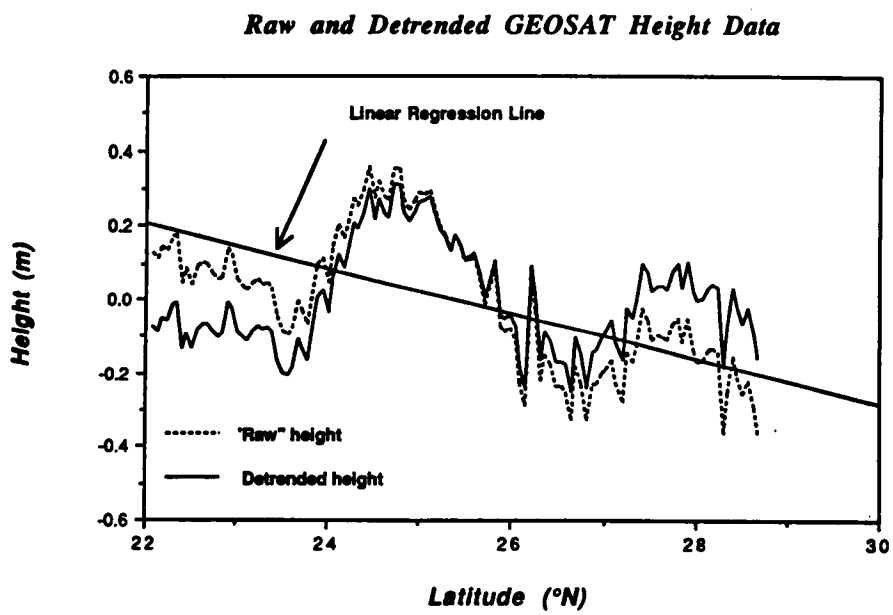

Figure 3.5-1. Raw and detrended GEOSAT height data from an October 8, 1988 descending pass in the central Gulf of Mexico. Subtraction of the linear regression line from the "raw" data gives detrended data.

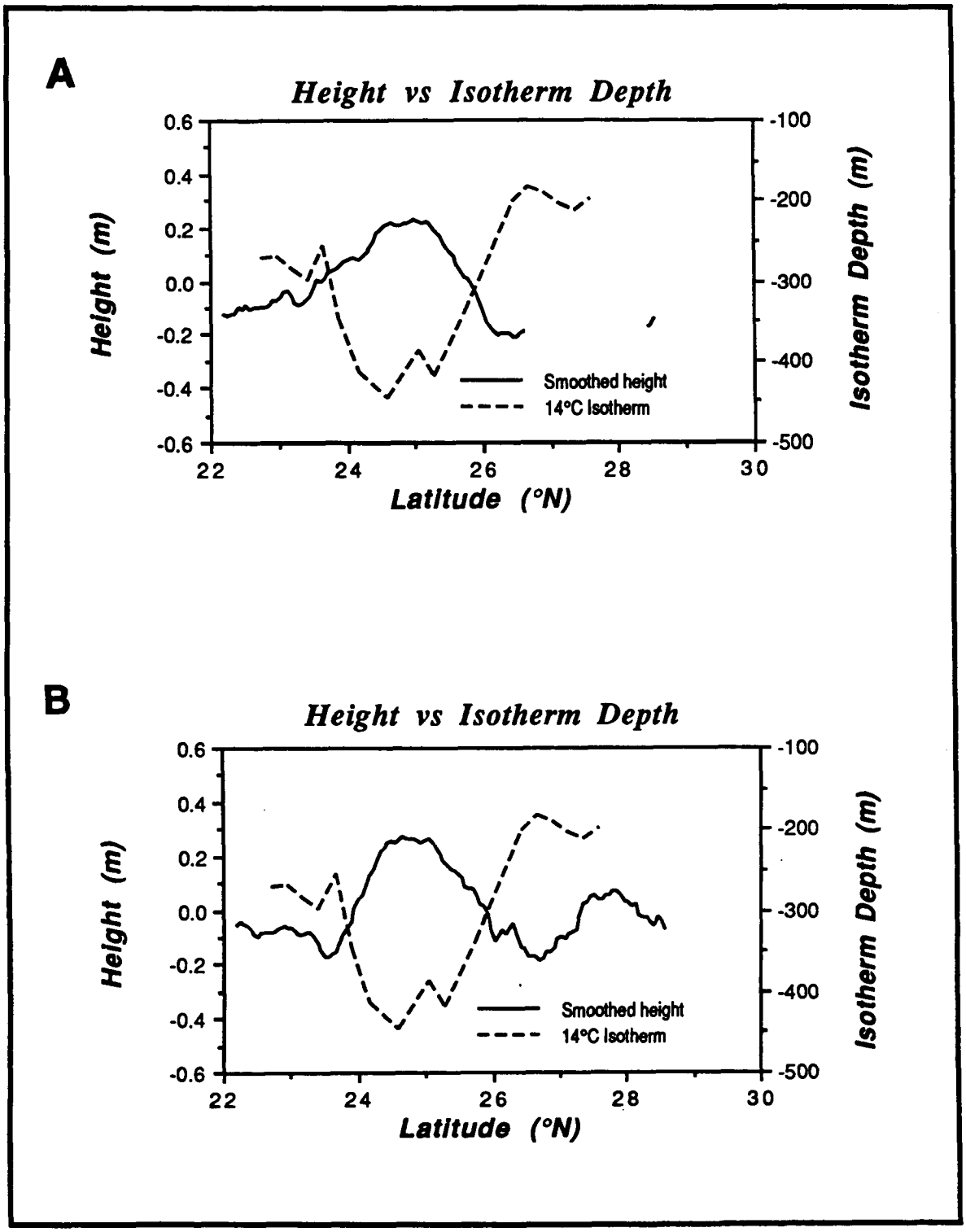

Figure 3.5-2. Sea surface height and isotherm depth for (a) concurrent sea surface height from an ascending pass and the 14°C isotherm depth from AXBT Stations 1 through 22 (Figure 2.3-3b) and (b) sea surface height data from a descending pass and 14°C isotherm depth from AXBT Stations 1 through 22.

pass and a descending pass are compared with the 14°C isotherm depth. The other ascending pass did not cross the warm eddy. The front position in the altimeter data was determined as the mid point of the line with maximum slope while the front was defined in the temperature data as the location of the 14°C water at 300 m.

The depth of the 14°C isotherm was fit with a polynomial, values were calculated at the same latitudes as the GEOSAT data, and correlations between isotherm depth and sea surface height were determined.

3.6 Subsurface Observations

3.6.1. Inverted Echo Sounder Data

Besides using the high resolution pressure record from IES #2 to analyze deep basin tides, the IES #1 travel-time record was used to relate to the upper ocean temperature structure and subsequently the passage of warm and cold eddies. An explanation of how this is accomplished is discussed below.

The IES emits 24 pings or sound pulses every sample period and records the travel time of each ping to the surface and back. The velocity of sound in the ocean is a strong function of temperature, and thus travel times are expected to be principally related to changes in the thermal structure of the water column. Travel times are an integrated measure of water column structure and thus are expected to better correlate with integrated measures of isotherm displacement, such as dynamic height, than with the depths of individual isotherms. Since seasonal warming has its major affects in the upper 20 m of the surface layer, it is expected to have only minor effects on travel times over the 3000 m depth of the water column. A statistical measure of each set of 24 pings is made to generate a representative travel time measurement for each sample period. Two measures were used, the median and the mode, and it was found that the time series were very similar with the median having slightly less high frequency noise. The median and mode are more robust estimates of the average travel time than the more usual arithmetic mean.

The relationship of the median travel times to isotherm depths and dynamic height was generated by finding all XBT and CTD casts that were close to the IES #1 site during the 18 months of deployment. The depths of the 8, 14 and 20°C isotherms were extracted from the profiles, and for temperature profiles, the pseudo-dynamic height between 150 and 650 dbars was generated using the method developed in Year 3 (SAIC, 1988; Section 3.3.2). On two occasions 3000 m CTD casts were made next to the site, but the travel times and dynamic heights were approximately the same, so a straight line could not be fitted. Subsequently, to increase the sample size, isotherm depths and pseudo-dynamic heights were obtained from stations taken by the JUSTO SIERRA on three cruises where four stations were taken (NE, NW, SE and SW) around the IES site. These data were approximately averaged in space and time to generate estimates of the isotherm depths at the site. Hydrographic data were taken from the PELICAN cruises, the second AXBT survey and the JUSTO SIERRA. The comparisons of isotherm depths and dynamic heights were made with travel

times made at the time (or estimated time) of the cast. Travel times were extracted from both the raw and 3-HLP filtered IES records.

The plots of raw and 3-HLP median travel times versus isotherm depths and pseudo-dynamic heights are given in Figure 3.6-1(a-d). The time series of 40-HLP median and mode travel times are given in Figure 3.6-2 which also notes the approximate times of the cruises. It can be seen that the hydrographic data were taken during times representing the full range of observed travel times. The 14°C and 20°C isotherm depths and pseudo-dynamic heights inversely correlate with travel times with R^2 values better than 0.85. The straight line least square fits were made with 3-HLP travel times. The depth of the 8°C isotherm shows more scatter and is less well correlated. Therefore, travel times correlate with upper layer thermal structure quite well, such that the more shallow the isotherms the colder the upper layer and the longer the travel times. Therefore, a warm eddy should be detected by relatively short travel times and a cold feature by relatively long travel times. The record in Figure 3.6-2 will be used in Chapter IV along with current meter and temperature data from Mooring GG, the composite maps of isotherm depth and the time series of SENATOR SOOP sections to discuss the occurrence of warm and cold features at Mooring GG.

3.7 Oceanic Frontal Analyses

3.7.1 SOOP Data

All of the available QUEENY transects are given in Figure 3.7-1 The majority cluster around a line from 24°N, 82°W to 27.4°N, 91°W. After removing the transects that deviate significantly from this mean line and any particularly short transects, 98 sections remain covering a period of 90 months. The majority of the QUEENY stations employed T6 XBT's (460 m depth), and station spacing ranged from about 15 to 30 km. An example of a QUEENY section showing both the Loop Current and a detached warm eddy off to the west is shown in Figure 3.7-2. The available transects for the New Orleans to Yucatan run are given in Figure 3.7-3. The transects divide into two lines, one favoring the Campeche Bank on the east side of the Yucatan Straits, and the other, the side near Cuba. Unfortunately, the tracklines did not alternate, so for long periods one line was favored over the other. However, since our primary interest is the northward extension of the Loop Current front, essentially all the track lines were used with the analysis of the position of the front restricted to north of 25°N. The NESTOR transect used T7 XBT's (760 m depth) with similar station spacing to the QUEENY transect. In all, 73 transects were run covering a period of 41 months.

Both the QUEENY and NESTOR transects were treated in the same manner. For each transect, the stations were projected onto the mean tracklines given in Figures 3.7-1 and 3.7-3. At each XBT station the depth of the required isotherm (i.e., 20°C, 15°C) was extracted. These depth values were then linearly interpolated to a regular spaced 20 km grid beginning at the marked origins. Points on this regular grid beyond the first or last station of the transect were flagged as having no valid data. The

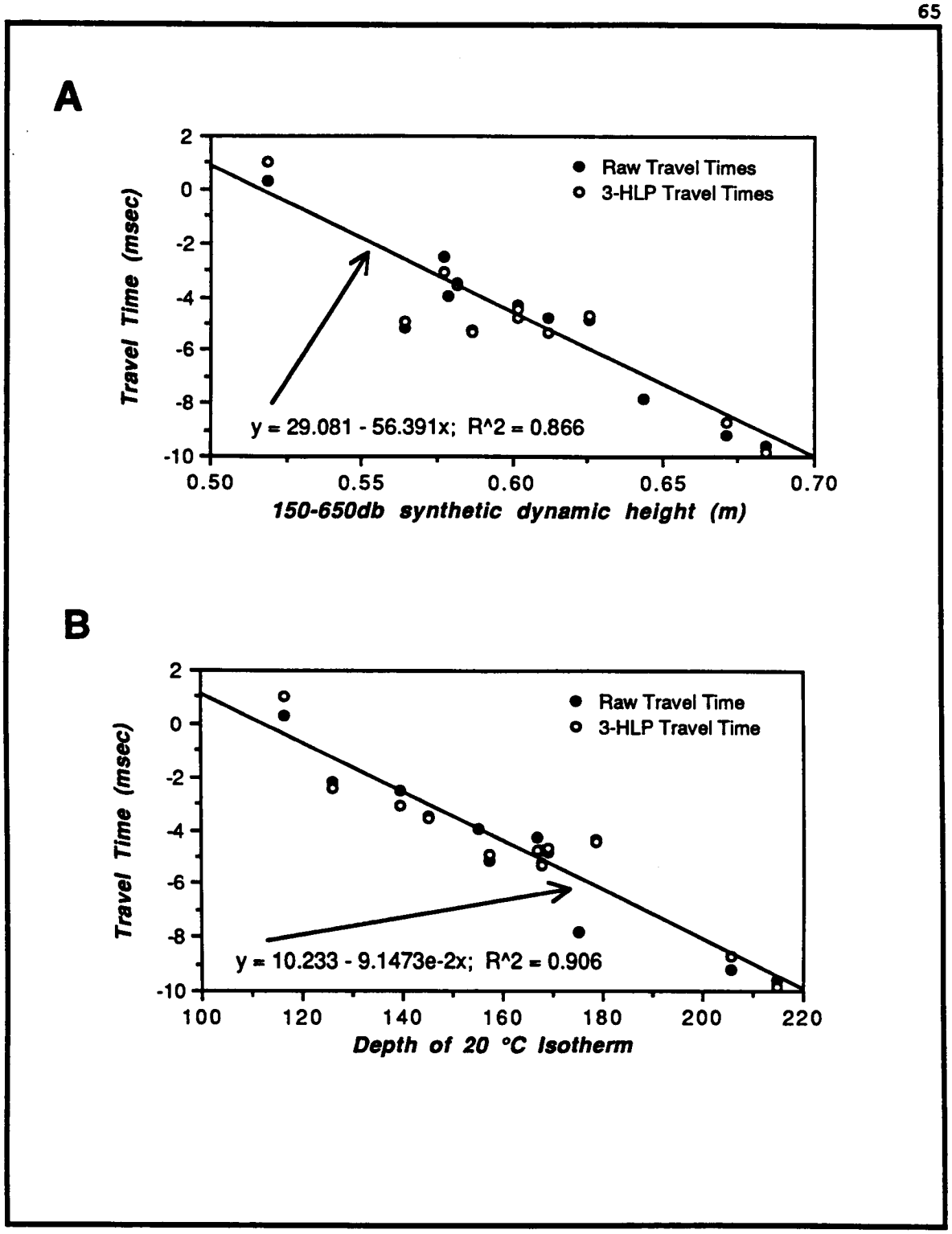

Figure 3.6-1a,b. Correlations from raw and 3-HLP median travel times from IES #1 record MGG6 and (a) synthetic dynamic heights and (b) the depth of the 20°C isotherm.

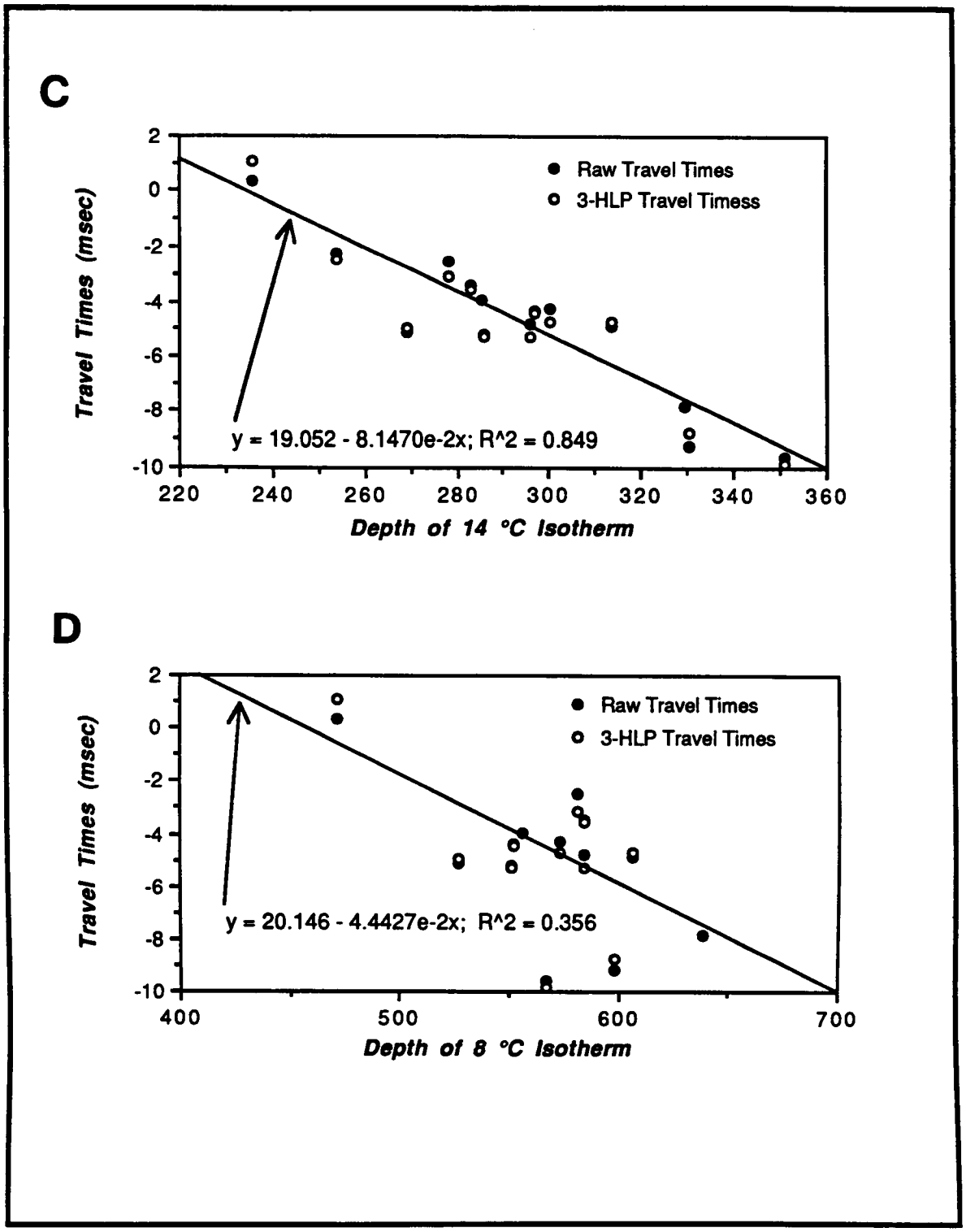

Figure 3.6-1c,d. Correlations from raw and 3-HLP median travel times from IES #1 record MGG6 and (c) the depth of the 14°C isotherm and (d) the depth of the 8°C isotherm.

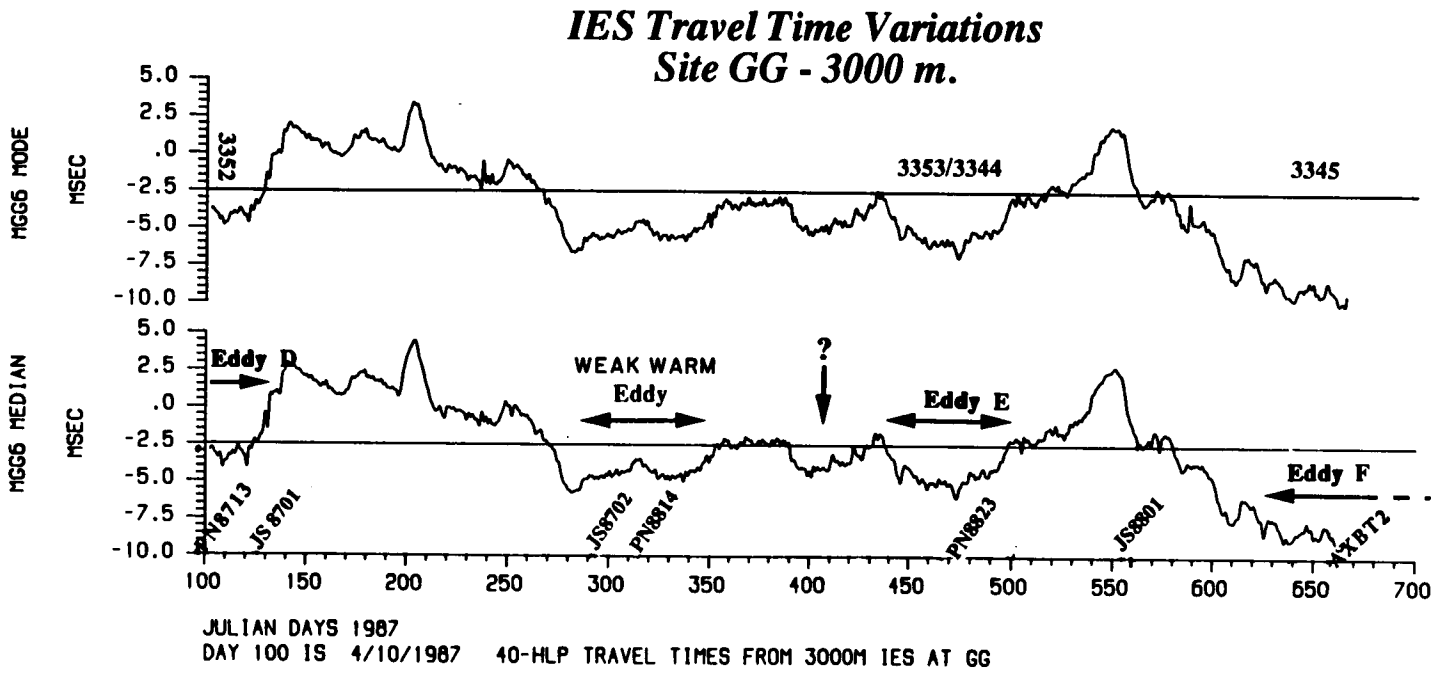

Figure 3.6-2. Forty-HLP IES #1 median and mode travel times for record MGG6. The eddies moving through the site are identified along with the approximate dates of hydrographic cruises and the occurrence of ARGOS drifters.

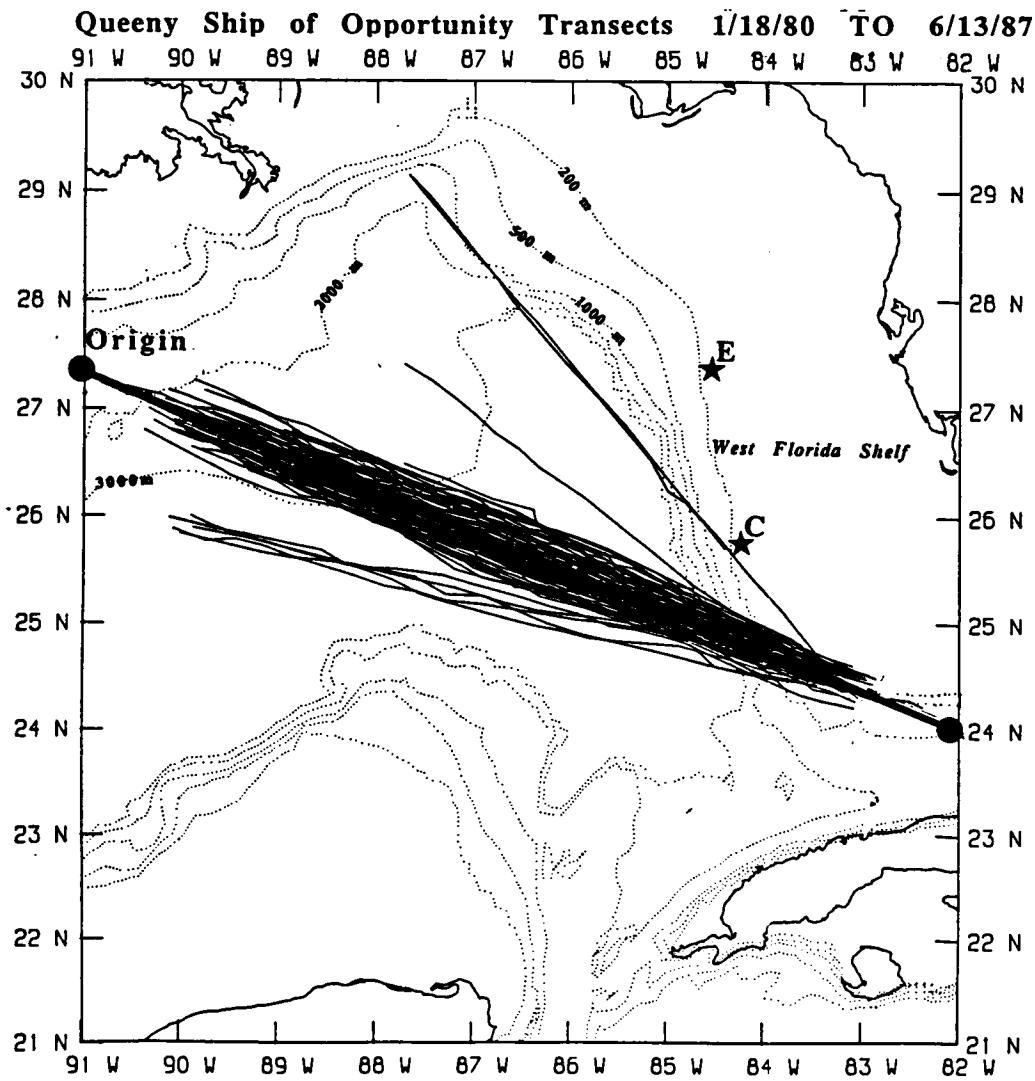

Figure 3.7-1. Available QUEENY east-west Ship-of-Opportunity transects between 1980 and 1987. The positions of Moorings C and E on the west Florida shelf are marked. The mean transect with the position of the origin used in the analysis is marked on the map.

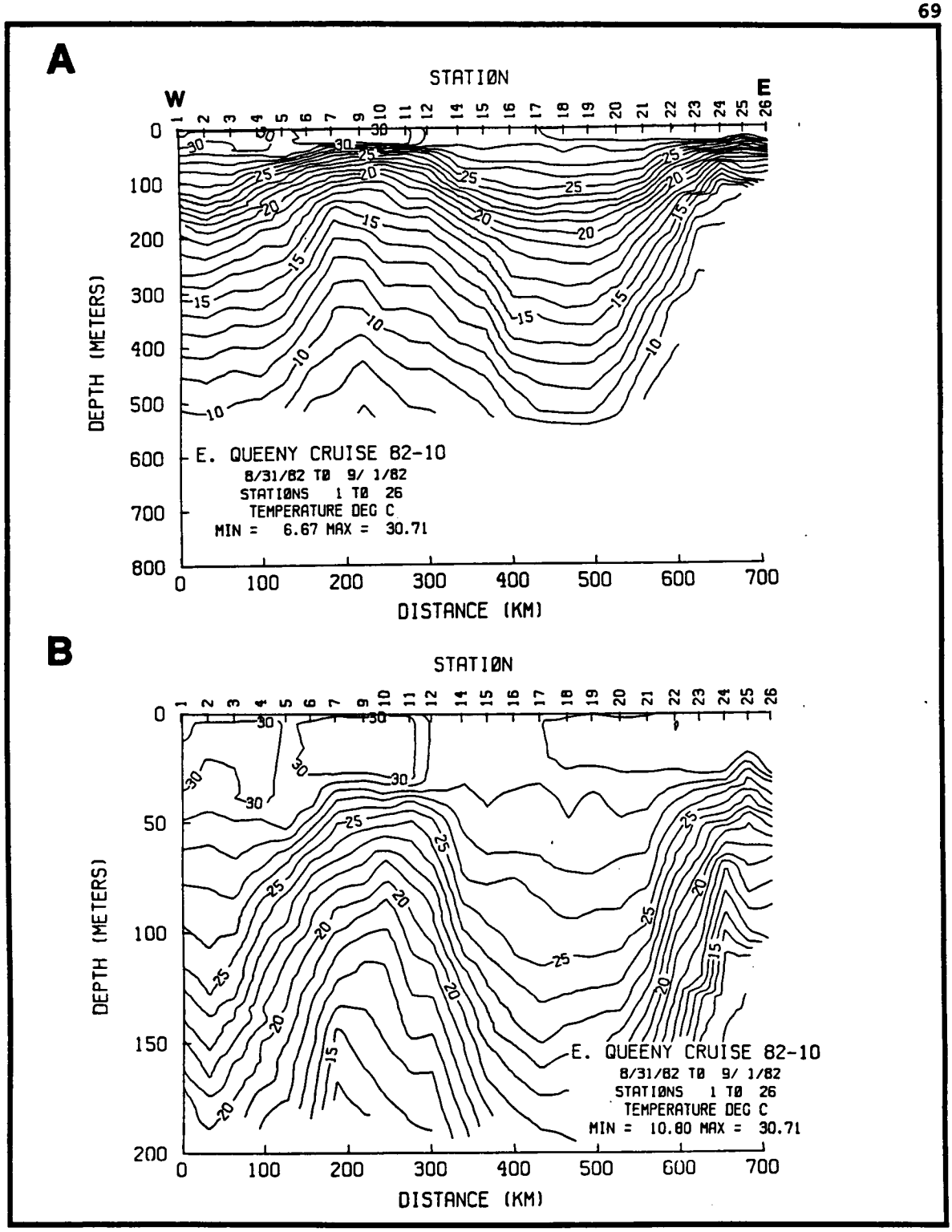

Figure 3.7-2. **A typical QUEENY section through the Loop Current and the eastern side of a detached warm eddy showing the (a) zero to 500 m isotherm structure and (b) zero to 200 m isotherm structure.**

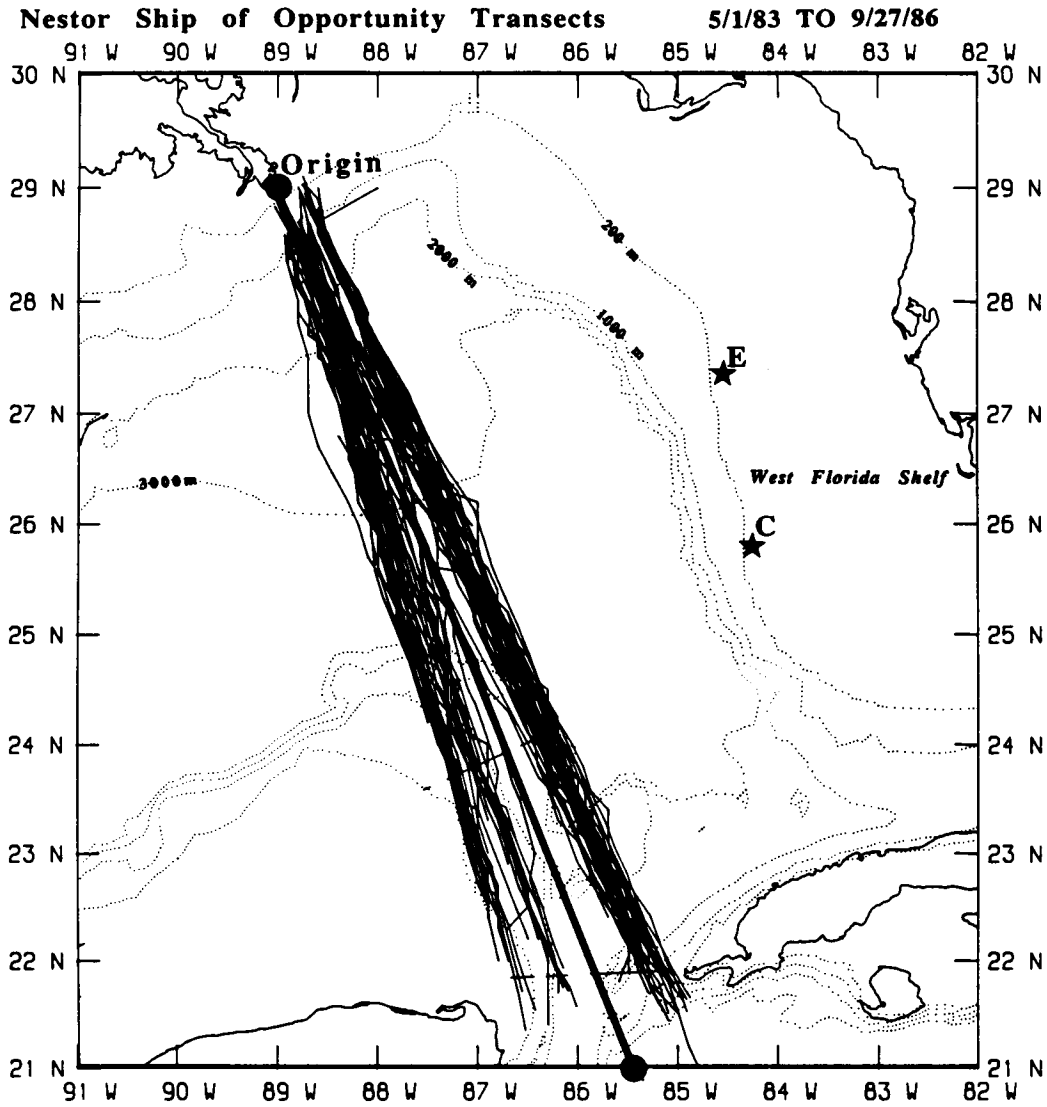

Figure 3.7-3. Available New Orleans to Yucatan Straits Ship-of-Opportunity transects from 1983 to 1986. The mean transect with the position of the origin used in the analysis is marked on the map.

results of this processing for the depth of the 20°C isotherm for the QUEENY transect in Figure 3.7-2 is given in Figure 3.7-4.

From Figure 3.7-2 it can be seen that a good definition of the position of the major temperature fronts is the position of the 20°C isotherm where it crosses the 125 m depth level. Figure 3.7-4 shows the positions of the eastern (LE) and western (LW) Loop Current fronts and the eastern warm eddy front (EE) obtained from the QUEENY 20°C isotherm depths. On occasions where an eddy is separated and the transect extends far enough to the west, the position of the western eddy front can sometimes be determined. This parameter is denoted EW. Other parameters defined in Figure 3.7-4 are the maximum isotherm depth in the Loop Current (DC), its position (LC) and the cross-sectional areas, AW and AE, defined by the isotherm between LW and LC and LC and LE, respectively. On occasion, the Loop Current does not extend across the QUEENY transect usually after the break off of an eddy. In this case LW, LC and LE contract to the same point which is estimated from examining the time sequence of the sections. The NESTOR transect is treated the same way, and the position where the 20°C isotherm slopes up to the north through the 125 m level is denoted LN. On a few transects the section crosses part of an eddy close to the Mississippi Delta slope. In these cases care is taken to choose the northern Loop Current front by cross checking the eddy positions with appropriate QUEENY sections.

3.7.2 Thermal AVHRR and Coastal Zone Color Scanner (CZCS) Imagery

The monthly frontal analysis maps were produced by RTI for the winter and early spring from AVHRR data for all years and for the summers of 1984 through 1985 from CZCS data. The maps were generated from two or three clear sky images in each month. For each image a frontal position line for the Loop Current, any warm eddies and shelf-slope features were hand drawn. The monthly composite was produced by subjectively averaging the fronts. This procedure usually only applies to the Loop Current front since each warm eddy was usually only present in one image. The shelf-slope front is defined as any sharp gradient that cannot be identified as the Loop Current or a major warm eddy. The precision of the analyst placing a line on the image is about ± 5km. The accuracy with which the surface front represents a subsurface front as determined from hydrography varies according to the type of feature present on the boundary of the major feature (i.e., shallow warm extrusions or filaments are not associated with major subsurface thermal structures). However, some comparisons with fronts located from SOOP transects and individual RTI AVHRR analyses of the Loop Current show an accuracy of approximately ± 10km. The accuracy of CZCS analysis is less since it is often unable to detect fronts seen in AVHRR images at similar times. It is conservatively estimated that CZCS front error bounds are about twice the AVHRR uncertainties. A comparison is made of monthly frontal positions from the QUEENY and NESTOR transects and the equivalent RTI analyzed positions (see below) and is discussed in Section 4.2.2.

The monthly frontal analysis maps were digitized or statistically analyzed as follows: A ½° latitude by ½° longitude grid was overlayed on each map covering a region bounded by 18°N and 31°N and 81°W and 98°W.

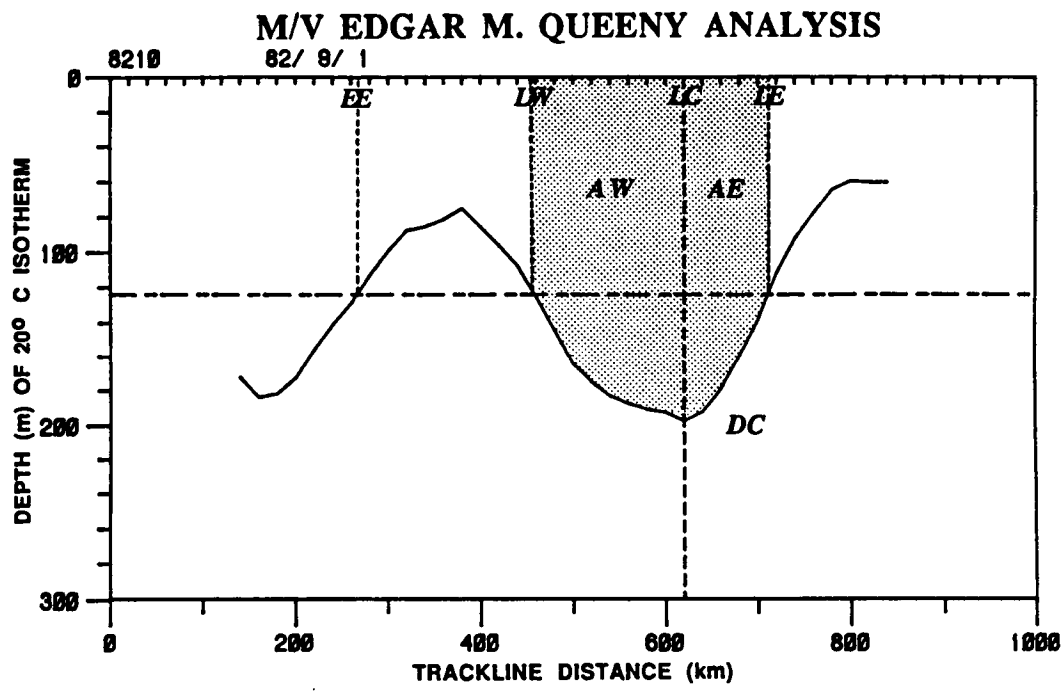

Figure 3.7-4. The analysis of the critical depth of the 20°C isotherm (125 m) from a representative QUEENY section. The designations: EE, LW, LC and LE are front positions; AW and AE are cross-sectional areas and DC is the maximum depth of the isotherm in the Loop Current.

Each type of front (Loop Current, warm eddy and shelf-slope) was digitized separately. The positions of the fronts were digitized by noting in which ½° by ½° cells they occurred. In addition, for the Loop Current and warm eddies, the cells completely within the front were also noted so that the area covered by the feature could be calculated. The assumption was made in calculating the area of the Loop Current and warm eddies that cells containing the front position were counted as a half cell area and that each cell had an area of 2740 km^2 corresponding to the area of the cell in the middle of the grid. Cell areas vary by about ± 3% between the top and bottom of the grid. An example of the front and interior cells counted for the Loop Current on a monthly map for December 1976 is given in Figure 3.7-5. The total area covered by the Loop Current for December 1976, from this figure, is 38 front cells x ½ + 57 interior cells = 76 x 2740 = 208,240 km^2. Similarly, the warm eddy centered at 26°N, 91.5°W has 14 front cells and 11 interior cells giving an area of 49,320 km^2.

The individual digitized frontal analyses (differentiated by front type) are averaged to produce for each cell the percentage of the total period (or probability) a front occurs, and the percentage of the total period the cell is covered by the warm water of the Loop Current or a warm eddy. A cell with a front is regarded as being half covered by warm water, similar to the area calculation above. The total period is represented by analyses from January 1976 to December 1985, if only the VHRR and AVHRR data are considered. Since there are seven thermal analyses per year, the total time covered by the maps is effectively five years or alternatively 10 years of winters and early springs. If the thermal imagery is combined with the CZCS data then a total of 80 analyses cover the same 10 year period with continuous monthly coverage between November 1983 and December 1985. The statistical results using the thermal and CZCS analyses are discussed in Chapter IV.

Figure 3.7-5 also shows the QUEENY and NESTOR mean transect lines discussed above. For the period November 1983 to December 1985, the distance of the Loop Current fronts relative to the west and north origins of the sections, respectively were measured from the maps. Thus, monthly imagery equivalents of LW, LE and LN were generated for comparison with the SOOP parameters.

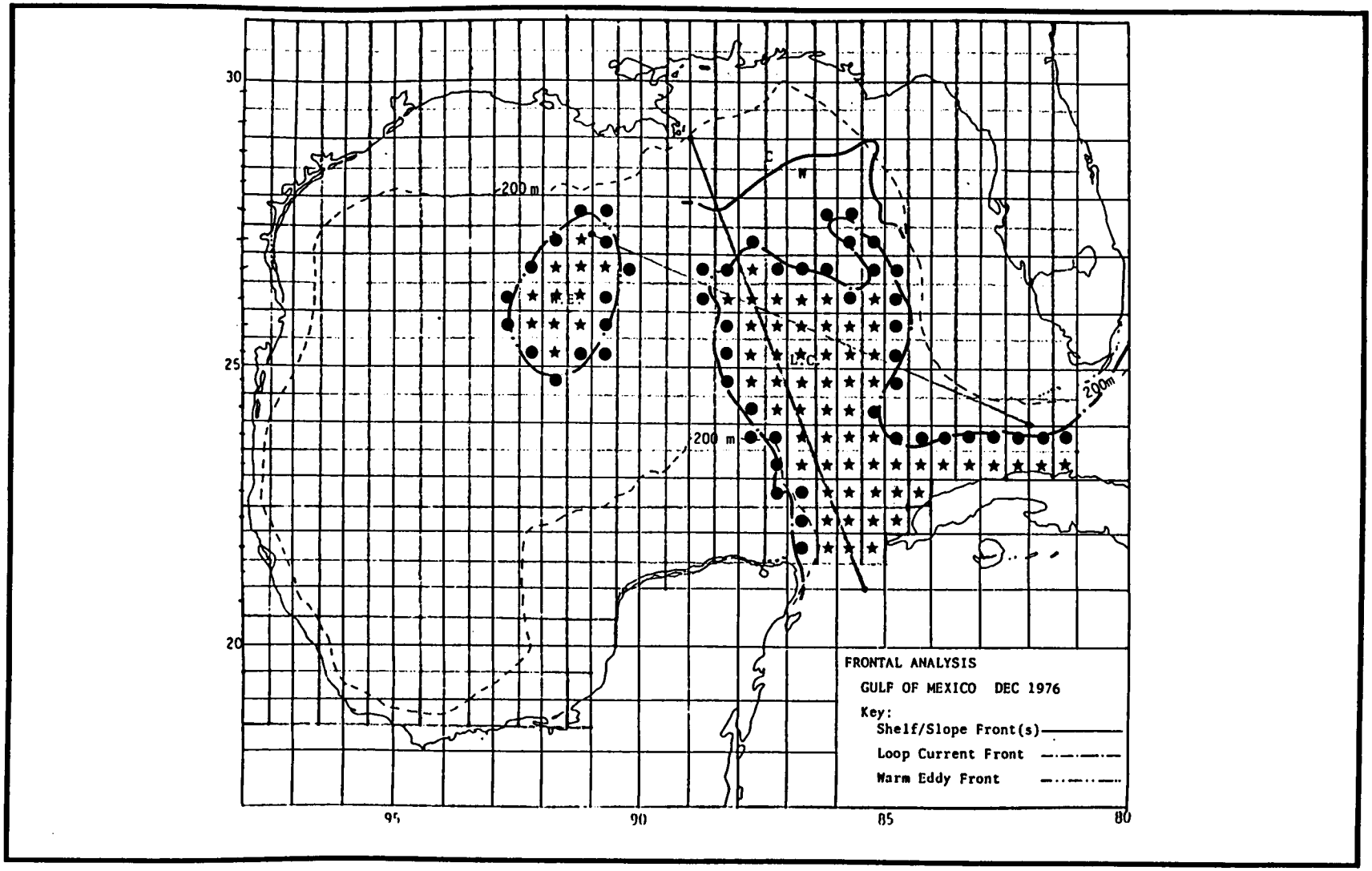

Figure 3.7-5. Example of the digitization, using a 1/2° x 1/2° grid, of the Loop Current and warm eddy fronts (•) and the areas contained by these fronts (*). The fronts are from monthly composites of thermal satellite imagery.

IV. TECHNICAL DISCUSSION

4.1 Introduction

Program Year 5 objectives are an improved understanding of the circulation patterns on the west Louisiana/east Texas shelf, slope and rise with regard to the specific elements listed below:

- **Long time series** - Provides information concerning the Loop Current movement and associated eddy shedding. The primary 7 material (SOOP transects) used in this presentation was taken over the entire multi-year program.

- **Deep Circulation** - Examines characteristics of circulation below 1500 m throughout the basin.

- **Loop Current Eddies** - Dynamics and kinematics providing insights to the evolution and structure of Loop Current anticyclones as they translate westward. This topic has been contained in each previous program year.

- **Slope Circulation**

  - **Loop Current eddies** - Isolating this topic acknowledges the considerable influence which episodic LC eddies and related events can have on the slope environment.

  - **Non-eddy related Slope Circulation** - In the absence of direct eddy influence, another suite of processes tend to govern the slope circulation patterns.

- **Shelf Circulation** - As a result of the shallow water depth and locally large variations in density, a suite of processes can occur on a shelf which are not expected in other environments.

- **Marine Optics** - The shelf is directly influenced by a large contribution of estuarine and riverine water which has a profound influence on the light penetration and other physically and biologically important processes.

Toward this end, the various data sets presented in Chapter II were taken and analyzed using techniques described in Chapter III. Results of these analyses have been used by the program principal investigators to identify key conditions and when possible to relate these conditions to circulation producing mechanisms. Chapter IV describes the results of this final synthesis effort.

The above organization provides an orderly presentation of new information while facilitating a comparison of the insights described in this report with those from previous program years. This is consistent with

the integrated nature of the various regional studies undertaken as parts of the overall Physical Oceanography Program.

4.2 Long-term Variability

4.2.1 Loop Current Variability

4.2.1.1 Introduction

The Loop Current (LC) is the major source of mesoscale variability in the Gulf of Mexico. The extension of the Loop Current to the north and subsequent pinching off of large warm anticyclonic eddies dominates the circulation of the eastern Gulf. Subsequent propagation of the warm eddies into the western Gulf is the major source of energy for upper layer circulation processes both in the deep basin and on the surrounding outer shelves. Loop Current variability is also a major source of topographic Rossby waves which dominate deep circulation below 1000 m in both the eastern and western Gulf (Section 4.4). The frequency of eddy shedding has been a matter of some controversy with early suggestions of an annual cycle (Leipper, 1970; Maul, 1977) which seemed to be confirmed by a regular 14-month cycle produced by Hurlburt and Thompson's (1980; 1982) two-layer numerical model results. Subsequent refinements of this model (Wallcraft, 1986) suggested that introducing variability in the form of winds or changing the input volume transport through the Yucatan Straits, especially in the lower layer, can make the eddy shedding period quite variable ranging from about six to 14 months. The regular seeding of warm eddies, with ARGOS drifters and the monitoring of the LC with satellite imagery, during the MMS Gulf of Mexico Program (SAIC, 1987; 1988), has indicated that the Loop Current can reform quite rapidly after an eddy detachment (Lewis and Kirwan, 1987) and that the period between the generation for warm eddies may be as short as six months (SAIC, 1988).

Little systematic effort has taken place to quantify the long-term LC variability and the eddy-shedding cycle. The major tool in previous studies has been AVHRR imagery (Sturges and Evans, 1983; Vukovich, 1988), but because of surface warming, the LC and eddies cannot be detected during the summer months (June through October). However, a reasonably consistent time series with data throughout the year and available over a number of consecutive years are the Ship-of-Opportunity (SOOP) XBT transects that have been maintained by National Marine Fisheries Service (NOAA) and MMS. These are composed of two transects across the Loop Current: the M/V E.M. QUEENY transect from the Straits of Florida to Galveston and the M/V NESTOR transect from the Straits of Yucatan towards New Orleans. This later transect was run with a number of other vessels besides the NESTOR, but since the NESTOR was one of the vessels that provided a long sequence of transects, the section will be referred to by that name. The cruise tracks and contoured sections for the period 1983 to 1987 are given in two MMS reports (Brown et al., 1986; 1989). The QUEENY data from 1980 to 1982 were obtained from NMFS.

4.2.1.2. Frontal Variability

The variation of Loop Current position parameters as a function of time for the QUEENY transect is given in Figure 4.2-1. The tick marks on the left hand axis show the times of the sections. The time interval between sections can be quite irregular with a few relatively large gaps of several months. Therefore, some likelihood exists that an eddy could have been missed due to the gaps in the transects or that an eddy detached to the south of the transect line. Thus, there is some uncertainty associated with using these QUEENY sections for characterizing low frequency Loop Current frontal motions. However, it is one of the few long, multi-year time series which has reasonable coverage through both summer and winter seasons that can be used for this purpose. Major features of interest in Figure 4.2-1 are that LE, LC and LW tend to move together with the amplitudes increasing westward; the eddies are most often shed when both east and west fronts are extended to the northwest. There is however, a good deal of interannual variability. Thus, the front positions and generation of eddies correspond to the picture suggested by Hurlburt and Thompson's (1982) numerical model results with the Loop Current extending as a body towards the northwest with the warm eddies shed in the region south of the Mississippi Delta. The early 1980s show relatively small variability compared to 1983 and the first half of 1984, which show that the Loop Current extended out to the northwest for a sustained period with apparently only one eddy detaching in September 1983. Beginning in 1985, there is again a quasi-regular period of growth and eddy births.

The birth of Eddies B, C and D, which were tracked by drifters and surveyed with XBT's, are indicated. The histories of Eddies B and C are described in the Year 3 report (SAIC, 1988) and in Lewis et al., (1989) and that of Eddy D in this report. Eddy A, which was first detected by Drifter 5495 in August 1985 in the southwestern Gulf (Lewis et al., 1989), was not directly observed as it detached from the Loop Current. There are, however, some suggestions from the SOOP data and imagery that Eddy A may have been shed in January 1985.

The variability of the QUEENY and NESTOR frontal parameters for their common period, 1983-1986 is given in Figure 4.2-2a and 2b respectively. Clearly, a close correspondence exists between the movement of the Loop Current along the QUEENY section and the movement of the front, LN, north along the NESTOR section. Thus, movements of the Loop Current towards the northwest are associated with the extension of the northern boundary towards the Mississippi Delta.

The basic statistics of the front parameters for both the QUEENY and NESTOR transects are given in Table 4.2-1. The increase in variability of the west front compared to the east front is reflected in the standard deviations of LW and LE. Despite the oblique angle at which the QUEENY transect cuts the Loop Current, the cross sectional areas east and west of the center line are about the same with similar standard deviations. The maximum depth, DC, of the 20°C isotherm in the section averages 234 m with a maximum of 323 m, which compares with the approximately 100 m undisturbed level of the isotherm outside the Loop Current.

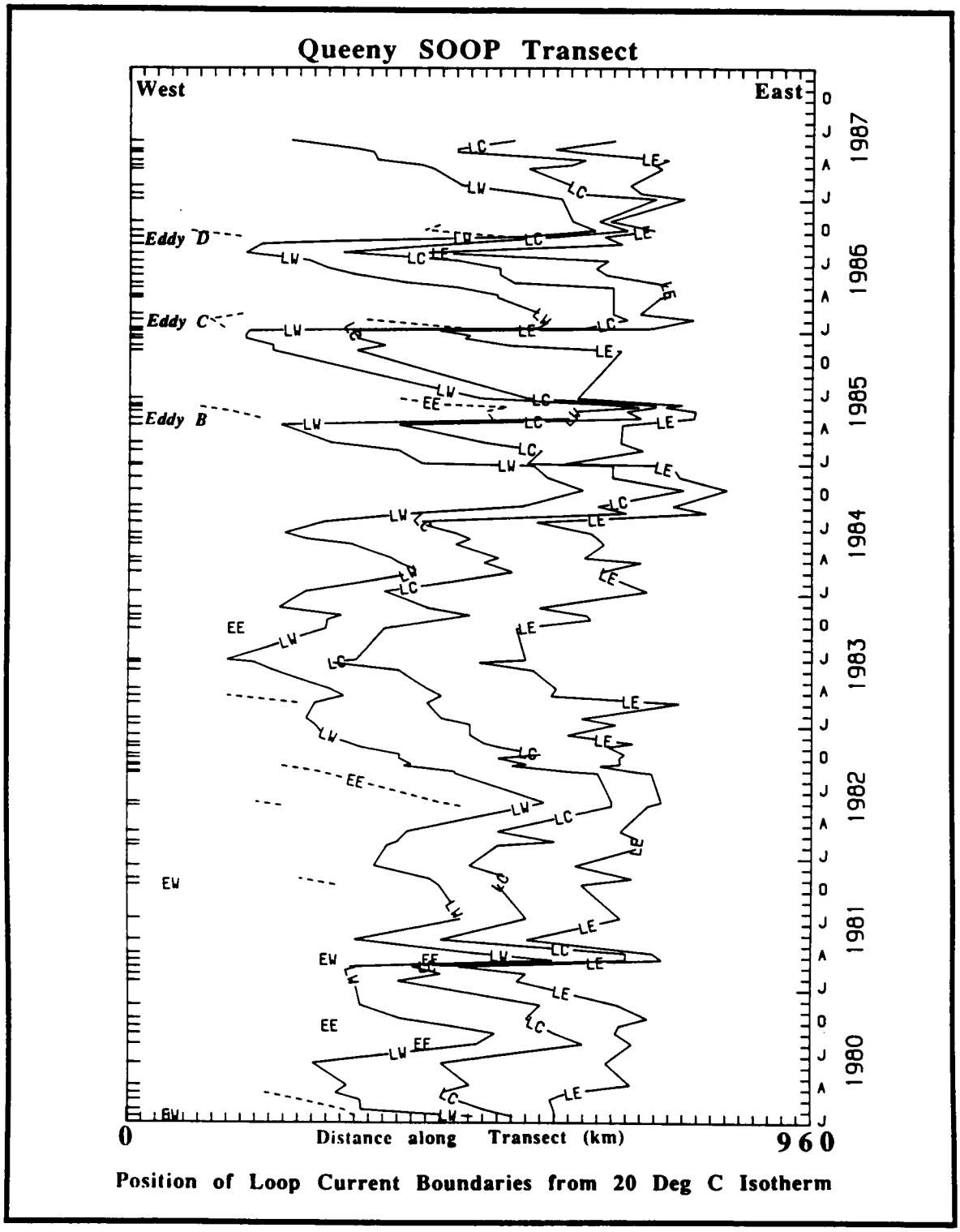

Figure 4.2-1. The variability of the positions of the frontal parameters derived from the QUEENY transects.

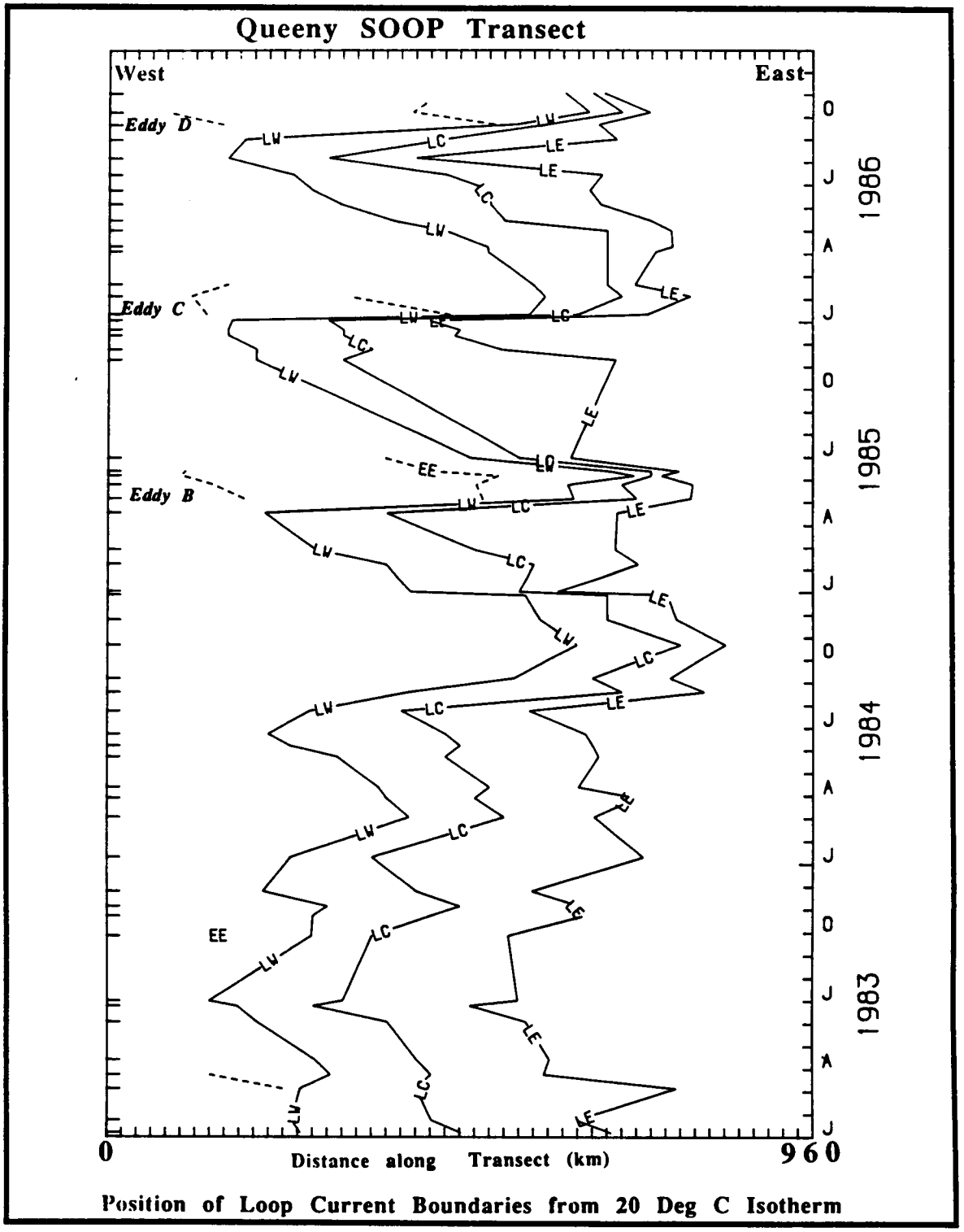

Figure 4.2-2a. The variability of the position of the frontal parameters (LW, LC and LE) derived from the QUEENY transects for 1983 through 1986.

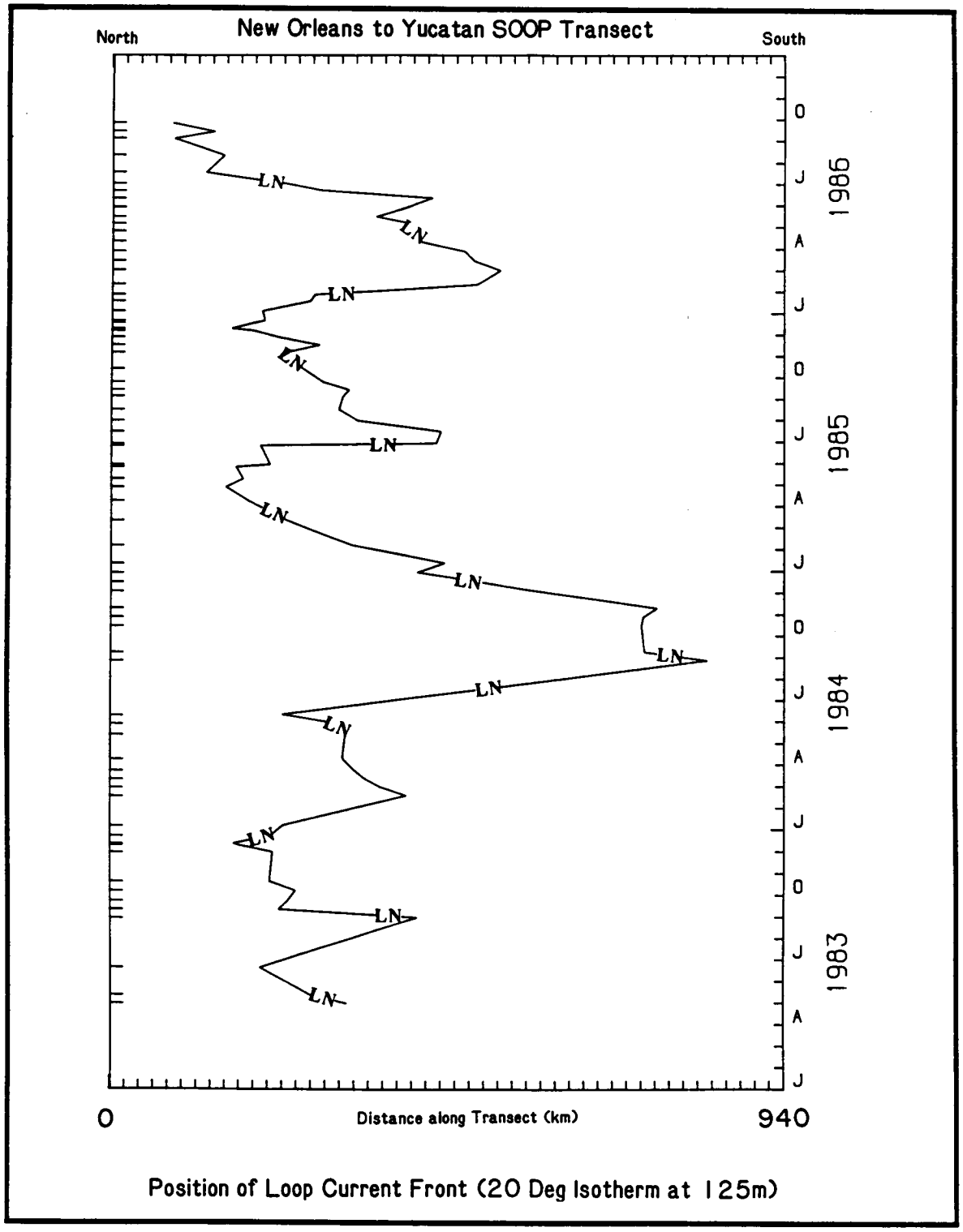

Figure 4.2-2b. The variability of the position of the frontal parameter (LN) derived from the NESTOR transects for 1983 through 1986.

Table 4.2-1. Loop Current statistics from 98 QUEENY transects (1/80-6/87) and 73 NESTOR transects (5/83-9/86).

Parameter	Units	Mean	Standard Deviation	Maximum	Minimum
North Boundary (LN)	km	331.5	162.60	832.2	83.4
West Boundary (LW)	km	385.3	140.45	716.8	138.9
East Boundary (LE)	km	672.3	85.48	841.1	419.0
Width (LE-LW)	km	287.0	93.20	479.6	61.6
Center (LC)	km	533.1	120.10	780.0	280.0
Depth Center (DC)	m	234.0	46.58	322.9	100.1
Area West (AW)	km^2	29.85	14.12	72.46	3.04
Area East (AE)	km^2	28.73	16.52	84.91	1.86
Total Area (AW+AE)	km^2	58.58	26.19	116.5	4.93
Eddy Period	months	9	-	19	6.5

Detached Eddies present in 28.6% of Queeny Transects
Number of Eddies = 10

A total of 10 eddies were detected over the 90-month period of M/V QUEENY transects giving an average of one eddy every nine months. The periods between the shedding of eddies ranged from 6.5 months to 19 months; however, a large part of this variability is due to the apparently anomalous 1983-1984 period. If this period is excluded, the eddy shedding periods range from 6.5 to 9.5 months with an average of about 7.5 months. In these calculations, Eddy A (SAIC, 1988) is excluded since the eddy fronts were not detected in the SOOP data. If Eddy A is assumed to detach in January, 1985 then the minimum, maximum and average eddy period would become four, 15 and eight months, respectively. Therefore, eddy shedding cycles from these data appear quite regular for two fairly long periods which are separated by an apparently anomalous period of Loop Current variability.

A more quantitative look at the variability of the fronts is to calculate the spectra of LW and LE. The positions were linearly interpolated to equally spaced time intervals of 30 days, and the power spectra, calculated by standard Fast Fourier Transform (FFT) techniques. The result, in variance preserving form, is given in Figure 4.2-3. The major peak in LW is at about 220 days, similar to the eddy shedding period. Lesser frequency peaks are harmonics of this peak due to the "saw-tooth" shape of the primary variability. LE is much less variable than LW, but with similar spectral peaks. Both records suggest a secondary low frequency peak at a period of about 400 days.

4.2.1.3 Loop Current Variability and Currents

During the three-year period, 1983 to 1985 a mooring array was maintained on the west Florida shelf. Moorings C, and E on the shelf break had three years of continuous current and temperature records, and previous analyses (SAIC, 1987) indicated substantial differences in the variability of the shelf edge current fields between the different years. The shelf break positions of Moorings C and E are given in Figures 3.7-1 and 3.7-3.

The variations of LW, LE and LN were given in Figure 4.2-2 for the 1983 to 1986 period. The time series of 40-HLP along isobath (V) components of the 50 m level currents and temperature for Moorings C and E are given in Figure 4.2-4. The Loop Current east and north boundary positions, with positive values increasing offshore and northwards, respectively (i.e., opposite convention to LW and LN), are shown also in Figure 4.2-4. The 1983 currents are characterized by relatively quiescent conditions with temperatures generally below 22.5°C at both moorings. Note that 50 m is below the seasonal thermocline, and, thus, seasonal warming and cooling do not affect the temperature records. The next year shows an increasing number of strong southward events culminating in the events centered on Day 600 at Mooring C and Day 630 at Mooring E which approach 100 cm s^{-1}. There is an abrupt warming at Mooring C and Mooring E to temperatures greater than 26°C associated with these two major events. The year 1985 is more like 1983 but with stronger currents with some northward events at Mooring C. The frontal boundary data show that for most of 1983, the Loop Current was extended to the west and north

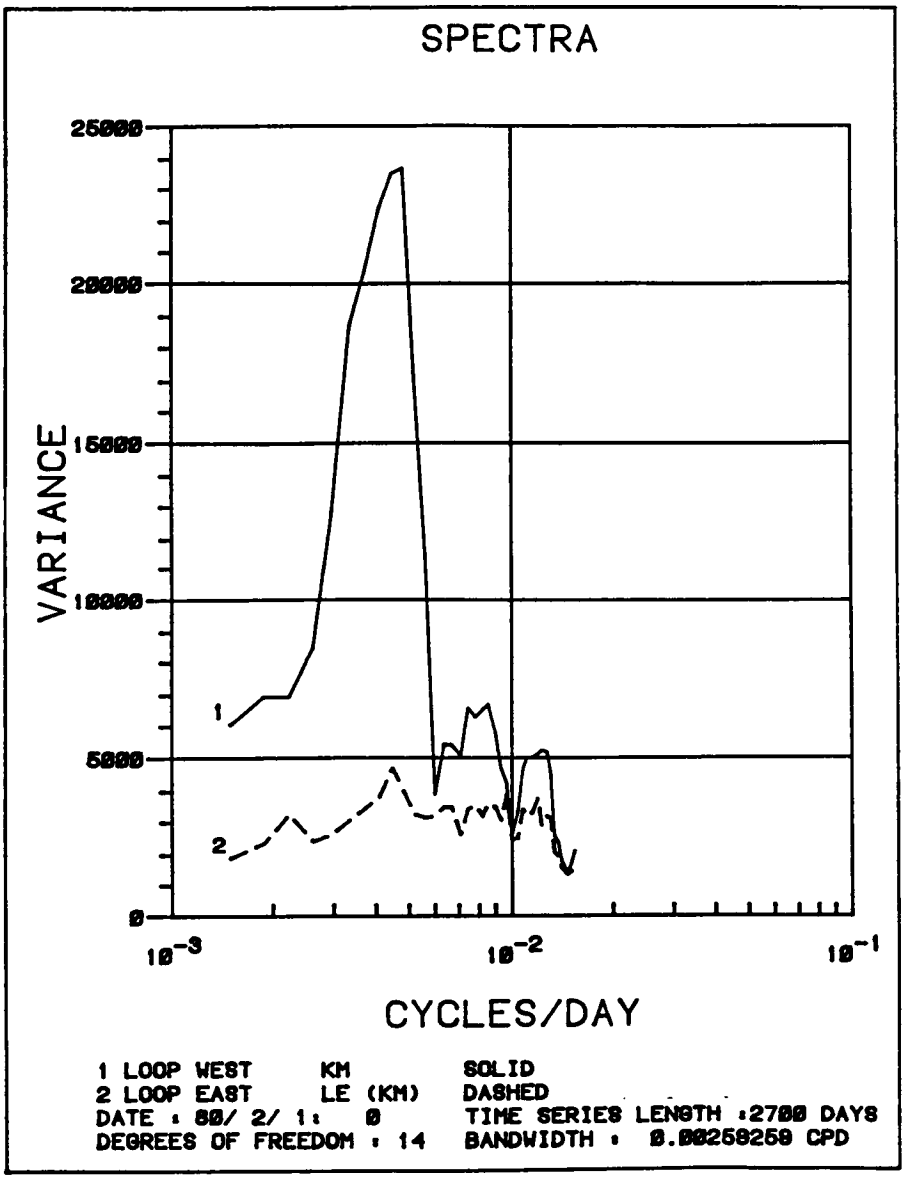

Figure 4.2-3. The variance preserving spectra of LW (solid) and LE (dashed) from the QUEENY analysis.

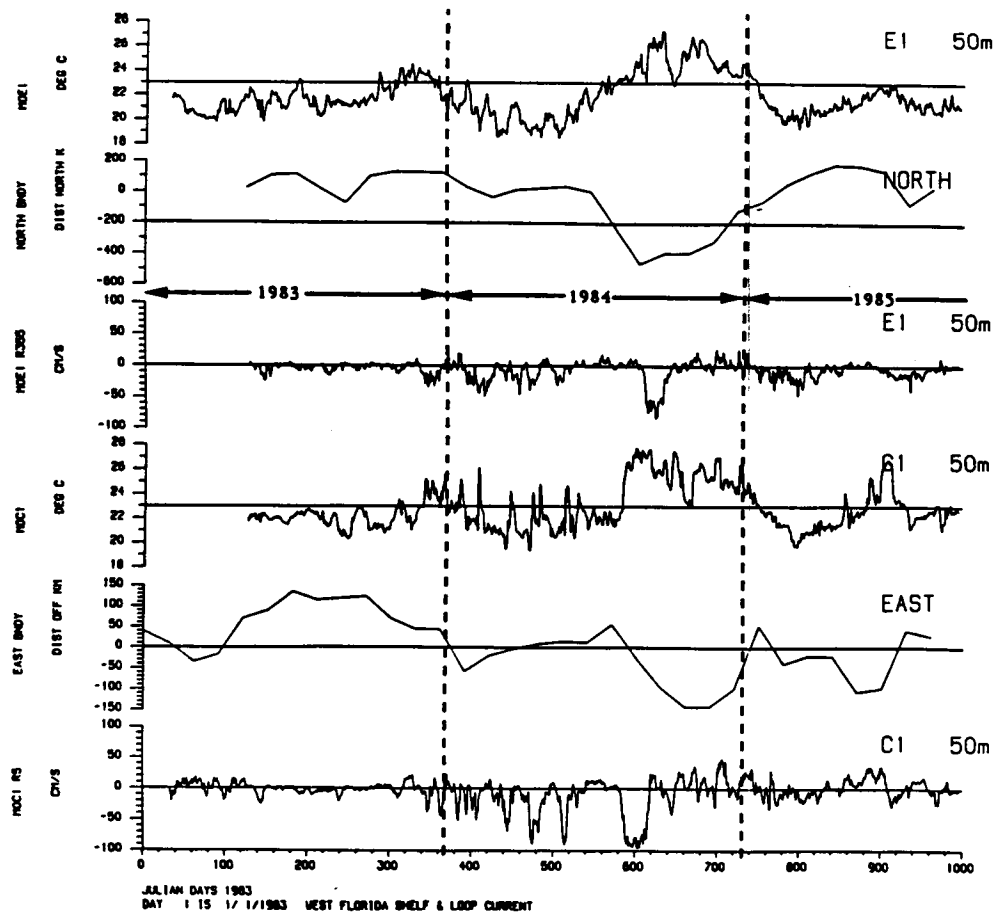

Figure 4.2-4. The 40-HLP along-shelf current velocity and temperature at the 50-m level for Moorings C and E for the years 1983 to 1985. The positions of the eastern Loop Current front (LE) and the north boundary (LN), from the QUEENY and NESTOR transects, are also plotted as time series.

with the eastern boundary being about 100 to 150 km offshore of the shelf break at Mooring C. During the first half of 1985, the eastern boundary moved closer to the shelf break, but the Loop Current was still extended to the north. In the second half of 1985, the body of the current withdrew from the New Orleans to Yucatan transect and moved onshore over the outer west Florida shelf. It is this movement that seems to trigger the major current events around Day 600 and is directly associated with the warming of the outer shelf. This suggests that the position and movement of the Loop Current, to a major extent, determines the current regime on the outer west Florida shelf both off Tampa and also further north where it might have been expected that the Loop Current would be less important.

4.2.2 Frontal Analysis Statistics

4.2.2.1 Loop Current

The occurrence of the Loop Current front derived from 10 years of RTIs monthly frontal analysis maps assembled by the Research Triangle Institute is given in Figure 4.2-5, and the occurrence of warm LC water is given in Figure 4.2-6. The mean position and standard deviation of the front derived from the NESTOR and QUEENY transects are also marked on Figure 4.2-5. It can be seen that the LW and LN means are quite close to each other, and, therefore, reasonably consistent despite the differing number of sections in the two transects. The XBT derived means are on the warmer side of the maximum probability of front occurrence. This is probably a reflection that the frontal analysis delineates maximum surface temperature gradients and that the sectional analysis is a measure of the maximum gradient at 125 m. Thus, the average position of the northern part of the front is closer to 26°N than to 27°N as indicated by the occurrence contours, and the mean eastern side of the Loop Current front (LE) is more likely to be offshore (west) of the 2000 m isobath than over the west slope of Florida.

A direct comparison of the time series of LW, LE and LN from XBT transects with equivalent frontal positions derived from the frontal analyses for the period November 1983 to December 1985 is given in Figure 4.2-7. The eastern boundary (LE) shows the best agreement. The disagreements around Days 600 and 900 are due mainly to the frontal analysis not detecting that an eddy had been shed. This may occur because there is often a thin layer of warm water between the LC and a newly shed eddy even though the subsurface fronts indicate that they have separated. However, even in non-eddy periods, the discrepancy between the frontal analysis and the true frontal position can be on the order of 50 to 100 km. This is again most likely because of warm filaments or shallow convoluted features that are attached to the main frontal boundary which the frontal analysis represents as the main front. The subsurface front, however, will be closer to the core of the current.

Noteworthy features of Figures 4.2-5 and 4.2-6 are that the LC rarely penetrates past 90°W and that the most likely outer shelf to be influenced by the LC is the southwest Florida shelf. The most northerly penetration generally occurs on the slope just south of Mobile, Alabama.

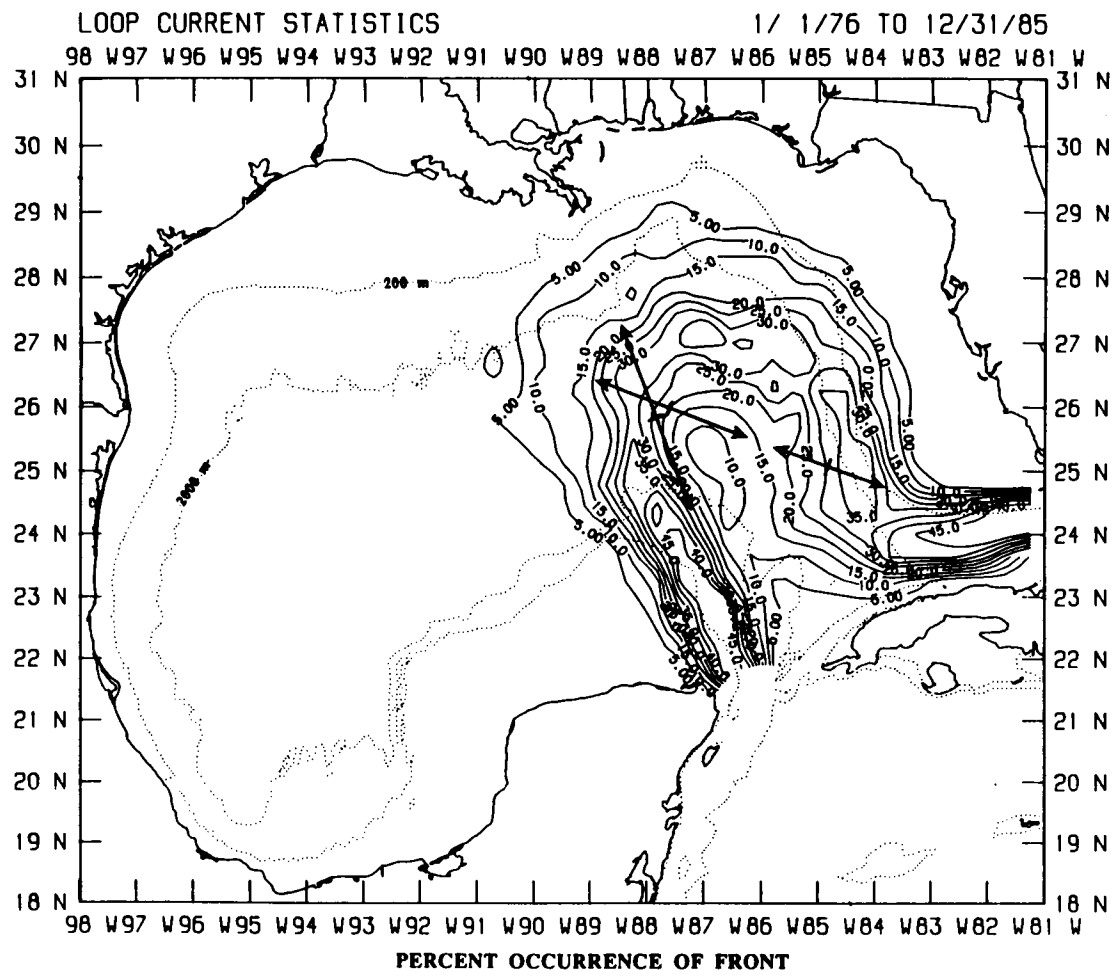

Figure 4.2-5. The percent occurrence of the Loop Current front from the 10 years of monthly frontal analyses. Superimposed are the mean and standard deviation of the frontal positions derived from the QUEENY and NESTOR transects.

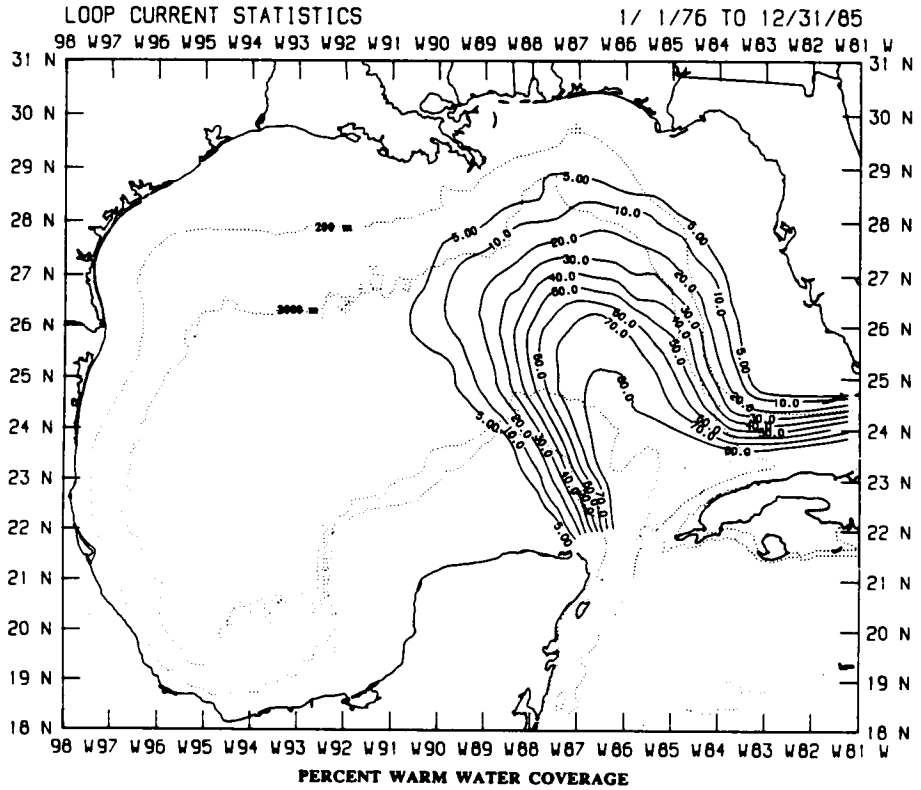

Figure 4.2-6. The percent occurrence of Loop Current water from the monthly frontal analyses.

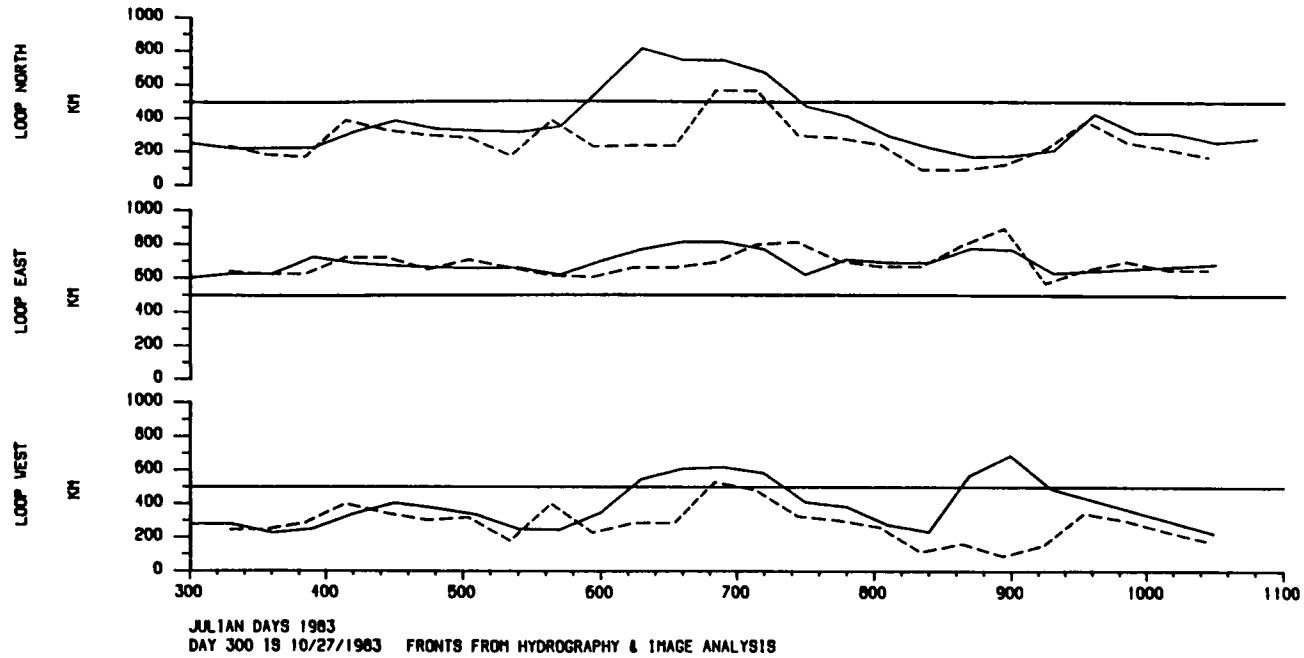

Figure 4.2-7. A comparison of the positions of the fronts (LN, LE and LW) derived from the QUEENY and NESTOR transects (solid) and from the monthly frontal analyses (dashed).

Figure 4.2-8 shows the relationship between the area covered by warm LC water and the maximum northward extension of the front. Not surprisingly, there is a strong linear relation between the maximum penetration of the LC and its areal coverage though the scatter is largest between 27° an 28°N where the LC is less confined by topography and is the region where eddies are usually shed. Table 4.2-2 gives summary statistics derived from the monthly frontal analyses for the Loop Current. Total water area of the ½° grid of the Gulf of Mexico is approximately 1,562 x 10^3 km^2.

4.2.2.2 Warm Eddies

The occurrence of fronts defining warm eddy boundaries and the coverage by warm eddy water are given in the probability maps of Figures 4.2-9 and 4.2-10, respectively. The percentages are low compared to the LC statistics because of the intermittent and non-stationary character of the eddy shedding and westward propagation processes. Some of the highest probabilities of finding warm eddy water occur south of the delta and in the deep region centered around 25°N, 92°W where eddies are located after being shed from the LC but prior to beginning to interact with the western Texas-Mexican slope. The contours of equal probabilities tend to follow the isobaths in the deep central Gulf and then turn towards the northwest corner. According to these charts, eddies have a low probability of being found south of 22°N in the Bay of Campeche. However, the Bay of Campeche is a notoriously cloudy region and slightly warmer surface water in the Spring makes eddy detection from AVHRR data difficult. Lagrangian drifter tracks often show eddies moving southwestward towards the Bay of Campeche (Kirwan et al., 1984). Therefore, not too much weight should be put on the lack of eddy fronts and warm eddy water in the southwest Gulf in Figures 4.2-9 and 4.2-10. There is a finite probability, < 5%, of finding an eddy front on most of the northern shelf regions, with the closest approaches to the coast being off the Mississippi Delta and southwest of Corpus Christi Bay. The statistics show something between the westerly and southwesterly eddy tracks suggested by the ARGOS drifters (Kirwan et al., 1984; Lewis et al., 1989).

Summary statistics of the frontal analysis are given in Table 4.2-3. The average eddy covers about 20% of the average area of the LC north of Yucatan Straits. The average eddy diameter, calculated from the area assuming a circular eddy, is similar to the 185 km estimated by Elliott (1982) from hydrography. The largest eddy found was in the eastern Gulf, presumably soon after being shed from the Loop Current. The maximum area covered by warm eddy water is about 15% of the total surface area of the Gulf.

4.2.2.3 Shelf-Slope Fronts

Finally, the occurrence of fronts that could not be directly associated with the LC or eddies are contained in Figure 4.2-11. The majority of these fronts were associated with the shelf or the slope though there is little or no information on their subsurface structure or dynamics. High probabilities of a shelf-slope front are found on most of the shelves,

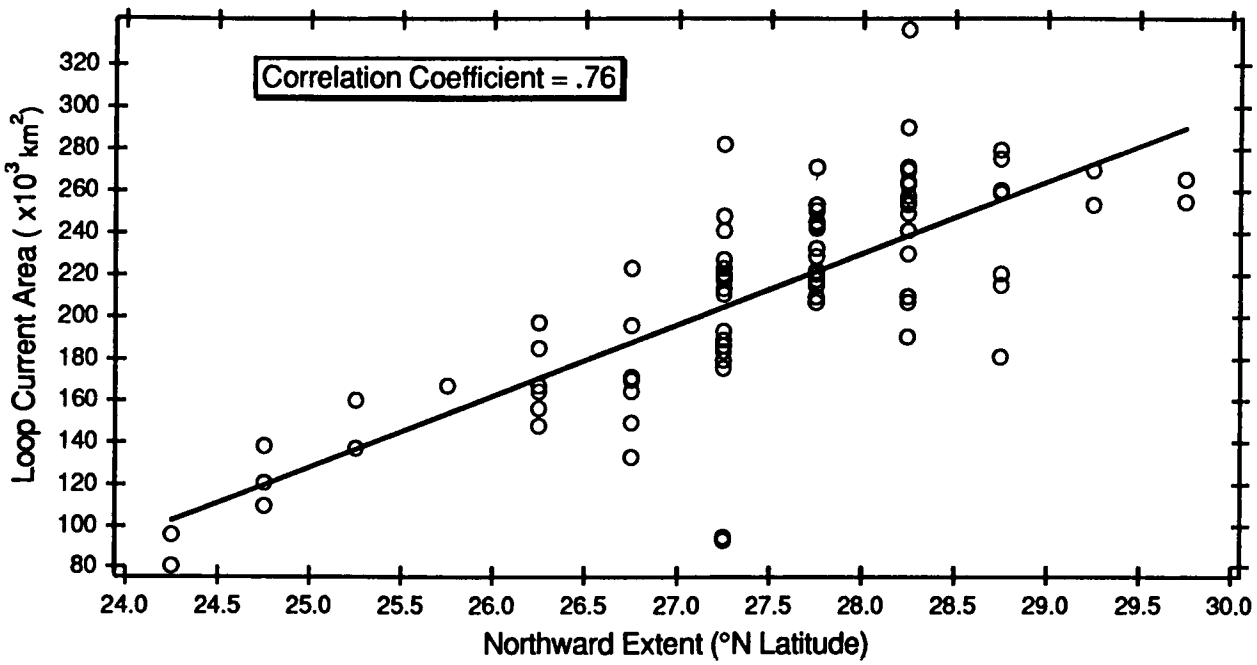

Figure 4.2-8. Scatter plot of the computed area versus the northward extent of the Loop Current from the frontal analyses.

Table 4.2-2. Loop Current summary statistics from frontal analysis.

		Date
Average Area	210.0 x 10^3 km^2	
Maximum Area	337.0 x 10^3 km^2	6/85
Maximum Northward Extension	29.75°N	2/82 5/82
Maximum Westward Extension	91.25°W	2/77

Table 4.2-3. Warm eddy summary statistics from frontal analysis.

		Date
Average Eddy Size	43,041 km^2	
Mean Diameter of Average Eddy	234 km	
Maximum Individual Eddy Size	128,780 km^2	5/81
Mean Diameter of Largest Eddy	405 km	
Average Area covered by Warm Eddy Water	45,731 km^2	
Maximum Area covered by Warm Eddy Water	234,270 km^2	11/85
Number of Eddies	4	

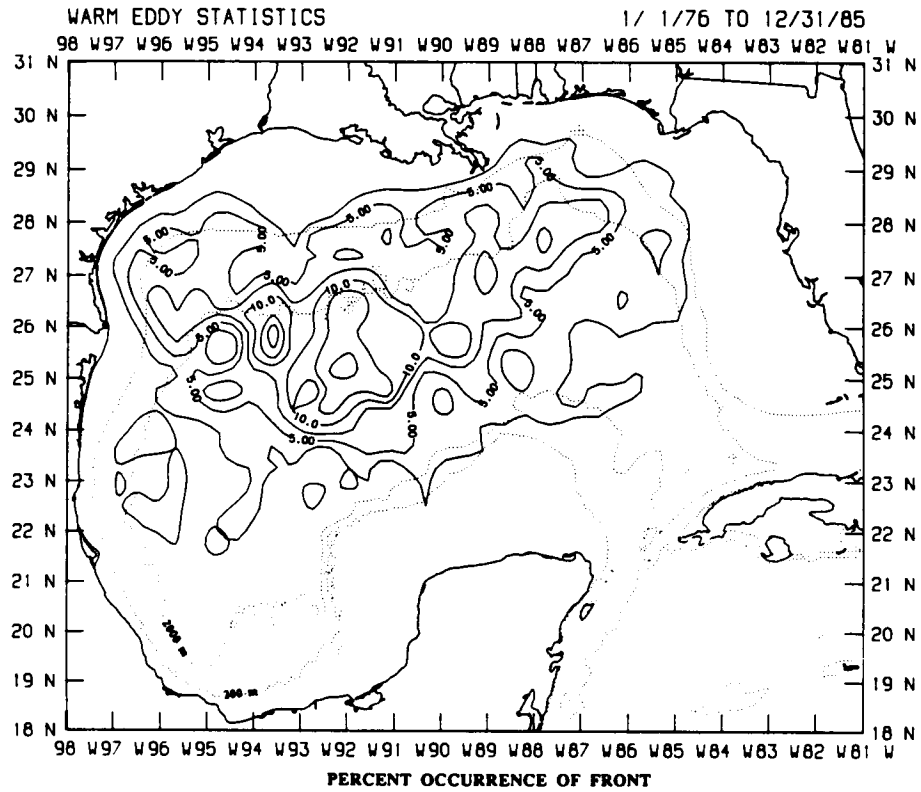

Figure 4.2-9. The percent occurrence of warm eddy fronts from monthly frontal analyses.

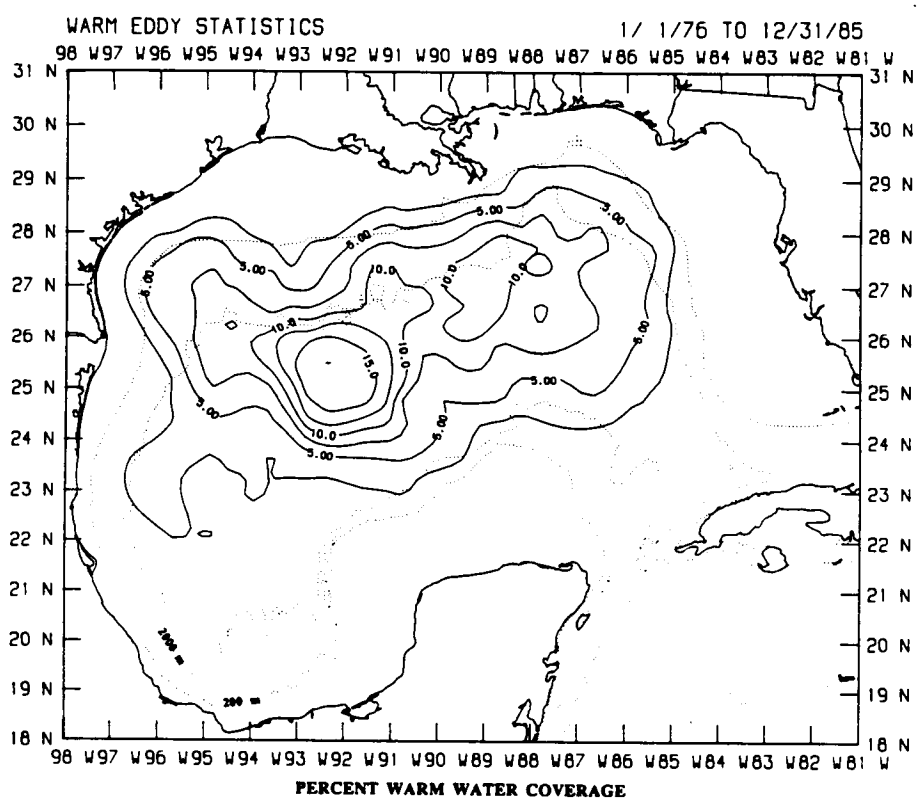

Figure 4.2-10. The percent occurrence of warm eddy water from monthly frontal analyses.

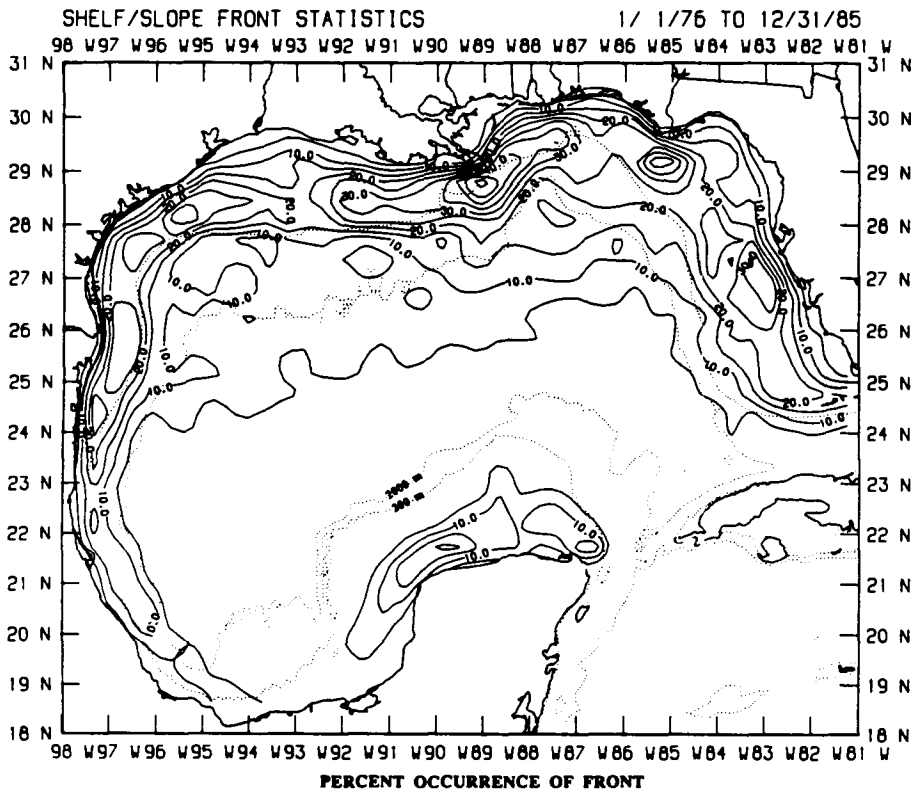

Figure 4.2-11. The percent occurrence of shelf-slope fronts from monthly frontal analyses.

but particularly around the Mississippi Delta. The majority of the monthly maps are for winter and spring which include the high spring run-off period of the Mississippi and Achafalaya Rivers. Therefore these mid-shelf fronts are probably associated with river runoff and the coastal boundary layer which is present west of the delta down as far as northern Mexico. The frontal occurrences off the Yucatan peninsula are possibly a result of persistent upwelling along this coast. There is a suggestion of enhanced exchanges between the shelf and slope off the delta on the Alabama/Mississippi slope and in the northwestern Gulf. The 10% contour line suggests that tongues of shelf water are extruded from the southwest Texas and Mexican slope at about 26.75°N and 25°N, similar in position to observations (Brooks and Legeckis, 1982; SAIC, 1988).

4.3 Eddy Movement and Dynamics

4.3.1 Gulf Eddies, August 1986-December 1988

A number of Loop Current eddies occurred in the Gulf of Mexico during the two-and-a-half year period after Eddy C reached the western Gulf (SAIC, 1988). These eddies were described using Lagrangian measurements, Ship-of-Opportunity XBT data, and hydrographic surveys. The following is a description of the movements of the various eddies based on the available data, beginning in August, 1986. This is directly after Eddy C is believed to have coalesced with the older Eddy B, (Lewis et al., 1989). The trajectory of Drifter 3379 from late-June through mid-September 1986 (Figure 4.3-1) shows large, anticyclonic motion with the drifter finally leaving the eddy flow field and moving into Campeche Bay. An XBT survey during the same period (Figure 4.3-2), shows the Loop Current reaching up to at least 27°N. This extension eventually resulted in the next Loop Current eddy.

During mid-September through late November 1986, Drifter 3379 made a slow cyclonic loop in the Bay of Campeche (Figure 4.3-3). At the same time, the Loop Current spun off another eddy, Eddy D. Lagrangian sea surface temperature (SST) and XBT data were used to show the conditions for 18 to 25 October 1986 in Figure 4.3-4. Here, note the cyclonic flow field in the Campeche Bay, Eddy D as defined by the 28°C isotherm and XBT data in the western Gulf, and the Loop Current shunting directly across to the Florida Straits. As Eddy D moved westward, Drifter 3379 once again became entrained in the flow field of Eddy C (Figure 4.3-5), with Drifter 3352 having been placed in Eddy D. However, this entrainment was short-lived. Conditions during late January 1987 are shown in Figure 4.3-6. The 24°C isotherm, XBT, and trajectory data imply a relatively large field of flow for Eddy D. Drifter 3379 was just leaving Eddy C in the western Gulf, and the Loop Current was beginning to extend beyond 25°N in the eastern Gulf.

The trajectories of Drifters 3379 and 3352 from late January through mid-March 1987 are shown in Figure 4.3-7. Drifter 3352 made some unusually large, elliptical loops around Eddy D and left the southern part of the eddy by the mid-March period. The conditions of March 31 to 7 April 1987 are shown in Figure 4.3-8. Drifter 3352 was in the western Gulf through which most Loop Current eddies pass on their way toward the

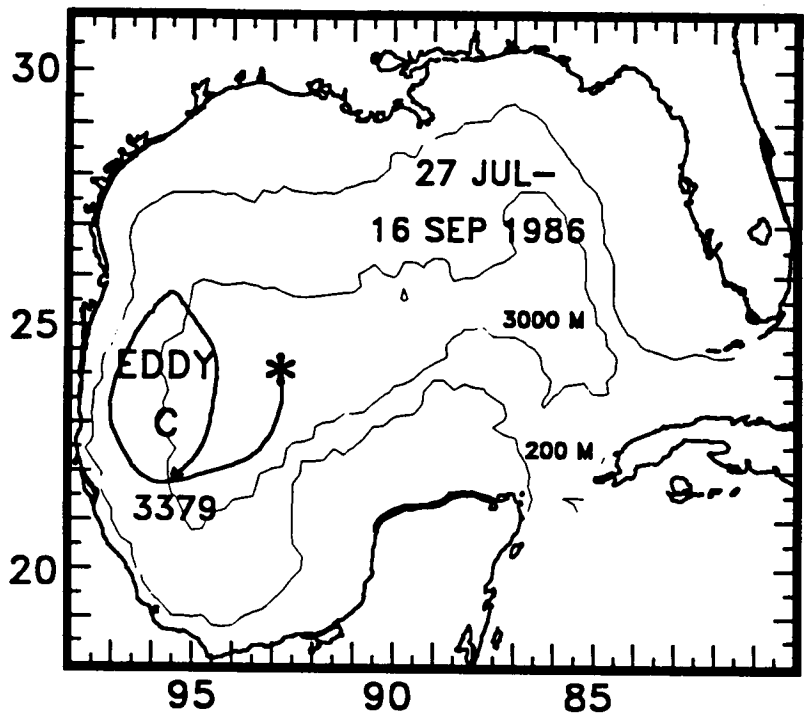

Figure 4.3-1. Drifter trajectory for July 27 to September 16, 1986. The asterisk represents the initial position of the drifter. Depth contours are in meters.

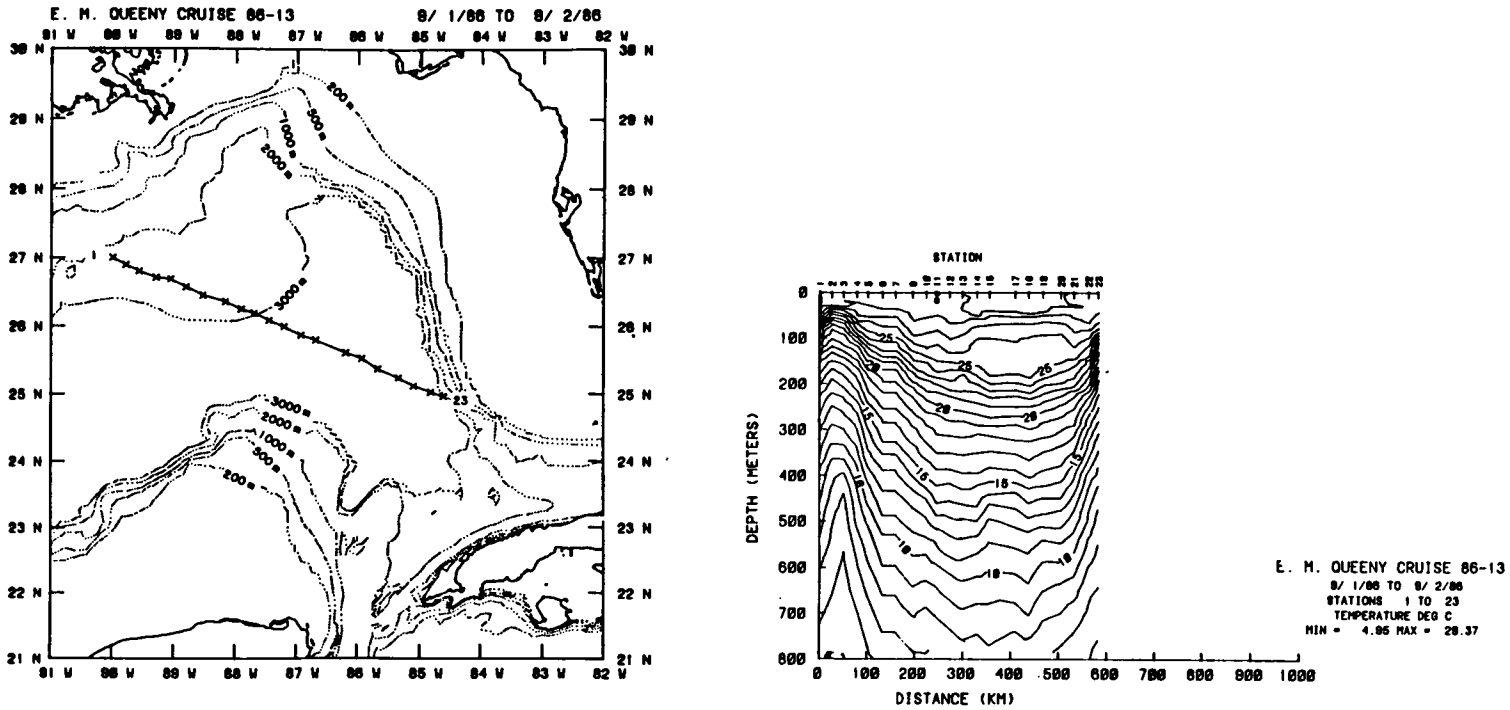

Figure 4.3-2. XBT transect through the Loop Current region for September 1 to 2, 1986.

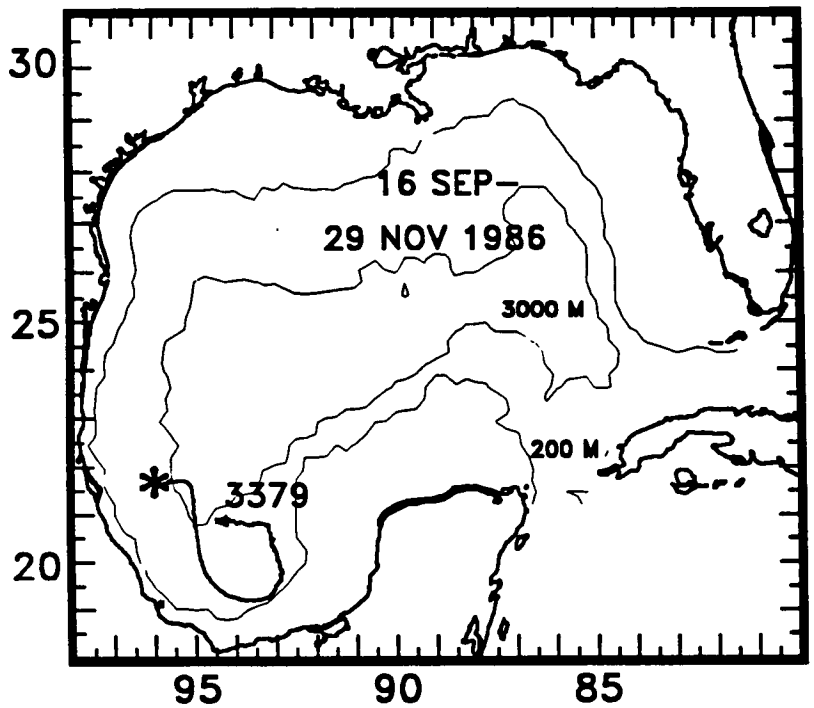

Figure 4.3-3. Drifter trajectory for September 16 to November 29, 1986. The asterisk represents the initial position of the drifter. Depth contours are in meters.

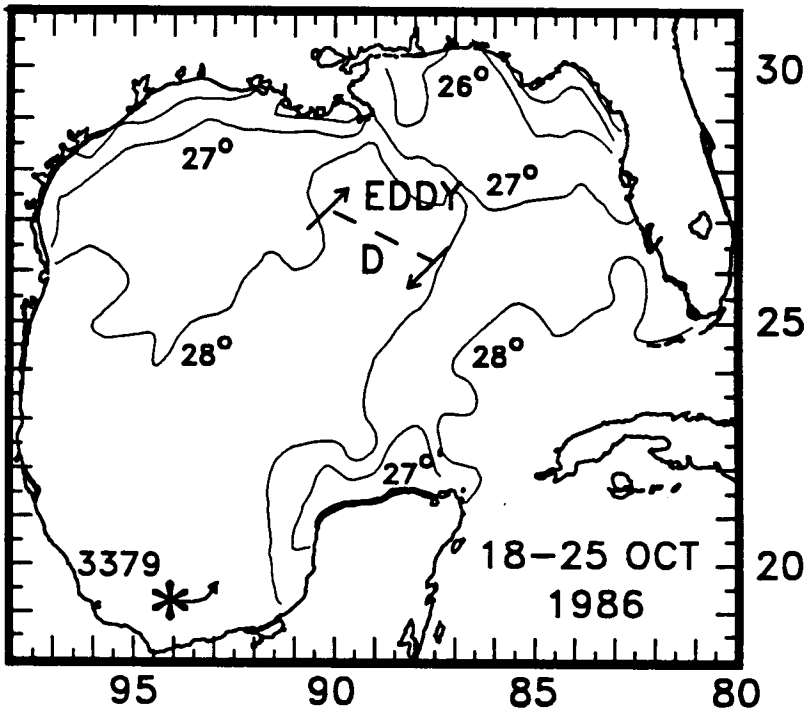

Figure 4.3-4. Conditions for October 18 to 25, 1986. SSTs are in °C and the asterisk represents the initial position of the drifter. Arrows denote flow at the edges of Eddy D. Dotted lines indicate the location of eddy water.

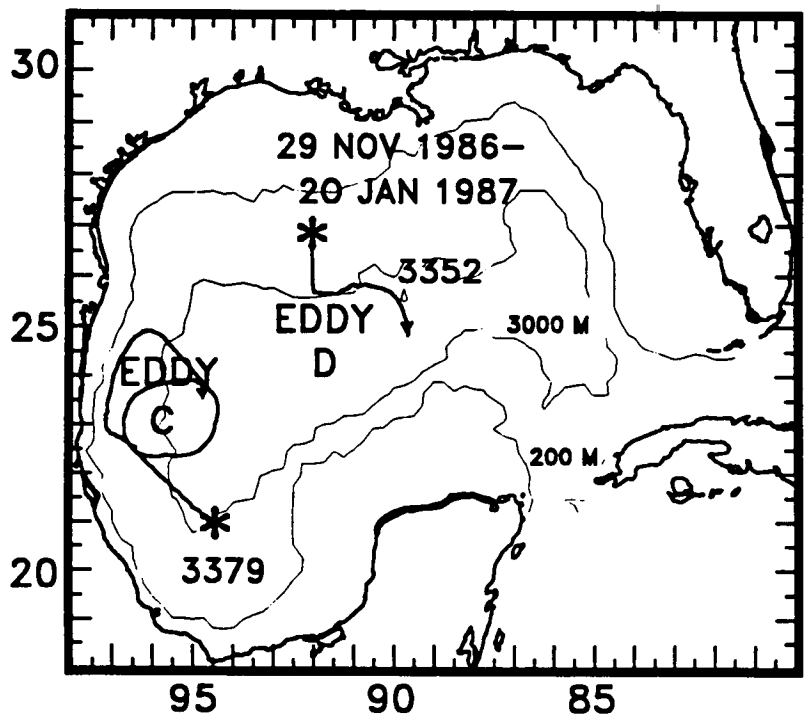

Figure 4.3-5. Drifter trajectories for November 29, 1986 to January 20, 1987. The asterisks represent the initial positions of the drifters. Depth contours are in meters.

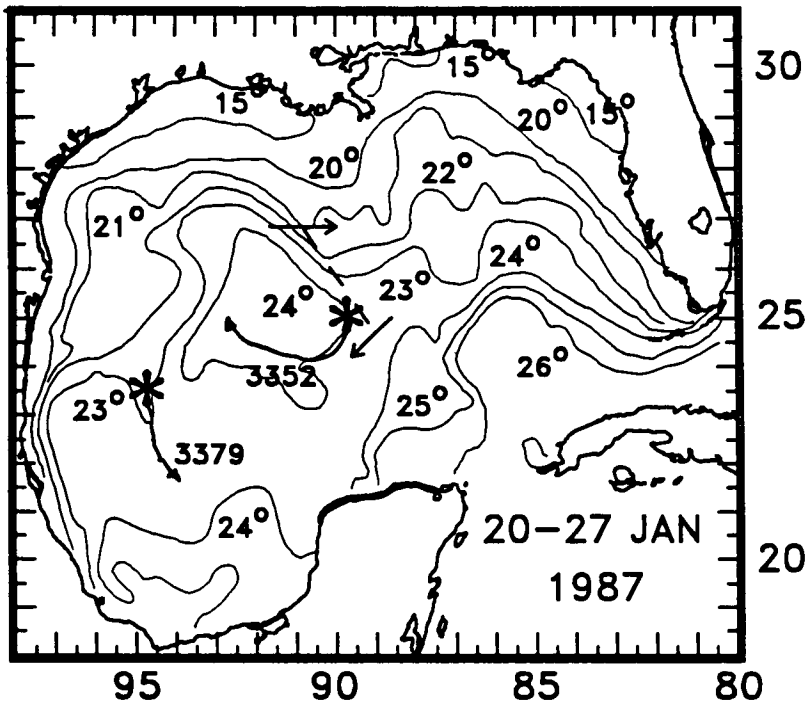

Figure 4.3-6. Conditions for the week of January 20 to 27, 1987. SSTs are in °C and the asterisks represent the initial positions of the drifters. Arrows denote flow at the edges of Eddy D. Dotted lines indicate the location of eddy water.

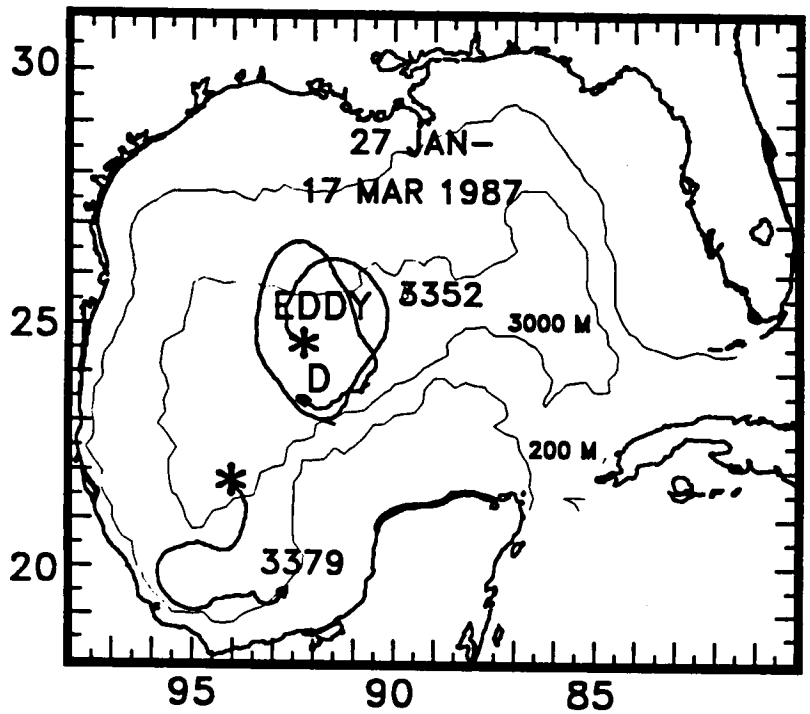

Figure 4.3-7. Drifter trajectories for January 27 to March 17, 1987. The asterisks represent the initial positions of the drifters. Depth contours are in meters.

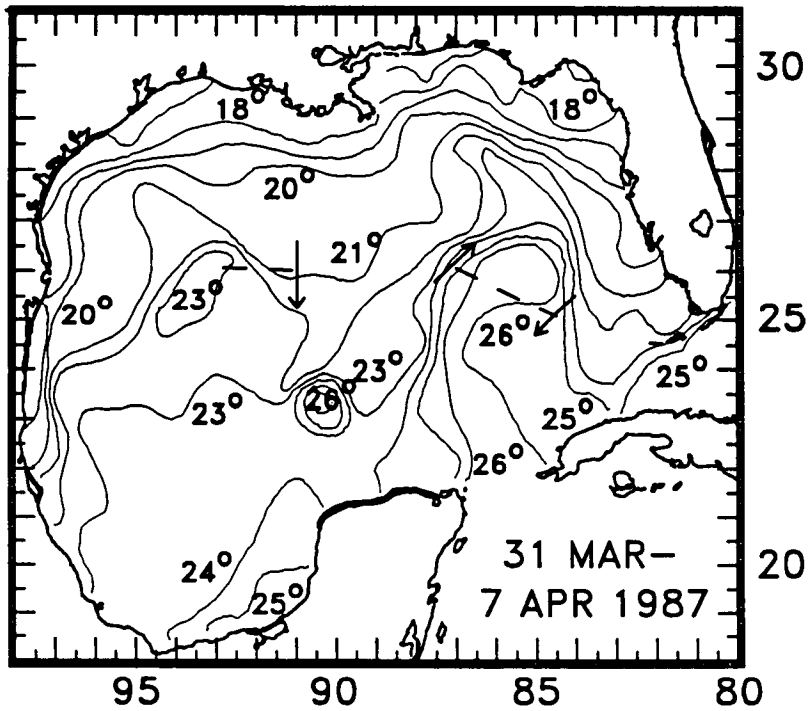

Figure 4.3-8. Conditions for the week of March 31 to April 7, 1987. SSTs are in °C. Arrows denote the flow at the edges of Eddy D (western Gulf) and the flow of the Loop Current (eastern Gulf) while dotted lines indicate the location of eddy water or Loop Current water (based on XBT data).

Mexican coast. The SST and XBT data show that Eddy D was in the region of about 25°N, 93°W. The Loop Current had continued its extension into the Gulf, reaching almost 27°N.

In mid-April 1987, Drifter 7234 was placed into Eddy D. Trajectory data from mid-April through early June 1987 (Figure 4.3-9) show Drifter 3352 slowing and moving westward toward the Mexican coast while Eddy D moved southward. Drifter 7234 made one rather large, anticyclonic loop beginning in mid-May 1987, reaching westward to 96.5°W. Drifter 7234 then moved eastward leaving the flow field of Eddy D. Past experience suggests that the large loop may indicate coalescence of Eddy D with the existing flow field (Eddy C) along the coast of Mexico. Composites of all XBT data collected during April-May 1987 are shown in Figure 4.3-10. The depth of the 15°C isotherm best shows the extent of Eddy D after it had moved southward.

In early June 1987, Drifters 5837 and 5839 were placed in the Gulf along 93°W. These locations were east of the flow field of Eddy D. All trajectory data for early June through mid-August 1987 are shown in Figure 4.3-11. Drifters 5837 and 5839 made a number of cyclonic rotations during that two-month period. The most significant of these were at the beginning of the period along the eastern edge of the flow field of Eddy D. These drifters moved southward and then westward, a pattern consistent with model studies (Hooker, 1987) which show that vortices of opposite signs will translate in the direction of the flow of water along their common boundary. As for Drifter 7234, XBT data show that it moved over the northern boundary of the extended Loop Current. The drifter eventually wandered southward along the break of the Florida continental shelf.

All trajectory data from mid-August through late October 1987 are shown in Figure 4.3-12. A number of points can be made from these data. First, Drifters 5837 and 5839 were pulled along the western edge of the flow field of Eddy D. Their trajectories clearly outline the extent of the anticyclonic field of rotation indicating a northern edge of 26.5°N in early September 1987. In the eastern Gulf, Drifter 7234 moved west at about the 24.5°N parallel implying the separation of a new eddy from the Loop Current. Drifter 7234 moved northward along the west side of the new eddy and then began making a series of cyclonic rotations. These cyclones were relatively small and weak in comparison to the new eddy called Eddy E. Eddy E was delineated for a short time by the trajectory of Drifter 3348.

A composite of XBT data from mid-October through mid-November 1987 is shown in Figure 4.3-13. The depth of the 8°C isotherm shows the remnants of Eddy D in the western Gulf as well as Eddy E in the eastern Gulf. Although no data exist to define the cyclonic flow field experienced by Drifter 7234, a second cyclonic flow field is suggested at ~27°N, 93°W. The center of this cyclone is in relatively shallow water approximately 1500 m deep. CTD data not included in this plot are further supportive of the existence of this cyclone feature.

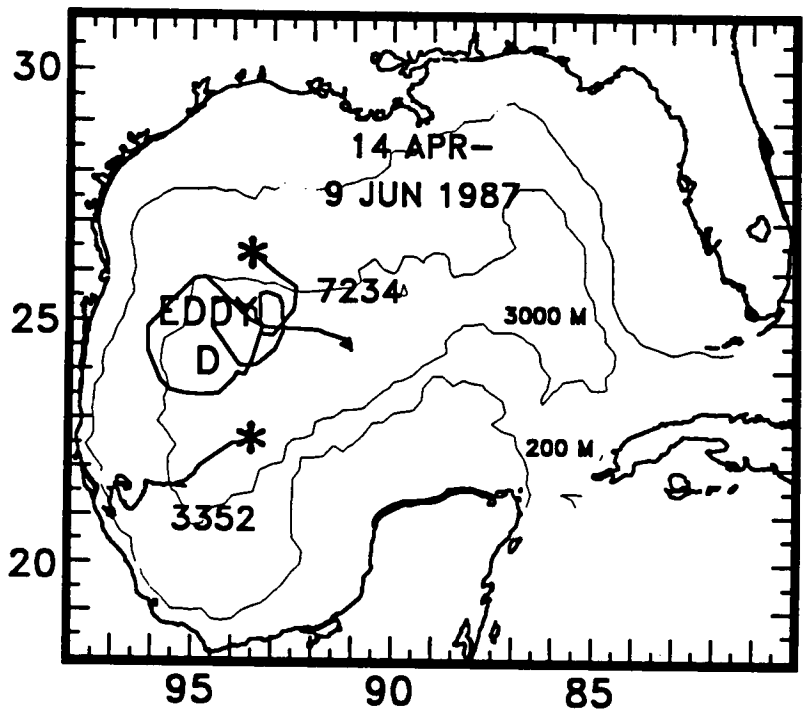

Figure 4.3-9. Drifter trajectories for April 14 to June 9, 1987. The asterisks represent the initial positions of the drifters. Depth contours are in meters.

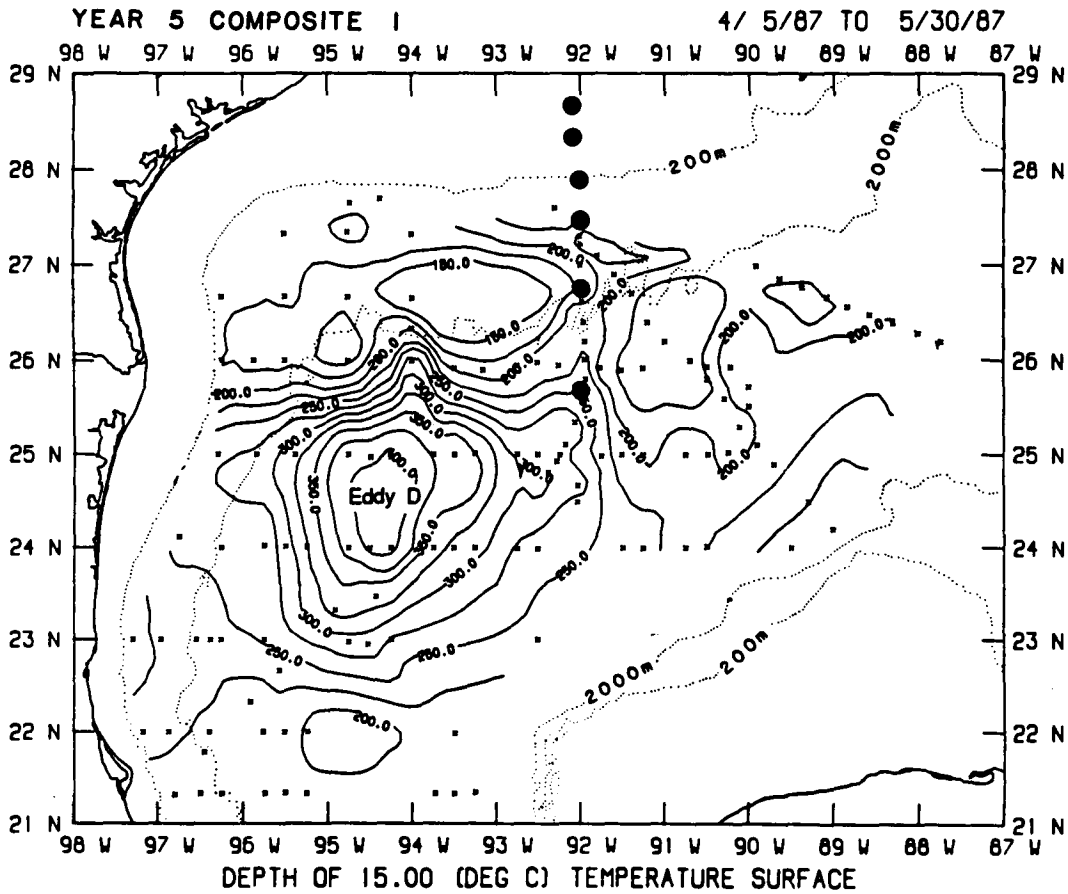

Figure 4.3-10. The depth of the 15°C isothermal surface as constructed from XBT data collected during the period of April 5 to May 30, 1987.

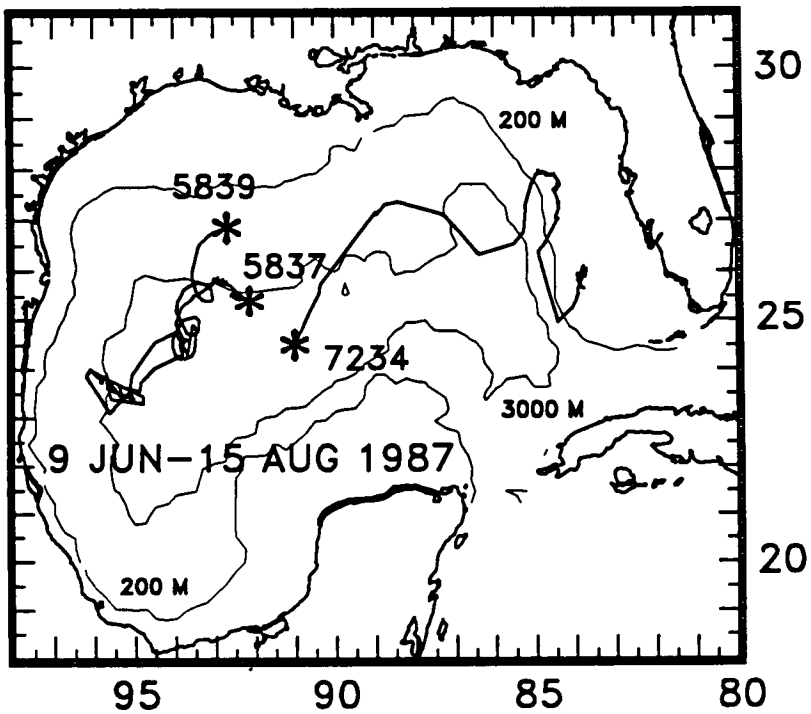

Figure 4.3-11. Drifter trajectories for June 9 to August 15, 1987. The asterisks represent the initial positions of the drifters. Depth contours are in meters.

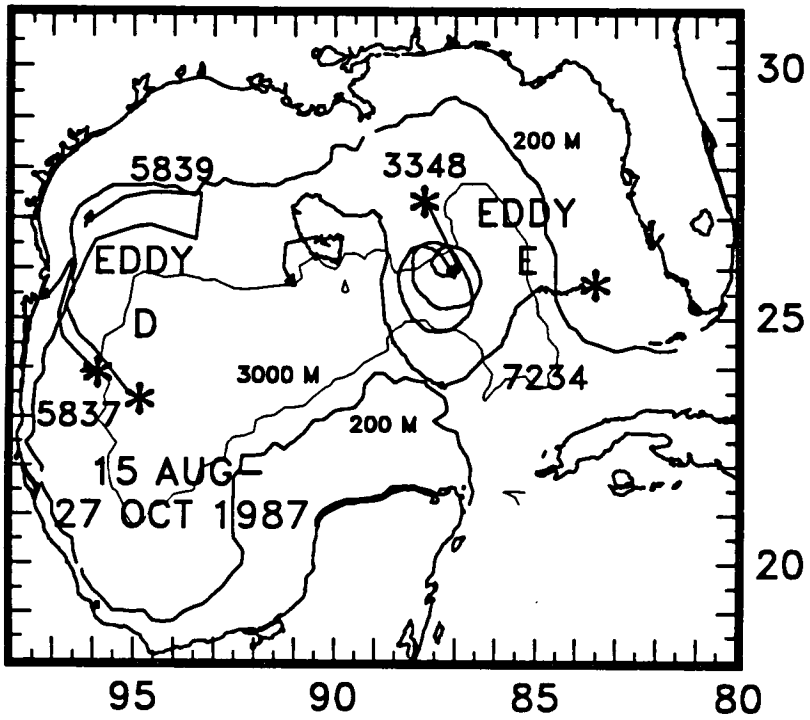

Figure 4.3-12. Drifter trajectories for August 15 to October 27, 1987. The asterisks represent the initial positions of the drifters. Depth contours are in meters.

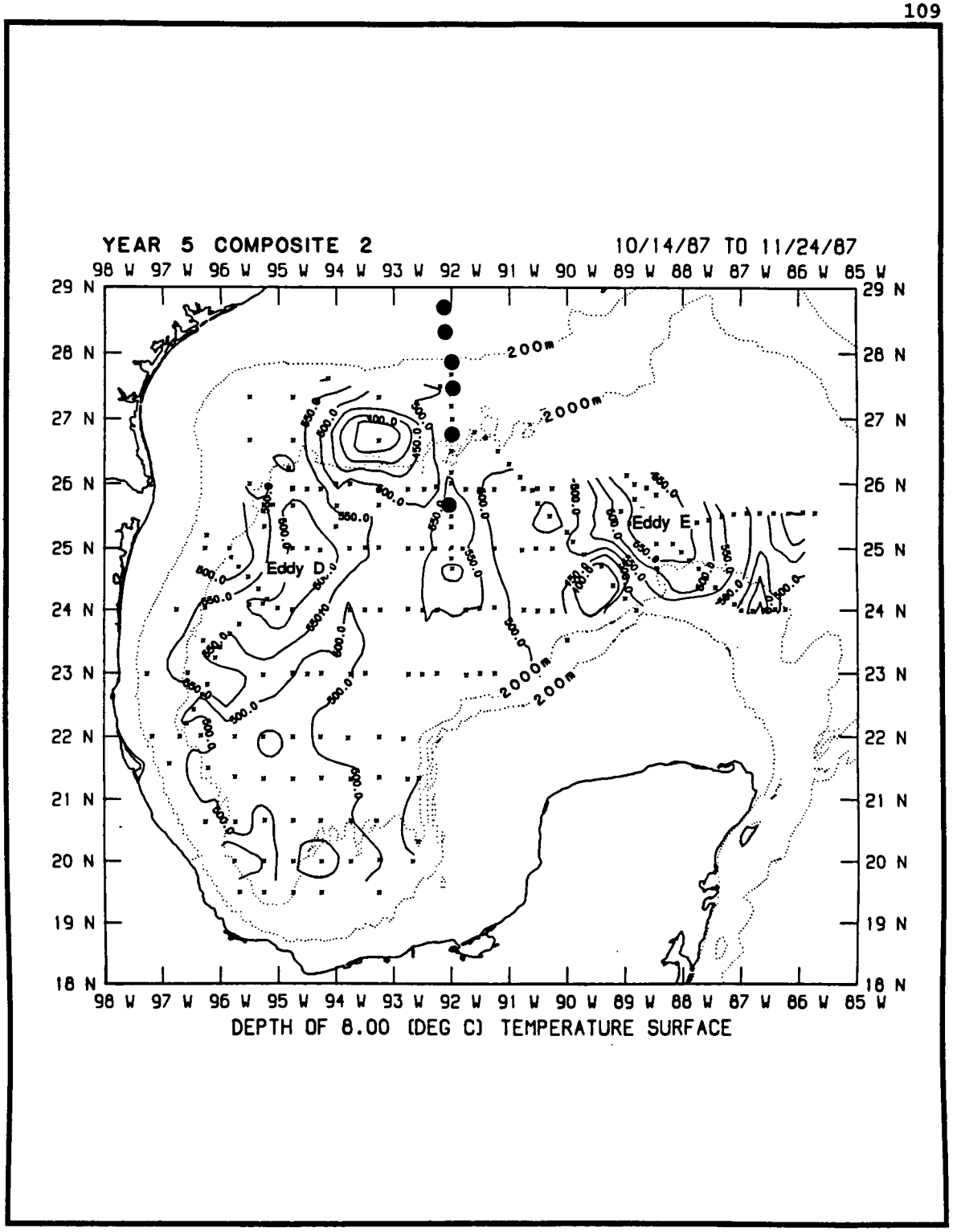

Figure 4.3-13. The depth of the 8°C isothermal surface as constructed from XBT data collected during the period of October 14 to November 24, 1987.

Eddy E had to be seeded a second time in mid-November 1987 (Drifter 3344). Trajectory data from the time of deployment to late March 1988 are shown in Figure 4.3-14. The eddy was stationary for over a month with a center of rotation at 25.5°N, 88.5°W. As it began to move westward, Drifter 3344 first moved closer to the center of rotation and then began making larger circles. By late March 1988, Drifter 3344 had left the flow field of Eddy E and began moving due west. Also shown in Figure 4.3-14 are the trajectories for Drifters 1392 and 1393 in the eastern Gulf. These drifters were in the water from mid-January through mid-March 1988. Their motion indicates a cyclonic flow field just east of the extension of the Loop Current as indicated by conditions during late March 1988 (Figure 4.3-15). As Drifter 3344 progresses steadily westward, XBT data show the edges of Eddy E in the vicinity of 25°N, 90°W. Loop Current water extends quite far northward with 25°C water reaching beyond 27°N. Within two months, this extension resulted in shedding another Loop Current eddy.

In mid-April 1988, Eddy E had to be seeded a third time. Figure 4.3-16 shows trajectory data from mid-April through mid-May 1988. Drifter 3353 was placed into Eddy E and made tight, anticyclonic loops while moving westward. At the same time, Drifter 3344 reached the Mexican continental shelf and rotated anticyclonically northward onto the Mexican coast. By the end of mid-May, a new eddy, Eddy F, had been shed from the Loop Current. The trajectories for Eddy E and Eddy F for mid-May through the first of September 1988 are shown in Figure 4.3-17. Both eddies translated slowly westward across the Gulf, with Eddy E approaching the Mexican coast at ~23°N. The structure of these eddies is shown in Figure 4.3-18 which is a composite of XBT data collected primarily during July 1988. The composite includes ship launched XBT data collected over 22 days (see Table 2.3-7) and AXBT data, which cover Eddy F, collected in four days (see Figure 2.3-3a). As can be seen in the composite, Eddy F is better resolved than Eddy E. Drifter 3345 has elliptical dimensions during mid July-early August of approximately 244 by 148 km. Figure 4.3-19 shows a vertical section of temperature along the major axis of Eddy F. Note that the drifter with its 100 m window shade drogue is not necessarily at the eddy front nor is it necessarily following the same parcel of water at all times. Taking the front location as the point where the 20°C isotherm crosses 125 m, the eddy front cannot be located in the 340 km section shown in Figure 4.3-19.

The trajectory of Drifter 3353 indicates that Eddy E was modified to some degree along the Mexican shelf. Figure 4.3-20 shows Drifter 3353 moving dramatically northward as far as four degrees of latitude and then making an anticyclonic loop. The abrupt northward turn coincided with the passage of Hurricane Gilbert to the south. Previously such northward movement has been associated in winter with a large amount of warm water moving from ~22°N to 27°N (Lewis and Kirwan, 1985; Lewis et al., 1989). An interaction between Eddy E and an existing flow field in the northwestern Gulf is suggested (possibly the remnants of Eddy D).

From mid-October to late December 1988, the trajectory from Drifter 3353 showed some different flow field characteristics, (Figure 4.3-21). This drifter, which had already made one anticyclonic loop along the northern

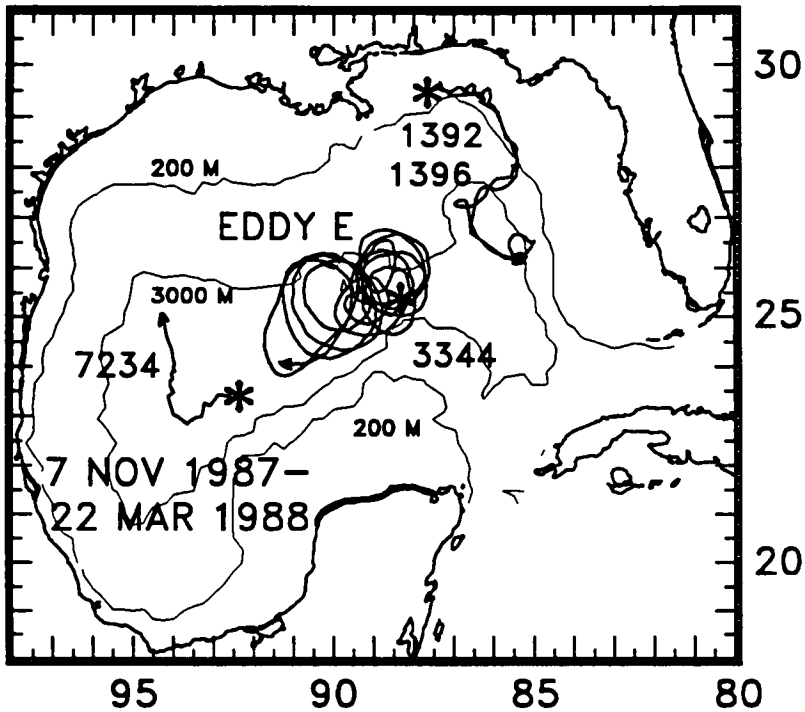

Figure 4.3-14. Drifter trajectories for November 7, 1987 to March 22, 1988. The asterisks represent the initial positions of the drifters. Depth contours are in meters.

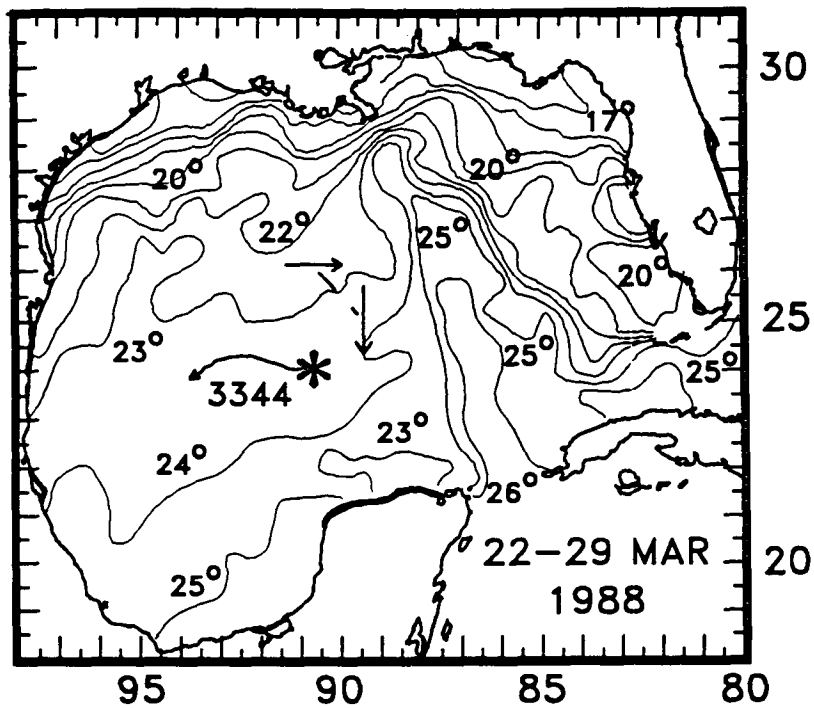

Figure 4.3-15. Conditions for the week of March 22 to 29, 1988. SSTs are in °C. Arrows denote the flow at the edges of Eddy E while dotted lines indicate the location of eddy water (based on XBT data).

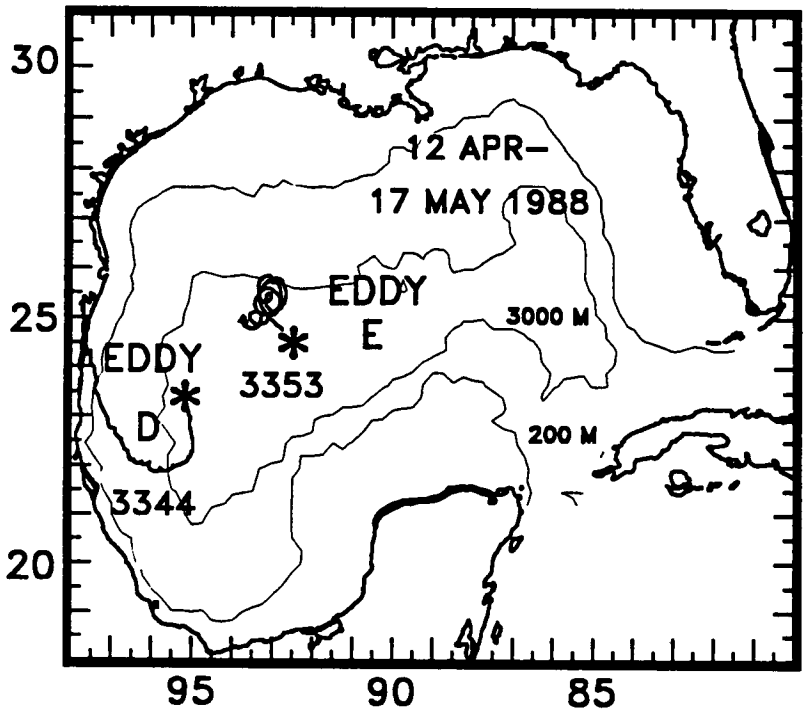

Figure 4.3-16. Drifter trajectories for April 12 to May 17, 1988. The asterisks represent the initial positions of the drifters. Depth contours are in meters.

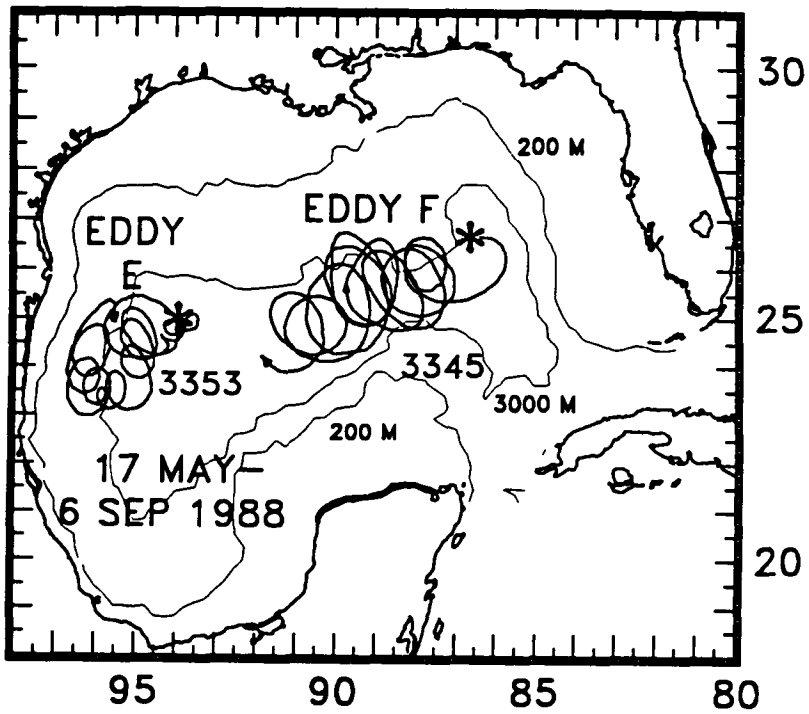

Figure 4.3-17. Drifter trajectories for May 17 to September 6, 1988. The asterisks represent the initial positions of the drifters. Depth contours are in meters.

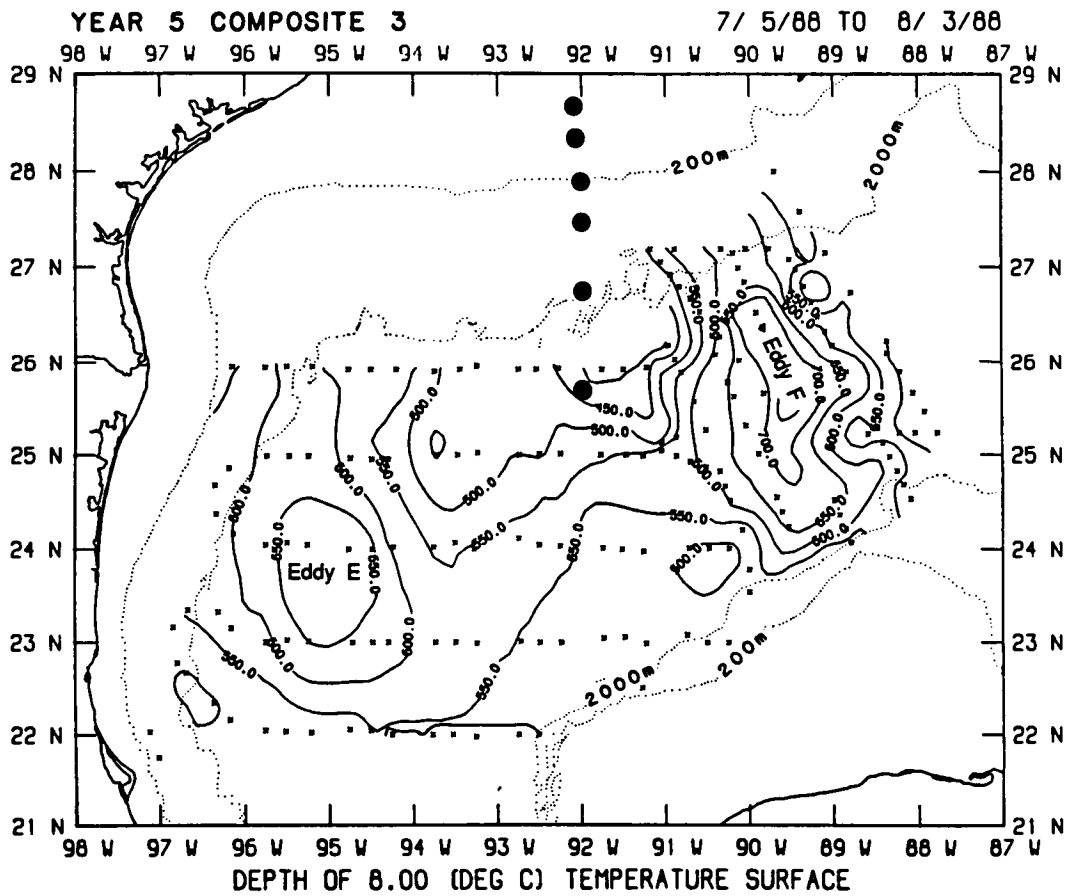

Figure 4.3-18. The depth of the 8°C isothermal surface as constructed from XBT data collected during the period of July 5 to August 3, 1988.

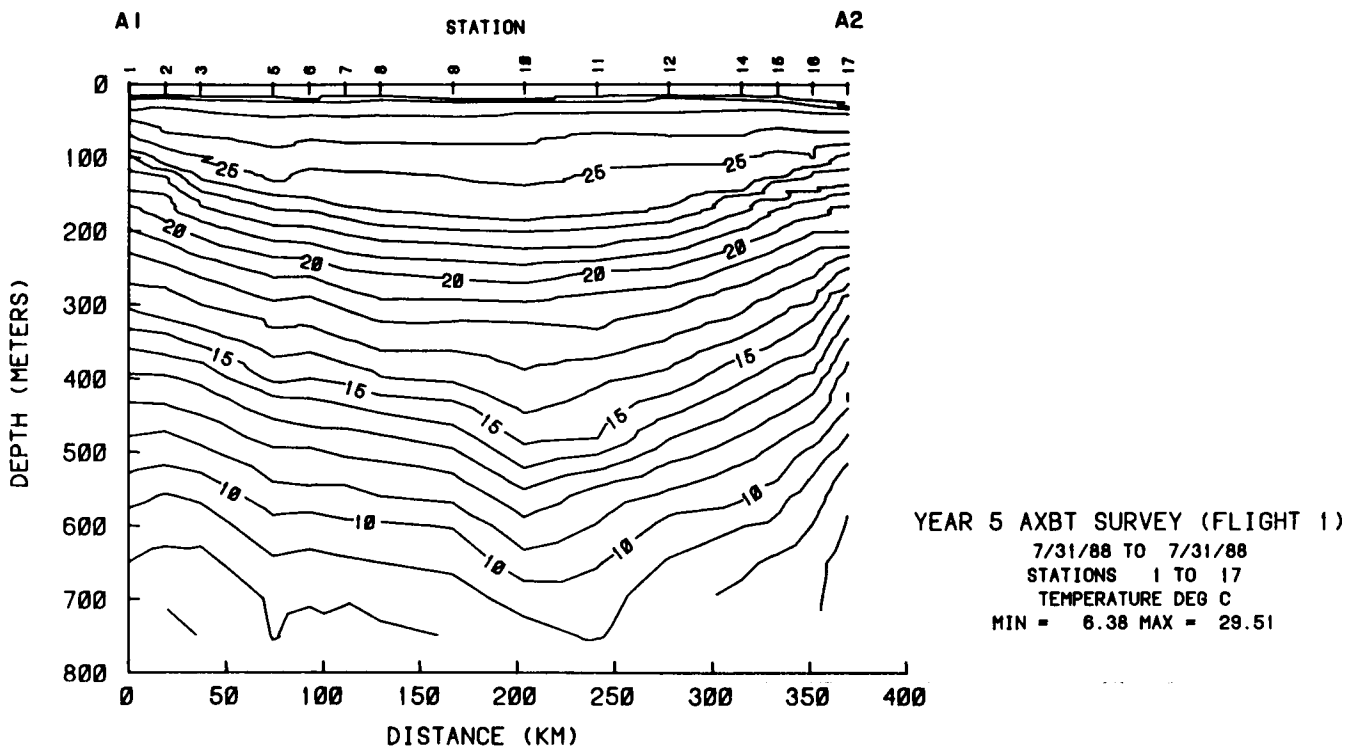

Figure 4.3-19. Vertical plot of temperature for Stations 1 to 17 for July 31, 1988 AXBT section in Eddy F.

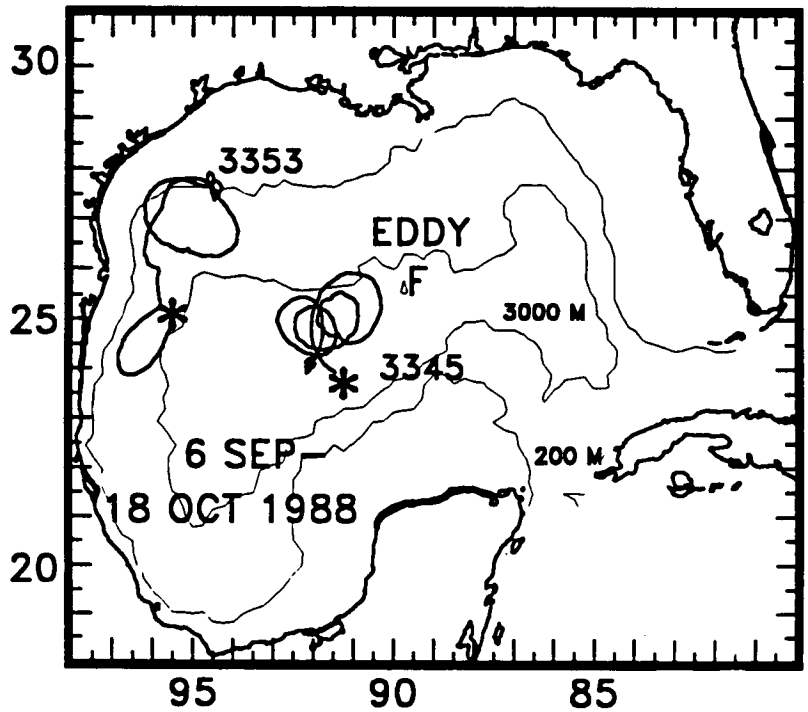

Figure 4.3-20. Drifter trajectories for September 6 to October 18, 1988. The asterisks represent the initial positions of the drifters. Depth contours are in meters.

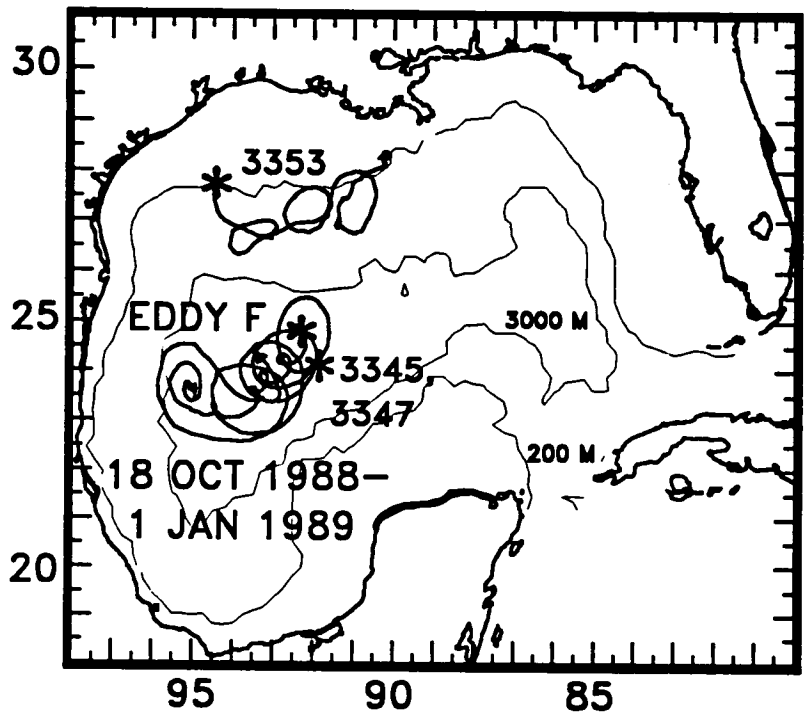

Figure 4.3-21. Drifter trajectories for October 18, 1988 to January 1, 1989. The asterisks represent the initial positions of the drifters. Depth contours are in meters.

Gulf shelf region (Figure 4.3-20), then moved eastward while making two cyclonic loops followed by an anticyclonic loop. It appears to have been moving between organized flow fields along the upper slope. This is the first time that such rotational, features have been documented along the northern shelf of the Gulf. The character of these features was constructed using available profile data from October 17 to 31, 1988 (Figure 4.3-22). In this figure, Eddy F is quite apparent in the deeper Gulf waters almost due south of Mooring GG. Depressions of the 8°C isothermal surface also occur in the northwestern Gulf. A cyclone along the northern shelf break is well defined.

A second series of AXBT tracks were made through Eddy F in mid-October such that three of the tracks were coincident with ascending GEOSAT tracks. GEOSAT altimeter data were available for two of the three ascending and two descending tracks. One descending track and an ascending track 10 days later crossed just north of the approximate center of Eddy F. These tracks have been illustrated in Figure 2.3-3b. The two ascending tracks were over Stations 1 to 22 and 35 to 56. GEOSAT track 189 (AXBT Stations 1 to 22) and descending track 061 are plotted in Figure 4.3-23b against the depth of the 14°C isotherm determined from AXBT Stations 1 to 22. Taking the eddy front location as the point where the 14°C isotherm crosses 300 m, the eddy was 300 km across. Using the midpoint of the slope in GEOSAT data, the eddy was approximately 215 km across with the northern front location within 25 km of that determined from the temperature structure. Using the position of the 20°C isotherm at 125 m as the eddy front location would make the GEOSAT and thermally derived front locations coincident, but the estimate of eddy dimension would be worse. Examination of vertical sections through the eddy suggests that the northern edge appears to be sharper or more distinct than the southern edge. These data illustrate some of the uncertainty in accurately determining eddy size and in correlating measurements from different sources.

In October, Eddy F which was seeded with an additional drifter, (Drifter 3347), moved westward, reaching 23°N, 94°W by the first week of December 1988 (Figure 4.3-21). Over the next two weeks, Eddy F elongated in an east-west direction with the net result that Drifter 3345 moved beyond the flow field of the eddy (Figure 4.3-24). Such a process has been seen with a number of satellite-tracked eddies in the Gulf since 1981. It may be related to Eddy F coalescing with the existing anticyclonic flow field along the Mexican coast (Nof, 1988; Lewis et al., 1989).

4.3.2 Kinematics of Eddies E and F

Kinematic analyses were performed on a number of drifters associated with Eddies E and F. Drifter 3344 was analyzed for that time after Eddy E had just separated from the Loop Current (Figure 4.3-14). The interesting feature is that Eddy E appeared to stall for approximately one month before beginning its westerly translation. In addition to Drifter 3344, Drifter 3353 was analyzed when Eddy E was approaching and along the Mexican coast (Figures 4.3-16 through 4.3-21). During this time, the drifter not only indicated the anticyclonic flow field of Eddy E but also an anticyclone in the northwestern Gulf and two cyclones along the

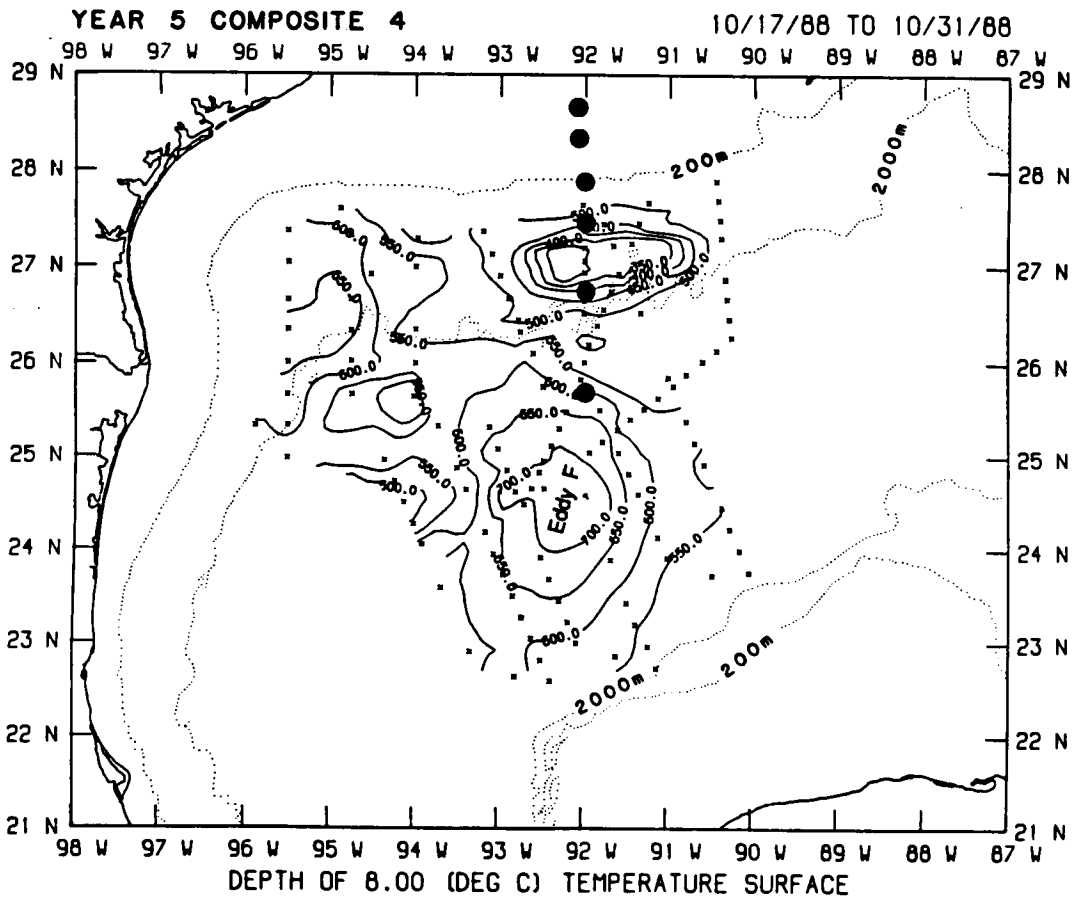

Figure 4.3-22. The depth of the 8°C isothermal surface as constructed from XBT data collected during the period of October 17 to 31, 1988.

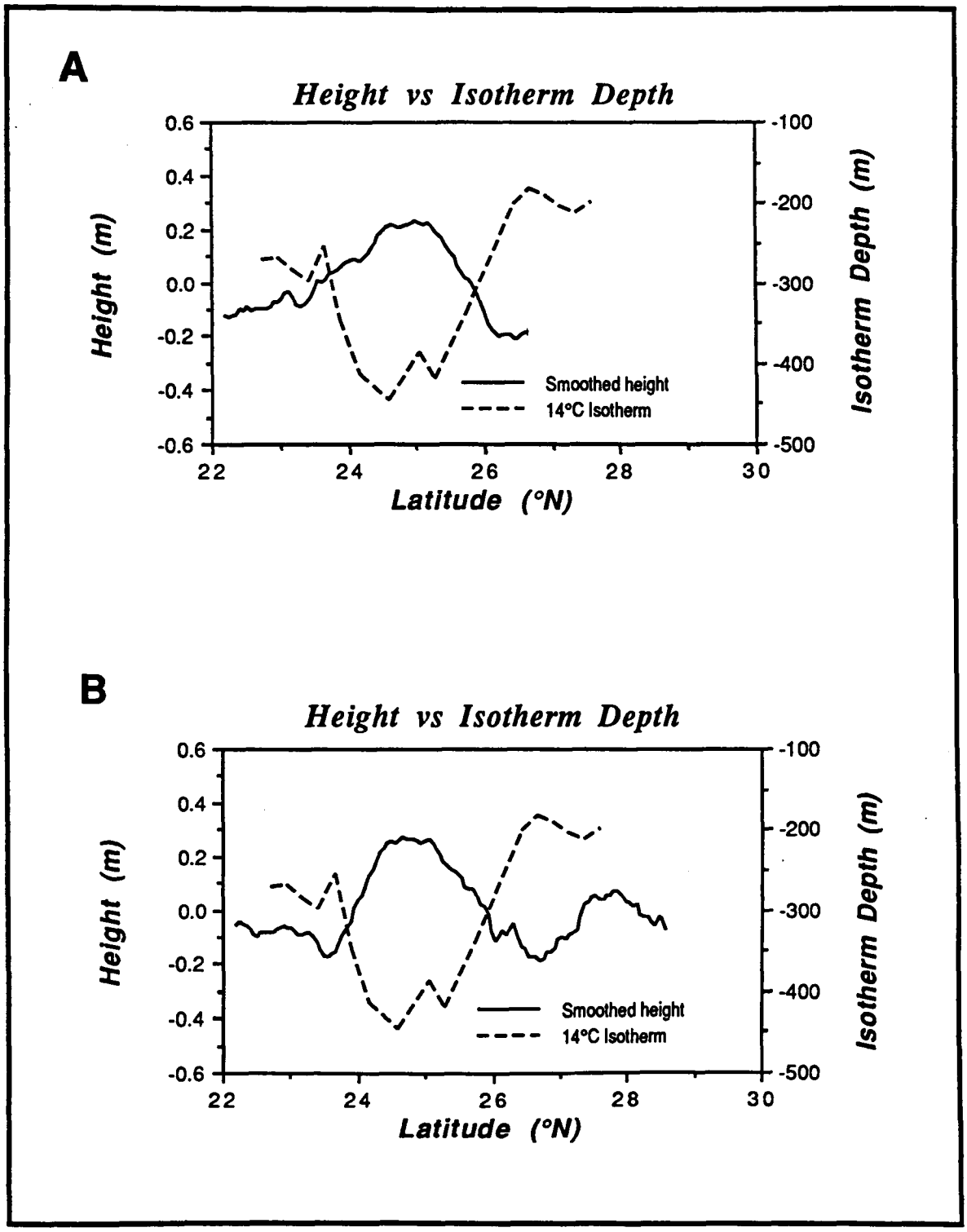

Figure 4.3-23a,b. Sea surface height and isotherm depth for (a) concurrent sea surface height from an ascending pass and the 14°C isotherm depth from AXBT Stations 1 through 22 (Figure 2.3-3b) and (b) sea surface height data from a descending pass and 14°C isotherm depth from AXBT Stations 1 through 22.

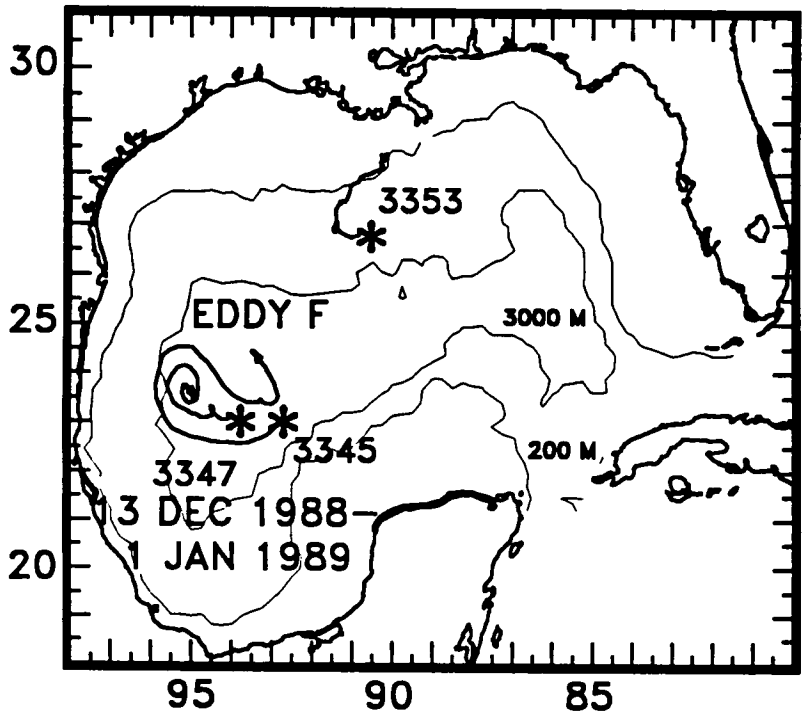

Figure 4.3-24. Drifter trajectories for December 13, 1988 to January 1, 1989. The asterisks represent the initial positions of the drifters. Depth contours are in meters.

northern Gulf shelf-break region. Finally, Drifters 3345 and 3347 were analyzed to study some of the flow characteristics of Eddy F (Figure 4.3-21). Of particular interest were differences associated with the trajectory of a drifter which remained in the flow field of Eddy F (3347) and the trajectory of a drifter which was apparently ejected from Eddy F (3345).

The initial kinematics of Eddy E are shown in Figures 4.3-25a and 4.3-25b. The vorticity (quite close to twice the angular speed of the eddy) is initially about -1.8×10^{-5} rad s^{-1} but slows to approximately -1.4×10^{-5} rad s^{-1} during Julian Days 360-380 relative to January 1, 1987 (note 2π radians = 360°). This change in vorticity coincided with the beginning of the eddies' westward translation. At the same time, the eddy was seen to be undergoing a change from a convergent flow field to a strong but short-lived divergent flow field (Figure 4.3-25). The east-west and north-south components of the swirl velocities are shown in Figure 4.3-26a. This figure indicates a general decreasing trend in the swirl velocities up to JD 365. However, as the eddy began moving westward, the swirl velocities increased ~10 to 20 cm s^{-1}. Minimum swirl velocities were recorded around JD 390 after which the swirl magnitudes increased to ~80 cm s^{-1}. At the same time that the swirl velocities were decreasing, the axes lengths (as seen by Drifter 3344) were decreasing (Figure 4.2-26b). These decreases were from a maximum of ~170 km to a minimum of ~50 km. As the eddy began moving westward, both axes increased in length for about five to 10 days.

Eddy E was tracked in the western Gulf with Drifter 3353. The recorded speed components of the drifter are shown in Figure 4.2-27. Between JDs 100 to 250, the speed variations were quite regular except during Days 160 to 170. After Day 250, Drifter 3353 moved northward toward the Texas shelf break (Figures 4.3-20 and 4.3-21) and traveled eastward moving between an anticyclone, two cyclones, and another anticyclone. As can be seen in Figure 4.3-27, the oscillations during this latter time period were longer in period and less well organized.

The kinematics of the flow field seen by Drifter 3353 are shown in Figures 4.3-28a and 4.3-28b. The vorticity was of the same order as that detected by Drifter 3344. Distinct periods existed during which the vorticity became more negative, about -3.0×10^{-5} rad s^{-1}. The two intervals of cyclonic rotation are well defined with positive vorticities as large as 4.0×10^{-5} rad s^{-1}. Yet, because of the larger values of deformation that were also occurring, the total rotation times were smaller than those seen in Eddy E. The variations in divergence (Figure 4.3-28b) appear to be relatively large during this portion in the evolution of Eddy E. Between JDs 200 and 250, the eddy converged, then diverged, and finally converged. After Day 250, a large divergence occurred. A second period of divergence occurred during Days 290 to 310. This was associated with the first cyclone.

The kinematics of Eddy F are shown in Figures 4.3-29a and 4.3-29b. The vorticity had slowly decreased in magnitude from its original mean value of about -1.5×10^{-5} rad s^{-1}. By JD 330 in 1988, the vorticity was around -1.2×10^{-5} rad s^{-1}. As the vorticity became more irregular at the end of

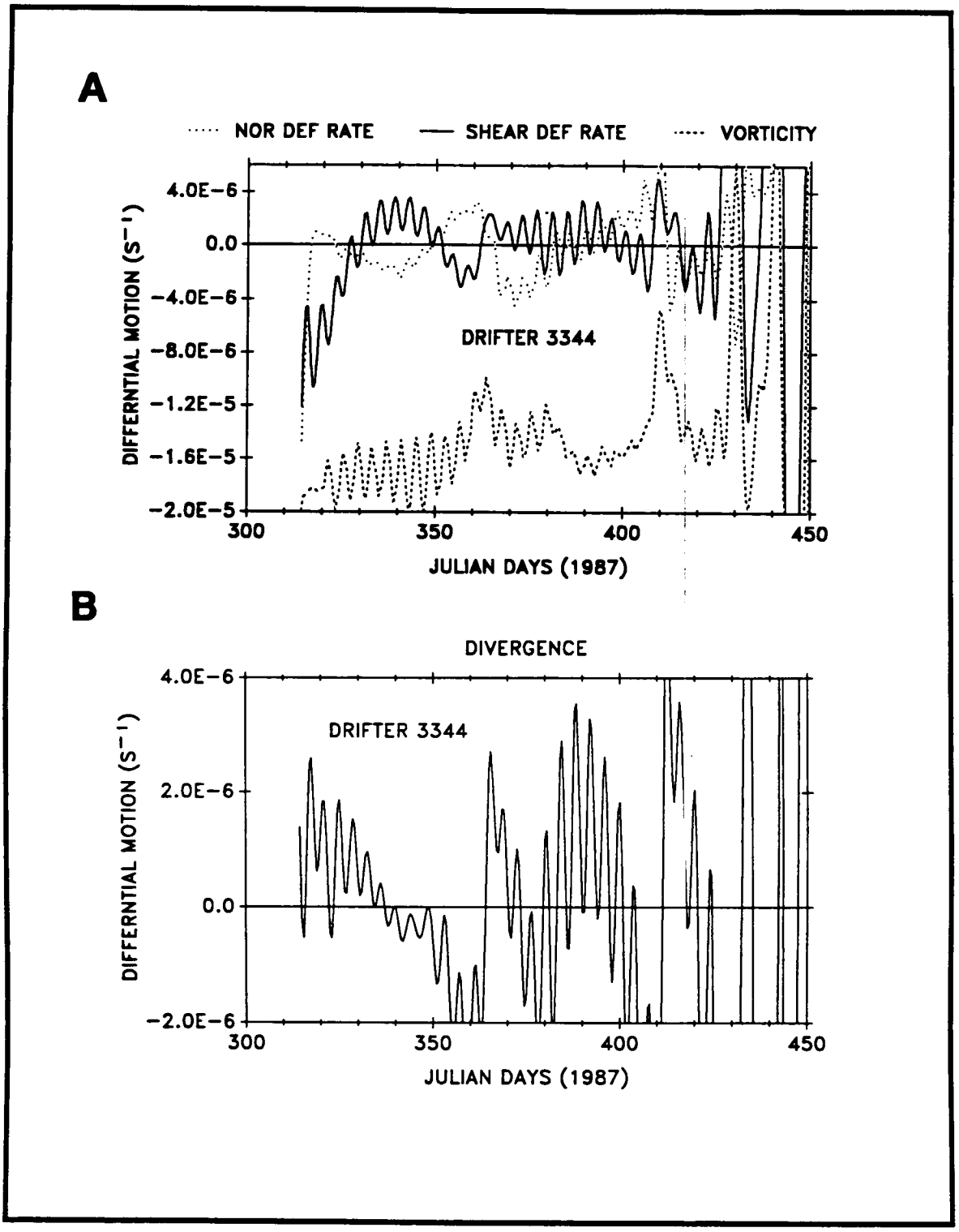

Figure 4.3-25. For Drifter 3344, the (a) vorticity, normal deformation rate and shear deformation rate for Eddy E, and (b) divergence for Eddy E.

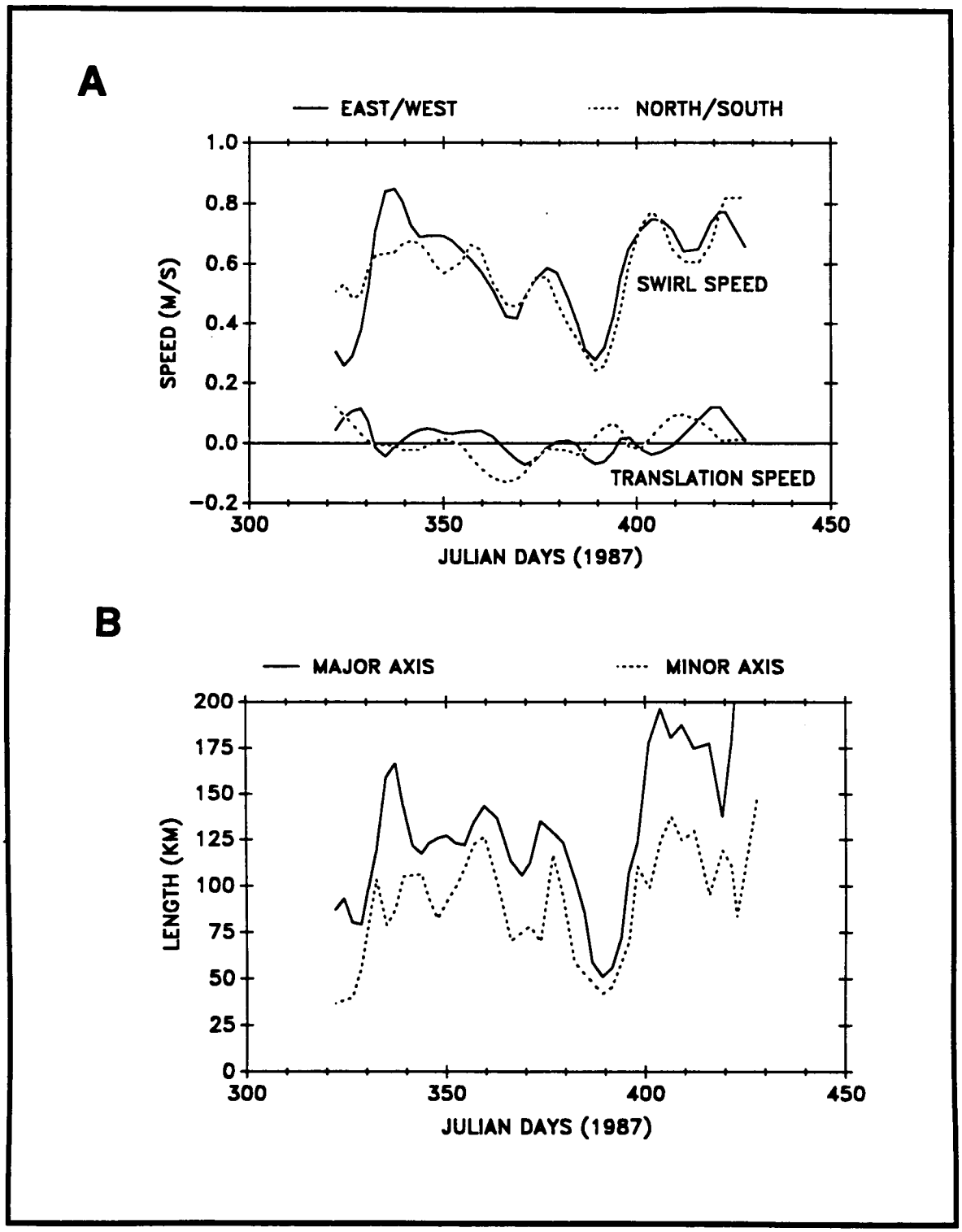

Figure 4.3-26. For Drifter 3344, the (a) east-west and north-south translation velocities and swirl magnitudes for Eddy E, and (b) variations in the lengths of the major and minor axes for Eddy E.

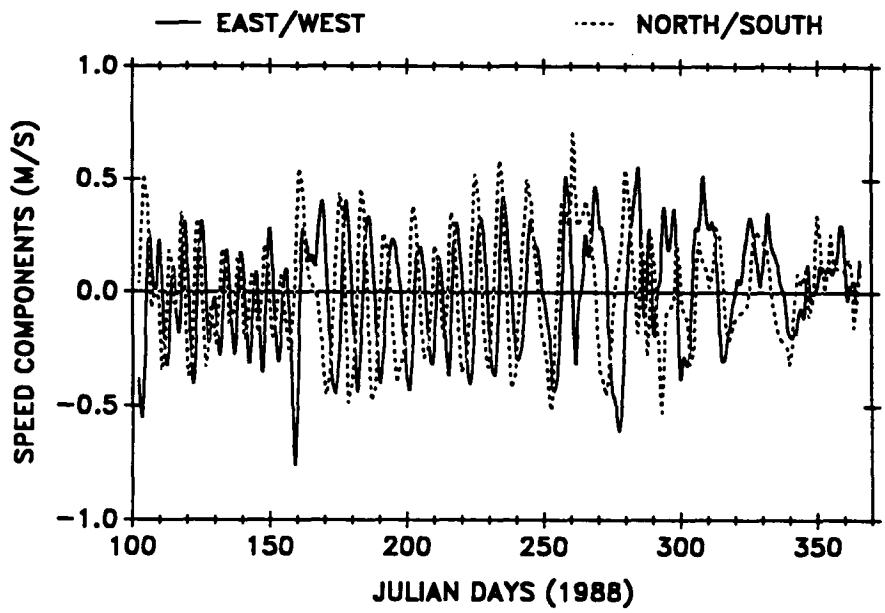

Figure 4.3-27. East-west and north-south speed components of Drifter 3353.

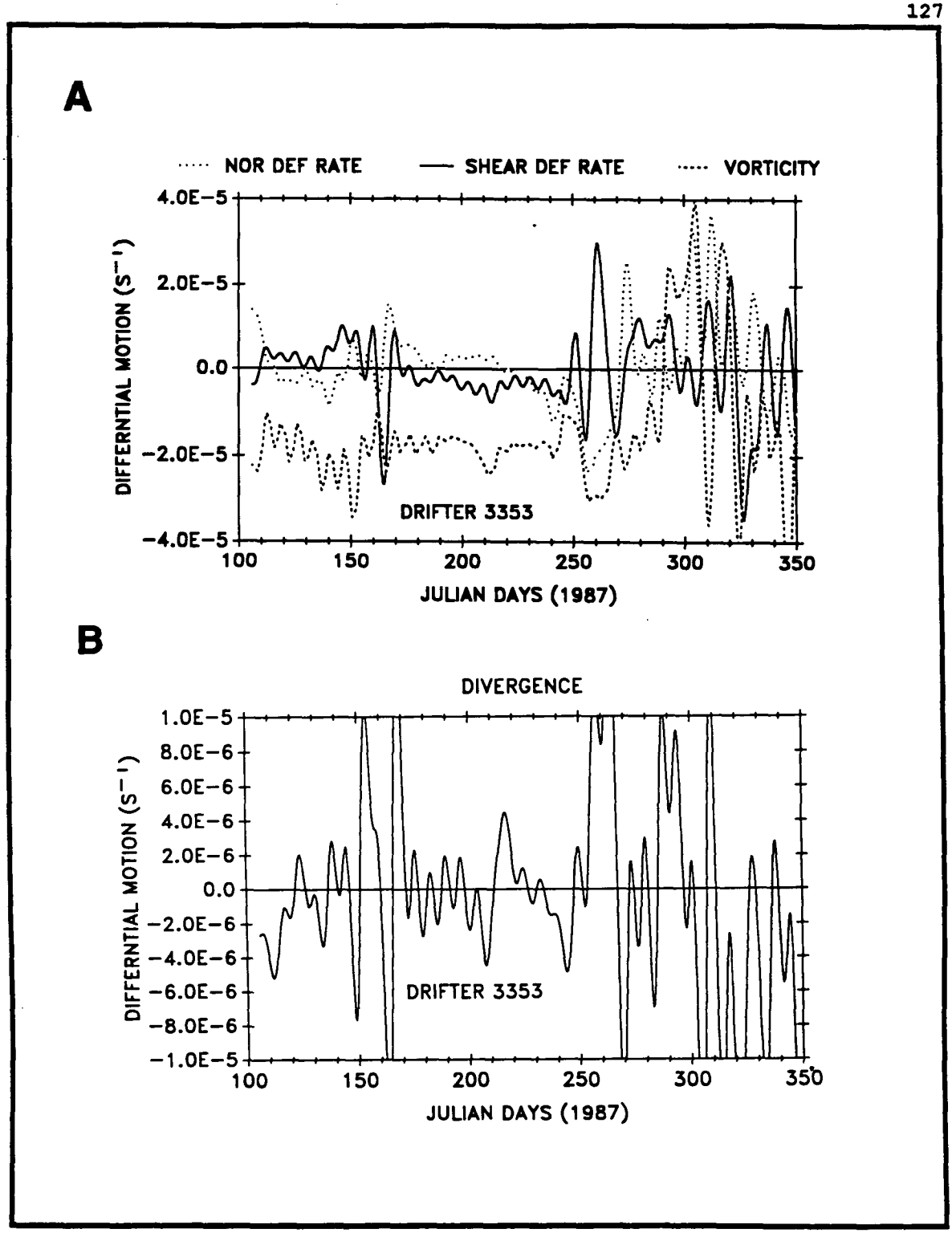

Figure 4.3-28. For Drifter 3353, the (a) vorticity, normal deformation rate and shear deformation rate for Eddy E, and (b) diverengence for Eddy E.

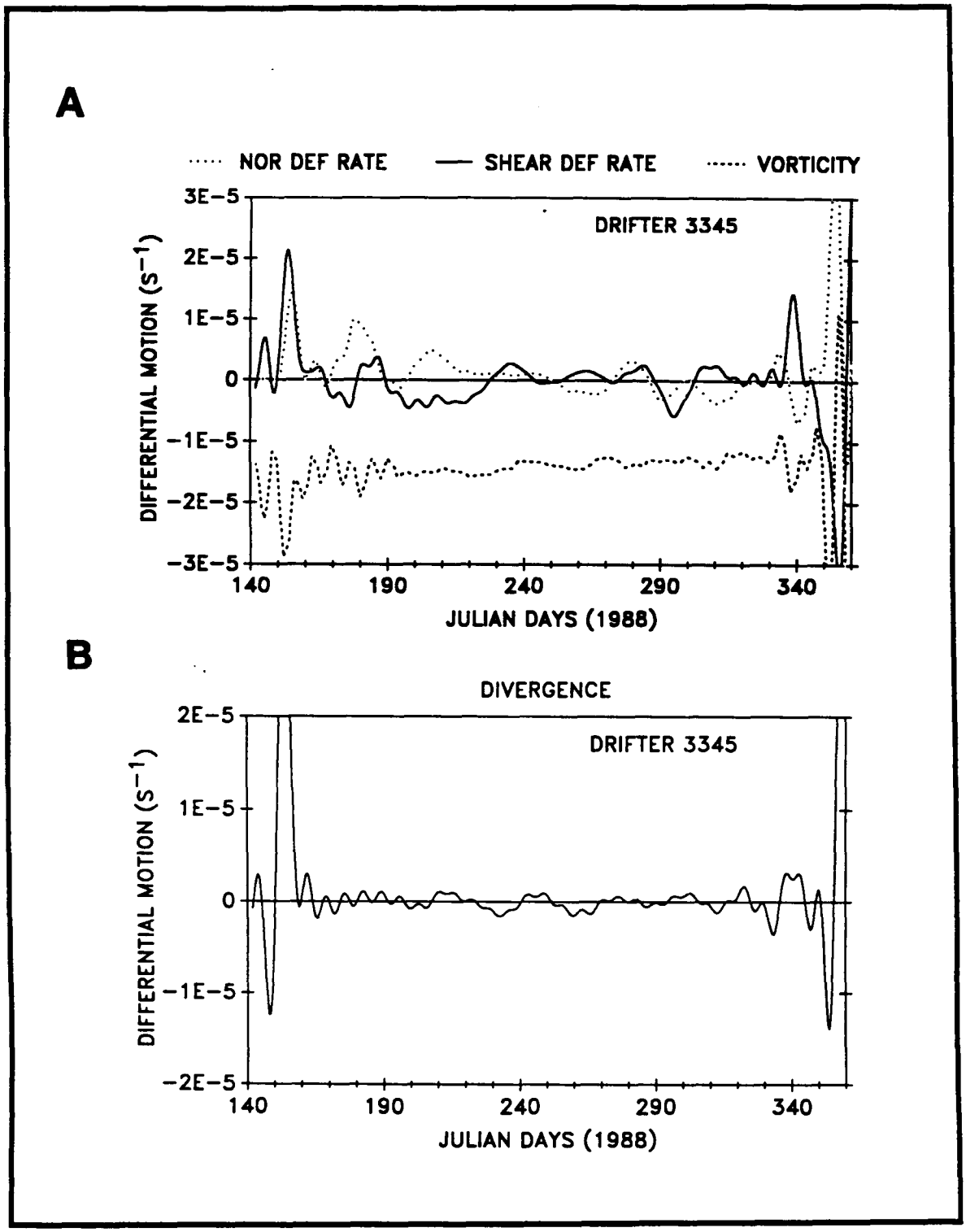

Figure 4.3-29. For Drifter 3345, the (a) vorticity, normal deformation rate and shear deformation rate for Eddy F, and (b) divergence for Eddy F.

the record, the eddy underwent greater deformation. A net divergence was distinctly detected as the drifter began to be spun out of the eddy (after Day 340). However, this divergence was not of the same magnitude as detected by Drifter 3347 (Figures 4.3-30a and 4.3-30b). The vorticity calculated using Drifter 3347 tended to be more negative than that calculated using Drifter 3345. Moreover, Drifter 3347 never encountered any positive vorticity.

4.3.3 Physical Processes of Interest

To discuss the physical processes in this data set, a quick review of the present understanding of eddies in the Gulf of Mexico is necessary. Gulf anticyclones are generated by the shedding from the Loop Current of a closed rotational feature, typically in the vicinity of 25.5°N, 87.5°W. The characteristics of the eddies' flow field appear to be established well before the shedding process. The intensity of the anticyclone can be expressed by the maximum depth of the 8°C isotherm. This maximum depth can range from 600 to 750 m. Since the undisturbed depth of the 8°C isotherm in the Gulf is ~500 m, these anticyclones are relatively intense rotational features. Thus, these eddies remain intact over long periods of time traveling all the way to the western Gulf at 5 to 8 cm s^{-1}.

The westward translation of Gulf eddies results from the spatial variations of the Coriolis parameter. As indicated in this data set, this translation process does not necessarily occur smoothly. Although Eddy F had a consistent westward motion, Eddy E's apparent hesitation at ~89°W was an unexpected phenomenon. A similar stalling of the westward motion of a Loop Current eddy has been reported (Lewis et al., 1989), but then the northern edge of the eddy was in relatively shallow water. As a result, non-linear acceleration would cause the eddy to move eastward against the Coriolis effect, the net result being the stalling of the westward motion of the eddy. However, in the case of Eddy E, the eddy was in relatively deep waters on all sides. Thus, apparently another process exists by which Loop Current eddies can have their westward motion arrested.

Another physical process pointed out by this data set is related to the interaction of eddies in the western GOM. As a "young" eddy approaches the western Gulf region, its flow field can interact with existing, older anticyclones along the Mexican coast (Lewis and Kirwan, 1985 and 1987; Lewis et al., 1989). This interaction may consist of two flow fields coalescing to form one anticyclone. Although the general nature of the coalescence process has been examined, Nof (1988) has only recently shown experimentally how such a coalescence can occur. The process has a "padlock" flow signature with motion that often has the outline of a peanut (see Figure 4.3-24). Even more recent work has shown that a coalescing process will likely result in ejecting some of the water from the two eddies (Cushman-Roisin, 1989). This ejection results from the need to conserve the mass, total energy and angular momentum of the original geostrophic eddies. In past studies, drifters have been observed to leave the anticyclonic field of motion after performing the peanut or padlock maneuver. It is quite likely that ejecting Drifter

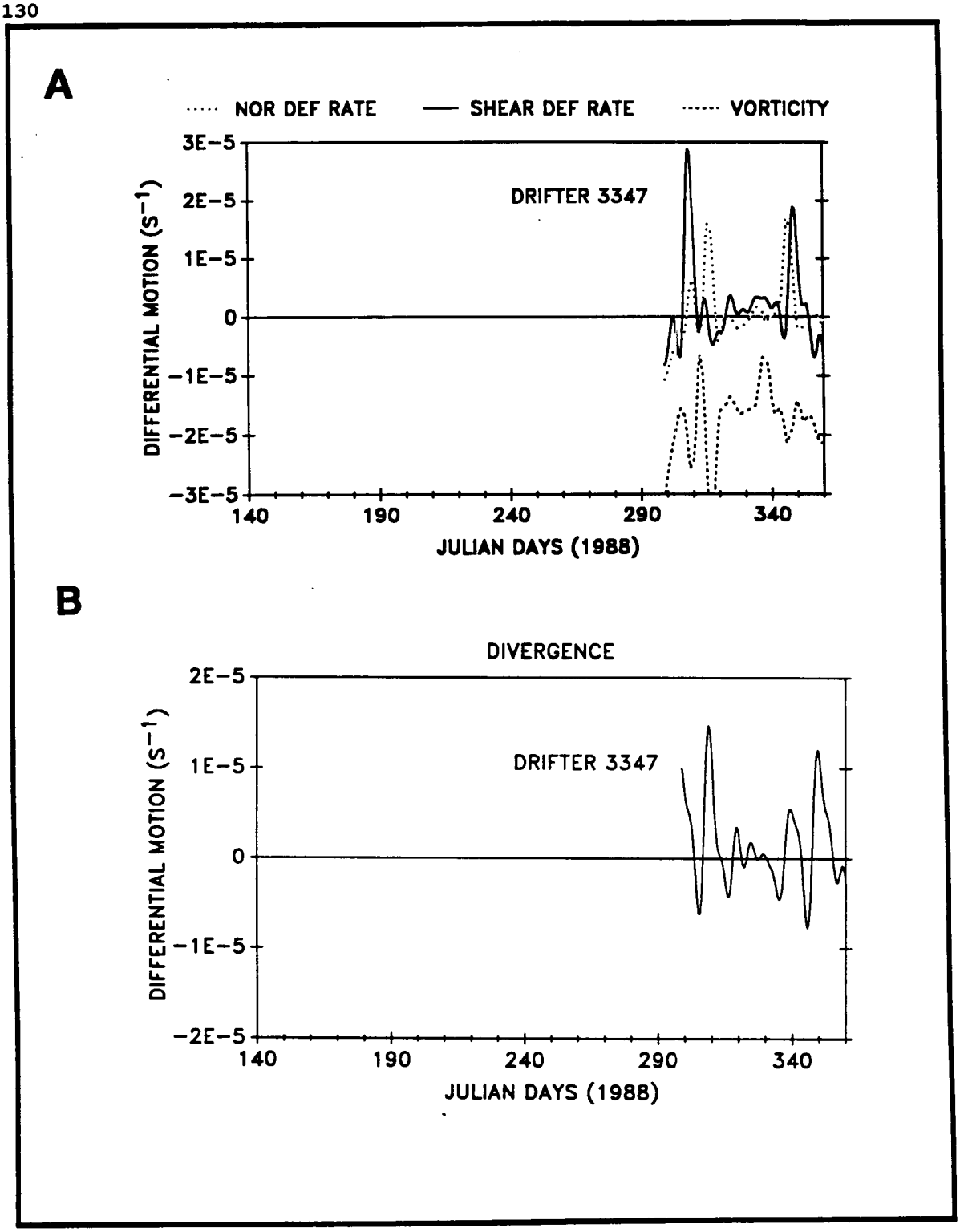

Figure 4.3-30. For Drifter 3347, the (a) vorticity, normal deformation rate and shear deformation rate for Eddy F, and (b) divergence for Eddy F.

3345 from Eddy F (and the corresponding retaining of Drifter 3347) reflected the need to eject some water but retain other water during coalescence in the western Gulf.

After a Gulf eddy moves onto the Mexican shelf slope, non-linear accelerations can cause the eddy to move northward (Figure 4.3-20). In many cases, water from the eddy will move rapidly northward as far as 28°N. At least in one instance, this phenomenon resulted from the interaction of a smaller, older eddy and a larger, newer eddy. This northern movement can be rather explosive and has cyclonic rotation associated with it (Lewis et al., 1989; see Figure 4.3-12). Next is the topic of Gulf cyclonic features as seen in this data set. The first cyclonic feature of interest is the Campeche Bay gyre. This cyclone is primarily wind driven and is not necessarily associated with the Loop Current anticyclones. However, interestingly, some exchange of waters between anticyclones along the Mexican coast and the Campeche Bay cyclone does occur (Figures 4.3-3 and 4.3-7).

A second set of cyclones are depicted by the trajectories of Drifters 5837 and 5839 on the western side of Eddy D (Figure 4.3-11). These cyclones are smaller than the other cyclones mentioned. These boundary vortices are likely associated with the western flow regime of Eddy D as the eddy interacts with bathymetry.

Finally, the more curious of the cyclones, those found along the northern shelf slope of the Gulf deserve comment. These eddies are depicted in both drifter trajectories (Figures 4.3-12 and 4.3-21) and hydrographic data (Figures 4.3-13 and 4.3-22). Such eddies may originate from the processes occurring in the western Gulf of Mexico. Cyclones generated in the western Gulf could move eastward as a result of the topographic beta effect (both the Coriolis effect and non-linear accelerations would cause cyclones to move westward). It is also possible that the cyclonic eddies result from the shedding of vortices as a Loop Current eddy moves westward (Smith and O'Brien, 1983). Yet, all the cyclones presented here are along the northern shelf slope as opposed to ones which are occasionally in deeper water just east of a westwardly moving anticyclone (a cyclone to the east of an anticyclone will tend to rotate in an anticyclonic nature, thus bringing it more to the southeast of the anticyclone [Hooker, 1987]).

The series of cyclones depicted in Figure 4.3-21 and the elongated nature depicted in Figure 4.3-22 suggest that the eddies might be generated by a barotropic instability. As the Loop Current eddies move westward, their northern flow regime (with its associated cyclonic vorticity) would induce a significant lateral shear. Under certain conditions, perturbations could grow into closed cyclonic vortices. These conditions are enhanced by the possibility that the densities of the two water masses can be significantly different (the 8°C isotherm within the eddy can be as deep as 750 m). Hooker (1987) studied such lateral instabilities numerically and showed that a series of closed cyclones form, and that these eventually coalesce to form the more elongated flow structures as seen in the hydrographic data of Figure 4.3-22.

4.3.3.1 Dynamics Related to the Stalling of Eddy E

Some of the kinematics related to the stalling of Eddy E were presented in Figures 4.3-25 through 4.3-26. Some additional data appear in Figure 4.3-31. Here, the period of rotation of the eddy began to increase from ~nine days to a maximum of about 13 days at the time Eddy E began moving westward. The eddy was almost circular during the entire time, but the drifter was continually moving closer to the center of rotation. The inward spiral of Drifter 3344 represents a convergence of the surface waters of Eddy E. If potential vorticity were being conserved, the convergence would be balanced by an increase in the absolute vorticity of the eddy. However, the rotation rate did not increase (indeed, it decreased), the eddy did not move northward, and it did not move into deeper water. This suggests that external factors could have been influencing Eddy E.

Lewis et al., (1989) have shown that entrainment of water into an eddy can cause convergence in the surface layers. However, for entrainment the absolute vorticity must decrease (Lewis et al., 1989). A decreasing vorticity implies an increasing rotation rate, and this is what occurred (Figure 4.3-31). Potential vorticity reflects the conservation of angular momentum on a geophysical scale, and the potential vorticity for Eddy E is shown in Figure 4.3-32. Potential vorticity gradually goes from positive to negative, reaching a maximum negative value right before JD 360. In effect, the isotherms were moving more downward with time. At Day 360, the eddy underwent rapid vortex compression, (i.e., divergence). It was as if the mechanism forcing the isotherms downward was rapidly extinguished, and the eddy responded by diverging (allowing the isotherms to move upward again).

Based on the above data and relationships, the entrainment of water by Eddy E up to JD 360 is a reasonable conclusion. However, still of concern is the mechanism which could keep Eddy E from moving westward up to JD 360. As of now, no candidate processes exist.

4.3.3.2 Ejection of Mass from Eddy F

As previously discussed, ejecting water from two coalescing, geostrophic eddies can be explained by the need to conserve mass, angular momentum, and energy (Cushman-Roisin, 1989). This topic is significant because of the amount of mass that could be ejected. Previously, it was assumed that almost all of the water of two coalescing eddies went into the new composite eddy. However, Cushman-Roisin (1989) show that if the eddies are of approximately the same size, more than 20% of the water of the eddies must be ejected. Considering the size of Loop Current eddies, this is a considerable amount.

Although Cushman-Roisin represented the ejected water as an annulus surrounding the new eddy, work by Hooker (1987) indicates that the ejected water would more closely resemble "tails" trailing the newly formed eddy. For two coalescing cyclones, a numerical simulation shows that the ejected water is spun off to the top left and bottom right of the newly formed cyclone. For two coalescing anticyclones, the tails

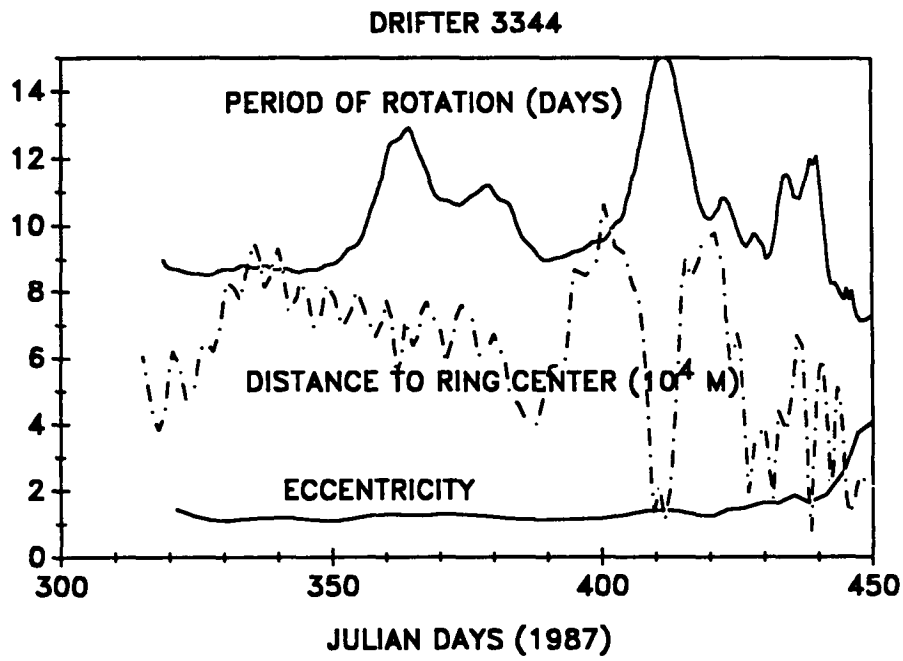

Figure 4.3-31. Period of rotation, distance to the center, and eccentricity for Eddy E as determined from the trajectory of Drifter 3344.

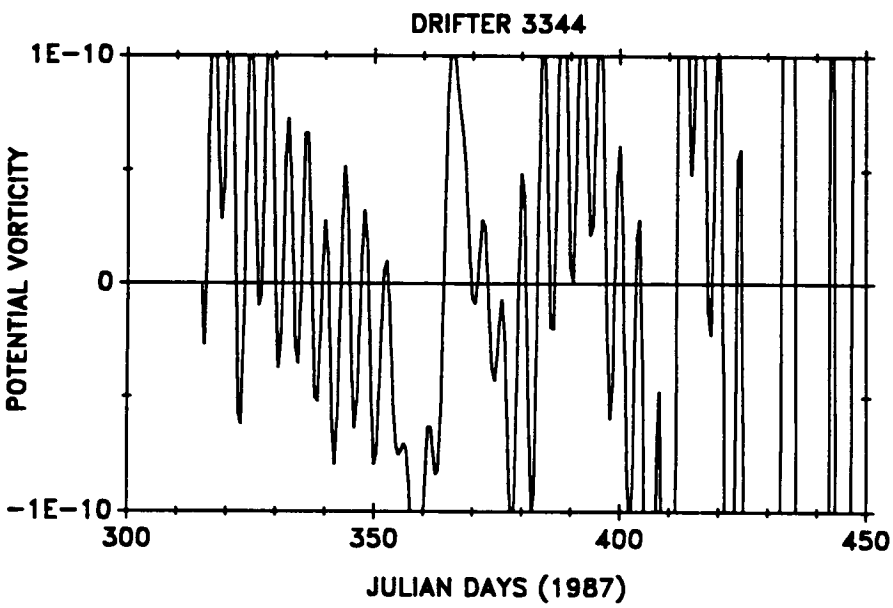

Figure 4.3-32. Potential vorticity for Eddy E as determined from the trajectory of Drifter 3344.

would be expected to the bottom left and top right of the new eddy (Griffiths and Hopfinger, 1987). The trajectory of Drifter 3345 shows the movement of the ejected water along the top right of Eddy F (Figure 4.3-24).

Some of the factors related to the coalescing process affecting Eddy F are shown in Figures 4.3-33a and 4.3-33b. Drifter 3345 varied from 45 to 100 km from the center of Eddy F while it was in the eddy. Its rotational period gradually increased from ~nine days in late May 1988 to ~13 days in December 1988. It is curious to note that Drifter 3347, which was deployed quite close to the center of rotation, indicated a period of rotation up to two days shorter than that indicated by Drifter 3345. This implies a cyclonic shear in the horizontal flow field between the two drifters. This in itself would promote a lateral diffusion of momentum toward the edge of the eddy, along with a corresponding ejection of water mass as the isotherms rise in response to a decrease in eddy velocity.

The effects of lateral shear are not considered in the balance of angular momentum as expressed by potential vorticity. Thus, a considerable imbalance might exist in the potential vorticity as seen by the two drifters in Eddy F. Figures 4.3-34a and 4.3-34b show this to be the case. The variations seen in these two figures are once again primarily a product of the oscillations of the stretching of the eddy vortex. Changes in relative and planetary vorticity were small.

From the trajectories of Drifters 3345 and 3347, reasonable hypotheses can be made about the ejection of water from two coalescing eddies in the western Gulf. Nof (1988) has shown that two coalescing anticyclones will send tentacles about one another as they join. For two anticyclones located west to east of one another, the tentacle of water leaves the top (northeast) corner of the western eddy and travels eastward around the northern half of the eastern eddy. Likewise, the eastern eddy has a tentacle of water leaving the bottom (southwest) corner of the eddy traveling westward around the southern half of the western eddy (Figure 4.3-35). These tentacles of water wrap around and encompass the adjoining eddy, pulling water from the interior of the eddies behind them. However, before the water from the interior of one eddy reaches the periphery of the other eddy, it is surrounded by the water of the tentacle of the other eddy (see Nof, 1988; Griffiths and Hopfinger, 1987). The final result is that water on the exterior of the new or combined eddy always comes from the exteriors of the two original eddies, and the water of the interior of the new eddy comes from the interiors of the two parent eddies. This would be intuitively expected. The lighter waters of the interiors end up in the center of the new eddy and the heavier waters of the exteriors end up on the exterior).

The trajectories of Drifters 3345 and 3347 (Figure 4.3-24) do indeed support the above scenario for the coalescing of anticyclones. As to the ejection of water, Drifter 3345 was ejected, as it must since only water on the exteriors of the parent eddies will end up on the exterior of the new eddy (where water can be readily ejected). Moreover, the diameter of the new eddy can only be at most ~25% greater than the parent eddies.

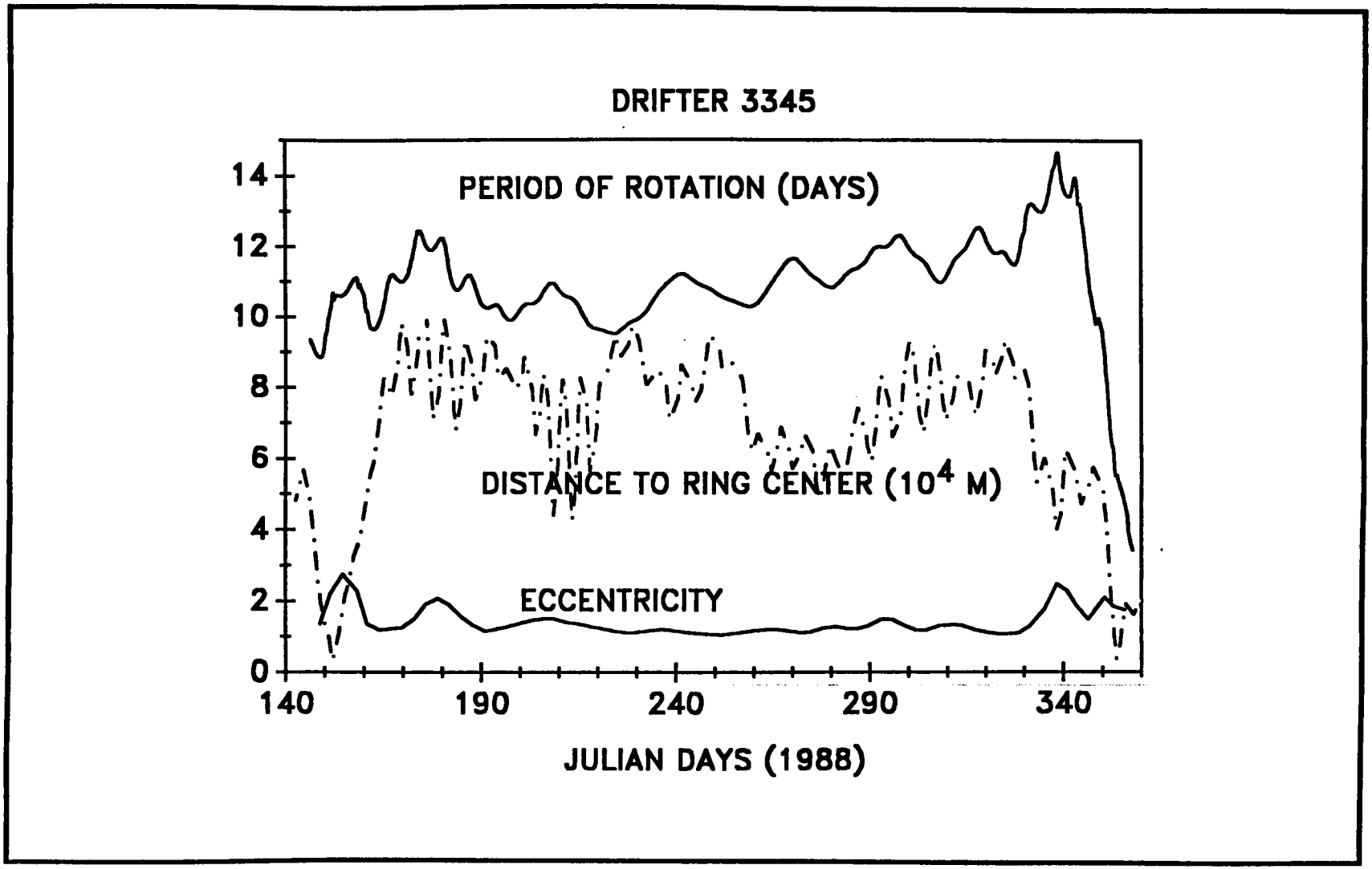

Figure 4.3-33a. Period of rotation, distance to the center and eccentricity for Eddy F as determined from the trajectory of Drifter 3345.

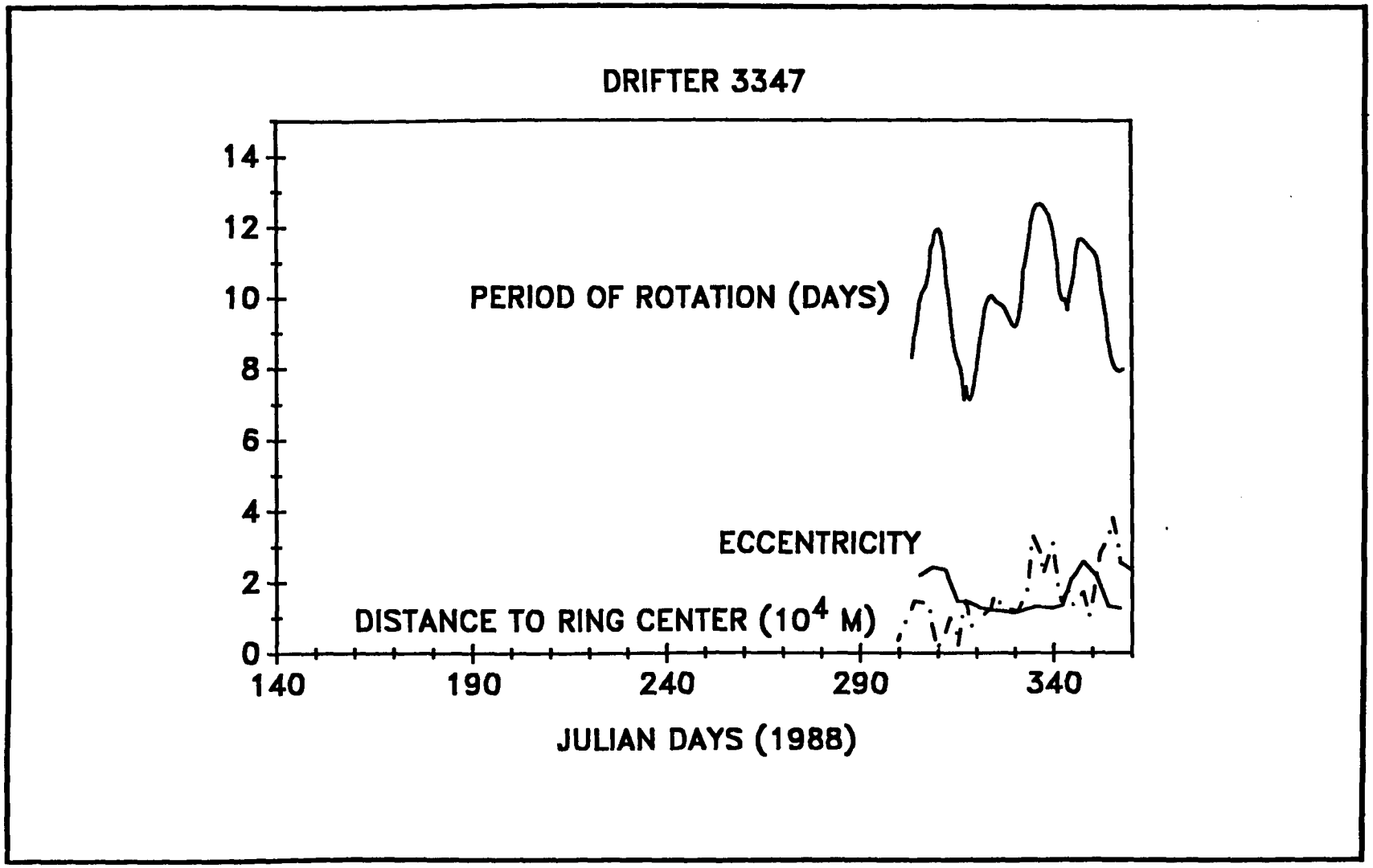

Figure 4.3-33b. Period of rotation, distance to the center and eccentricity for Eddy F as determined from the trajectory of Drifter 3347.

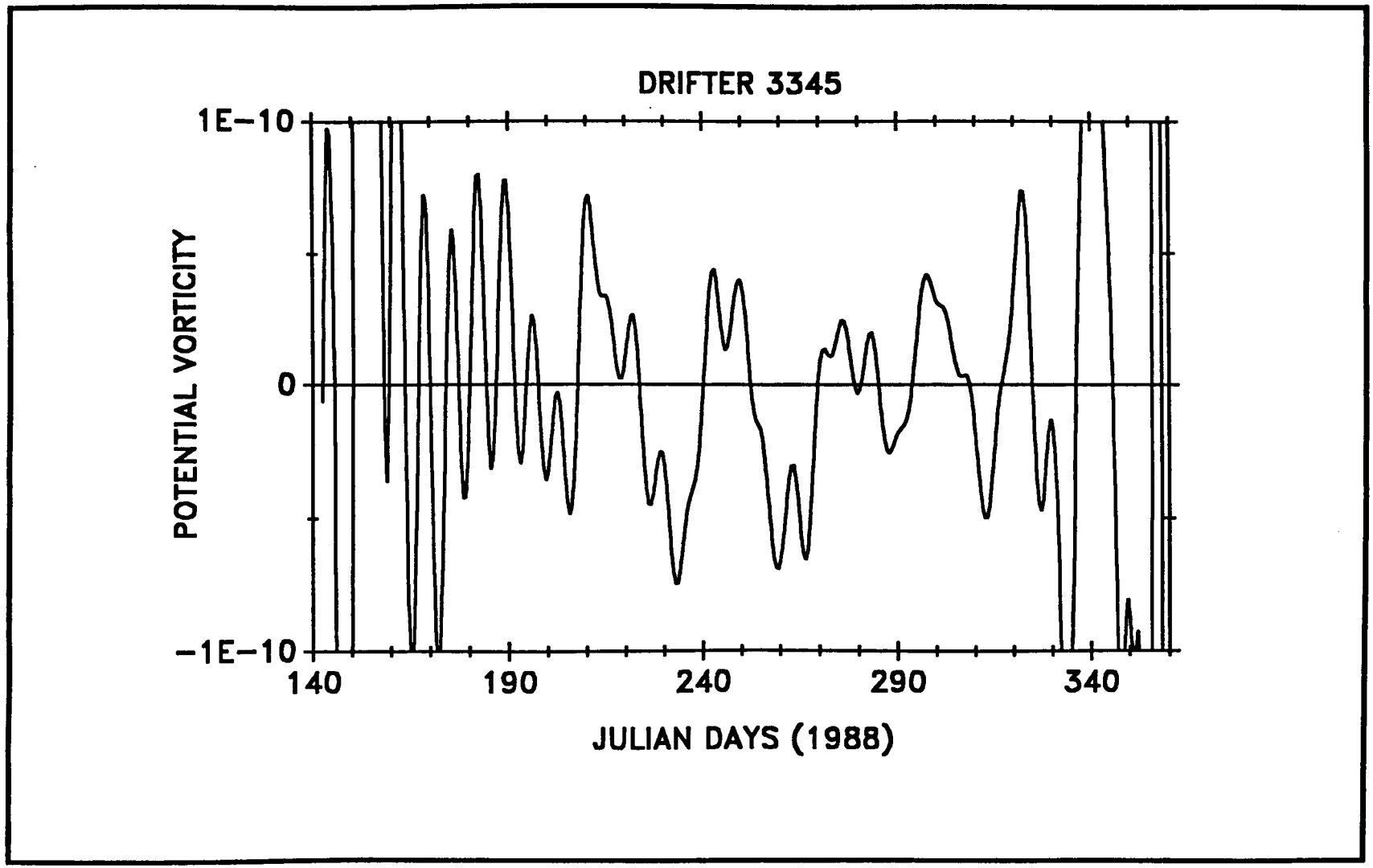

Figure 4.3-34a. Potential vorticity for Eddy F determined from Drifter 3345.

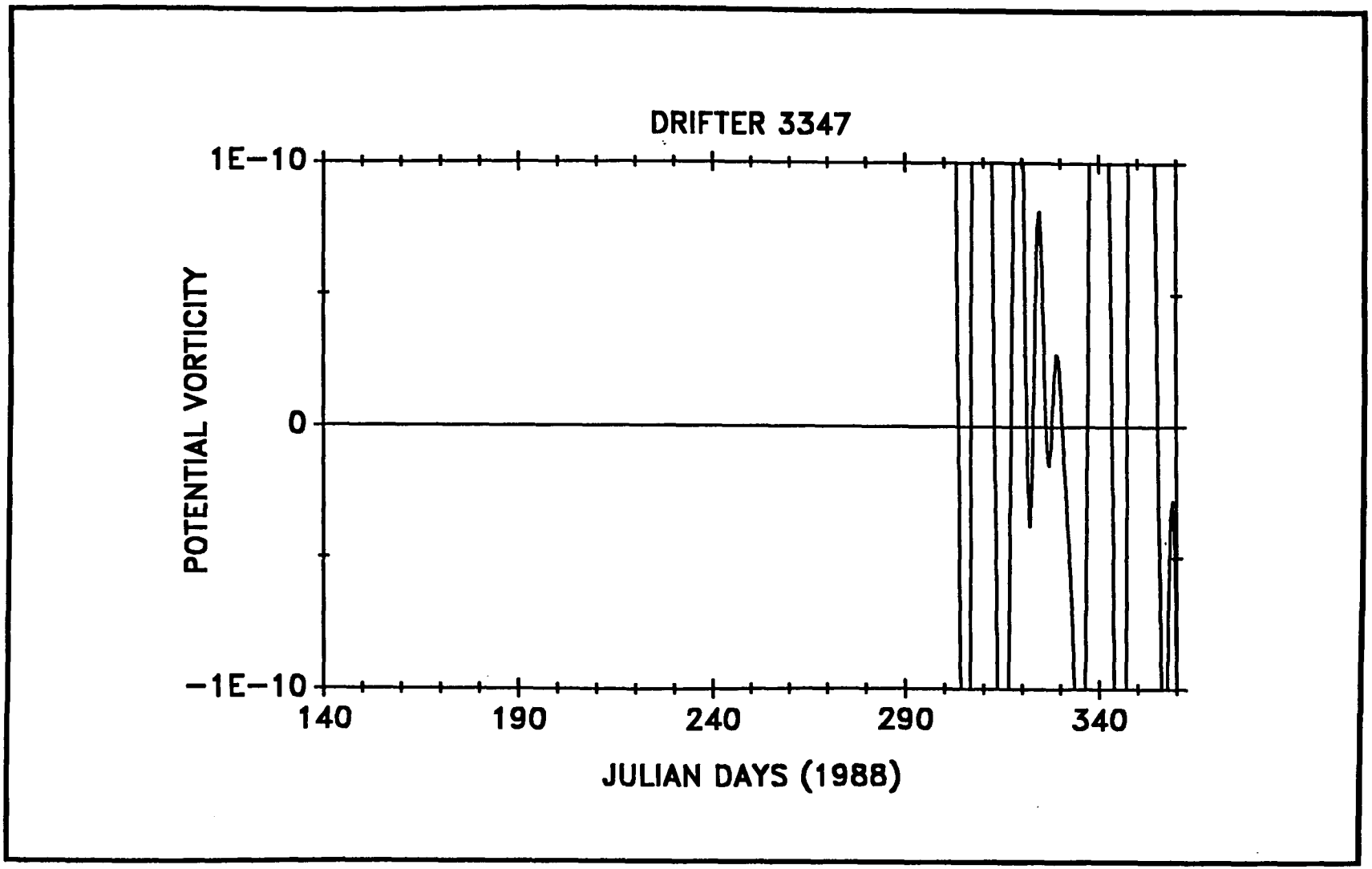

Figure 4.3-34b. Potential vorticity for Eddy F determined from Drifter 3347.

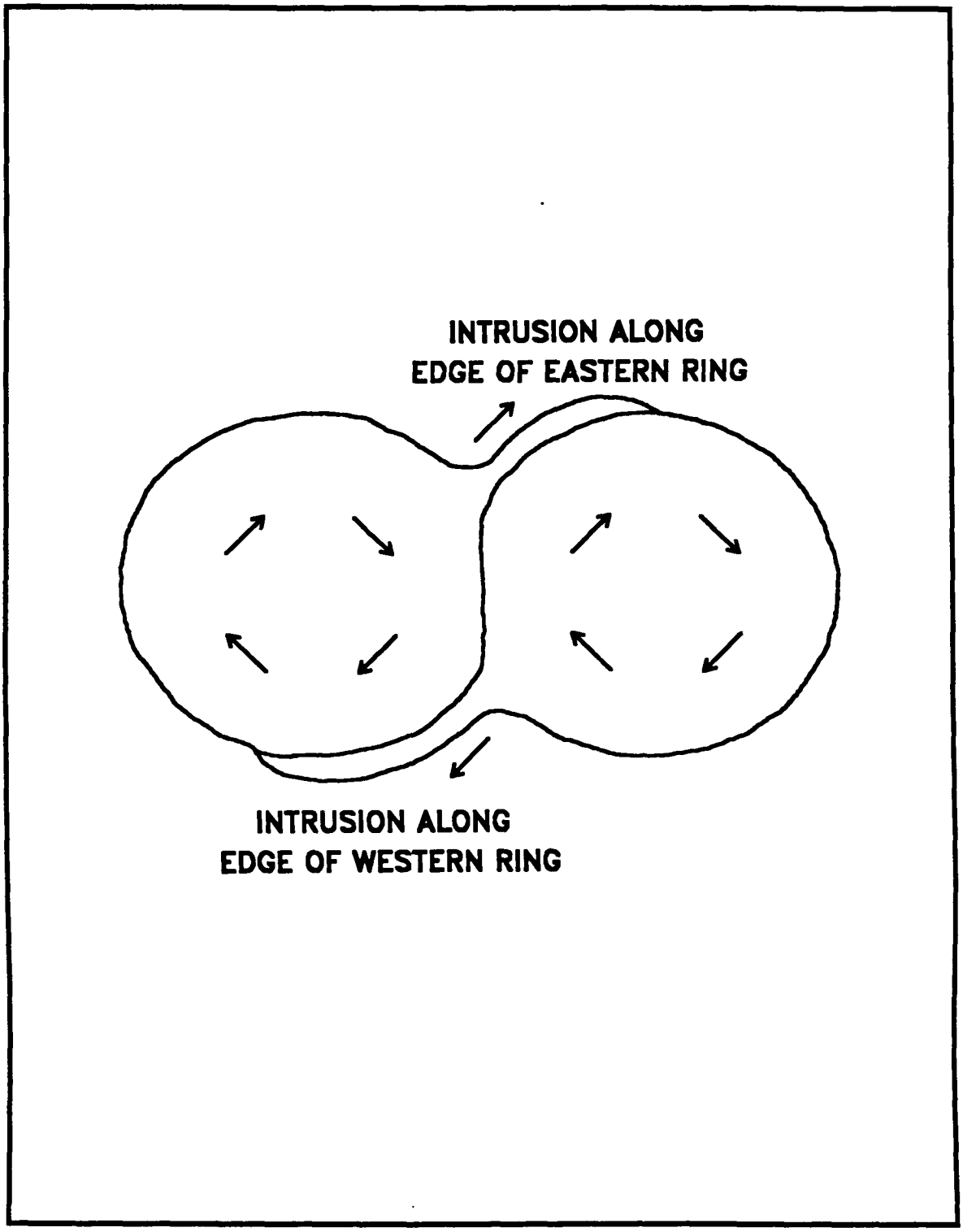

Figure 4.3-35. A schematic indicating the initial conditions of the coalescing of two anticyclones. Shown are tentacles of water from the exteriors of each eddy which flow outward to wrap around the other eddy.

Thus, the exterior water of the new eddy will be formed only from the waters on the northern and western exterior of the more westward parent and the waters on the southern and eastern exterior of the more eastward parent. This implies that the water ejected from coalescing anticyclones in the deep western Gulf will come only from that water lying on the northern and western exterior of the more westward parent and the waters lying on the southern and eastern exterior of the more eastward parent at the time coalescing begins. In this scenario, had Drifter 3345 been on the western or northern edges of Eddy F when coalescing began, it could not have been ejected from the flow field.

4.3.3.3 Dynamics of Cyclones on the Northern Slope

The data presented here have provided a far better documentation of cyclones along the Louisiana-Texas slope than was presented by Lewis et al., (1989). It is now known that these cyclones may have a diameter of ~100 km, exist in depths between the 2000 m and 200 m isobaths, and occur from 89° to 95°W. Thus, at issue here is how these cyclones form and what their fate is.

Cyclonic vorticity can be induced as old Loop Current eddies move northward along the Mexican coast. A good example of this is shown in Figure 4.3-12 where both Drifters 5837 and 5839 make abrupt cyclonic turns along the western and northern edges of Eddy D. To understand such a process, it is necessary to begin with the effects of non-linear acceleration on a Loop Current eddy along the Mexican coast. The restricted flow between the eddy center and the coast of Mexico results in the non-linear advective terms becoming important in the balance of forces. The net effect is an increase in the inertia of the water in this restricted region of flow. The increase in inertia carries the water farther north than it would normally go before turning offshore and eastward. After going offshore into deeper water, the non-linear advective terms become negligible again with the net effect of the eddy flow field having moved northward.

Non-linear acceleration forces water on the westward side of an anticyclone beyond 26°N, a region in which the bottom topography begins an abrupt change from a north-south oriented steep shelf slope to an east-west oriented gentle shelf slope. (Non-linear acceleration is not the only process that can cause such a northward movement. Lewis et al., (1989) have shown that the interactions of two anticyclones can also force water from a Loop Current eddy to move beyond 26°N and induce cyclonic vorticity. As the northward movement carries the water into shallower regions, the flow field must adjust. First, it is essential to consider such an adjustment in terms of potential vorticity conservation. This conservation can be expressed as

$$d(\zeta + f)/dt + D\ (\zeta + f) = 0$$

or, in finite difference form with the Coriolis parameter f approximately constant,

$$\zeta_{new} = \zeta_{old} - \Delta t\ D\ (\zeta + f)$$

where ζ = relative vorticity, t = time, and D = divergence.

As the water flows into shallower regions, the water column must diverge ($D > 0$). For Loop Current eddies, $\zeta + f < 0$. Thus, ζ_{new} becomes more negative with time. However, this induction of negative vorticity has the limit of $\zeta = -f$ regardless of whether the flow continues into shallower water. Thus, northward translation into shallower water and the conservation of potential vorticity will increase the negative vorticity of the flow field, but it cannot alone induce a net cyclonic vorticity. Thus, although we understand the basic effects of topography on eddies, there appears to be an additional mechanism about which we can only speculate. Yet, a mechanism of cyclone generation in this region of the Gulf provides a closure for our understanding of the fate of Loop Current eddies. It is understood that these large, powerful, anticyclonic eddies continuously pump momentum and mass into the Gulf of Mexico. However, it is necessary to realize that the Gulf is not continuously building in its anticyclonic vorticity and its mass of water with Loop Current characteristics. Therefore, mechanisms must exist which balance the negative vorticity and mix the Loop Current water. It would appear that the bathymetry of the northwestern corner of the Gulf may provide such a mechanism.

4.3.3.4 A Possible Scenario

Based on observations and calculations, the following may be an appropriate scenario. The Loop Current anticyclones move westward (sometimes sporadically) as a result of the planetary beta effect. The eddies can entrain water during their westward passage, but this mixing does not appear to modify their flow structure (e.g., relative vorticity and maximum swirl speed: Lewis et al., 1989). As they reach the western Gulf, they interact and coalesce with older anticyclones. The coalescing process can result in the ejection of water from the eddies, another process that has the net effect of mixing Loop Current water with Gulf common water. Interaction with the slope in the western Gulf weakens them somewhat, and they move northward due to non-linear acceleration effects. As the flow fields of these eddies move across 26°N and into shallower water, at least some of the negative vorticity is converted into cyclonic vorticity. This cyclonic vorticity wraps the Loop Current water around a central core of water from the Texas continental slope. The results are the formation of cyclonic eddies and the further mixing of Loop Current and Gulf Common waters. The cyclones then move eastward between the 200 m and 2000 m isobaths. The cause of the eastward movement could be one of several possibilities. Topographic beta effect would drive cyclones eastward along the Texas shelf slope. In addition, the dispersion of energy eastward via Rossby waves could carry a feature that was of the order of the Rossby radius (the mean Rossby radius of deformation in the Gulf is ~50 km, the same as the radius of these cyclones). However, it is also possible that these cyclones are simply pushed eastward by the arrival of more recently-shed Loop Current eddies. In a fashion, the process can be thought of as a conveyer in which anticyclones move west along a southerly route in the Gulf and then convert to cyclones which move east along a northerly route. The

presence of a younger eddy moving northward along the Mexican coast might simply produce a pressure head that pushes the most recent cyclone eastward.

4.4 Slope Circulation

4.4.1 Current Meter Statistics

In order to facilitate the discussion of the current meter data, Table 4.4-1 has been compiled for the respective time periods.

Table 4.4-1. Comparative time periods discussed for Moorings EE, FF and GG.

Time Period	Dates	Filtering
I	11/11/87 - 09/05/88	3-HLP
II	04/10/88 - 10/30/88	3-HLP
III	11/15/87 - 09/01/88	40-HLP
IV	04/14/88 - 10/26/88	40-HLP
V	11/15/87 - 10/26/88	40-HLP

In addition, a useful way of characterizing the basic statistics of a velocity record is in a table of joint distribution of speed and direction and its graphical form, the current rose. Figures 4.4-1, 4.4-2 and 4.4-3 show the data in this form at 100 m and 725 m for Moorings EE, FF and GG, respectively. The percentages of joint frequency were computed from hourly values of time series of U and V that were three-hour low pass filtered. The time period is November 11, 1987 through September 5, 1988 (Period I). The speed ranges were selected so as to provide an optimum resolution in the lower ranges (Those for MGG1 are double those of the other current records). Calm conditions are defined as speeds lower than typical instrument thresholds of about 1 cm s^{-1}. Each value in the joint frequency table represents the percentage of observations that fell in a given speed range and direction sector. The total for a given row gives the percentage of observations that fell in that direction sector regardless of speed (e.g., NE is from 22.5 degrees to 67.5 degrees). The scalar average speed (as opposed to vector average) for each direction sector is given on the far right side of each row. The total for a given column gives the percentage of observations that fell in a given speed range regardless of direction. For ease in visualizing the table, a rose diagram is plotted above it. Each directional element corresponds to a direction sector in the table. A segment of each directional element corresponds to a speed range, and the length of each segment is proportional to the percentage expressed in the

A

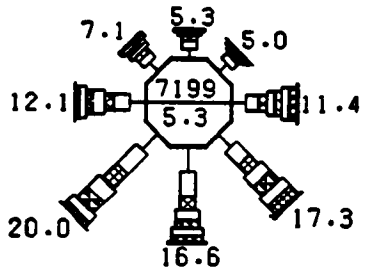

CURRENT ROSE, MEE1
87/11/11 (0000) - 88/09/05 (2200) (GMT)

DIR	RANGE (CM/S) F.Q. 1< V ≤5										AVG SPEED
	1-5	5-10	10-15	15-20	20-25	25-30	30-40	40-50	50+	TOTAL	
N	1.7	1.5	0.9	0.5	0.2	0.3	0.2			5.3	10.5
NE	1.9	1.3	0.5	0.3	0.2	0.4	0.4	+		5.0	11.1
E	2.5	2.1	1.5	1.2	1.3	1.2	1.3	0.3	+	11.4	16.2
SE	3.1	3.2	2.1	2.3	2.3	1.9	2.1	0.4		17.3	16.7
S	4.3	4.3	2.4	1.7	1.2	1.4	1.1	0.3	+	16.6	13.3
SW	3.8	4.7	3.5	2.8	2.6	1.5	1.0	+		20.0	13.8
W	2.8	2.8	1.6	2.0	1.2	1.2	0.7	+		12.1	13.6
NW	2.2	1.3	1.0	0.8	0.8	0.7	0.4			7.1	12.6
TOTAL	22.2	21.1	13.5	11.5	9.8	8.5	7.1	1.1	+	94.7	13.4
CALM										5.3	

B

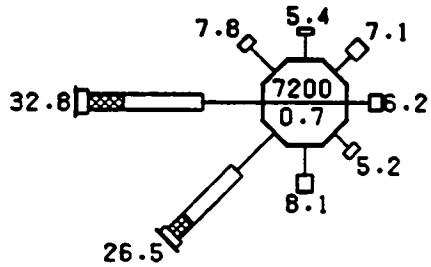

CURRENT ROSE, MEE3
87/11/11 (0000) - 88/09/05 (2200) (GMT)

DIR	RANGE (CM/S) F.Q. 1< V ≤5										AVG SPEED
	1-5	5-10	10-15	15-20	20-25	25-30	30-40	40-50	50+	TOTAL	
N	4.4	1.0								5.4	3.2
NE	4.1	2.9	0.2							7.1	4.5
E	4.0	2.1	+							6.2	4.0
SE	3.6	1.5	+							5.2	3.9
S	5.1	2.8	0.1							8.1	4.3
SW	9.3	11.8	3.8	1.4	+	0.1	+			26.5	7.0
W	10.4	14.0	6.1	2.0	0.2	+	+			32.8	7.4
NW	6.2	1.7	+							7.8	3.4
TOTAL	47.2	37.9	10.3	3.4	0.3	0.1	+			99.3	5.9
CALM										0.7	

Figure 4.4-1. Current rose and table of joint frequency distribution of speed and direction for the period from November 11, 1987 through September 5, 1988 (Period I) at Mooring EE at depths of (a) 100 m and (b) 725 m (based on hourly 3-HLP currents).

A

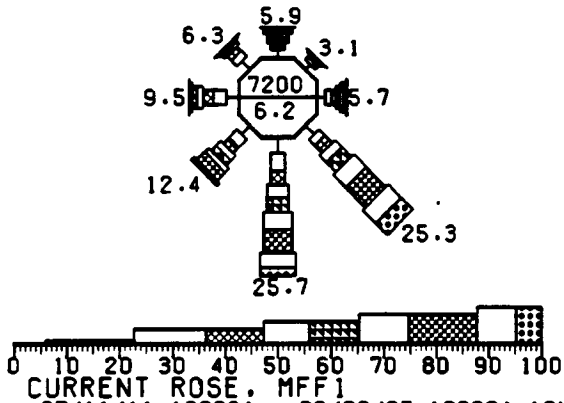

CURRENT ROSE, MFF1
87/11/11 (0000) - 88/09/05 (2200) (GMT)

DIR	RANGE (CM/S) F.G. 1< V ≤5										AVG SPEED
	1-5	5-10	10-15	15-20	20-25	25-30	30-40	40-50	50+	TOTAL	
N	1.5	0.6	0.7	0.7	1.0	0.7	0.6	+		5.9	15.7
NE	1.3	0.8	0.5	0.3	0.1	+	+			3.1	8.6
E	1.6	1.2	0.8	0.4	0.5	0.6	0.5	0.3		5.7	14.9
SE	2.3	1.6	1.9	1.8	2.6	3.3	5.2	3.5	3.1	25.3	29.1
S	2.9	3.3	2.4	2.4	2.7	3.2	4.3	2.9	1.6	25.7	24.0
SW	2.3	2.1	1.5	1.3	1.3	1.0	2.1	0.6	0.1	12.4	18.3
W	2.4	2.5	2.0	1.1	0.8	0.4	0.3	+		9.5	11.5
NW	2.2	1.5	1.2	0.6	0.4	0.2	0.2	+		6.3	10.0
TOTAL	16.5	13.6	11.0	8.6	9.4	9.3	13.2	7.3	4.8	93.8	19.6
CALM										6.2	

B

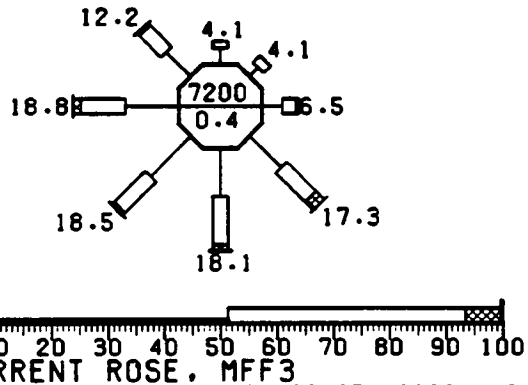

CURRENT ROSE, MFF3
87/11/11 (0000) - 88/09/05 (2200) (GMT)

DIR	RANGE (CM/S) F.G. 1< V ≤5										AVG SPEED
	1-5	5-10	10-15	15-20	20-25	25-30	30-40	40-50	50+	TOTAL	
N	2.9	1.2								4.1	5.5
NE	2.2	1.7	0.2							4.1	4.5
E	3.6	2.4	0.5							6.5	4.9
SE	7.9	7.3	2.0	+						17.3	5.5
S	8.5	8.4	1.0	0.2	+					18.1	5.2
SW	10.1	7.8	0.5	0.2						18.5	4.6
W	9.4	7.9	1.4	+						18.8	5.0
NW	6.2	5.4	0.6	+						12.2	4.9
TOTAL	50.8	42.1	6.1	0.5	+					99.6	4.9
CALM										0.4	

Figure 4.4-2. Current rose and table of joint frequency distribution of speed and direction for the period from November 11, 1987 through September 5, 1988 (Period I) at Mooring FF at depths of (a) 100 m and (b) 725 m (based on hourly 3-HLP currents).

A

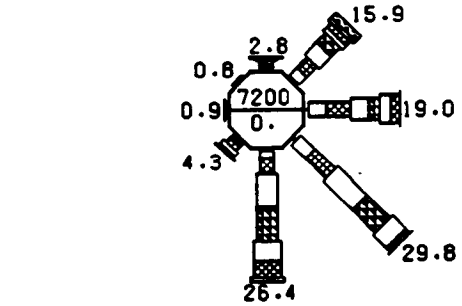

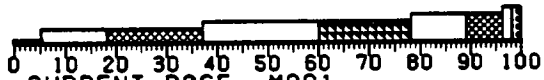

CURRENT ROSE, MGG1
87/11/11 (0000) - 88/09/05 (2200) (GMT)

DIR	RANGE (CM/S) F.D. 1< V ≤10										AVG SPEED
	1-10	10-20	20-30	30-40	40-50	50-60	60-70	70-80	80+	TOTAL	
N	0.7	0.7	0.7	0.4	+	+		+	0.3	2.8	25.5
NE	0.7	2.1	2.8	3.4	2.5	1.0	1.2	0.8	1.4	15.9	41.0
E	1.0	3.5	4.8	3.6	2.1	2.1	1.8	+		19.0	33.4
SE	1.0	4.0	5.6	8.0	6.3	3.6	1.2	0.1		29.8	35.3
S	0.7	1.5	3.2	6.4	6.6	3.9	3.2	0.8	0.2	26.4	42.4
SW	0.4	0.7	1.5	1.0	0.5	0.2				4.3	27.9
W	0.3	0.2	0.4	0.1						0.9	19.4
NW	0.5	0.3	+							0.8	9.3
TOTAL	5.2	12.9	19.0	22.9	18.1	10.8	7.3	1.8	1.8	100.0	36.7
CALM											

B

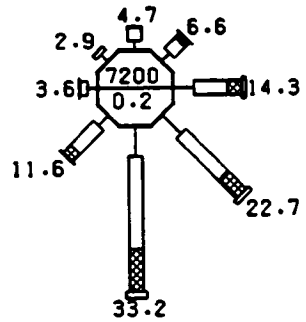

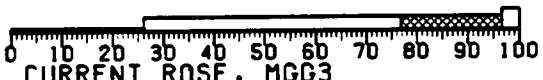

CURRENT ROSE, MGG3
87/11/11 (0000) - 88/09/05 (2200) (GMT)

DIR	RANGE (CM/S) F.D. 1< V ≤5										AVG SPEED
	1-5	5-10	10-15	15-20	20-25	25-30	30-40	40-50	50+	TOTAL	
N	1.8	2.7	0.2							4.7	5.6
NE	2.3	3.0	1.3	+						6.6	6.8
E	4.1	6.6	2.8	0.8						14.3	7.6
SE	5.2	11.6	5.0	0.9	+					22.7	7.9
S	5.8	17.9	8.2	1.3	+					33.2	8.3
SW	2.8	6.6	2.1	0.2						11.6	7.3
W	1.9	1.5	0.2	+						3.6	5.1
NW	1.9	0.9								2.9	4.0
TOTAL	25.9	50.8	19.7	3.4	+					99.8	7.5
CALM										0.2	

Figure 4.4-3a,b. Current rose and table of joint frequency distribution of speed and direction for the period from November 11, 1987 through September 5, 1988 (Period I) at Mooring GG at depths of (a) 100 m and (b) 725 m (based on hourly 3-HLP currents).

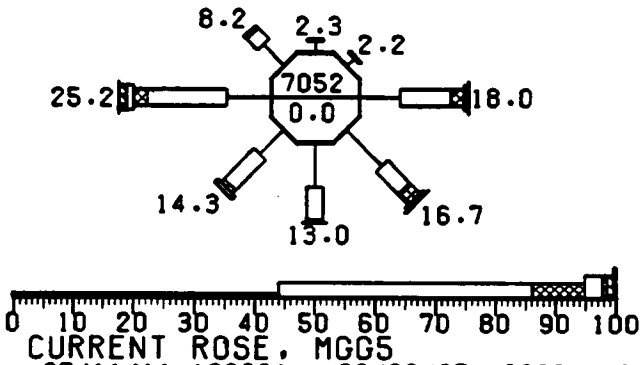

CURRENT ROSE, MGG5

87/11/11 (0000) - 88/09/05 (2200) (GMT)

DIR	RANGE (CM/S) F.Q. 1< V ≤5										AVG SPEED
	1-5	5-10	10-15	15-20	20-25	25-30	30-40	40-50	50+	TOTAL	
N	1.9	0.3	+							2.3	2.7
NE	1.8	0.4								2.2	3.1
E	6.7	8.3	2.2	0.6	0.1	0.1	+			18.0	5.7
SE	8.4	5.1	2.4	0.3	0.3	0.3				16.7	6.2
S	7.2	5.4	0.4	+						13.0	4.7
SW	5.7	6.9	0.8	0.7	+					14.3	6.2
W	7.4	13.0	2.3	1.2	1.3	+				25.2	7.7
NW	5.0	2.6	0.7							8.2	4.4
TOTAL	44.0	42.1	8.7	2.9	1.8	0.4	+			00.0	6.2
CALM										+	

Figure 4.4-3c. Current rose and table of joint frequency distribution of speed and direction for the period from November 11, 1987 through September 5, 1988 (Period I) at Mooring GG at a depth of 2500 m (based on hourly 3-HLP currents).

table. The total percentage in that direction is printed at the tip of each directional element. A cumulative speed graph is plotted below each rose. It expresses the percentage of observations that fell in a given speed range regardless of direction, and it corresponds to the row of totals (second row from the bottom) in the table. The graph runs from zero to 100 percent. The scale of the graph and the scale of the directional elements are the same. Thus, if all the directional elements of a rose are laid end-to-end, the length would equal the length of the graph, less the percentage of calms. The total number of observations on which the percentages are based is printed in the upper half of the center of the rose. The percentage of calms is printed in the lower half.

At Mooring GG at 100 m (Figure 4.4-3a), the dominant direction is SE. Current has an eastward component (NE, E or SE) about 65% of the time, and a southward component (SE, S or SW) about 61% of the time. The dominant speed range is 30 to 40 cm s^{-1}. Speed exceeds 40 cm s^{-1} about 40% of the time, and it exceeds 50 cm s^{-1} about 22% of the time. At least for the 300-day period of this record, the location of Mooring GG is very energetic in the near surface layer. This is because the outer portions of at least two Loop Current anticyclones and one cyclone spent time in the area. The direction statistics indicate that an anticyclone lay west-southwest of Mooring GG and/or a cyclone lay east-northeast of it during much of the period of the record. At 725 m (Figure 4.4-3b), the dominant direction rotates clockwise to the south. Speed is in the 5 to 10 cm s^{-1} range about 51% of the time and rarely exceeds 15 cm s^{-1}, reflecting the current meter's proximity to the zero point of the first baroclinic mode (see below). The dominant direction sector at 2500 m (Figure 4.4-3c) rotates further clockwise to the west, suggesting the along isobath or V-component has a counter-flow in the deep water. Speeds less than 5 cm s^{-1} occurs 44% of the time and are probably typical of the background, non-event value. However, it exceeds 10 cm s^{-1} about 14% of the time, and occasionally exceeds 20 cm s^{-1}. These values are probably related to the eddy events discussed later.

At Mooring FF at 100 m (Figure 4.4-2a), current has a southerly component more than 63% of the time. The dominant speed range is 1 to 5 cm s^{-1}, and speed exceeds 40 cm s^{-1} about 12% of the time. Overall average speed is about 20 cm s^{-1}, whereas it was about 37 cm s^{-1} at Mooring GG located 120 km to the south. The speed at 725 m, at Mooring FF (Figure 4.4-2b), falls below 10 cm s^{-1} about 93% of the time and rarely exceeds 15 cm s^{-1}. The distribution of speed and direction for Mooring EE at 100 m (Figure 4.4-1a) is similar to that for FF, but speed is somewhat less energetic, and direction is more broadly distributed. Current has a southerly component more than 54% of the time. The dominant speed range is 1 to 5 cm s^{-1}, and a value above 40 cm s^{-1} occurs about 1% of the time. The overall average speed is about 13 cm s^{-1}. At 725 m (Figure 4.4-1b), current is westward or southwestward more than half the time. Speed at 725 m is slightly more energetic than at Mooring FF, as it exceeds 10 cm s^{-1} about 15% of the time and 15 cm s^{-1} about 4% of the time. In general, the joint probability distributions of speed and direction at Moorings EE and FF are similar, but they are distinctly different from that at Mooring GG.

4.4.2 Warm Eddies and Cold Cyclones Over the Lower Slope

4.4.2.1 General Overview

The succession of cold and warm features passing over Mooring GG is illustrated by the travel time record in Figure 4.4-4. Warm eddies were independently verified from ARGOS drifter tracks and hydrographic surveys. Eddies D, E and F are noted and the related drifters identifiers are given in the top panel. Only Eddy F was comprehensively surveyed while in the vicinity of 92°W (Year 5 AXBT 2 survey). This leaves two warm features in Figure 4.4-4 which were not identified.

The event between Days 275 and 350 apparently depressed the isotherms as much as Eddy E. However, only the northern part of Eddy E passed over the mooring, thus the full strength of the eddy "signal" was not sensed. The depth of the 15°C isotherm from the hydrographic surveys of Composite Two is given in Figure 4.4-5 which shows Eddy D in the western Gulf centered at 24.5°N, 94.5°W and the recently detached Eddy E in the eastern Gulf. Just south of Mooring GG is a weak warm feature with maximum depth of the 15°C isotherm at 275 m. The upper layer (100 m) current observations at Mooring GG show easterly and southeasterly flows with speeds of about 30 cm s^{-1} for Days 320 to 340. This is consistent with Mooring GG being on the northern side of a weak anticyclone. There is no indication from AVHRR imagery where this weak anticyclone may have originated, but it may be either the remnant of an old eddy, and thus has come from the west or southwest, or it is a secondary circulation spun up by the passage of Eddy D.

The small warm feature at approximately Day 400 (Figure 4.4-4), just prior to the arrival of Eddy E, was not surveyed and the only indication of its origin is images from January 26 and 27, 1988 (Days 391 and 392). These show a warm feature centered at 25°N, 94°W intruding over the mooring site from the west. The currents from the upper three levels of Mooring GG are southwestward and southward with 20 to 30 cm s^{-1} velocities; again consistent with the eastern edge of an anticyclonic eddy moving over the site from the west and then withdrawing as Eddy E approaches. The origin of this warm feature is again uncertain. It could be Eddy D moving off the western slope or a secondary gyre spun up during the interaction of Eddy D with slope topography. There is evidence from later imagery that this feature may have become a slope anticyclone. It is, however, fairly clear that this warm feature comes from the west or southwest and not from the east as do the major vigorous anticyclonic eddies shed from the Loop Current.

During the summers of 1987 and 1988, cold features, which seem to be characteristic of cyclones, were observed in the IES record. These cold features will be further discussed in terms of supporting hydrographic and current data in the following sections.

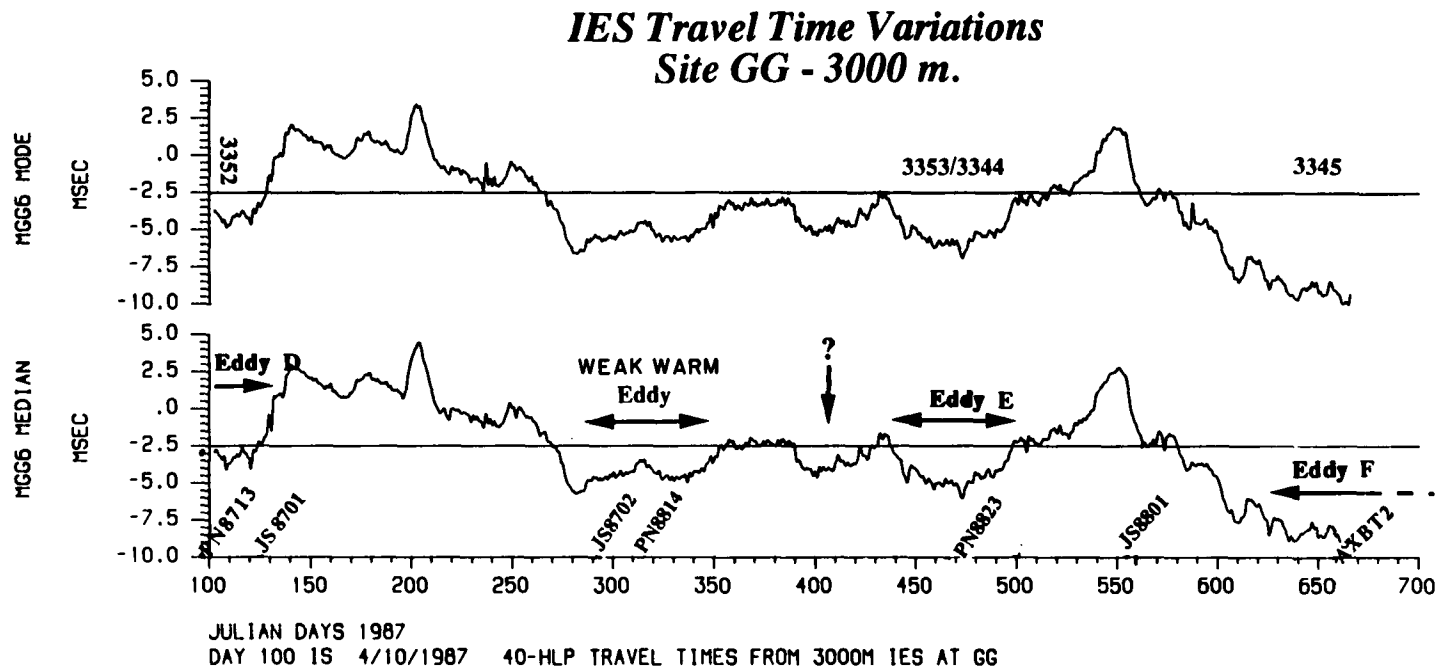

Figure 4.4-4. Forty-HLP IES #1 median and mode travel times for record MGG6. The eddies moving through the site are identified along with the approximate dates of hydrographic cruises and the occurrence of ARGOS drifters.

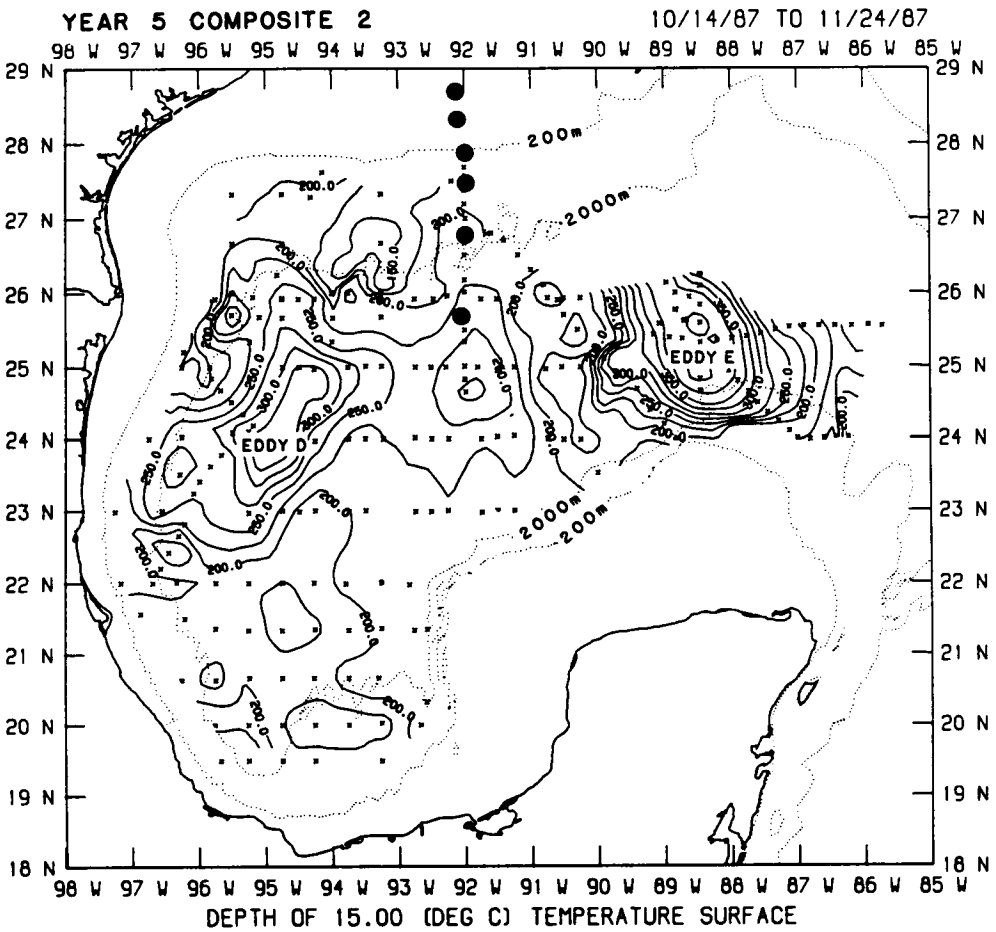

Figure 4.4-5. Depth of the 15°C isotherm from Composite Two.

4.4.2.2 Summer 1987

The IES record in Figure 4.4-4 shows two or three apparent cold features (long travel times) between Days 130 and 230. The only hydrographic survey during this period was just prior to the arrival of the feature at Mooring GG. The 15°C and 8°C isotherm depths for Composite One during April and May 1987 suggest a deep cold feature centered on 26.5°N, 91°W, just east of the mooring line. They also suggest a weak cold feature on the slope north of Eddy D around 93° to 94°W (Figure 4.4-6). Composite One contains the SOOP transect of the M/V SENATOR which primarily defines the deep cold feature. The available SENATOR transects are given in Figure 4.4-7. These were treated in exactly the same manner as the QUEENY and NESTOR transects discussed in Section 4.2. The SENATOR sections cut obliquely across the deep water channel into the western Gulf and were well suited to detecting both warm and cold features passing either from the western to eastern Gulf or vice-versa.

The depth of the 8°C isotherm from the sequence of SENATOR transects is given in the contour plot of Figure 4.4-8a. The time series of isotherm depths clearly shows the passage of Eddy D between November 1986 and February 1987. In October 1986, a cold feature was over the northern slope just prior to the arrival of Eddy D, and in April 1987, over the deep basin. The strong cold feature seen in Figure 4.4-6 is observed to the northeast (Day 140 - April 20) of Eddy D prior to the first major cold peak in the IES record (Day 140 - April 20) at Mooring GG. This is directly south of the northern part of the SENATOR transect (Figure 4.4-7). Therefore, a reasonable scenario is that the cold cyclone observed in April 1987 at 26.5°N, 91°W moved south through Mooring GG under the influence of the anticyclonic southward flow on the east or trailing side of Eddy D. There are, however, no upper layer current measurements at this time to document southward movement of a cyclonic feature through Mooring GG. It is unlikely that the cold features to the northwest and northeast of Eddy D (Figures 4.4-6 and 4.4-8a) are the same feature. If they were, the SENATOR sections should show movement of the northwest cyclone over the slope around to the northwest side of Eddy D. There is no evidence of such a connection in Figure 4.4-8a. It may be that the October 1986 cyclone in Figure 4.4-8a became the weak cold feature seen over the slope between 93°W and 94°W in April-May 1987 (Figure 4.4-6). This would have required that it moved west along the slope as Eddy D moved west into the western Gulf.

Figure 4.4-8b shows the depth of the 20°C isotherm as determined from the SENATOR transects. Clearly there are virtually no signs of the two cyclones in the upper layers of the water column though the warm-core anticyclones have strong signals. Indeed, these data show cyclones to be middle and lower layer phenomena with little surface layer expression in the temperature field. Subsequently, they are not likely to be immediately apparent in winter AVHRR imagery except by the indirect effects of their circulation on adjacent contrasting water masses (i.e., shelf or slope water). The strong cold feature on Days 200 to 210 (19 to 29 July 1987) at Mooring GG, however is not detected by the SENATOR sections (July-August, 1987) in Figure 4.4-8 and, therefore, is unlikely to have originated in the eastern Gulf.

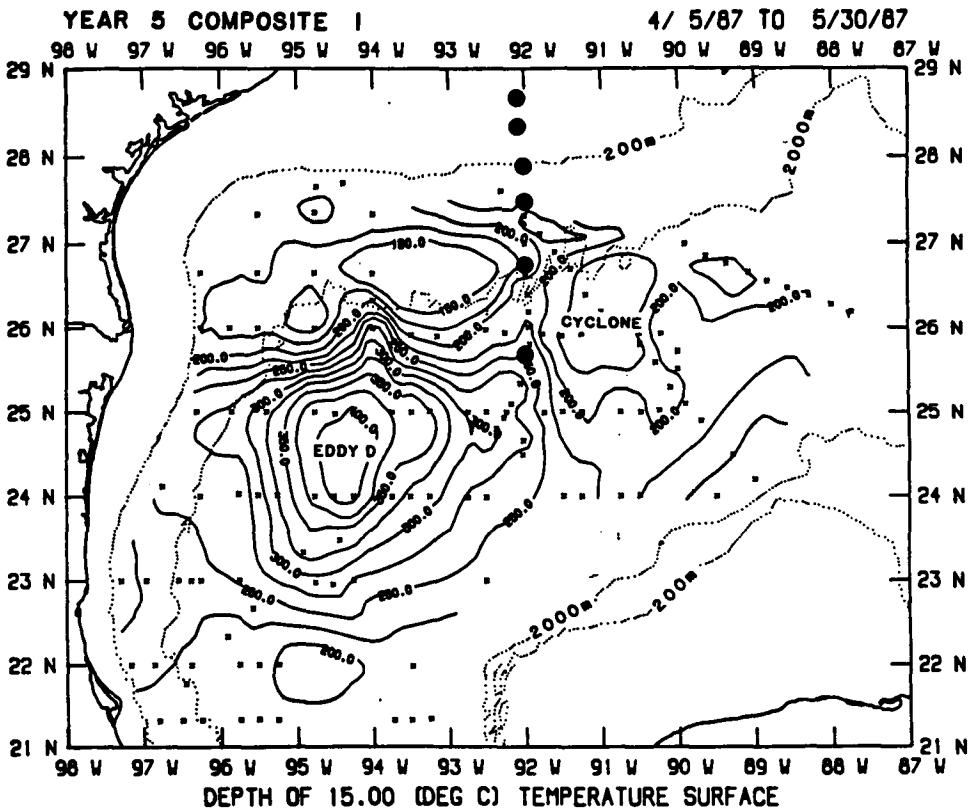

Figure 4.4-6a. Depth of the 15°C isotherm from Composite One.

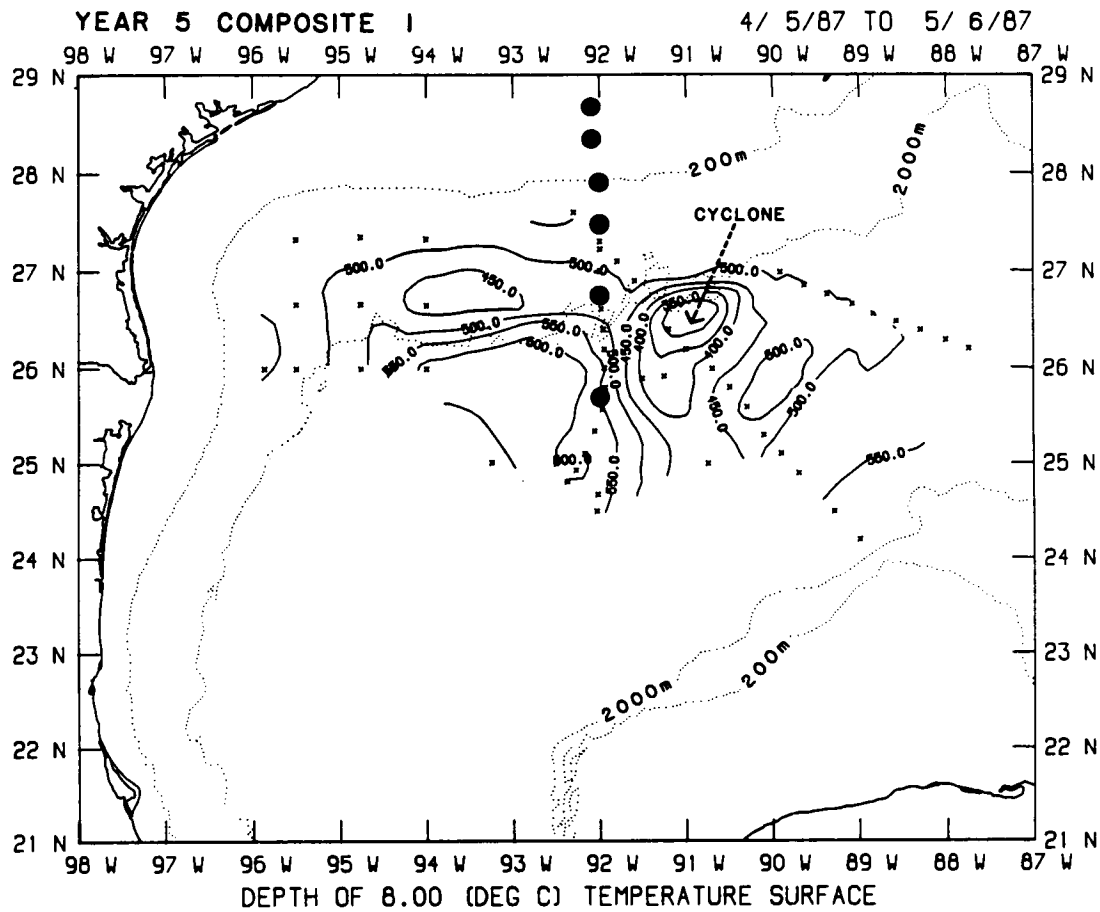

Figure 4.4-6b. Depth of the 8°C isotherm from Composite One.

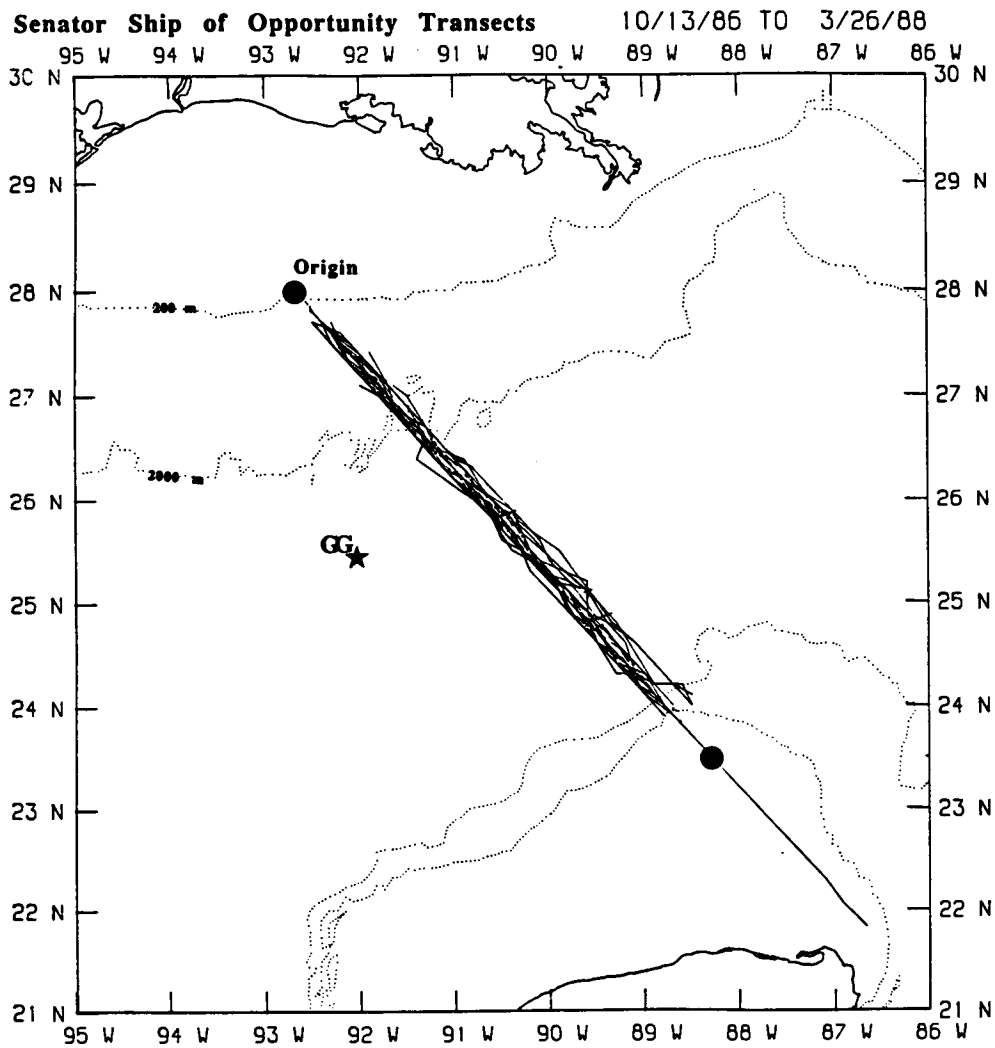

Figure 4.4-7. Available SENATOR Ship-of-Opportunity transects with the mean transect and origin marked. The position of Mooring GG is noted.

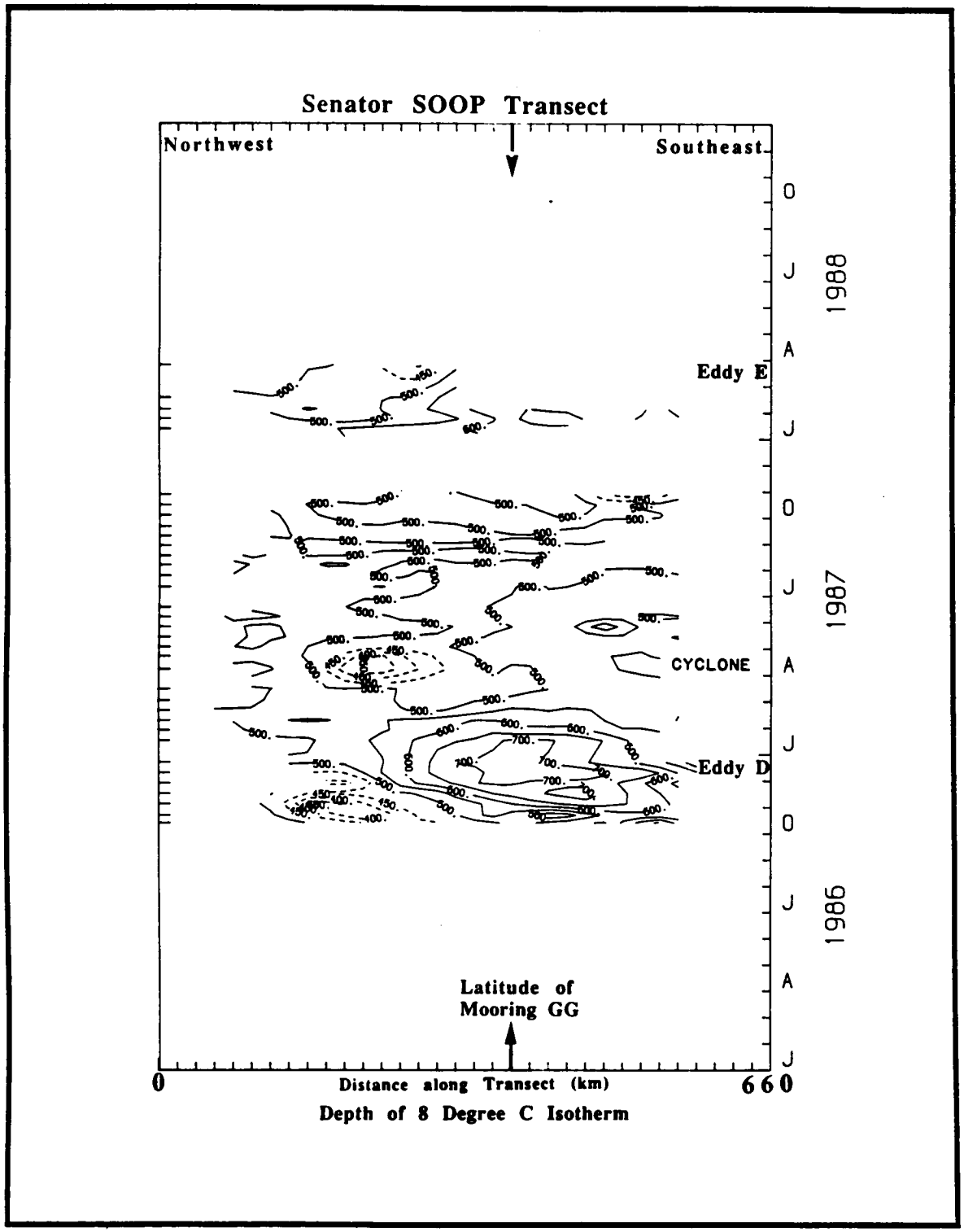

Figure 4.4-8a. Contours of the depth of the 8°C isotherm as a function of distance along the transect, and time for the SENATOR sections.

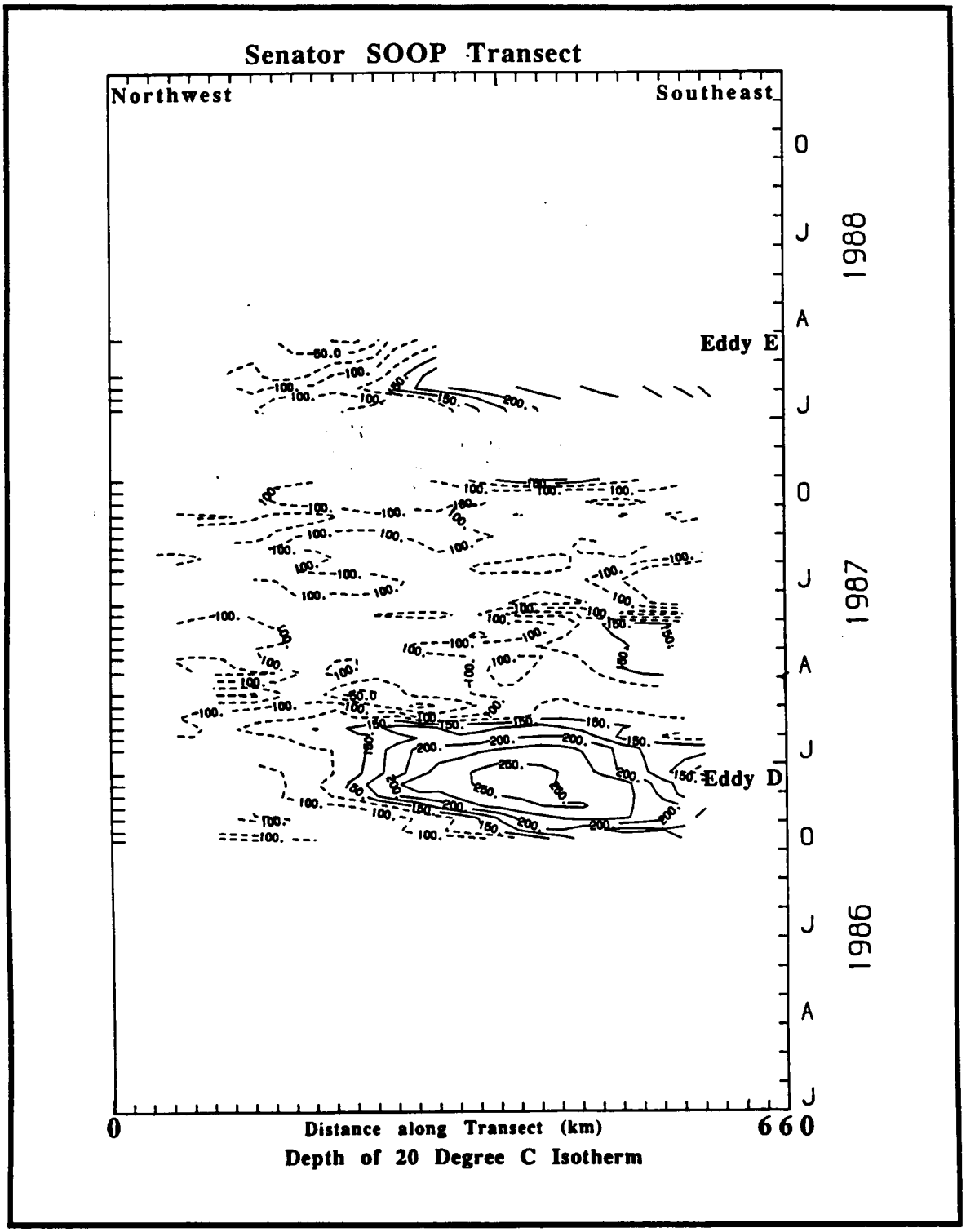

Figure 4.4-8b. Contours of the depth of the 20°C isotherm as a function of distance along the transect, and time for the SENATOR sections.

The weak warm feature (Days 270 to 350; September 27 to December 16, 1987) detected by the IES and Composite Two (Figures 4.4-4 and 4.4-5) appears in the 20°C but not the 8°C isotherm depth contours at the beginning of November 1987 on the SENATOR transect (Figure 4.4-8b). This is just before the break in the time sequence. It appears later at this more eastern section than its first detection at Mooring GG, which was at the end of September. Therefore, this gives further tentative support to the interpretation that this weak anticyclone (see Figure 4.4-5) moved slowly eastward into the vicinity of 92°W from the western Gulf.

4.4.2.3 Summer 1988

In July 1988, after the passage of Eddy E into the southwestern Gulf and prior to the arrival of Eddy F at 92°W, a strong cold feature is observed in both the IES travel time and the upper layer temperature records at Mooring GG. The coincidence and strong correlation of the IES record with the (linearly) interpolated depths of the isotherms from the three current meters (Figure 4.4-9) give further support that the IES travel times are good detectors of middle and upper layer displacements of the isotherms. There is, however, no cold temperature signal around Day 550 (July 3, 1988) at Mooring FF, 120 km to the north, suggesting that the feature is quite localized.

The sequence of events affecting the current and temperature measurements at Moorings GG and FF between Days 480 and 600 in Figure 4.4-9 are complex and subject to differing interpretations of the movement of this major deep water cold eddy. Some insight is gained from AVHRR image for May 7, 1988, (JD 128 = Day 493) which shows Eddy F having just been shed from the Loop Current in the eastern Gulf with a cyclonic circulation between Eddy F and 92°W. The center of the cyclone appears to be about 100 km east of Mooring GG. Eddy E is not directly observable due to clouds but drifter information indicates that its northeast quadrant is just west of Mooring GG. The SST image also shows a cold cyclone over the slope just south of the delta and north of Eddy F. A sketch of this situation is given in Figure 4.4-10, including 10 days of ARGOS Drifter 3353 in Eddy E.

Currents and temperature for this period from Moorings EE, FF and GG are given in stick plot and component form in Figure 4.4-11. At the time of the image (JD 128), flow at Moorings GG and FF (300 m level) are south-southeastward and south-southwestward, respectively. This is consistent with Moorings GG and FF being on the western and northwestern side of a cyclone. Between Days 520 and 540 (JD 155 to 175), flows at Mooring GG switched from SE to NE and the temperature dropped. At Mooring FF a cold event is seen with flows rotating from SW to NW implying that the cyclone moved northwestward towards the slope with Mooring GG being closer to the cyclone center. After Day 500 (JD 185), when the lowest temperatures were found at Mooring GG, flows switched again to the SE, with a mid-level temperature rise, with virtually no signal at Mooring FF. This implies that the cyclone moved eastward with the region south of the center affecting Mooring GG.

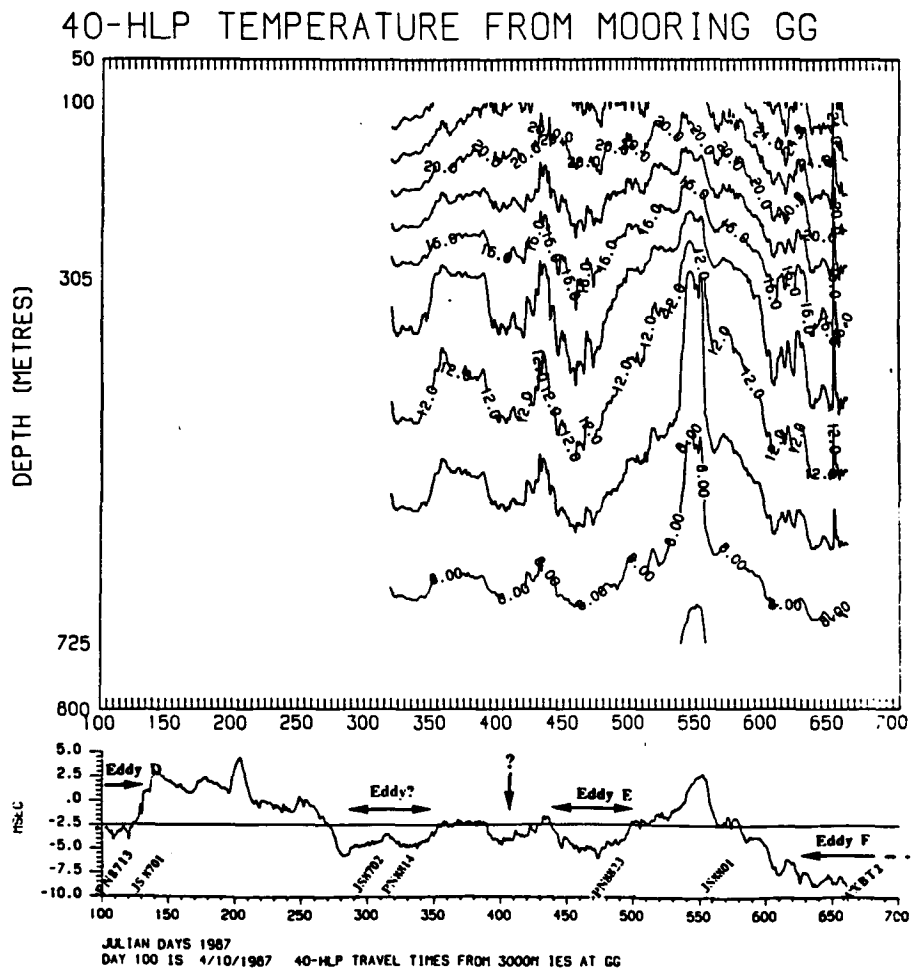

Figure 4.4-9. A plot of 40-HLP isotherm depths from the upper three current meters at Mooring GG and the IES #1 travel time record.

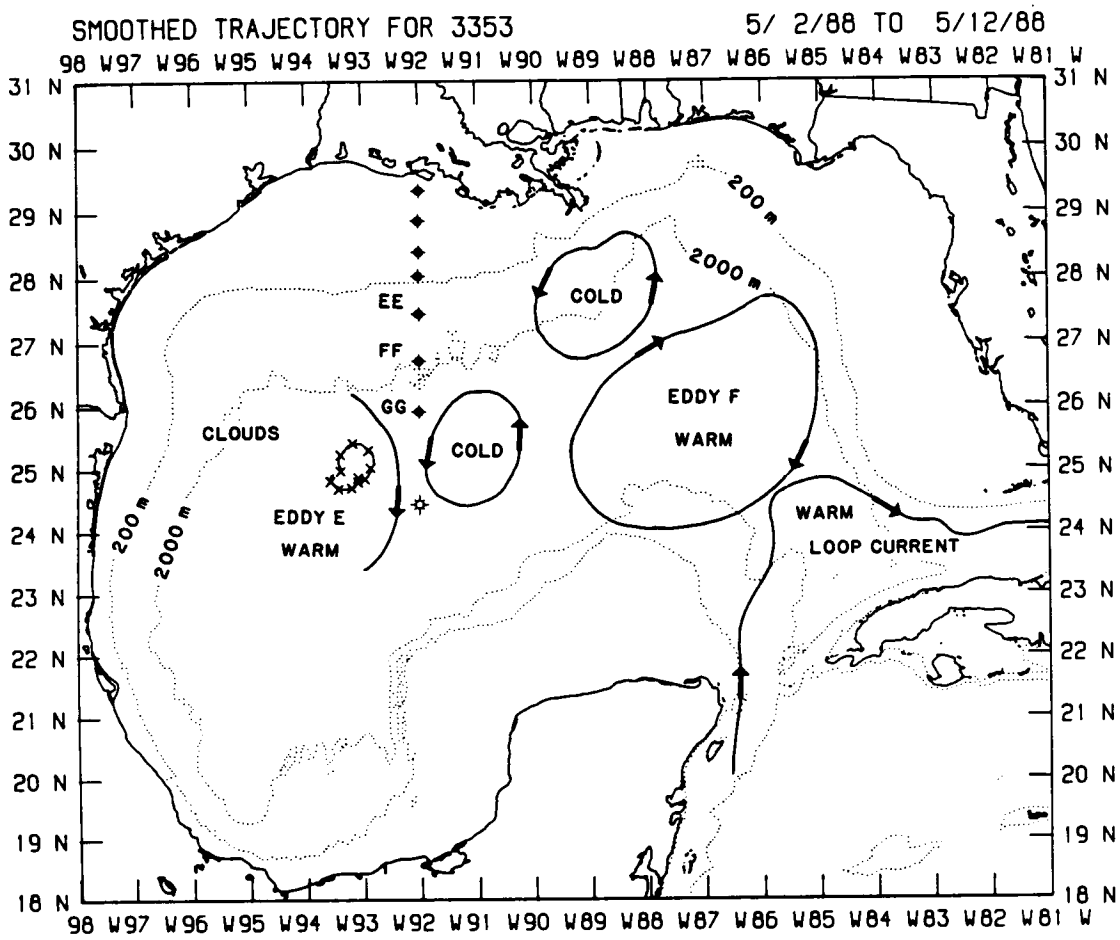

Figure 4.4-10. A sketch of the eddy features observed in a NOAA 9 image for May 7, 1988 (JD 128). The smoothed trajectory for ARGOS Drifter 3353, in Eddy E, is shown for the period May 2 to 12, 1988 with crosses marking the beginning of each day.

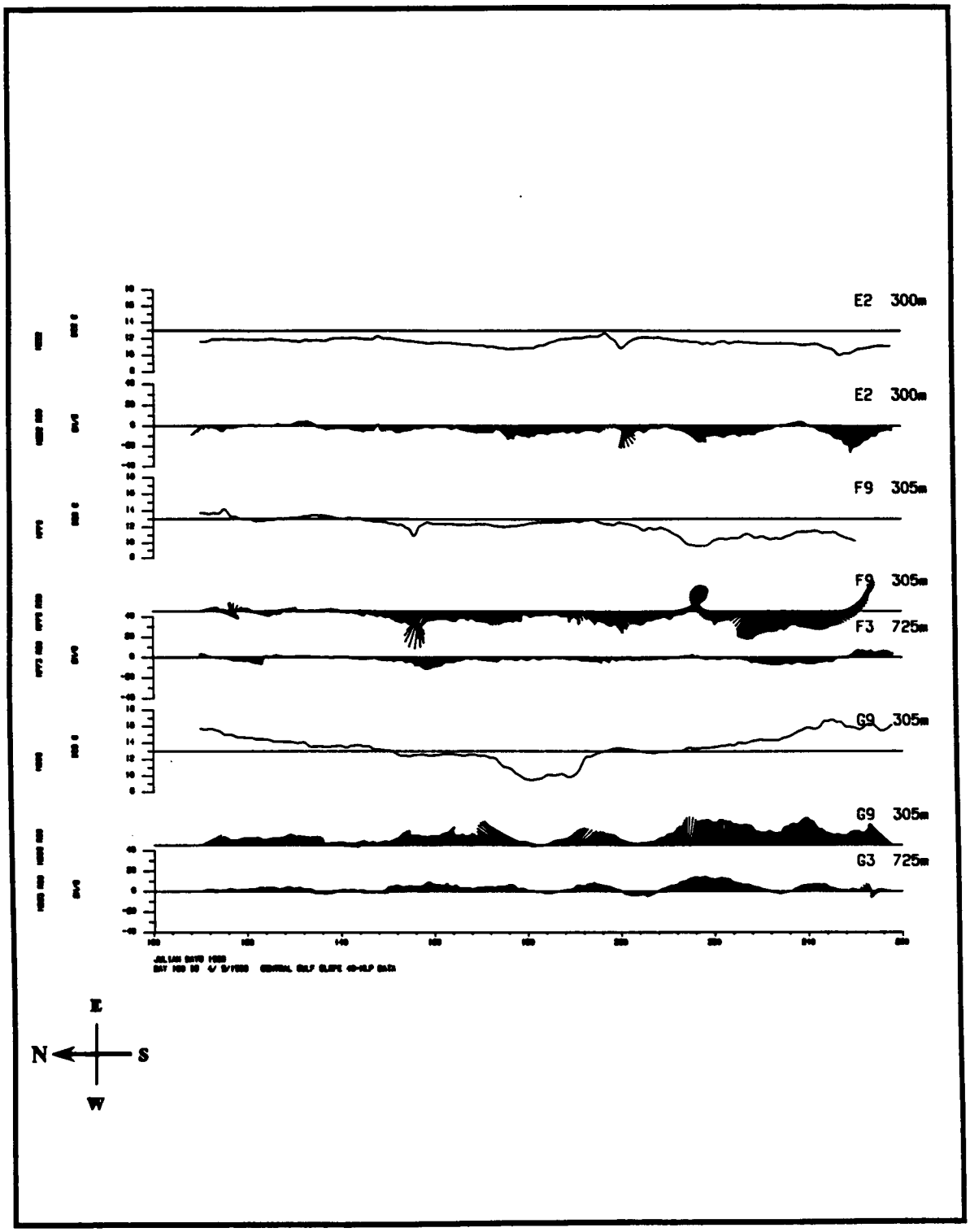

Figure 4.4-11a. Forty-HLP stick and temperature data from the indicated slope instruments for April to October 1988.

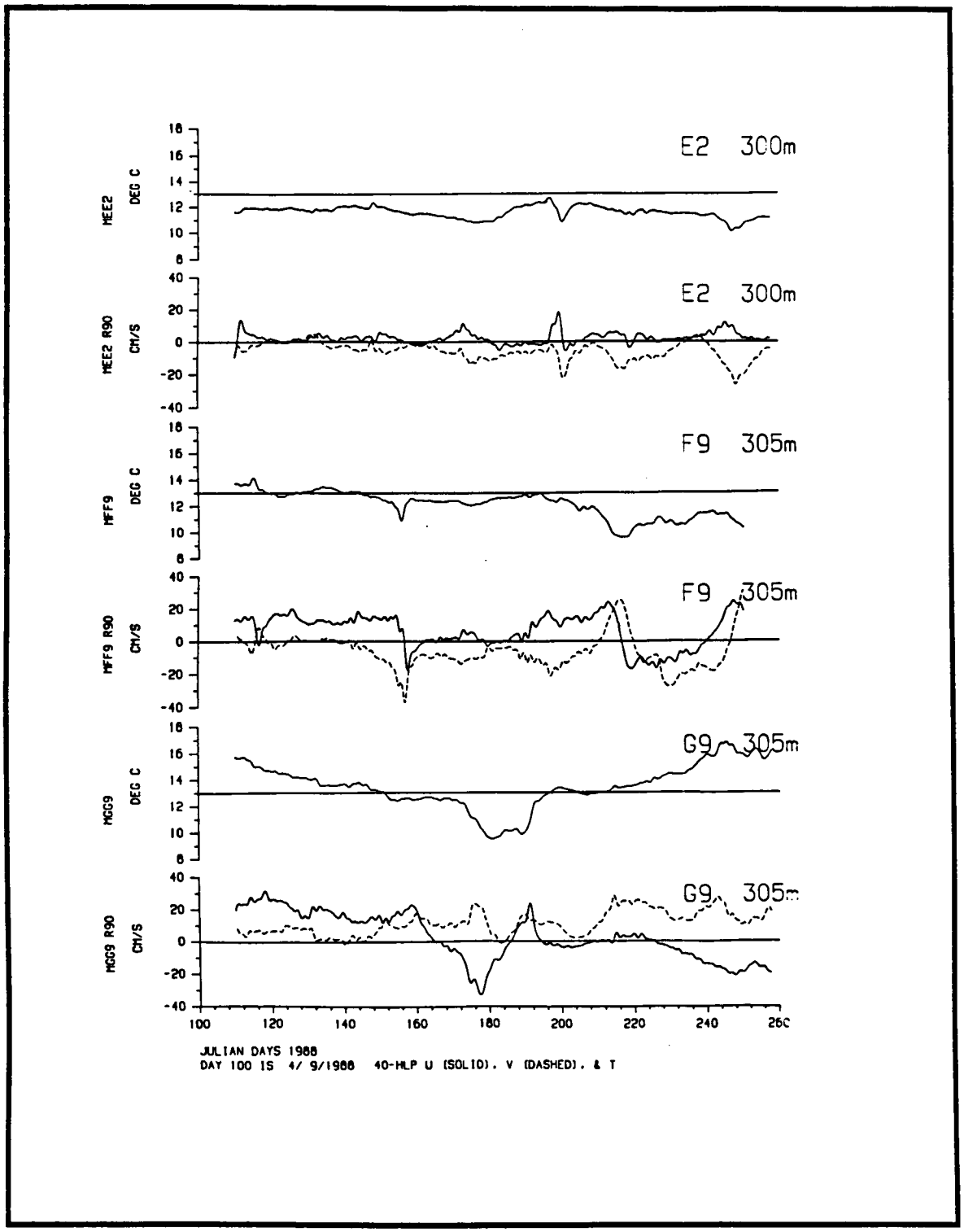

Figure 4.4-11b. Forty-HLP U (solid), V (dashed) and temperature data for the indicated slope instruments for April to October 1988.

The hydrographic surveys of Composite Three, though not providing dense coverage near the mooring line (Figure 4.4-12), suggest a large cold cyclone centered east of 92°W with the SW quadrant affecting Mooring GG. This consistent with the SE flows observed there. Figure 4.4-12 suggests that the cyclone is linked with Eddy F and is possibly being moved eastward or northeastward by the clockwise circulation of the northern part of the anticyclone. The relative positions of the cyclone and warm eddy are similar to, and seem to be consistent with the surmised positions of the cyclones observed in the SENATOR transects (Figure 4.4-8a) that seemed to be associated with Eddy D.

After Day 570 (JD 205), the eastward currents of the northern part of Eddy F begin to dominate flows at Mooring GG. Around JD 215 a cyclonic event is observed at Mooring FF with flows moving from SW to NW as temperature falls and rises (Figure 4.4-11). This implies a cold cyclone moving westward on the slope with some upslope-downslope movement so that the southern part, with eastward current, affects Mooring FF on JD 215. The increasing and decreasing westward flows at Mooring EE are consistent with westward and/or upslope-downslope movement of the northern part of a cyclone through this mid-slope mooring. Because of the close proximity in time, the event at Mooring FF would appear to be the same cyclone now up on the slope and being moved westward by the advance of Eddy F. The anticyclonic circulation of Eddy F with eastward flows at Mooring GG from JD 220 to 245 are opposed by northwest flows at Mooring FF. This along with relatively cool temperatures, implies that the northeast quadrant of the cyclone is still over Mooring FF. The currents drift back to southwestward, implying eastward translation of the northern part of the cyclone through Mooring FF. Between JD 240 and 260, exactly the same type of cyclonic rotary event occurred as observed on JD 210 to 230. This was accompanied by increasing westward flows at Mooring EE and low temperatures (extremely low at FF9 at 305 m) at both moorings which implies that the cyclone again shifted to the west with an even more vigorous translation onto the middle slope. Forty days later, around JD 300, the hydrographic surveys of Composite Four (Figure 4.4-13) show a prominent cold cyclone over the lower half of the slope between Moorings FF and EE with Eddy F centered about 24.5°N, 92.5°W. This may be the same cyclone that generated the events on JD 215 to 230 and 240 to 260 at Mooring FF. There is no evidence from Figure 4.4-13 of any other vigorous cyclones on the slope to the west of the mooring line. There is, however, further evidence of the persistence and position of this cyclone during November 1988, as ARGOS Drifter 3353 made a cyclonic loop (Figure 4.4-14) between the positions of Moorings EE and FF, almost exactly in the same position as the cold feature in Figure 4.4-13.

4.4.2.4 Discussion of Cyclones on the Slope

Evidence from moored current and temperature records, hydrographic surveys, and satellite thermal imagery, indicates that a cyclone between Eddies E and F in the deep basin moved westward and eastward through the mooring transect between May and July 1988 (Figure 4.4-9), eventually ending up on the lower slope just east of Mooring FF. As Eddy F passed to the southwest, the cyclone apparently moved quickly to the west with

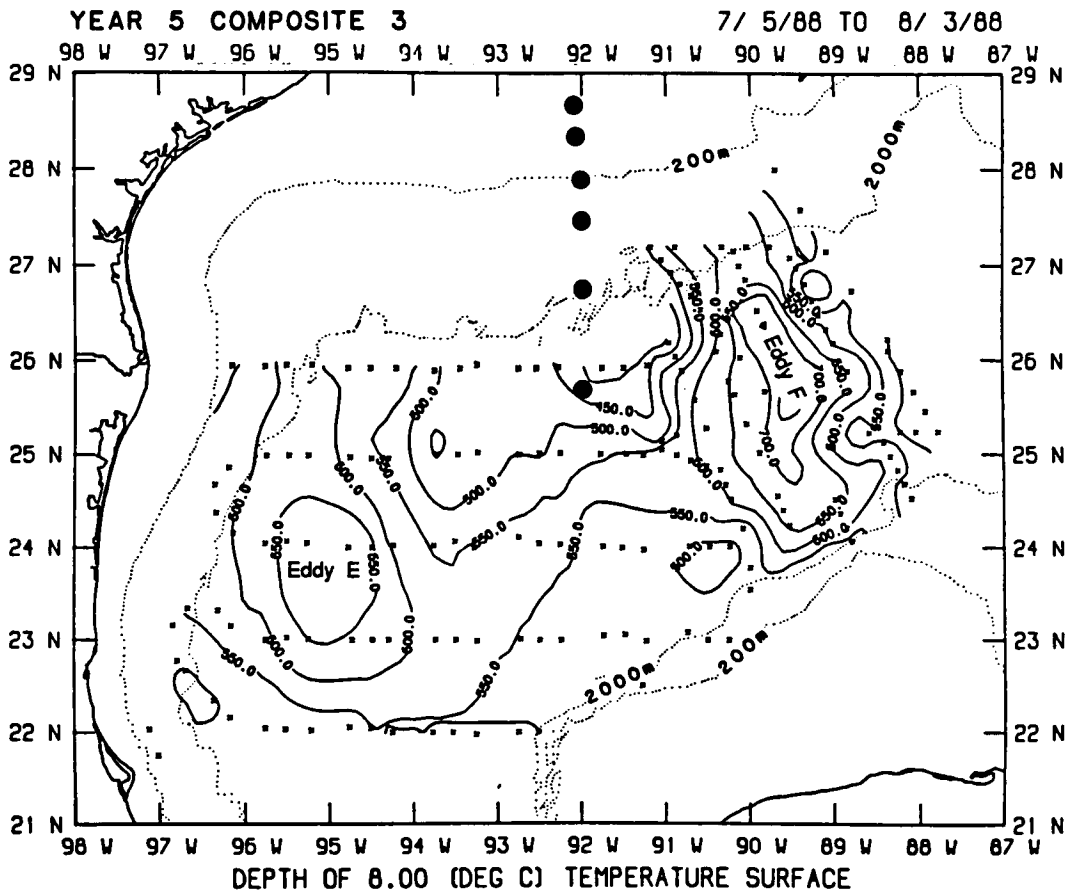

Figure 4.4-12. Depth of the 8°C isotherm from Composite Three.

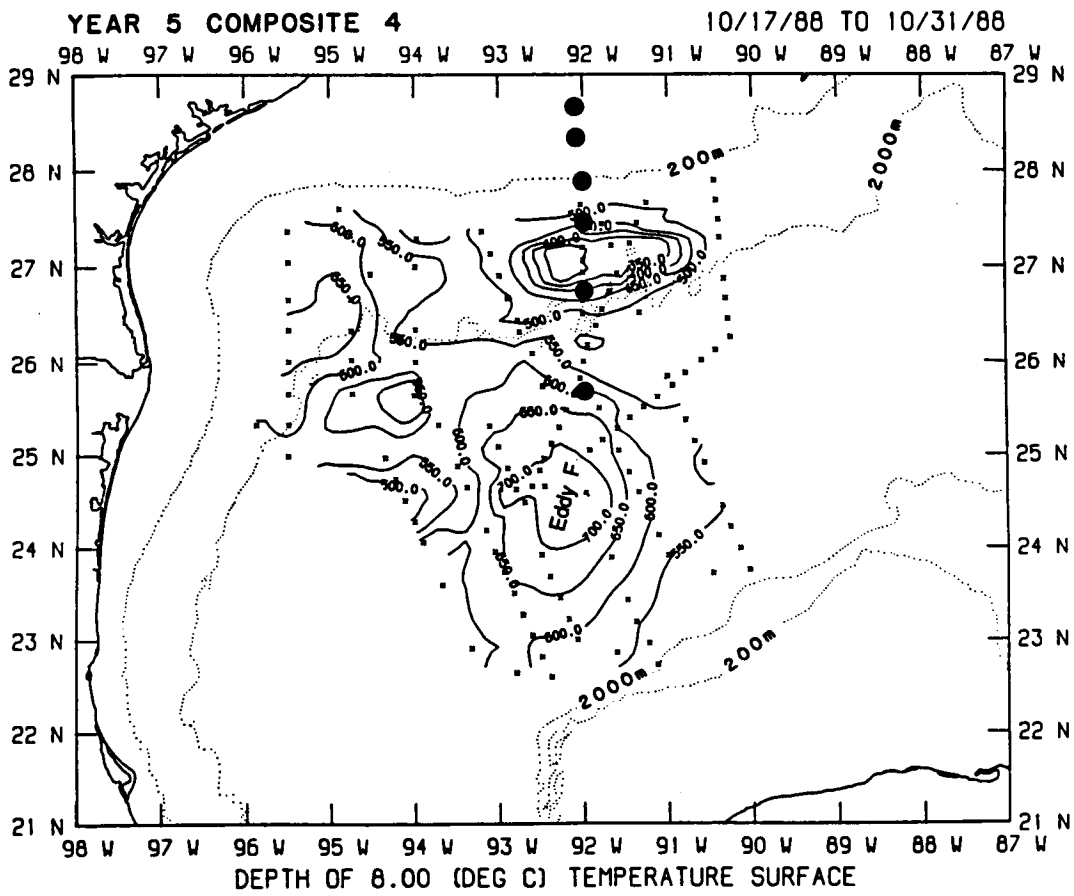

Figure 4.4-13a. Depth of the 8°C isotherm from Composite Four.

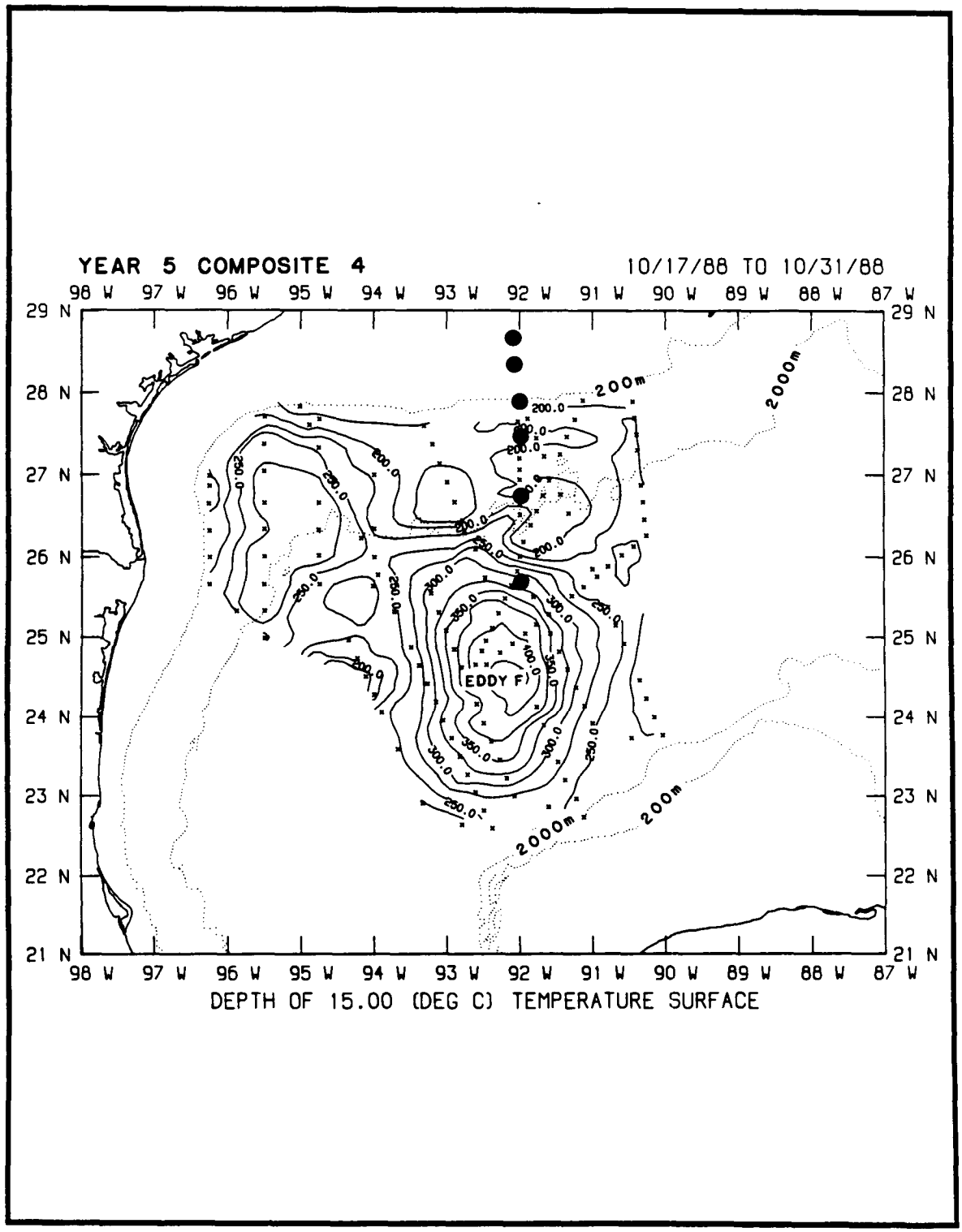

Figure 4.4-13b. Depth of the 15°C isotherm from Composite Four.

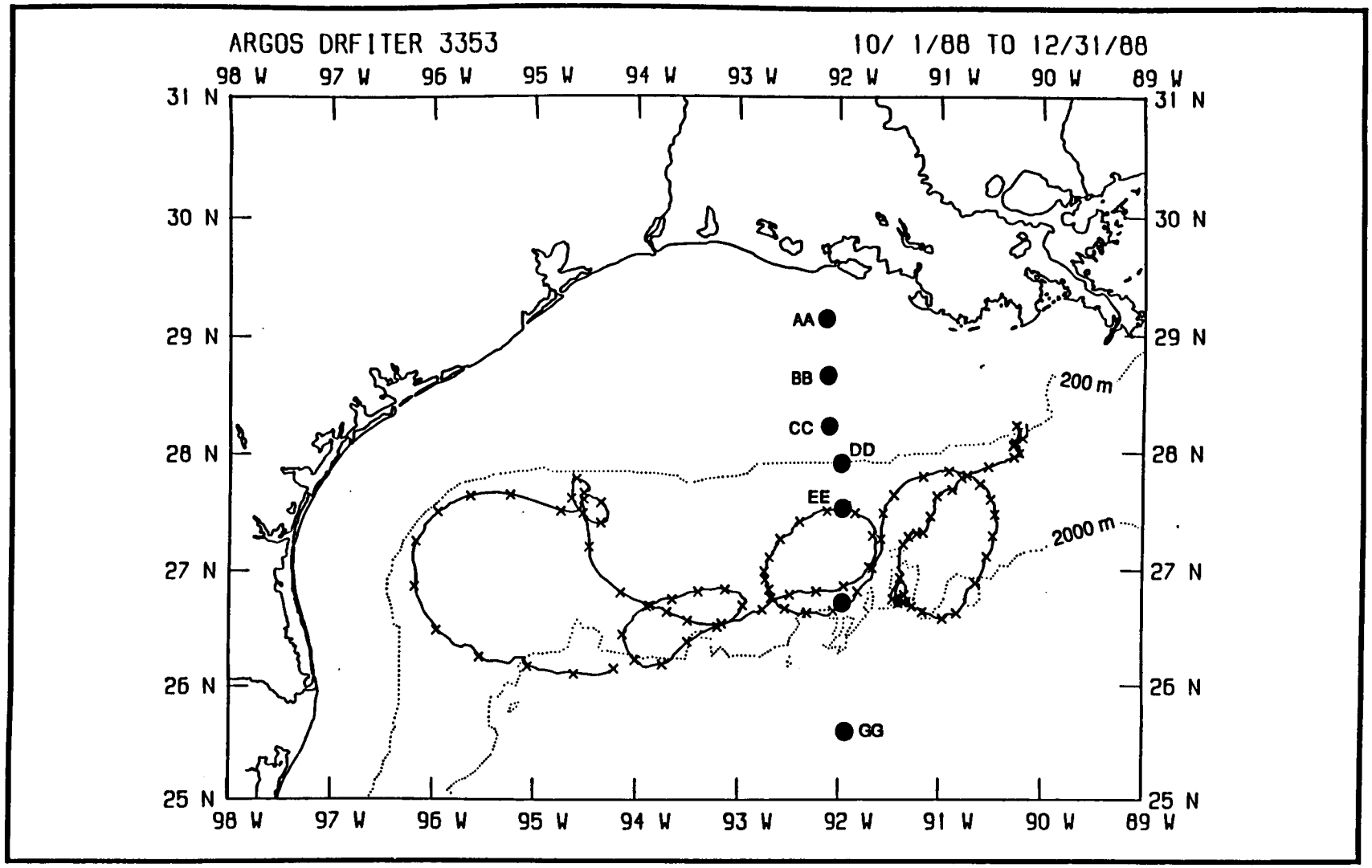

Figure 4.4-14. The track of ARGOS Drifter 3353 for October to December 1988. The ticks are at daily intervals.

an accompanying displacement onto the middle slope and then drifted back east, at least twice during August and September. By the beginning of November a cyclone, which seems likely to be the same cyclone, was over the mid- to lower slope and persisted there for at least the month of November. Thus, if this scenario is accepted, the cyclone was affecting the circulation over the slope and deep basin around 92°W for over 200 days with relatively small total movement. This sort of phenomena may explain why characteristic northern Gulf slope currents have long time scales (several months) but short coherence scales. The origin and fate of this substantial cyclonic feature is unknown.

The interpretation of the cyclonic features for summer 1987 given above indicates that cyclones may be quite common in the deep central Gulf and northern slope. Their origin is possibly more associated with the eddy shedding processes of the Loop Current and the propagation of large warm anticyclones between the Yucatan and Louisiana slopes rather than being spawned by the interaction of warm eddies with the Mexican slope (SAIC 1988) subsequent movement of cyclones eastward along the slope to 92°W. This latter mechanism is not, of course, excluded but it does not account for cyclones in the deep central basin. The interpretation given above would argue that the cyclone in Figure 4.4-13 originated as a deep water cyclone that moved onto the lower slope and persisted there as a relatively stationary feature, rather than originating in the northwest corner of the Gulf and propagating eastward along the slope. However, the data base is still far too sparse in space and time to resolve definitively the structure and movements of these Gulf cyclones. There is no indication whether the cyclonic events of the summer of 1988 are characteristic of the circulation or a relatively infrequent occurrence over the slope.

4.4.2.5 Warm Eddies

The discussion above has concentrated on the prominent cold features found in the various data records and surveys. However, the track of ARGOS Drifter 3353 (Figure 4.4-14) shows the presence of a warm anticyclone of similar size to the cyclones (diameter 100 to 150 km) over the lower slope. The drifter seems to move from a cyclone to an anticyclone as it moves eastward along the northern slope. It is known that the remnants of major warm eddies often seem to occupy the northwestern slope region. For example, Figure 4.4-13b shows a large warm eddy in this region (possibly Eddy D), and thus anticyclonic circulations could be generated over the northwestern slope by this mechanism.

To complete the event analysis of the current meter records at Moorings EE and FF, it is necessary to consider the first six months of the record prior to arrival of the cold cyclone which dominates the latter half of the record. Unfortunately, the hydrographic survey coverage is not as useful as for the summer of 1988, but AVHRR imagery coverage is quite good and offers some clues to an event analysis of this data. Figure 4.4-15 gives the 40-HLP upper layer currents and temperature data for the slope moorings, both in the stick plot and component form. An example of a sustained eastward flow event is seen at Mooring FF between Days 400

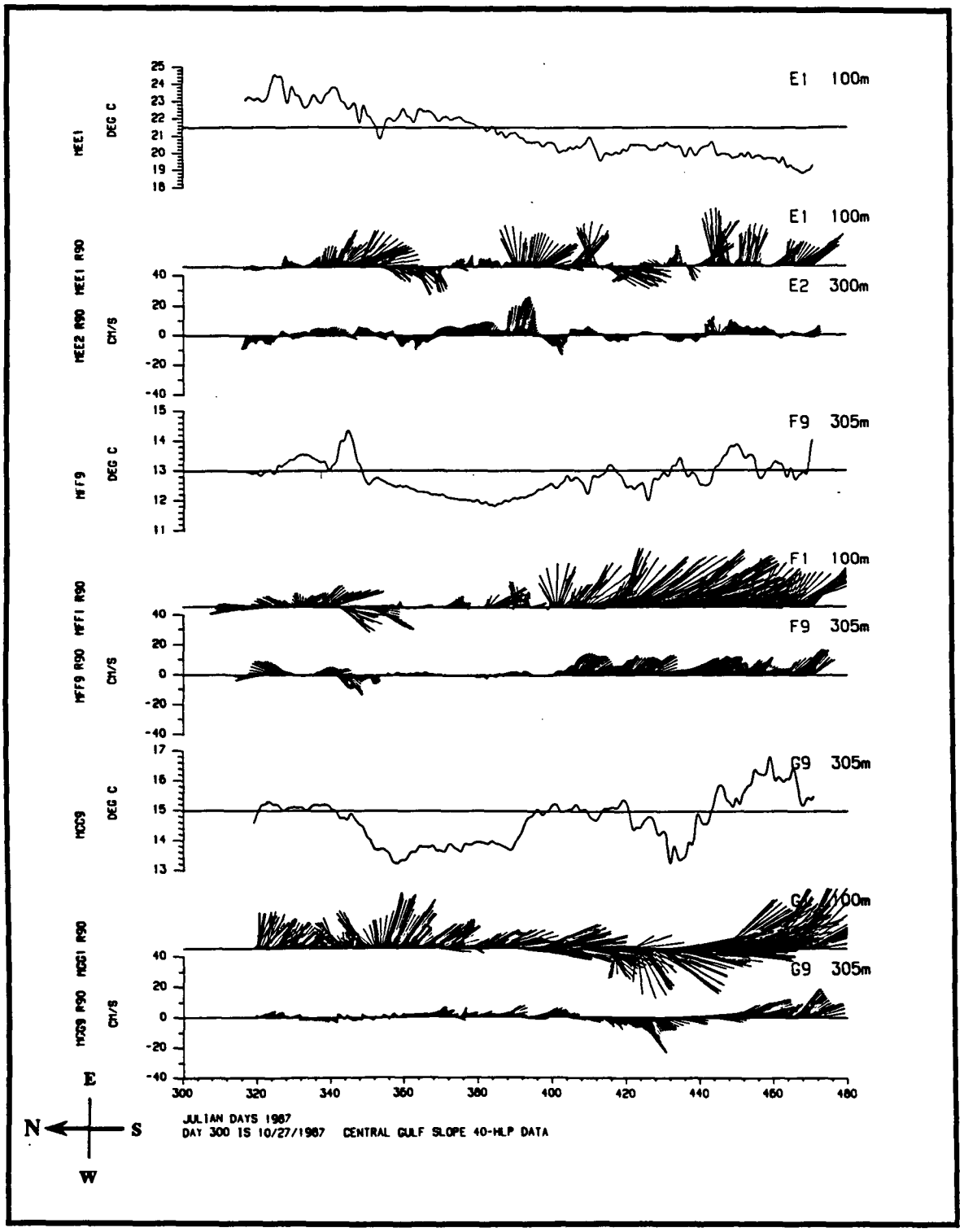

Figure 4.4-15a. Forty-HLP stick and temperature data from the indicated slope instruments for October 1987 to May 1988.

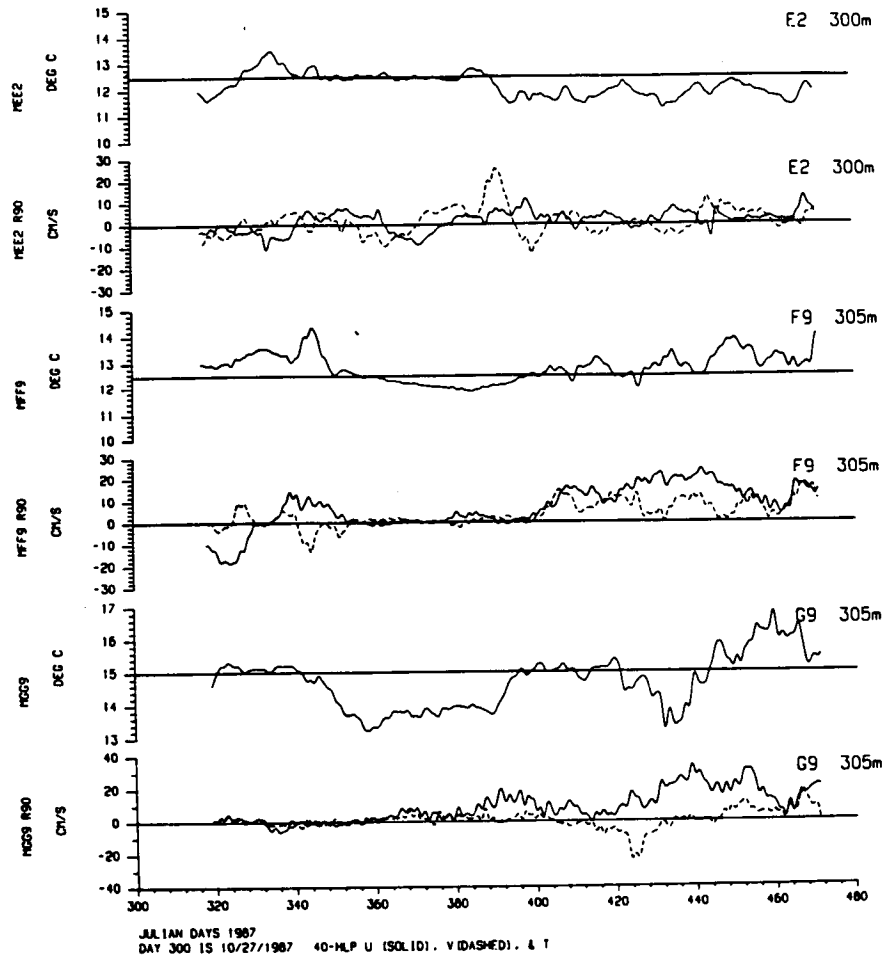

Figure 4.4-15b. Forty-HLP U (solid), V (dashed) and temperature data from the indicated slope instruments for October 1987 to May 1988.

and 470. This event is unlikely to be caused by Eddy E, discussed in the context of Mooring GG (Figure 4.4-4), because the hydrographic and drifter information indicate that Eddy E flows were south of the base of the slope. Therefore, other explanations of this sustained event at Mooring FF must be sought.

The images for JD 44, 47, 53, 71 and 84 (Days 409, 412, 418, 436 and 449) all show a warm feature over the lower slope apparently pulling cold outer shelf water over the slope in the vicinity of 92°W. This implies that the eddy center is to the west of the mooring array. Flows at Mooring FF are generally southeastward whereas at Moorings GG the flows are southwestward until the arrival of Eddy E about Day 430. Thus, currents at Moorings FF and GG are consistent with being on the eastern side of an anticyclone. A warm temperature signal is seen at Mooring GG (Days 390 to 430) but with only slight warming at Mooring FF and relatively cool temperatures at the 100 m level at Mooring EE (20°C). Flows at Mooring EE are more event like with both eastward and southward flows indicating that it may be intermittently affected by the northwestern quadrant of an anticyclonic circulation and is probably being affected by offshore flows of cool shelf water.

There is some evidence from thermal images from January 26 and 27, 1988, that this anticyclone was centered over deep water at 25°N, 94°W just prior to affecting flows at Moorings GG and FF. This raises the possibility, like the summer 1988 cyclone, that this lower slope secondary anticyclone which dominated flows at Mooring FF for about two months, moved onto the slope from offshore. Its origin, however, was much further to the west than the cyclone.

Only one further event can be analyzed from the imagery and this occurs at the beginning of the record in Figure 4.4-15. A circular feature is observed over the slope to the west of the mooring line, in a very similar position to the warm anticyclone discussed above (on JD 309). Some images as early as the middle of October (JD 289) indicate that this feature was present at the same longitude but on the middle and upper slope. Later, rather obscured images, up to JD 324, indicate that the feature was still present, a little closer to the moorings and on the mid-slope. The image for JD 309 shows a warm circular band of water with a cool center, but the majority of the other images show a warm feature.

Between Days 320 and 360, flows at Mooring FF rotate clockwise from north to SE going through zero with a rise and fall in temperature. This implies that the northern side of the center part of an anticyclone moved westward through the mooring line. Flows at Mooring GG, however, seem not to be a part of this flow. Weak eastward flows and warmer temperatures at Mooring EE, between Days 330 and 360, are consistent with this mooring being on the northern side of an anticyclone. The event at Mooring FF, between Days 320 and 360, appears to have moved relatively rapidly through the mooring, and did not return even though imagery suggests it was persistent on the lower and middle slope.

Therefore, on the evidence of two warm events at Mooring FF, with supporting data from Mooring EE and GG, as well as AVHRR imagery, both

quasi-stationary and moving anticyclones can cause two different types of flow events. There is no obvious reason that the same anticyclone can not exhibit both types of behavior depending on unknown external influences. Slope circulation, possibly being dominated by relatively small warm and cold eddies of the order of 100 to 150 km in diameter, explains the long periodicities of the current and temperature fluctuations and the lack of cross shelf and (by implication) alongshelf coherence. This set of flow fields is not very amenable to standard statistical and spectral analysis as the event nature of the description in this section has emphasized.

4.4.2.6 A Note on Tides

The 3-HLP pressure record from MHH1 in the deepest part of the basin was harmonically analyzed for tidal constituents using the least square fits to the astronomical constituents as described by Godin (1972) and implemented by Foreman (1978). The principal diurnal and semi-diurnal constituents are given in Table 4.4-2. The units are millibars which can be directly converted to centimeters of seawater.

Table 4.4-2. Tidal analysis of MHH1 (IES #2) pressure record.

Constituent	Period (hrs)	Amplitude (mb)	Greenwich Phase
Q1	26.868	3.83	352.1°
O1	25.819	15.52	9.6°
P1	24.066	4.87	20.2°
K1	23.934	15.80	16.0°
N2	12.658	1.20	208.8°
M2	12.421	3.91	228.6°
S2	12.000	1.14	157.5°

Number of Points Analyzed = 8765
Separation = 1 hour
Position 24° 29.57'N 92° 0.95'W

The amplitudes and phases are consistent with an earlier analysis of Gulf tides by Reid and Whitaker (1981) which included a benthic gauge east of the present site at 25°N, 90°W. The amplitudes are about 10% larger for the O1 and K1, and nearly four times as large for the M2. However, 25°N, 90°W is near an M2 amphidromic point just north of the Yucatan, thus amplitudes and phases of the semi-diurnal tide are expected to vary over short distances in this region.

4.4.3 Eddy Current Structure

4.4.3.1 Introduction

In this section, subsurface currents and temperatures measured at Moorings EE, FF and GG are analyzed and used to characterize the general circulation and identify some of the dominant processes that seem to be governing it. Strong mesoscale events, i.e., Loop Current anticyclones, cyclones and filaments, influence the records for a significant portion of time. The typical methods of analyzing and presenting a time-series record, such as basic statistics and spectral analyses, are difficult to interpret when the record is dominated by relatively different events. This is because the assumptions that the governing processes are stationary and stochastic are violated.

Mesoscale events such as Loop Current eddies are very baroclinic. That is, a significant proportion of their current strength is directly related to the presence and strength of horizontal density gradients (the baroclinic component). Thus, hydrographic and XBT sections through such features are a principal data source for estimating the size and vertical velocity structure of eddies. However, there can also be a barotropic component to the velocity field, the portion of the horizontal current that is independent of depth. This cannot be determined by calculating relative geostrophic velocities. Current meter time series taken in this study are sufficiently long and spatially dense enough to permit both components to be estimated. As a review, the baroclinic component of velocity exhibits vertical shear (velocity gradients) and the barotropic component of velocity is constant top to bottom, that is, depth independent.

To estimate barotropic and baroclinic components, the mean (or basic state) vertical profile of stratification for the whole Gulf of Mexico was computed. From this profile, a set of orthonormal, vertical modes was computed. The modes, or structure functions, reveal the basic vertical structure of currents that the given stratification can support. The observed currents were fitted to these modes in order to separate the barotropic and baroclinic components and to estimate their instantaneous amplitudes. The modes also proved useful in interpreting the results of correlations between currents at various locations and depths. In the following portions of this section, the data are first presented in a standard Eulerian time-series format. Characteristic features are noted and basic statistics are described. Next, the mean stability profile for the Gulf of Mexico is presented together with the vertical structure functions of current velocity derived for depths corresponding to the locations of Moorings EE, FF and GG. The results of the modal decomposition of the currents are presented.

4.4.3.2 Subsurface Circulation from Current Meter Records

Section 2.6.2 shows the locations of Moorings EE, FF and GG and summarizes the data return for each of the variables at each instrument depth. The variables are designated U, V and T for the south-north and east-west components of currents and temperature, respectively. Positive

U and V correspond to south and east, respectively. Note that the along isobath direction is E-W. The following mooring-depth designator is adopted: MEE1 corresponds to Mooring EE at a depth of 100 m, MEE2 to Mooring EE at a depth of 300 m, etc. The five possible depths are 100, 300, 725, 1650, and 2500 m. For the analyses of this section, two time periods or sub-intervals are used. The first covers the 300 days from November 11, 1987 through September 5, 1988 (Period I) during which the continuous data return is greatest. Data at MGG4 are excluded from the analyses because a tight rotor attenuated the speeds during half the period. However, direction values are good, and the data are qualitatively useful. For a modal analysis, a six-day current gap at MGG5 for April 3 to 9, 1988 was zero-filled, and the temperature data were not used. The second sub-interval covers the period during which the data return at Mooring GG is continuous at all five levels, April 10 through October 30, 1988 (Period II). This data set permits the barotropic and the first three baroclinic modes to be estimated and includes the influence of a large Loop Current eddy towards the end of the record.

The U, V and T series were filtered with a symmetric, Lanczos-squared, 40-HLP filter and were subsampled at 12 hours. The filtering process removes four days from each end of a time series. Figures 4.4-16a-c and 4.4-17a-c show the stick vectors for Moorings EE and FF, respectively, for the common data period (after filtering) of November 15, 1987 through September 1, 1988 (Period III). Figure 4.4-18a-d shows stick vectors for Mooring GG from November 15, 1987 through October 26, 1988 (Period V).

The most pronounced event in the data set occurs at Mooring GG during the latter part of the record as Eddy F moves into the array. The Year 5 Composite Four temperature surface for 8°C, during late August 1988, (Figure 4.4-19) indicates that the baroclinic component of Eddy F has a radius of influence of about 180 km. Its center is about 120 km south of Mooring GG. Indeed, the center of the path of Drifter 3345 (Section 4.2) suggests that Mooring GG should be influenced by baroclinic currents of Eddy F about mid-August 1988. This is exactly what happened as on Day 222 (Figure 4.4-18c) when the currents began to show a reversal below 725 m. During the preceding two weeks, the currents had about the same direction throughout the water column, and a magnitude that decreased by about a factor of three between 100 and 725 m, but then remained almost constant down to 2500 m. The form suggests a strong barotropic component. Similar events, but reversed in sequence, occur late in the current records, corresponding to the time that the trailing side of Eddy F passes Mooring GG. This type signature was also observed during the Year 3 study (SAIC, 1988; Figure 4.3-19) at Mooring R, in 3500 m of water (about 220 km west of Mooring GG), as the leading edge of a Loop Current eddy began to cross it.

Other events are evident in the deep current records of the three moorings, but it is difficult to establish if a given event is caused by the passage of a particular eddy, an eddy byproduct such as a filament or some other process such as wave propagation, particularly at Moorings EE and FF. The temperature at 305 m, however, provides some additional information about events. Figure 4.4-20a-d shows the temperature series

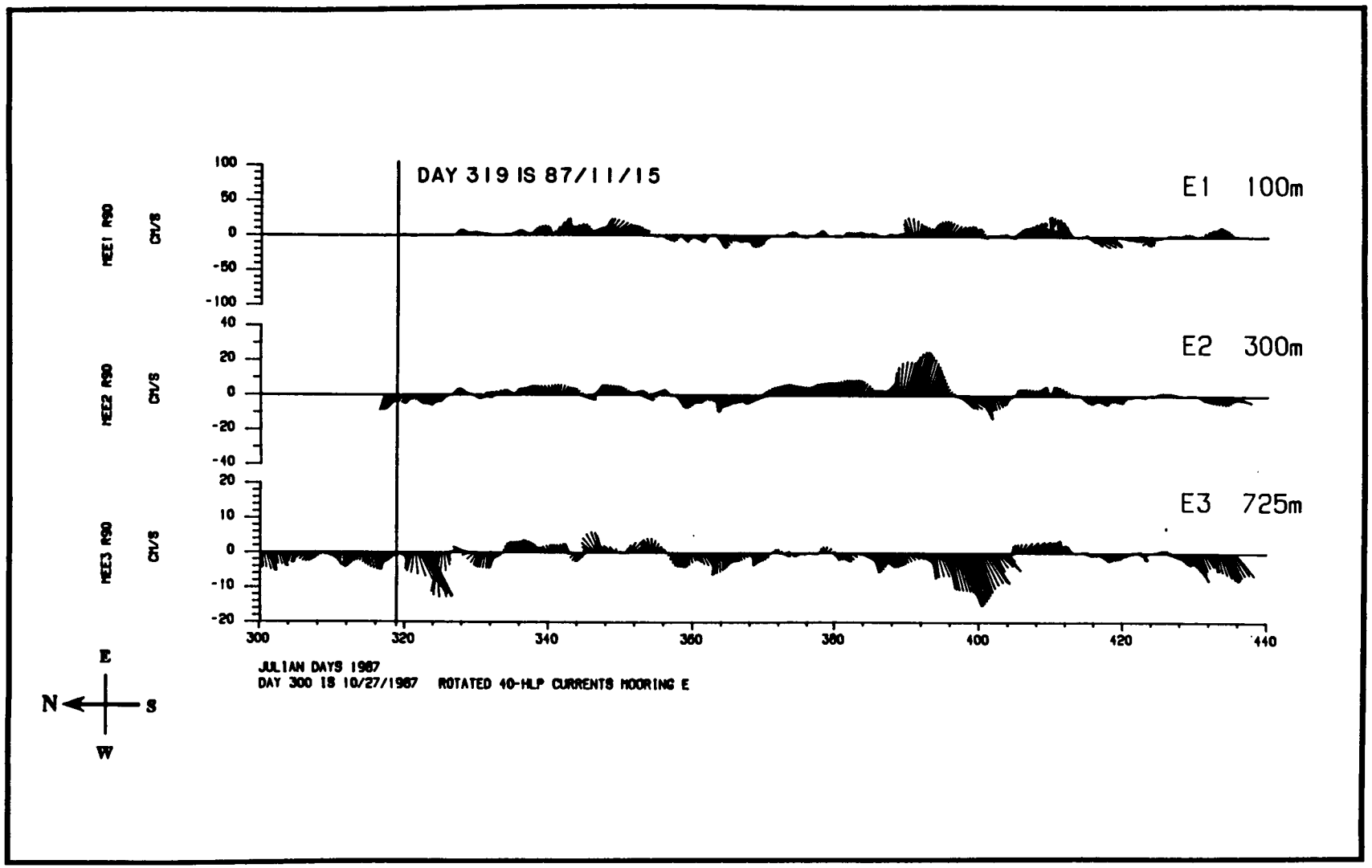

Figure 4.4-16a. Stick vector plots of 40-HLP currents at Mooring EE for the period from October 27, 1987 through March 11, 1988. Vertically up (+V) is east.

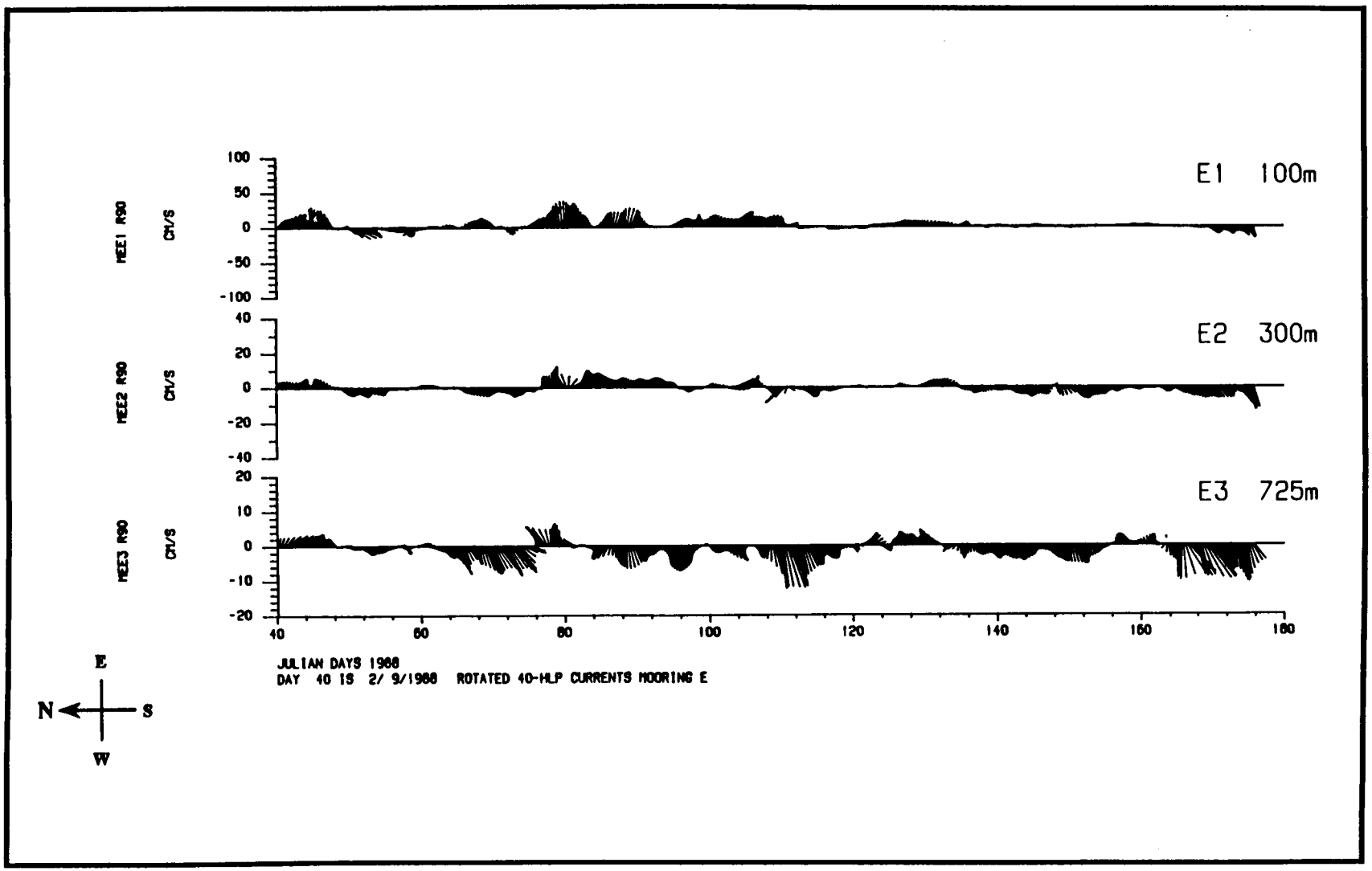

Figure 4.4-16b. Stick vector plots of 40-HLP currents at Mooring EE for the period from February 9, 1988 through June 24, 1988. Vertically up (+V) is east.

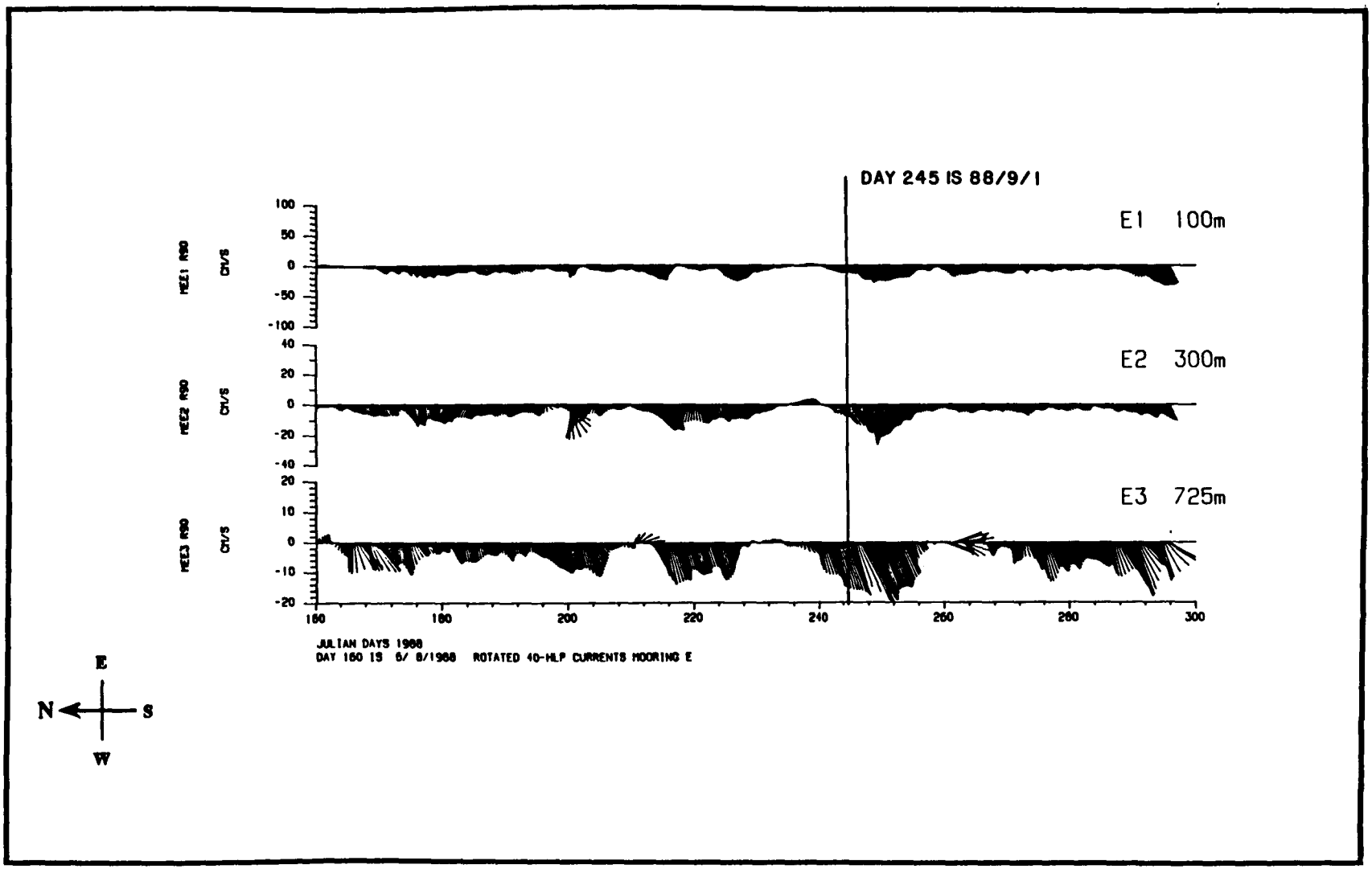

Figure 4.4-16c. Stick vector plots of 40-HLP currents at Mooring EE for the period from June 8, 1988 through October 22, 1988. Vertically up (+V) is east.

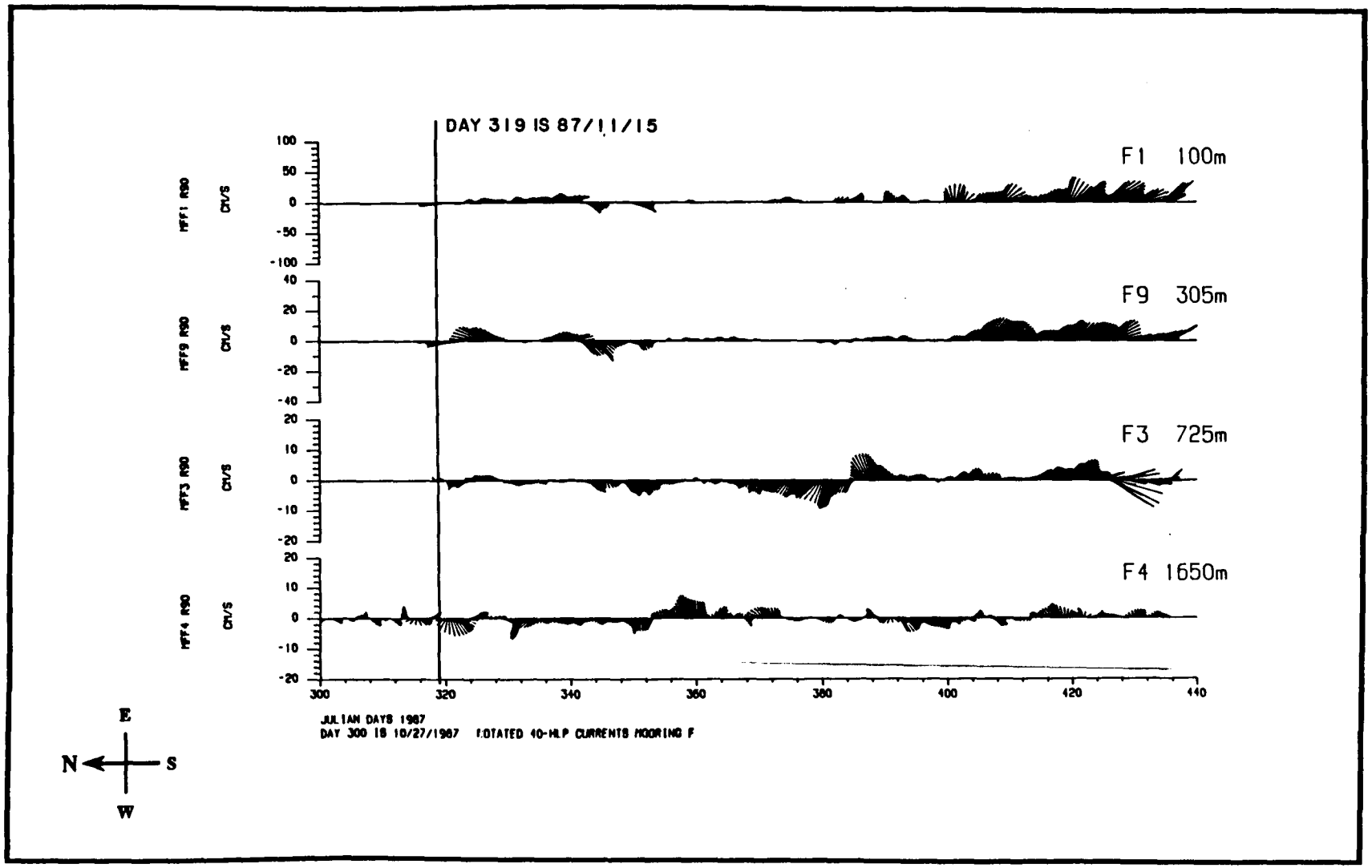

Figure 4.4-17a. Stick vector plots of 40-HLP currents at Mooring FF for the period from October 27, 1987 through March 11, 1988. Vertically up (+V) is east.

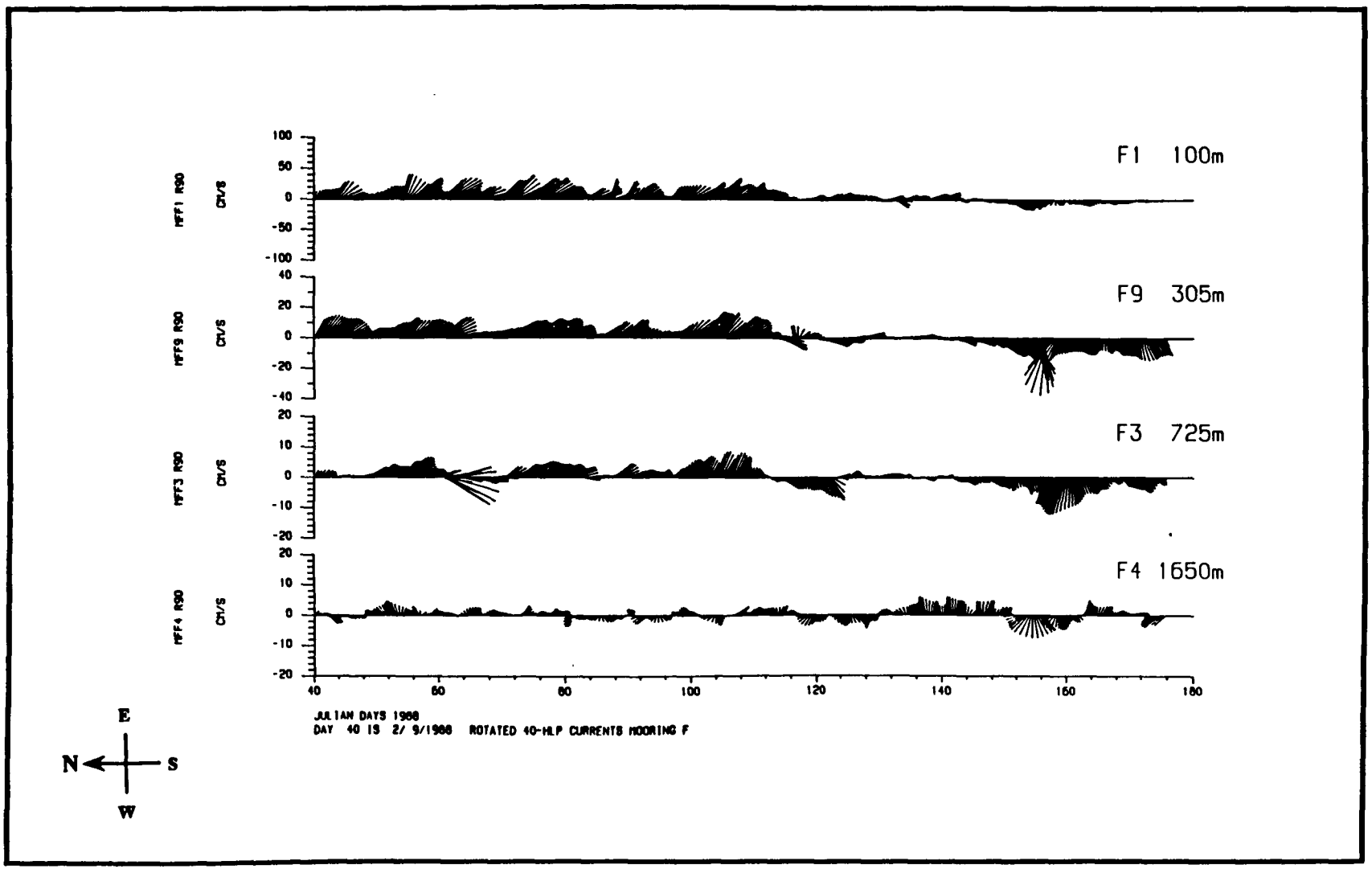

Figure 4.4-17b. Stick vector plots of 40-HLP currents at Mooring FF for the period from February 9, 1988 through June 24, 1988. Vertically up (+V) is east.

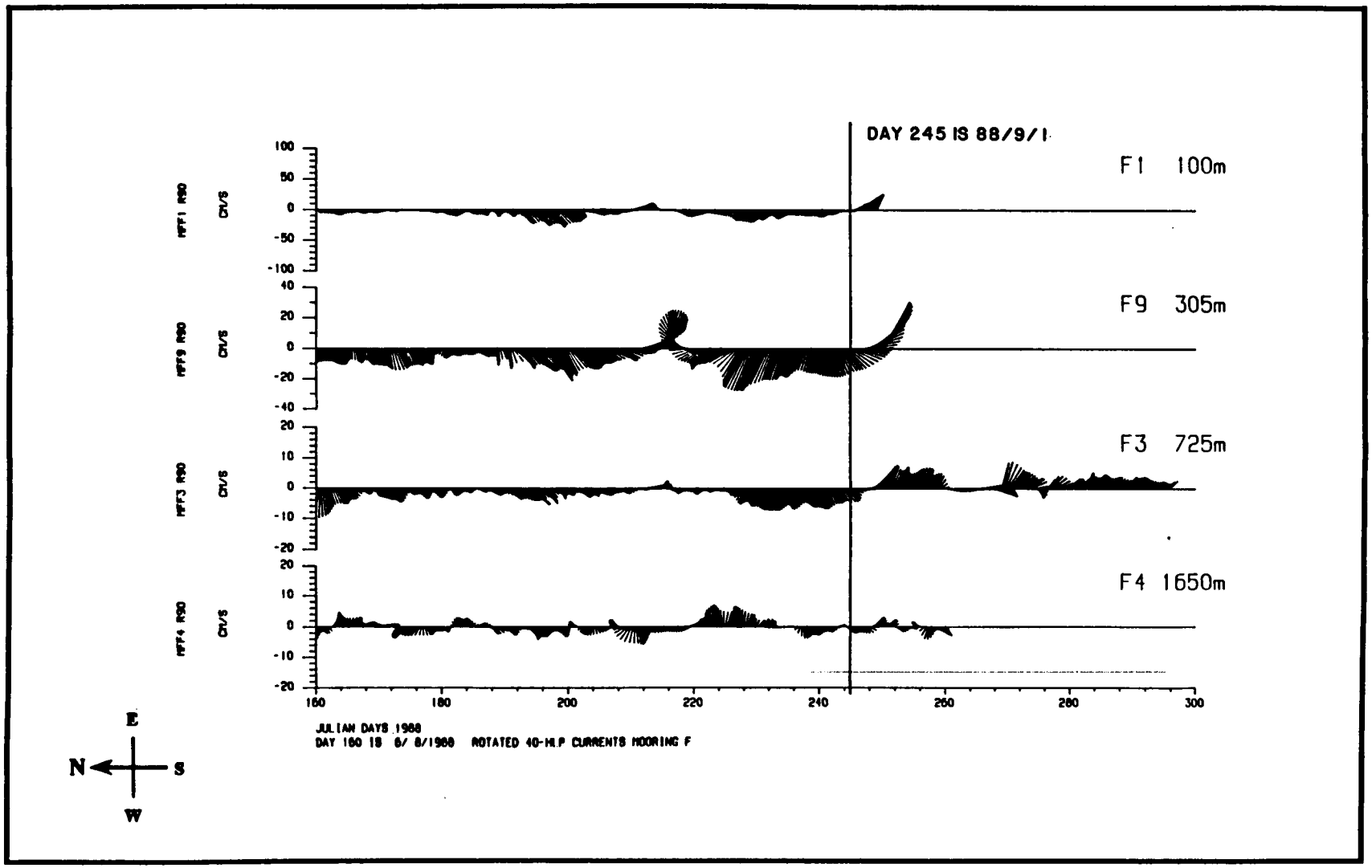

Figure 4.4-17c. Stick vector plots of 40-HLP currents at Mooring FF for the period from June 8, 1988 through October 22, 1988. Vertically up (+V) is east.

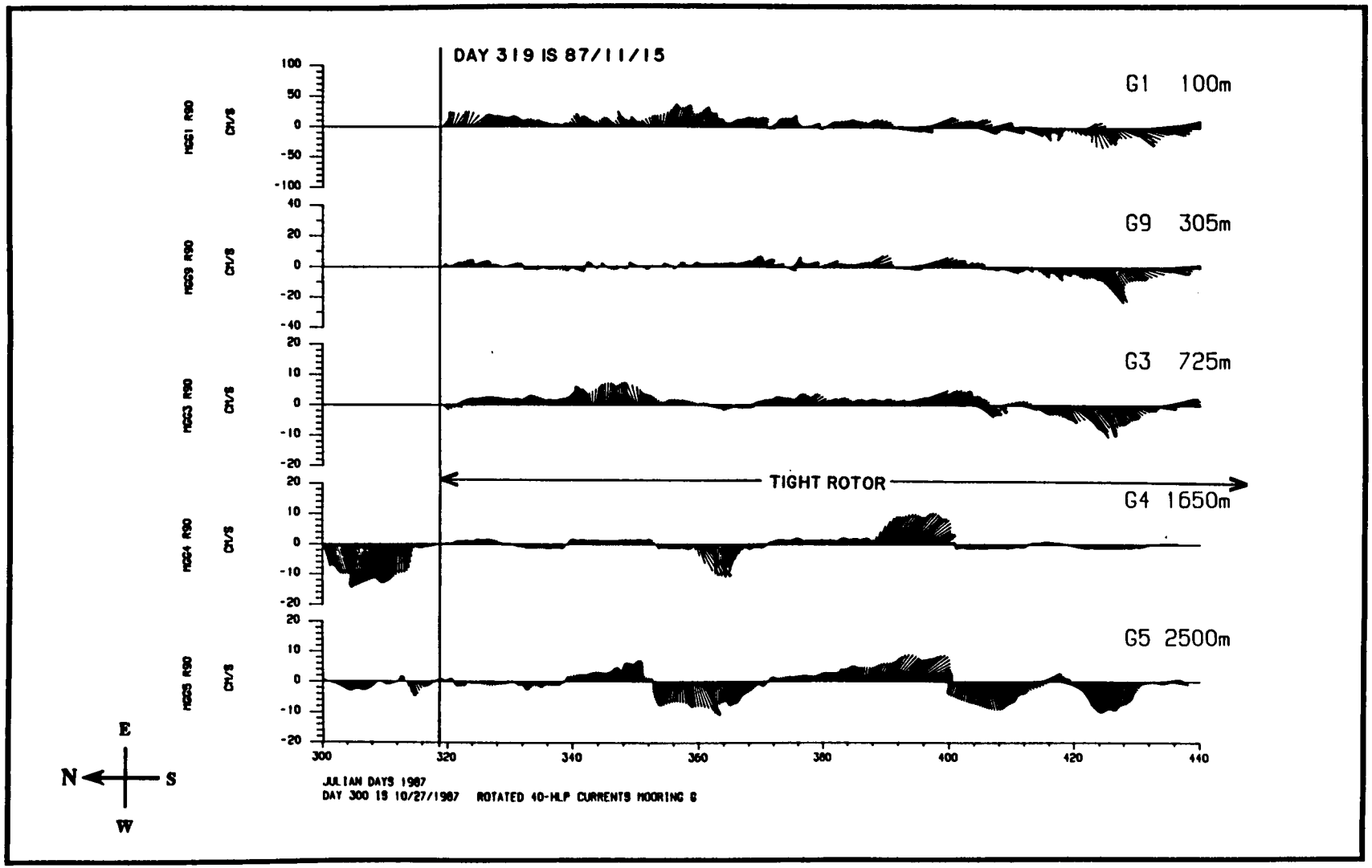

Figure 4.4-18a. Stick vector plots of 40-HLP currents at Mooring GG for the period from October 27, 1987 through March 11, 1988. Vertically up (+V) is east.

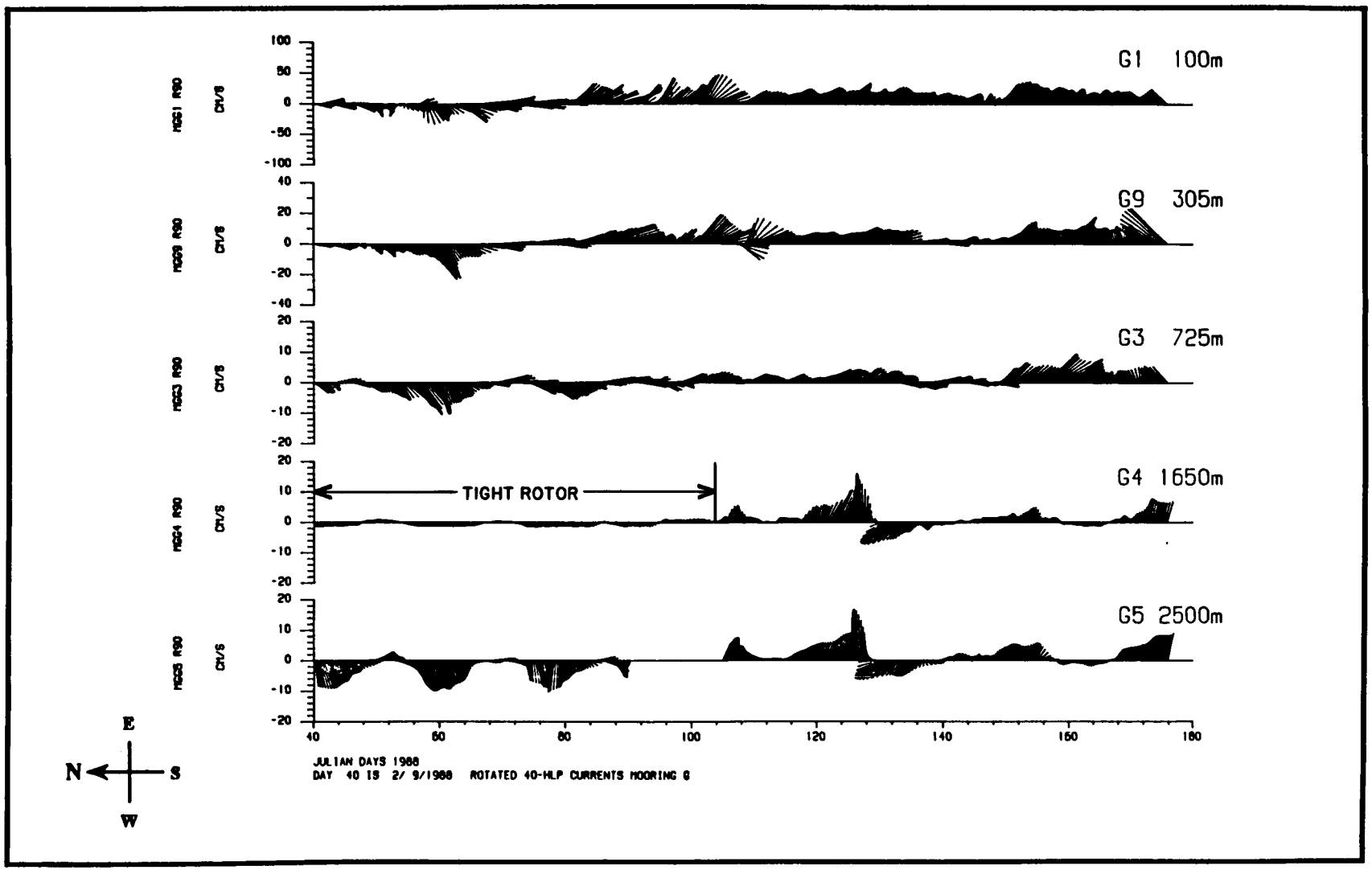

Figure 4.4-18b. Stick vector plots of 40-HLP currents at Mooring GG for the period from February 9, 1988 through June 24, 1988. Vertically up (+V) is east.

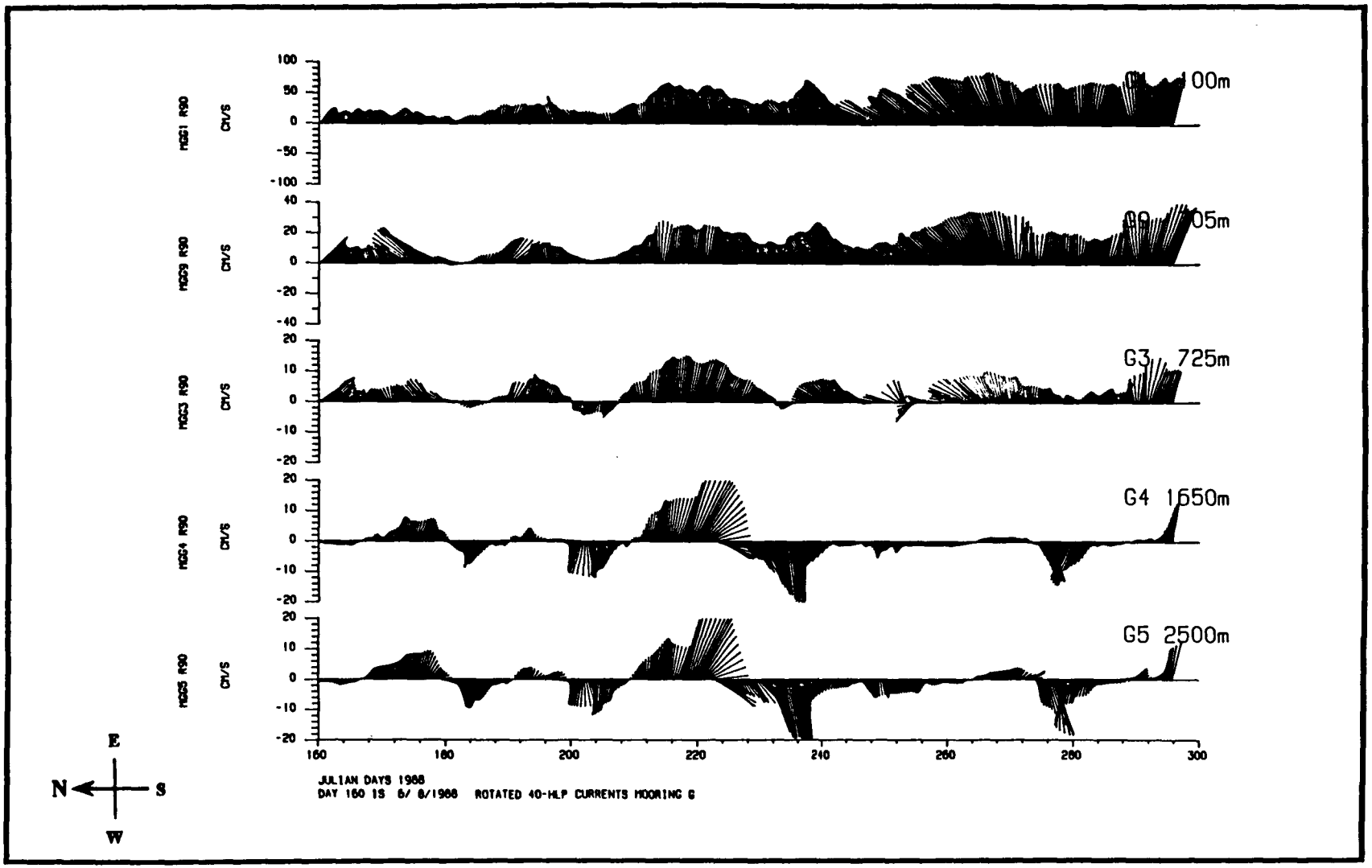

Figure 4.4-18c. Stick vector plots of 40-HLP currents at Mooring GG for the period from June 8, 1988 through October 22, 1988. Vertically up (+V) is east.

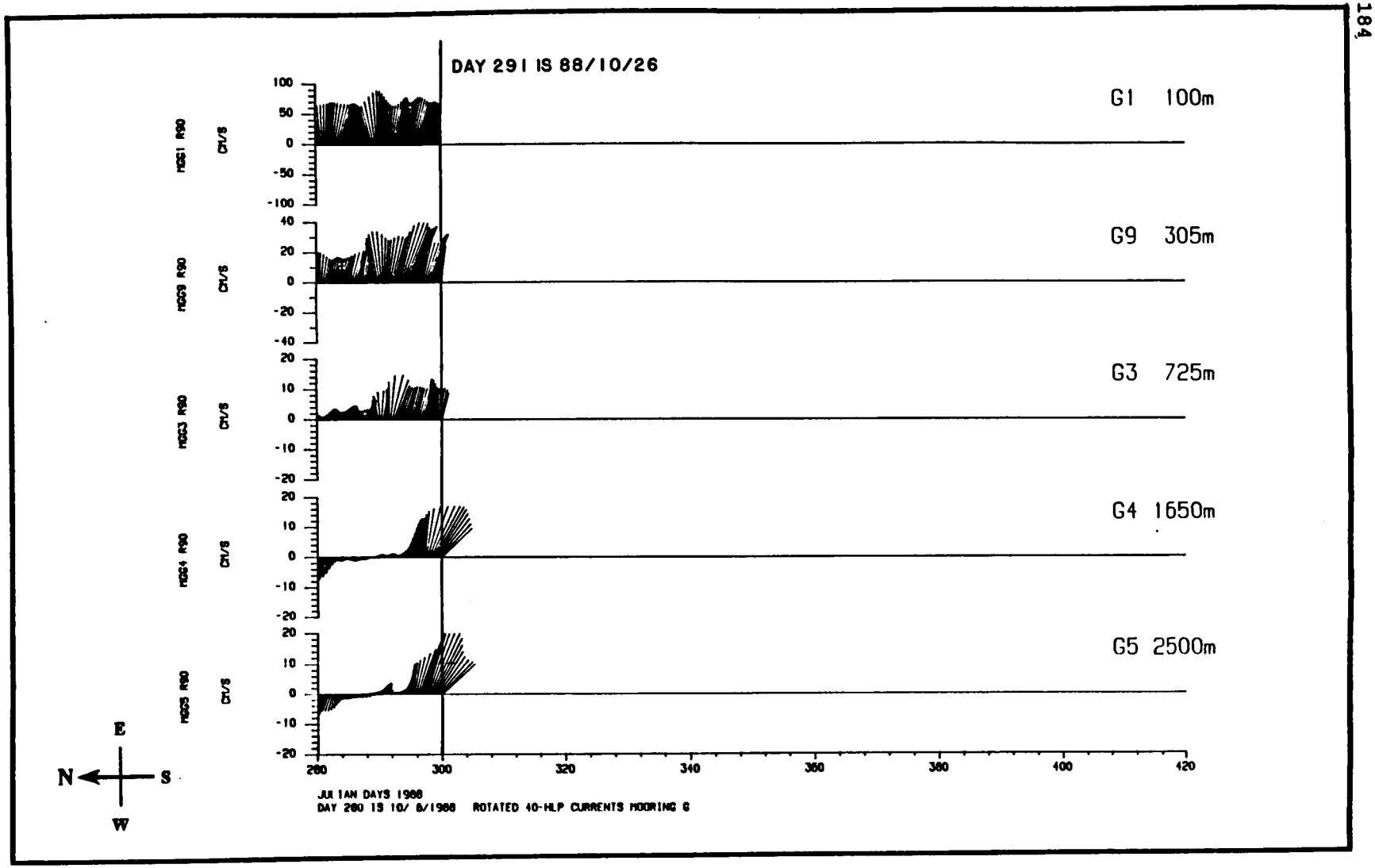

Figure 4.4-18d. Stick vector plots of 40-HLP currents at Mooring GG for the period from October 6, 1988 through October 26, 1988. Vertically up (+V) is east.

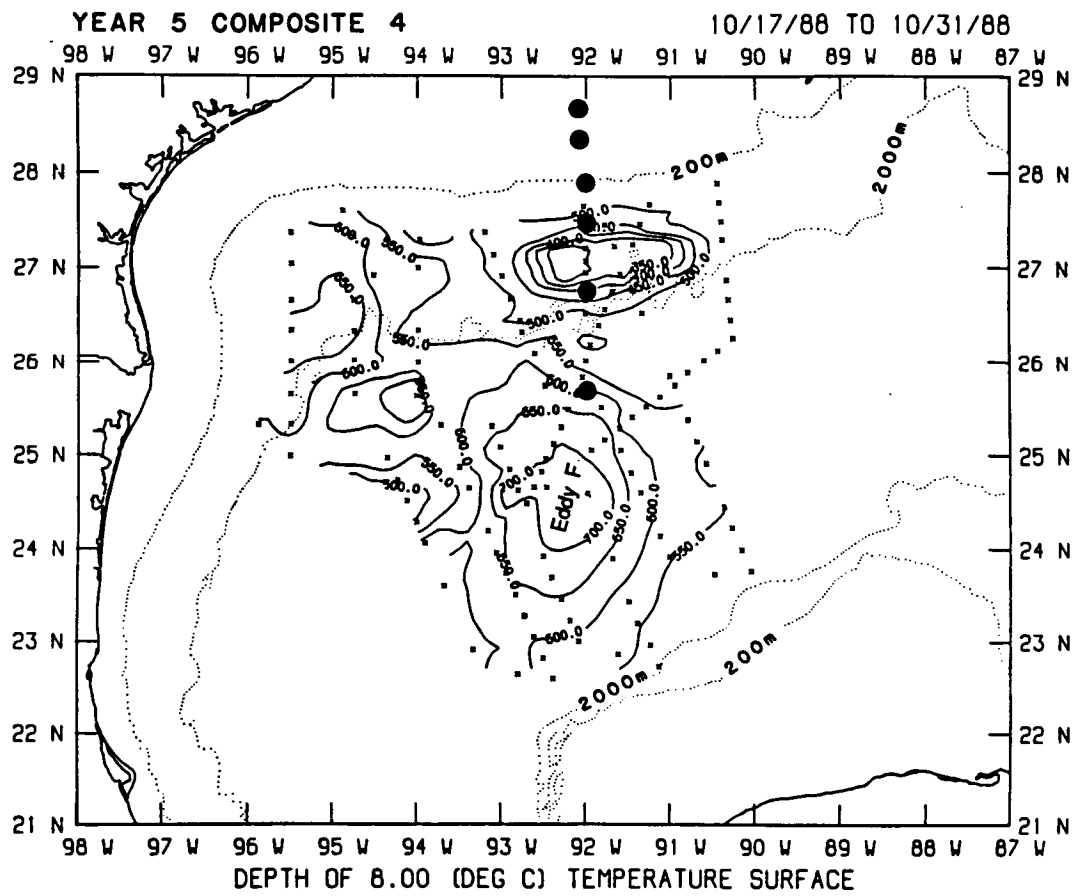

Figure 4.4-19. Topography of the 8°C temperature surface based on a composite of XBT data sets collected during the period from October 17 to 31, 1988.

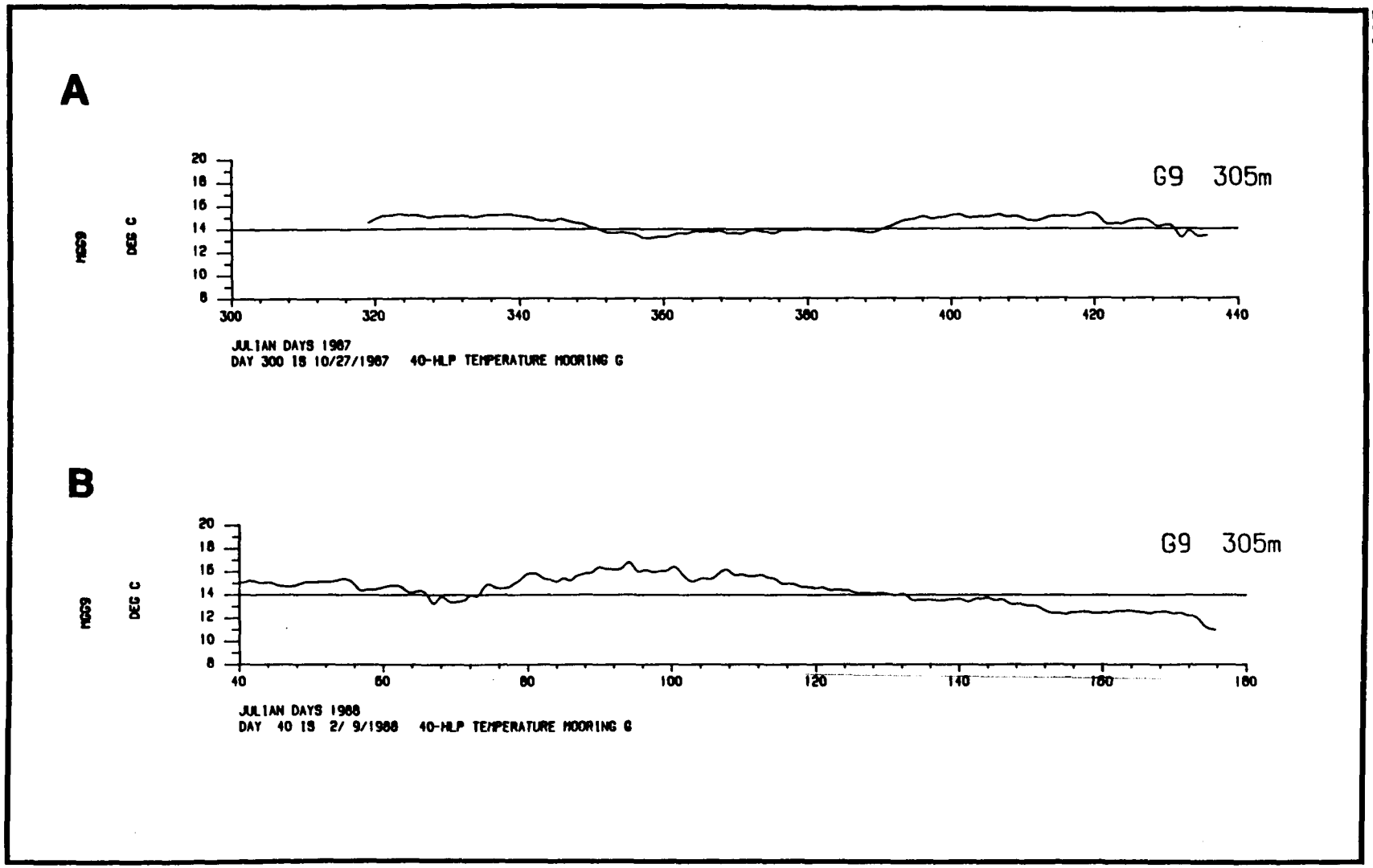

Figure 4.4-20a,b. Forty-HLP temperature series at 305 m at Mooring GG for the period from (a) October 27, 1988 through March 11, 1988 and (b) February 9, 1988 through June 24, 1988.

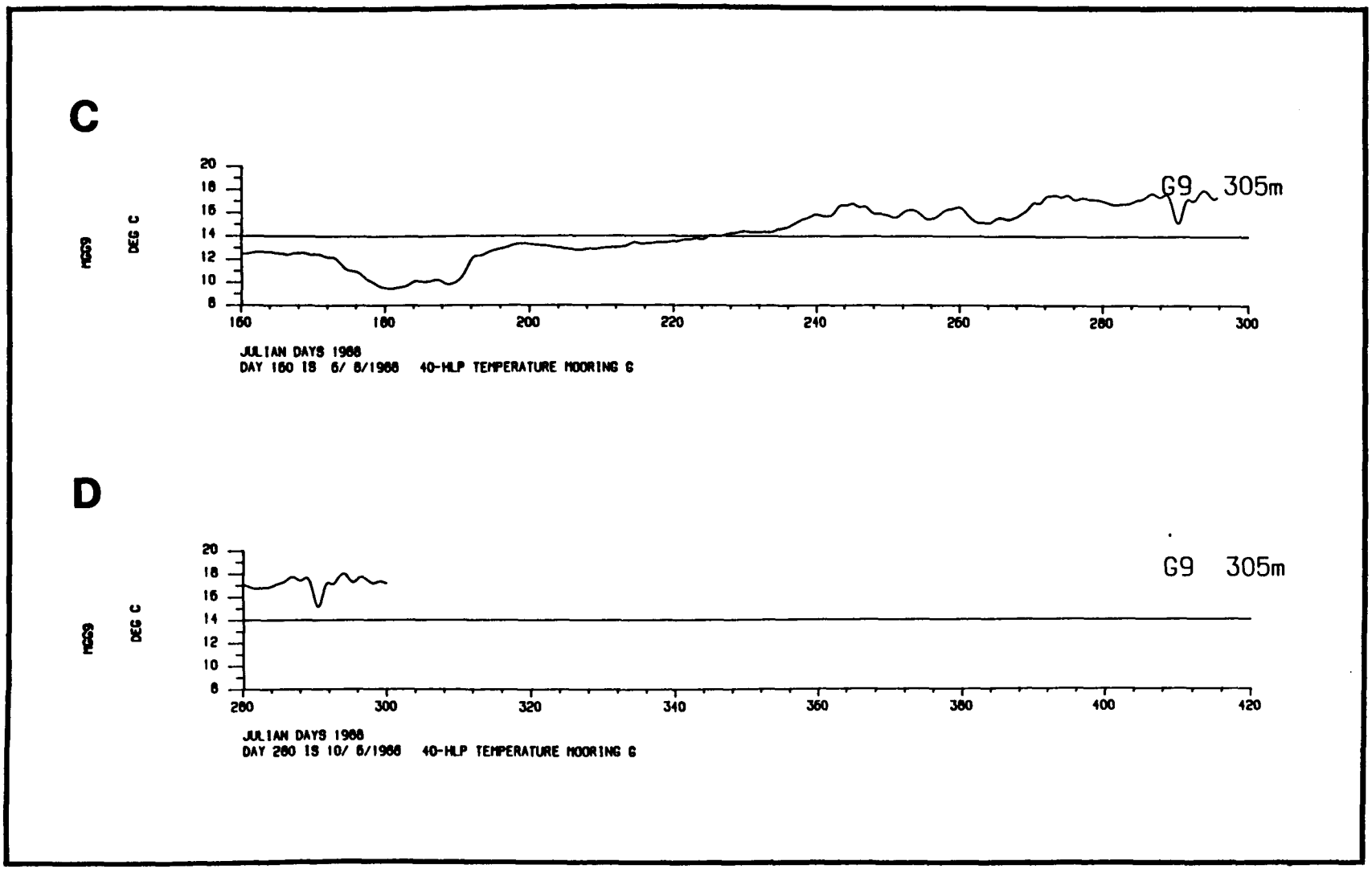

Figure 4.4-20c,d. Forty-HLP temperature series at 305 m at Mooring GG for the period from (c) June 8, 1988 through October 22, 1988 and (d) October 6, 1988 through October 26, 1988.

for 305 m at Mooring GG. The temperature increases beginning about Day 220 (August 7, 1988) as Eddy F approaches. The maximum deviation is about 4°C. Between Days 72 and 124, the influence of the passage of Eddy E (Figure 4.4-21) is evident as the temperature rises (Figure 4.4-20b). The change is only about 2°C, so only the fringe of Eddy E crosses the mooring. In addition, some cold-core or cyclonic events are suggested by negative fluctuations in temperature as, for example, between Days 145 and 190. In this particular case, the deviation also is as much as 4°C. Composite Three for the depth of the 15°C isotherm (Figure 4.4-22), suggests cyclonic circulation in the vicinity of Moorings GG and FF during this time period, and, indeed the upper currents are eastward at Mooring GG and westward at Mooring FF. Less pronounced events can be found in the temperature series for Moorings EE and FF (not shown).

An obvious characteristic of the vertical structure of the currents in Figure 4.4-18 is that a zero point, or level of no motion, lies between 725 and 1650 m. Currents at 100, 305 and 725 m are similar in direction and have a magnitude that decreases with depth while currents at 1650 and 2500 m are similar in both magnitude and direction but are distinctly different from those at shallower depths. The currents recorded at Mooring R in the Year 3 study (SAIC, 1988; Figure 4.3-19) imply that the zero point is probably above 1000 m because currents, in that case, are similar in magnitude and direction from 1000 m downward. In the deep Gulf, therefore, available direct observations indicate that a level of no motion may lie between 725 and 1000 m. Hofmann and Worley (1986) analyzed historical hydrographic data in the Gulf of Mexico by empirical search and inverse techniques and found that the depth of the density surface corresponding to the optimum reference level varies between 800 and 950 m in the deep western Gulf. In shallower regions the zero point is shallower. At Moorings EE and FF the records for 305 and 725 m, respectively, each have the characteristic of being more similar to the upper currents during some portions of the record and to deeper currents during other portions. Each is located, therefore, close to the zero point of its respective vertical current structure.

A third characteristic visible in Figure 4.4-18 for Mooring GG, particularly in the deep records, is a long-period fluctuation of between 20 and 25 days. It also occurs in the records for Moorings EE and FF (Figures 4.4-16 and 4.4-17), but less obviously so. One can expect this period to be prominent in the spectral analyses.

Table 4.4-3 presents the basic statistics for U, V and T for the common 300-day interval (Period I) so that some quantitative comparisons can be made. However, the records are clearly dominated by long period events, and 300 days is not sufficient to characterize the climatology of the region. The most consistent property in Table 4.4-3 is that the mean cross isobath (U) velocities are positive (southward) at all three locations and at all depths. The mean cross isobath components at 100 m increase southward indicating a mean divergence north to south along the line of the moorings at this depth. The mean along isobath (V) velocities at 100 m are all positive (eastward) and increase southward. The horizontal shear of the mean along isobath velocity is 4.0×10^{-7} s^{-1} between Moorings EE and FF and 12.0×10^{-7} s^{-1} between Moorings FF and

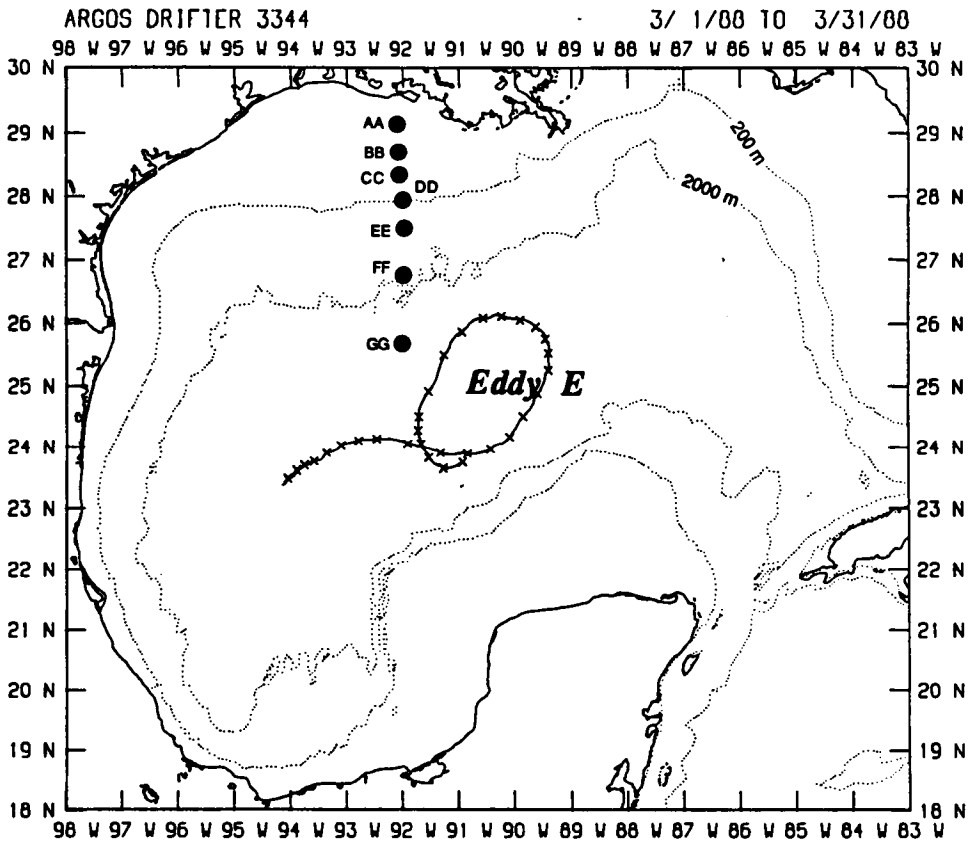

Figure 4.4-21. Trajectory of Drifter 3344 during the month of March 1988. Each X indicates a one-day interval.

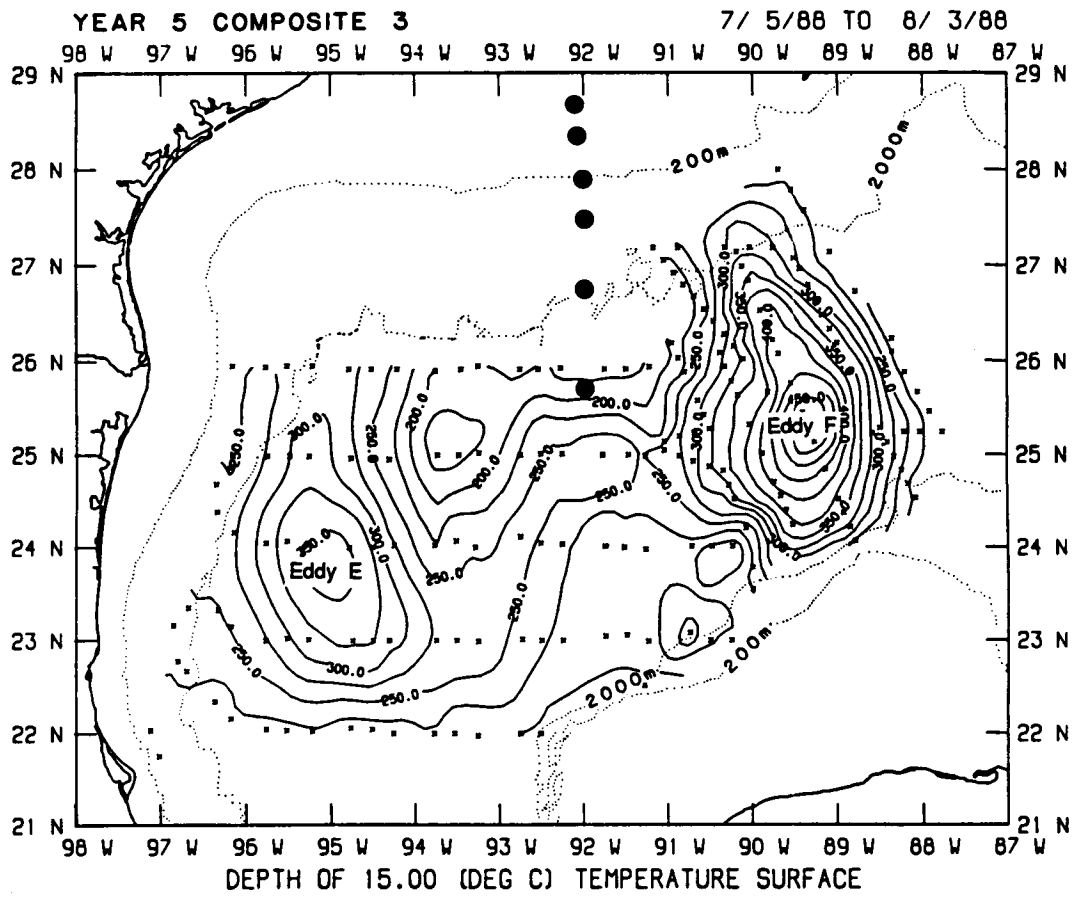

Figure 4.4-22. Topography of the 15°C temperature surface based on a composite of XBT data sets collected during the period from July 5 to August 3, 1988.

Table 4.4-3. Statistics for deployments three and four (common data period: November 11, 1987 through September 5, 1988 (Period I); 7200 observations).

METER ID	U(CM/S)				V(CM/S)				T(DEGREE C)			
	MIN	MAX	MEAN	VAR	MIN	MAX	MEAN	VAR	MIN	MAX	MEAN	VAR
EE1	-37.1	54.2	4.75	110.3	-40.6	50.8	0.16	156.1	18.57	24.97	20.7	1.91
EE2	-15.5	21.5	1.71	24.9	-30.9	30.1	-2.23	56.9	9.7	13.7	11.89	0.48
EE3	- 8.7	15.1	1.34	10.1	-28.7	1.1	-3.45	27.8	5.7	6.7	6.1	0.02
FF1	-40.2	65.1	11.87	290.6	-46.9	49.2	3.25	188.2	19.5	24.1	21.37	1.11
FF2	-23.8	32.2	6.43	112.7	-43.8	30.6	-1.17	109.2	-	-	-	-
FF3	- 9.1	19.1	1.55	14.1	-16.1	13.6	-8.68	17.9	5.4	6.8	6.11	0.07
FF4	- 7.9	7.8	0.1	6.3	- 9.9	12.2	-0.01	9.5	4.1	4.2	4.17	0.01
GG1	-92.5	87.3	14.29	802.6	-36.8	76.3	17.79	335.3	19.9	26.9	22.73	2.56
GG2	-36.6	41.9	6.44	168.3	-33.8	32.3	5.65	80.1	9.1	17.2	14.1	2.27
GG3	-13.3	20.1	4.04	27.3	-14.7	19.1	1.89	22.7	5.5	7.2	6.6	0.12
GG5	-12.9	1.6	1.74	10.3	-24.9	28.9	- 0.79	43.6	-	-	-	-

GG. At 300 and 725 m the mean along isobath velocity at Moorings EE and FF on the slope are negative (westward).

4.4.3.3 Dynamic Normal Mode Decomposition of Currents

Vector plots ("stick plots" Figures 4.4-16, 4.4-17 and 4.4-18) show that currents in the central Gulf can have a complicated vertical structure, particularly when strong mesoscale eddies are present. Vertically sheared baroclinic currents resulting from horizontal density differences combine with a vertically constant barotropic current, which at times has a significant amplitude, to produce the observed vertical velocity structure. The baroclinic part depends on the presence of a basic state of stable stratification in which lighter fluid overlies denser fluid. The degree of stratification is measured by the stability frequency, N, defined as

$$N = \left[g\left(-\frac{1}{\rho_0}\frac{\partial \rho}{\partial z} - \frac{g}{c^2} \right) \right]^{\frac{1}{2}} \tag{1}$$

where g is the acceleration of gravity, ρ_o the reference density, ρ the in-situ density, z the vertical coordinate and c is the local speed of sound. N is the natural frequency of oscillation of a parcel of fluid given a small vertical displacement from its equilibrium position. The fluid is statically stable when N^2 is greater than zero. The corresponding period, $2\pi/N$, varies from a few minutes in the thermocline to many hours in the deep oceans, where the water is nearly neutrally stable. Phillips (1977) regards the distribution of N as one of the most important dynamical characteristics of the ocean. For the large scale dynamics of ocean currents of interest here, N determines the Rossby radius of deformation and is a parameter controlling the baroclinic instability of currents (Pedlosky, 1979).

One way to analyze and interpret the vertical structure of currents is to decompose it using a set of basic functions that are derived from linear quasigeostrophic theory and a known stability profile (Kundu et al., 1975; Flierl, 1978; Inoue, 1985; McWilliams et al., 1986). For inviscid flow in a stratified, unbounded ocean with negligible mean flow over a flat bottom, the horizontal and time variables can be separated from the vertical variable in the equations for horizontal velocity or pressure. The equations for the vertical structure of horizontal velocity and for surface and bottom boundary conditions are then

$$\frac{d}{dz}\left[\left(\frac{f^2}{N^2(z)}\right)\frac{d}{dz}F_n(z)\right] + \lambda_n F_n(z) = 0 \tag{2}$$

$$\frac{dF_n}{dz} = 0 \quad \text{at} \quad z = -H, 0$$

where F_n (z) is the vertical structure eigenfunction for the nth mode, λ_n the eigenvalue, H the bottom depth, and N(z) the mean vertical profile

of stability discussed above. This is a Sturm-Liouville eigenvalue problem, and for an arbitrary N(z) profile it must be solved numerically. The eigenvalues of the solution are related to the Rossby radii of deformation by

$$\lambda_n = \frac{1}{\left(R_{d_n}\right)^2} \tag{3}$$

where Rd_n is the Rossby radius Rd of the nth mode. The eigenfunctions, $F_n(z)$, form a complete orthogonal set. A modal representation for a variable such as velocity then has the form

$$v(z,t) = \sum_{n=1}^{\infty} D_n(t) F_n(z) \tag{4}$$

where D_n (t) is the amplitude of the nth normal mode at time t. The $F_n(z)$ are usually normalized in a depth averaged sense by dividing by

$$\left[\frac{1}{H}\int_{-H}^{0} F_n^2(z)dz\right]^{\frac{1}{2}} \tag{5}$$

This makes the set orthonormal

$$\int_{-H}^{0} F_m F_n = \delta_{m,n} \tag{6}$$

where $\delta_{m,n}$ is the Kroneker delta, so that

$$\frac{1}{H}\int_{-H}^{0} v^2(z,t)dz = \sum_{n=1}^{\infty} D_n^2(t) \tag{7}$$

Then, the square of each $D_n(t)$ is the instantaneous depth-integrated kinetic energy. The utility of any modal representation lies in the fact that mesoscale currents usually have most of their energy in a few vertical modes and the above summation can be truncated after relatively few terms.

A mean stability profile for the entire Gulf of Mexico was determined from historical data in the following manner. The Levitus (1982) climatological data set provides mean values for temperature and salinity at standard depths for each one degree square in the world ocean. The data for the Gulf of Mexico were extracted and edited. Squares with instabilities in their mean density profiles were eliminated. The potential density profile referenced to 3000 m ($\sigma_3(z)$) was calculated for each one degree square. A set of σ_3 values was chosen that had increasing resolution for higher (deeper) ranges, and the depth of each one was determined by interpolation (i.e., $z(\sigma_3)$ was interpolated from $\sigma_3(z)$) for each one degree square. Thus the depth (topography) of each

σ_3 surface was determined for the Gulf. The average depth of each surface, $z_{avg}(\sigma_3)$, was then computed, and finally, $\sigma_{3avg}(z)$ was interpolated from $z_{avg}(\sigma_3)$. The net result is a Gulf-wide mean (i.e., ''leveled'') vertical density profile from which the mean stability profile ($N_{avg}(z)$) was then computed using Equation (1). Below 2000 m, the values for $N_{avg}(z)$ differed slightly from those of Nowlin (1972), which are based on the best available Gulf-wide data for the basin waters, and so Nowlin's values were substituted below 2000 m. Figure 4.4-23a shows the profile of $N_{avg}(z)$. The peak value of 14.4 cycles hour^{-1} at 25 m is a result of the ''leveling'' process, which, in essence, spreads the less dense shelf waters into a shallow layer over the whole Gulf. The advantage of this approach is that the mean stability profile represents the basic state for the entire Gulf. Differences between this basic state and the stability actually observed at any location and time are perturbations which are responsible for the baroclinic component of motion (The mean flow is also a perturbation about the basic rest state in this approach).

Equation (2) for the vertical structure functions ($F_n(z)$) was then solved numerically by means of the computer code ''SLEIGN'' (Bailey, 1978). The structure functions of the barotropic and first three baroclinic modes, F_0, F_1, F_2 and F_3 were determined for each of the mooring depths and are shown in Figure 4.4-23b-d. The value of F_0 is constant (equal to one after normalization) and hence its horizontal velocities are independent of depth. The mode number of each of the baroclinic modes corresponds to the number of times it crosses zero. Note that in the deep layers, the amplitudes of the baroclinic modes are not zero; they have a small but finite value. In the framework of quasigeostrophic dynamics, baroclinic modes have zero vertically integrated horizontal mass flux, so the area between vertical axis and the positive portions of a given curve must be compensated by an equal area between the vertical axis and the negative portions of the curve. When the water depth is 3000 m, the baroclinic modal amplitudes below the deepest zero crossing increase to a small constant value in the homogenous region below about 2000 m, where there can be no vertical shear. The amplitude of F_1 in Figure 4.4-23b is 3.48 at the surface, -0.55 at 1500 m, and -0.57 at 3000 m. The absolute ratio of surface to deep amplitudes is about six, so if the surface speed of the first baroclinic mode is in the range of 30 to 40 cm s^{-1}, which is the dominant speed range in Figure 4.4-3a, it is about five to seven cm s^{-1} in the deep layers. Nowlin (1972) computed the geopotential anomaly of the 1000db surface relative to 1500db and found relative current speeds generally less than 10 cm s^{-1}. As indicated in Equation (3), each eigenvalue of Equation (2) corresponds to the Rossby radius of deformation for that mode. The Rossby radii of the first three baroclinic modes for each location are listed in Table 4.4-4. For comparison, the first baroclinic Rossby radius of deformation in the MODE region of the Atlantic Ocean is about 46 km (Flierl, 1978), which has a latitude and stability profile similar to that in the Gulf. In the Drake Passage of the Southern Ocean, where the stratification is weak, and the value of the Coriolis parameter larger (Inoue, 1985) this radius of deformation is seven to 17 km. The distances between Moorings GG and FF and between Moorings FF and EE are 120 km and 80 km, repsectively. This

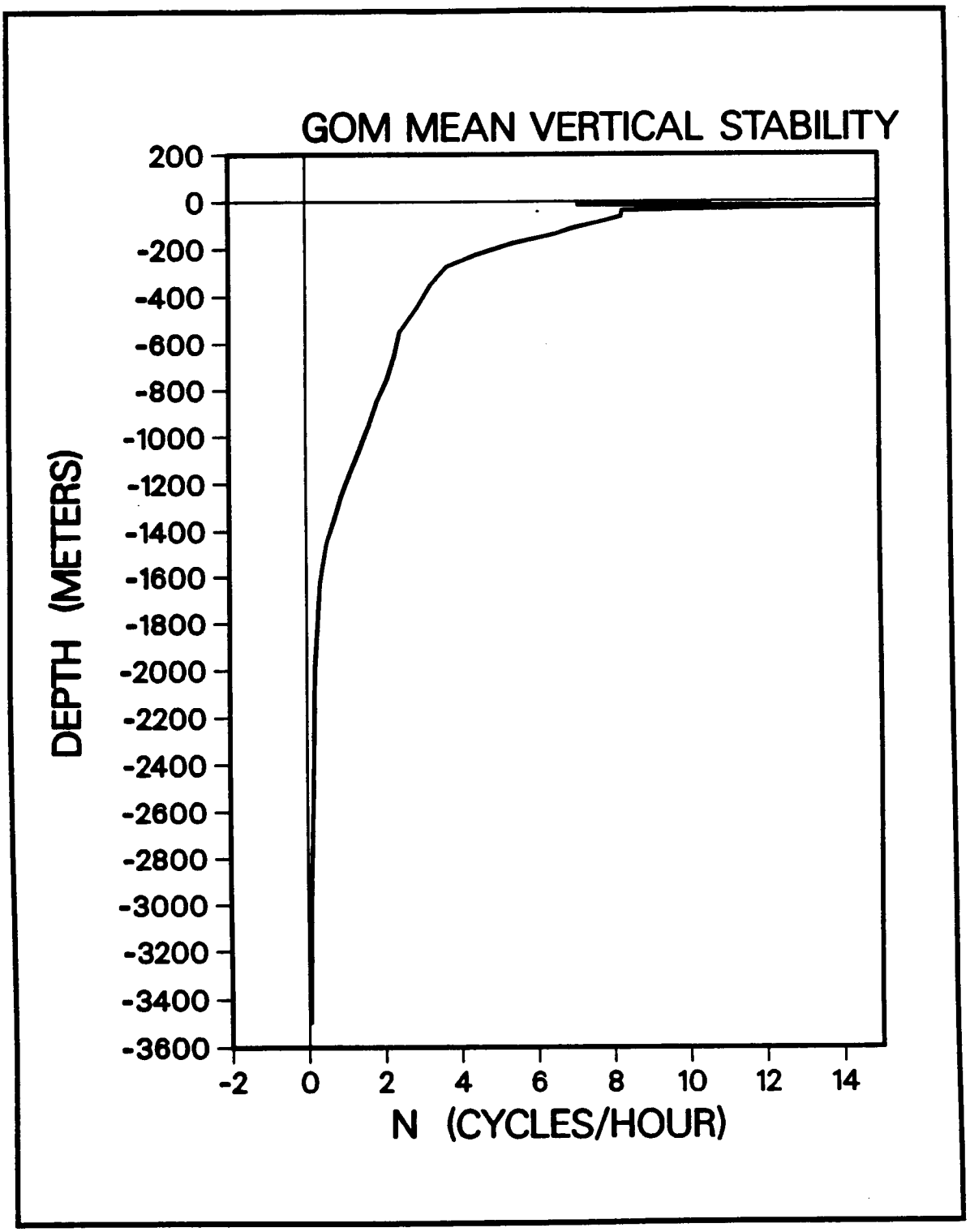

Figure 4.4-23a. Gulf of Mexico mean vertical stability profile.

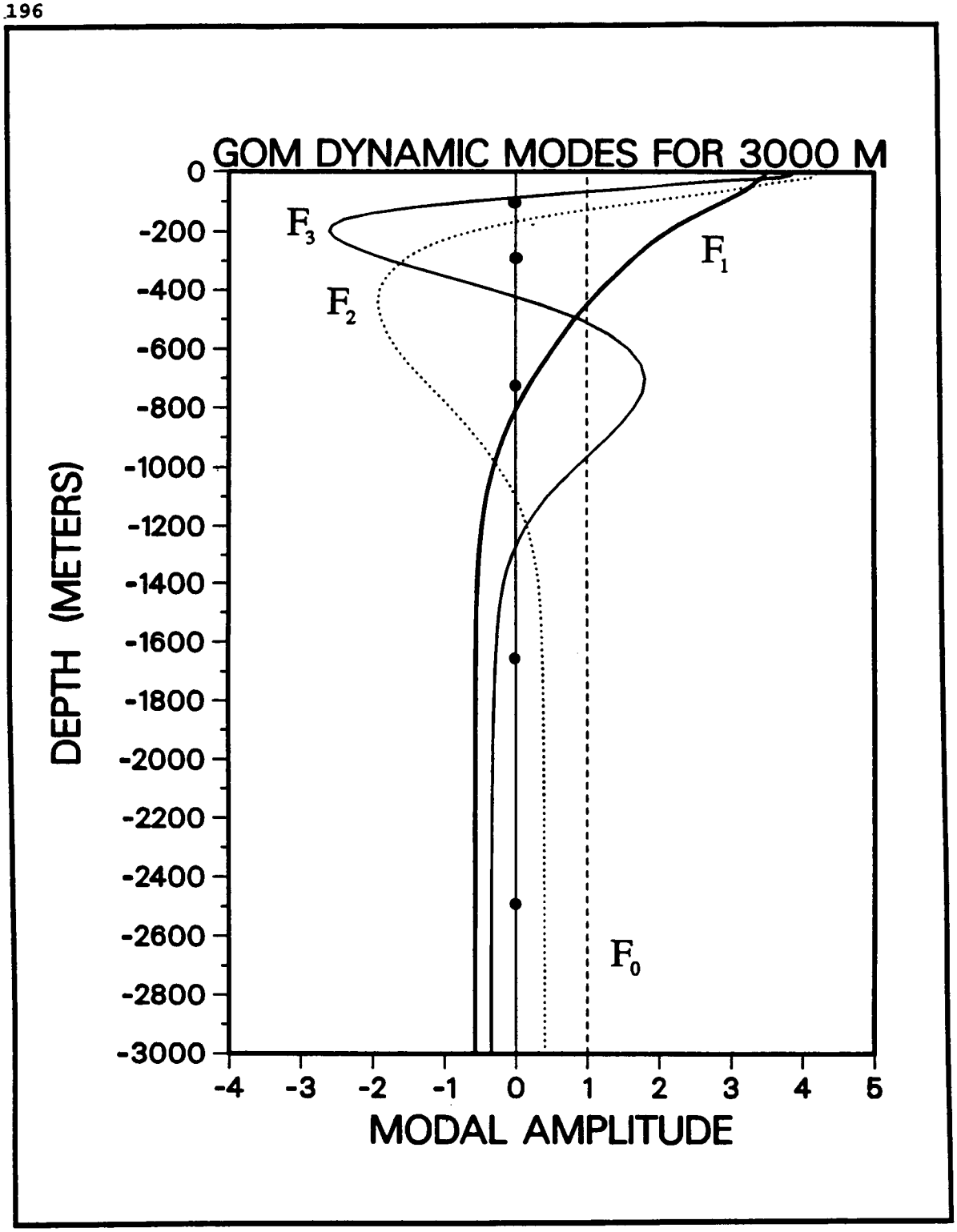

Figure 4.4-23b. Gulf of Mexico modal structure functions for the barotropic (F_0) and first three baroclinic modes (F_1, F_2 and F_3) for Mooring GG. The solid dots on the vertical axis indicate the depths at which current meters were located.

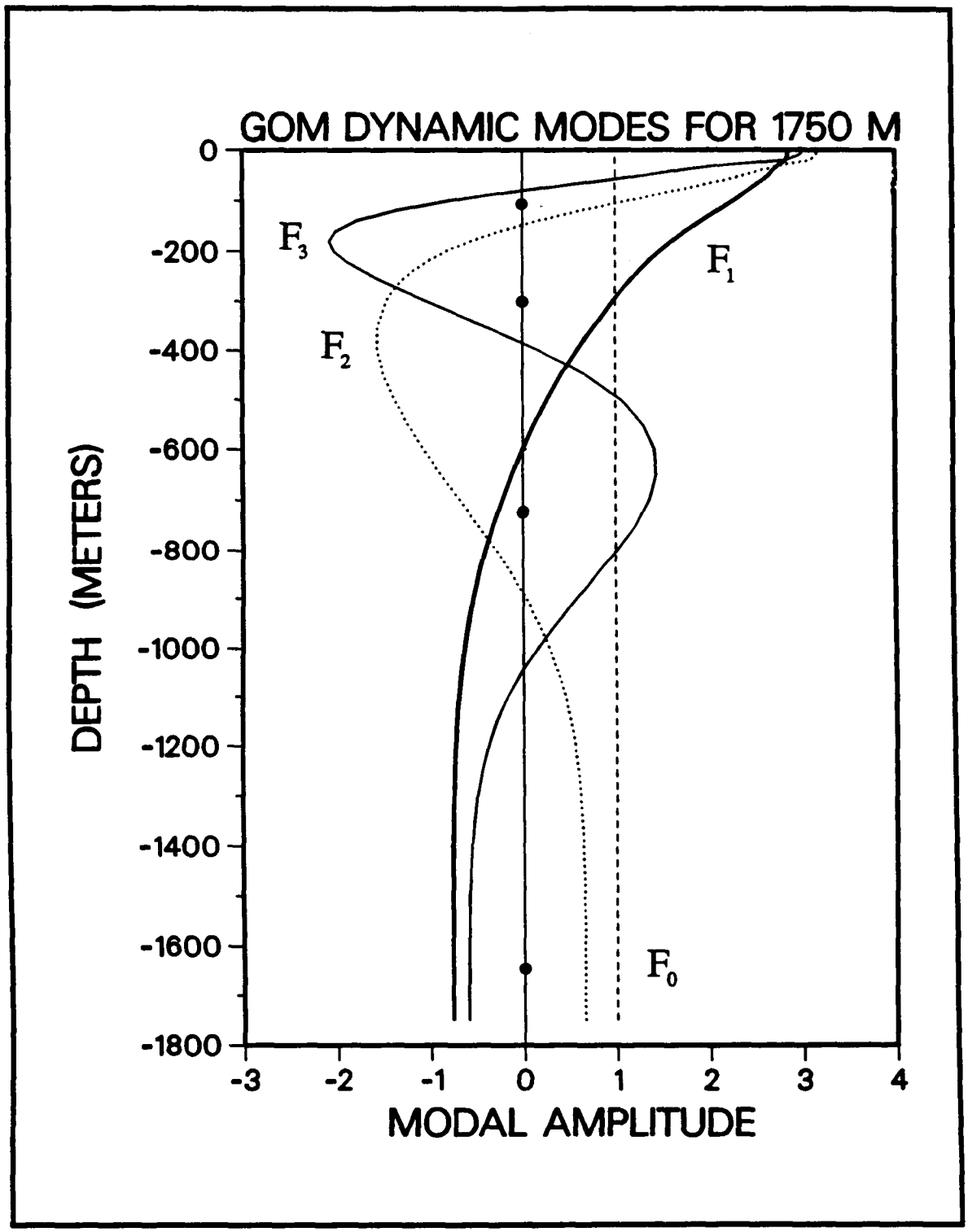

Figure 4.4-23c. Gulf of Mexico modal structure functions for the barotropic (F_0) and first three baroclinic modes (F_1, F_2 and F_3) for Mooring FF. The solid dots on the vertical axis indicate the depths at which current meters were located.

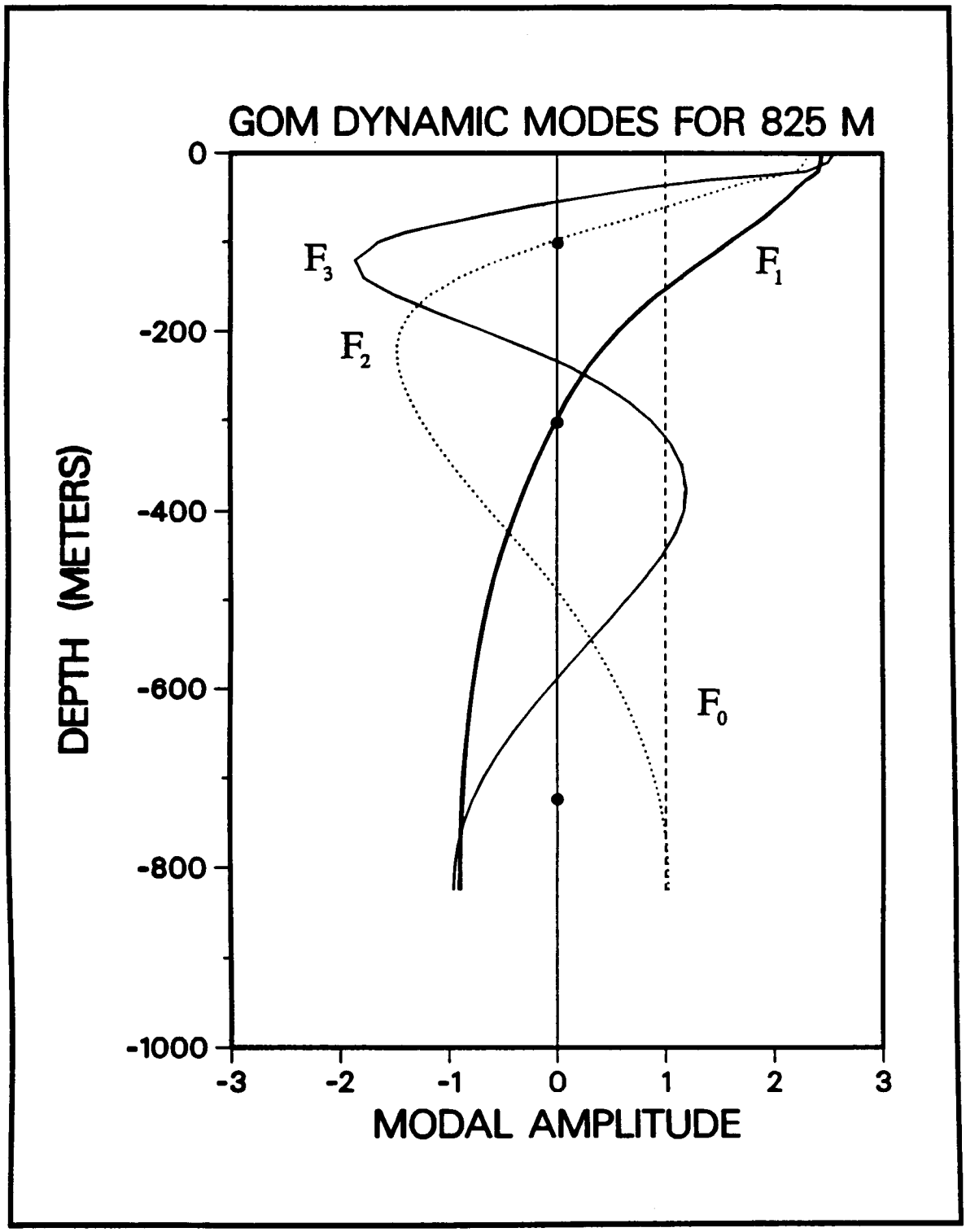

Figure 4.4-23d. Gulf of Mexico modal structure functions for the barotropic (F_0) and first three baroclinic modes (F_1, F_2 and F_3) for Mooring EE. The solid dots on the vertical axis indicate the depths at which current meters were located.

Table 4.4-4. Rossby radii for the first three baroclinic modes.

Depth	Mooring	R_{d_1}	R_{d_2}	R_{d_3}
3000m	GG	40.0km	20.6km	13.1km
1750	FF	35.5	19.1	12.3
825	EE	26.9	14.2	9.5

is 2.5 to three times the local first baroclinic Rossby radius. Low coherences might, therefore, be expected between the moorings.

The zero of the first mode for 3000 m water depth is located at about 800 m (Figure 4.4-23b). Above this point the F_1 velocity increases almost linearly to the surface, while below about 1200 m it is constant. This result is consistent with the depth of the zero point estimated from the time-series plots of current. The zeros of the first mode for Moorings EE and FF lie at 300 m and 600 m, respectively. The vertical structure of the first baroclinic mode at each mooring is consistent with the characteristics observed in the time-series plots. They exhibit a somewhat linear decrease in speed with little change in direction down to a depth corresponding to the zero point of the first baroclinic mode and then a fairly constant speed with depth and, frequently, a reversal in direction. The location of the current meters relative to the zero point of the first mode will affect the results of cross-spectral analyses. The current from an instrument at or near a zero point cannot be expected to be very coherent with one well above the zero point on a different mooring, as, for example, in the case of MEE2 and MFF2. Both are at 300 m, but the former is at the zero point of the first baroclinic mode for the location of the mooring, whereas the latter is well above its corresponding zero point.

The next step is to decompose the current records using the modal shapes in Figure 4.4-23b-d so as to determine the amplitudes of the D_n in Equation (4) as a function of time. From a time series plot of the D_n, one can then see the relative strengths of the barotropic and baroclinic parts during the major events. Although the modes are orthogonal in the continuous sense of Equation (6), they do not necessarily satisfy a discrete analog of Equation (6). If z_j are the specified sampling depths it may be that

$$\sum_{j=1}^{J} F_n\left(z_j\right) \neq \delta_{m,n} \qquad (8)$$

Therefore, the orthogonality properties cannot be used to determine the D_n as is usually done, for example, in the case of Fourier transforms. Instead a least squares method is used that minimizes the error

$$\sum_{j=1}^{J}\left[v(z_j,t)-\sum_{n=1}^{N}D_n(t)F_n(z_j)\right]^2 \qquad (9)$$

The depths of the current meters on the moorings, indicated by the dots on the vertical axis in Figures 4.4-23b-d, are well placed to resolve at least the first two baroclinic modes at Moorings GG and FF and the first mode at Mooring EE.

Period IV data were analyzed first in order to investigate the effect of using successively two to four modes in the decomposition of the U and V components. The maximum number of modes that can be fit is one less than the number of depths at which there are current observations, in order to have one degree of freedom and a residual that can be used to judge the quality of the fit. The amplitudes for D_0, D_1, D_2 and D_3 are shown in Figure 4.4-24a,b. The sign convention for the amplitudes follows that of the currents. Thus, a positive barotropic V-component flows eastward; a positive first baroclinic amplitude for the V-component signifies positive shear such that surface layer flows eastward while the bottom layer flows westward. The actual velocity in cm s^{-1} of any component at any instant and depth may be found by multiplying the value of D_n at that instant by the value of F_n for that depth (Figure 4.4-23b-d). Since the magnitude of F_0 is a constant of value one, the amplitude of D_0 gives the barotropic velocity directly. It is readily seen that the amplitudes of the barotropic mode D_0 and the first baroclinic mode D_1 are much larger than the amplitudes of the second and third baroclinic modes throughout the records of both U and V (Figure 4.4-24a,b). An estimate of the relative square residual left after fitting a given number of modes to the data series is given by

$$r(z_j,t_k)=\left[\frac{\left[v(z_j,t_k)-\sum_{n=1}^{N}D_n(t_k)F_n(z_j)\right]^2}{\frac{1}{K}\sum_{k=1}^{K}v^2(z_j,t_k)}\right] \qquad (10)$$

where K is the number of time samples. An overall or mean square residual is found by taking the time and depth average of Equation (10). Table 4.4-5 lists the residuals calculated for two, three and four mode fits to data set GG3. Although the barotropic and first baroclinic modes dominate, the contribution of the second baroclinic mode is not negligible, since including it significantly reduces the residual. The amplitude of the second mode is largest in early September 1988, rising to 30-50% of the value of the first mode when Eddy F makes its closest approach to Mooring GG. The third mode, however, contributes very little to the overall fit.

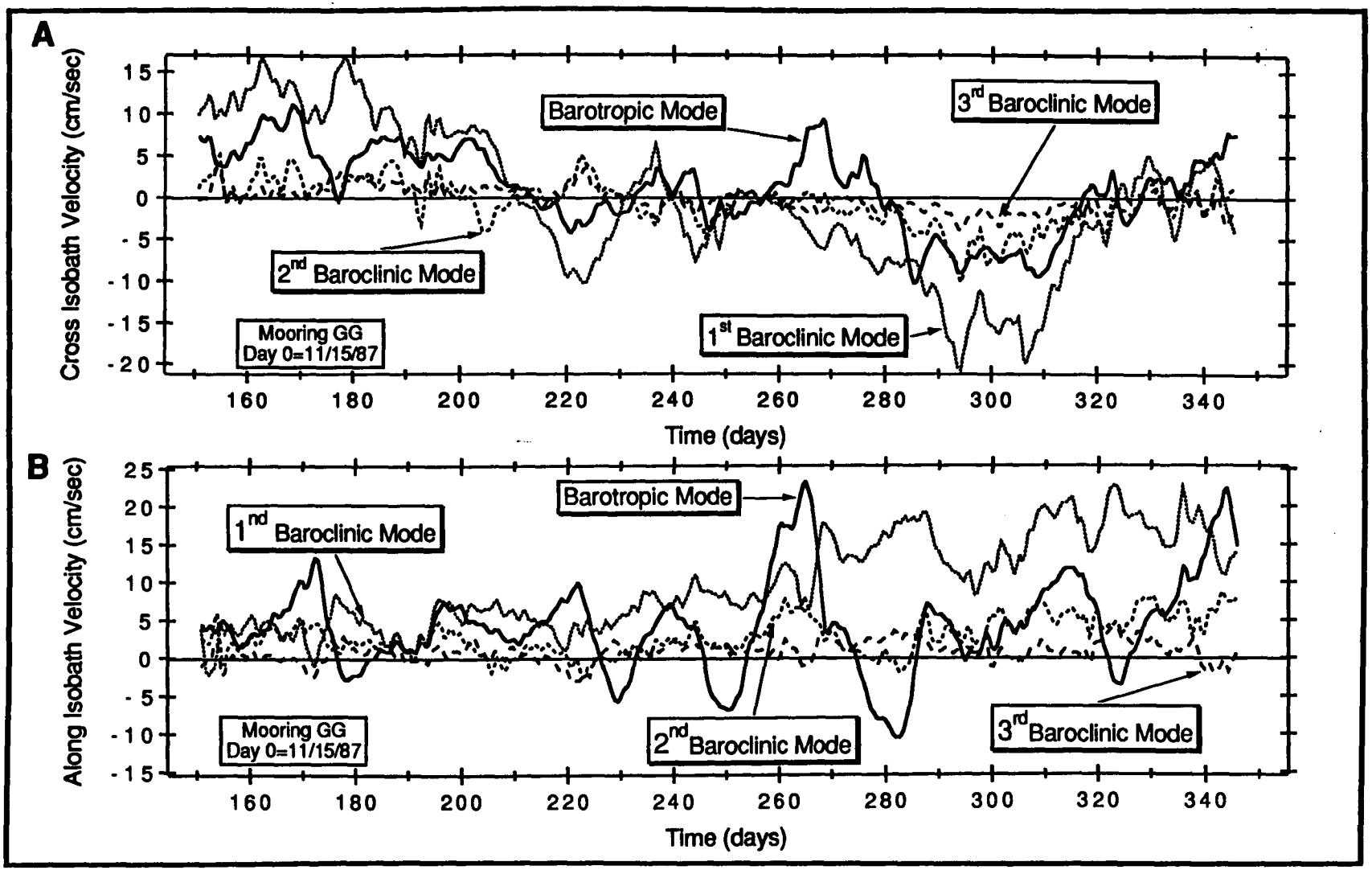

Figure 4.4-24. Amplitudes of the barotropic (D_0) and first three baroclinic modes (D_1, D_2 and D_3) at Mooring GG for the period from April 14, 1988 through October 26, 1988 (Period IV) for the (a) U component (cross isobath component) of current velocity and (b) V component (along isobath component) of current velocity.

Table 4.4-5. Relative mean square residuals after fitting the given number of modes.

Data Set	No. of Modes	Percent Relative Mean Square Residual U	V
GG3	2	17.3	17.1
GG3	3	9.4	2.6
GG3	4	5.4	1.5
GG2/3	3	14.6	3.8
FF2/3	3	32.0	20.8
EE2/3	2	25.0	9.2

The amplitude of the first baroclinic mode of the U and V components begins to signal the arrival of Eddy F on about August 8, 1988 (Day 267, Figure 4.4-24). For the V component it increases rapidly to about 19 cm s^{-1} (positive means eastward), while the U component begins a gradual increase in the negative direction (northward). The U component reverses to positive (southward) on October 6, 1988 (Day 326, in Figure 4.4-24a) whereas the V component remains positive to the end of the record. The pattern of signs indicates that the northern side of the baroclinic part of the eddy crossed Mooring GG. Peak values of U and V for the amplitude of the first mode are -21 cm s^{-1} and 22 cm s^{-1}, respectively. Multiplying by $F_1(z)$ gives the current of the first mode at a specific depth. Thus, peak values of the first mode at the surface are -73.1 for U and 76.6 for V. At the bottom they are 12.0 for U and -12.5 for V.

The V component of the barotropic mode reaches a maximum value of 23 cm s^{-1} (eastward) on August 6, 1988 (Day 265 in Figure 4.4-24b), just before the onset of the baroclinic signal of Eddy F. The barotropic current at the bottom has the same value since F_0 equals one at all depths. The barotropic V component changes to westward on August 15 (Day 274) and then becomes mostly eastward again and rises to 22 cm s^{-1} on October 24, 1988 (Day 344). The barotropic U component is southward until August 20 (Day 279), northward until September 27 (Day 317), and then southward again. The combination of the U and V components does not indicate a single large barotropic eddy, coaxial with the baroclinic one. However, one possible interpretation of the barotropic data is that an eddy pair, rotating in opposite directions, crossed the mooring. The leading eddy would be cyclonic and the trailing one anticyclonic. The line representing the path the mooring would trace across the pair as they move by would cut diagonally from the southwest region of the leading cyclone to the northeast region of the trailing anticyclone. Figure 4.4-25a shows the stick vectors for the barotropic mode at Mooring GG for the period July 20, 1988 through October 26, 1988. The stick vectors were produced by combining the U and V components shown in Figure 4.4-24. Figure 4.4-25b shows the hypothetical vortex pair and line of movement. This construct would explain the pattern of the U component well but it is a little strained in accounting for the variations exhibited by the V

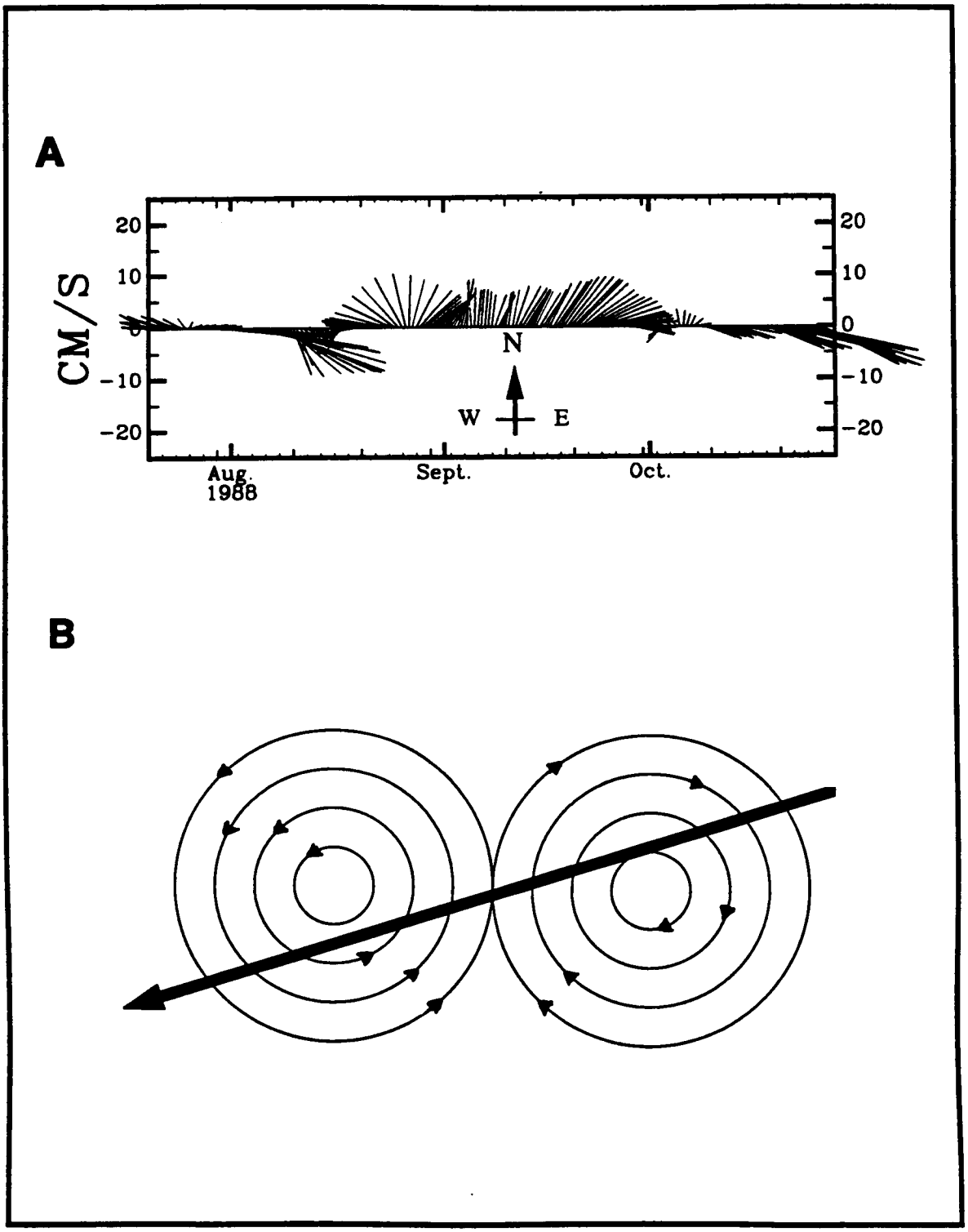

Figure 4.4-25. Cartoon showing (a) stick vectors for the barotropic mode of current at Mooring GG for the period from July 20, 1988 through October 26, 1988 and (b) a hypothetical vortex pair that would produce a time series of current velocity similar to that shown above, if it moved across a fixed mooring in the direction shown by the heavy line.

component, but plausible, especially if the path were not quite a straight line. It is also suggested that the barotropic eddy pair is not independent of the baroclinic eddy, but rather coupled to it. The currents recorded at Mooring R in 1985 (SAIC, 1988) exhibited a pattern quite like that described here, as the leading half of a Loop Current anticyclone (Eddy B) approached Mooring R. The possible observation of a barotropic vortex pair that is coupled to a Loop Current anticyclone lends some support to a similar and rather robust result of numerical models (e.g., Smith, 1986; Wallcraft, 1986).

The modal decomposition was also performed on the set of currents at each mooring that were continuous for the 300-day period from November 15, 1987 through September 1, 1988. Three modes were fit to the data of Mooring GG and the results are shown in Figures 4.4-26. The residuals are listed in Table 4.4-5. For Mooring GG, the residuals for the three-mode fit with only four instrument levels (the data from 1650 m is omitted) are higher than for the three-mode fit with five instrument levels. The time series of the barotropic and first baroclinic modes are visually uncorrelated for both U and V components, and, indeed, the cross-spectral analysis between the modes (not shown) was incoherent except for the U component at the lowest frequencies resolved. This means that the two modes are independent. Modes can become coupled, or linearly dependent, through non-linear interaction and through the effects of changing bottom topography. Nonlinearity should be generally small for Mooring GG for the time period of this study. The Rossby number, U/fL, has an upperbound of about 0.2 for the case of a U of 100 cm s^{-1} and an L of 50 km, which is an upperbound on the internal Rossby radius of deformation. Since the modes are uncoupled, topographic effects also appear to be insignificant at Mooring GG. This is not the case for Moorings FF and EE, as shown below. For March 12, 1988 (Day 118) to May 3, 1988 (Day 170), the influence of Eddy E can be seen mostly in the barotropic and baroclinic modes of the U component. Both of them remain positive during the period of influence, which means southward flow in the upper layers. The modes of the V component are generally smaller. These results suggest that Eddy E passed well south of Mooring GG and then moved northward. Thus, only the eastern side of it affected the currents at Mooring GG, resulting in persistent southward flow. The cold core cyclone's effects between May 24 and July 8, 1988 are also seen principally in the first baroclinic mode of the U component. Flow in the upper layer is first southward and then northward.

Figure 4.4-27 shows the results of a three-mode decomposition for the four levels of current meter data for Mooring FF. The residual for the U component (Table 4.4-5) is a large 32%. The barotropic and first baroclinic modes are coupled, which is to be expected because U is the cross-isobath component. Cross-spectral analysis demonstrates strong coherence at all frequencies below 0.1 cpd and in the 0.3 to 0.5 cpd band. The fit for the V component produces a more reasonable residual, but the coherence of the cross spectra between the modes, although less marked than that of the U component, is significant at 0.25 cpd, 0.1 cpd and below 0.05 cpd. Since the modes are coupled, a question is 'which mode is driving which?' This is difficult to decide with the given data. The topographic coupling is related in part to the along isobath gradient

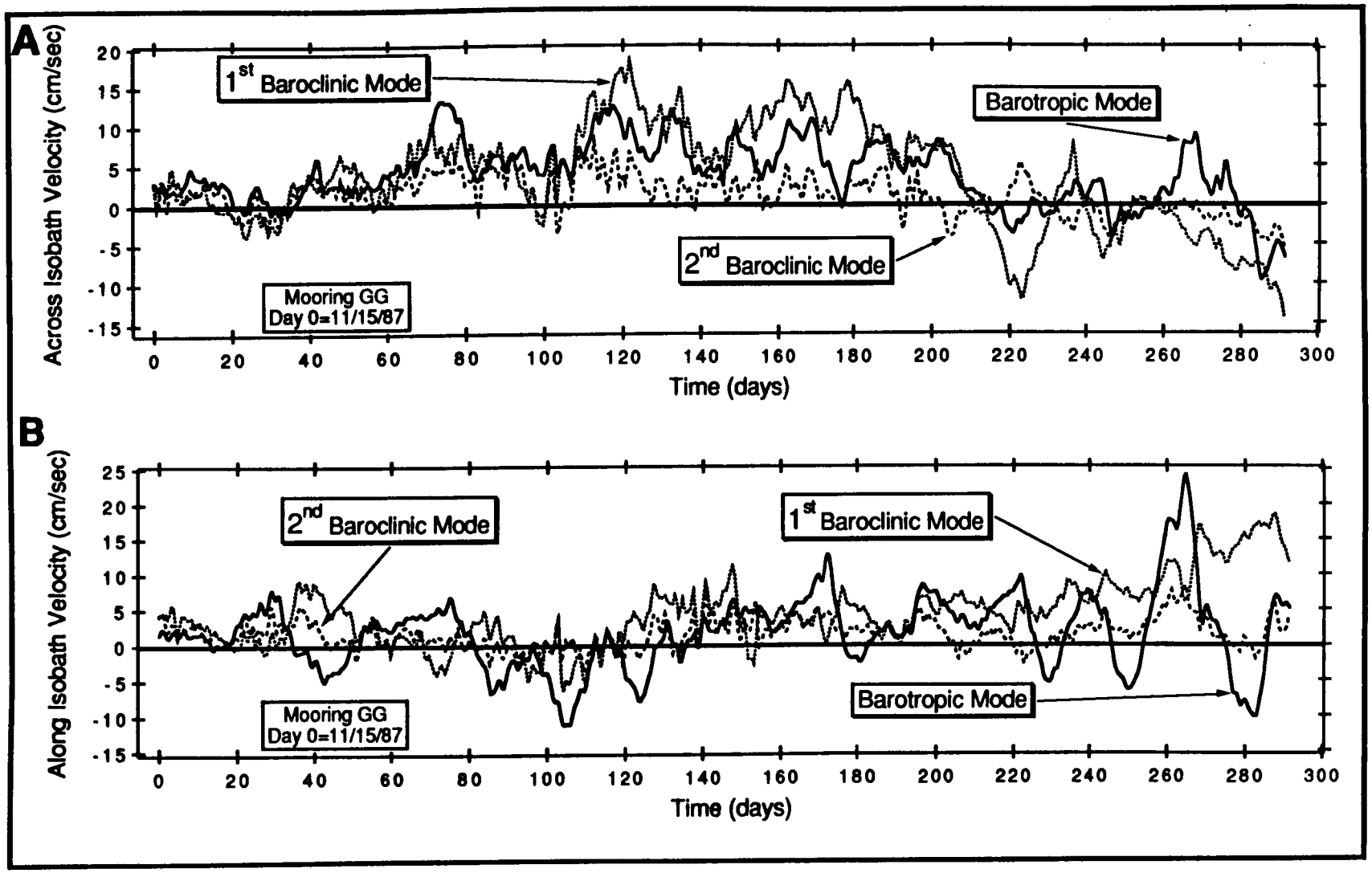

Figure 4.4-26. Amplitudes of the barotropic (D_0) and first two baroclinic modes (D_1 and D_2) at Mooring GG during the period from November 15, 1987 through September 1, 1988 (Period III) for (a) the U component (cross isobath component) of current velocity and (b) the V component (along isobath component) of current velocity.

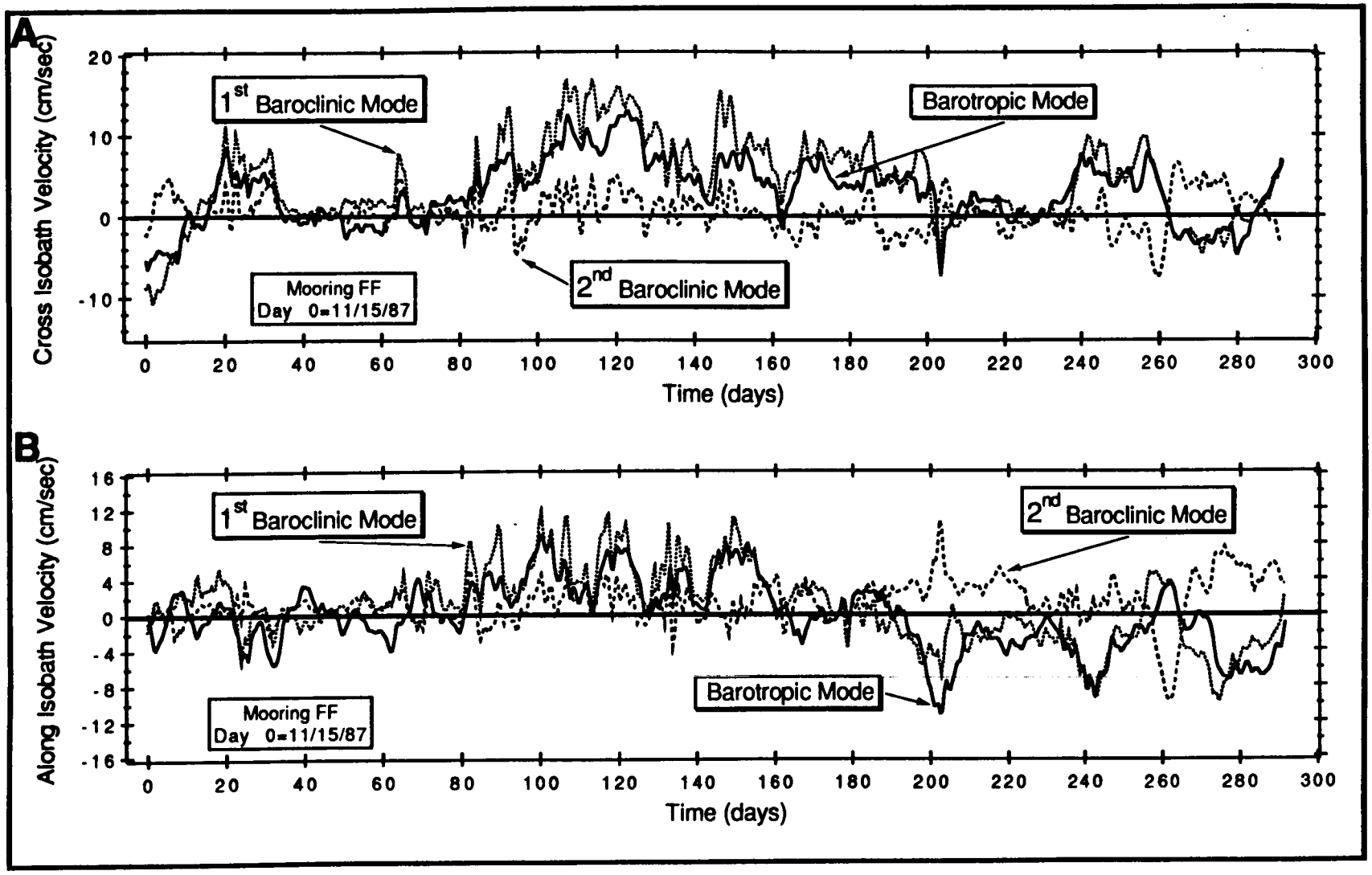

Figure 4.4-27. Amplitudes of the barotropic (D_0) and first two baroclinic modes (D_1 and D_2) at Mooring FF during the period from November 15, 1987 through September 1, 1988 (Period III) for (a) the U component (cross isobath component) of current velocity and (b) the V component (along isobath component) of current velocity.

of velocity which is not known. Also, the characteristic length scales are smaller over the slope, and the potential increases for nonlinearities to become more important. It is noted without comment that the amplitude of the barotropic mode is frequently about 3/4 that of the first baroclinic mode and that the value of $F_1(-H)$ is 0.76.

A two-mode fit to the three levels of currents at Mooring EE is shown in Figure 4.4-28. The residual is relatively large for the U component but small for the V component. The difference is probably attributable to differences in the degree of coupling as indicated by the coherence from the cross-spectral analysis (Figure 4.4-29). The most interesting aspect of the results for Mooring EE is that frequently the amplitude of the barotropic mode of the V component is larger than that of the first baroclinic mode and uncoupled from it. It is not known what is driving this barotropic mode, but the mode is clearly an important part of the V-component kinetic energy at this location on the slope.

4.4.3.4 Frequency Domain Description

4.4.3.4.1 Introduction

For the U, V and T time series of the 292-day (after filtering) data set, (Period III), cross spectral analysis was performed on each of the possible horizontal and vertical combinations for that variable. Combinations between variables and slant combinations (across depths between moorings) were excluded. The results of cross-spectral analysis between moorings at a given depth for each of the variables is basically that the variables are horizontally incoherent in all cases. Given that the moorings are separated by about 2.6 to three times the local Rossby radius of the first baroclinic mode, the lack of significant coherence is reasonable. Significant vertical coherence, however, was found for U and V between various depths on a given mooring. Below, representative U and V autospectra are described; then the vertical coherences are presented.

4.4.3.4.2 Autospectra

The 300 m level autospectra were selected as representative of the U and V data for the upper layer at each mooring (Figures 4.4-30 and 4.4-31), and the 2500 m level at Mooring GG was chosen to represent deep ones (Figure 4.4-32). All the autospectra are ''red'' in that they have most of their energy at the lowest frequencies, and energy decreases by two to three orders of magnitude between the lowest and highest frequencies resolved. This type of autospectrum is characteristic of time series that are dominated by aperiodic events of relatively long duration. The U components all exhibit some ''structure'', i.e., peaks and inflection points, between about 0.05 cpd and 0.15 cpd, as Figure 4.4-30 indicates, but there is no consistent or preferred frequency. Several autospectra, such as MEE2 (Figure 4.4-30a), have a maximum value at a peak at 0.025 cpd. For the V components (Figure 4.4-31), there is frequently a peak (MEE2) or an inflection point (MGG2) near 0.05 cpd and a peak near 0.1 cpd. These features are also found in the deep layer (Figure 4.4-32) in autospectra of both U and V components.

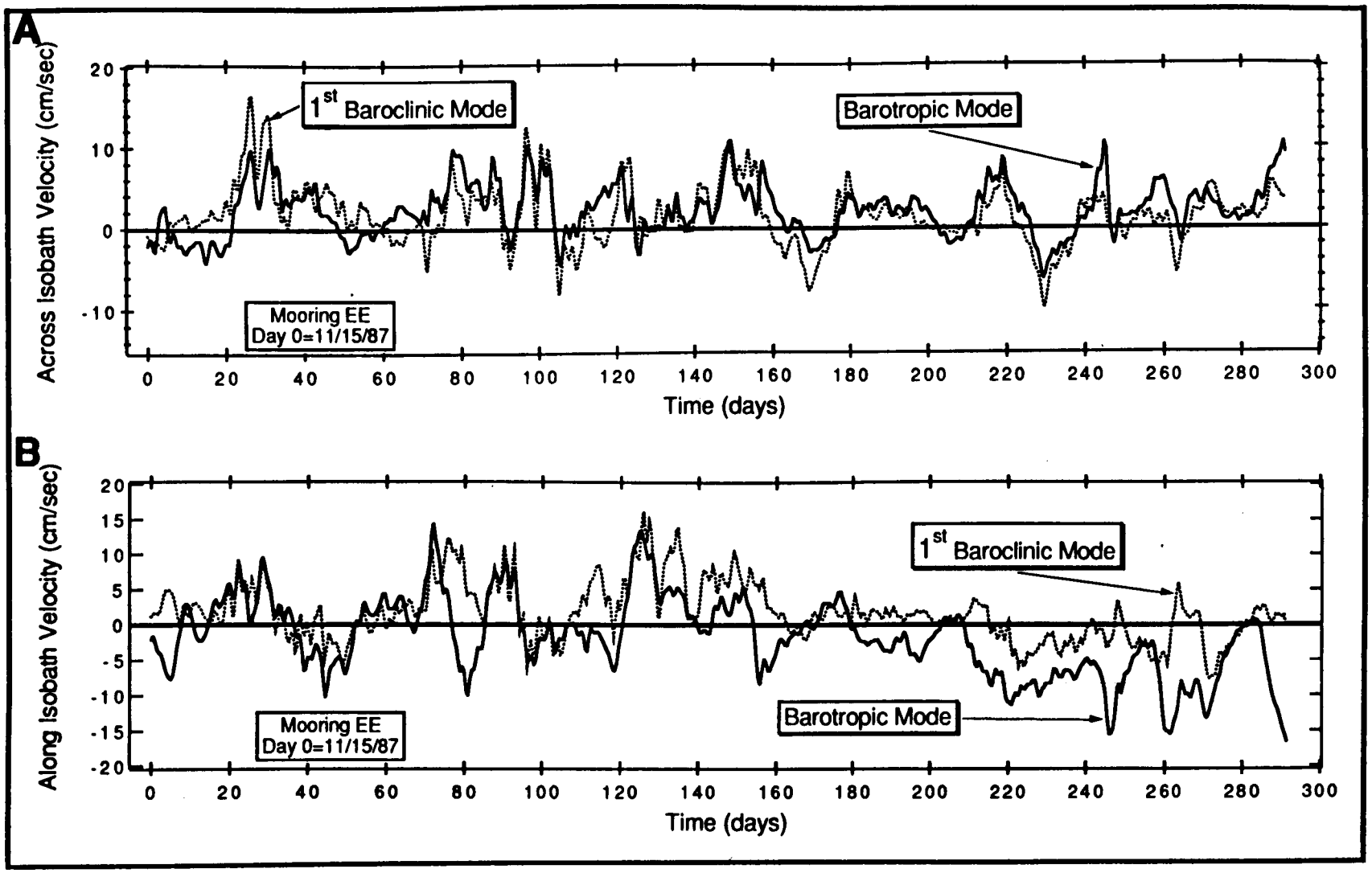

Figure 4.4-28. Amplitudes of the barotropic (D_0) and first baroclinic mode (D_1) at Mooring EE during the period from November 15, 1987 through September 1, 1988 (Period III) for (a) the U component (cross isobath component) of current velocity and (b) the V component (along isobath component) of current velocity.

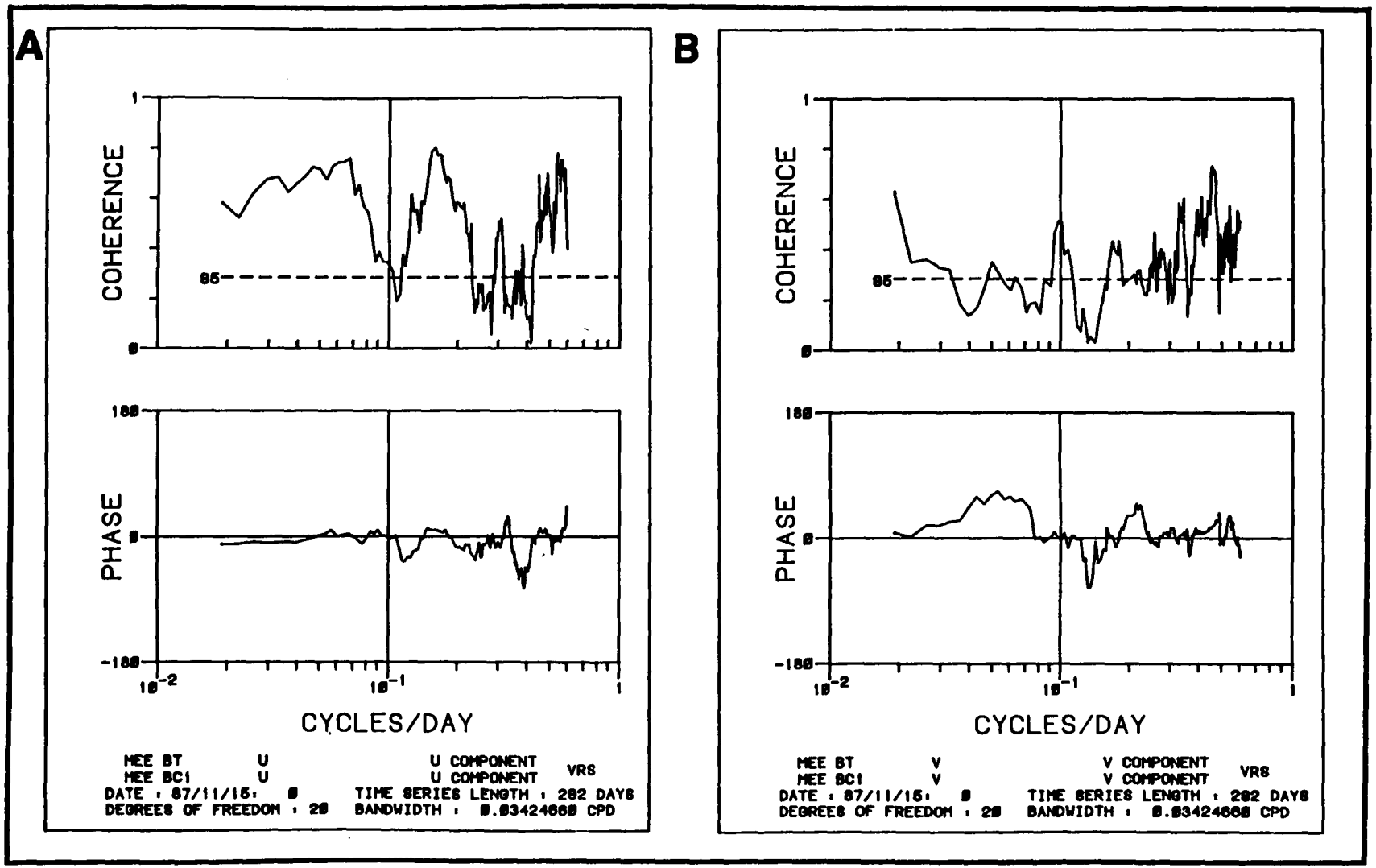

Figure 4.4-29. Spectral coherence between the barotropic and first baroclinic modes at Mooring EE for 292 days beginning on November 15, 1987 for the (a) U component of current velocity and (b) V component of current velocity.

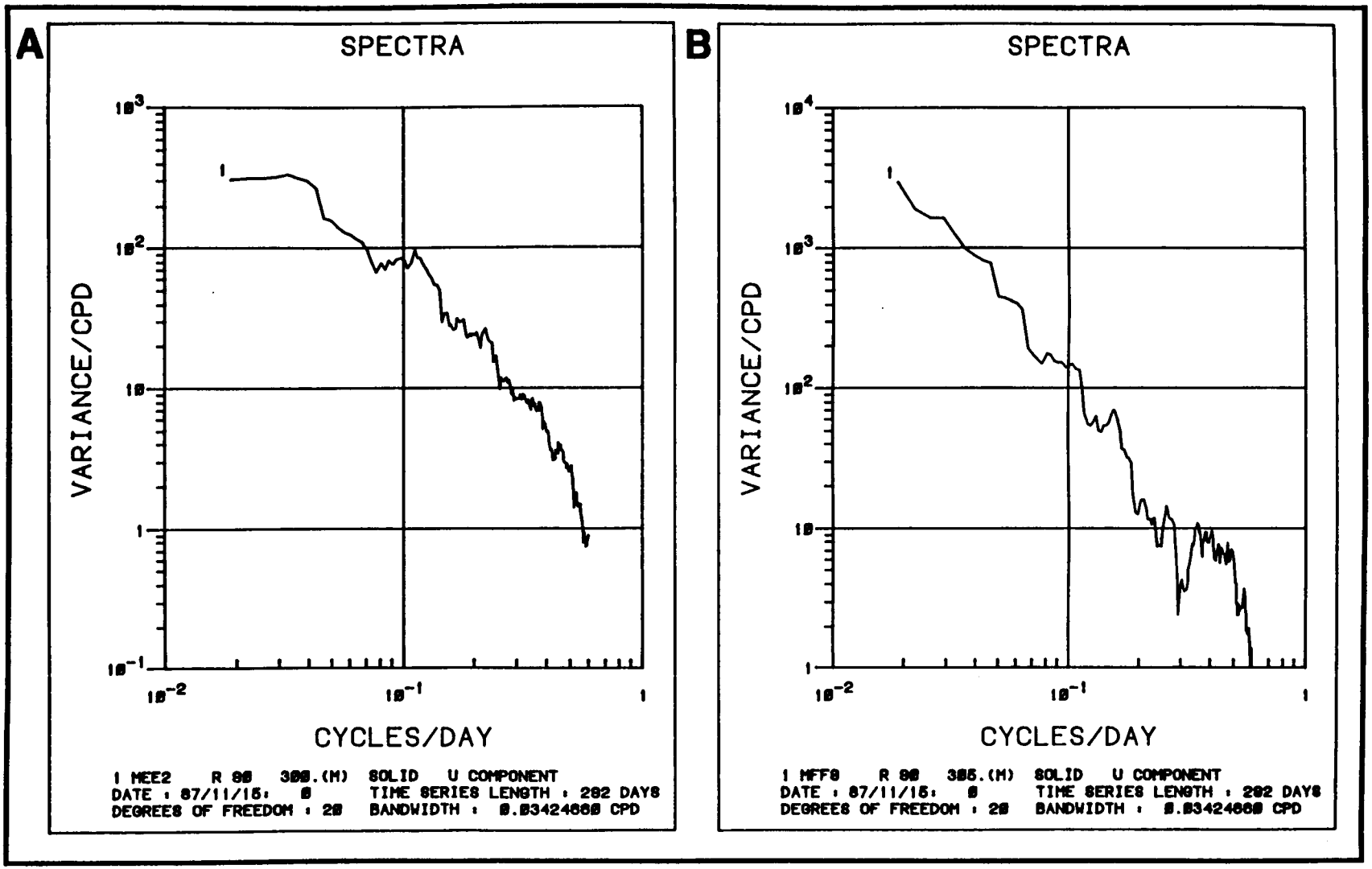

Figure 4.4-30a,b. Autospectra of the U component of current velocity at 300 m for 292 days beginning November 15, 1987 for (a) Mooring EE and (b) Mooring FF.

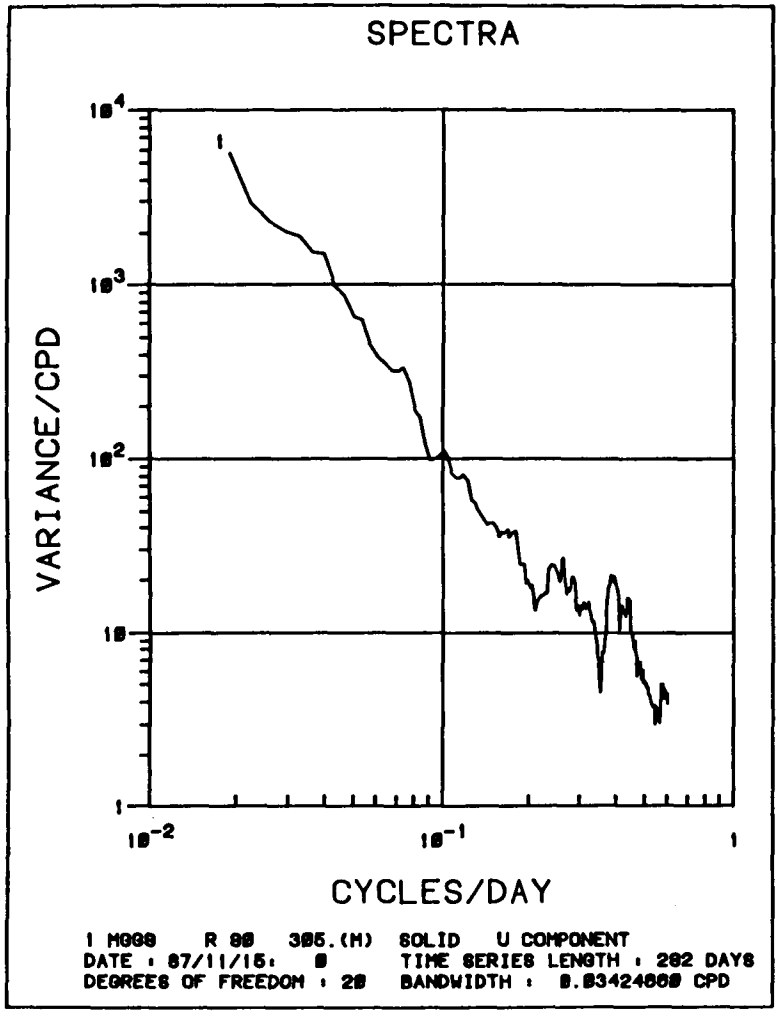

Figure 4.4-30c. Autospectrum of the U component of current velocity at 305 m for 292 days beginning November 15, 1987 for Mooring GG.

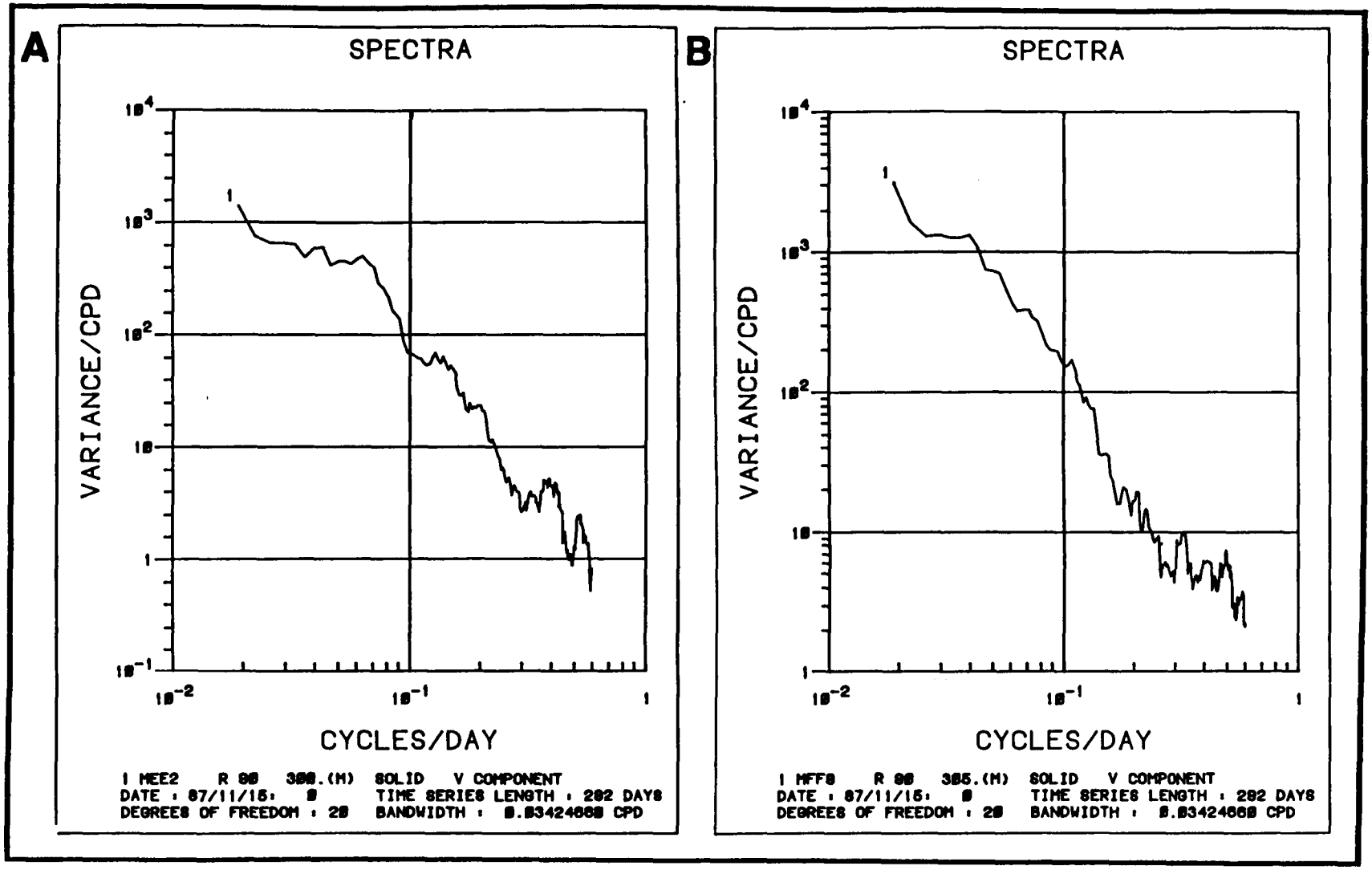

Figure 4.4-31a,b. Autospectra of the V component of current velocity at 300 m for 292 days beginning November 15, 1987 for (a) Mooring EE and (b) Mooring FF.

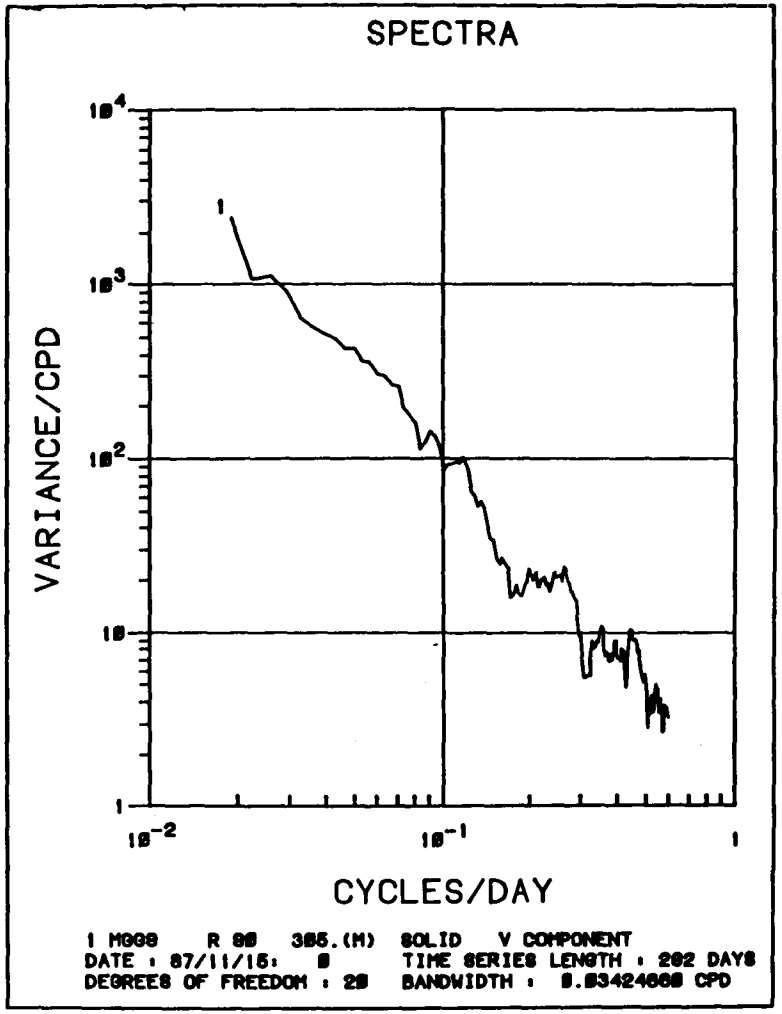

Figure 4.4-31c. Autospectrum of the V component of current velocity at 305 m for 292 days beginning November 15, 1987 for Mooring GG.

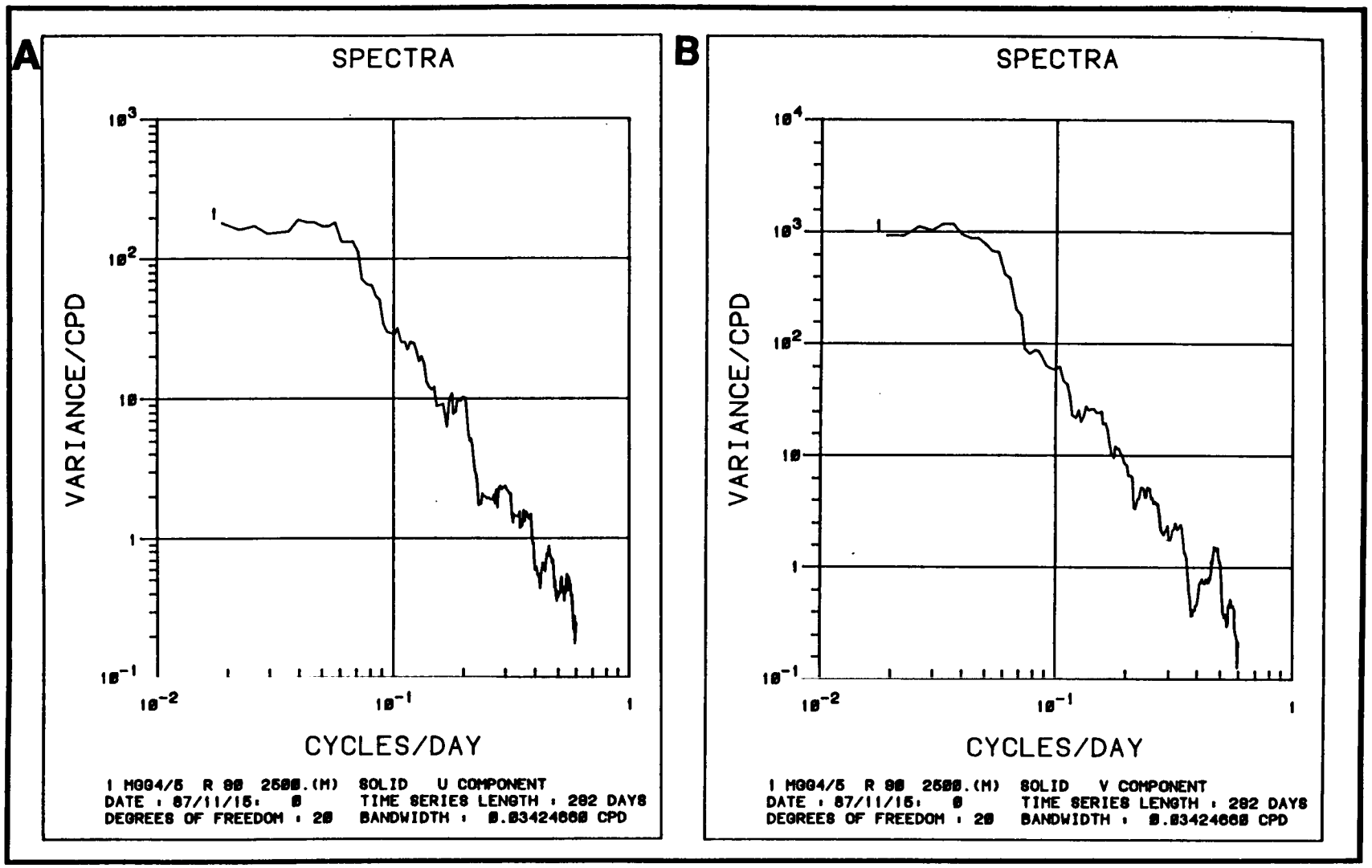

Figure 4.4-32. Autospectra of current velocity at 2500 m for Mooring GG for 292 days beginning November 15, 1987 for (a) the U component of current velocity and (b) the V component of current velocity.

4.4.3.4.3 Vertical Coherence of U and V

Figures 4.4-33 through 4.4-36 show a selected set of results of the phase and coherence squared (referred to hereafter as coherence) in the vertical direction for the U and V components. Within the upper layer, i.e., from the surface to the depth of the zero crossing of the first baroclinic mode, the most frequent pattern (Figure 4.4-33) is for the coherence to rise well above the 95% significance level at the lowest frequencies, drop below it near 0.04 cpd and then rise to a peak between about 0.05 and 0.1 cpd. Across the zero point, e.g., MFF2 versus MFF4 (not shown), both U and V components are typically incoherent, except for the V component at Mooring GG. In this latter, striking case, there is a strong peak of coherence at 0.05 cpd. Furthermore, the phase is not statistically different from zero. This particular result indicates the presence of a barotropic wave mode in the V component at Mooring GG.

4.4.3.4.4 Discussion

Moorings EE, FF and GG were located on the continental slope in order to study the processes that affect slope circulation, particularly in the presence of eddies. The moorings had current meters at three to five depths and the data return was excellent. The horizontal separation between moorings was equivalent to about three times the local Rossby radius of deformation. Because of the spacing between moorings and differences in bottom depth, a different dynamical regime governed the currents at each location; thus currents were relatively uncorrelated horizontally between moorings as various analyses demonstrated. The interpretation of the data, therefore, focused on their temporal and vertical spatial characteristics. The dominant ones were visually evident in comparative time-series plots of the currents and temperature. Eddies E and F and a cold-core eddy each passed close enough to Mooring GG to significantly influence its data records. The vertical structure of currents at each mooring was clearly barotropic during some periods, i.e., current velocity was relatively uniform from top to bottom. At other times, it was clearly baroclinic, i.e., current velocity decreased in magnitude from the surface to some depth, below which it reversed direction. Quasi-periodic fluctuations, with a period on the order of 20 days, were identifiable at times in a number of the records, particularly at Mooring GG. The analyses quantified these characteristics and brought out other less obvious ones.

Basic statistics and current roses demonstrated that the level of kinetic energy increased southward from Mooring EE to Mooring GG. Mean U components were southward at all moorings and depths, and the values increased southward, indicating mean divergence of this component. Despite the east-west orientation of the isobaths, currents with a significant southward component were frequent at all moorings and depths. At 100 m, mean V components were eastward at the three moorings. These values also increased southward, and, therefore, so did the horizontal shear of V. At Moorings EE and FF, mean V components below 100 m were westward. Because of the effect of eddies at Mooring GG, current speed at 100 m exceeded 40 cm s^{-1} about 40% of the time, and at 2500 m it exceeded 10 cm s^{-1} about 14% of the time.

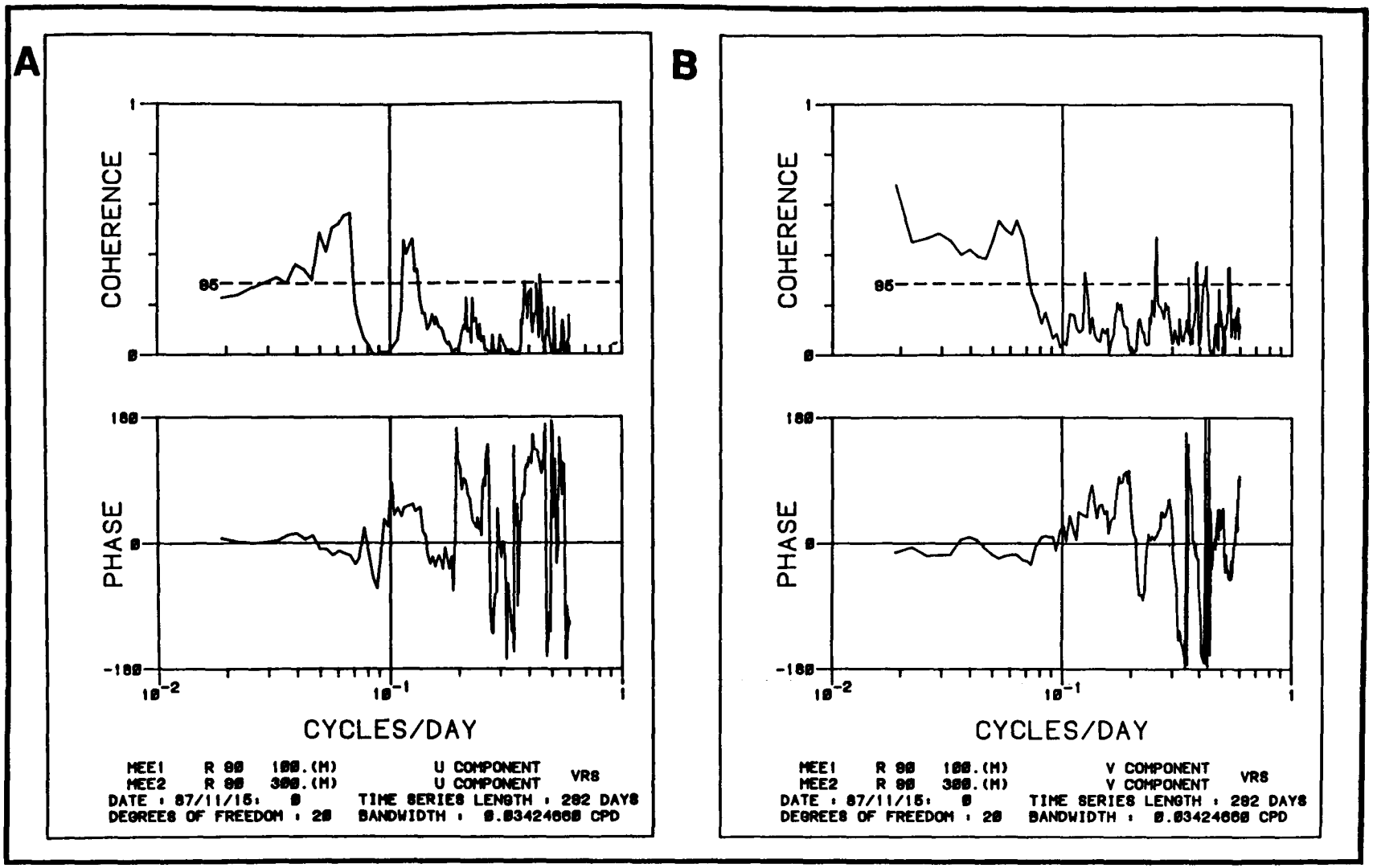

Figure 4.4-33. Phase and coherence squared at Mooring EE for 292 days beginning November 15, 1987 between (a) the U components of current velocity at 100 m and 300 m and (b) the V components of current velocity at 100 m and 300 m.

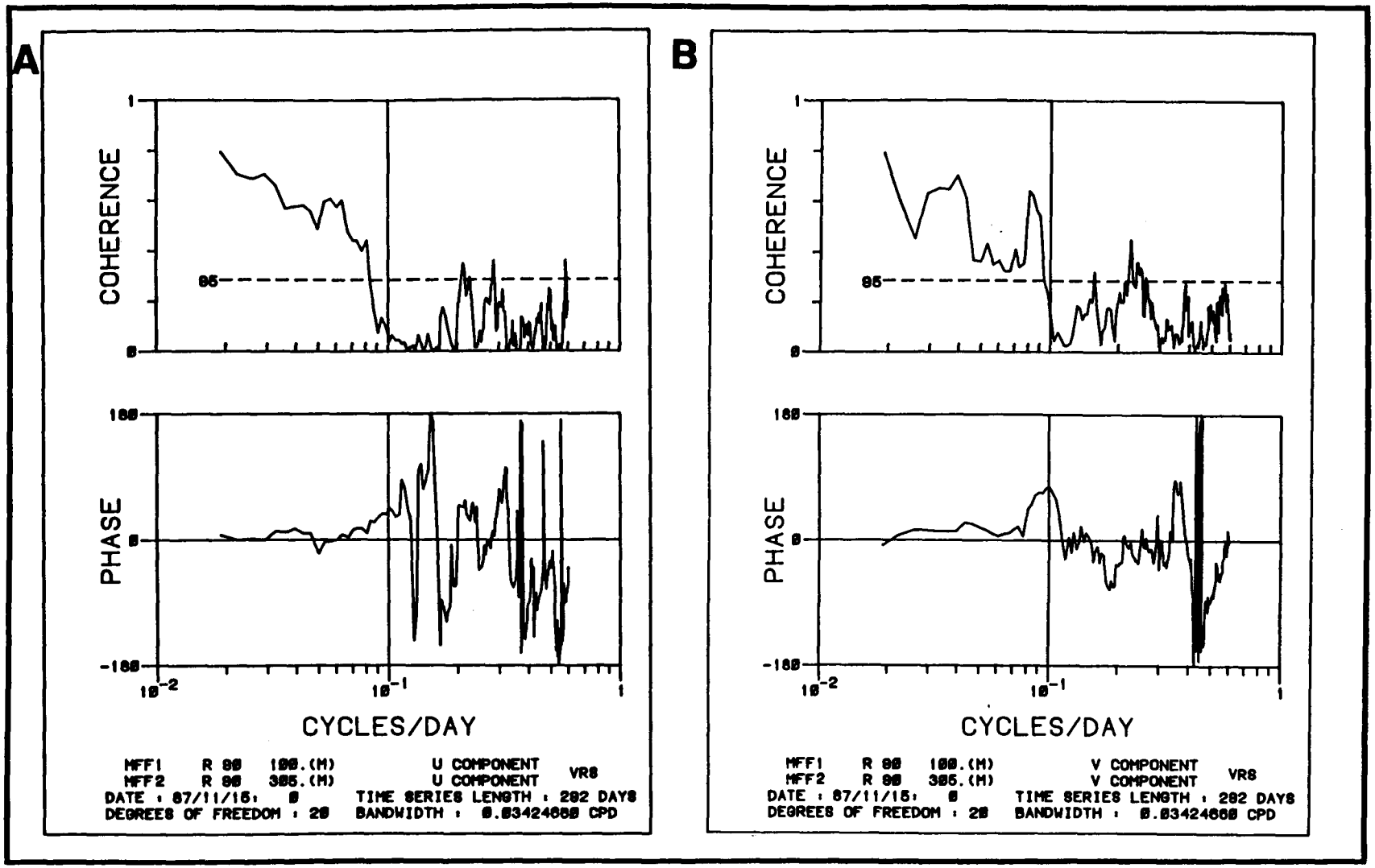

Figure 4.4-34. Phase and coherence squared at Mooring FF for 292 days beginning November 15, 1987 between (a) the U components of current velocity at 100 m and 305 m and (b) the V components of current velocity at 100 m and 305 m.

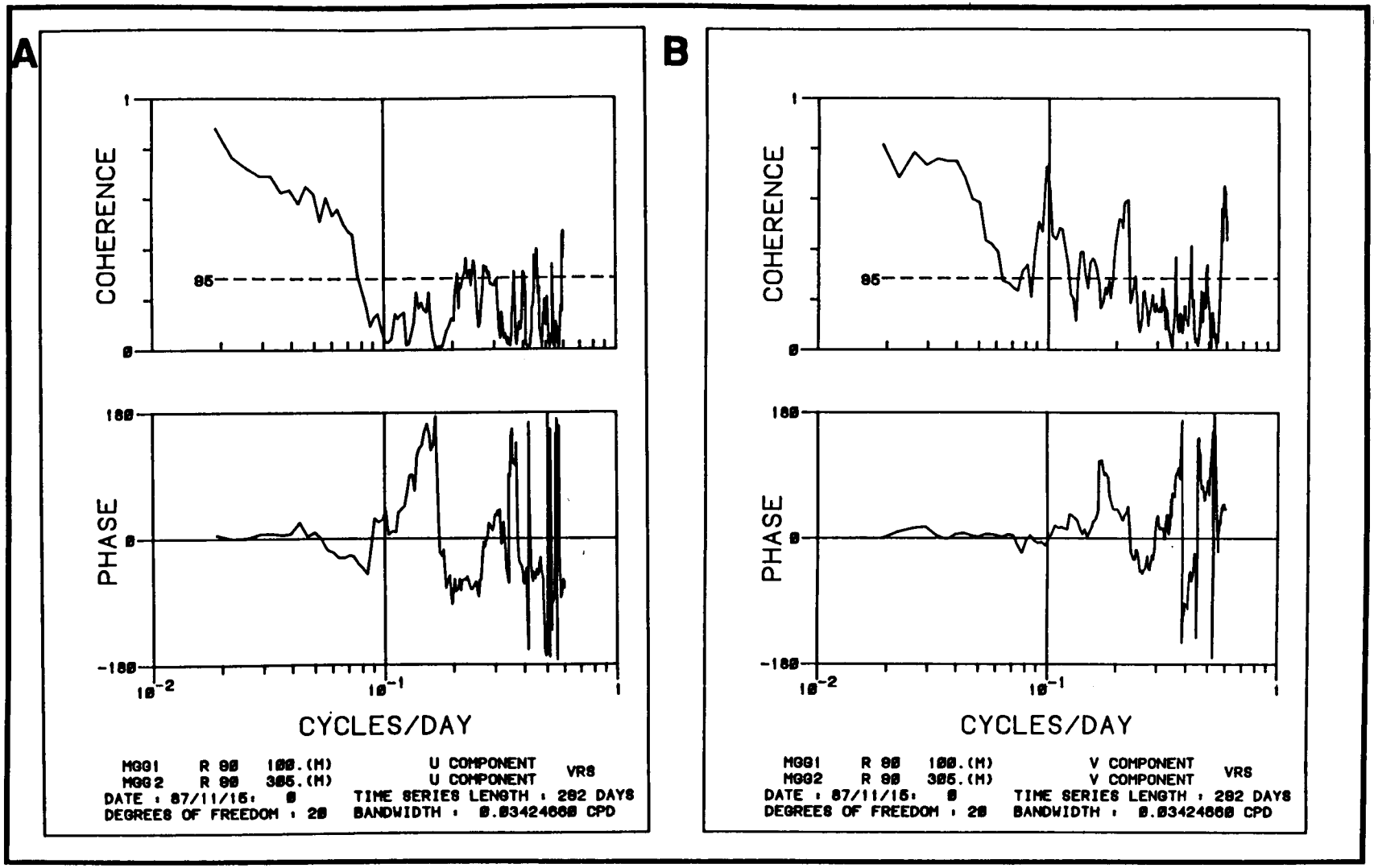

Figure 4.4-35. Phase and coherence squared at Mooring GG for 292 days beginning November 15, 1987 between (a) the U components of current velocity at 100 m and 305 m and (b) the V components of current velocity at 100 m and 305 m.

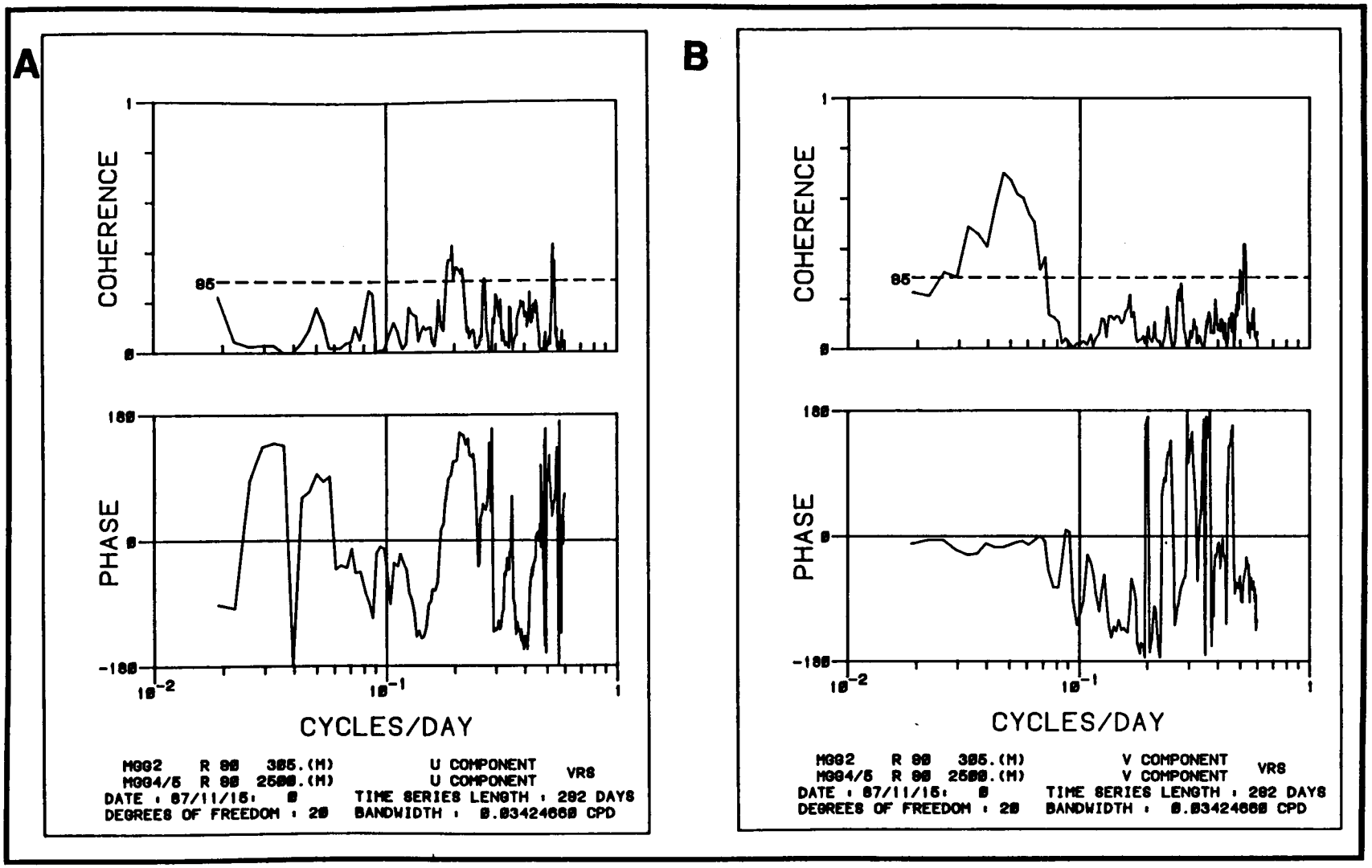

Figure 4.4-36. Phase and coherence squared at Mooring GG for 292 days beginning November 15, 1987 between (a) the U components of current velocity at 305 m and 2500 m and (b) the V components of current velocity at 305 m and 2500 m.

The results of cross-spectral analyses between instruments at a given depth for each of the variables were incoherent in all cases. Significant coherence, however, was found for U and V between various depths on a given mooring. Within the upper layer, current was typically coherent, between 0.05 and 0.1 cpd and at the lowest frequencies resolved. Across the zero point, both U and V components were typically incoherent; except for the V component at Mooring GG where there was a strong peak of coherence at 0.5 cpd with zero phase lag. This suggests a barotropic wave mode.

The properties of quasigeostrophic normal modes were used to investigate the vertical structure of current velocity at each mooring. As a first step, the mean vertical stability profile (Brunt-Väisäliä frequency) of the Gulf of Mexico was calculated from historical climatological data. With this stability profile, the vertical structure functions for the barotropic and first three baroclinic modes were numerically computed for depths corresponding to the location of each mooring. Most of the energy of currents is typically contained in the barotropic and first baroclinic modes. Since the barotropic mode is constant with depth, the vertical structure function for the first baroclinic mode provides considerable insight into the constraints that are dynamically imposed on the currents at each location. The zero crossing of the first baroclinic mode establishes the level of no motion to be 800 m at Mooring GG, 600 m at Mooring FF and 300 m at Mooring EE. Above this point, current velocity increases almost linearly to the surface. Below this point, direction changes sign and current magnitude increases to a small asymptotic value. This structure reflects the mean density profile and the fact that in the framework of quasigeostrophic dynamics, baroclinic modes have zero vertically integrated horizontal mass flux. For each baroclinic mode there is an associated Rossby radius of deformation, and for the first mode the values at Moorings EE, FF and GG are 27, 36 and 40 km, respectively.

The amplitudes of the modes for each mooring were obtained at each instant of time by a least-squares fit of the modes to the observed current profile. U and V components were individually fit and the resulting time series were plotted. Although the barotropic and first baroclinic modes were always dominant, the second mode was significant at times, particularly in the presence of eddies. The third mode was insignificant. An overall residual value was calculated to indicate the quality of the fit. For Mooring GG, it was low for a three-mode fit, indicating that the modes were not coupled, i.e., they were linearly independent. The residuals were higher and the modes coupled at Mooring FF, particularly for the U component. Since U is the cross-isobath direction, topographically induced coupling is to be expected. At Mooring EE the residual for the U component was high but for the V component it was low. Frequently the amplitude of the barotropic mode of the V component was not only uncoupled from the first baroclinic mode, but also larger than it. It is not known what was driving this barotropic mode, but the mode was clearly an important part of the V-component kinetic energy at this location on the slope.

The largest modal amplitudes occurred during the period that Eddy F affected the currents at Mooring GG. The barotropic mode of the V component reached values of 23 cm s^{-1} at times, which accounts for the strong pulses of current observed at 2500 m. The peak value of the amplitude of the first baroclinic mode for both U and V was about 22 cm s^{-1}. To get the magnitude of the baroclinic mode at a specific depth, one multiplies the amplitude by the value of the vertical structure function at that depth. Thus the peak value of the first mode is about 76 cm s^{-1} at the surface and 12 cm s^{-1} at the bottom. The first baroclinic mode, therefore, contributes to the observed bottom currents, but not as effectively as the barotropic mode.

The pattern of the barotropic mode of the U and V currents was analyzed during the time of Eddy F's influence. The combination of the U and V components did not indicate a single large barotropic eddy coaxial with the baroclinic one. However, one possible interpretation of the barotropic data is that an eddy pair, rotating in opposite directions, crossed the mooring. The leading one would be cyclonic and the trailing one anticyclonic. The possible observation of a barotropic vortex pair that is coupled to a Loop Current anticyclone is an important result of this study, because it would support a similar and rather robust result of numerical models (e.g., Smith, 1986; Wallcraft, 1986).

4.5 Deep Currents

4.5.1 Introduction

This section will present current measurements taken below 1000 m in the eastern, central and western part of the Gulf of Mexico, and makes a preliminary investigation of the importance of Rossby waves in different parts of the basin. This multi-year, regionally phased field program has produced the first direct measurements of deep currents below the sill depth of the Yucatan Straits in the Gulf of Mexico. Previous current meter moorings have been restricted to the mid-and upper continental slope (800 to 1000 m) off Texas (Brooks, 1984), Alabama and the west Florida shelves at (Molinari and Mayer, 1982). The deep circulation has been inferred using inverse methods, from a Gulf-wide hydrographic survey (Hofmann and Worley, 1986) showing transport patterns composed of several small cells with a cyclonic gyre in the western Gulf opposing the clockwise upper layer circulation. Hofmann and Worley (1986) caution against putting much significance in their inferred deep circulation since it is sensitive to their empirically determined reference levels and there were no current meter data available for verification.

4.5.2 Water Column Analysis

Seven-Day Low Pass (DLP) stick vectors for currents measured at eastern Gulf Moorings A and G in Program Years 1, 2, and 4 are presented in Figure 4.5-1. Immediately striking is the high degree of coherence between the different levels at both Moorings A and G and the episodic nature of the events at G. There is also, generally, a small increase in current speed between bottom instruments G4 and G5, and A4 and A5.

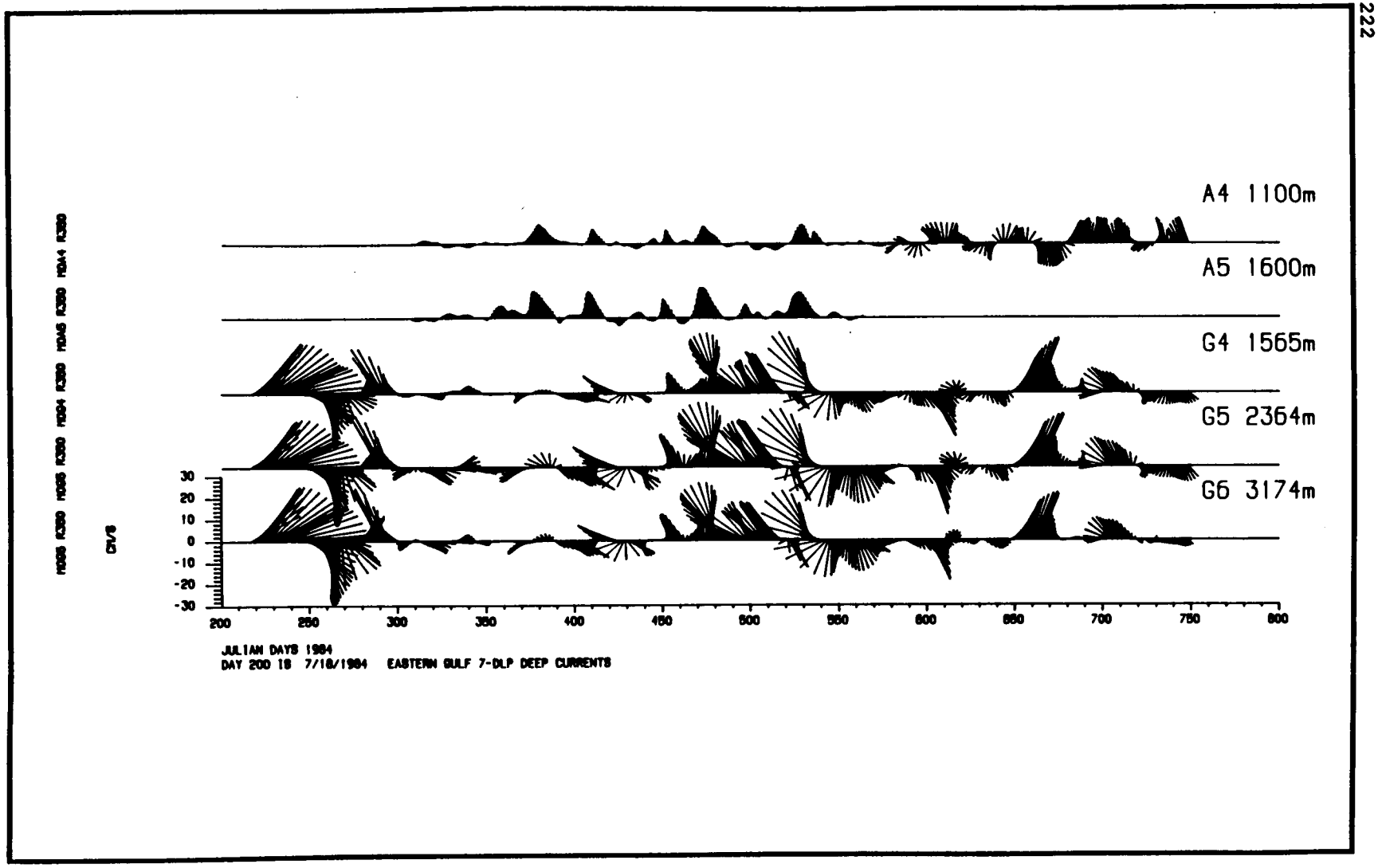

Figure 4.5-1. Seven-DLP stick plots from eastern Gulf Moorings A and G.

Some of the events at Mooring G also occur at Mooring A (i.e., Days 470, 530 and 710) but other energetic events at Mooring G such as Days 610 and 660, seem to correspond to flows in the opposite direction at Mooring A. The current fluctuations at Mooring A, which is on the lower part of the steep west Florida continental slope, are much less energetic than at Mooring G, which is often under the Loop Current, where the bottom slope of the continental rise is small.

The kinetic energy (KE) spectra in variance preserving form for the velocity time series from Mooring G are given in Figure 4.5-2. The increase in KE between G4 and G5, and to a lesser extent between G4 and G6, is apparent at all frequencies below 0.1 cycle per day (cpd). Instrument G6 is 25 m from the bottom, and since the stratification is very weak near the bottom, it is likely that G6 is often within the bottom boundary layer. Prominent spectral peaks occur at about 0.04, 0.02-0.03 and 0.01 cpd. The rapid decrease in energy at frequencies above 0.05 cpd indicates that high frequency motions above about 0.07 cpd are not supported above the Rossby wave cut-off frequency given by $N\alpha$, where N is the Brunt-Vaisala frequency of the lower water column and α the bottom slope. It will be shown that there is negligible energy between 10 days and the inertial period in most of these deep records. Figure 4.5-2 shows that the 18-month record does not resolve the lowest frequencies present in the deep currents. This is may be expected since the Loop Current eddy shedding cycle is usually estimated to be between nine and 15 months (Hurlburt and Thompson, 1980). The coherence squared between velocity components for G4 and G5, and G4 and G6 is greater than 0.9 for frequencies less than 0.07 cpd, with phase differences not significantly different from zero. These motions are characteristic of Topographic Rossby Waves (TRW) in the vertical and frequency structure. Fluctuations are highly columnar with bottom intensification and negligible energy present above a cut-off frequency of about 0.07 cpd.

Seven-DLP stick plots for the Program Year 3 western Gulf current measurements are shown in Figure 4.5-3. Moorings Q and R (see Figure 2.5-1 in SAIC (1988)) again show highly coherent motions with depth with evidence of bottom intensification. Current magnitudes are smaller than under the Loop Current, but fluctuations are less episodic. Mooring P currents, at the base of the slope, are less energetic and show much less coherence between the 1000 m and 1500 m levels than the essentially columnar motion in deeper water. Typical of deep water wave motions, energy is unevenly distributed, and horizontal coherence between events over relatively short distances (~50 to 100 km) is not at all obvious (Hogg, 1981; Hamilton, 1984). Figure 4.5-4 shows the KE spectra for Moorings R and P. The records at R are short (116 days), and thus only the first major peak at 0.05-0.06 cpd is resolved. However the increase in energy with depth is apparent for all three instruments along with the lack of energy at periods shorter than seven days. Mooring P has longer records and shows a decrease in KE with depth and resolves peaks at about 0.03-0.04 cpd. The records at Mooring R show coherence squared of better than 0.9 with zero phase differences at frequencies below 0.1 cpd, but at Mooring P, the components of the P3 and P4 records have coherence squared of only 0.4-0.6 at about 0.04 cpd. The small magnitude of deep currents over the lower slope of the southern Mid-Atlantic Bight has been

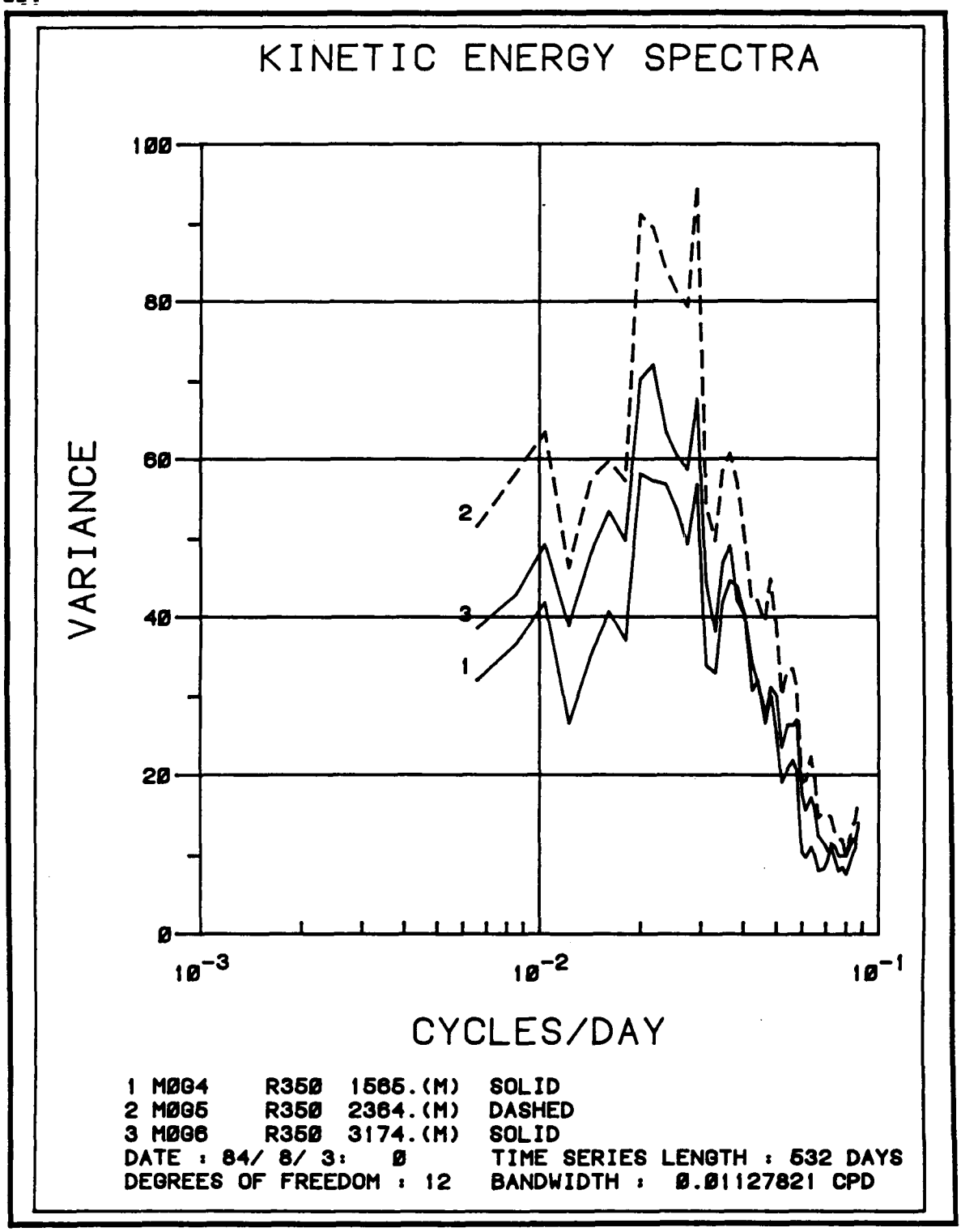

Figure 4.5-2. Kinetic energy spectra in variance preserving form for deep current records at Mooring G.

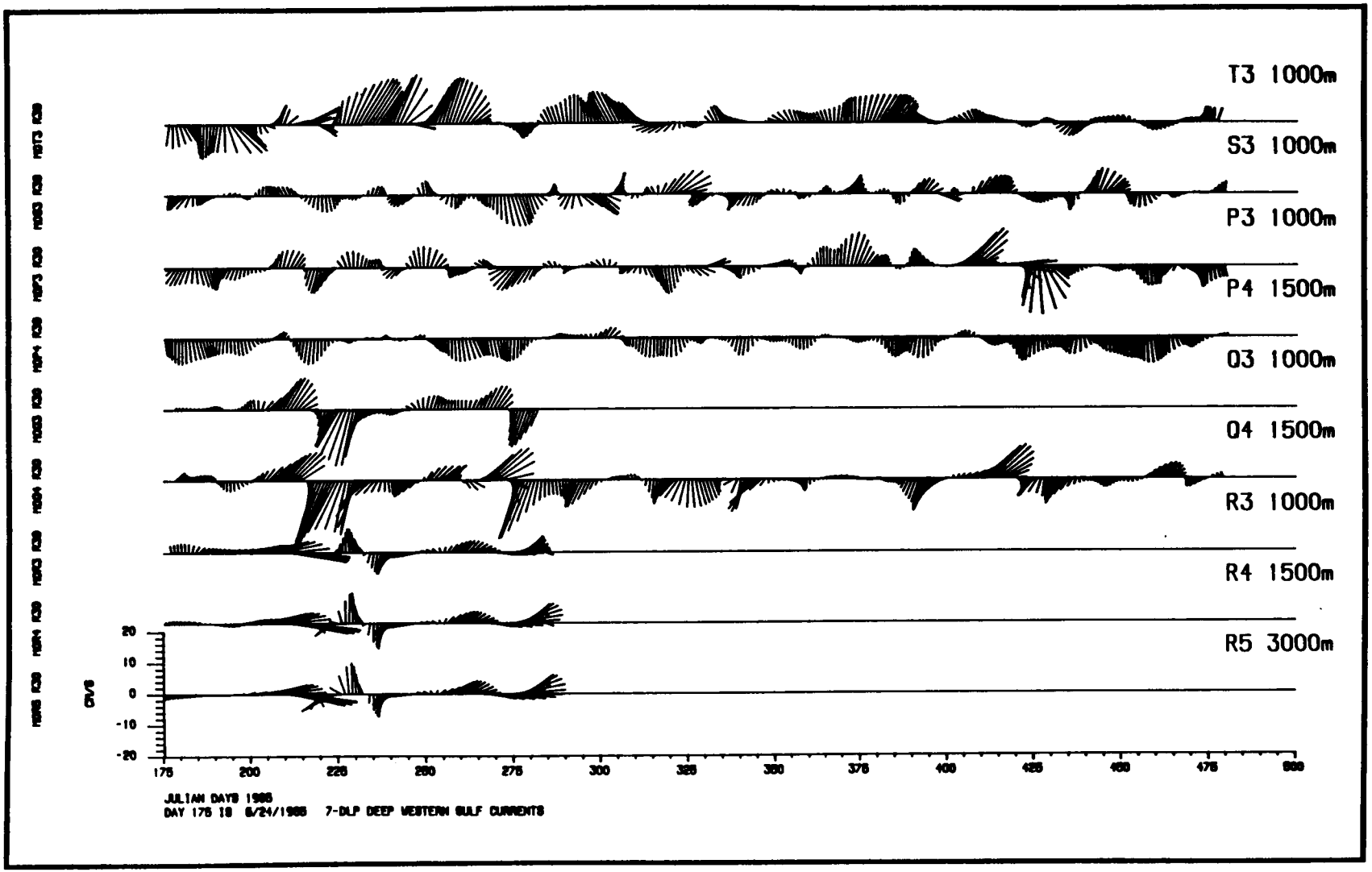

Figure 4.5-3. Seven-DLP stick plots from western Gulf Moorings P, Q, R, S and T.

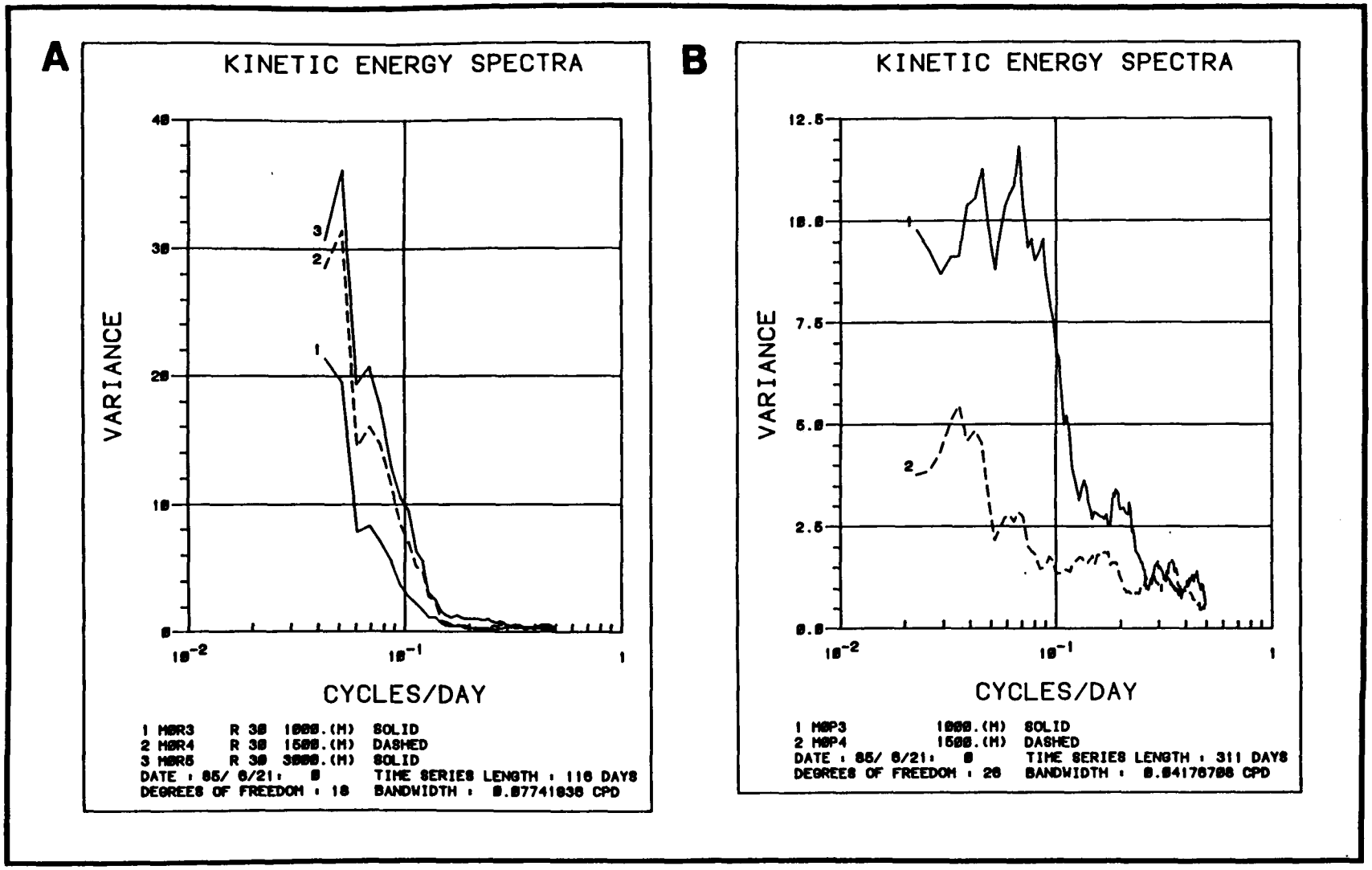

Figure 4.5-4. Kinetic energy spectra in variance preserving form for deep current records at (a) Mooring R, and (b) Mooring P.

noted previously by Csanady et al., (1988). It has been related to the refraction of onshore propagating TRWs as they encounter steeper topography (Shaw and Csanady, 1988).

In the central Gulf, the composite GG4/5 record is shown along with the last deployment of GG5; the currents from FF4 and the 40-HLP IES travel time records (GG6) are given in Figure 4.5-5. Where GG4 and GG5 overlap after Day 470, the record at 2500 m shows larger magnitudes and very high coherence with the record at 1650 m similar to the other continental rise stations discussed above. The mooring on the slope, FF4, has much weaker velocities (~5 cm s^{-1}) than observed on the other slopes at similar depths. The regular nature and the 20 to 25 day period of the fluctuations at both Moorings GG and FF is quite remarkable. The spectra of these records will be discussed below.

Currents in the lower part of the water column clearly have the bottom intensified character and periodicities expected of TRWs in all three regions of the Gulf. This suggest along with differences in amplitude that Loop Current fluctuations, in analogy with mid-Atlantic Gulf Stream meanders, is a source of TRWs which propagate westward into the Gulf However, large warm eddies also propagate westward after detaching from the Loop Current and interact with topography, particularly the southwest Texas - Mexican slope (SAIC, 1988; Lewis et al., 1989). Thus, anti-cyclonic eddies could also be a source of Rossby wave energy.

4.5.3 Horizontal Energy Distribution

The variance ellipses for 40-HLP near bottom current records are given in Figure 4.5-6. As noted above, the highest energy is found under the Loop Current at Mooring G. The variance ellipses at this mooring show the increase of KE and the alignment of the principal axis of the fluctuations with depth. The central and western moorings are less energetic with similar variances at equivalent depths. The central and eastern arrays show decrease of energy towards the slope as does the Mooring P-Q pair in the west; however, there seems to be a relative increase in variance towards the south southeast along the general trend of the 2000 m isobath. Yet, some uncertainty exists because of the differing depths of water and the bottom instruments at Moorings P, S and T.

Since Mooring G (eastern Gulf) and GG (central Gulf) have the longest continuous records, the difference between the KE spectra at low frequencies will be examined first (Figure 4.5-7a). The dominance of the 0.04-0.05 cpd peak in the central Gulf (GG) and the lack of energy compared to Mooring G at frequencies lower than 0.04 cpd, (period = 40 days) even though peaks at ~0.02 cpd occur in both records, is immediately apparent. When the comparison between Moorings Q, GG and G is made with shorter records (Figure 4.5-7b), the 0.04 cpd peak is much less prominent at Mooring Q than at the other moorings. There is, however, a higher spectral peak at about 0.025 cpd which has greater energy than that at Mooring GG. A similar comparison (Figure 4.5-7c) for the moorings at the base of the slope shows much lower variances with the dominant peaks at about 0.03 cpd in the eastern and western Gulf and

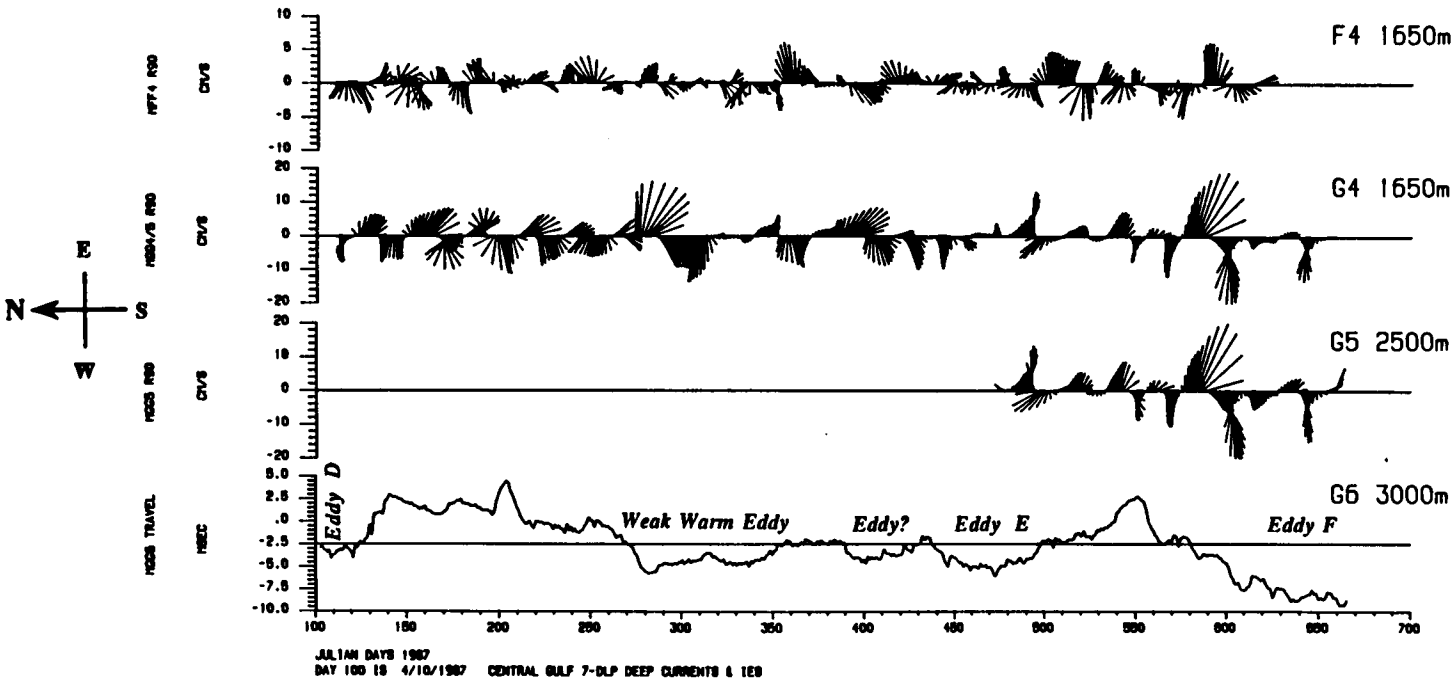

Figure 4.5-5. Seven-DLP deep currents from central Gulf Moorings GG and FF. The travel time record from IES #1 (MGG6) at Mooring GG is also shown.

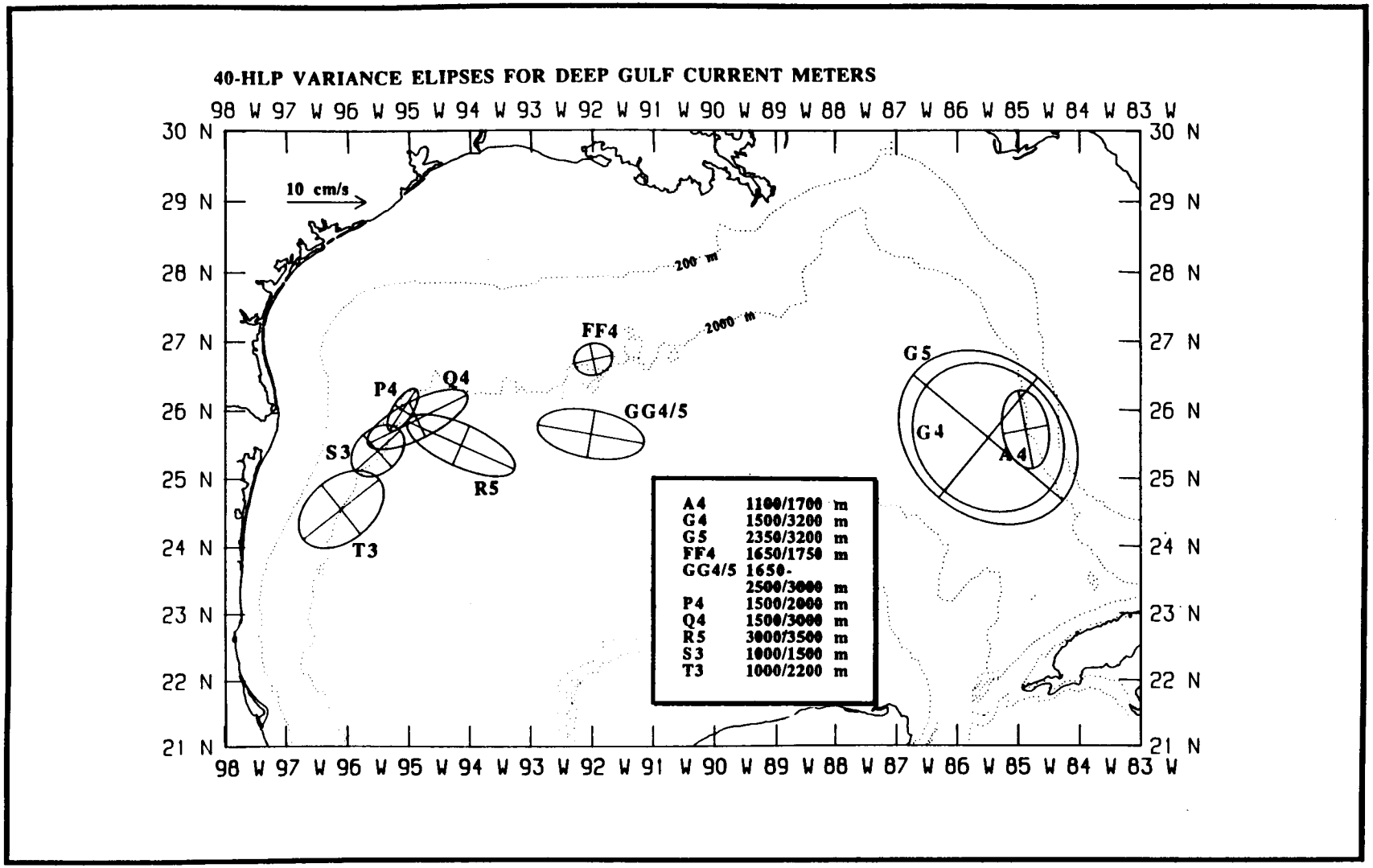

Figure 4.5-6. Forty-HLP variance ellipses for the indicated records where the half axis lengths are equal to the standard deviation of the velocity fluctuations along the principal axes.

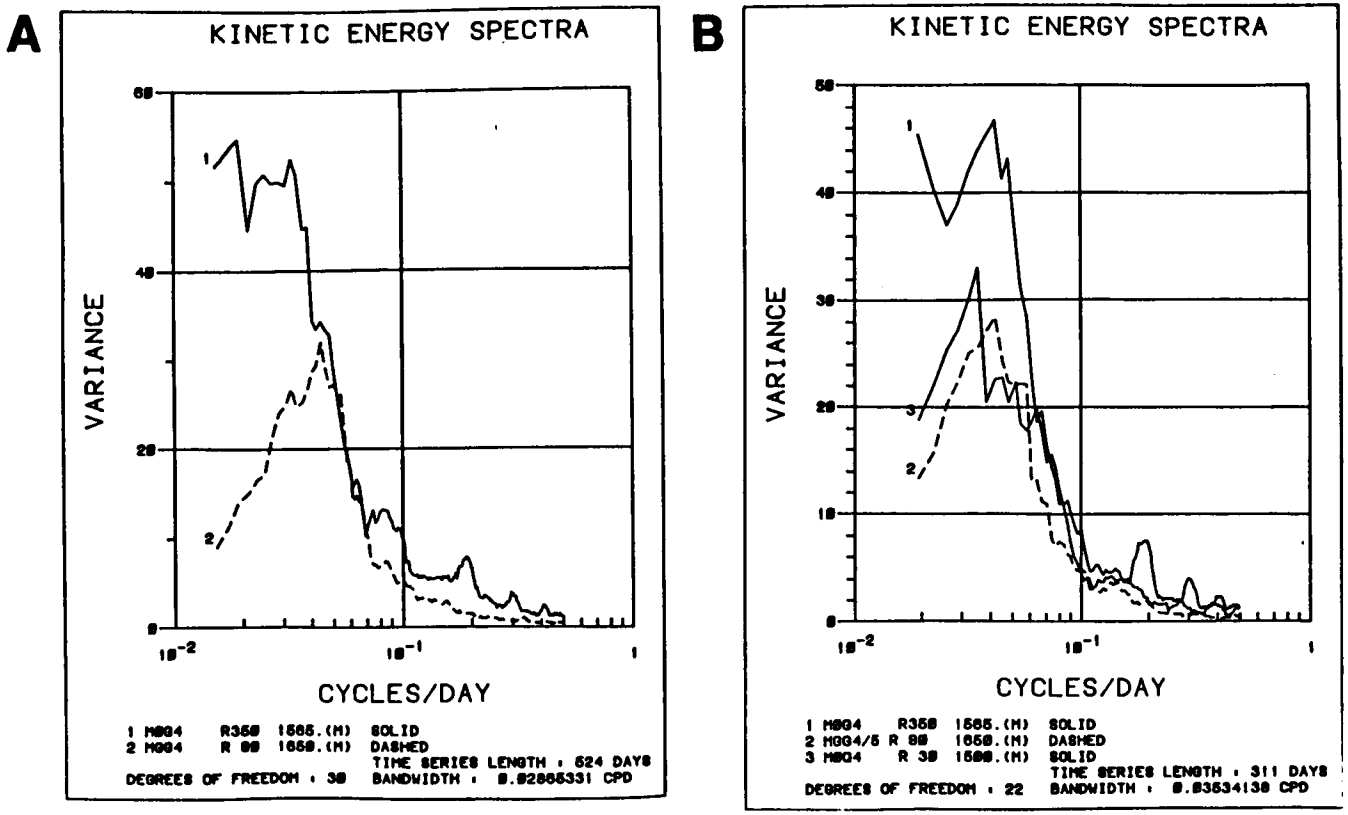

Figure 4.5-7a,b. Kinetic energy spectra in variance preserving form for records (a) MOG4 and MGG4; and (b) MOG4, MGG4/5 and MOQ4.

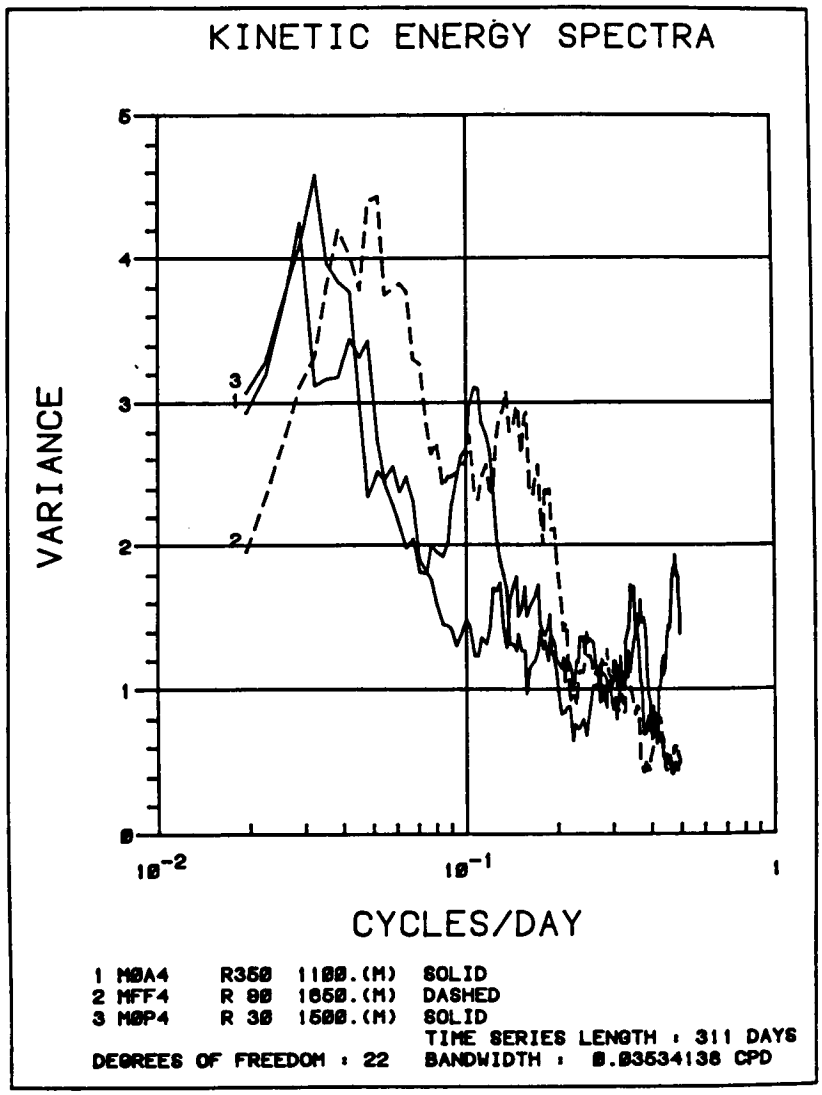

Figure 4.5-7c. Kinetic energy spectra in variance preserving form for records MOA4, MFF4 and MOP4.

0.04-0.05 cpd in the central Gulf. The gentler slopes of the central and western Gulf, unlike the steep slope at Mooring A, apparently support some energy at frequencies higher than the deep-water cut-off of about 0.08 cpd. Since the cut-off frequency is proportional to bottom slope, the northern slope region would be expected to allow higher frequency TRW motions than the deep basin. Very steep slopes seem to constrain the vorticity such that only small amplitude motions can exist. The theory (Rhines, 1970) breaks down for steep bottom slopes.

Therefore, the distribution of KE is uneven with 0.04-0.05 cpd (period = 20 to 25 days) motions present in most records. There is a tendency for lower frequency motions of ~0.02 cpd to be slightly more important in the western Gulf and to dominate the spectra, along with even lower frequency fluctuations, under the Loop Current. The highest TRW frequency band of 0.04-0.05 cpd on the continental rise of the Gulf is lower than the 16 day period wave motions found at Mooring Site D on the Continental rise of the Mid-Atlantic Bight (Thompson, 1977).

4.5.4 Local Phase Propagation and Wave Numbers

If the current in all three regions of the Gulf are primarily TRWs, then they should exhibit the proper phase propagation characteristics. The dispersion relation is

$$\omega = - k\alpha \, N/K \coth (NHK/f) \qquad (1)$$

where ω is the wave frequency, the wave number $K = (k^2 + l^2)^{\frac{1}{2}}$ with components k, l directed along isobath (x) and normal to the isobath (y, positive towards shallower water), respectively. N is the (constant) Brunt-Väisälä frequency, and the bottom slope is defined by $H - \alpha y$ (Rhines, 1970) where H = water depth and f = Coriolis parameter. It can be shown that for stable stratification, k is always negative (thus westward propagation), and if the energy flux has an upslope component then l is also negative which implies offshore propagation of phase (Thompson, 1977). The difference in energy levels between the continental rise and slope stations is consistent with a small upslope energy flux. The theory predicts that TRWs are plane transverse waves, and, thus, the major principal axis of the velocity fluctuations is perpendicular to the wave number, K.

The spectra 18 to 37 day and 38 to 300 day bands were analyzed using EOFs, considering each of the three regional data sets. The spectra were normalized and the cross spectral matrix calculated for both U and V components of the velocity records. The phase differences were taken from the first eigenmode, and since generally the V-component had higher coherence between onshore and offshore stations, only the V-component was used to estimate the wave number components. Exceptions are noted in Table 4.5-1. Only the western array has along isobath information from which to calculate k. For this array, the wave number components were estimated by least squares. Similar calculations for estimating wave numbers have been performed for Mid-Atlantic Bight current data by Hamilton (1984) and Thompson (1977). The results are given in Table 4.5-1.

Table 4.5-1. Topographic Rossby wave number estimates.

Mooring Arrays	Offshore Separation (km)	Percentage of Total Normalized U & V Variances Explained by Mode 1	Degrees of Freedom	Wave Number (Cycles/km) k	l	Wavelength (km)	Angle w.r.t y axis
18-37 Day Period							
MOG4, MOA4 Loop Current	63	46.3	24	-	-0.00454	220	-
MGG4, MFF4 Central Gulf	120	48.4	28	-	-0.00576	174	-
MOP4, MOQ4	29	50.9	18	-0.00074	-0.00633	157	187°
MOS3, MOT3 Western Gulf				-0.00104	-0.00902	110*	187°
38-300 Day Period							
MOG4, MOA4 Loop Current	63	49.4	24	-	+0.00337	297+	-
MGG4, MFF4 Central Gulf	120	44.7	28	-	-0.00611	164	-
MOP4, MOQ4 MOS3, MOT3 Western Gulf	29	40.1	18	-0.00034	-0.00827	121	182°

* Estimated from both U and V Components.
\+ Estimated from U Components.

Offshore propagation of phase is unambiguous for the Loop Current and western Gulf arrays in the higher frequency band. The central Gulf produces ambiguous results because of the large separation. However, it is assumed that the larger negative phase angle generates an offshore wave number that is consistent with the other regions, with the assumption of westward propagation, and with the calculated direction of the principal axis of the current fluctuations. The first mode eigenvector for each EOF analysis is used to calculate the hodograph of the wave motion at each current meter. This is done in a manner similar to constructing tidal current ellipses from the harmonic analysis of two orthogonal current components (Foreman, 1978). For each analyzed array, therefore, the hodographs represent coherent motions and the arrow on the ellipses gives the relative phase and direction of rotation (Figure 4.5-8). The percentage of the total normalized variance of the arrays, explained by the Mode 1 eigenvector, is given in Table 4.5-1. The normalized amplitudes were multiplied by the standard deviations of the frequency band for each component time series to convert to velocity units.

Since the major principal axis of the current hodographs is at only a slight angle to the general trend of the isobaths for each region (Figure 4.5-8), the offshore wave number, *l*, is the major component of the total wave number, K. Thus it is a good estimate (though an underestimate) of K and hence, the wave length of the 0.04 and 0.015 cpd TRWs. Wave lengths range from about 150 to 220 km for the higher frequency band and 120 to 300 km for the lower band with an apparent decrease westward. These are similar to the approximately 200 km estimates for 16-day waves in the Mid-Atlantic Bight (Thompson, 1977; Hamilton, 1984).

Figure 4.5-8a illustrates the westward decrease in amplitude of the 0.04 cpd waves and the transverse nature of the oscillations particularly for the central and western measurements. The energy of the fluctuations on the 3000 m isobath decreased from G4 to GG4 to Q4 in the ratios 1.76: 1.4: 1. Since Moorings GG and Q are 656 and 942 km west of Mooring G, respectively, about ¼ of the initial energy is dissipated in the western third of the Gulf as against 20% between 86°W and 92°W. As mentioned above, the small inclination of the major axis of the fluctuations to the trend of the isobaths is consistent with westward propagation of phase and energy (i.e., the wave number vector is in the fourth quadrant).

Therefore, the 18 to 37 day period motions have wave number vectors that are consistent with the westward and upslope energy flux of TRWs. Wave lengths are short (~150 to 200 km) and there is evidence of enhanced dissipation in the western third of the basin.

The lower frequency motions centered on 0.015 cpd (period = 67 days) have a more complex energy distribution with a minimum in the central Gulf (Figure 4.5-8b) and the fluctuations are less transverse. Thus, the hodographs in Figure 4.5-8b have a smaller major to minor axis ratio than for the higher frequency hodographs in Figure 4.5-8a. This would suggest either secondary sources in the western Gulf, perhaps due to topographic interaction of large warm eddies with the Mexican slope

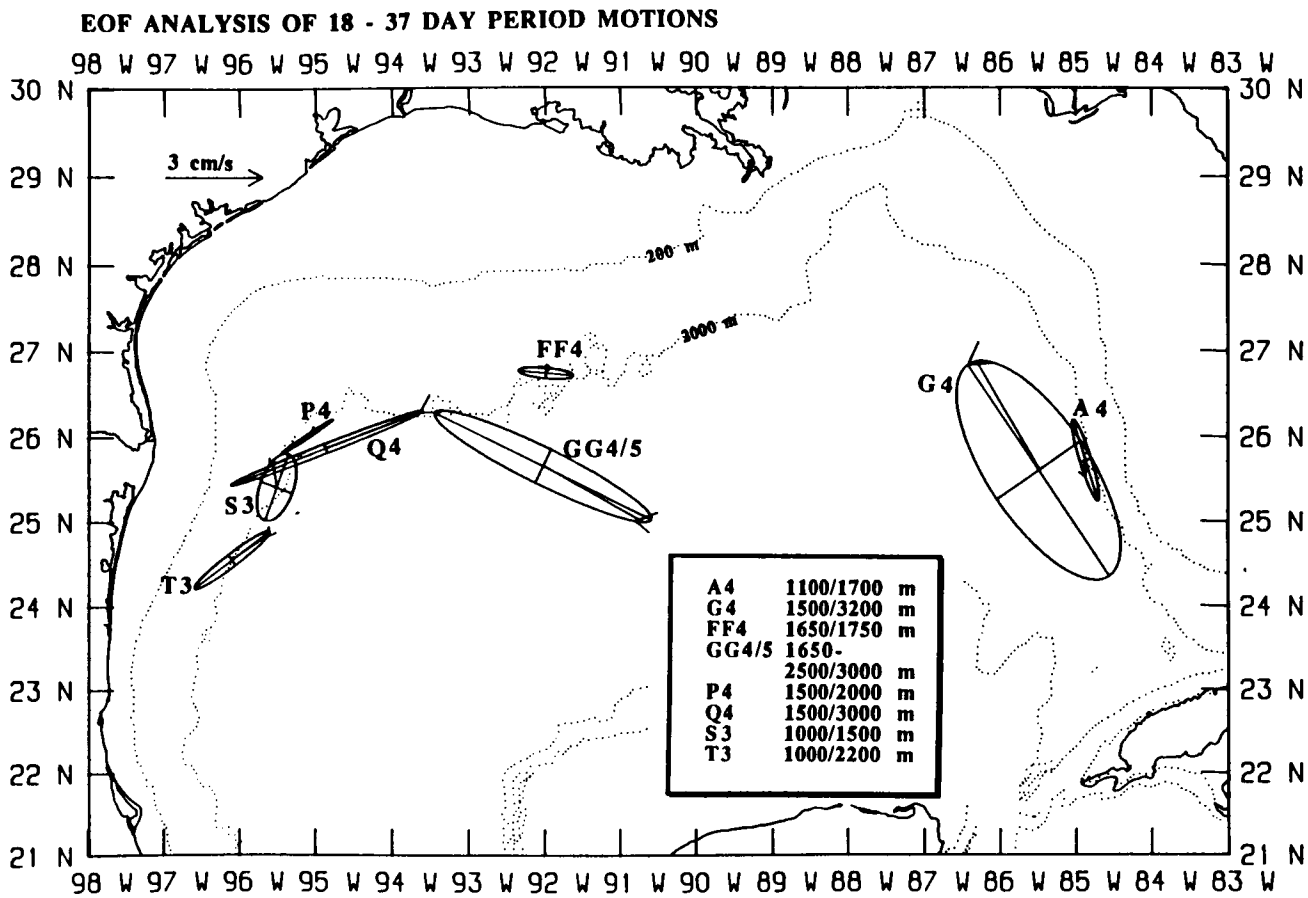

Figure 4.5-8a. The velocity hodographs from the EOF analysis of the deep current records for 18 to 37 day period motions.

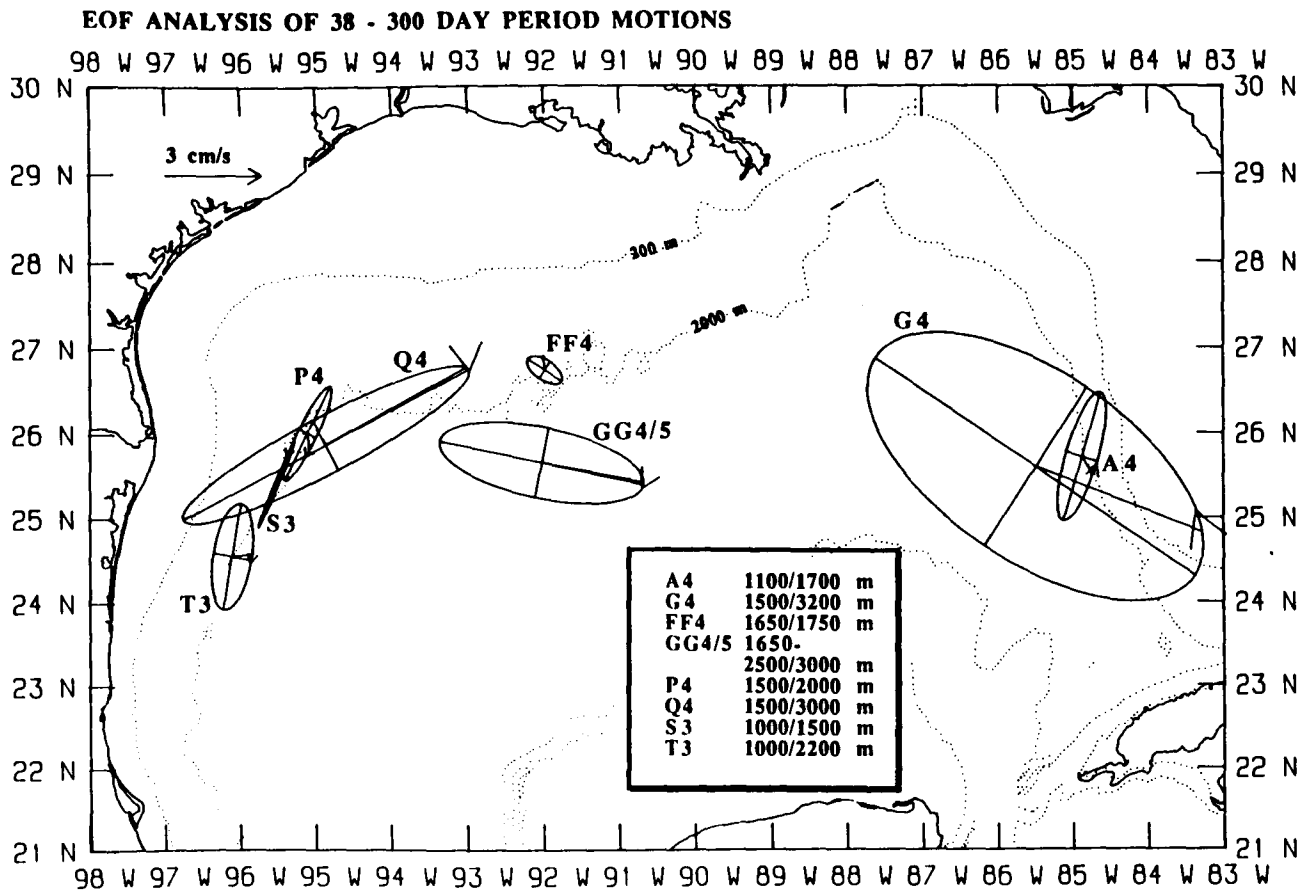

Figure 4.5-8b. The velocity hodographs from the EOF analysis of the deep current records for 38 to 300 day period motions.

(SAIC, 1987), or a more complex propagation path of these lower frequency waves. Otherwise, the western and central Gulf hodographs are similar in character to the high frequency band (Figure 4.5-8a). The eastern Gulf low frequency motions have about a factor of two greater KE than the 18 to 37 day motions, and there is onshore propagation of phase (Table 4.5-1) and thus, an offshore component of energy flux. However, the closed nature of the isobaths and the relatively small distance between the Yucatan and west Florida slopes make it difficult to draw any conclusions on the source of the fluctuations.

4.5.5 Energy Propagation

The last section presented evidence that current signals are consistent with the westward propagation of TRWs. Since the time series from the eastern and western Gulf overlap (Figure 4.5-9) and a packet of TRWs would be expected to traverse the basin in approximately three to six months, it seems reasonable to look for coherent signals between eastern and western arrays with the appropriate lag. A significant correlation was found between G4 and Q4 records after the G4 record was lagged by 106 days. The exact lag was found by computing the maximum lagged correlation coefficient for the seven-DLP V-component time series. The stick plots for Q4 and lagged G4 are given in Figure 4.5-10. It can be seen that the contributions to the positive correlation come from the more energetic events between Days 200 and 300, and Days 375 and 450 (relative to Mooring Q). The coherence squared between Q4 and the lagged G4, V components, as well as the P3, U component and the A4, V component is given in Figure 4.5-11. The lagged G4 versus Q4 coherence squared is significant for the 0.04 - 0.06 cpd interval. The coherence squared for lagged A4 vs P3 is coherent at frequencies below 0.03 cpd. There is some other significant coherence (i.e., the G4 and S3), but Figure 4.5-11 illustrates the main point that some of the eastern Gulf signal from under the Loop Current is predictable in the western Gulf after allowing for a propagation time of about 106 days.

The coherence between lagged A4 and P3 at frequencies below 0.03 cpd implies that lower frequency waves also propagate across basin, but in this case, unlike the 0.04-0.05 cpd band, there is no significant spectral peak in the central Gulf at these lower frequencies. This propagation of low frequency waves appears to be more complex than the 0.04 cpd waves and may be influenced by the closed and small extent of the basin.

The 106-day lag time gives a direct estimate of the lower bound in the group velocity, which is 9 km day^{-1}. Group velocity can be estimated from the dispersion relation (Equation 1) using the wave number estimates of Table 4.5-1. A reasonable value for the bottom slope of the rise, α, is about 5×10^{-3}, and the average N for 1500 m to 3000 m depth, calculated from CTD casts taken near Mooring GG, is about 5×10^{-4} s^{-1}. The group velocity, ($\underline{c}_g$), components ($\partial w/\partial k$, $\partial w/\partial l$) are calculated to be -8.45, and 0.3 km day^{-1}, respectively, for the 0.04 cpd waves furthermore, since the U-component is not very sensitive to k and K as long as $k/K \ll 1$, the 0.015 cpd wave has almost the same value. Thus, estimates of the westward propagation velocity for waves generated under the Loop Current

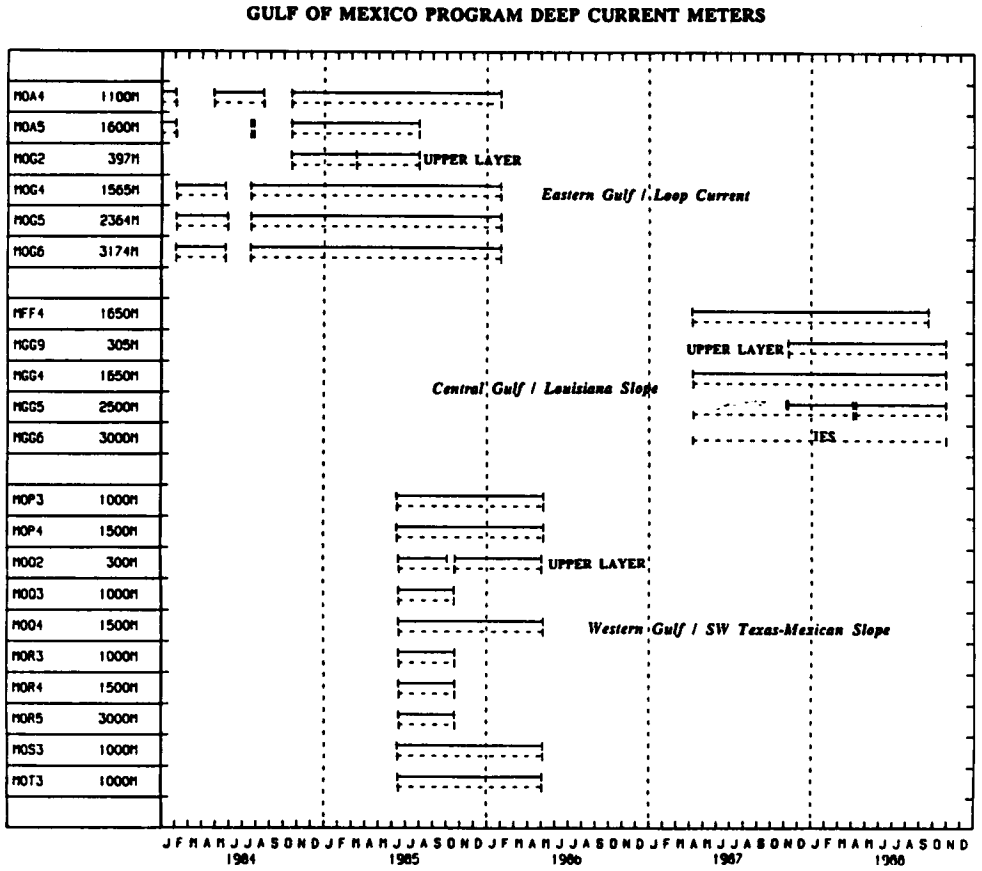

Figure 4.5-9. Time lines of deep current records with selected upper layer records from 1986 to 1988 for the MMS Gulf of Mexico Physical Oceanography Program. Solid lines are velocity and dashed lines are temperature.

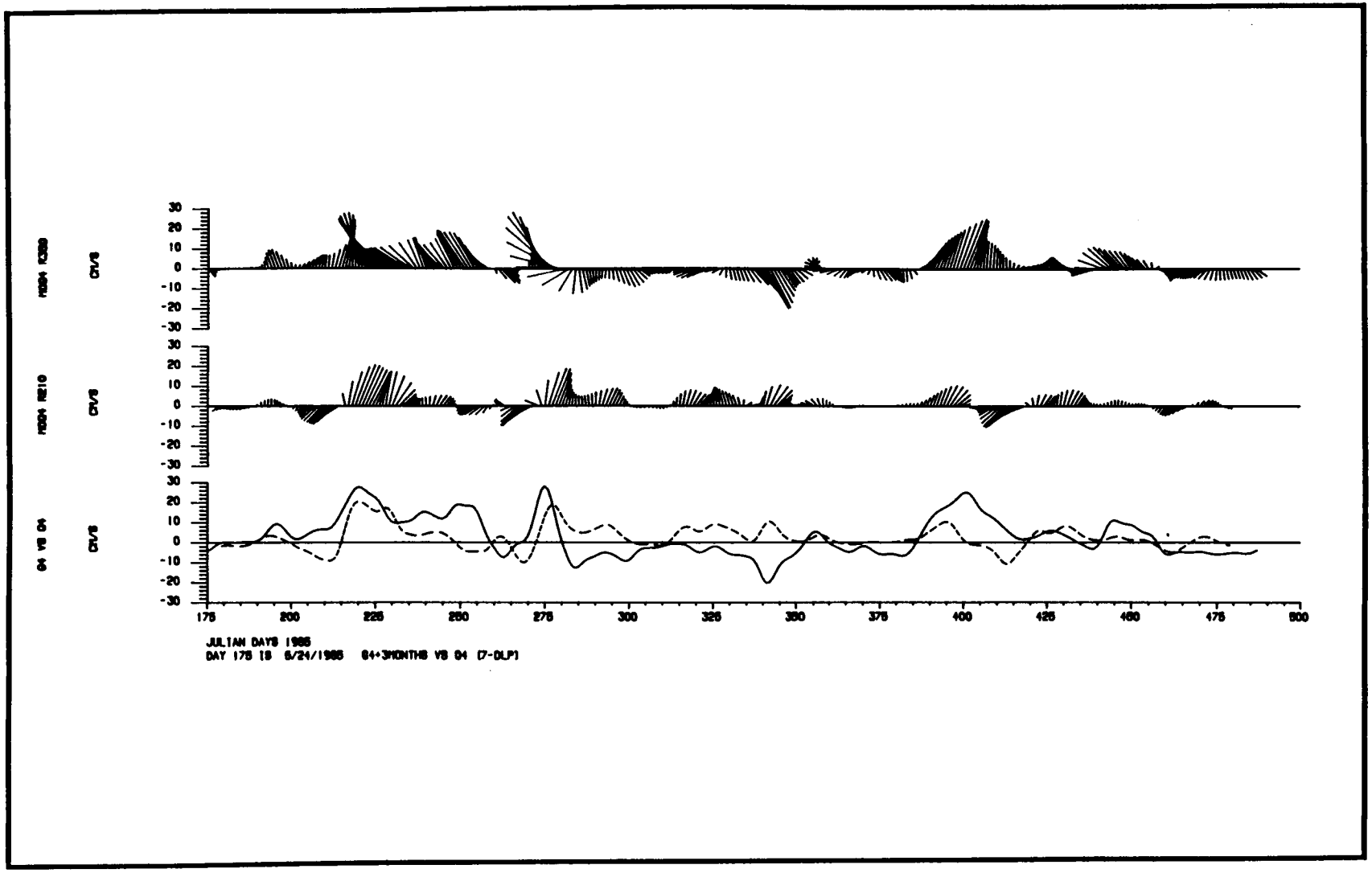

Figure 4.5-10. Seven-DLP stick plots of records M0Q4, and M0G4 lagged by 106 days. The lower panel shows the along isobath (V) components. The lagged M0G4 is solid and M0Q4 is dashed.

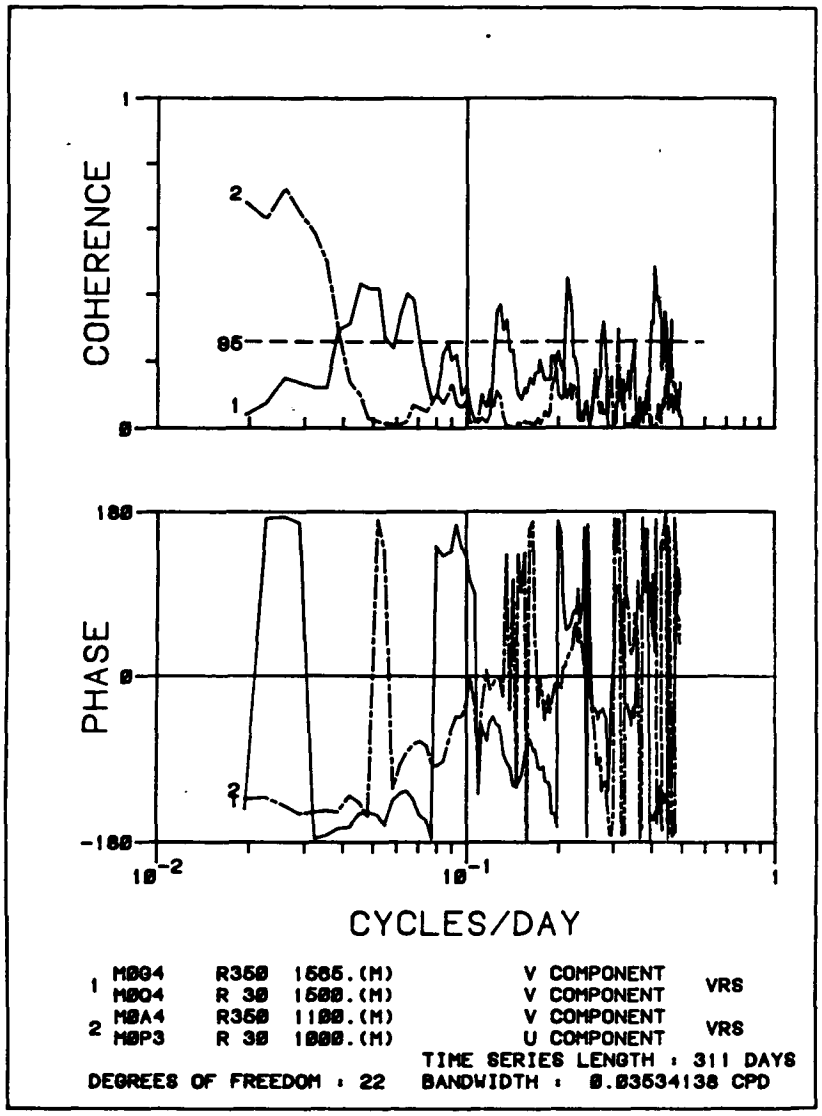

Figure 4.5-11. Coherence squared and phase differences for the indicated eastern and western Gulf records. Eastern Gulf records have been lagged by 106 days.

based on the correlation of currents from the eastern and western Gulf, and direct calculations directly from the dispersion relation agree quite closely. The upslope group velocity is very small compared with the along isobath component indicating there is only a small energy flux towards the slope from the deep basin. The dispersion relation also indicates that the along isobath component of $\underline{c}_g$ is not sensitive to frequency as long as $k/K << 1$ (see Table 4.5-1). This help explain why the low frequency coherence between A4 and P3 have about the same lag as the 0.04 cpd motions.

4.5.6 Deep Currents and Warm Eddies

The relationship of the deep currents to the shedding and westward propagation of major anticyclones can be partially investigated with these data. The model that has emerged from the above analysis is that TRWs are generated by motions of the Loop Current and more energetic waves might be expected to be generated by extensions to the northwest resulting in the shedding of major anticyclonic eddys. Louis et al., (1982) associated bursts of TRW energy on the Scotian continental slope with warm eddys shed by the Gulf Stream, and the Loop Current may be supposed to generate TRWs similarly. TRWs propagate westward relatively undisturbed as do the upper layer warm eddies. However, the average translation velocity of a warm eddy ranges from three to six km day^{-1} (Kirwan et al., 1984; SAIC, 1987) as against the nine km day^{-1} TRW westward group velocity. Thus, the lower layer current fluctuations might be expected to become increasingly decoupled from the upper layer velocities as the eddies move west.

During the period of the eastern and western current measurements, a large eddy (Eddy B from SAIC (1988)) detached from the Loop Current at the end of June 1985 and was centered about 26°10'N and 89°20'W on July 17, 1985 (day 564 in Figure 4.5-1). The period from Day 450 to 560 was a period of large fluctuations at Mooring G under the Loop Current (Figure 4.5-1). Eddy B was tracked with ARGOS drifters and was surveyed four times between July 1985 and February 1986 (SAIC, 1988; Lewis et al., 1989). The center arrived at about 25°20'N and 93°W on October 25, 1985 (Day 298 in Figure 4.5-3) as determined from the CTD survey of the R/V PELICAN Cruise 85-02 (see Figure 4.3-14 in SAIC, 1988). The eddy was evident in the upper layer currents of Mooring R (see Figure 4.3-19 in SAIC, 1988). Therefore, the average translation speed was 3.7 km day^{-1} across the central and western Gulf. During the same time period the packet of TRWs generated under the Loop Current had traveled a greater distance (250 km) at higher speed and arrived just prior to the eddy at the western slope (i.e., coherent energetic events around Day 275 at Mooring Q in Figure 4.5-120). Therefore, the difference in propagation speeds between the upper eddy and the lower layer TRWs, even though both were energetic events spawned by the Loop Current at approximately similar times, indicates that upper and lower layer currents become largely independent of each other in the western Gulf. Eddy B subsequently interacted with the topography from November 1985 through May 1986, generating a cyclone-anticyclone pair of eddies. The remnants of Eddy B eventually coalesced with Eddy C in 1986 at about 23°N. Eddy C

was shed from the Loop Current in January 1986 and took the more usual southwest trajectory across the Gulf (SAIC, 1988; Lewis et al., 1989).

During 1987 and 1988, three eddies and a number of smaller warm and cold features passed over Mooring GG in the central Gulf. Figure 4.5-5 shows the upper layer features detected by the IES travel time record which is inversely proportional to dynamic height. Eddies D, E and F were tracked by ARGOS drifters and were surveyed by ship and aircraft. The centers of all the eddies passed to the south of Mooring GG. The warm event seen between Days 270 and 350 was mapped by hydrographic surveys between Days 290 and 310 and was found not to be an eddy, but a weak anticyclonic feature. Eddy F was a very large (300 km diameter) vigorous warm eddy which was shed from the Loop Current in April 1988. There is no obvious correspondence between the approach and departure of a Loop Current eddy and deep currents at GG. Strong events are observed just prior to the arrival of Eddy F but are not observed for the smaller Eddy E. The event around Day 275 is not associated with a vigorous anti-cyclone.

The upper layer current data for Moorings G, GG and Q are not as extensive as the lower layer data, however, the degree of coherence of the columnar motions below 1000 m with the 300 to 400 m level currents can be checked with these shorter records. The time lines for G2, GG9 and Q2 are given in Figure 4.5-9, and the coherence squared and phase differences between U and V components of these records with the lower layer velocities from G5, GG4/5 and Q4, respectively are given in Figure 4.5-12. The upper to lower layer coherence provided some support for the model of TRWs being progressively unrelated to the upper layer currents moving west of presumed generation by the Loop Current. At Mooring G, both components are moderately coherent over most of the low frequency band. At Mooring GG, coherence is seen at the dominant 0.04 to 0.06 cpd TRW peak in the along isobath component only, and at Mooring Q, coherence for the U components is only barely significant. Note that where coherences are significant, upper to lower layer phase differences are not significantly different from zero. None of the slope moorings (Moorings A, FF and T) with upper layer records show any significant coherence with the respective bottom currents. Thus, at Moorings GG and Q the upper layer eddy currents are supplanting the TRW motions, which theoretically occupy the whole water column (Rhines, 1970). The Loop Current upper layer flows at Mooring G, however, are quite closely related to the deep currents at all TRW frequencies.

4.5.7 Mean Currents

The mean velocities for the bottom current records are given in Figure 4.5-13. The means are small compared with the 40-HLP variances (Figure 4.5-6) and despite the 11 to 20 month long records, the means have little statistical significance. Mean flows are northward along the west Florida slope. This agrees with near bottom current measurements made on the 1000 m isobath west of Tampa (27.5°N, 88.5°W) and south of Mobile (29°N, 88°W) by Molinari and Mayer (1982). These data showed northwestward and westward mean velocities of about 2.5 cm s^{-1} and 1.5 cm s^{-1} for 306 and 358 day records, respectively. At 92°W, mean flows are

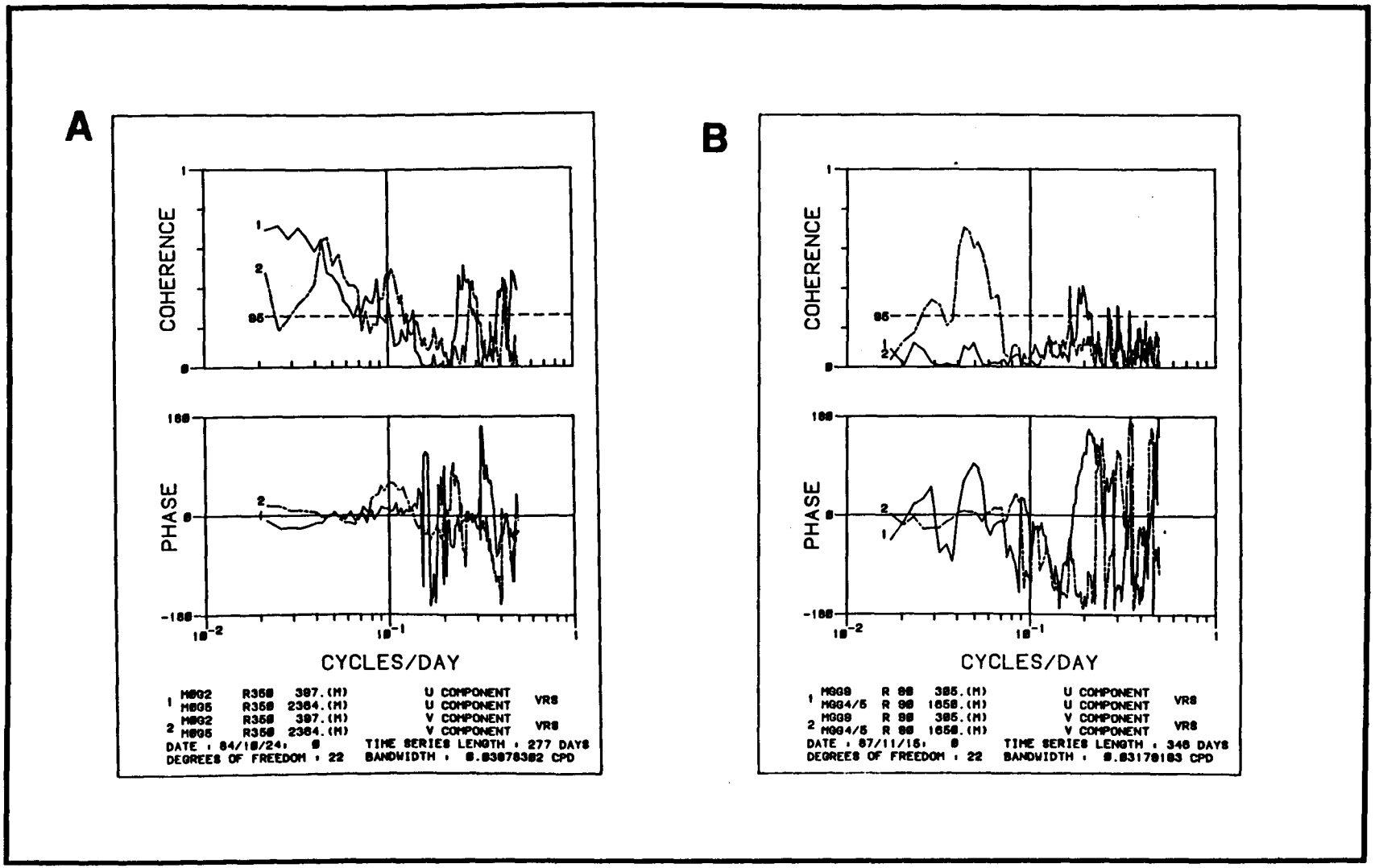

Figure 4.5-12a,b. Coherence squared and phase differences between upper and lower layer currents in the (a) eastern Gulf of Mexico and (b) central Gulf of Mexico.

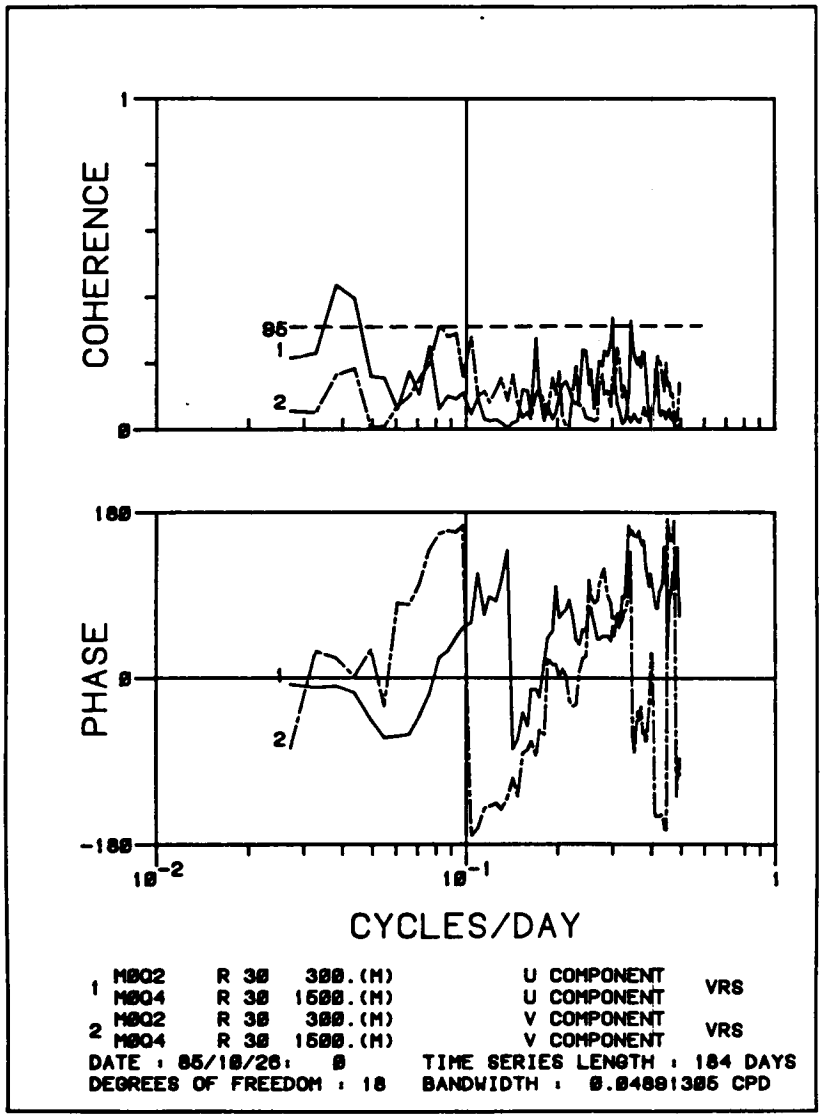

Figure 4.5-12c. Coherence squared and phase differences between upper and lower layer currents in the western Gulf of Mexico.

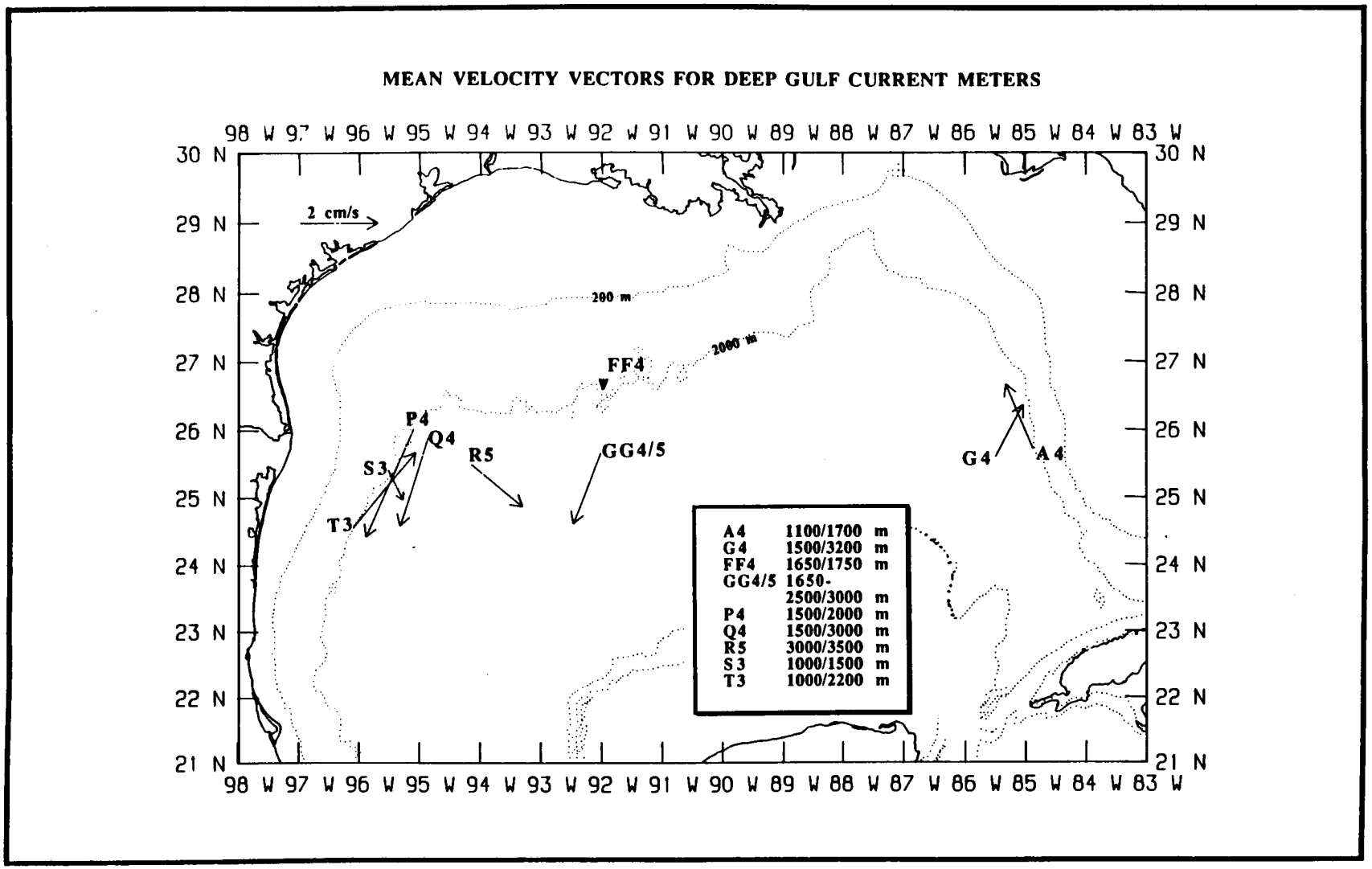

Figure 4.5-13. Mean velocity vectors for the indicated records (all available data).

southward, normal to the slope, and in the western Gulf, mean currents are southward north of 25°N and northward south of there at Mooring T. The convergence of the mean flows in the western Gulf may be a result of interaction of Eddy B with the Mexican slope topography and the subsequent formation of a cyclone anticyclone pair (SAIC, 1988). A cyclone-anticyclone pair has been observed previously in this region with an offshore directed surface jet being observed at about 25°N (Brooks, 1984; Brooks and Legeckis, 1982; Merrell and Morrison, 1981).

The lower layer transports have been calculated from hydrographic data for the Gulf of Mexico Basin by empirical search and inverse techniques to determine the reference level (Hofmann and Worley, 1986). Their results showed a cyclonic gyre in the western Gulf with a number of smaller cells in the northwest corner and in the east. There is some correspondence between the current meter means and Hofmann and Worley's (1986) transport results. The offshore flow at 92°W roughly corresponds to the northern part of the cyclonic gyre. Some indication of offshore transport with convergence between two cells along the western slope at about 25°N exists. There is no indication in their results of the northward flow along the base of the west Florida shelf as indicated by Moorings A and G and Molinari and Mayer (1982).

4.5.8 Summary

Moored current meter measurements have been made on the lower continental slope and deep basin of the Gulf of Mexico. Three regions have been analyzed; under the Loop Current, the north central Gulf along 92°W and the western Gulf. The low frequency currents in the lower water column have been interpreted as topographic Rossby waves with fluctuating KE confined to periods greater than about 10 days and bottom intensification of highly columnar motions. Eighteen to 37 day motions were present at all three sites with longer period motions, 38 to 300 days, dominating in the eastern and western Gulf. There was offshore propagation of phase, which is characteristic of TRW motions on the Mid-Atlantic Bight continental rise, and the wave hodographs indicated along isobath phase propagation with shallower water to the right of the direction of propagation. Direct calculation of westward phase propagation was only possible for the western Gulf array. Calculated wavelengths ranged from approximately 150 to 250 km, similar to estimates made from current meter data in the northwest Atlantic (Thompson 1977; Hamilton, 1984).

Currents showed moderate coherence between eastern and western sites. This was consistent with a directly estimated group velocity of about nine km day^{-1}. Group velocity calculated from the dispersion relation for TRWs agreed with this estimate quite closely. The 18 to 37 day TRWs showed energy decay in the western Gulf, and increasingly the hodographs more closely approximated plane transverse waves. The 38 to 300 day waves showed an energy minimum in the central Gulf. This suggests more complex propagation paths into the western Gulf or secondary generation of TRWs along the Mexican slope, probably due to the topographic interaction of large warm anticyclonic eddies.

The analysis suggests a tentative model of deep water current fluctuations due to TRWs generated by motions of the Loop Current, with possibly more energetic events being generated during eddy shedding periods. The TRWs propagate westward at higher group velocities than the typical warm eddy translation velocity of three to six km day^{-1}, and thus appear to be independent of the westward movement of the eddies. However, the eddies have a "head start", so to speak, since they are often shed around 89°W, whereas TRWs generated by large excursions of the Loop Current have their apparent source nearer the west Florida shelf. Thus, an energetic TRW packet may seem to precede immediately the arrival of an eddy in the western slope region. There is inconclusive evidence from the current measurements that this may occur in some cases. The two-layer numerical model studies of Hulburt and Thompson (1982) suggest that lower-layer cold and warm eddy-like circulations generated during the eddy shedding cycle propagate westward faster than the upper-layer eddies. Calculation of coherence between upper- and lower-layer currents for Moorings G, GG and Q in the east, central and western Gulf, respectively indicate that the lower-layer motions do become more decoupled from the upper-layer circulations as the TRWs move westward.

The data are not extensive enough in time or space to indicate the fate of TRWs within the basin. However, it is noted that for water depths greater than about 2000 m, the basin is closed for bottom intensified TRW motions, and there is some indication that 0.04 cpd waves dissipate in the western Gulf. In the west, wave trajectories will tend to follow the isobaths south into the Bay of Campeche. Where the topography slopes up to the south, the topographic restoring force opposes the planetary beta effect as opposed to reinforcing it in the northern Gulf. Thus, the propagation characteristics of Rossby waves may be quite different in the Bay of Campeche from that off the Yucatan Peninsula. Further investigations into deep currents in the Gulf may be quite fruitful for further studies of TRWs in enclosed basins.

4.6 Shelf Circulation and Hydrography

4.6.1 Introduction

Five current meter moorings were maintained across the upper slope and shelf during 1987 and 1988. This section will focus primary attention on the variability of the 40-HLP, currents although the tidal band currents also present some interesting processes. First, the general statistics and then results of frequency domain analysis will be discussed. When possible, all available data are used initially in the analyses. The variability introduced by seasonal and inter-annual modulations of external forcing restricts the ability to interpret analyses of these long data sets. The effects of multiple, time-varying forcings are confounding, and the time series are non-stationary. In an attempt to minimize these problems, focus will be placed on three intervals when current measurements were reasonably complete and external forcing was moderately stationary. The trade-off is that these component records are shorter and the available degrees of freedom are reduced. The time periods are the summer of 1987, a time of weak winds and moderate river runoff; the winter of 1987-1988, a period of high runoff

and strong wind forcing; and the summer of 1988, a time of very low river runoff and moderate to strong wind forcing. In this section, these time periods will be referred to as Period VI, Period VII and Period VIII, respectively (see Table 4.6-1). Finally, Empirical Orthogonal Functions (EOF) will be computed for these three intervals.

Table 4.6-1. Comparative time periods discussed for the shelf Moorings (AA, BB, CC and DD) along with Mooring EE.

Time Period	Dates
VI	07/21/87 - 11/10/87
VII	01/05/88 - 05/16/88
VIII	05/14/88 - 10/27/88

4.6.2 General Current Meter Statistics

Long-term means from all data at each current meter on Moorings AA, BB, CC, DD and EE are presented in Figure 4.6-1 and Table 4.6-2. The southerly and easterly components were considered to be statistically significant if they were greater in absolute value than twice the standard error of the mean. The standard errors were estimated by an expression of the form

$$\langle u'^2 \rangle^{\frac{1}{2}} / (T/\tau)^{\frac{1}{2}}$$

where $\langle u'^2 \rangle$ is the variance of the current component, T is the record length, and τ is the correlation time-scale of the current component. The correlation time-scales for the velocities were estimated as the lag at which the auto-correlation function dropped within two standard errors of zero for the first time. For all meters within 100 m of the sea surface, the correlation time for southerly flow was about one week, and it was slightly more than twice this for the easterly component of flow. At the deeper meters, the correlation time-scale for southerly flow was slightly more than two weeks and approximately one week for the easterly flow.

It must be noted that the significance levels reflect on the likelihood that these sample means are statistically meaningful estimates of the true mean. However, the quantity computed as a mean gives a true estimate of volume transport for the indicated periods and is not influenced by statistical significance.

The mean pattern which emerges is one of statistically significant, cyclonic circulation above about 100 m over the shelf and upper slope, and a westerly flow below 100 m on the outer shelf and upper slope. This should be compared with the mean sea-surface flow hypothesized by

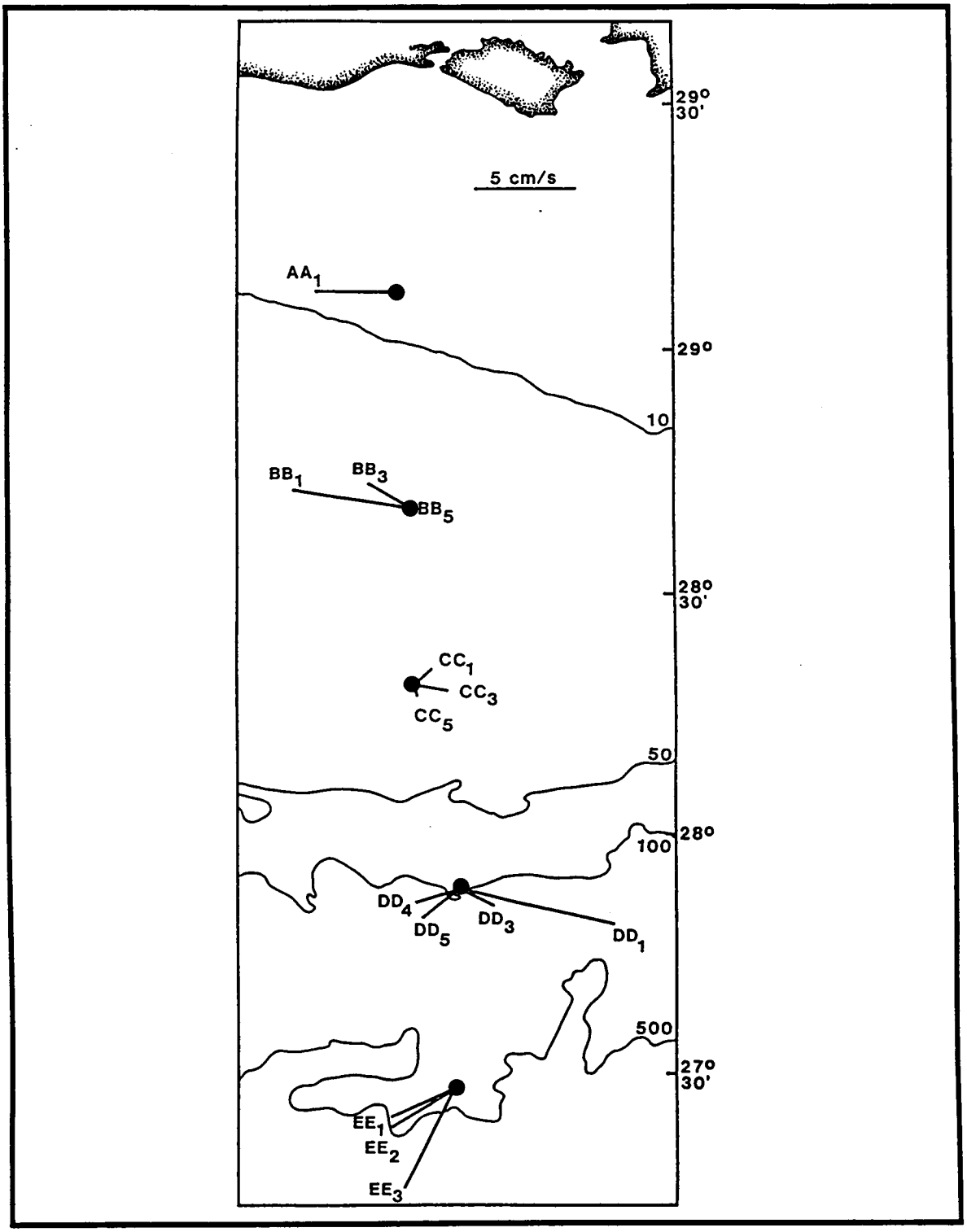

Figure 4.6-1. Mean current vectors from all available data for the shelf and upper slope moorings. Current vectors originate at the mooring site and flow toward the letters denoting the individual meters.

Table 4.6-2a. Low frequency statistics, all available data.

Inst. ID	U Mean (cm sec^{-1})	V Mean (cm sec^{-1})	$\langle u_r^2 \rangle$ (cm^2 sec^{-2})	$\langle v_r^2 \rangle$ (cm^2 sec^{-2})	Principal Axis (°)
AA1	-0.07*	-3.45	14.46	230.23	5.35
BB1	-0.84	-5.63	63.48	145.27	-2.30
BB3	-1.19	-2.06	36.36	95.27	-4.80
BB5	-0.05*	0.09*	16.09	43.17	10.84
CC1	-0.75	0.88	43.43	82.68	-6.32
CC3	0.61	1.52	22.65	58.15	-16.39
CC5	0.35*	0.15*	14.71	26.10	7.15
DD1	1.57	7.40	79.00	187.62	-13.23
DD3	0.76	1.79	22.77	107.60	11.80
DD4	0.61	-1.88	11.45	75.91	13.12
DD5	1.13	-1.53	2.15	22.46	8.14
EE1	4.89	-2.31	75.15	153.39	0.58
EE2	1.91	-2.97	14.21	45.41	6.36
EE3	1.32	-3.14	2.99	23.40	19.58

* Indicates a mean value that is not statistically significant.

Table 4.6-2b. Low frequency statistics, time Period VI.

Inst. ID	U Mean (cm sec^{-1})	V Mean (cm sec^{-1})	$\langle u_r^2 \rangle$ (cm^2 sec^{-2})	$\langle v_r^2 \rangle$ (cm^2 sec^{-2})	Principal Axis (°)
BB1	-0.31*	0.98*	52.45	99.10	-9.11
BB3	-0.88*	0.77*	39.43	85.60	11.87
CC1	1.26*	1.01*	64.88	122.11	-21.61
CC3	2.66*	4.54*	37.79	106.28	-31.84
DD1	7.97	14.56	66.60	266.19	-20.70
DD4	1.88	-3.50*	2.09	64.07	15.18
EE3	0.41*	-1.90	1.54	14.37	17.64

* Indicates a mean value that is not statistically significant.

Table 4.6-2c. Low frequency statistics, time Period VII.

Inst. ID	U Mean (cm sec^{-1})	V Mean (cm sec^{-1})	$\langle u_r^2 \rangle$ (cm^2 sec^{-2})	$\langle v_r^2 \rangle$ (cm^2 sec^{-2})	Principal Axis (°)
AA1	-1.09*	-5.76*	12.00	233.15	8.70
BB1	-1.54*	-10.23	76.72	183.83	-8.93
BB3	-1.54*	-4.05*	31.48	108.98	-8.35
BB5	-0.16	0.59*	8.87	33.38	42.24
CC1	-1.91*	0.71*	35.04	54.14	-7.56
CC3	-0.88*	-0.38*	6.64	34.03	-2.79
CC5	0.02*	-0.27*	8.44	28.57	12.36
DD1	-0.57*	7.79*	110.48	205.15	0.04
DD3	1.10*	1.51*	55.82	74.17	-17.19
DD4	1.11	-2.05*	2.24	58.78	11.68
EE1	4.86	6.18*	91.11	108.80	-18.19
EE2	2.02	1.53*	14.51	35.75	1.17
EE3	1.43*	-2.46	3.45	16.45	15.07

* Indicates a mean value that is not statistically significant.

Table 4.6-2d. Low frequency statistics, time Period VIII.

Inst. ID	U Mean (cm sec^{-1})	V Mean (cm sec^{-1})	$\langle u_r^2 \rangle$ (cm^2 sec^{-2})	$\langle v_r^2 \rangle$ (cm^2 sec^{-2})	Principal Axis (°)
AA1	0.34*	-2.89*	10.17	236.02	4.66
BB1	-5.35	6.45*	59.79	152.21	26.72
BB3	-2.09*	-1.34*	36.67	103.76	-8.88
BB5	0.02*	-0.03*	14.86	52.98	1.34
CC3	0.59*	2.18*	21.96	54.11	5.93
CC5	1.33*	0.41*	24.49	37.54	37.95
DD1	-0.69*	3.92*	37.37	90.00	-11.43
DD4	-0.82*	-2.28*	30.18	51.16	15.94
EE1	4.24	-10.08	36.60	87.97	30.40
EE2	2.44	-6.94	10.26	26.87	14.61
EE3	2.60	-6.16	3.65	28.32	19.69

U and V are the mean speeds in the southward and eastward directions, respectively.

$\langle u_r^2 \rangle$ and $\langle v_r^2 \rangle$ are the variances along the minor and major principal axes, respectively. PHI is the rotation of the principal axes measured positive in a clockwise direction.

* Indicates a mean value that is not statistically significant.

Cochrane and Kelly (1986). They suggest a series of ephemeral cyclonic and anticyclonic gyres over the Texas-Louisiana shelf. These patterns, though, always show easterly flow near the surface over the outer shelf along 92° W and generally show westerly flow over the inner shelf at the same longitude.

During Period VI, mean flow over the shelf was generally to the east (Table 4.6-2b). Only at instruments DD4 and EE3 was the mean flow westward. Most of the estimated means were statistically insignificant. Only the mean currents over the outer shelf and upper slope were statistically different from zero. The summer months covered by Period VI, though, are the time period when the very low-frequency flow over the inner shelf may be expected to reverse for nearly one month (Cochrane and Kelly, 1986; Smith, 1980; Crout et al., 1984). Thus, a statistically insignificant mean flow over the inner shelf is not unexpected.

During time Period VII, the mean currents were generally westerly and onshore over the inner shelf and easterly and offshore over the outer shelf and upper slope (Table 4.6-2c). Meter EE3 showed westerly offshore flow. This pattern is consistent with that predicted by Cochrane and Kelly. These means, though, are not generally statistically different from zero because of the large current variances driven, presumably, by the winter storms. Wiseman and Dinnel (1989) also found statistically insignificant mean flows in this area during the winter season.

During time Period VIII, the currents were again generally not statistically different from zero (Table 4.6-2d). Only at Mooring EE was there vertically coherent and statistically significant mean flow. At this site the flow was to the west southwest. With the exception of BB1, the mean flow was to the west over the inner shelf and to the east over the mid and outer shelf which is consistent with the model of Cochrane and Kelly.

The mean flows during the course of this field program, then, are consistent with the patterns suggested by Cochrane and Kelly. The large current variances and long correlation time scales over the shelf, however, imply that a statistically significant seasonal mean can be obtained only after combining the seasonal flows from many years of data collection.

The raw current meter records were initially filtered into three different bands: a low-passed band, periods longer than 40 hours; an intermediate band, periods between 40 and 10 hours, which contains the diurnal and semi-diurnal tidal components, the inertial oscillations and a natural oscillation of the Gulf of Mexico at periods near 30 hours; and a high-passed band, periods shorter than 10 hours. The distribution of variance for both the eastward and southward current components at each meter and for the indicated deployment is shown in Figure 4.6-2. For alongshore components most of the variance in the easterly flow is contained in the low-passed signals except at Mooring CC where there is nearly equal distribution of variance between the low-passed and intermediate bands. The high-passed band is an important contributor to

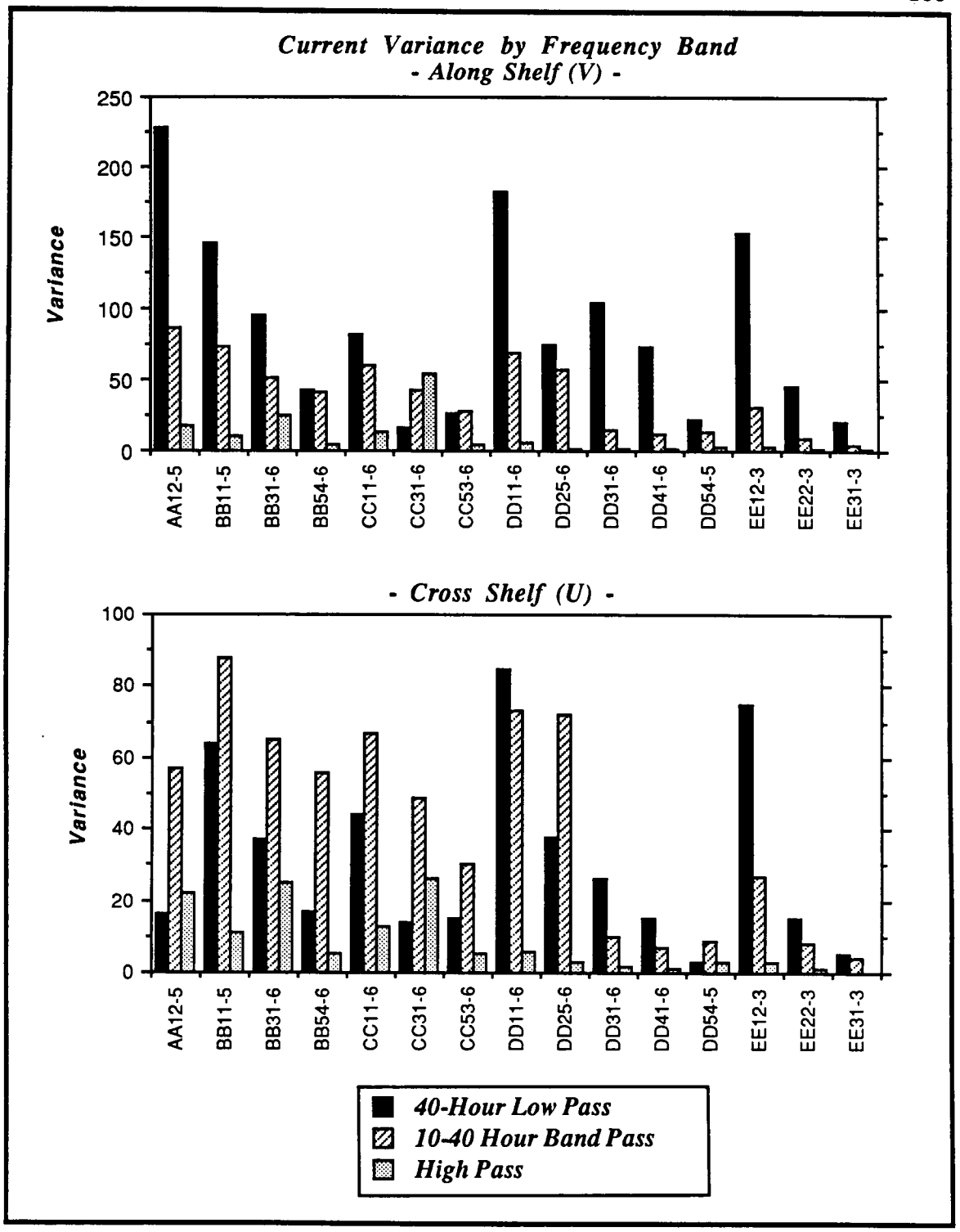

Figure 4.6-2. Variance distribution for current meter records by band and by component.

the total variance only in the alongshelf flow at CC3, a location of weak mean flow.

When the entire data set is considered, the principal axes of the low-passed current field all lie within 20° of east (Table 4.6-2, Figure 4.6-3). There is, though, an apparent decrease in the kinetic energy level of the fluctuating part of the signals as one approaches Mooring CC either from the inner shelf or the outer shelf. Furthermore, the distribution of energy is more vertically isotropic on Mooring CC than either north or south of the mooring. During Periods VI, VII and VIII, the principal axes of the low-passed currents do not deviate from east by more than 42° and most by less than 20°. Topographic steering of the subtidal flow, as evidenced by the anisotropy of the variance ellipse, is strong nearshore where the coastal constraint (Csanady, 1981) is important and over the outer shelf and upper slope where, presumably, conservation of potential vorticity is important. The mid-shelf minimum in kinetic energy of the low-passed fluctuations is not as clear in Period VI as in the other two seasonal periods.

4.6.3 Spectrum Analysis Results

Initially, an attempt was made to analyze current velocity using complex spectrum analysis. The results were disappointing and it was believed that the weaker cross-shelf signals might be degrading the quality of the results. As a consequence, all analyses presented here are scalar analyses for either the eastward or southward component of the velocity. Analyses are carried out with 20 degrees of freedom.

The winds used in the analyses came from Sabine Pass and Southwest Pass. Only the water level was collected at Galveston. Wind data from sites closer to the mooring array than Sabine Pass were either not yet available, were incomplete or interrupted, were derived from improperly installed meters or were from inland stations which were not representative of shelf winds. Chuang and Wiseman (1983) suggest that highly correlated wind patterns occur over the region from Galveston to the Mississippi Delta. While the winds at Sabine Pass (SRST2) and Southwest Pass (BURL1) were highly coherent, the relative energy distribution within different frequency bands varied significantly between the two sites. In particular, there is a strong relative peak in eastward wind stress at Southwest Pass in the one-week band (Figure 4.6.4)

Spectra of individual low-passed current meter records in variance conserving form show either a uniform distribution of energy at the lowest frequencies with a decay towards higher sub-tidal frequencies or a broad peak in the synoptic weather band, e.g., Figure 4.6-5a,b. The wind-stress spectra exhibit a spectrum peak at periods from four to 20 days with sharper secondary peaks at three to four, seven and 12 to 14 days. The apparent difference in variance in the wind-stress field at Southwest Pass (Figure 4.6-4, solid curves) and Sabine Pass (Figure 4.6-4, dashed curves) is, at least partially, due to the higher anemometer height at the former site. The mean winds were also different at the two sites.

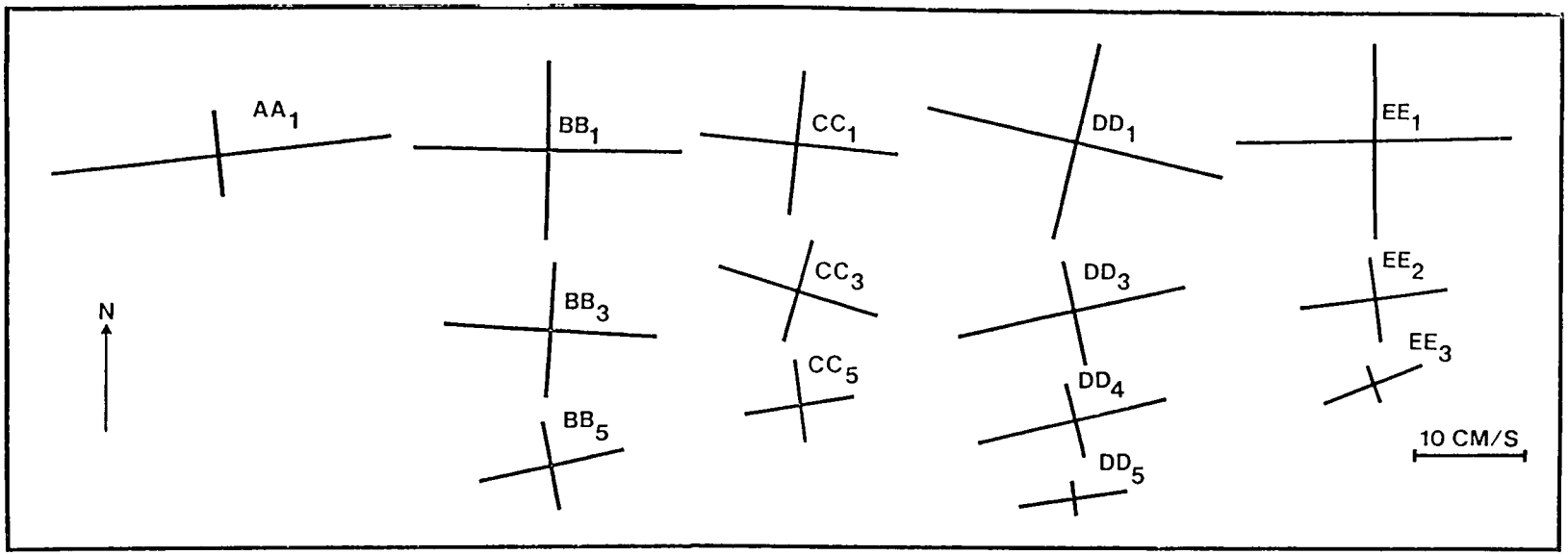

Figure 4.6-3. Principal axes of the low-passed current variance ellipses from all available data for the shelf and upper slope moorings.

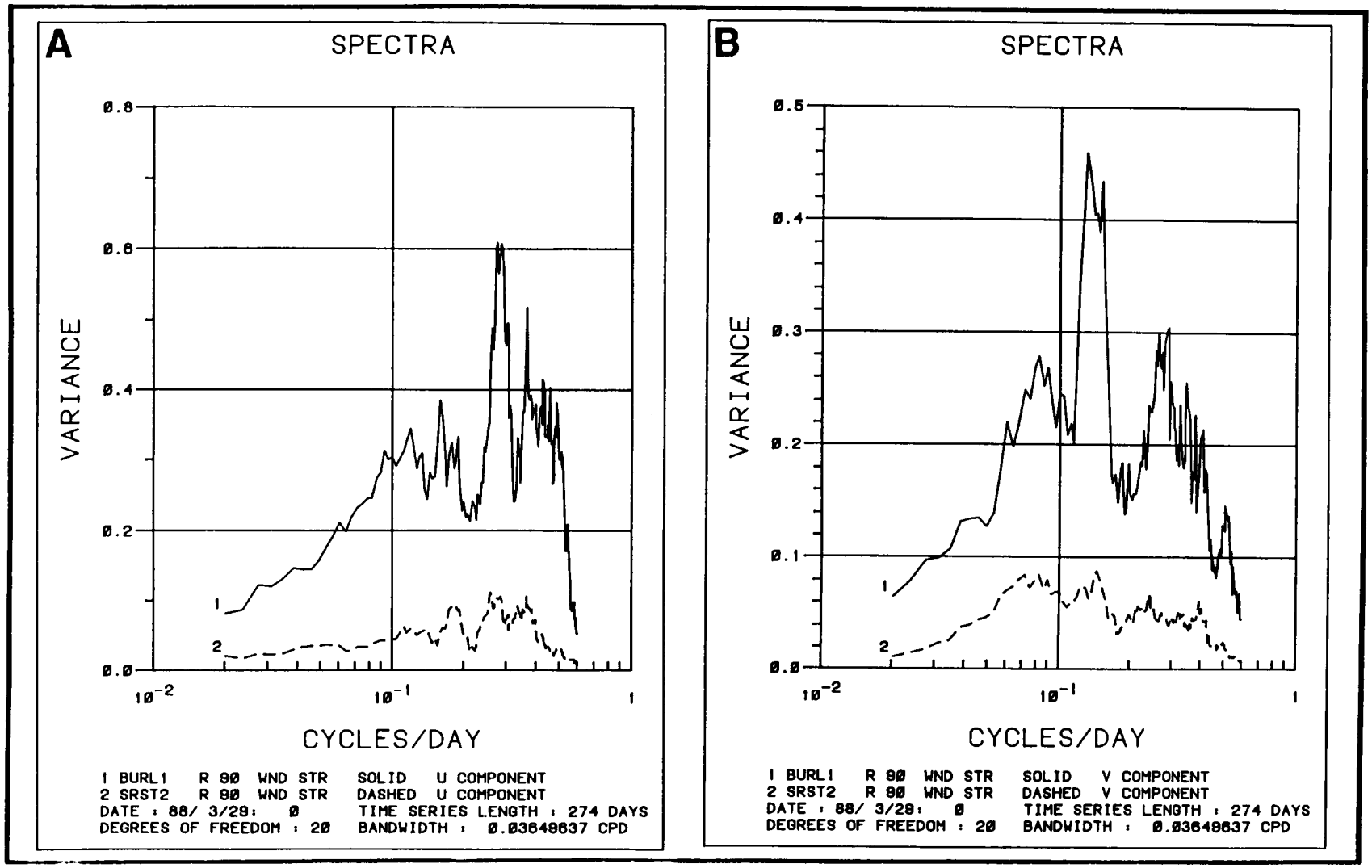

Figure 4.6-4. Variance preserving spectra for 274 days, beginning March 29, 1988, at Sabine Pass (SRST2) and Southwest Pass (BURL1) for (a) the U component of wind stress and (b) the V component of wind stress

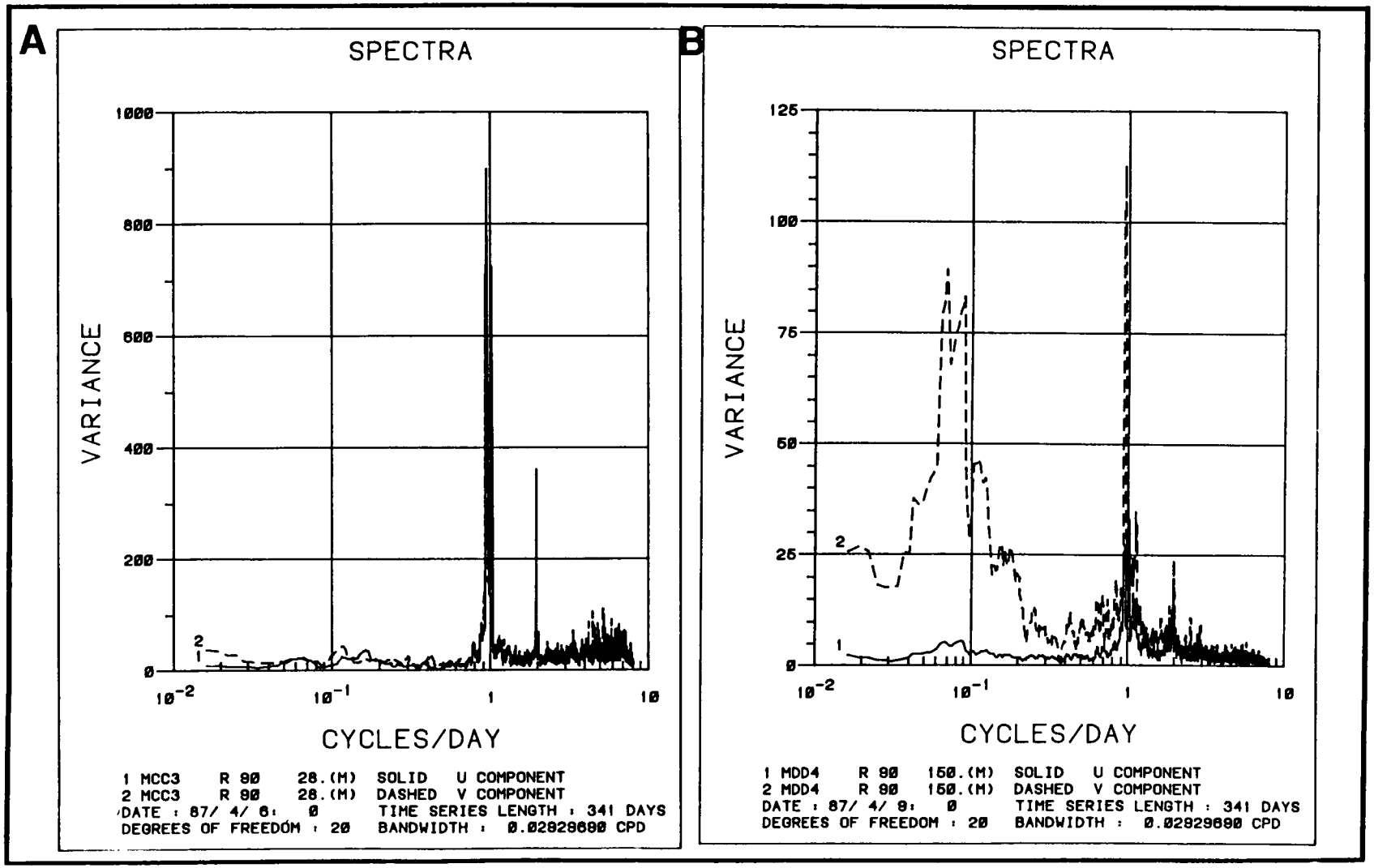

Figure 4.6-5. Variance preserving spectra for 341 days, beginning in April 1987, from the current meter records at (a) Mooring CC at 20 m depth (record MCC3) and (b) Mooring DD at 150 m depth (record MDD4). Spectra are estimated using 20 degrees of freedom.

The spectrum of water-level variations at Galveston is red below periods of about six days. Minor spectrum peaks occur at periods of approximately seven and 14 days. In the energy containing portion of the spectrum, the water levels are coherent with the eastward wind stress, at periods longer than 2.5 days, with a phase near 180° as previously seen by Chuang and Wiseman (1983). Water level is also coherent with the cross shelf wind at the synoptic weather periods, 3 days and 7 days.

When the Galveston water-level records were compared with the longest current meter records, they were found to be coherent with the alongshore flow at Meter BB3 at time periods between 10 and 30 days. The phase was near 180°, suggesting a simple quasi-geostrophic balance. No significant coherences were found near periods of seven days between the water level and (alongshore) flow at BB3, CC3 or DD4.

Vertical coherence between long records of easterly flow at a single mooring was generally significant at the 95% level within the synoptic weather band, e.g., Figure 4.6-6b. For the cross-shelf components, significant vertical coherence was also often found (Figure 4.6-6a). As shown in Figure 4.6-6, the phase was near zero degrees when the current meters were both near the surface or near the bottom and often near 180° when they were widely separated in the vertical. This is consistent with wind-driven Ekman transport and continuity.

Within the near-surface and near-bottom layers, the horizontal coherence of the alongshore currents was often significant between neighboring moorings, e.g., Figure 4.6-7. This was not the case for the cross-shelf flow.

For the longest records, statistically significant coherence was observed between the alongshore currents and the alongshore wind stress at Southwest Pass at periods longer than 5 days. (The coherence with the wind stress at Sabine Pass was less clear. This site was closer to the moorings, but downcoast of them.) The coherence levels decreased and the phase lag of the currents with respect to the wind increased at the offshore moorings.

In many cases when the coherence was statistically significant, the linear model relating the two signals left a major portion of current variance unexplained. (This may be seen in Figure 4.6-8. This figure presents stick diagrams for the wind stress and currents during a 100-day period beginning in late July 1988. There was a strong eastward wind event in mid-August, a westward wind event in early September and a southward event in early October. The response of the currents was not appropriate to a purely wind-driven, linear system. At Meter AA1, the currents are directly driven by the eastward event and possibly by the westward event. No response to the southward event is observed. A clear response to all three events, though, is observed at Meter BB3 somewhat further offshore. Over the outer shelf, at Mooring DD, the uppermost meter exhibits a response to all three events, but the strength of the response is not directly proportional to the strength of the wind stress. Deeper in the water column, at Meter DD4, there does not appear to be a coherent response to any of the three wind events.) A number of possible

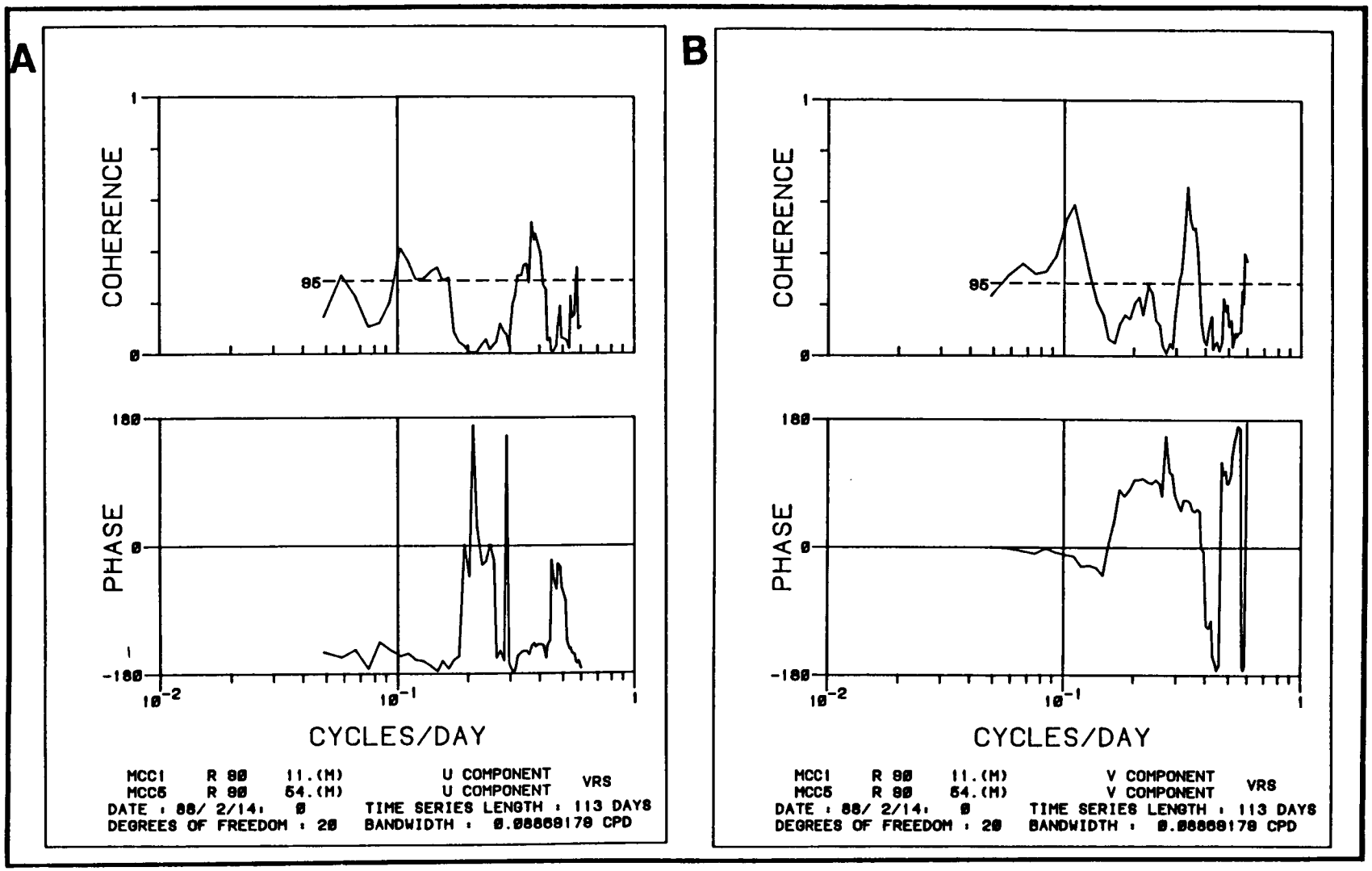

Figure 4.6-6a,b. Vertical coherence and phase, estimated using 20 degrees of freedom, for the concurrent portions of current records at Mooring CC at 11 and 54 meters depth for (a) the southward component of current velocity and (b) the eastward component of current velocity.

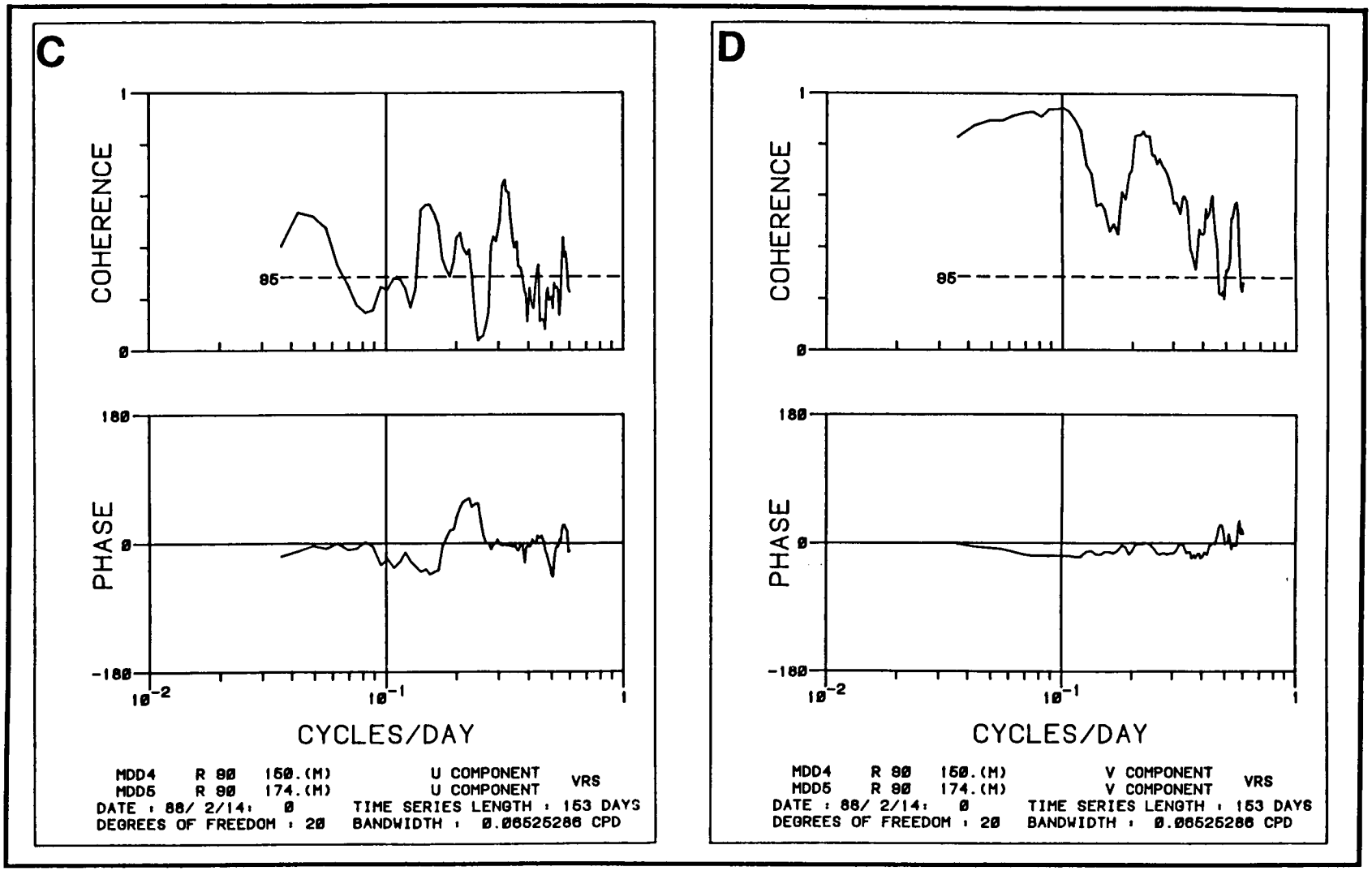

Figure 4.6-6c,d. Vertical coherence and phase, estimated using 20 degrees of freedom, for the concurrent portions of current records at Mooring DD at 150 and 174 meters depth for (a) the southward component of current velocity and (b) the eastward component of current velocity.

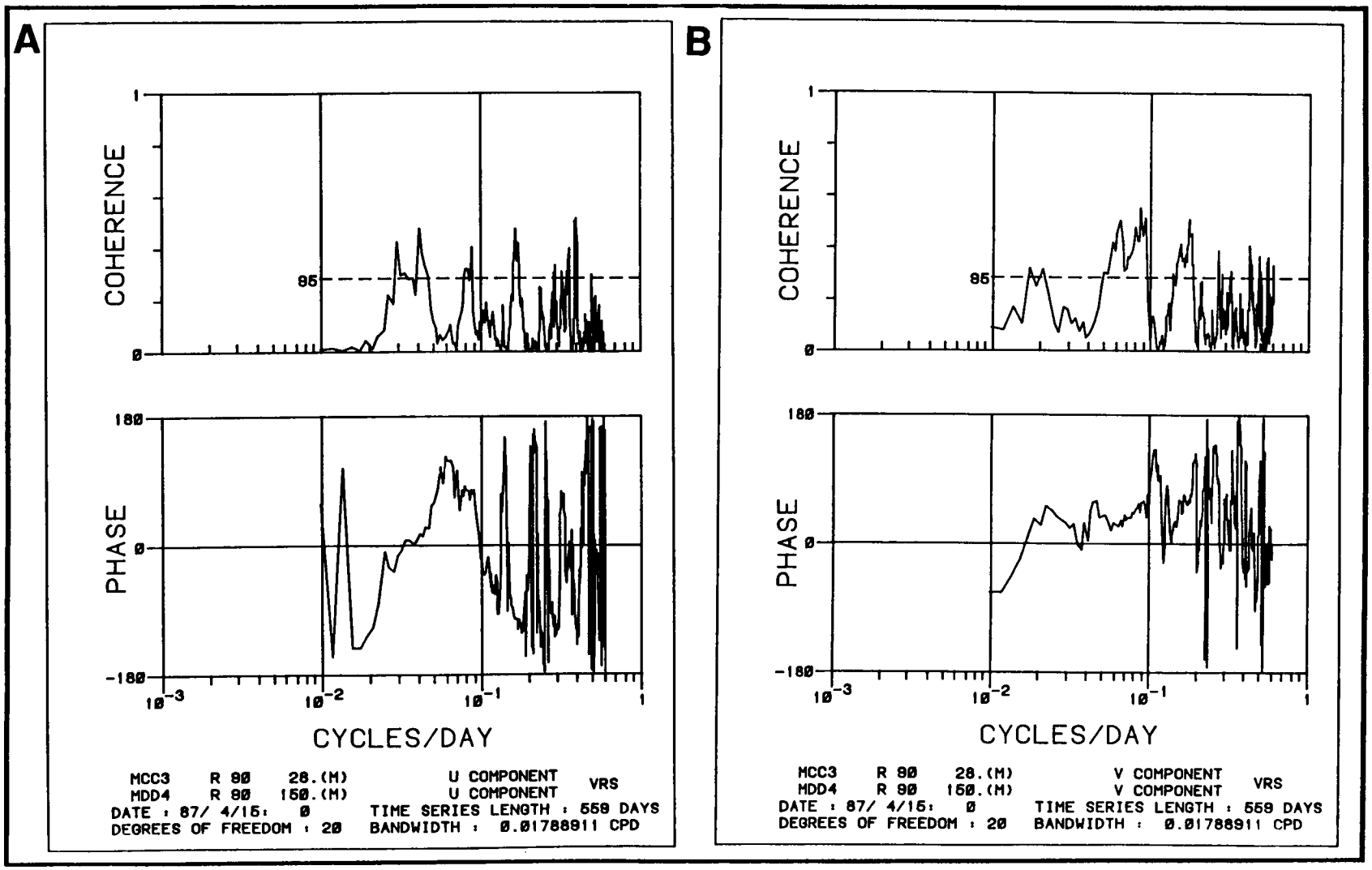

Figure 4.6-7. Horizontal coherence and phase, estimated using 20 degrees of freedom, for the concurrent portions of the current records at Mooring CC at 28 m and Mooring DD at 150 m for (a) the southward component of current velocity and (b) the eastward component of current velocity.

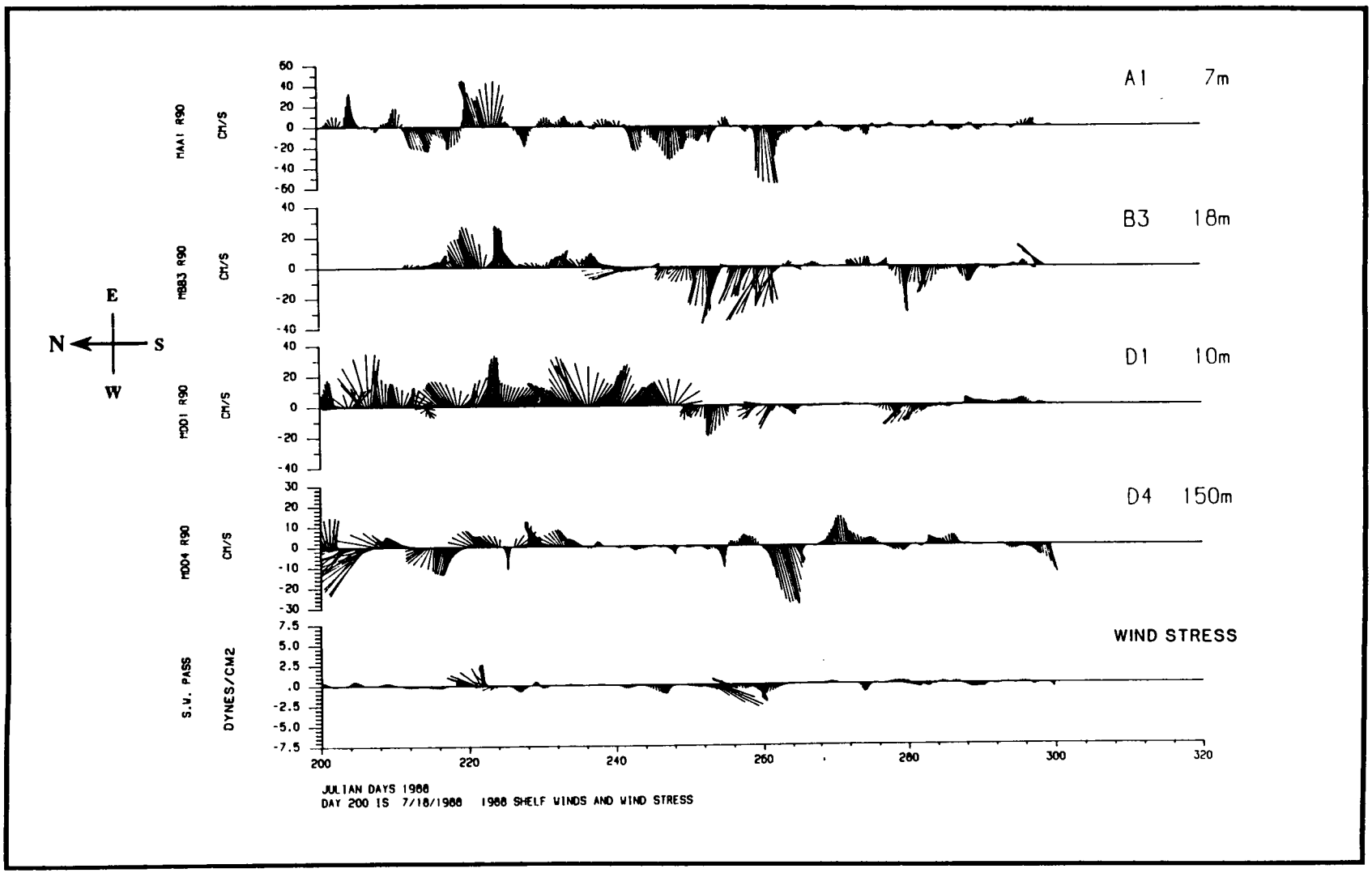

Figure 4.6-8. Winds for Southwest Pass and the last 100 days of currents at Meters MAA1 (7 m), MBB3 (18 m), MDD1 (10 m) and MDD4 (150 m).

explanations for the low coherences are plausible. The current forcing may be from the very far field, possibly further up-coast (east) than the Mississippi Delta. The time series may be non-stationary. The current meters may at different times be found above, within, or below the pycnocline. This would introduce a random phase relation between the currents and the winds and result in low apparent coherence. This is structurally similar to the situation offshore where eddies intermittently affected the instruments. In an attempt to avoid some of these problems, similar frequency domain analyses were performed on the data from time Periods VI, VII and VIII.

Time Period VI was a period of relatively weak winds and low to moderate river runoff. Both components of the currents at Moorings BB and CC were vertically coherent with a phase near zero degrees (Figure 4.6-9). Coherence between the current components and the corresponding Southwest Pass wind-stress components was generally weak and narrow and or insignificant. The only moderately strong coherence was observed at meter BB3. The easterly winds and currents were coherent at periods between 5 and 8 days. In the cross-shelf direction, coherence was significant between 12 and 20 days. Occasionally, other current meter pairs exhibited significant coherence among themselves. For example, the eastward components of flow at current Meters DD4 and EE3 were coherent at periods near four days. During this interval, the wind stress at Southwest Pass exhibited a broad spectral peak at periods longer than three days, and the easterly component showed an intense secondary peak at three days. Hydrographic conditions measured in July 1987 were dominated by a broad pycnocline in the upper 40 m of the water column across which the density changed by five sigma-t units. The meters at Moorings BB and CC were certainly within this pycnocline region while those at DD4 and EE3 were well below it.

Period VII had strong wind and riverine forcing. The Mississippi River runoff was high during the entire period. The wind-stress variance was two to three times as large as that during Period VI; the character of the wind stress changed as well. During Period VI, the cross-shelf wind stress was dominant. During Period VII the two stress components were nearly equal in variance with the alongshelf component being slightly more energetic. Comparisons of near-surface and near-bottom current meters at Moorings BB, CC, and DD exhibited bands of marginally coherent alongshore flow at periods longer than ten days. The near-surface and near-bottom southerly components at Mooring CC were also coherent at periods of three and ten days with a phase near 180°.

The meters over the shelf generally exhibited bands of significant coherence between the along isobath components of current and Southwest Pass wind stress. The coherence was strongest at mid-shelf and at the deeper meters (Figure 4.6-10). The low coherence over the inner shelf was surprising since past studies of the shallow nearshore regions of the Louisiana shelf have shown very strong coherence with the local wind (Crout et al. 1984; Kelly et al, 1983). It is possible that the local wind over the inner shelf was not well represented by the winds at Southwest Pass. More likely, the offshore moorings were in a well-mixed, wind-driven portion of the shelf while the proximity of the Atchafalaya

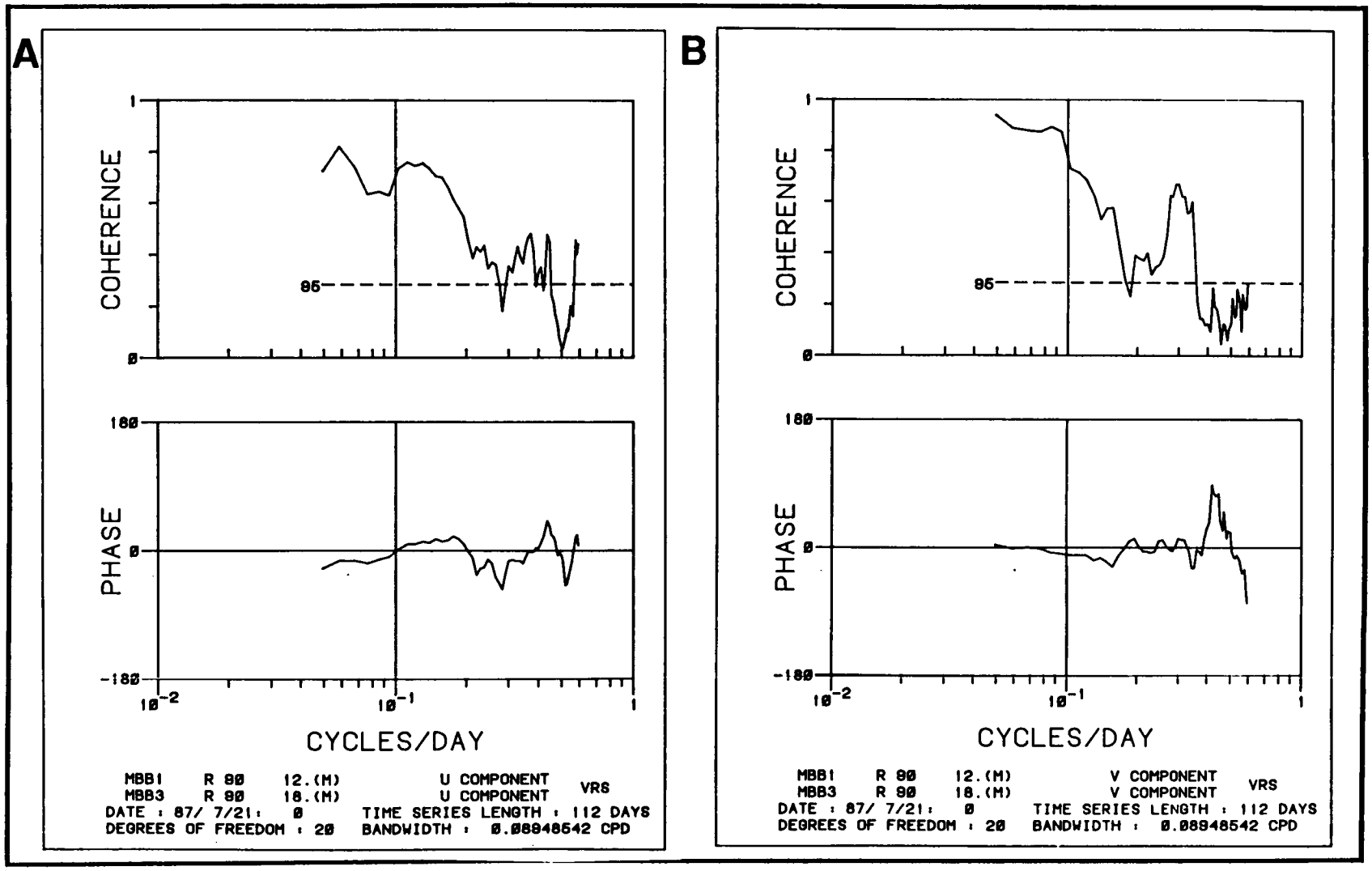

Figure 4.6-9. Vertical coherence and phase between (a) cross isobath and (b) along isobath Mooring BB current meter records MBB1 (12 m) and MBB3 (18 m) for Period VI, estimated using 20 degrees of freedom.

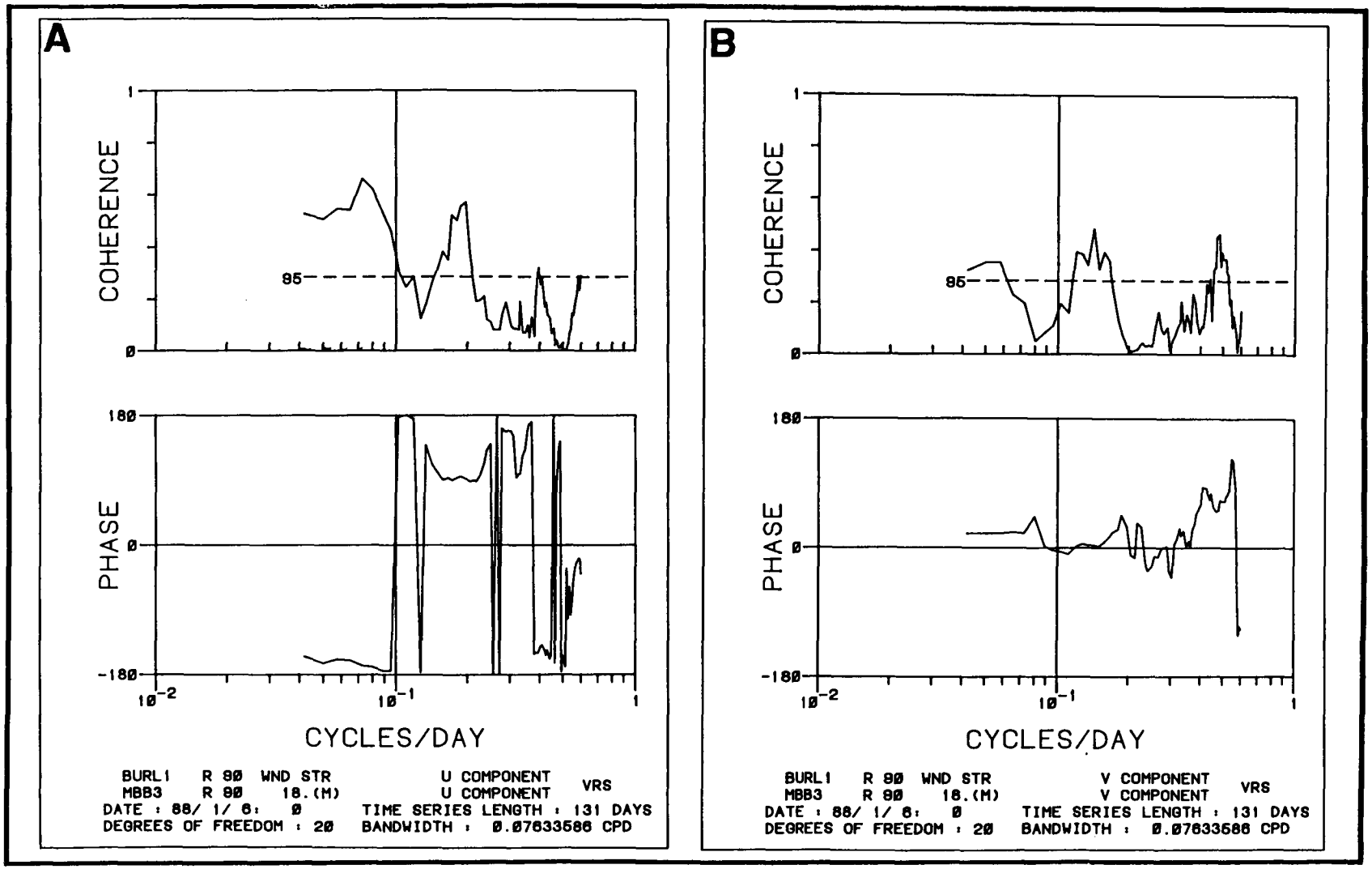

Figure 4.6-10a,b. Coherence and phase between (a) cross isobath and (b) along isobath current meter records from Mooring BB Meter MBB3 (18 m) and Southwest Pass (BURL1) wind stress during Period VII, estimated using 20 degrees of freedom.

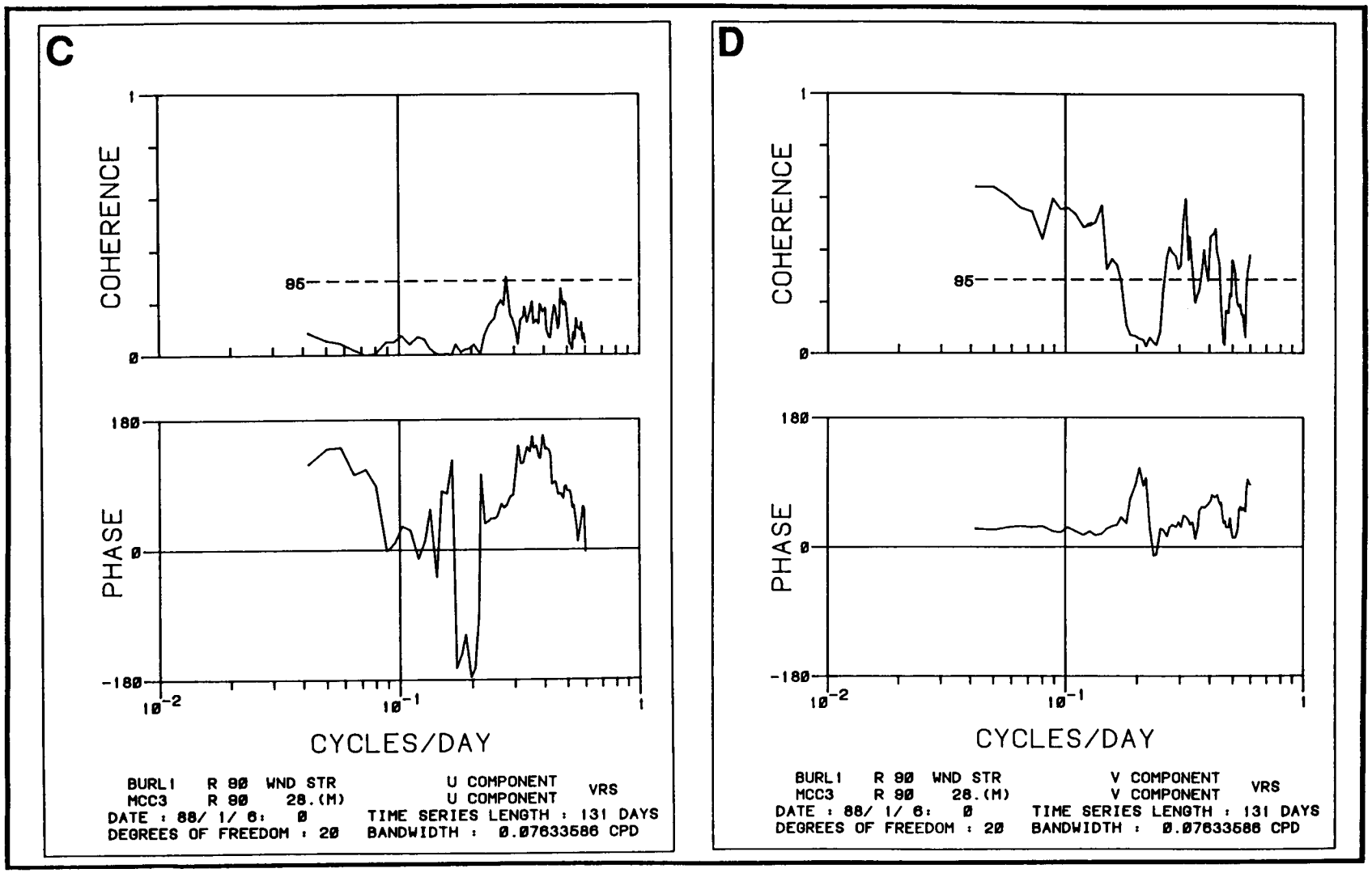

Figure 4.6-10c,d. Coherence and phase between (c) cross isobath and (d) along isobath current meter records from Mooring DD Meter MCC3 (28 m) and Southwest Pass (BURL1) wind stress during Period VII, estimated using 20 degrees of freedom.

Delta resulted in significant stratification variability closer to shore. This would modulate the effectiveness of wind-forcing and reduce the coherence between wind and current records.

Data from the November 1987 cruise showed vertical near-homogeneity of the water column over the shelf to depths of 60 m. Below 75 m, thermal stratification was observed, but no salinity data were available with which to assess the density stratification. It can reasonably be assumed, however, that the waters were stratified below these depths since any mixing would have altered both the temperature and salinity fields. The February 1988 cruise again observed vertical near-homogeneity to depths of 100 m. Below this depth the waters were weakly stratified. Over the shelf, modest stratification was observed at 10 to 20 m depth in waters 20 to 40 m deep. This is believed to be a time-dependent phenomenon with the Atchafalya River plume probably contributing directly to this stratification.

Winter season winds associated with cold-air outbreaks stir and homogenize the water column with isopycnals (lines of constant density) becoming nearly vertical at these times. In calmer periods between storms, the stratification can re-establish itself as the frontal boundaries relax and assume a more horizontal position in the water column. It is also noteworthy that a mass of dense water (>26 sigma-t) was observed over the mid-shelf. This water is often observed to form over the west Louisiana and east Texas shelves during winter. The resultant low in dynamic topography is consistent with and may be responsible for the cyclonic circulation proposed by Cochrane and Kelly (1986) during this season.

It has been suggested that in these very shallow waters the dominant response may be due to the cross-isobath component of wind (Chuang and Wiseman, 1983; Lewis and Reid, 1985). Indeed, significant coherence exists between the southward (offshore) wind stress at Southwest Pass and southward current at Mooring BB at 18m depth. Coherence was significant at approximately 5-day periods and at periods longer than 10 days. The phase was near 180° at the longer periods. It was closer to 90° in the 5-day band.

During time Period VIII, the summer of 1988, the United States was suffering from a severe drought. The Mississippi River stage was extremely low. Hypoxia, a normal summertime occurrence along the Louisiana inner shelf, was absent. Nearshore waters which are normally turbid were quite clear. Thus, riverine forcing was at a minimum. Wind forcing, though, was about twice as strong as that during the summer of 1987.

Vertical coherence of the flow was apparently weak during this period. The coherence between the cross-shelf current components at BB1 and BB3 was significant at periods longer than six days while the coherence between the easterly components at EE1 and EE3 was significant at periods longer than ten days. Both components of flow were coherent between currents at DD1 and DD4. No other regions of strong vertical coherence were noted.

The inner shelf current records exhibited significant coherence between the alongshore components of flow and the eastward (alongshore) wind stress at Southwest Pass at periods longer than 5 days (Figures 4.6-11 and 4.6-12). Significant coherence between the cross-shelf wind stress and current was generally weak and narrow band. The wind stress during this period had noticeable spectral peaks at periods of two to three days in the cross-shelf direction and five to 14 days in both components. While no salinity data were available during this period, strong thermal stratification was noted across the shelf between 20 and 40 m within the water column during the July 1988 cruise. Similar thermal stratification persisted into October.

4.6.4 Empirical Orthogonal Function Results

For each of the three time periods, an Empirical Orthogonal Function analysis was run for the alongshore and cross-shelf velocity components of current and wind. Each analysis was run once with the Galveston low-passed barometrically adjusted water level added as an additional observable and once with it left out of the analysis. The analyses were also run with data from Mooring EE included and omitted to determine the degree to which flow over the upper slope was correlated with that over the shelf.

The presence of data from Mooring EE in the analysis did not significantly affect the results. In fact, weightings of the signals from Mooring EE for the most important mode, the first mode for eastward flow, were small. Similarly, adding Galveston adjusted water level as an observable did not significantly alter the modal patterns. Weightings for the water level were often high but consistent with the interpretation of the patterns which had been determined without the water level included in the analysis. Therefore, in the following, results from the analysis of shelf currents, wind stress at Southwest Pass and adjusted water level at Galveston are stressed. The most significant modes are described in Table 4.6-3.

In the eastward direction, the most important mode (Mode 1 (V), Table 4.6-3) consistently accounts for more than 40% of the variance in the correlation matrix. It describes a pattern in which the water moves back and forth along the shelf in response to the wind, i.e., the components of the Mode 1 eigenvector are positive at all current meters and at the Southwest Pass anemometer, indicating positive correlation of wind and current at all stations. The component associated with adjusted water level at Galveston is negative for this eigenvector. Thus, when the fluctuating currents are positive (eastward) the fluctuating water level is below the mean (negative). This is consistent with Ekman flow in which eastward winds are correlated with eastward flow and falling coastal water levels. The second mode (Mode 2 (V), Table 4.6-3) accounts for approximately 10-20% of the variance and describes lateral shear over the mid or outer shelf, i.e., the components of the eigenvector associated with the current meters change sign (alongshore direction) as one moves seaward. This mode is only weakly correlated with the wind except during Period VIII when the pattern is best developed and the wind appears to drive the nearshore flow.

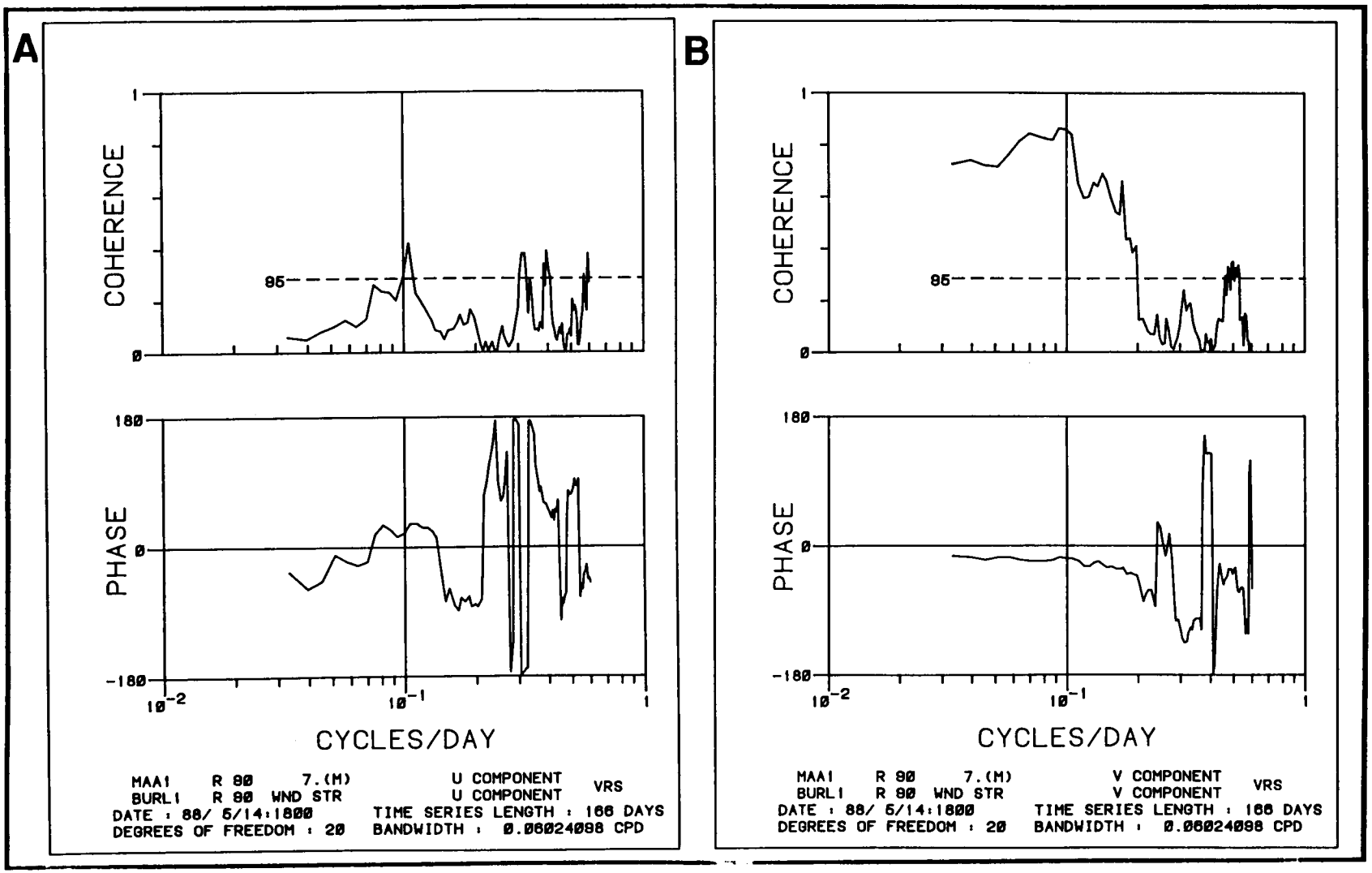

Figure 4.6-11. Coherence and phase between (a) cross isobath and (b) along isobath current meter records from Mooring AA Meter MAA1 (7 m) and Southwest Pass (BURL1) wind stress during Period VIII, estimated using 20 degrees of freedom.

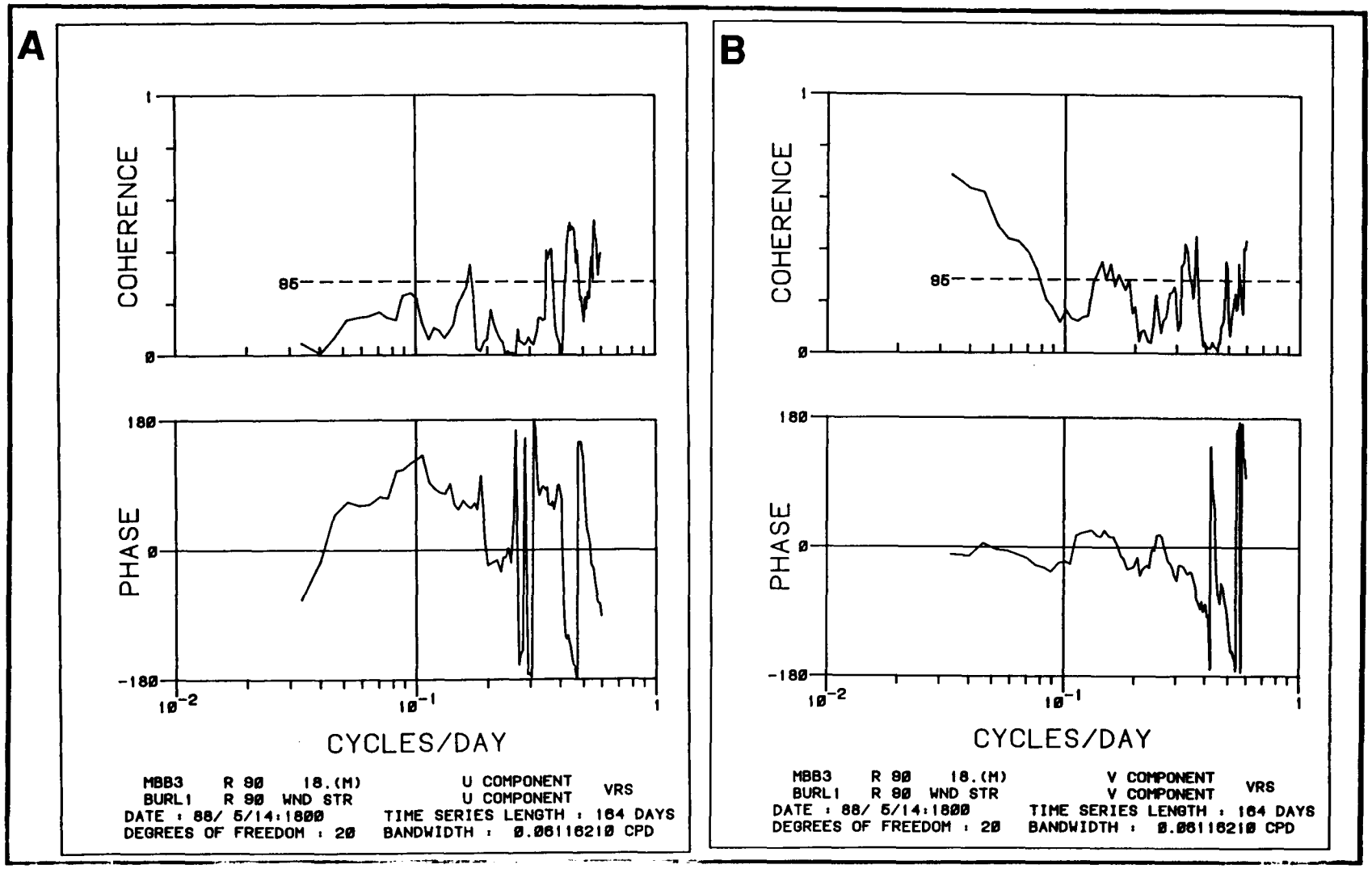

Figure 4.6-12. Coherence and phase between (a) cross isobath and (b) along isobath current meter records from Mooring BB Meter MBB3 (18 m) and Southwest Pass (BURL1) wind stress during Period VIII, estimated using 20 degrees of freedom.

Table 4.6-3a. Empirical orthogonal functions, time Period VI.

Station	Mode 1 (V)	Mode 2 (V)
BB1	0.98	0.03
BB3	1.00	0.03
CC1	0.50	1.00
CC3	0.44	0.97
DD1	0.57	-0.41
DD4	0.73	0.34
SWP*	0.75	-0.23
GVN*	-0.96	0.35
%*	0.70	20.95

* SWP represents the appropriate windstress component at Southwest Pass, GVN is water level at Galveston, Texas, and % indicates the percent or the variance represented in the correlation matrix which is explained by the mode.

Table 4.6-3b. Empirical orthogonal functions, time Period VII.

Station	Mode 1 (V)	Mode 2 (V)
BB1	0.71	-0.12
BB3	0.92	-0.25
CC3	1.00	0.02
CC5	0.92	-0.05
DD1	0.20	1.00
DD3	0.31	0.88
DD4	0.64	0.60
SWP*	0.79	-0.37
GVN*	-0.91	0.24
%*	45.43	17.23

* SWP represents the appropriate wind stress component at Southwest Pass, GVN is water level at Galveston, Texas, and % indicates the percent of the variance represented in the correlation matrix which is explained by the mode.

Table 4.6-3c. Empirical orthogonal functions, time Period VIII.

Station	Mode 1 (V)	Mode 2 (V)
AA1	-0.84	-0.66
BB3	-0.94	-0.16
BB5	-0.90	-0.11
CC3	-0.69	1.00
DD1	-0.75	0.72
DD4	-0.42	0.93
SWP*	-0.87	-0.67
GVN*	1.00	0.25
%*	53.45	13.50

* SWP represents the appropriate wind stress component at Southwest Pass, GVN is water level at Galveston Texas, and % indicates the percent of the variance represented in the correlation matrix which is explained by the mode.

In the cross-shelf direction, none of the first three modes accounts for more than 26% of the observed variance or less than 14%. No simple interpretation of the modes is apparent nor are the modal patterns consistent between the three periods. It is probable that both the variations in stratification and the variations in correlation between the wind stress components are contributing to the difficulty in interpreting the modal patterns.

4.6.5 Discussion and Interpretation

The mean flows observed during the study are consistent with the general pattern of flow suggested by Cochrane and Kelly (1986). When considered on seasonal times scales, the mean currents are also consistent with these patterns, but not statistically significant. The measured currents describe the flow along a single cross-shelf line of longitude. If it can be concluded that the observed cyclonic shear is indicative of a closed shelf gyre, then the transport in the bottom boundary layer would tend to accumulate material at mid-shelf in the absence of intense "events" which create mixing and hence dilution. The dense water found over the mid- and outer shelf during the February 1988 cruise is indicative of such accumulation. Much of this modified water, when initially formed, sinks and flows offshelf providing a mechanism for periodically flushing material from the shelf.

No clear evidence of strong oceanic forcing exists in the data set. Some coherence does exist between upper slope and shelf current meters, however, no pattern of consistent lateral coherence occurs at stations across the shelf. In fact, cross-shelf coherence patterns are very difficult to interpret. The cross-shelf coherence length scales appear to be extremely small. Station separation during this study did not support a rough estimate of the coherence scale magnitude.

Vertical coherence of the eastward currents was often significant. Although the data were analyzed in seasonal time periods to improve coherences and to interpret more easily the underlying dynamics, these coherences were greater for the longer time series which extended across seasons.

Vertical coherence of cross-shelf flow was generally less than for the stronger alongshore flow. This may be partially attributed to the variations in the density structure over the shelf. As fronts and pycnoclines move back and forth past a meter, the phase relation between current pairs or currents and wind stress usually changes. For these computations, unless the phase relation is consistent throughout the time series, coherence analysis will have a difficult time estimating a meaningful linear relationship. Furthermore, topographic steering will tend to focus current energy in the alongshore direction. Also, wind forcing is principally in this alongshore direction which supports a more vigorous forcing-response relationship except during the winter season. As a result, our understanding of the eastward flow is superior to that of the cross-shelf flow.

The coherence analysis of the Galveston water level suggests that simple Ekman dynamics are important at subinertial time scales. At periods greater than 2.5 days, the flows are coherent with the alongshore winds. The water level and alongshore currents are also coherent at subinertial frequencies.

The coherence of the currents and the winds is far superior when the winds measured at an upstream location such as Southwest Pass are used rather than the more local but downstream winds measured at Sabine Pass. This is consistent with the concept of coastally trapped waves generated east of the measurement site travelling alongshore (downcoast) past the mooring array. Whether these might be forced at the Mississippi Delta [similar to forcing waves at the Florida Keys as described by Mitchum and Clarke (1986)], or further east so that they must propagate past the delta is not clear.

The Empirical Orthogonal Function analysis for each season consistently finds that a simple model of wind forcing of the entire shelf accounts for a significant portion of the observed eastward current variations. The second mode describes lateral shear over the mid- and outer shelf. The forcing for this mode is not readily apparent. In the cross-shelf direction, the EOF analysis did not provide any structured insight to shelf current patterns.

Much of the variance in the current field is left unexplained by any of the simple statistical analyses presented above. A similar situation has been noted during the analysis of the CASP data set (Anderson et al., 1989) which was collected along the Nova Scotian shelf. Either a vital forcing function has been left out of consideration, or the important dynamics are considerably more complex than the statistical analyses used can account for, much of which assumed a linear relationship between variables.

One possibility is that the Louisiana shelf in this region is so broad and flat that the curl of the wind stress becomes an important forcing function for shelf circulation. Preliminary analyses of wind data from several offshore oil platforms suggest that wind stress and the wind stress curl are equally important in vertically-integrated, barotropic models. Unfortunately, the wind data necessary to assess the importance of this forcing were not available for the time period of the present study. The NDBC buoys are quite far off the shelf, previous observations from platforms were not of a consistent quality, and the C-MAN stations are within the transition region of the atmospheric coastal boundary layer.

Another possibility is that the dynamics are controlled by coupled shelf wave modes. The available data set is marginally acceptable to explore this possibility. Attempts to hindcast the data using such a model need to be explored. Furthermore, any future studies in this region would do well to utilize bottom-mounted pressure sensors in their experimental design. The absence of open coast tide gauge recorders restricts the interpretation of the available data. The observed cross-shelf phase relationships and modal structures of the observed currents may also be

more readily explained with the incorporation of good pressure measurements.

4.6.6 Shelf Hydrography

4.6.6.1 Introduction

Five shelf hydrographic cruises were conducted seasonally during the first year of observations. Information from these cruises and temperature data from the in-situ current meters will be discussed in the following section. The cruise dates have been related to the appropriate days in the time series of temperatures as measured by the current meters.

4.6.6.2 Seasonal Thermal Structure

As shown by the 40-HLP temperatures in Figure 4.6-13 an annual cycle of temperature occurs at inner (Mooring BB) and mid-shelf (Mooring CC) locations. As is often seen on mid-latitude shelves, temperature is vertically homogeneous during the period when cooling is occurring. This results from vertical mixing due to mechanical (winds and waves) and buoyancy (density) processes. The resulting overturning causes the entire water column to cool down as a unit.

During the warming portion of the annual cycle, inner and mid-shelf waters become increasingly stratified in the vertical. This tends to inhibit vertical mixing and means that less thermal energy is required to warm the surface waters. As would be expected during the warmer months, the temperature difference between the top and bottom of the water column increases with increasing bottom depth. Note that at Mooring DD the top to bottom (depth=180 m) temperature difference in summer is approximately 14°C while in winter it is as little as 3° to 4°C.

In contrast to the vertical homogeneity as the water column cools, the across-shelf horizontal stratification increases. This can been seen in Figure 4.6-14 which shows the 40-HLP filtered temperatures at a nominal depth of 10 m at Moorings BB, CC and DD across the shelf. This horizontal pattern of temperature gradients is opposite to, or out-of-phase with, the vertical stratification. During the cooling process, the near surface waters tend to be warmer at the outer shelf than at the inner shelf. This is understandable since the offshore continental slope can be a major source of warm water. In contrast, the horizontal gradients are virtually absent as shelf waters seasonally warm. This indicates that the surface waters are quickly heated and become isothermal across shelf while stratifying vertically.

The pattern discussed above was seen in discrete cruise data and from other prior observations on this shelf, however, the present data are believed to be the first continuous long-term temperature records which provide concurrent information on the vertical and horizontal distribution of temperature. Temperature is only one of the two

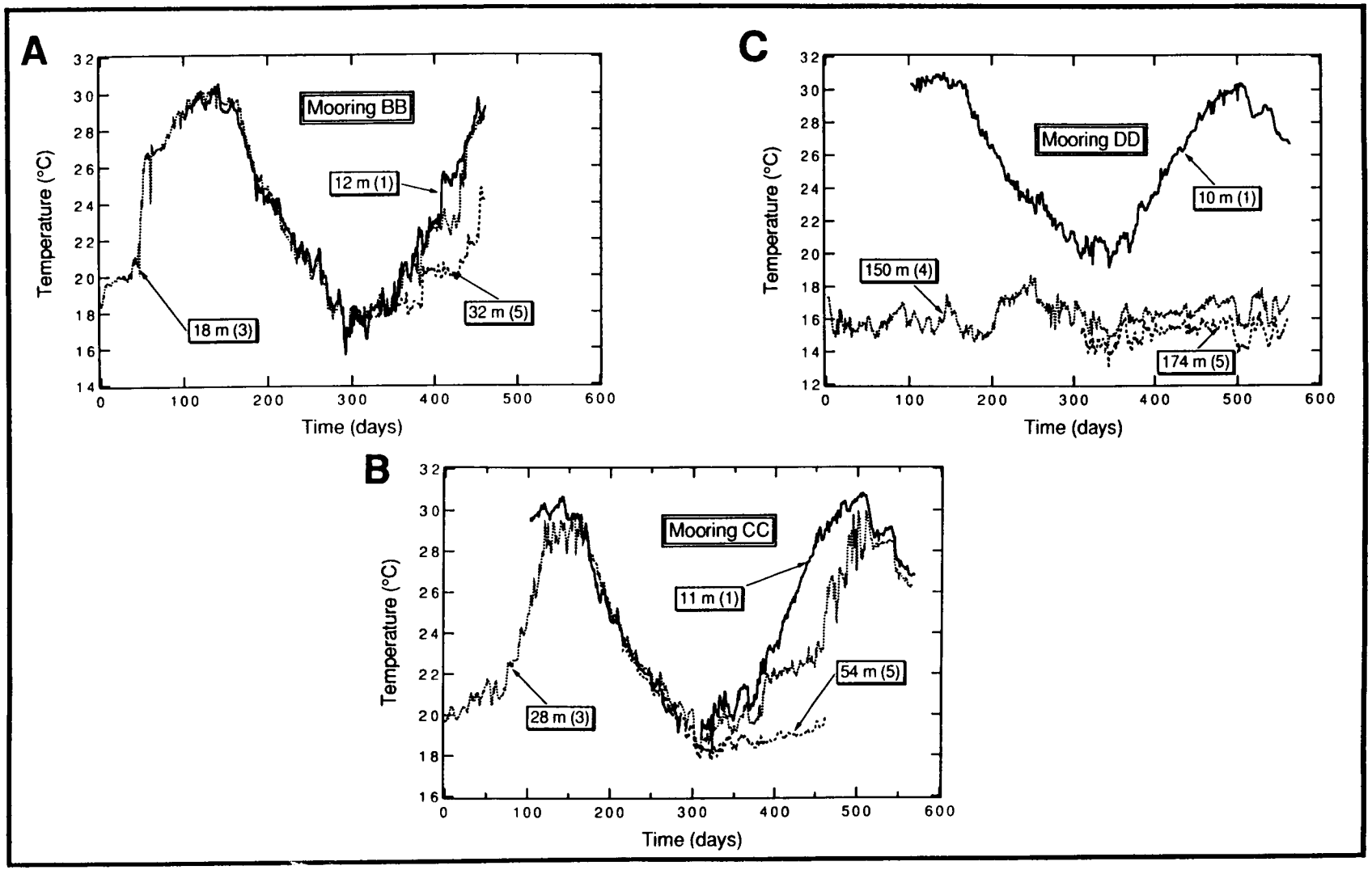

Figure 4.6-13. Forty-HLP time series plots at indicated depths for (a) Mooring BB, (b) Mooring CC and (c) Mooring DD. Note the temperatures are vertically uniform during cooling and vertically stratified during warming.

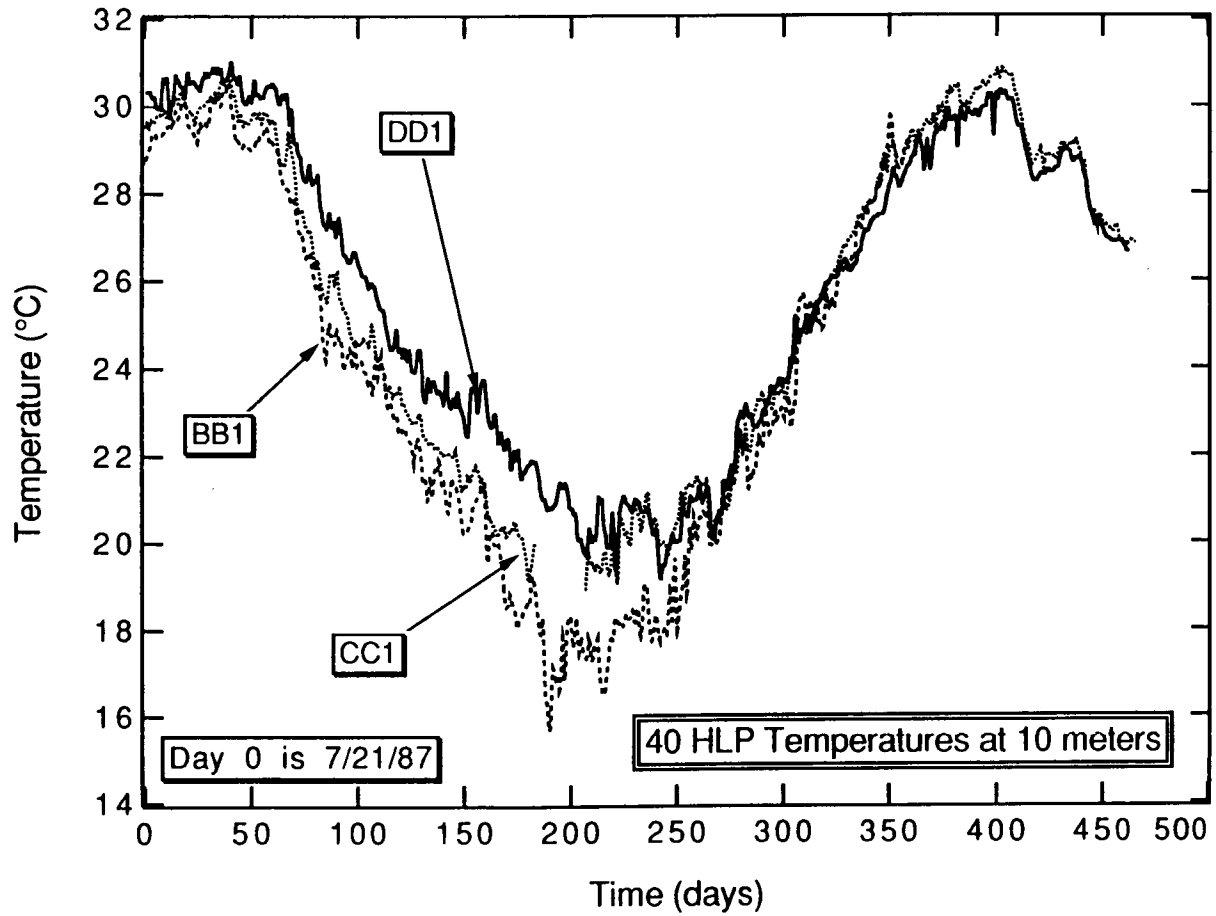

Figure 4.6-14. Forty-HLP time series plots of temperatures at a nominal depth of 10 m for the indicated moorings. Note that during shelf cooling a horizontal gradient develops while during warming the near surface layer is approximately isothermal.

variables affecting water density, thus this pattern does not provide comprehensive information about the spatial distribution of mass.

4.6.6.3 Temperature, Salinity and Density

The initial cruise which involved the deployment of the current-temperature sensors occurred in Spring 1987 (April) coinciding approximately with Day 0 in Figure 4.6-13. The water was weakly stratified in temperature for the initial portion of the annual warming cycle. However, local riverine-estuarine discharge provided a large volume of fresh water to the inner and mid-shelf. This was confined to 120 km from shore and the upper 25 to 30 m of the water column (Figure 4.6-15). This salinity dominated regime caused a strongly stable lens of water which was not readily diluted by vertical mixing (It is worth noting that the contouring scheme used to create these figures linearly interpolates between points, thus, what may appear as diffuse fronts between stations may have been quite strong and localized. The spreading in this presentation may well result from the station spacing in conjunction with the interpolation scheme). Note that seaward of about 125 km the temperature and salinity structure are vertically homogeneous and density gradients are weak or absent.

A second cruise was conducted in April 1987 (Day 16 in Figure 4.6-13) to support concurrent optical measurements. As can be seen in Figure 4.6-16, this cross shelf section is still weakly thermally stratified, however, the lens of fresher water has extended further offshore while remaining in the upper 30 m of the water column. During both April cruises, the largest vertical extent of low salinity water occurred at water depths of 30 to 35 m approximately 40 km offshore of the inner shelf (Mooring AA). During the second cruise the outer boundary of the low salinity water was more diffuse with the gradient occurring over several stations. The minimum salinity during this second cruise was slightly higher than during the first.

The July cruise (Figure 4.6-17), which coincides with Day 98 in Figure 4.6-13, showed strong vertical thermal stratification. The top-to-bottom temperature change in 40 m of water was approximately 9°C. The isotherms were approximately horizontal with the strongest vertical gradients approximately 20 to 30 m below the water surface. A relatively fresh mass of water was located over the inner 90 km of the shelf. A comparison of Figure 4.6-16 and 4.6-17 suggests that the salinity fields are somewhat similar. Note, however, that the minimum salinity measured during July was much less than measured in April. This is because a fresher water mass (salinity less and 23 ppt) was documented at the surface, at the shoreward most station, and is probably associated with a local discharge from estuaries just to the east. This is in contrast to a more diffuse low salinity coastal boundary layer in April, which extended approximately more than half way across the shelf. The density section shows that vertical stratification extended deeper at locations further offshore in July than in April.

The Fall cruise (Figure 4.6-18), in November 1987 (Day 220 in Figure 4.6-13) illustrates conditions after frontal related winds vertically mix the

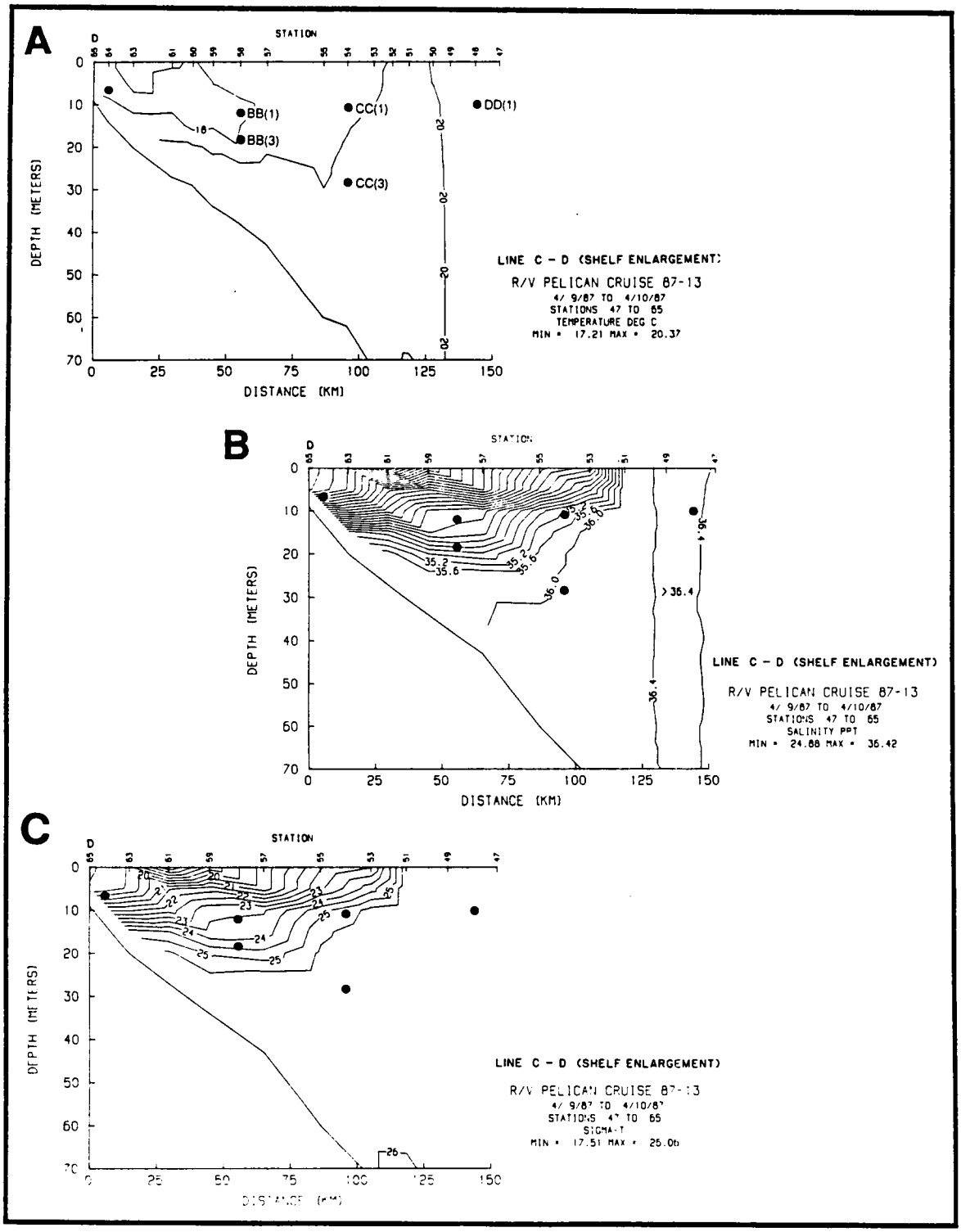

Figure 4.6-15. Cross-shelf sections of (a) temperature, (b) salinity and (c) sigma-t (density) taken during cruise PN8713 on April 9 to 10, 1987. Current meter locations are indicated and labelled.

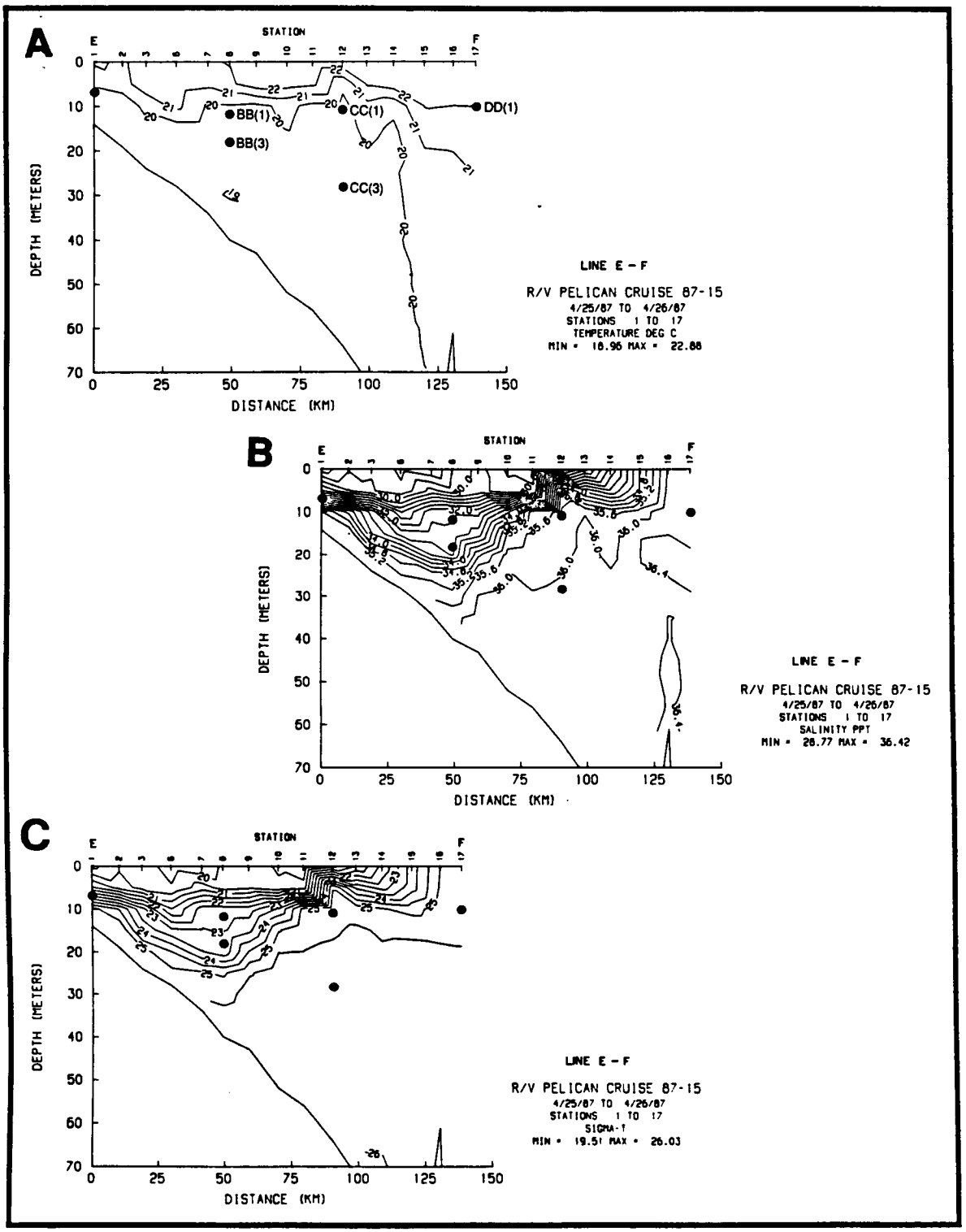

Figure 4.6-16. Cross-shelf sections of (a) temperature, (b) salinity and (c) sigma-t (density) taken during cruise PN8715 on April 25 to 26, 1987. Current meter locations are indicated and labelled.

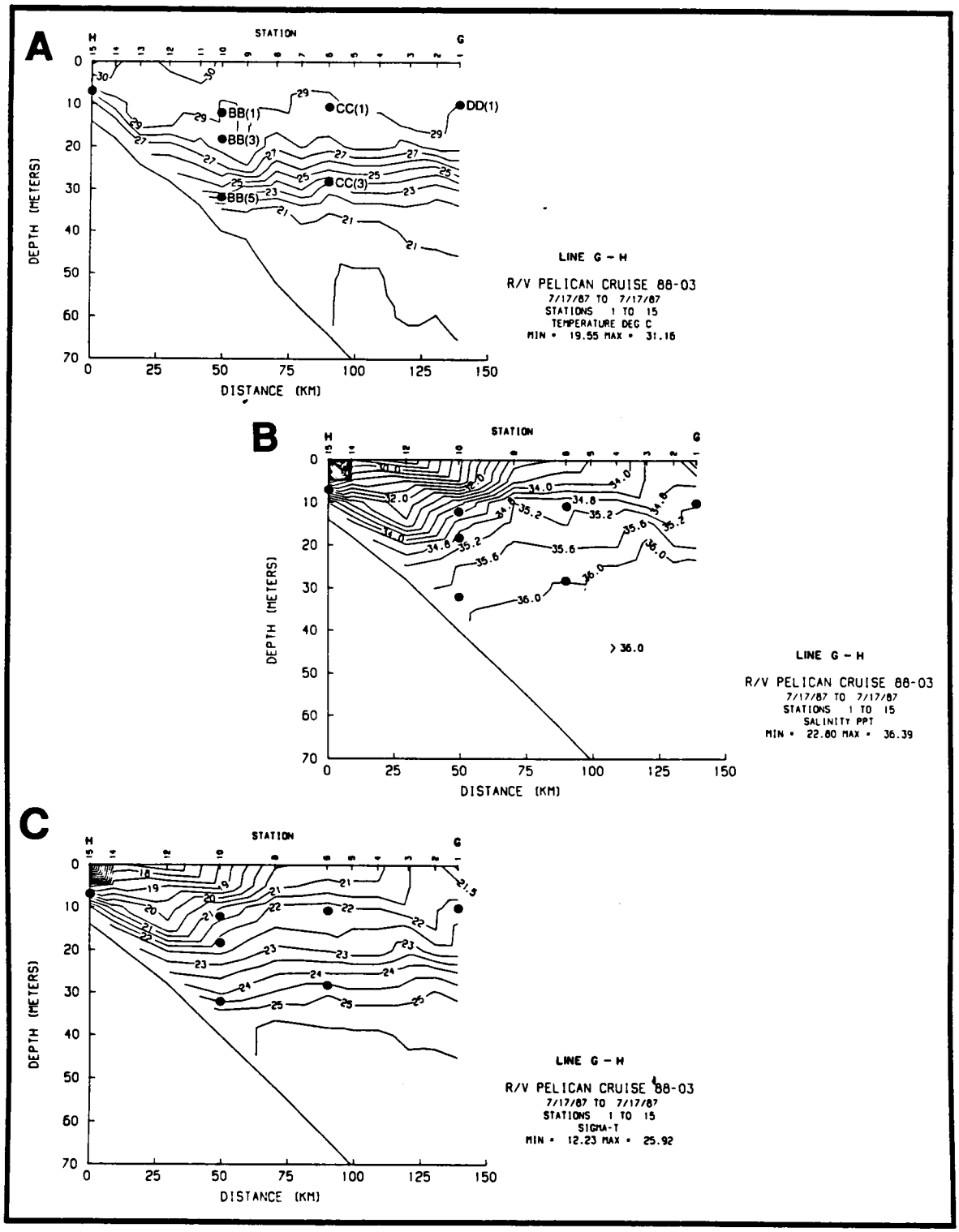

Figure 4.6-17. Cross-shelf sections of (a) temperature, (b) salinity and (c) sigma-t (density) taken during cruise PN8803 on July 17, 1987. Current meter locations are indicated and labelled.

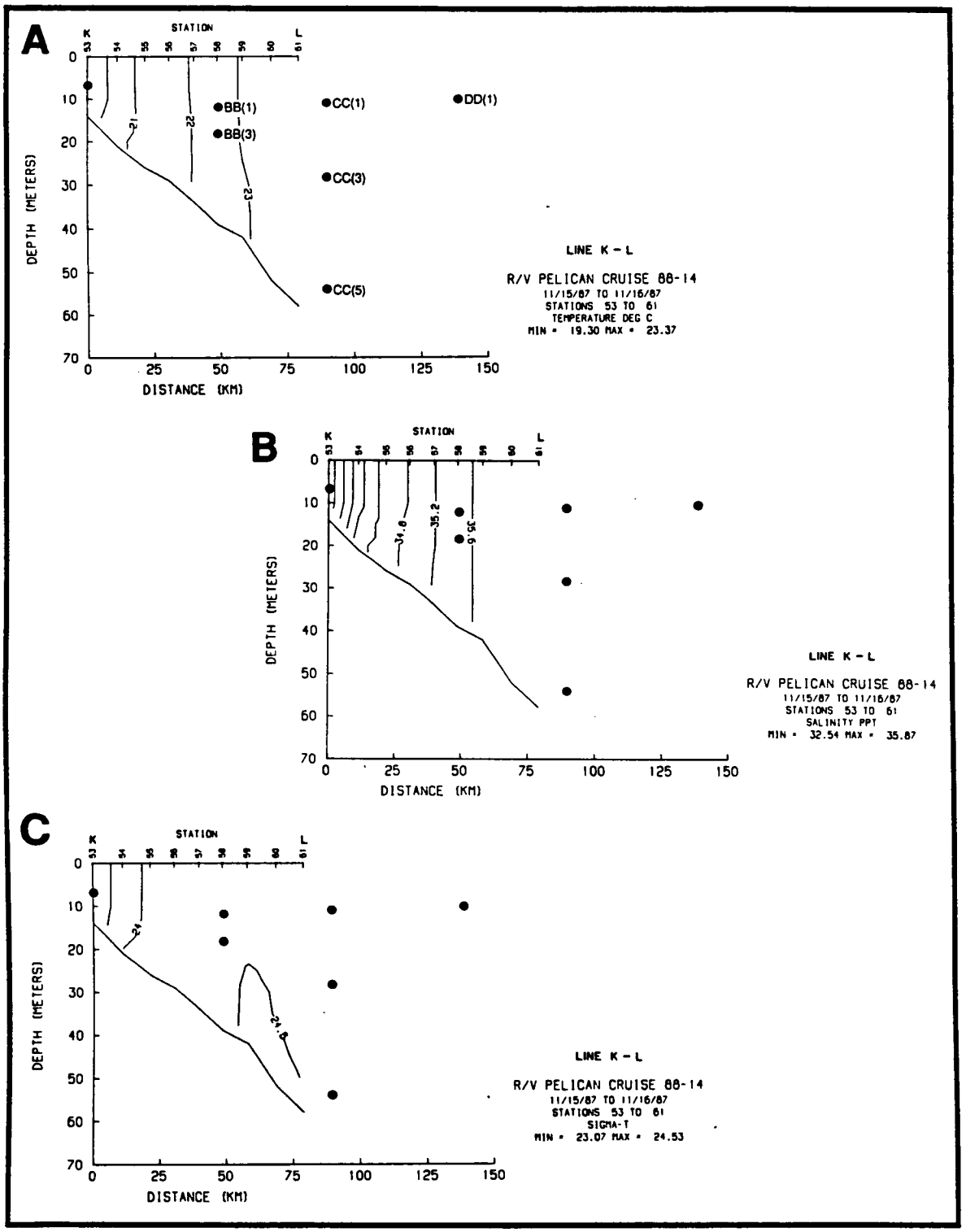

Figure 4.6-18. Cross-shelf sections of (a) temperature, (b) salinity and (c) sigma-t (density) taken during cruise PN8814 on November 15 to 16, 1987. Current meter locations are indicated and labelled.

water column. Temperature and salinity are vertically homogeneous with relatively weak horizontal gradients. There is a direct relationship between water depth and temperature/salinity/density. The coldest temperature is between 19° and 20°C and occurs at the most shoreward station. The freshest water, 32.5 ppt, also occurs at the shoreward end of the transect. As compared to previous surveys, horizontal and vertical density gradients are weak.

The final cruise (Figure 4.6-19) in February 1988 (Day 305 in Figure 4.6-13) showed the same general structure seen in November 1987. The temperatures decreased while remaining generally isothermal in the vertical. Minimum temperature decreased by about 5°C and minimum salinities decreased about 1.5 ppt. Note that in the latter two cruises, salinities of 35.6 ppt or greater extended on shore as far as the 40 m isobath.

Both the above cruise data and the in-situ data are coincident in magnitudes and exhibit the same general patterns. The time series of measurements at spatially discrete points allow documentation of the evolution of the patterns shown by these cross-shelf surveys.

4.6.6.4 Dissolved Oxygen

Dissolved oxygen data are available for the same five cruises as discussed above plus a sixth cruise in July 1988. These data are presented in Figures 4.6-20 and 4.6-21. As with temperature, salinity and density data, seasonal trends are apparent.

Initially on April 9-10, 1987 (Figure 4.6-20) near surface dissolved oxygen concentrations as high as 6.41 ml l^{-1} were observed, possibly associated with photosynthesis from a phytoplankton bloom. Later that same month on April 25-26 (Figure 4.6-20), these concentrations dropped to a maximum of 5.95 ml l^{-1}. In addition, the near bottom minimum dropped from 2.97 ml l^{-1} to 2.70 ml l^{-1} at the shallowest station. On July 17 (Figure 4.6-20) the oxygen maximum had again dropped, this time to 5.48 ml l^{-1}, but more significantly the near-bottom oxygen minimum had fallen to nearly anoxic conditions at 0.41 ml l^{-1}. This hypoxia phenomenon has been previously reported and is known to occur in July in this region.

In November 1987 and February 1988 (Figure 4.6-21a,b) when the water column was vertically well mixed, the oxygen concentrations over the entire shelf were generally around 5.00 to 5.50 ml l^{-1}. By July 21, 1988 (Figure 4.6-21) thermal stratification had re-established. The maximum oxygen concentrations (5.45 ml l^{-1}) were nearly identical to those observed a year earlier (5.48 ml l^{-1}), but the hypoxic near-bottom conditions of July 1987 were not duplicated. This may be due to an actual difference in conditions or simply an artifact of the bottle sampling. It is noted, however, that the summer of 1988 was characterized by a severe drought and that the runoff from the Mississippi River was greatly reduced from its norm.

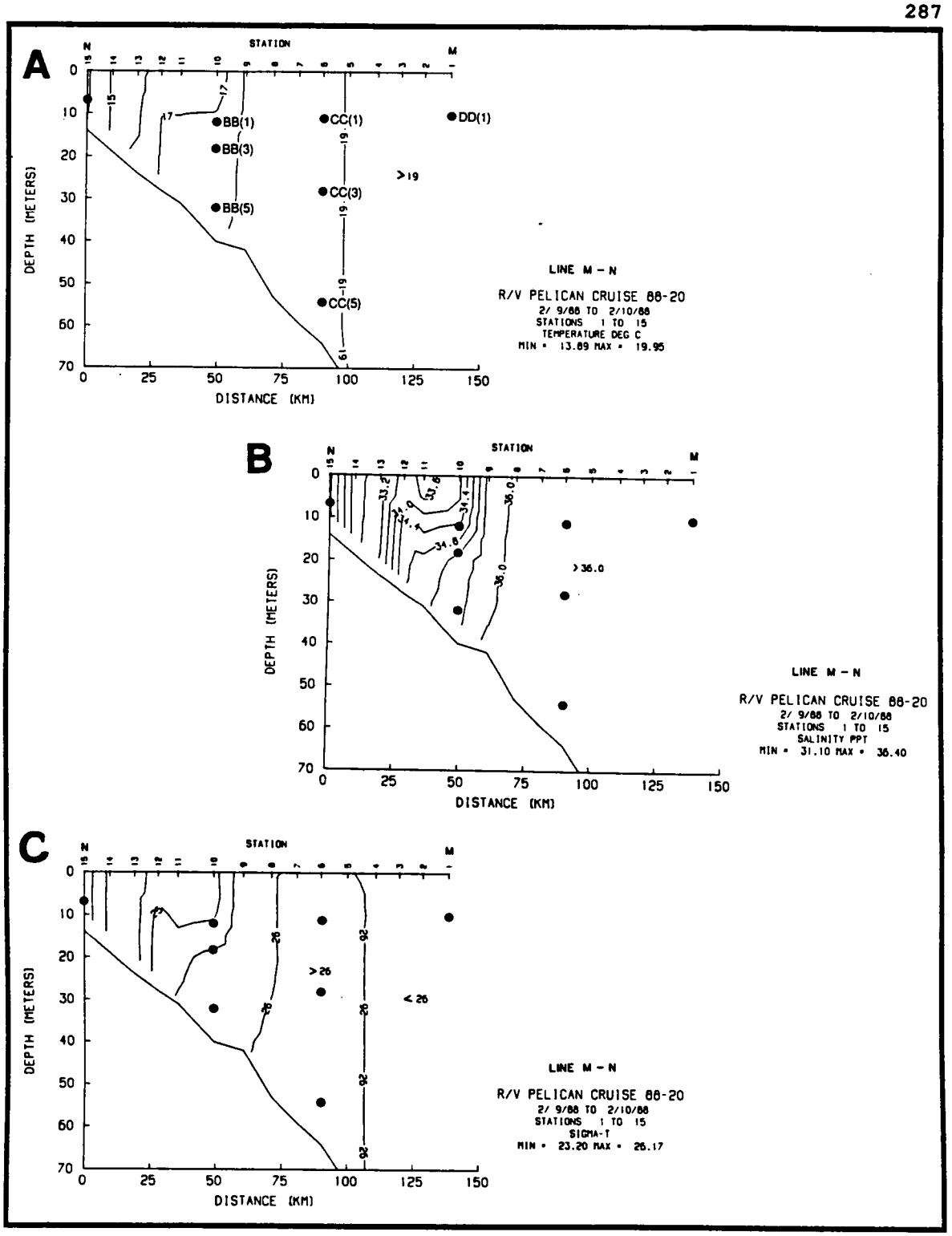

Figure 4.6-19. Cross-shelf sections of (a) temperature, (b) salinity and (c) sigma-t (density) taken during cruise PN8820 on February 9 to 10, 1988. Current meter locations are indicated and labelled.

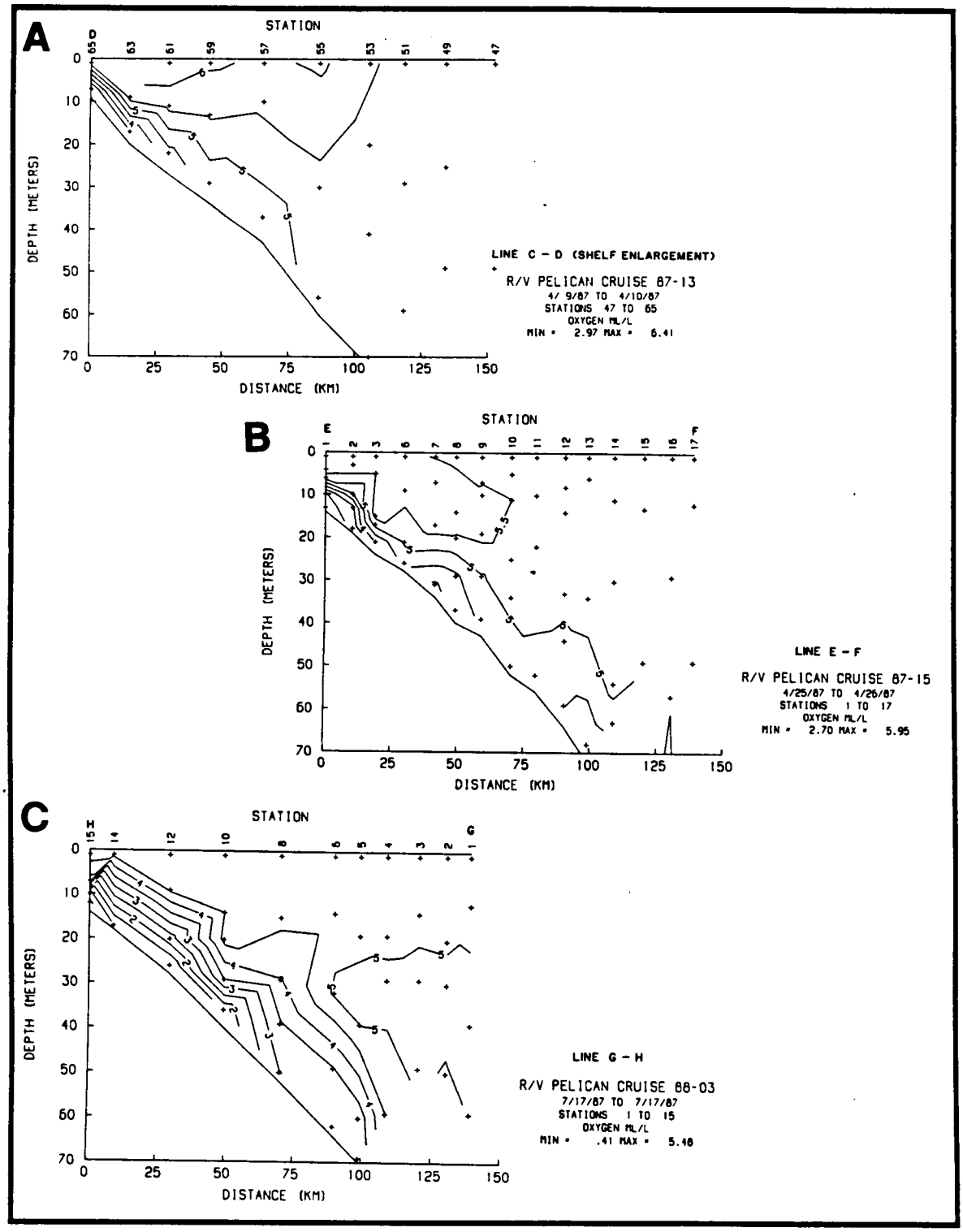

Figure 4.6-20. Cross-shelf sections of dissolved oxygen (DO) for cruises: (a) PN8713 (April 9 to 10, 1987), (b) PN8715 (April 25 to 26, 1987) and (c) PN8803 (July 17, 1987).

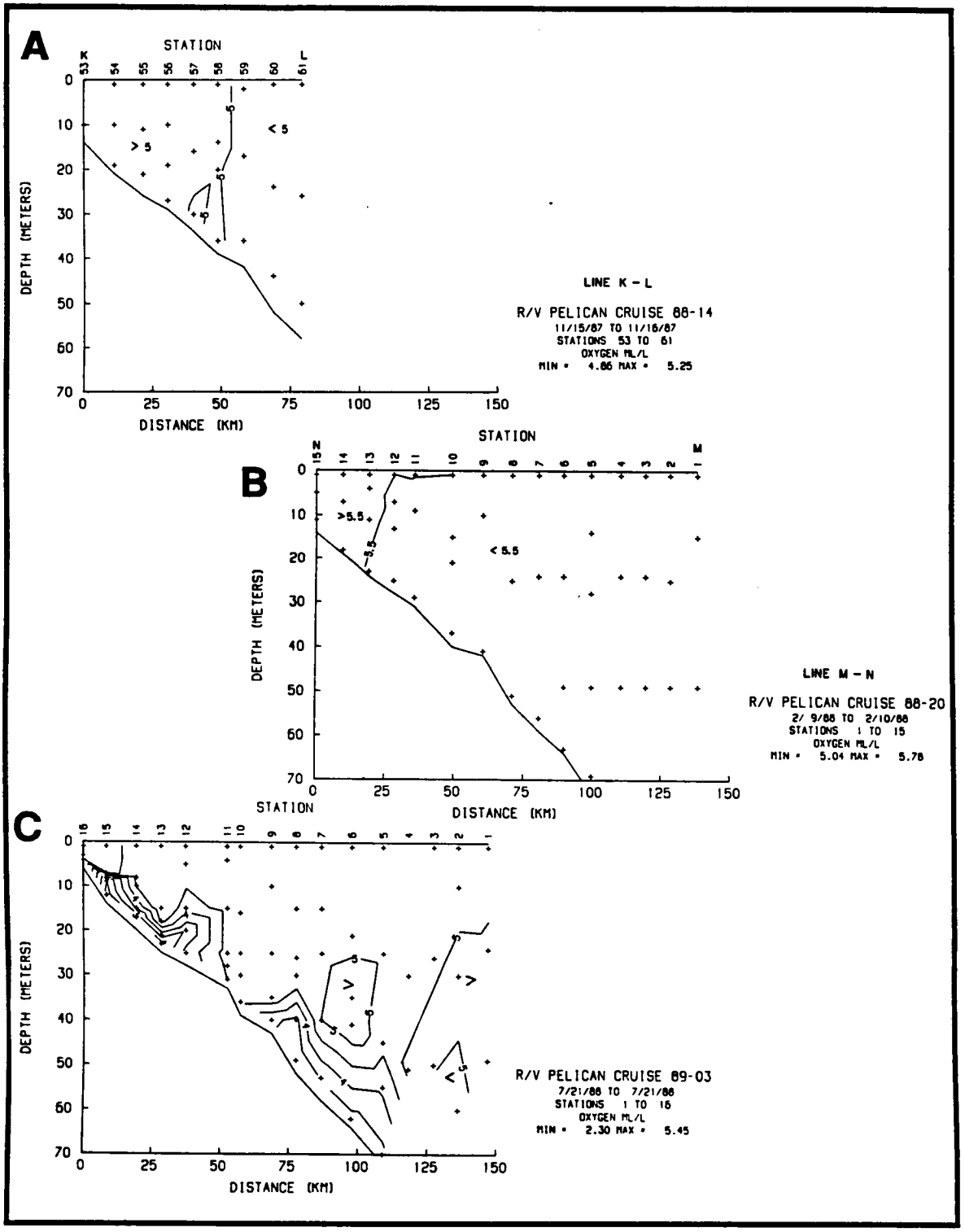

Figure 4.6-21. Cross-shelf sections of dissolved oxygen (DO) for cruises: (a) PN8814 (November 15 to 16, 1987), (b) PN8820 (February 9 to 10, 1988), and (c) PN8903 (July 21, 1988).

4.6.6.5 Suspended Solids

Suspended solids data were collected with the intent of supporting the in-situ transmissometry measurements. However, because of heavy fouling and periodic bottle sampling in vertical gradients it is not meaningful to pursue such an analysis. It is worthwhile, however, to report the results of the filtrations at the various mooring sites, as these give some general site specific ranges for total suspended and volatile suspended solids. It is emphasized, as well, however, that the data provided are only a small sampling and that some of these date reveal great variability over short periods of time, both vertically and horizontally.

The total suspended (TSS) and volatile suspended solids (VSS) data are presented in Tables 4.6-4 through 4.6-7. From these, it is obvious that insufficient data are available to reliably detect seasonal trends, but general across-shelf trends are obvious. These are summarized in Table 4.6-8, revealing that the highest concentrations of both total and volatile suspended solids generally occur at Mooring AA and decrease offshore towards the Mooring DD site. In particular the highest observed concentrations of both total and volatile suspended solids occurred at Mooring AA in July 1988 during the period when the Mississippi River runoff was low because of an extended period of drought. The ratio of volatile suspended solids to total suspended solids for this maximum observation was 0.23. During other periods this ratio varied from a low of 0.15 to a high of 0.68.

4.7 Shelf Optics

4.7.1 Introduction

Weather conditions were fair and seas were calm during all three cruises in April 1987, and in February and July 1988. A total of 33 optical stations were occupied on the various cruises during the first year. At the four shelf mooring sites (AA, BB, CC and DD) a full optical measuring program was always performed. Several other stations were occupied and a lesser set of observations was made depending on available time. The parameters measured are described in Chapter II. All the daylight measurements were normalized against a deck photometer which recorded continuously.

4.7.2 Inter-Station Comparison

The following intercomparison is presented in order of seasons rather than the order taken.

- Winter

In February 1988 (Figure 4.7-1) the fluorescence measurements on the shelf show moderately high values at Station AA and relatively low and similar values at Stations BB, CC and DD as depicted in Figure 4.7-2. In all four cases there are virtually no changes (structure) in fluorescence with depth. This leads to the interpretation that the

Table 4.6-4. Summary of suspended solids data near Mooring AA site.

Sta/Depth(m)*	Date (GMT)	Time (GMT)	TSS(mg l^{-1})	VSS(mg l^{-1})
15C/9.5	07/17/87	2314	2.80	1.10
15C/9.5	07/17/87	2314	2.45	1.10
51X/9.5	11/12/87	2330	1.45	0.40
51X/9.5	11/12/87	2333	1.60	0.38
16C/9.5	02/10/88	1528	4.04	0.79
16C/9.5	02/10/88	1528	4.11	0.64
16C/9.5	02/10/88	1528	4.11	0.61
16C/9.5	02/10/88	1528	4.11	0.71
AA/9.5	04/14/88	2346	3.73	0.90
AA/9.5	04/14/88	2346	3.63	0.83
15C/9.5	07/21/88	2110	19.00	4.35
15C/9.5	07/21/88	2110	18.00	4.00
15C/9.5	07/21/88	2110	18.55	4.20
15C/9.5	07/21/88	2110	18.05	4.05

* All stations are located near the Mooring AA site in approximately 14 m depth for the different time periods. Refer to Figure 2.3-1.

Table 4.6-5. Summary of suspended solids data near Mooring BB site.

Sta/Depth(m)*	Date (GMT)	Time (GMT)	TSS(mg l^{-1})	VSS(mg l^{-1})
BB/13.5	07/16/87	0250	0.81	0.38
BB/19.5	07/16/87	0256	0.75	0.40
10C/14.0	07/17/87	1918	4.00	0.74
10C/20.0	07/17/87	1918	4.08	0.74
58C/14.0	11/15/87	2015	0.68	0.21
58C/20.0	11/15/87	2015	0.64	0.21
10C/14.0	02/10/88	0410	1.03	0.20
10C/14.0	02/10/88	0410	0.95	0.25
10C/20.0	02/10/88	0408	1.08	0.28
10C/20.0	02/10/88	0408	1.15	0.28
17C/14.0	02/10/88	1918	0.61	0.16
17C/20.0	02/10/88	1918	0.71	0.16
BB/14.0	05/05/88	0327	0.51	0.25
BB/20.0	05/05/88	0325	0.47	0.24
10C/14.0	07/21/88	1550	2.54	0.58
10C/14.0	07/21/88	1550	2.73	0.59
17C/14.0	07/22/88	1338	2.80	0.59

* All stations are located near the Mooring BB site in approximately 40 m depth for the different time periods. Refer to Figure 2.3-1.

Table 4.6-6. Summary of suspended solids data near Mooring CC site.

Sta/Depth(m)*	Date (GMT)	Time (GMT)	TSS(mg l^{-1})	VSS(mg l^{-1})
12C/14.4	04/26/87	0430	4.58	0.81
12C/32.5	04/26/87	0430	0.38	0.20
18C/14.3	04/26/87	1800	2.15	0.35
18C/32.8	04/26/87	1800	0.32	0.14
CC/14.5	07/16/87	1158	5.02	1.04
CC/32.5	07/16/87	1158	0.63	0.27
6C/13.5	07/17/87	1515	0.92	0.34
6C/32.0	07/17/87	1515	0.77	0.32
42X/13.5	11/12/87	1704	1.50	0.28
42X/13.5	11/12/87	1707	1.70	0.33
6CB/13.5	02/09/88	2145	0.68	0.16
6CB/32.0	02/09/88	2141	1.18	0.23
6CB/32.0	02/09/88	2141	1.05	0.23
CC/13.5	05/04/88	2224	0.36	0.17
CC/32.0	05/04/88	2222	0.39	0.21
6C/13.5	07/21/88	1104	2.14	0.44

* All staions are located near the Mooring CC site in approximately 64 m depth for the different time periods. Refer to Figure 2.3-1.

Table 4.6-7. Summary of suspended solids data near Mooring DD site.

Sta/Depth(m)*	Date (GMT)	Time (GMT)	TSS(mg l^{-1})	VSS(mg l^{-1})
17C/11.5	04/26/87	1100	0.18	0.12
DD/11.5	07/17/87	0120	2.14	0.51
1C/11.5	07/17/87	0920	1.98	0.41
36X/15.0	11/12/87	1338	1.45	0.26
1C/15.0	02/09/88	~1400	0.15	0.08
DD/15.0	04/14/88	1541	0.40	0.23
DD/15.0	04/14/88	1541	0.34	0.23
1C/17.0	07/21/88	0322	2.47	0.51
1C/17.0	07/21/88	0322	2.42	0.49

* All stations are located near the Mooring DD site in approximately 181 m depth for the different time periods. Refer to Figure 2.3-1.

Table 4.6-8. Summary of observed maximums, minimums and averages of total and volatile suspended solids data near the Mooring AA, BB, CC and DD sites.

Station	TSS(mg l^{-1})			VSS (mg l^{-1})		
	max	min	avg	max	min	avg
AA	19.00	1.45	3.04*	4.35	0.38	0.76*
BB	4.08	0.47	1.58	0.74	0.16	0.38
CC	5.02	0.32	1.50	1.04	0.14	0.36
DD	2.47	0.15	1.25	0.51	0.08	0.30

* Not including extreme maximum data from July 21, 1988.

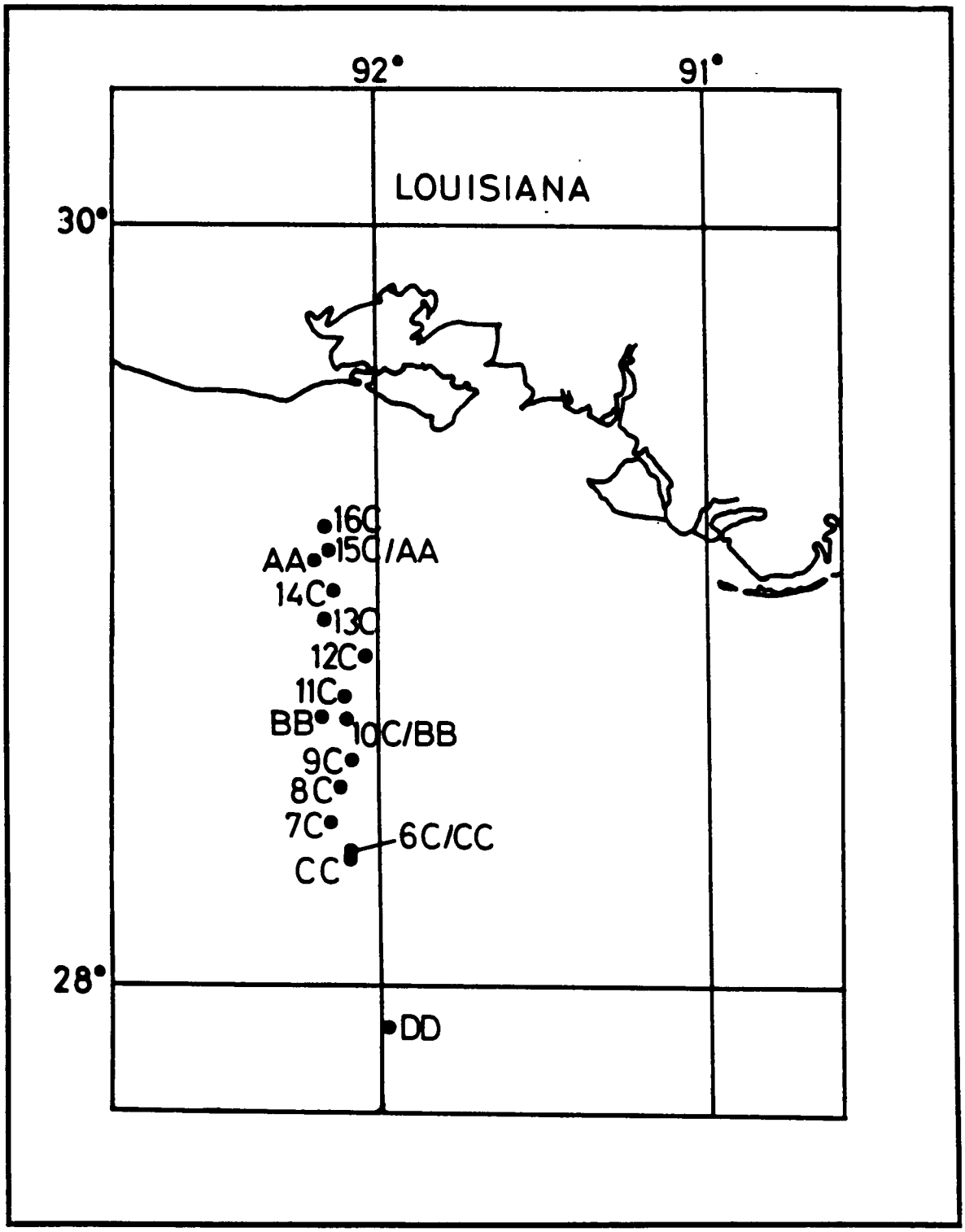

Figure 4.7-1. Station locations for the February 1988 study of the optical properties of the Louisiana shelf.

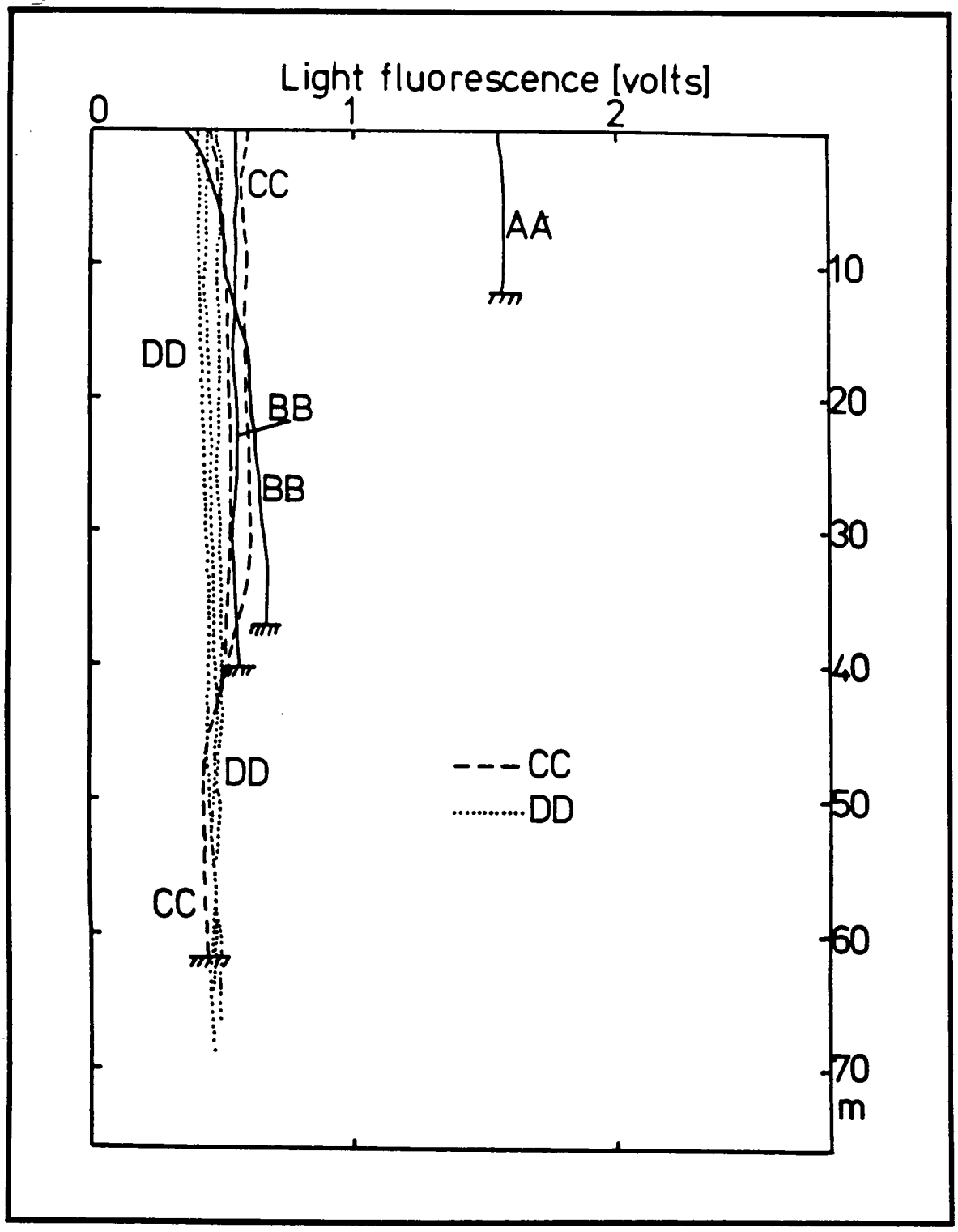

Figure 4.7-2. The vertical distribution of light fluorescence at Stations AA, BB, CC and DD in February 1988. A signal output of one Volt corresponds approximately to 10 mg m^{-3} of chlorophyll-like pigments depending on the pigment composition.

suspended organic matter consists mainly of detritus. Figures 4.7-3 and 4.7-4 show increased values of suspended matter with depth, as well as considerably decreasing values with distance from shore. This can be explained by resuspension of sea floor sediments and sediment discharges from land to sea, respectively. Note especially the low values in the clear blue water at Station DD.

As shown in Figure 4.7-5 and Table 4.7-1, the depth of the euphotic zone ($z_q(1\%)$) varies by a factor of 10 across the shelf with the smallest variation between Stations BB and CC. The reason for this is a small variation in suspended matter as the horizontal variation of yellow substance is high (see Figure 4.7-6). It can thus be concluded that there exists both a yellow substance oceanic front between Stations BB and CC and a sediment oceanic front between Stations CC and DD. Note that the E(310) profiles are represented by almost straight lines in Figure 4.7-6, meaning that K(310) is almost invariable with depth. This means, in turn, that the yellow substance is well mixed in the upper layers as was the suspended matter.

- Spring

In April 1987 (Figure 4.7-7), the fluorescence measurements on the shelf reveal high values and structure with depth at Station AA, in particular, as well as at Stations BB and CC near the bottom (Figure 4.7-8). In contrast, the situation at Station DD resembles the one from February 1988. All the surface values at Stations BB, CC and DD are about the same, but lower than those from almost a year later in February 1988. Plankton blooms are obviously developing on the shelf in the spring and are most pronounced in the vicinity of Station AA. The difference in the surface fluorescence values between April 1987 and February 1988, at Stations BB, CC and DD, presents an example of the annual variation of the biomass. Note the very sharp vertical gradients at Station AA, declining at Stations BB and CC and vanishing at Station DD. Figures 4.7-9 and 4.7-10 depict pronounced variations with depth too, except at Station DD. Note especially, the strong near-bottom gradient at Station CC in Figures 4.7-9 and 4.7-10 and its absence in Figure 4.7-8. This is clear evidence of resuspension, indicating a strong bottom current at Station CC.

In Figure 4.7-11 and Table 4.7-2, the depth of the euphotic zone across the shelf resembles the situation from February 1988, except that no sediment oceanic front can be located with the same certainty as for the winter case. However, the yellow substance oceanic front has not shifted position between Stations BB and CC as seen in Figure 4.7-12. Note that K(310) decreases with depth; most noteworthy at Station CC. Deep, clear oceanic water has obviously penetrated into the shelf since the deep K(310) values at Stations CC and DD are about the same.

- Summer

In July 1988 (Figure 4.7-13), the fluorescence measurements show plankton blooms over the entire shelf. Figure 4.7-14 depicts two deep fluorescence maxima with the deepest one at Station DD where the water

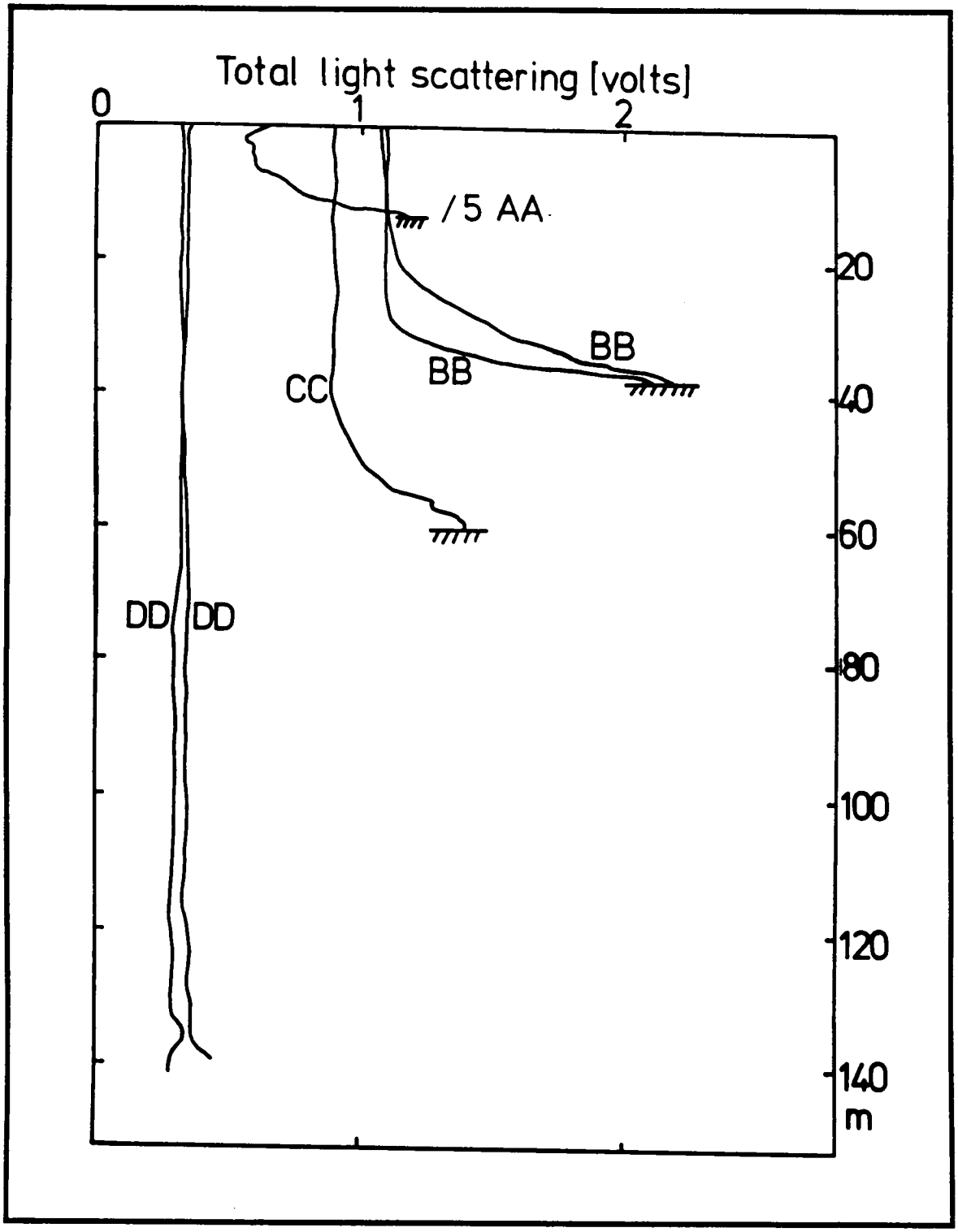

Figure 4.7-3. The vertical distribution of total light scattering at Stations AA, BB, CC and DD in February 1988. A signal output of one Volt corresponds approximately to b = 0.140 m^{-1} depending on the particle composition and distribution. The wavelength centers around 655 nm.

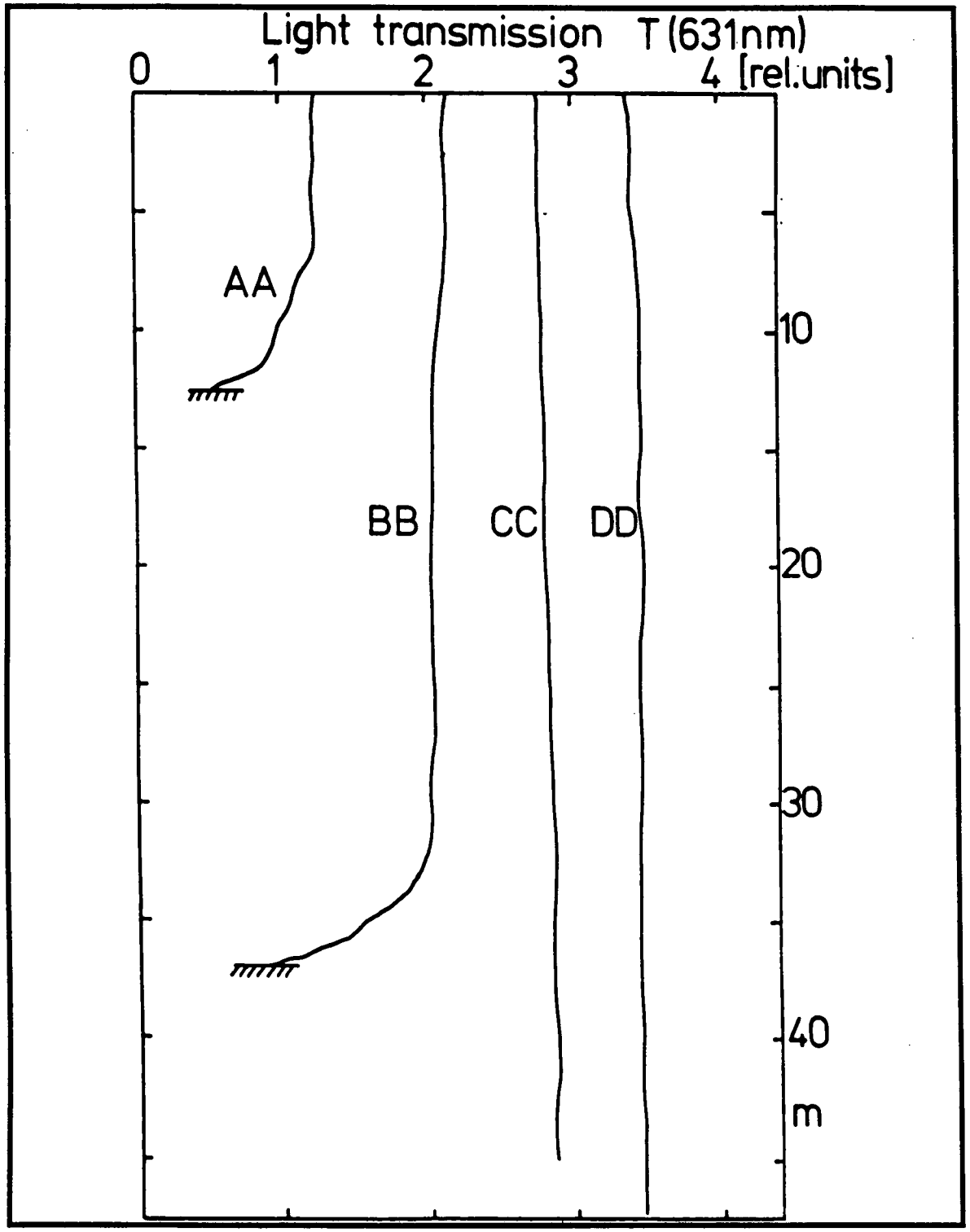

Figure 4.7-4. The vertical distribution of the light transmission at Stations AA, BB, CC and DD in February 1988. When the signal output from the transmissometer having a total path length of 0.5 m amounts to one relative unit, the light transmission T(0.5 m) = 0.242. The following relations are valid: $T(1.0\ m) = e^{-c.1} = (T(0.5\ m))^2$ in which c is the beam light attenuation coefficient (m^{-1}). The wavelength applied centers around 631 nm.

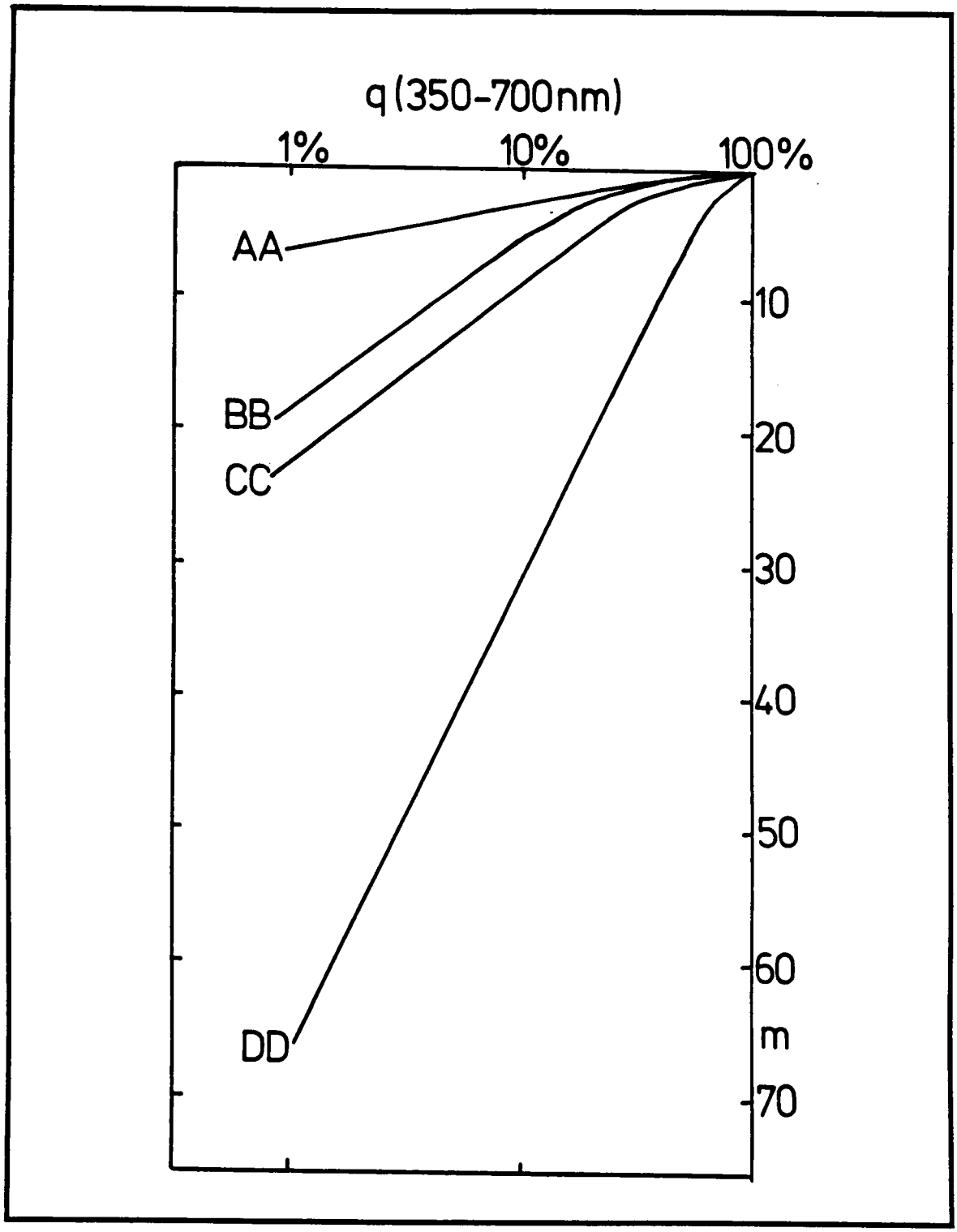

Figure 4.7-5. Relative downward quanta irradiance (350 to 700 nm) versus depth at Stations AA, BB, CC and DD in February 1988. The 100% value is taken to be Q (350 to 700 nm) just below the water surface. The quanta irradiance is a measure for the amount of photons available for photosynthesis (= Photosynthetically Active Radiation, or PAR).

Table 4.7-1. Gulf of Mexico optical observations for February 1988.

Stations	Station Depth (m)	Dates	F_1 -	F_2 -	D m	Z_q (1%) m	Z (1%) m	h_s degr.	H m
DD	184	2/9	1.85	-	20-21.5	66.7	37.3	"	0.5
2C	108	2/9	1.67	3.02	17	-	-	"	0.5-1
3C	107	2/9	1.55	2.25	16	-	-	"	0.75
4C	86	2/9	1.10	-	10	-	-	"	0.5-1
5C	73	2/9	1.12	2.20	10.5	-	-	"	0.5-1
CC	64	2/8	0.84	1.78	7	22.7	17.3	clouds	0.5
6C	64	2/9	1.04	1.92	8.5	-	-	"	0.5
CC	64	2/9	0.92	2.39	8	-	-	"	0.5
BB	40	2/10	0.46	0.87	8.5	18.4	4.0	"	0.5-1
AA	14	2/10	0.41	0.56	2.5	6.44	3.3	"	0.5

F_1 equals the ratio of the water leaving nadir radiances at 447 nm and 521 nm, respectively.

F_2 equals the ratio of the water leaving nadir radiances at 447 nm and 550 nm, respectively.

D is the Secchi depth, Z_q (1%) is the depth of the euphotic zone defined at the depth where the PAR is reduced by a factor 100, Z (1%) is the depth at which the downwelling UV-B light around 310 nm is reduced by a factor 100, h_s is the solar elevation in degrees measured from the horizontal and H is the wave height (2 x wave amplitude).

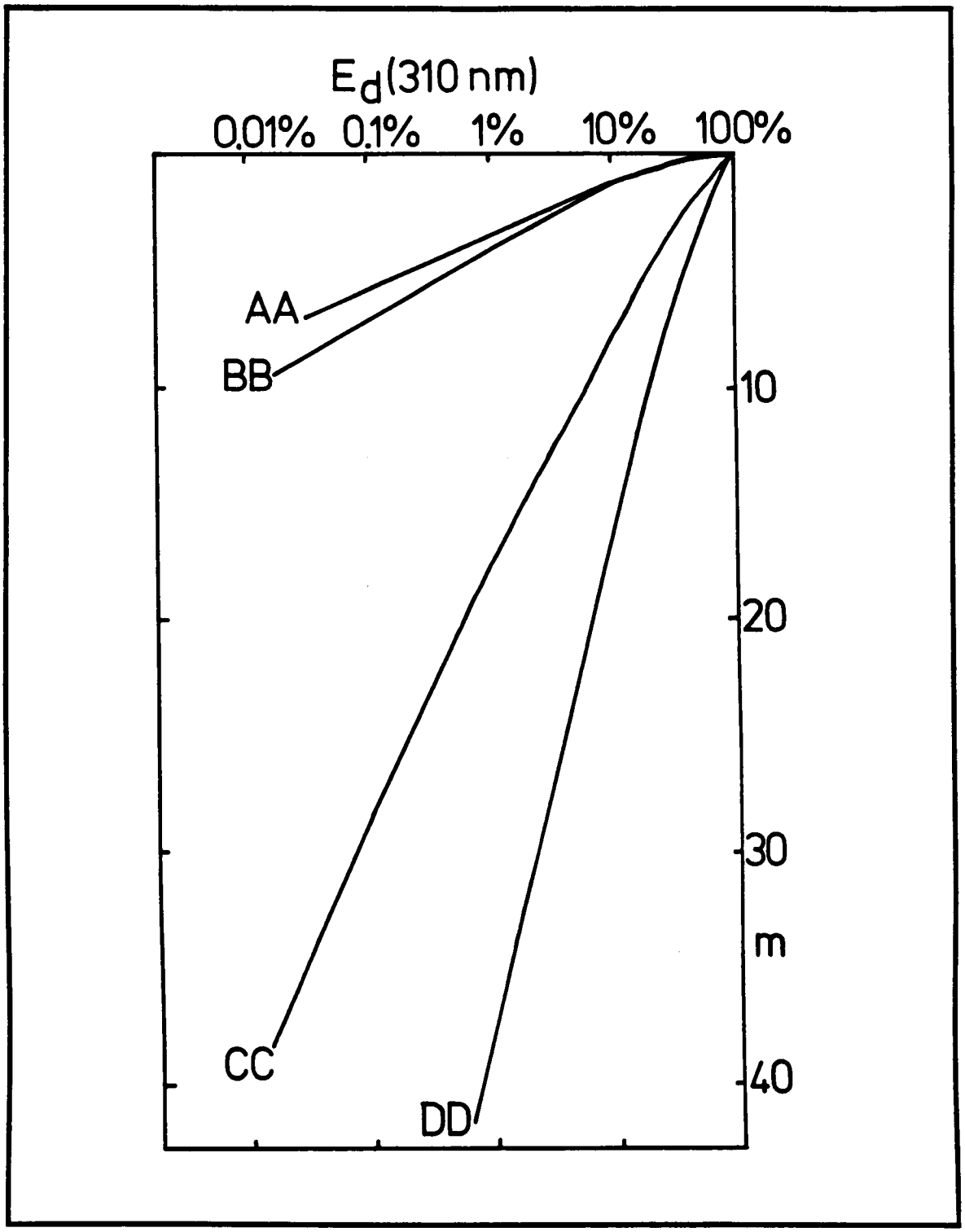

Figure 4.7-6. Relative downward UV-B irradiance versus depth at Stations AA, BB, CC and DD in February 1988. The 100% value is taken to be E_d (310 nm) just below the water surface. In the upper meters an averaging procedure is required at stations where the light absorption is high i.e. always at Station AA, sometimes at Station BB depending on the season, but never at Stations CC and DD.

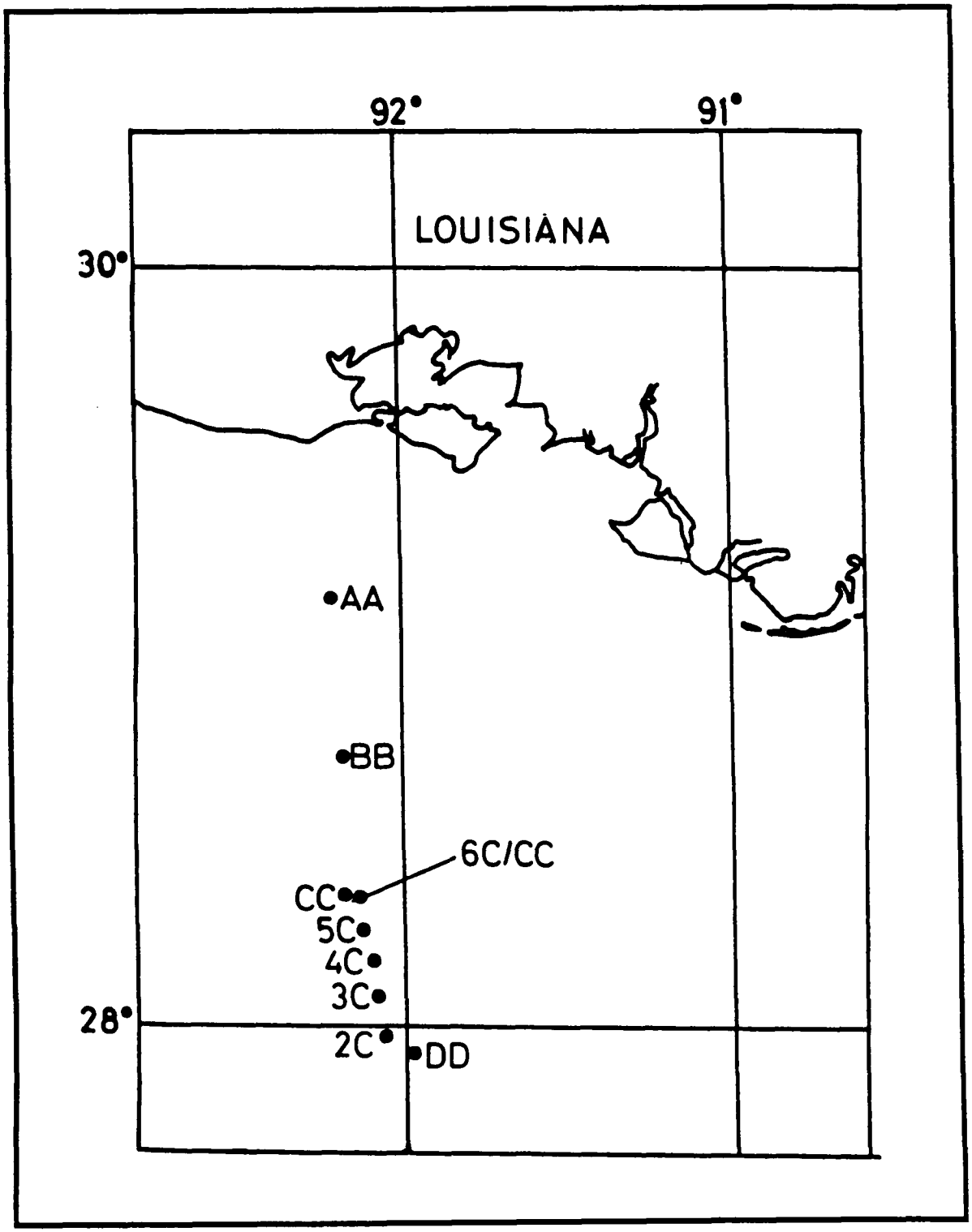

Figure 4.7-7. Station locations for the April 1987 study of the optical properties of the Louisiana shelf.

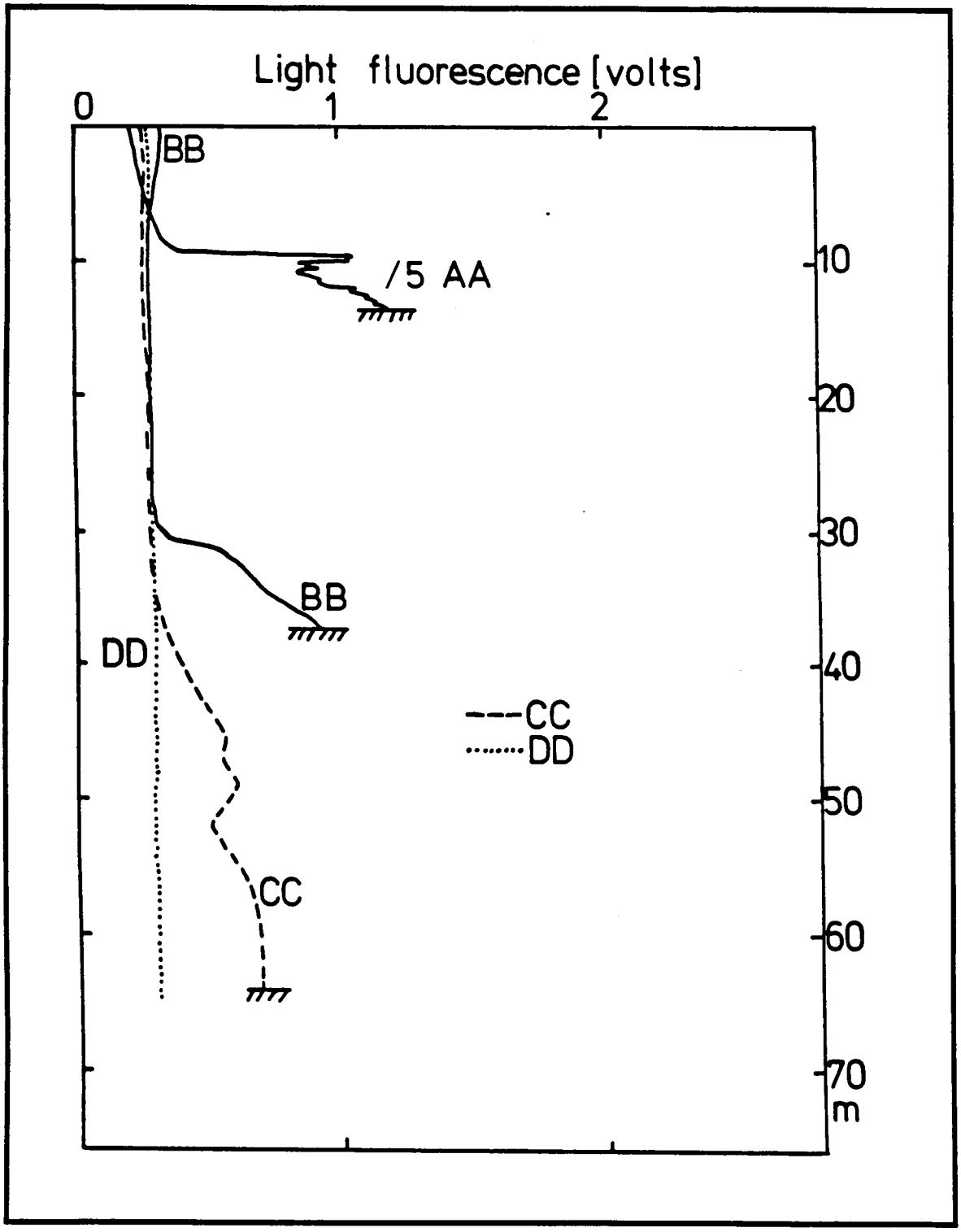

Figure 4.7-8. The vertical distribution of light fluorescence at Stations AA, BB, CC and DD in April 1987. A signal output of one Volt corresponds approximately to 10 mg m^{-3} of chlorophyll-like pigments depending on the pigment composition.

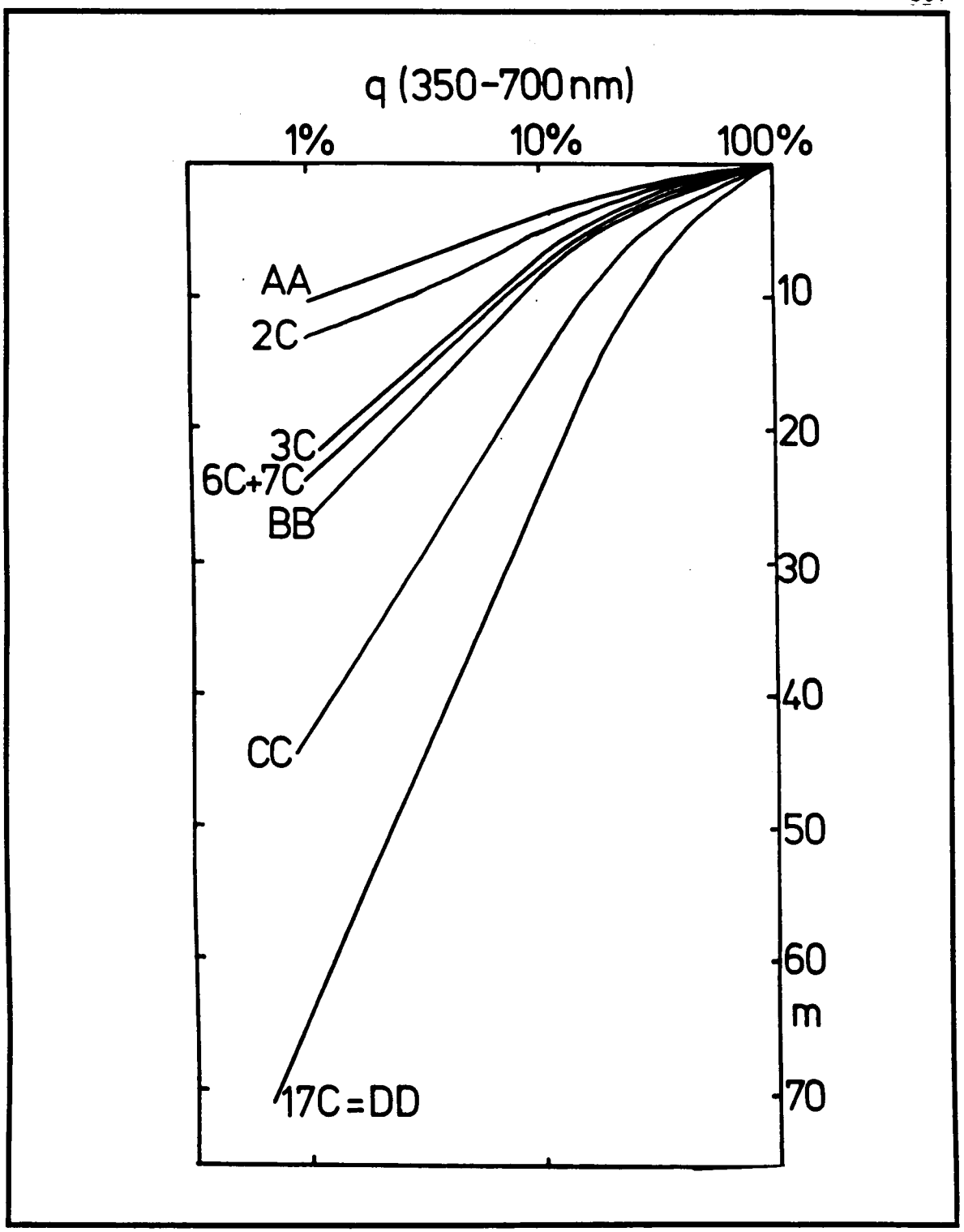

Figure 4.7-11. Relative downward quanta irradiance (350 to 700 nm) versus depth at Stations AA, BB, CC and DD in April 1987. The 100% value is taken to be Q (350 to 700 nm) just below the water surface. (See caption to Figure 4.7-5 for further discussion.)

Table 4.7-2. Gulf of Mexico optical observations for April 1987.

Stations	Station Depth (m)	Dates	F_1 -	F_2 -	D m	Z_q (1%) m	Z (1%) m	h_s degr.	H m
AA	14	4/25	0.52	0.54	-	10.2	3.33	20	-
2C	19	4/25	0.37	0.48	-	13.3	3.33	38	-
3C	24	4/25	0.46	0.63	-	22.2	3.86	65	-
6C	28	4/25	0.43	0.75	-	23.2	3.86	75	-
7C	34	4/25	0.48	0.69	-	23.3	4.5	68	-
BB-8C	40	4/25	0.52	0.76	-	26.7	4.8	48	-
9C	43	4/25	0.54	0.66	12	-	-	15	-
CC	64	4/26	0.60	0.53	14	43.1	8.1	70	-
DD-17C	190	4/26	2.30	3.70	26	64.4	44.4	8	0.5
"		"	2.38	3.57	26	-	-	-	"
"		"	2.09	-	-	-	-	16	"
"		"	2.08	3.70	-	-	-	-	"
"		"	2.16	-	-	-	-	19	"
"		"	2.11	-	-	-	-	-	"
"		"	2.07	-	-	-	-	22	"
"		"	2.23	4.83	-	-	-	-	"
"		"	2.15	-	-	-	-	25	"
"		"	2.06	-	-	-	-	-	"
"		"	2.04	5.07	-	-	-	-	"
"		"	2.00	-	-	-	-	32	"

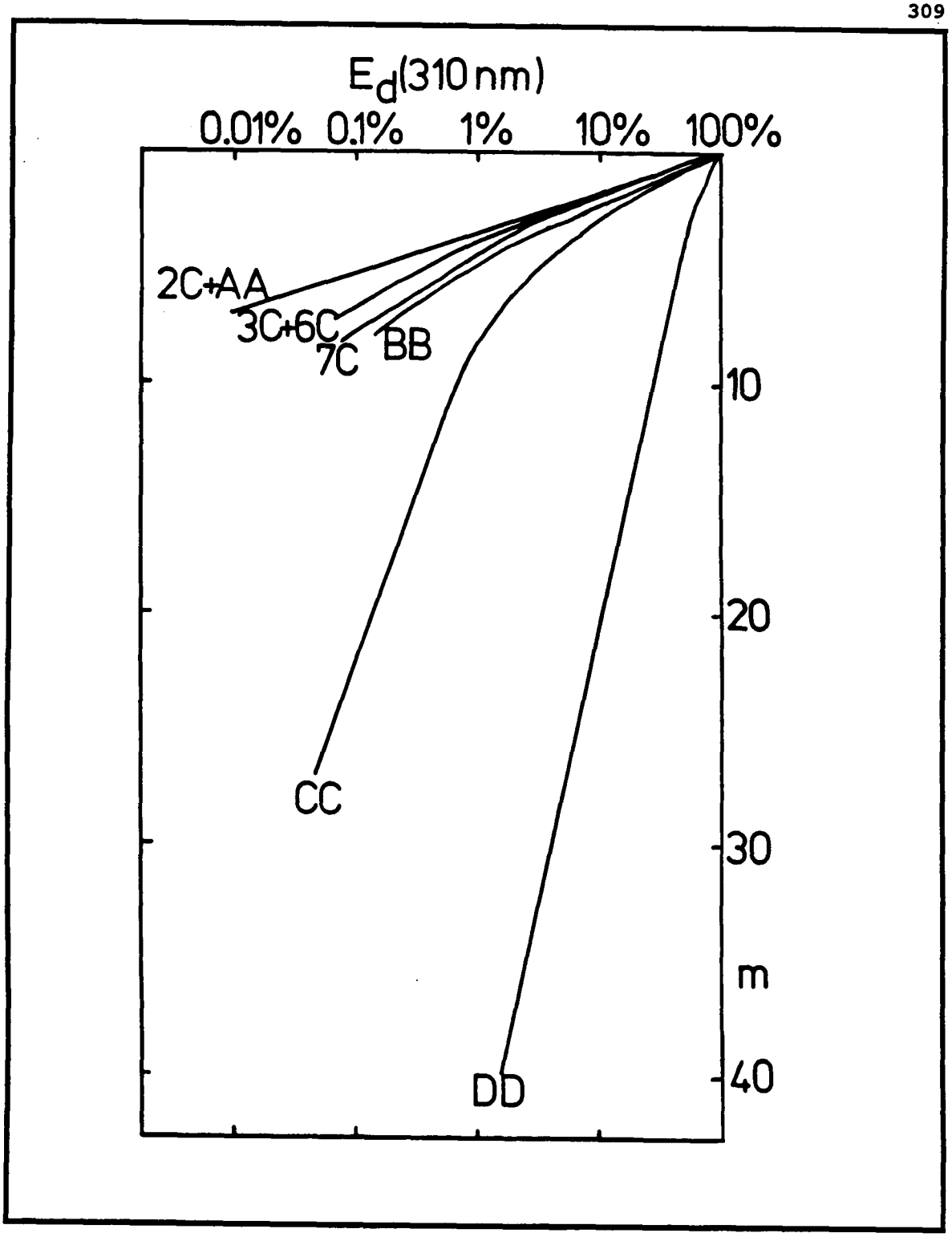

Figure 4.7-12. Relative downward UV-B irradiance versus depth at Stations AA, BB, CC and DD in April 1987. The 100% value is taken to be E_d (310 nm) just below the water surface. (See caption to Figure 4.7-6 for further discussion.)

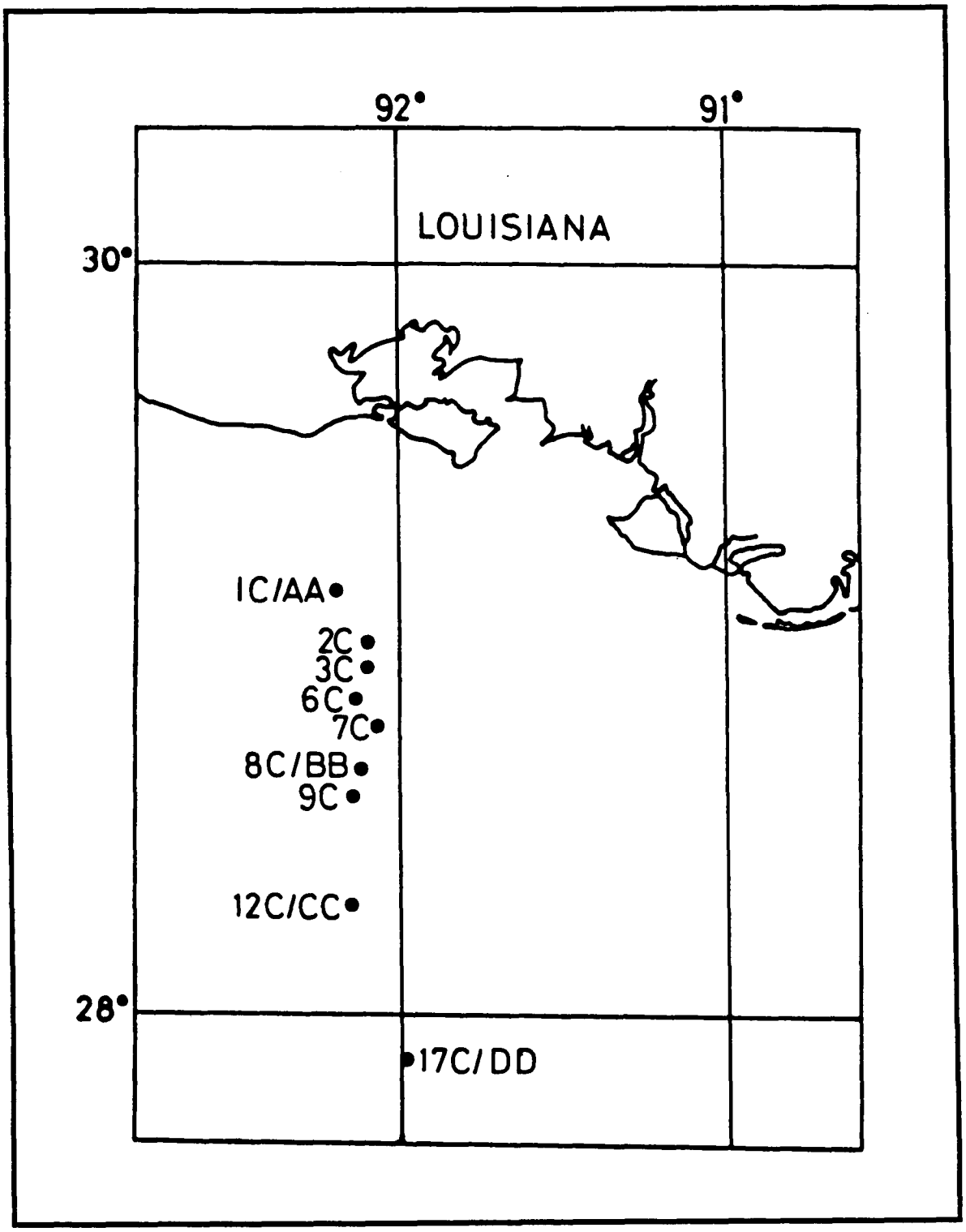

Figure 4.7-13. Station locations for the July 1988 study of the optical properties of the Louisiana shelf.

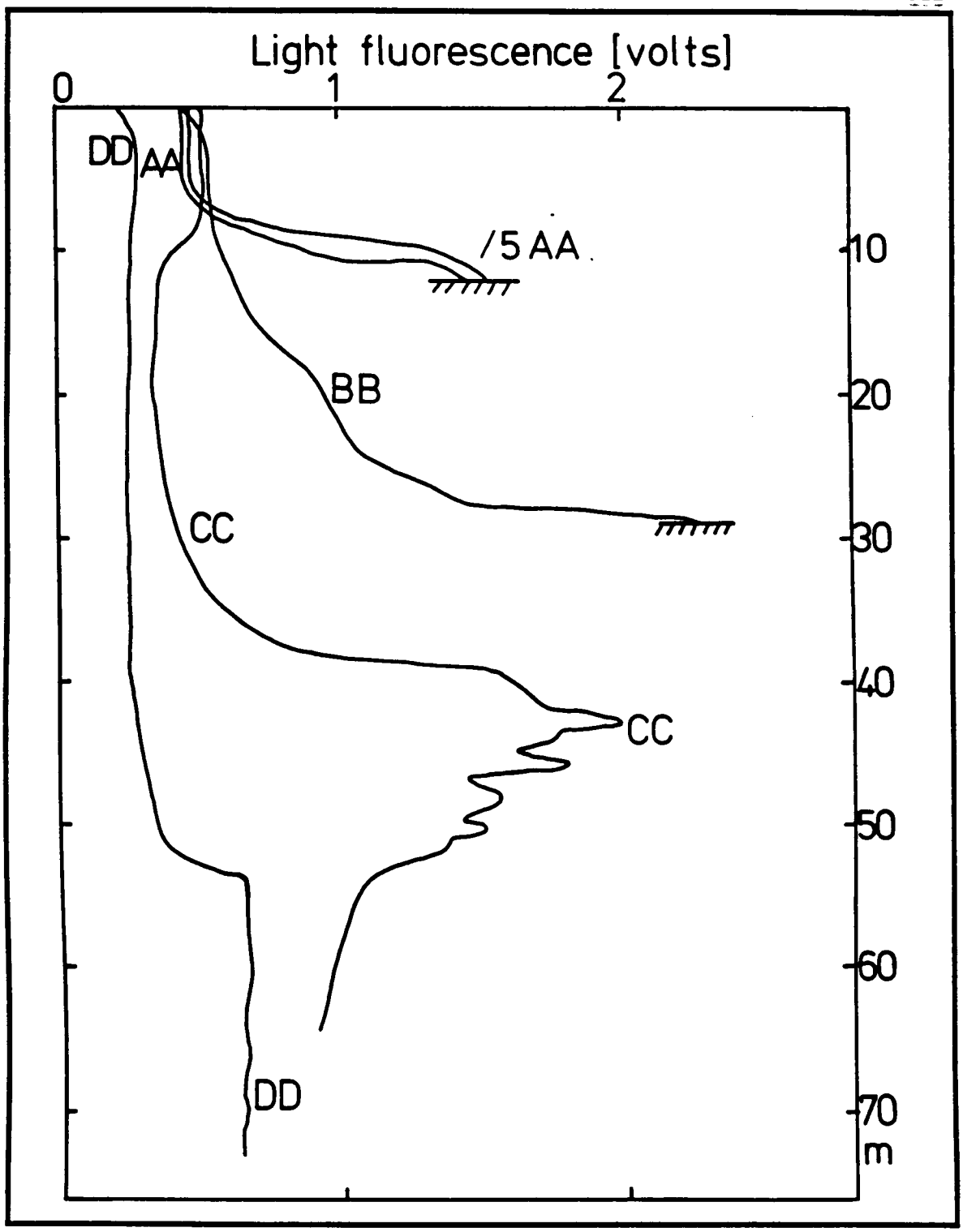

Figure 4.7-14. The vertical distribution of light fluorescence at Stations AA, BB, CC and DD in July 1988. A signal output of one Volt corresponds approximately to 10 mg m^{-3} of chlorophyll-like pigments depending on the pigment composition.

is most transparent. Note also the structure in the maximum at Station CC (e.g., Højerslev, 1985).

Figures 4.7-15 and 4.7-16 indicate possible resuspension due to bottom currents at Station CC, but not at Station BB where the increased bottom values are solely caused by the presence of plankton as depicted in Figure 4.7-14. The intermediate maximum due to suspended inorganic matter at Station AA is remarkable and is possibly caused by the presence of a pycnocline.

The depths of the euphotic zone have not changed much across the shelf since April 1987. Of interest is the measurement in July 1988 from Station 16C (Table 4.7-3), it being closer to land. Figure 4.7-17 suggests a sediment oceanic front between Stations 16C and AA although the concentration of yellow substance is about the same at these two stations (Figure 4.7-18). Unlike before, in the two former cases for February 1988 and April 1987, the yellow substance oceanic front has moved shorewards and is now situated between Stations AA and BB rather than between Stations BB and CC. This is explained by a decreased freshwater discharge into the region. Combining the findings in Figures 4.7-6, 4.7-12 and 4.7-18 and Tables 4.7-1, 4.7-2 and 4.7-3 shows that the amount of yellow substance in the area varies seasonally at all four stations with maximum values occurring in the spring and minimum values in summer. The remarkably low K(310) values of 0.069 m^{-1} at Station DD in July 1988, estimated from the slope in Figure 4.7-18, calls for attention because it represents a much lower value than earlier reported (see Table 4.7-4). The UV-B meter has been checked for instrumental failures, but none could be observed. As before, it is concluded that deep oceanic water has penetrated onto the shelf, shorewards, up to Station DD and CC but without having reached Station BB.

4.7.3 Optical Water Mass Classification

The water masses encountered on the Louisiana shelf can be classified according to Jerlovs (1976) optical classification scheme (see also Højerslev, 1986b for more details). According to the findings depicted in Figures 4.7-19, 4.7-20 and 4.7-21 the waters at Station AA belong to Coastal Type 7 in February 1988, Coastal Type 5 in April 1987 and to Coastal Type 3 on average in July 1988. At Station BB the water masses belong to Coastal Type 3 in February 1988, Coastal Type 1 in April 1987 and to Oceanic Type III on average in July 1988. At Station CC the water masses belong to a Coastal Intermediate Type 1 and 3 in February 1988, Coastal Type 1 in April 1987 and to an Intermediate Oceanic Type III and II in July 1988. Finally, the waters at Station DD belong to Oceanic Type IB, most likely throughout the year. Consequently, according to this classification scheme the shelf waters become more transparent for those wavelengths important to photosynthesis with the distance from the coast and from winter to spring to summer.

The color indices F_1 and F_2 (See Chapter III for definition) increase with the distance from the coast and reach their maximum values at Station DD (see Tables 4.7-1, 4.7-2 and 4.7-3; and Figure 4.7-22). The color indices, F_1, measured at Station DD shows that the waters here are

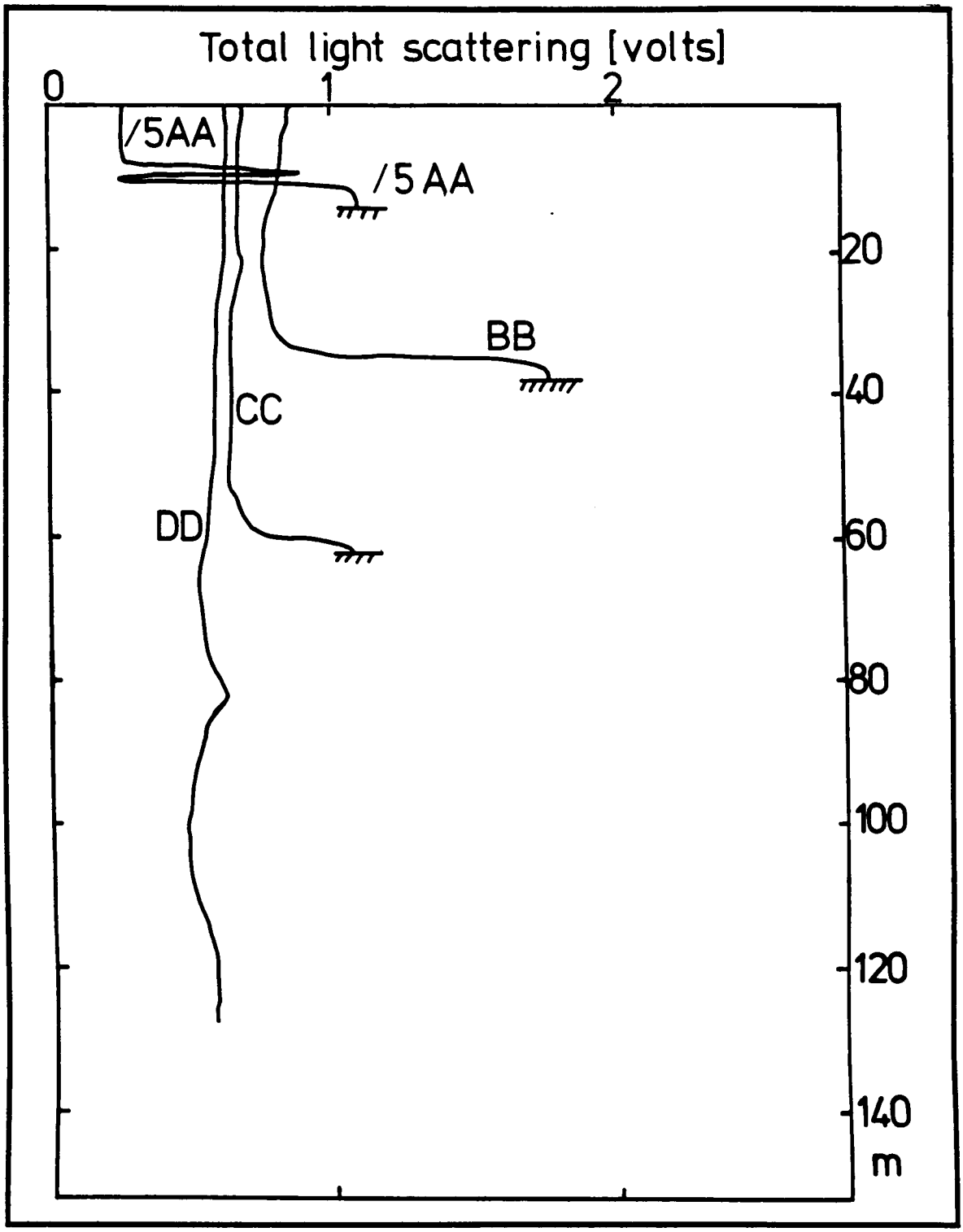

Figure 4.7-15. The vertical distribution of total light scattering at Stations AA, BB, CC and DD in July 1988. A signal output of one Volt corresponds approximately to b = 0.140 m^{-1} depending on the particle composition and distribution. The wavelength applied centers around 655 nm.

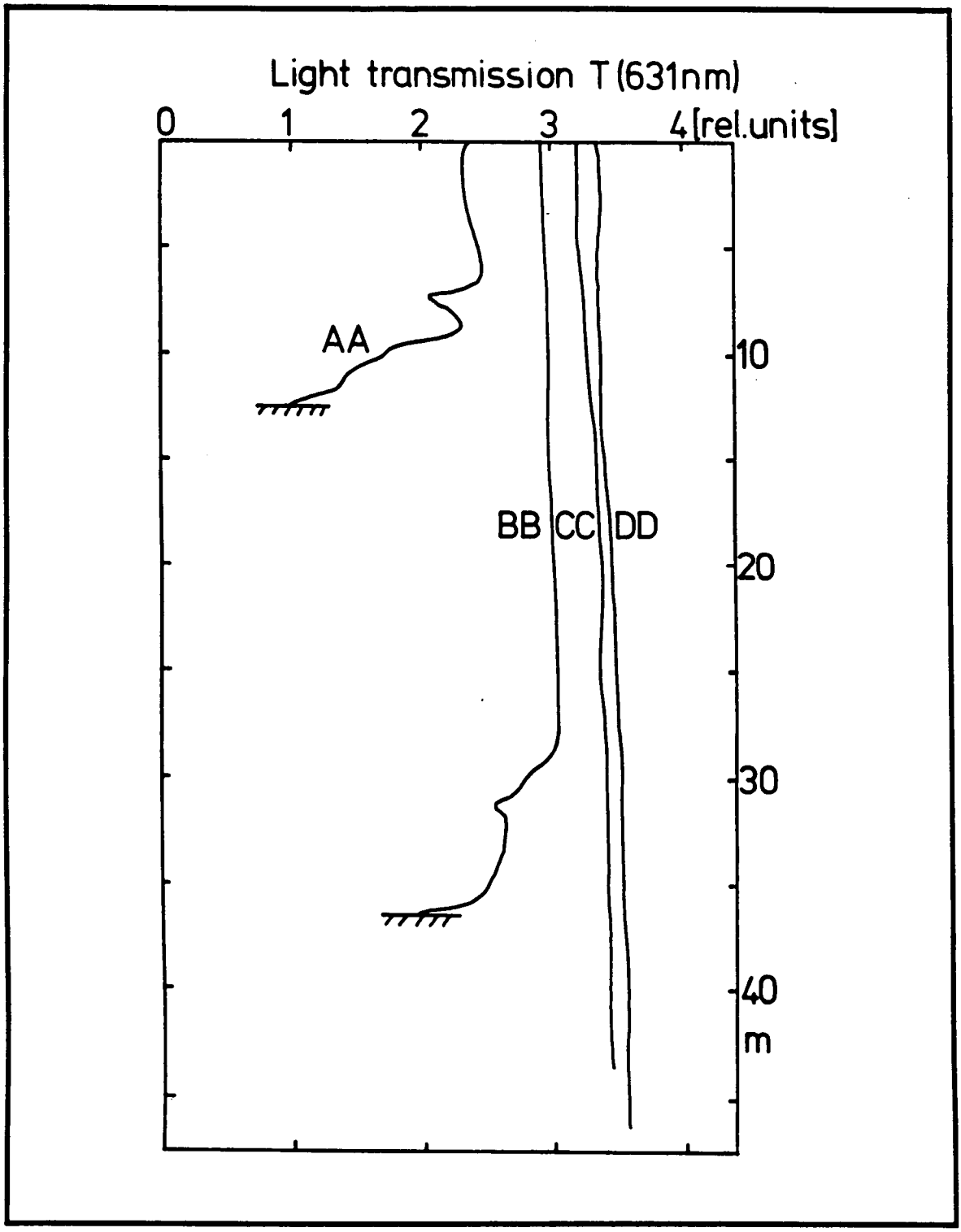

Figure 4.7-16. The vertical distribution of the light transmission at Stations AA, BB, CC and DD in July 1988. (See caption to Figure 4.7-4 for further discussion.)

Table 4.7-3. Gulf of Mexico optical observations for July 1988.

Stations	Station Depth (m)	Dates	F_1 -	F_2 -	D m	Z_q (1%) m	Z (1%) m	h_s degr.	H m
DD	183	7/20	2.40	-	30	66.8*	66.7*	20	0.5
CC-6C	64	7/20	1.88	-	26	52.2*	38.0	85	0.5
7C	58	7/21	1.00	-	26	-	-	11	-
8C	52	7/21	1.00	-	18	-	-	-	-
9C	43	7/21	1.11	-	20-22	-	-	32	-
BB-10C	40	7/21	1.16	-	26	-	17.3	48	-
BB	40	7/22	0.88	-	18	40.7*	17.3	clouds	-
11C	33	7/21	0.94	-	25	-	-	65	-
12C	28	7/21	0.59	-	15-17	-	-	78	-
13C	25	7/21	0.58	-	14	-	-	85	-
14C	20	7/21	0.48	-	12	-	-	70	-
AA	14	7/19	0.38	0.42	5-6.5	24.4*	2.93	60	0.5
AA-15C	14	7/21	0.42	-	6.5	-	-	50	-
16C	6	7/21	0.36	-	4.0	6.22	2.67	35	0.5-1

* Extrapolated values.

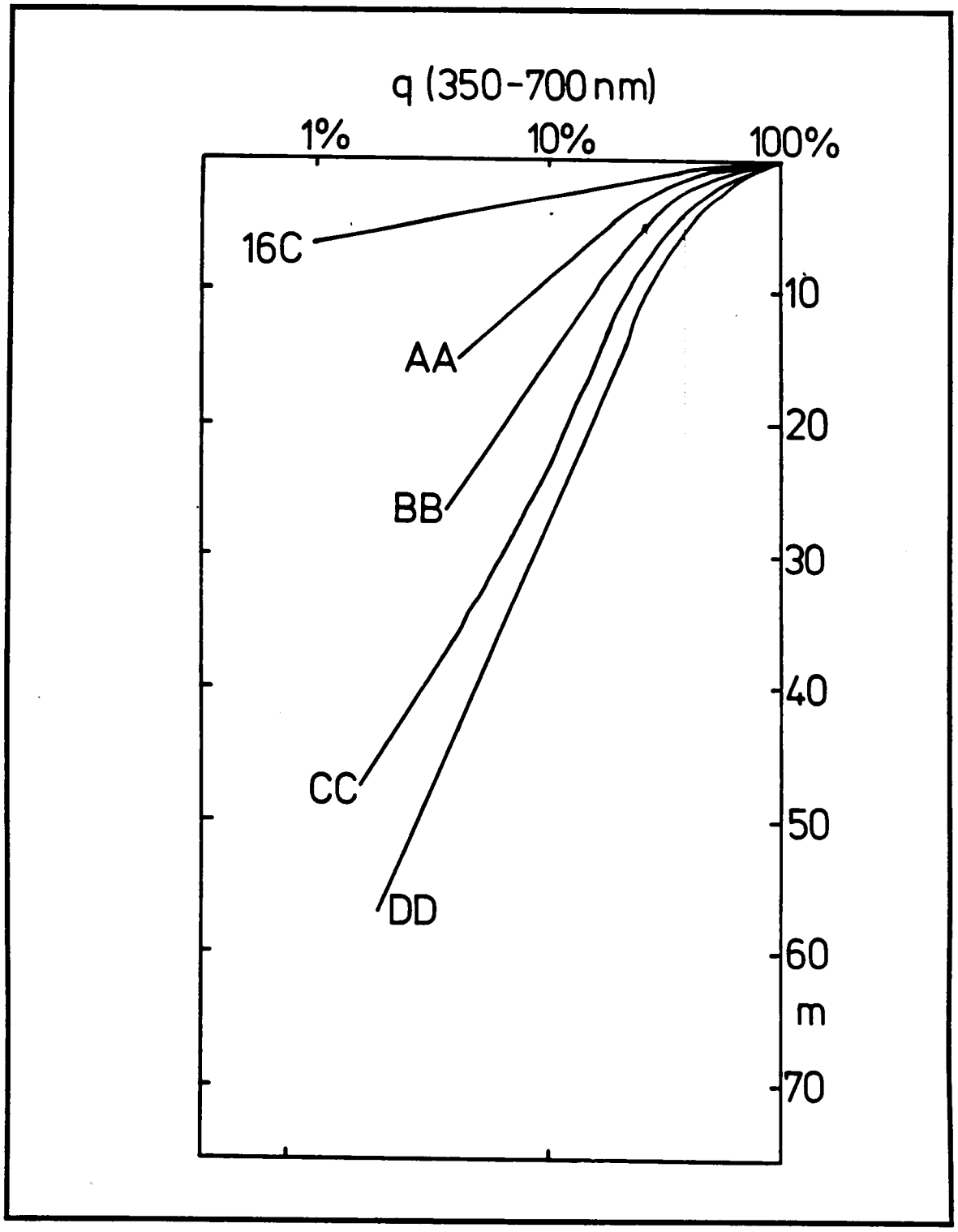

Figure 4.7-17. Relative downward quanta irradiance (350 to 700 nm) versus depth at Stations AA, BB, CC and DD in July 1988. The 100% value is taken to be Q (350 to 700 nm) just below the water surface. (See caption to Figure 4.7-5.)

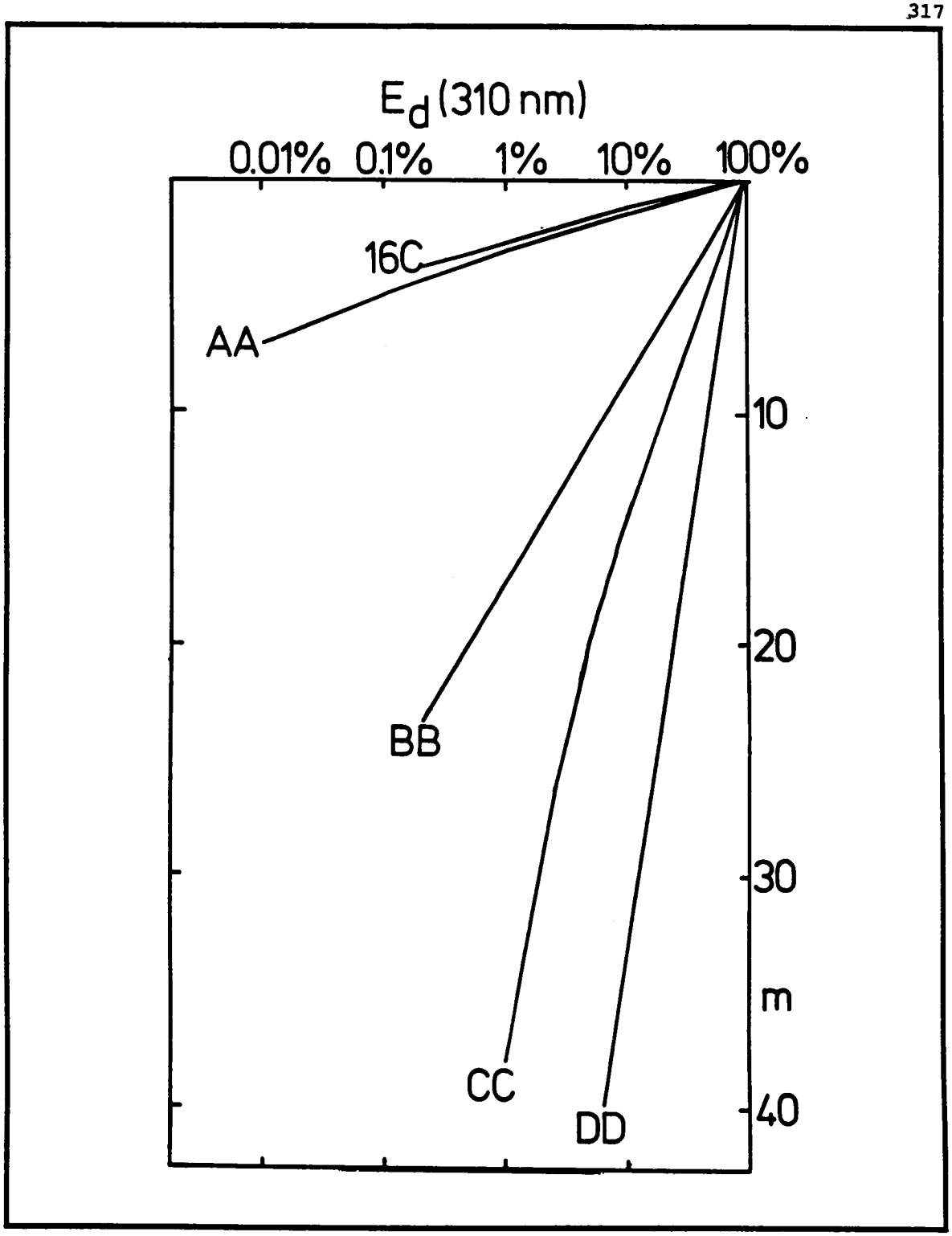

Figure 4.7-18. Relative downward UV-B irradiance versus depth at Stations AA, BB, CC and DD in July 1988. The 100% value is taken to be the E_d (310 nm) just below the water surface. (See caption to Figure 4.7-6.)

Table 4.7-4. Spectral values of vertical attenuation coefficient for the downward irradiance k_w, light absorption coefficient, a_w, for the clearest natural ocean waters, and light scattering coefficient, b_w, for pure artificial sea water. After Morel (1974), Smith and Baker (1981).

λ nm	K_w m^{-1}	a_w	b_w m^{-1}	λ nm	K_w m^{-1}	a_w	b_w m^{-1}
300	0.154	0.141	0.0262	650	0.350	0.349	0.0010
310	0.116*	0.105	0.0229	660	0.400	0.400	0.0008
320	0.0944	0.0844	0.0200	670	0.430	0.430	0.0008
330	0.0765	0.0678	0.0175	680	0.450	0.450	0.0007
340	0.0637	0.0561	0.0153	690	0.500	0.500	0.0007
350	0.0530	0.0463	0.0134				
360	0.0439	0.0379	0.0120	700	0.650	0.650	0.0007
370	0.0353	0.0300	0.0106	710	0.834	0.839	0.0007
380	0.0267	0.0220	0.0094	720	1.170	1.169	0.0006
390	0.0233	0.0191	0.0084	730	1.800	1.799	0.0006
				740	2.380	2.38	0.0006
400	0.0209	0.0171	0.0076	750	2.47	2.47	0.0005
410	0.0196	0.0162	0.0068	760	2.55	2.55	0.0005
420	0.0184	0.0153	0.0061	770	2.51	2.51	0.0005
430	0.0172	0.0144	0.0055	780	2.36	2.36	0.0004
440	0.0170	0.0145	0.0049	790	2.16	2.16	0.0004
450	0.0168	0.0145	0.0045				
460	0.0176	0.0156	0.0041				
470	0.0175	0.0156	0.0037				
480	0.0194	0.0176	0.0034				
490	0.0212	0.0196	0.0031				
500	0.0271	0.0257	0.0029				
510	0.0370	0.0357	0.0026				
520	0.0489	0.0477	0.0024				
530	0.0519	0.0507	0.0022				
540	0.0568	0.0558	0.0021				
550	0.0648	0.0638	0.0019				
560	0.0717	0.0708	0.0018				
570	0.0807	0.0799	0.0017				
580	0.109	0.108	0.0016				
590	0.158	0.157	0.0015				
600	0.245	0.244	0.0014				
610	0.290	0.289	0.0013				
620	0.310	0.309	0.0012				
630	0.320	0.319	0.0011				
640	0.330	0.329	0.0010				

* Compared with the measured value of 0.069 found in the present data (See Section 4.7.2).

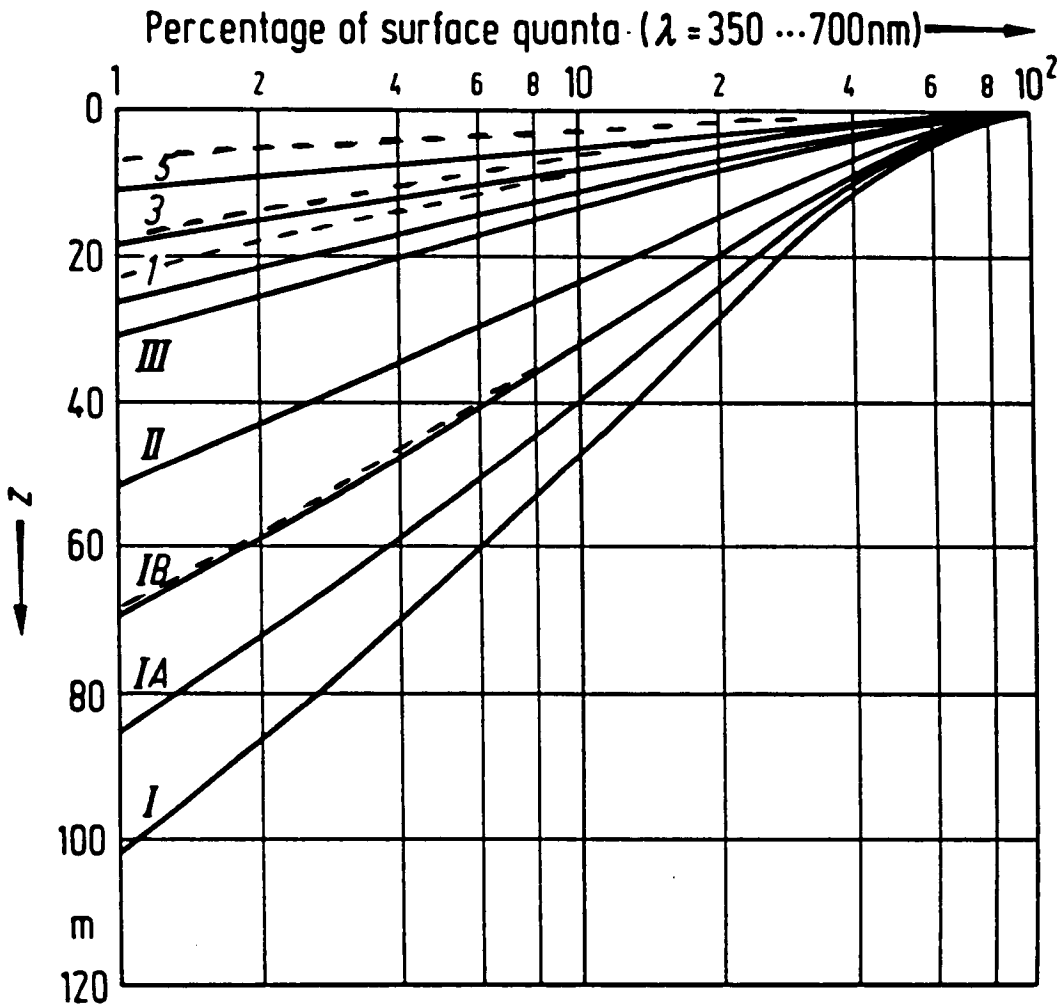

Figure 4.7-19. Profiles of downward quanta irradiance Q as percent of surface value for different optical water types (Jerlov, 1976) together with Q as measured at Stations AA, BB, CC and DD in February 1988. Dashed curves taken from above and downwards represent quanta irradiance profiles from Stations AA, BB, CC and DD (reading down).

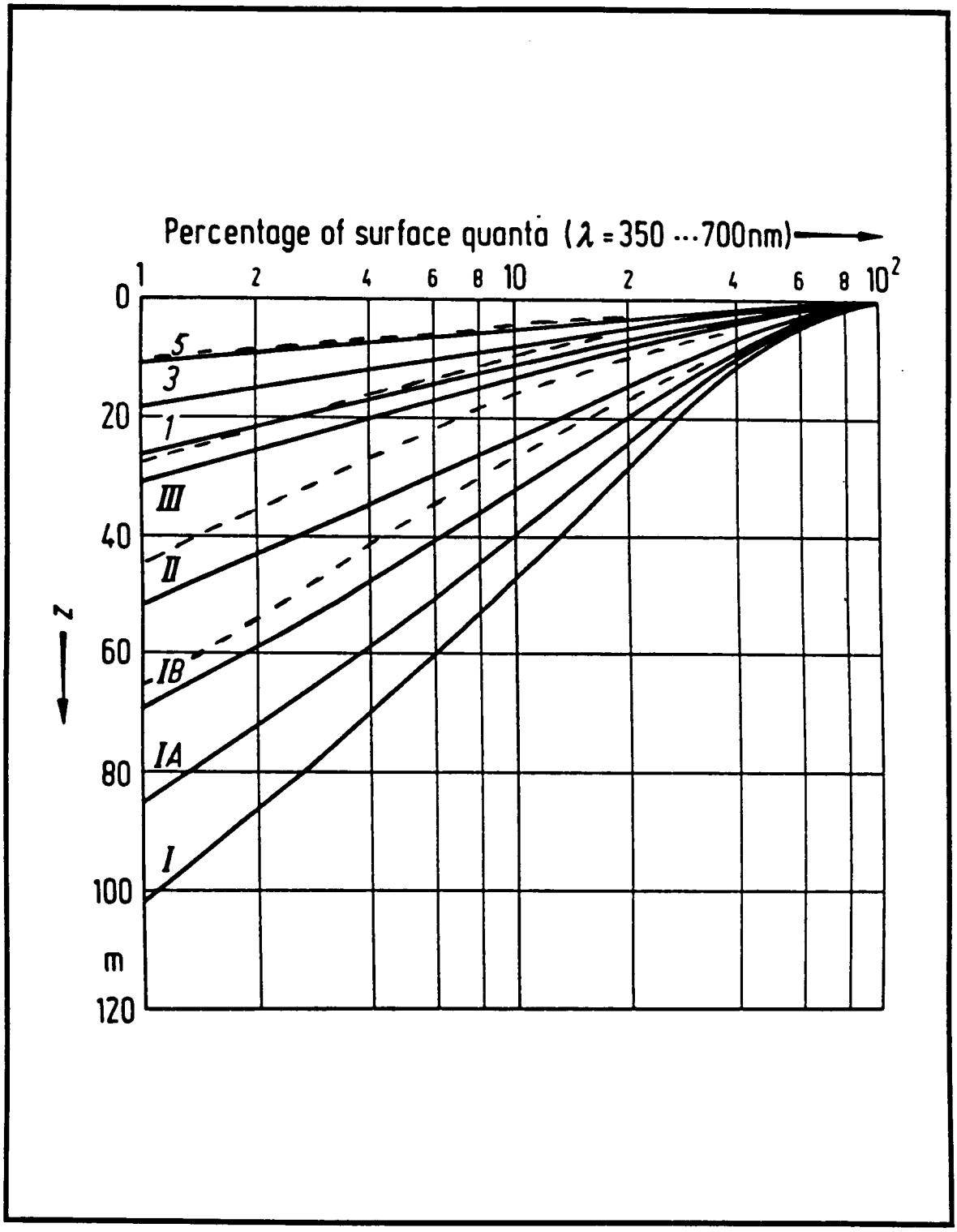

Figure 4.7-20. Profiles of downward quanta irradiance Q as percent of surface value for different optical water types (Jerlov, 1976) together with Q as measured at Stations AA, BB, CC and DD in April 1987. Dashed curves represent quanta irradiance profiles from Stations AA, BB, CC and DD (reading down).

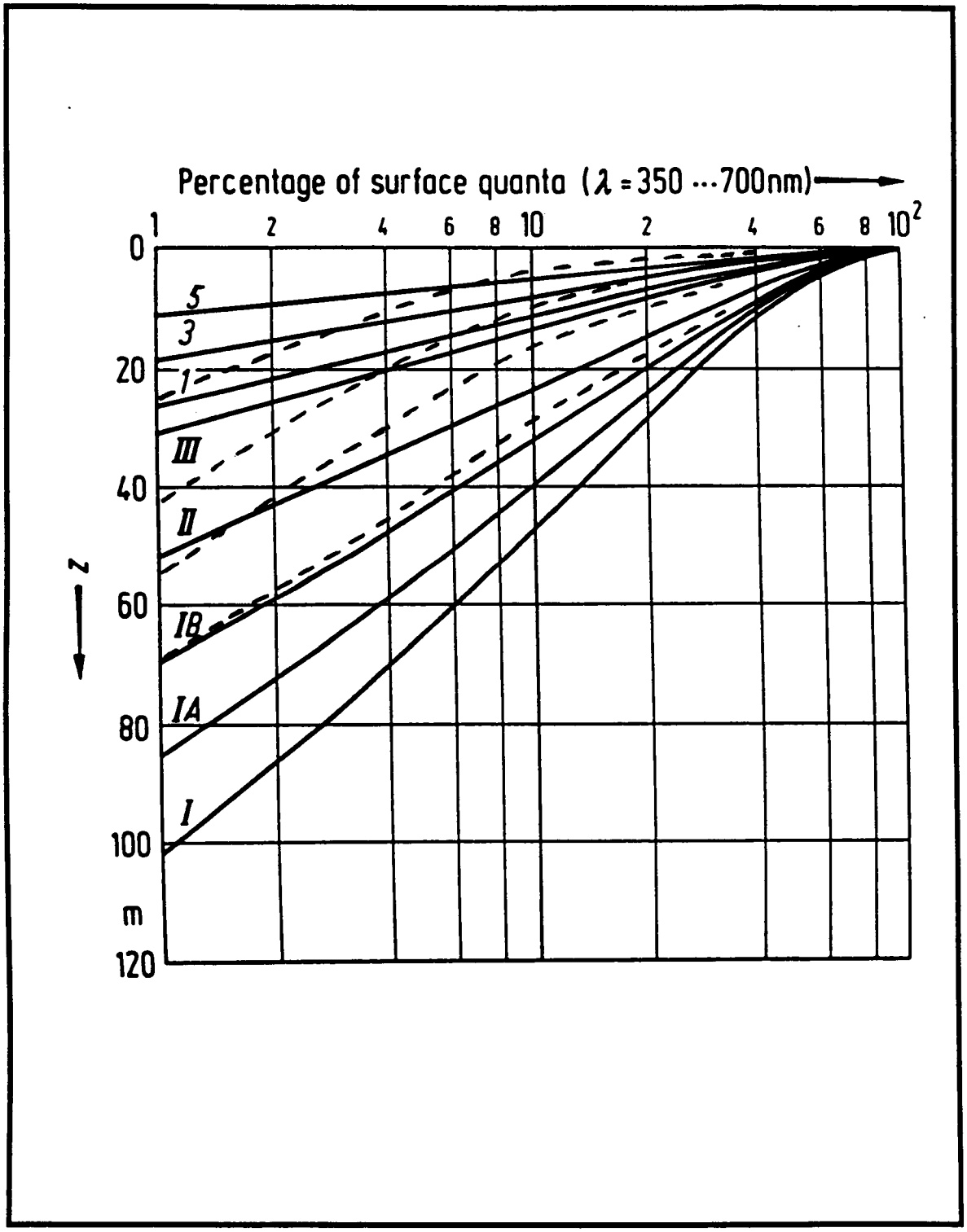

Figure 4.7-21. Profiles of downward quanta irradiance Q as percent of surface value for different optical water types (Jerlov, 1976) together with Q as measured at Stations AA, BB, CC and DD in July 1988. Dashed curves represent quanta irradiance profiles from Stations AA, BB, CC and DD (reading down).

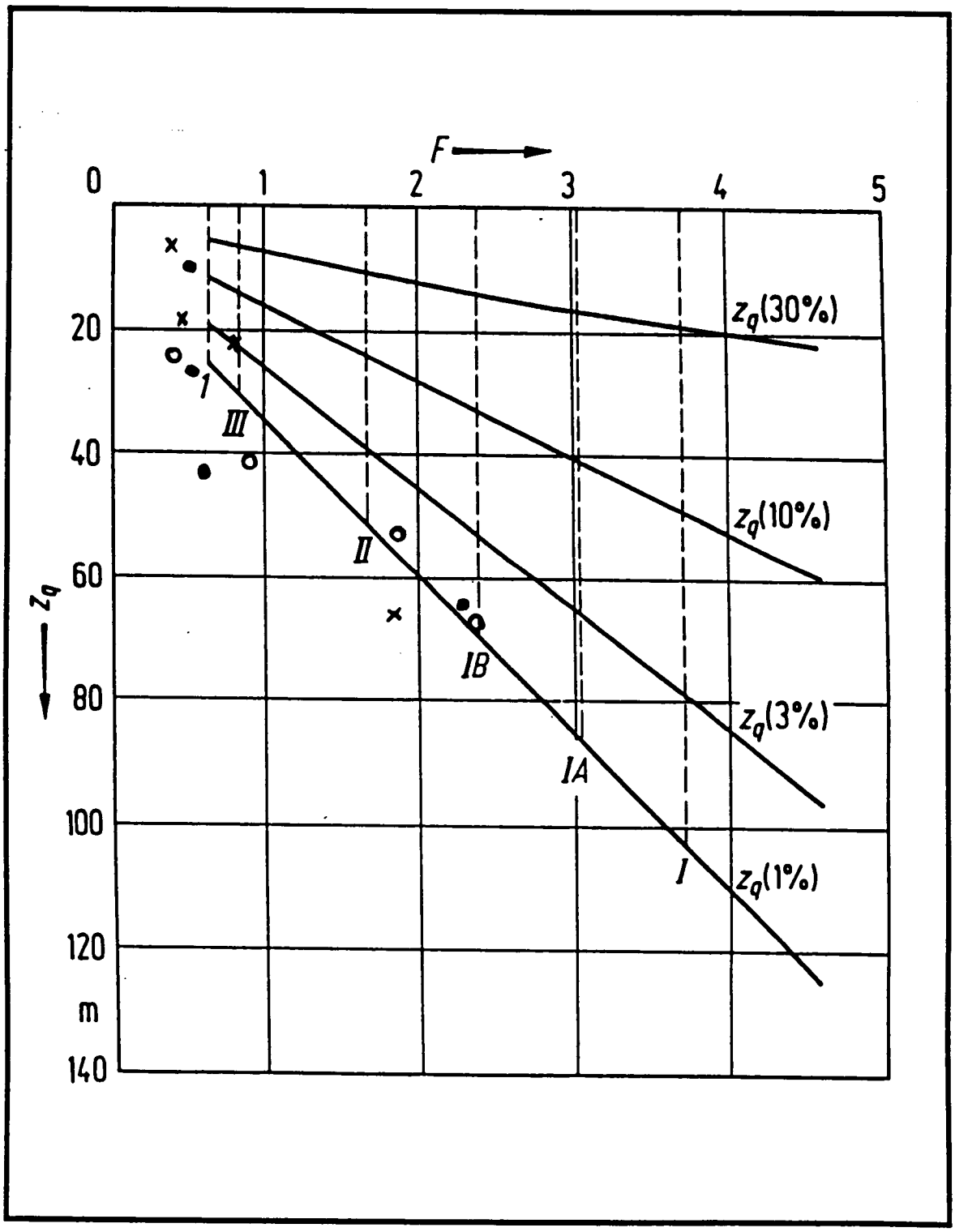

Figure 4.7-22. Empirical relations between the color index F, obtained at zero m depth and selected levels for the downward quanta irradiance Q. Included are the optical water classes I, IA, IB, II, III Oceanic, and 1 Coastal (Hojerslev, 1980). x=F^1 versus Z_q (1%) in February 1988. •=F^1 versus Z_q (1%) in April 1987. o=F^1 versus Z_q (1%) in July 1988.

predominantly of the Oceanic Type IB. The remaining color index measurements at Stations AA, BB and CC do not fit well into Højerslev and Jerlov (1977) optical classification scheme depicted in Figure 4.7-22. This is mainly due to the high near-coastal concentrations of both yellow substance and suspended matter combined with their concurrent decrease seawards. This causes only slight variations in F_1, but large increases in the Z_q (1%) values when the water becomes gradually more transparent seawards.

Figure 4.7-23 demonstrates that the concentration of total suspended matter can be expressed in optical terms like b and c, both of which are easy and rapid parameters to measure. From Figure 4.7-23, the following empirical relations are approximately valid:

$$TSS = 10.5 \cdot b(655) \qquad (mg\ l^{-1})$$

in which the unit for b is m^{-1} and

$$\frac{a_y + a_p}{b_p} = 4$$

in the red part of the spectrum at 631 nm.

This relation states that the combined light absorption is due to yellow substance a_y and to suspended organic material as light scattering, due to the total suspended matter b_p (biomass, detritus and sediments) by a factor of four being usually a much lower value. For this reason, it is postulated that organic suspended matter and dissolved organic substances, as a rule, are dominating the inorganic fraction at the depths where the water samples were taken, (i.e., at intermediate depths where the Sea Tech transmissometers were deployed). Finally, the above relation can be rewritten as

$$c - c_w = c - 0.320 = 5 \cdot b$$

valid at 631 nm.

It has been assumed then that $b = b_p$ (compare with Table 4.7-4) and that $b_p(655) = b_p(631)$.

4.7.4 Conclusions

The water on the Louisiana shelf is characterized by variety in its content of biomass, sediments and yellow substance. From the coast seaward, the color of the ocean changes from yellow-green to blue. The near-coastal waters have a high concentration of yellow substance which decreases with depth and with distance from shore. This suggests that the Mississippi and Atchafalia Rivers are the main source for the presence of yellow substance for the study area, and that deep oceanic blue water, at times, penetrates well onto the shelf. The amount and the distribution of yellow substance as measured during winter, spring and summer reveals a seasonal dependency attributed to the fresh water

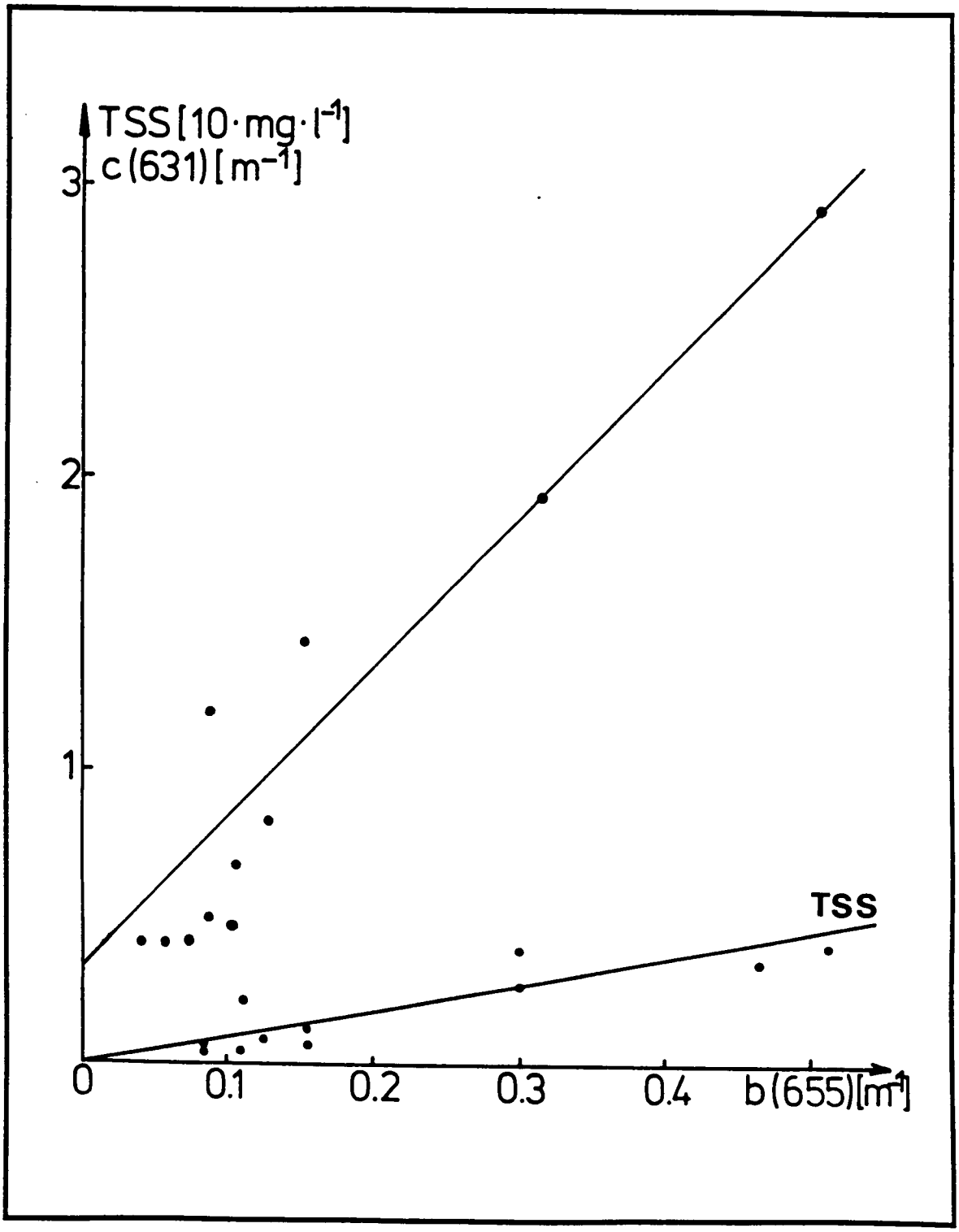

Figure 4.7-23. Total suspended solids (TSS) (note that the unit is 10 mg l^{-1}) and c(631) (m^{-1}) versus the total light scattering coefficient at 655 nm [b(655) (m^{-1})], respectively.

discharge onto the shelf. Thus, the lowest concentrations and minimum horizontal spread were found in the summertime; intermediate concentrations, in winter and the highest ones, in spring.

In the winter, the vertical variation in the bio-optical properties was small. Fairly persistent in all seasons, the main variations occur across the shelf. During the spring cruise, indications are that the plankton bloom season had started and developed at locations near the shore where the water was most stratified. Later, during the season, the plankton blooms reached the waters on the deep shelf and near the shelf edge. In the summer, fairly deep chlorophyll maxima were fully developed.

Passive remote sensing of chlorophyll and biomass of the NIMBUS-7, CZCS type is questionable. Near the coast, the water leaving nadir radiancy are interfered with by both yellow substance chlorophyll-like pigments. Well off the coast, where the yellow substance is negligible or at least small, the chlorophyll maxima are not observable remotely. In this context, it is interesting to note that one of the first remote sensing chlorophyll algorithms derived, was derived from sea-truth data east of the area in question, an area characterized by typically deep chlorophyll maxima, and negligible amounts of yellow substance (Carder et al., 1989).

The present investigation shows a great need for extended and intensified measurements. Thus, a station grid rather than a station section would provide valuable information about the spreading of the yellow substance coming mainly from the Atchafalia and Mississippi Rivers. Such measurements combined with conventional hydrography would allow calculations of water mass mixing. Such calculations cannot be made by applying the usual T-S analysis because the temperature is not a conservative property on the shelf. This and other investigations suggest that yellow substance has conservative properties so that a Yellow Substance - S analysis could form the basis for calculating the dilution of Mississippi River water on the Louisiana shelf.

Routine measurements of yellow substance measured in a spectrophotometer in terms of absorbance on glass filtered water samples combined with standard CTD measurements are strongly recommended in future work. Intensified measurements are further believed to be mandatory if sedimentation processes and plankton dynamics are to be studied. Moreover, for an area like the Gulf of Mexico where oxygen depletions and cultural contaminants are a matter of concern, knowledge especially of plankton dynamics is essential for evaluating environmental impact. Measurements like fluorescence, light scattering and/or light attenuation are possible and practical steps in the right direction.

Finally, the investigated area is a most suitable test site for developing future remote sensing algorithms for chlorophyll-like pigments and biomass, since a very large variety of water masses is encountered in a restricted region, assuming that the sea truth data sampling can be made almost synoptically.

REFERENCES

American Public Health Association, American Water Works Association and Water Pollution Control Federation. 1985. Standard methods for the examination of water and wastewater. Sixteenth Edition. Washington, D.C.: American Public Health Association. 1268 pp.

Anderson, C., F. Dobson, W. Perrie, P. Smith, and B. Toulany. 1989. Storm response in the coastal ocean. The Oceanography Report. EOS 70 (18):562-572.

Austin, R. W. 1980. Gulf of Mexico ocean-color surface-truth measurements. J. Bound. Layer Meteor. 18(1):269-286.

Bailey, P. B. 1978. SLEIGN: eigenvalue-eigenfunction code for Strum-Louisville problems. Sand 77-2044 Sandia Lab., Livermore, Calif.

Brooks, D. A. 1984. Current and hydrographic variability in the northwestern Gulf of Mexico. J. Geophys. Res. 89:8022-8032.

Brooks, D. A., and R. V. Legeckis. 1982. A ship and satellite view of hydrographic features in the western Gulf of Mexico. J. Geophys. Res. 87(C6):4195-4206.

Brown, M., E. Waddell, and R. J. Wayland. 1989. Gulf of Mexico Ship-of-Opportunity data report, update: October 1985 - March 1988. OCS Study/MMS 89-0013. 598 pp.

Brown, M., E. Waddell, J. Karpen and R. J. Wayland, 1986. Gulf of Mexico Ship-of-Opportunity data report, January 1983 - October 1985. OCS Study/MMS 86-0028. 632 pp.

Brown, O. B., B. Olson, J. Brown, and H. Evans. 1983. Satellite infrared observations of the kinematics of a warm-core ring. Aust. J. Mar. Fresher. Res. 34:535-545.

Carder, K. L., R. G. Steward, G. R. Harvey, and P. B. Ortner. 1989. Marine humic and fulvic acids: Their effects on remote sensing of ocean chlorophyll. Limnol Oceanogr. 34(1):68-81.

Chuang, W.-S. and W. J. Wiseman, Jr. 1983. Coastal sea level response to frontal passages on the Louisiana-Texas shelf. J. Geophys. Res. 88: 2615-2620.

Cochrane, J. D. and F. J. Kelly. 1986. Low-frequency circulation on the Texas-Louisiana shelf. J. Geophys. Res. 91:10645-10659.

Crout, R. L., W. J. Wiseman, and W.-S. Chuang. 1984. Variability of wind-driven currents, west Louisiana inner continental shelf: 1978-1979. Contr. in Mar. Sci. 27:1-11.

Csanady, G. T. 1981. Circulation in the coastal ocean. Adv. in Geophys. 23:101-183.

Cushman-Roisin, B. 1989. On the role of filamentation in the merging of anticyclonic lenses. J. Phys. Oceanogr. 19:253-258.

Elliott, B. A. 1982. Anticyclonic rings in the Gulf of Mexico. J. Phys. Oceanogr. 12:1293-1309.

Flierl, G. R. 1978. Models of vertical structure and the calibration of two-layer models. Dyn. Atmos. Oceans 2:341-381.

Foreman, M. G. G. 1978. Manual for tidal currents analysis and prediction. Pacific Marine Science Report 78-6, Institute of Ocean Studies, Patrician Bay, Sydney BC. 70 pp.

Godin, G. 1972. The analysis of Tides. University of Toronto Press, Toronto.

Griffiths, R. W. and E. J. Hopfinger. 1987. Coalescing of geostrophic vortices. Journal Fluid Mech. 178:73-97.

Hamilton, P. 1984. Topographic and inertial waves on the continental rise of the Mid-Atlantic Bight. J. Geophys. Res. 89(C1):695-710.

Harvey, G. B., D. A., Boran, L. A. Chesal and J. M. Tokar. 1983. The structure of marine fulvic and humic acids. Elsevier Science Publ. B.V. Amsterdam. pp. 119-132.

Hofmann, E. E., and S. J. Worley. 1986 An investigation of the circulation of the Gulf of Mexico. J. Geophys. Res. 91(C12):14221-14236.

Hogg, N.G. 1981. Topographic waves along 70°W on the continental rise. J. Mar. Res. 39:627-649.

Højerslev, N. K. 1978. Daylight measurements appropriate for photosynthetic studies in natural sea water. J. Cons. Int. Explor. Mer. 38:131-146.

Højerslev, N. K. 1980. Water color and its relation to primary production. J. Bound. Layer Meteor. 18(1):203-220.

Højerslev, N. K. 1982a. Yellow substance in the sea. In: The role of solar ultraviolet radiation in marine ecosystems. Ed. J. Calkins, Plenum Press. pp. 263-282.

Højerslev, N. K. 1982b. Bio-optical properties of the Fladen Ground: "Meteor"-FLEX-75 and FLEX-76. J. Const. Int. Explor. Mer. 40:272-290.

Højerslev, N. K. 1985. Bio-optical measurements in the southwest Florida shelf ecosystem. J. Cons. Int. Explor. Mer. 42:65-82.

Højerslev, N. K. 1986a. Visibility of the sea with special reference to the Secchi disc. SPIE Vol. 637 Ocean Optics VIII (1986). pp. 294-305.

Højerslev, N. K. 1986b. Optical properties of sea water. In: Oceanography, Ed. J. Sündermann, New Series, Group V, Vol. 3. Subvol. a. Landolt - Börnstein, Spinger Verlag, Berlin - Heidelberg - New York - London - Paris - Tokyo. pp. 383-462.

Højerslev, N. K. 1988. Natural occurrences and optical effects of Gelbstoff. Rep. Inst. Phys. Oceanogr., Univ. of Copenhagen. 50:30 pp.

Højerslev, N. K. and N. G. Jerlov. 1977. The use of the colour index for determining quanta irradiance in the sea. Rep. Inst. Phys. Oceanogr., Univ. of Copenhagen. 35:12.

Højerslev, N. K. and K. Larsen. 1980. On the optical instruments developed at the Institute of Physical Oceanography - University of Copenhagen. Rep. Inst. Phys. Oceanogr., Univ. Copenhagen. 42:155-191.

Hooker, S. B. 1987. Mesoscale eddy dynamics by the method of point vortices. Ph.D. dissertation, Univ. of Miami, Coral Gables, Fla. 158 pp.

Hundahl, H. and J., Holck. 1980. A new in-situ fluorometer for detection of rhodamine B and chlorophyll. Rep. Inst. Phys. Oceanogr., Univ. Copenhagen. 42:145-153.

Hurlburt, H. E. and J. D. Thompson. 1980. A numerical study of Loop Current intrusions and eddy shedding. J. Phys. Oceangr. 10:1611-1651.

Hurlburt, H. E. and J. D. Thompson. 1982. The Dynamics of the Loop Current and shed eddies in a numerical model of the Gulf of Mexico. In: Nihoul, J. C. J. ed., Hydrodynamics of semi-enclosed seas. Elsevier. pp. 243-298.

Inoue, M. 1985. Modal decomposition of the low-frequency currents and baroclinic instability at Drake Passage. J. Phys. Oceanogr. 15: 1157-1181.

Jerlov, N. G. 1961. Optical measurements in the eastern north Atlantic. Medd. Inst. Oceanogr. Gothenburg, Ser. B. 8:40 pp.

Jerlov, N. G. 1974. Significant relationships between optical properties of the sea. In: Optical Aspects of Oceanography. Jerlov, N. G. and E. S. Nielsen, eds. New York, Academic Press. pp. 77-94.

Jerlov, N. G. 1976. Marine optics 2nd ed. Amsterdam: Elsevier. 203 pp.

Jerlov, N. G. and K. Nygard. 1969. A quanta and energy meter for photosynthetic studies. Rep. Inst. Phys. Oceanogr., Univ. of Copenhagen. 10:29 pp.

Kelly, F. J., J. E. Schmitz, R. E. Randall and J. D. Cochrane. 1983. Physical oceanography. In: Hann, R. W., Jr. and R. E. Randall, eds. Evaluation of brine disposal from the Bryant mound site of the Strategic Petroleum Reserve Program. Annual Report for September 1981 through August 1982 to the Department of Energy, Vol. 1, Texas A&M University and Texas A&M Research Foundation.

Kirwan, A. D., W. J. Merrell, Jr., J. K. Lewis, and R. E. Whitaker. 1984. Lagrangian observations of an anticyclonic ring in the western Gulf of Mexico. J. Geophys. Oceanogr. 89(C3):3417-3424.

Koopmans, L. H. 1974. The spectral analysis of time series. New York: Academic Press. 353 pp.

Kundu, P. K., J. S. Allen, and R. L. Smith. 1975. Modal decomposition of the velocity field near the Oregon coast. J. Phys. Oceanogr. 5:683-704.

Leipper, D. F. 1970. A sequence of current patterns in the Gulf of Mexico. J. Geophys. Res. 75(3):637-657.

Levitus, S. 1982. Climatalogical atlas of the world ocean. NOAA Professional Paper 13. Washington, D. C.: U.S. Government Printing Office. 173 pp.

Lewis, J. K. and A. D. Kirwan, Jr. 1985. Some observations of ring topography and ring-ring interactions in the Gulf of Mexico. J. Geophys. Res. 90(C5):9017-9028.

Lewis, J. K. and R. O. Reid. 1985. Local wind forcing of a coastal sea at subinertial frequencies. J. Geophys. Res. 90 (C1):935-944.

Lewis, J. K. and A. D. Kirwan, Jr. 1987. Genesis of a Gulf of Mexico ring as determined from kinematic analyses. J. Geophys. Res. 92(C11): 11727-11740.

Lewis, J. K., A. D. Kirwan, Jr., and G. Z. Forristall. 1989. Evolution of a warm-core ring in the Gulf of Mexico: Lagrangian observations. J. Geophys. Res. 94(C6):8163-8178.

Louis, J. P., B. D. Petrie, and P. C. Smith. 1982. Observations of topographic Rossby waves on the continental margin off Nova Scotia. J. Phys. Oceanogr. 12:47-55.

Luyten, J. R. 1977. Scales of motion in the deep Gulf Stream and across the continental rise. J. Mar. Res. 35:49-74.

Maul, G. A. 1977. The annual cycle of the Loop Current, Part I: observations during a one-year time series. J. Marine Res. 35:29-47.

McWilliams J. C., W. B. Owens, and B. L. Hua. 1986. An objective analysis of the POLYMODE Local Dynamics Experiment. Part I: general formalism and statistical model selection. J. Phys. Oceanogr. 16:483-504.

Merrell, W. J. and J. M. Morrison. 1981. On the circulation of the western Gulf of Mexico with observations from April 1978. J. Geophys.Res. 86:4181-4185.

Mitchum, G. T. and A. J. Clarke. 1986. Evaluation of frictional, wind-forced long-wave theory on the west Florida shelf. J. Phys. Oceanogr. 16:1029-1037.

Molinari, R. L. and D. Mayer. 1982. Current meter observations on the continental slope at two sites in the eastern Gulf of Mexico. J. Phys. Oceanogr. 12:1480-1492.

Morel, A. 1974. Optical properties of pure water and pure sea water. In: Optical aspects of oceanography. Jerlov, N. G. and E. S. Nielsen, eds. New York: Academic Press. pp. 1-24.

Nof, D. 1988. The fusion of isolated non-linear eddies. J. Phys. Oceanogr. 18:887-905.

Nowlin, W. D., Jr. 1972. Winter circulation patterns and property distributions. In: Capurro, L. R. A. and J. L. Reid. eds. Contributions on the physical oceanography of the Gulf of Mexico. Houston: Gulf Publishing Co. pp. 3-51.

Nowlin, W. D., Jr. and C. A. Parker. 1974. Effects of a cold-air outbreak on shelf waters of the Gulf of Mexico. J. Phys. Oceanogr. 4:467-486.

Pedlosky, J. 1979. Geophysical fluid dynamics. Springer-Verlag. 624 pp.

Phillips, O. M. 1966. The dynamics of the upper ocean. New York: Cambridge University Press.

Phillips, O. M. 1977. The dynamics of the upper ocean, 2nd ed. New York: Cambridge University Press. 336 pp.

Reid, R. O. and R. E. Whitaker. 1981. Numerical model for astronomical tides in the Gulf of Mexico. Vol. I: theory and application. Tech. Report, Department of Oceanography, Texas A&M University.

Rhines, P. B. 1970. Edge, bottom, and Rossby waves in a rotating stratified fluid. Geophys. Fluid Dynam. 1:273-302.

Science Applications International Corporation. 1986. Gulf of Mexico physical oceanography program, final report: years 1 and 2. Volume II: technical report. MMS Contract No. 14-12-0001-29158, OCS Report/MMS 5-0094 (SAIC Report No. SAIC-86/1023). 378 pp.

Science Applications International Corporation. 1987. Gulf of Mexico physical oceanography program, final report: year 4. Volume II: technical report. MMS Contract No. 14-12-0001-29158, OCS Report/MMS 87-0007 (SAIC Report No. SAIC-87/1027). 226 pp.

Science Applications International Corporation. 1988. Gulf of Mexico physical oceanography program, final report: year 3. Volume II: technical report. MMS Contract No. 14-12-0001-29158, OCS Report/MMS 88-0046. 241 pp.

Shaw, P-T. and G. T. Csanady. 1988. Topographic waves over the continental slope. J. Phys. Oceanogr. 18:813-822.

Shaw, P-T. and C. Y. Peng. 1987. A numerical study of the propagation of topographic Rossby waves. J. Phys. Oceanogr. 17:358-366.

Smith, D. C., IV. 1986. A numerical study of Loop Current eddy interaction with topography in the western Gulf of Mexico. J. Phys. Oceanogr. 16:1260-1272.

Smith, D. C., IV and J. J. O'Brien. 1983. The interaction of a two-layer isolated mesoscale eddy with bottom topography. J. Phys. Oceanogr. 13: 1681-1697.

Smith, N. P. 1980. On the hydrography of the shelf waters of the central Texas Gulf coast. J. Phys. Oceanogr. 10:806-813.

Smith, P. C. and B. D. Petrie. 1982. Low-frequency circulation at the edge of the Scotian Shelf. Phys. Oceanogr. 12:28-46.

Smith, R. C. and K. S. Baker. 1981. Optical properties of the clearest natural waters (200-800 nm). Appl. Optics. 20(2):1177-184.

Strickland, J. D. H. and T. R. Parsons. 1972. A practical handbook of seawater analysis. Fisheries Research Board of Canada, Ottawa. 310 pp.

Sturges, W. and J. C. Evans. 1983. On the variability of the Loop Current in the Gulf of Mexico. J. Mar. Res. 41:639-653.

Thompson, R. O. R. Y. 1977. Observations of Rossby waves near site D. Prog. Oceanogr. 7:135-162.

Tracey, K. L., M. Cronin, and D. R. Watts. 1986. On Gulf Stream meander characteristics near Cape Hatteras. J. Geophys. Res. 91:7587-7602.

Vukovich, F. M. 1988. Loop Current boundary variations. J. Geophys. Res. 93:15585-15591.

Vukovich, F. M., B. W. Crissman, M. Bushnell and W. J. King. 1979. Some aspects of the oceanography of the Gulf of Mexico using satellite and in situ data. J. Geophys. Res. 84:7749-7768.

Wallcraft, A. J. 1986. Gulf of Mexico circulation modeling study, annual progress report: year 2. Progress report by JAYCOR submitted to the Minerals Management Service, Metairie, La. MMS Contract No. 14-12-0001-300073. 94 pp.

Wiseman, W. J., Jr. and S. P. Dinnel. 1989. Subtidal flows over Gulf of Mexico shelves. Presented at AGU Chapman Conference on the Physics of the Gulf of Mexico, 5-7 June 1989, St. Petersburg, Fla.

The Department of the Interior Mission

As the Nation's principal conservation agency, the Department of the Interior has responsibility for most of our nationally owned public lands and natural resources. This includes fostering sound use of our land and water resources; protecting our fish, wildlife, and biological diversity; preserving the environmental and cultural values of our national parks and historical places; and providing for the enjoyment of life through outdoor recreation. The Department assesses our energy and mineral resources and works to ensure that their development is in the best interests of all our people by encouraging stewardship and citizen participation in their care. The Department also has a major responsibility for American Indian reservation communities and for people who live in island territories under U.S. administration.

The Minerals Management Service Mission

As a bureau of the Department of the Interior, the Minerals Management Service's (MMS) primary responsibilities are to manage the mineral resources located on the Nation's Outer Continental Shelf (OCS), collect revenue from the Federal OCS and onshore Federal and Indian lands, and distribute those revenues.

Moreover, in working to meet its responsibilities, the **Offshore Minerals Management Program** administers the OCS competitive leasing program and oversees the safe and environmentally sound exploration and production of our Nation's offshore natural gas, oil and other mineral resources. The MMS **Minerals Revenue Management** meets its responsibilities by ensuring the efficient, timely and accurate collection and disbursement of revenue from mineral leasing and production due to Indian tribes and allottees, States and the U.S. Treasury.

The MMS strives to fulfill its responsibilities through the general guiding principles of: (1) being responsive to the public's concerns and interests by maintaining a dialogue with all potentially affected parties and (2) carrying out its programs with an emphasis on working to enhance the quality of life for all Americans by lending MMS assistance and expertise to economic development and environmental protection.